Ab Initio Study of Intercalated TMDCs and their Superlattices

Submitted by Conor Jason Price, to the University of Exeter as a thesis for the degree of Doctor of Philosophy in Physics, October 2023.

I certify that all material in this thesis which is not my own work has been identified and that any material that has previously been submitted and approved for the award of a degree by this or any other University has been acknowledged.

. . . . . .

Conor Jason Price

This is for Katie and Kiean.

Abstract

In this thesis, the structures and properties of layered transition metal dichalogenide (TMDC) materials are investigated at the atomic scale using *ab initio* density functional theory methods, with a focus on determining their suitability for intercalation electrodes in lithium-ion and beyond-lithium-ion batteries. Layered materials with a van der Waals spacing have already demonstrated a lot of success as intercalation electrodes, owing to the natural channels through which foreign ions can move during cell cycling and be stored in when fully charged or discharged. As a result, the fundamental function and working of batteries have changed little since the 1970s and 1980s. The TMDCs represent a particularly broad family of such layered materials that have received a lot of attention in a wide range of applications, but only selected materials have been considered as intercalation electrodes. We therefore provide a comprehensive study of these materials and several key electrode properties, including the volume expansion, the voltage, and the reversible intercalation capacity. From this, we conclude TMDC sulfides to be the best in general for lithium intercalation, highlighting the Group IV, V, and VI in particular for their low volumetric expansion, moderate intercalation voltages, and high stability against conversion reactions. TMDCs composed of early transition metals are also shown to offer the best performance for magnesium intercalation. We extend this investigation to consider how the elastic and mechanical properties change with intercalation. Such properties are particularly important for electrode modelling beyond the atomic scale, and we find that the introduction of an intercalant reduces elastic anisotropy but increases the bulk, shear, and Young's moduli of the host material. Out of these broad studies, we identify ScS_2 in particular to be a promising material for consideration as a cathode due to its high voltages and high intercalation stability, though it has received little attention previously. Consequently, we present a more thorough study of this material, employing a mix of machine learning and *ab initio* techniques, and consider other beyond-lithium intercalants. Ultimately, we find that ScS_2 is able to compete with current market leaders and that the introduction

of scandium into the structure of other cathodes could be used to improve their performance. Finally, we consider how the formation of TMDC superlattices affects the properties of the TMDCs. From of a study of 50 pairings, we are able to show that, in general, many key of the key electrode properties of van der Waals superlattice structures can be well approximated with the average value of the equivalent property for the component layers. Thus, we conclude that superlattice formation can be used to improve material properties through tuning of intercalation voltages towards specific values, and by increasing the stability of conversion-susceptible materials.

Acknowledgements

The thesis presented here along with all of the work that went into it would not have been possible without the incredible support of colleagues, friends, and family over the past few years.

I would first like to thank all current and past members of my group; Ned Taylor, Francis Davies, Shane Davies, Quinton Chan, Edward Baker, Joe Pitfield, and William Borrows. They have each been incredibly helpful with the development of this work, and also with the preservation of my sanity. I would like to express particular thanks to Edward Baker for the near-daily discussions on all of the work presented in this thesis, each of which have made the work better than it would have otherwise been.

I would like to thank Deregallera Ltd. for their useful discussions at the start of the PhD and for showing me that there is actually something going on where I grew up, and to Lambda Ltd. for the industrial studentship they funded me for. I would like to thank all of the leaders of the QSN group for any wisdom they may have unwittingly passed on to me, with particular thanks going to Prof. G. P. Srivastava and Dr. Sharon Strawbridge for their expertise in many of the core ideas that this work is built upon. I am also grateful for the motivation Prof. Misha Portnoi provided for me to write the thesis. I also want to thank my assessors, Prof. Monica Craciun and Prof. David Scanlon, for taking the time to read my thesis, for their insightful viva discussions, and for seeing me across the finish line of my PhD journey. Of course, I could not go without thanking my supervisor Dr. Steven Paul Hepplestone, without whom this work would not have been possible.

Rachel has been a close friend since the start of our undergraduate degree and I have been very glad to have that friendship throughout the PhD, even if that has come at the cost of an "I told you so". I will forever owe Dean and Hannah for the countless trips to Aldi, for their support through the dark days of the COVID lockdowns, and for the date nights that I will miss. I could also not go without mentioning the Lads and Dads of Dean, Jamie, Ollie, and Andy for their shared

suffering marking problem sets and dealing with landlords.

Finally, my greatest gratitude has to go to my family who have been providing support to me since long before I started on this PhD journey. Katie and Kiean have always inspired me, and without my Auntie Nicola, Grumpy, Nan, and Grampy I would not have made it as far as I have. I am eternally grateful for all that you have done.

Funding Acknowledgements

I would like to thank the XM^2 Exeter Centre for Doctoral Training in Metamaterials (Grant No. EP/L015331/1) for providing additional financial and training support, as well as for allowing me to be part of a collaborative and friendly community of PhD students; the skills that I have learnt through the courses they have offered have been invaluable.

The work detailed in this thesis has been supported by the UK's HEC Materials Chemistry Consortium and their funding from the EPSRC (Grant numbers EP/L000202, EP/R029431, EP/X035859), which has enabled us to use both the ARCHER and ARCHER2 UK National Supercomputing Services. Simulations have also been performed using both the University of Exeter High-Performance Computing facilities, and the Isambard 2 UK National Tier-2 HPC Service, which is also funded by EPSRC (EP/T022078/1). Finally, I would like to thank Lambda Energy for funding me during a 12-month studentship during my PhD. I am very grateful for these organisations who, due to their large contributions, allowed me to conduct research in a range of varied fields.

Author's Declaration

Analysis of all work presented in this thesis was performed by Mr. Conor Jason Price.

The work in Chapter 3 formed the basis of a publication: First Principles Study of Layered Transition Metal Dichalcogenides for Use as Electrodes in Li-Ion and Mg-Ion Batteries, *Journal of Materials Chemistry A*, **11**, 23, (2023). This was completed to obtain a single, consistent study of the whole family of TMDC materials, and their application as lithium-ion and magnesium-ion intercalation electrodes. Most of the work was completed by Mr. Price, and analysis of results was shared between Mr. Price and Mr. Edward Allery David Baker.

The work in Chapter 4 formed the basis of a publication: Intercalation-Dependent Elastic Properties of Transition Metal Dichalcogenides, *Journal of Materials Chemistry C*, **11**, 41, (2023). This was completed in an extension to that achieved in Chapter 3. All calculations and analysis of results were completed by Mr. Price.

The work in Chapter 5 formed the basis of a publication: First Principles Study of Layered Scandium Disulfide for use as Li-ion and Beyond-Li-ion Batteries, *Physical Chemistry Chemical Physics*, **25**, 3, (2023). This work was motivated by results obtained in the work towards Chapter 3 and Chapter 4, which highlighted ScS_2 as a promising electrode material. Mr. Joe Pitfield developed the RAFFLE software and performed the random structure search investigation, and Mr. Baker completed all calculations concerning scandium-oxide materials.

The work in Chapter 6 formed the basis of a publication: Properties of Layered TMDC Superlattices for Electrodes in Li-Ion and Mg-Ion Batteries (in submission). This was motivated as an extension to the work of Chapter 3. Most of the work was completed by Mr. Price, with analysis of results shared between Mr. Price and Mr. Baker.

Contents

List of Figures

List of Tables

List of Symbols

The following list describes several symbols that are commonly used within the body of this work.

h	Planck's Constant	$6.62607004 \times 10^{-34}\,\mathrm{J\,s}$
$\hbar$	Reduced Planck's Constant	$1.05457182 \times 10^{-34}\,\mathrm{J\,s}$
e	Elementary Charge	$1.60217662 \times 10^{-19}\,\mathrm{C}$
k_B	Boltzmann Constant	$1.380649 \times 10^{-23}\,\mathrm{m^2\,kgs^{-2}\,K^{-1}}$
m_e	Electron Mass	$9.10938356 \times 10^{-31}\,\mathrm{kg}$
ε_0	Permittivity of Free Space	$8.85418782 \times 10^{-12}\,\mathrm{Fm^{-1}}$
F	Faraday Constant	$9.64853321 \times 10^{4}\,\mathrm{Cmol^{-1}}$
R	Universal Gas Constant	$8.31446262\,\mathrm{JK^{-1}\,mol^{-1}}$

List of Abbreviations

The following list describes several abbreviations that are commonly used within the body of this work.

2D	Two-dimensional
3D	Three-dimensional
BZ	Brillouin Zone
CI-NEB	Climbing Image Nudged Elastic Band
DFT	Density Functional Theory
DOS	Density of States
GGA	Generalised Gradient Approximation
HF	Hartree-Fock
HOMO	Highest Occupied Molecular Orbital
HSE	Heyd–Scuseria–Ernzerhof
LDA	Local Density Approximation
LUMO	Lowest Unoccupied Molecular Orbital
NCA	$LiNi_xCo_yAl_{1-x-y}O_2$
NEB	Nudged Elastic Band
NMC	$LiNi_xMn_yCo_{1-x-y}O_2$

OC Open Circuit

PBE Perdew-Burke-Ernzerhof

PES Potential Energy Surface

RAFFLE pseudoRandom Approach For Finding Local Energetic minima

SEI Solid Electrolyte Interphase

SO Spin-Orbit

TMDC Transition Metal Dichalcogenide

VASP Vienna *Ab initio* Simulation Package

vdW van der Waals

VESTA Visualization for Electronic and Structural Analysis

VRH Voigt-Reuss-Hill

ZPE Zero-Point Energy

List of Publications

- Ned Thaddeus Taylor, Francis Huw Davies, Shane Graham Davies, Conor Jason Price, and Steven Paul Hepplestone, The Fundamental Mechanism Behind Colossal Permittivity in Oxides, *Advanced Materials*, **31**, 51, (2019).
  DOI:10.1002/adma.201904746.

- Ned Thaddeus Taylor, Conor Jason Price, Alexander Petkov, Marcus Ian Romanis Carr, Jason Charles Hale and Steven Paul Hepplestone, The Potential of Overlayers on Tin-Based Perovskites for Water-Splitting, *The Journal of Physical Chemistry Letters*, **11**, 10, (2020).
  DOI: 10.1021/acs.jpclett.0c00964.

- Ned Thaddeus Taylor, Francis Huw Davies, Isiah Edward Mikel Rudkin, Conor Jason Price, Tsz Hin Chan, and Steven Paul Hepplestone, ARTEMIS: Ab initio Restructuring Tool Enabling the Modelling of Interface Structures, *Computer Physics*, **257**, (2020).
  DOI:10.1016/j.cpc.2020.107515.

- Francis Huw Davies, Conor Jason Price, Ned Thaddeus Taylor, Shane Graham Davies, and Steven Paul Hepplestone, Band Alignment of Transition Metal Dichalcogenide Heterostructures, *Physical Review B*, **103**, 4, (2021).
  DOI:10.1103/physrevb.103.045417.

- Edward Allery David Baker, Joe Pitfield, Conor Jason Price, and Steven Paul Hepplestone, Computational Analysis of the Enhancement of Photoelectrolysis Using Transition Metal Dichalcogenide Heterostructures, *Journal of Physics: Condensed Matter*, **34**, 37, (2022).
  DOI: 10.1088/1361-648x/ac7d2c

- Conor Jason Price, Joe Pitfield, Edward Allery David Baker, and Steven Paul Hepplestone, First Principles Study of Layered Scandium Disulfide for use as Li-ion and

Beyond-Li-ion Batteries, *Physical Chemistry Chemical Physics*, **25**, 3, (2023).
DOI: 10.1039/D2CP05055B

- Conor Jason Price, Edward Allery David Baker, and Steven Paul Hepplestone, First Principles Study of Layered Transition Metal Dichalcogenides for Use as Electrodes in Li-Ion and Mg-Ion Batteries, *Journal of Materials Chemistry A*, **11**, 23, (2023).
  DOI: 10.1039/D3TA00940H

- Conor Jason Price, and Steven Paul Hepplestone, Intercalation-Dependent Elastic Properties of Transition Metal Dichalcogenides, *Journal of Materials Chemistry C*, **11**, 41, (2023).
  DOI: 10.1039/D3TC02106H

- Conor Jason Price, Edward Allery David Baker, and Steven Paul Hepplestone, Properties of Layered TMDC Superlattices for Electrodes in Li-Ion and Mg-Ion Batteries: *In Submission*.

Chapter 1

Introduction

"It is important to realize that in physics today, we have no knowledge of what energy is."

Richard Feynman, 1964

The success of early human civilisation can broadly be attributed to the development of agriculture ($\sim$10,000 B.C.E.) and the domestication of a diverse range of animals ($\sim$8,500 B.C.E.). Following this, the discovery and application of new materials allowed for further development, allowing for growth out of the colloquially-termed Stone Age into the Bronze Age ($\sim$3,300 B.C.E.) and Iron Age ($\sim$1,200 B.C.E.). However, much more recent developments have centred around the generation and utilisation of energy. The earliest evidence of water-driven wheels dates back to Greek engineer Philo of Byzantium ($\sim$280-220 B.C.E.), and the first technical description of a watermill comes from the Roman engineer Vitruvius ($\sim$10 B.C.E.). These made use of the energy of flowing water to drive a mechanism, and The Domesday Book (1086 C.E.) lists 5,624 water mills in England — one per 350–400 people. Along a similar vein, windmills became popular in Europe between $\sim$800-1100 C.E. and exploited the energy of moving air. The Industrial Revolution in Europe and the USA across the 18^{th} and 19^{th} centuries provided a significant increase in energy use, resulting in a transition from hand production methods to machine-based methods. These modern alternatives used water and steam power, generated from the combustion of coal. This period also provided large-scale access to a form of energy that is the basis of almost all modern technology: electricity.

The wide-spread availability of electrical energy in commercial and domestic settings, along with the development of more powerful electronics, has seen a corresponding rise in the use of devices such as televisions, smart phones, and computers. This has resulted in households being consistently ranked as the largest electricity final users. In 2021, for example, households in the UK consumed nearly 109 terawatt-hours of electricity, accounting for roughly 38% of the total energy consumption. There is also significant energy demand from a wider range of industries, including mining, chemical processing, and transport, of all which are requiring a greater consumption of energy to meet the demands of growing populations and growth of consumer industries.

With energy usage undergoing dramatic change over the last few decades, and larger changes expected over the coming years, forecasts of energy demand and carbon emissions vary wildly. However, numerous reports by both public and private organisations conclude the same thing: the global energy demand is rising and we are in the middle of an energy crisis [1–4]. Currently, fossil fuels provide for approximately 70-80% of the total global energy consumption [1–3], resulting in over 35 Gt of CO_2 being released into the atmosphere throughout 2020 alone [5]. As the rise in the Earth's average temperature is primarily caused by human activity [6], there is a serious need to move away from our reliance on fossil fuels. Coupled with this, fossil fuels are finite resources, and so natural deposits will eventually be depleted.

As a consequence of the negative environmental effects of fossil fuel use and rising prices due to depletion of reserves, new sources of energy are being considered. Fortunately, many projections are optimistic in the share of energy production these alternatives will provide, predicting renewables as the fastest growing source of energy [4], and an overall decarbonisation of the energy sector as fossil fuels are replaced by green electricity and hydrogen [3]. For example, across the member states of the European Union, more than 35% of consumed energy is now generated from renewable energy sources, and over 80% of this renewable energy is provided by wind, hydro or solar energy. This is, in part, a result of cooperative international efforts to reduce the impact of climate change, such as with the Paris Agreement and the recent COP27 Conference. There is, however,

still much work to do to reduce the strain on energy production, and facilitate an effective transition to green, renewable alternatives [7].

Obvious alternatives to the non-renewable energy sources build on the early ideas of wind and water mills, with modern equivalents being wind turbines and hydropower dams. Whilst these have long been overlooked due to their low energy and power output compared to fossil fuel combustion, they are clean, renewable, and can largely provide a passive supply of energy. Many of these green, renewable alternatives to energy generation, however, are dependent upon variable factors such as the weather, meaning there could be extended periods of time for which there is no power output (for example, when there is little wind). If instead the energy harvested during active periods was able to be safely and reliably stored, the variability would no longer be an issue. The challenge is then not the harvesting of energy from renewable sources, but cost-effective and efficient ways to store the energy produced during peak production times for later use [8, 9].

1.1 Electrochemical Energy Storage

Within the field of electrical energy storage, there are two main types of electrochemical cell: batteries and capacitors. Batteries are characterised by Faradaic electron transfer, achieved by accessing different oxidation states of (typically) metal atoms constituting the material being employed. Capacitors on the other hand use electric double layers at the surfaces of materials to non-Faradaically store charge [10]. However, the rapidly increasing number of materials that have been presented to the community has started to lead to ambiguous boundaries between these, with many materials displaying both capacitive and Faradaic electrochemical characteristics, so-called 'pseudo-capacitors' [11]. One way to begin categorising the mechanism of charge storage is through the use of electrochemical techniques such as cyclic voltammetry, which shall be discussed later in this section. The work in this thesis does not consider the surfaces of the materials in question, nor the interaction with any potential electrolyte, and so the results will be presented with only the Faradaic electron transfer in mind. However, it is

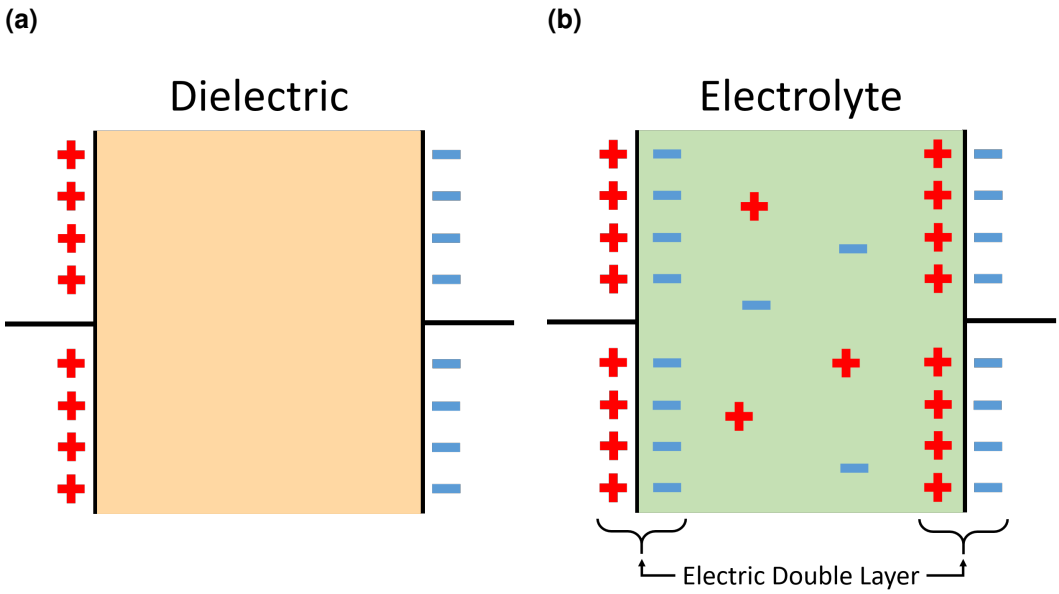

Figure 1.1: 1.1a shows a conventional capacitor, consisting of two oppositely charged plates separated by a dielectric material (orange). 1.1b shows an electric double layer capacitor (EDLC), consisting of two opposing plates separated by an electrolyte (green), where the electric double layer formed at each plate is indicated.

important that we are aware of the different processes that can occur in these cells to better understand experimental results and how the results presented here may be modified in an experimental setup.

1.2 Capacitors

Electrochemical capacitors, sometimes referred to as supercapacitors or ultracapacitors, are a form of energy storage device consisting of two opposing electrodes separated by an electrolyte. Patents for such devices date back to the 1950s [12]. Whilst conventional capacitors store charge on opposing plates or through polarisation of a dielectric material (see Figure 1.1a), electrochemical capacitors establish a so-called 'electric double layer' at the boundary between a conductive electrode and an adjacent liquid electrolyte. At this interface, opposing charges accumulate into two opposing layers, one within the electrode and one within the electrolyte [10], hence the term 'double-layer' (see Figure 1.1b).

Capacitors offer high charge-discharge efficiency, remain robust after repeated

cycling, and therefore have long lifetimes [13]. As the charge storage mechanism is based on reactions that occur at the surface of an electrode (instead of ionic diffusion through a material), capacitors are able to achieve high power densities [14, 15], and are best suited for applications where fast energy delivery is required [16]. Unfortunately, as the charge storage mechanism is restricted to surfaces [17], they typically have low charge capacities, and hence low energy densities of up to 10 Whkg^{-1} [14, 15].

1.3 Batteries

Perhaps the most well-known and most widely available form of electrochemical energy storage is the battery. This ubiquitous electrical component can be found in devices ranging from personal phones and laptops, to medical equipment and power tools. Batteries are able to store charge through chemical reactions, typically through the conversion of a material or through storage of ions in a host material. As these devices rely on chemical reactions and the transport of ions into a crystal framework, they tend to have limited charging rates and hence low power densities. However, as these reactions are not limited to a surface (as with electrochemical capacitors), they are able to achieve higher energy densities relative to capacitors.

With an ever-increasing demand for more powerful electronic devices, the need for suitable batteries has also increased. Unfortunately, batteries have developed at a much slower pace than other areas of electronics [18, 19]. This has meant that low capacities and short life-times still plague modern batteries, and hence modern electronics. On top of this, the past two decades have seen a rapid increase in research and investment into the development of electric vehicles [20], with the hope being for a move away from their more widely-used, fossil-fuel consuming cousins. One of the largest hurdles faced by the electric-vehicle industry, however, is the need for higher capacity batteries: the energy density of batteries has improved in a roughly step-wise manner, and is currently at about 200 Whkg^{-1} [21, 22], but energy densities of at least 500 Whkg^{-1} [23–25] are required to satisfy the demand of vehicle electrification. Thus, there is a clear need

for higher capacity, more robust, longer-life batteries.

Modern batteries rely on the insertion ('intercalation') of lithium or other elements into layered materials, as we shall see in the following discussions. Beyond direct battery application, the intercalation of ions into a host structure raises a range of fundamental questions, the answers to which could be of immense value throughout physics, chemistry and materials science. For example, the processes by which an ion enters a material, the diffusion of ions through the material once it is intercalated, and the removal of those ions from a material during discharge, are all properties that change between materials. Intercalation has also been used as a method to modify the optical [26–28], thermal [29,30], and magnetic [31] properties of materials, and there is evidence for new, metastable, superdense phases of lithium forming when intercalated into layered materials such as graphite [32,33]. These new material phases could hold novel properties that have not been previously observed. Clearly, being able to understand how a host material interacts with an intercalated species and how this changes the properties of the host material would be useful for a wide range of applications. The intercalation of layered materials, in the context of intercalation batteries, will form the main focus and motivation of this thesis.

1.3.1 Function of Batteries

A typical Li-ion cell is shown in Figure 1.2 to highlight the two main components to a battery: the electrodes and the electrolyte. Other components may be included during manufacture, such as the 'separator', which physically separates the electrodes to prevent a shorting of the cell, the 'current collector', which connects the components that collect electrical current generated at the electrodes with external circuits, and the 'binder', which binds the active materials in the electrodes together. However, these additional components do not take part in the electrochemical processes; instead, they act to increase the efficiency, lifetime, and performance of the cell. Therefore, we will only discuss the electrodes and electrolyte here.

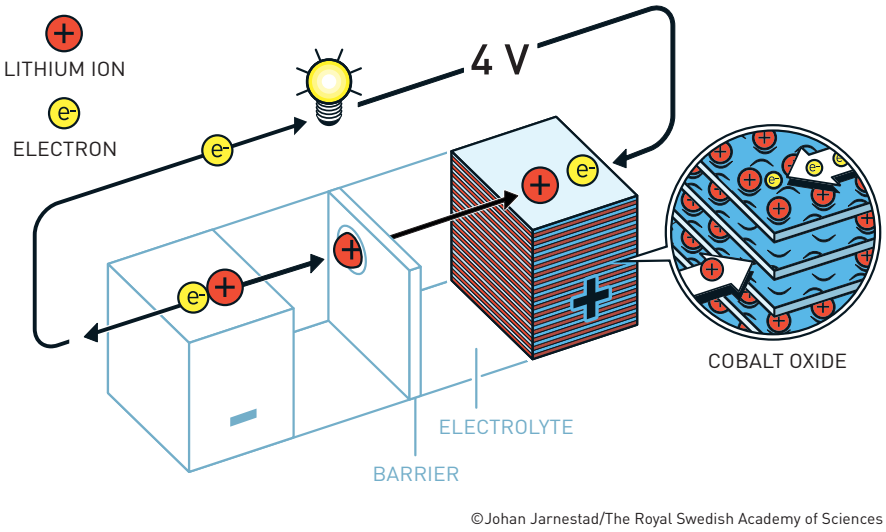

Figure 1.2: Schematic of Goodenough's battery during discharge, with a Li_aCoO_2 cathode. Lithium ions travel through the electrolyte from one electrode to the other. Electrons, unable to travel through the electrolyte, travel through an external circuit and power a connected device. Figure reproduced from the Nobel Prize Website [34].

Electrodes

The electrodes of electrochemical cells are the sites at which the electrochemical reactions take place. In an intercalation battery, the reactions taking place are the intercalation and deintercalation of ions. The electrodes act to 'house' the intercalated ions in between charging and discharging. Whilst there is in principle no limit to what these intercalated ions can be, we will use the example of lithium in the following discussions.

There are two electrodes in a battery, the anode and the cathode, characterised by the redox process they facilitate. The anode is the electrode at which the oxidation of lithium atoms takes place, producing positively charged lithium ions, and releasing the removed electrons to an external circuit. Conversely, the cathode is the electrode at which reduction takes place, accepting electrons from an external circuit to reduce lithium ions to lithium atoms. During discharge of the cell the anode is the negative electrode and the cathode is the positive electrode. The direction of ion and electron flow is reversed during the charging process

and so this assignment is switched, however to avoid confusion and to maintain consistency, we will only refer to the discharge process within this thesis.

For the specific case of intercalation electrodes, Whittingham was the first to suggest that materials with a layered structured and van der Waals spacings would be ideal for the storage of intercalant species [35], as their spacings provide natural channels for the lithium to be held in, and allow for reversible intercalation reactions that do not break any bonds. For typical lithium-ion batteries, composed of a graphitic anode and a $LiCoO_2$ cathode, the discharge of the battery can be described by the following reactions:

$$\begin{aligned} \text{Cathode:} \quad & \mathrm{CoO_2} + a\mathrm{Li^+} + a\mathrm{e^-} \rightarrow \mathrm{Li}_a\mathrm{CoO_2} \\ \text{Anode:} \quad & \mathrm{Li}_a\mathrm{C_6} \rightarrow \mathrm{C_6} + a\mathrm{Li^+} + a\mathrm{e^-} \\ \text{Full Reaction:} \quad & \mathrm{Li}_a\mathrm{C_6} + \mathrm{CoO_2} \rightarrow \mathrm{C_6} + \mathrm{Li}_a\mathrm{CoO_2}. \end{aligned} \tag{1.1}$$

This reaction, or an equivalent reaction with other electrode materials, produces a potential difference across the cell. The potential difference is an important quantity in electrochemistry, and can be useful for describing and comparing different electrode materials. For easy comparison of intercalation potentials between different materials a reference anode of lithium metal is typically used. This will then give the electrode half-cell potential for any given material, which is the voltage given with respect to the Li/Li^+ redox potential [10].

Ideal cathode materials will demonstrate a high voltage versus the Li/Li^+ redox level, with current market leaders achieving voltages of 3 - 5 V [36–42]. Ideal anodes, on the other hand, will demonstrate a low (but positive) voltage. The voltage obtained from a pairing of any two materials can then be calculated from their difference. As $LiCoO_2$ possesses a voltage of $\sim$4 V [42], and graphitic carbon achieving voltages as low as 0.01 V [43], cells utilising these materials as opposing electrodes allows the battery to provide a voltage of 4 V.

Electrolytes

The electrolyte is a medium connecting the two electrodes of the cell, and whilst a range of electrolytes exist, for example liquid organics [44], ionic liquids [45] and inorganic solids [46], their basic function is the same. The electrolyte must

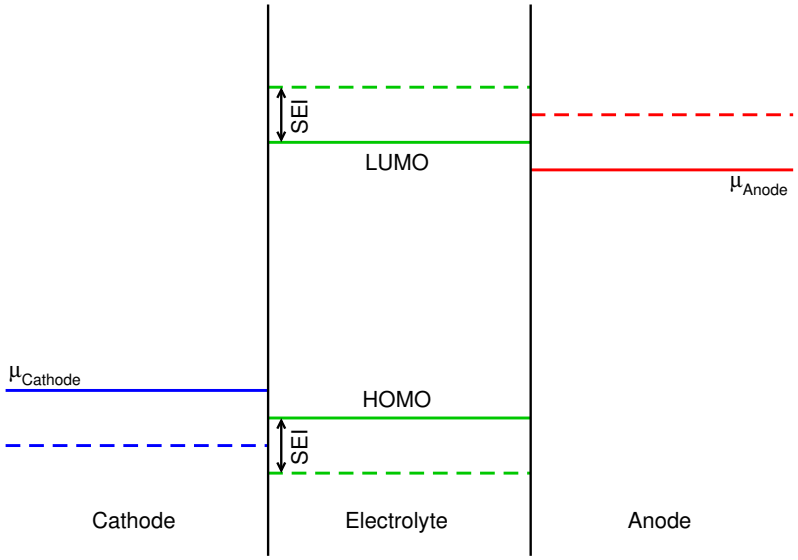

Figure 1.3: Schematic illustrating the open-circuit energy diagram associated with the cathode, electrolyte and anode of a cell. $\mu_{Cathode}$ indicated with a solid blue line is the electrochemical potentials of the cathode, μ_{Anode} indicated with a solid red line is the electrochemical potentials of the anode, and HOMO and LUMO indicate the highest occupied molecular orbital and lowest unoccupied molecular orbital of the electrolyte, respectively, both indicated with solid green lines. The effect of the formation of a solid-electrolyte interphase (SEI) layer (green dashed lines) is allows the positions of $\mu_{Cathode}$ and μ_{Anode} to shift, as indicated with the respective dashed lines.

prevent electronic conduction between the electrodes (which would result in a short of the cell), whilst allowing ionic conduction. Electrolytes are subject to their own practical restrictions and shortcomings, and the search for better electrolytes is the subject of many different studies. Whilst electrolytes are not the focus of this work, it is important that they are addressed for context and awareness of any restrictions they may impose on electrodes.

Within the electrically-resisting electrolyte, there will be a gap between the lowest unoccupied molecular orbital (LUMO) and the highest occupied molecular orbital (HOMO), which is often referred to as the window of stability of the electrolyte [45, 47]. It is required that the electrochemical potential of the cathode ($\mu_{Cathode}$) be higher in energy than the HOMO of the electrolyte, and the electrochemical potential of the anode (μ_{Anode}) be lower in energy than the LUMO of the electrolyte. This is indicated in Figure 1.3. If the electrochemical potential of the anode is higher than the LUMO of the electrolyte, electrons will be able to flow

from the anode to the electrolyte and the electrolyte will be chemically reduced. Similarly, if the electrochemical potential of the cathode is lower than the HOMO of the electrolyte, electrons will be able to flow from the electrolyte to the cathode, and the electrolyte will be oxidised. Both of these processes cause degradation of the electrolyte and cell.

A passivation layer at the interface between the electrode and electrolyte, known as a solid-electrolyte interphase (SEI), can be formed. A successful SEI layer will be electronically insulating but ionically conducting, and act as solid electrolyte [48]. If this material is conductive to ionic lithium but electrically insulating, then normal battery operation can take place. The electrical insulator property of the SEI can add electrochemical stability to the electrolyte by raising the effective LUMO of the electrolyte and lowering the effective HOMO. This in turn allows the position of $\mu_{Cathode}$ (μ_{Anode}) to move to a lower (higher) energy, thus allowing for a larger open-circuit voltage to be obtained, as indicated by the dashed lines in Figure 1.3. However, the specific properties of the SEI and the effect of its formation on device function will depend heavily on the electrolyte, the electrode, and the local chemistry at their interface. The formation of a SEI may also require consumption of lithium, the active electrode, and/or the electrolyte, resulting in higher internal resistance of the cell and capacity fading. This usually manifests as a larger charge capacity being achieved in the first few charge-discharge cycles of a cell compared to following cycles [49].

Electrochemical Testing

A popular tool for investigations of the complex reactions in a material is cyclic voltammetry. This involves linearly varying the potential across the cell in time and recording the resultant current. Once one potential sweep between two defined potentials is completed, the potential is varied in the opposite direction back to the starting potential, hence ‘cyclic’ voltammetry. When the potential is far from the potential of a redox-reaction, only non-Faradaic currents can flow. However, as the potential sweeps through any redox-reaction potentials, Faradaic currents lead to spikes. These can be identified in the voltammetry plots, giving insight into the nature of reactions that occur during charging/discharging [10], and can help

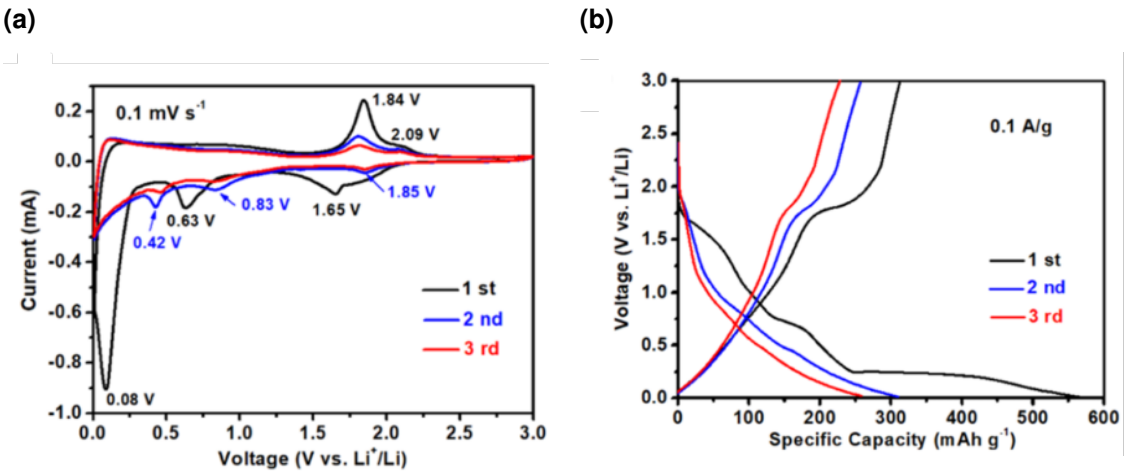

Figure 1.4: Figures of electrochemical tests on $NbSe_2$ during lithium intercalation. Figure 1.4a shows the cyclic voltammetry plots (scan rate of 0.1 mV/s) during the first three cycles, with key potentials identified. Figure 1.4b shows the galvostatic test (constant current of 0.1 A/g) for both charging and discharging of $NbSe_2$ in the same work. Figures reproduced from [50].

with the determination of whether a material is Faradaic, capacitive, or pseudocapacitive [11]. An example cyclic voltammetry plot is shown in Figure 1.4a, reproduced from [50].

Another popular tool is galvanostatic testing, which can be useful for the evaluation of a material's specific capacity and cyclability. This involves the application of a constant current to the cell electrodes, and measurement the resultant potential between them as a function of the total charge supplied. The produced plot often consists of a series of plateaus, each indicating structural changes in the electrode [10]. An example galvanostatic test plot is shown in Figure 1.4b, also reproduced from Peng [50].

As is evident from these figures, there can be several redox peaks appearing for a single material. These can arise from intercalation, conversion of the host material into other products, further reduction/oxidation of these conversion products, SEI formation, or reactions taking place in the electrolyte, to name a few possible sources of redox peaks. For example, in Figure 1.4, the peaks/plateaus in the range 0.01-1.70 V are attributed to the reversible conversion of the layered Li_aNbSe_2 structure to Li_2Se and metallic Nb, and the peaks/plateaus close to 1.85 V are are attributed to the oxidation-reduction reaction between Li_2Se and

polyselenides [50]. Special care should therefore be taken when assigning these peaks to any particular redox reaction.

1.3.2 A Brief History of Batteries

Benjamin Franklin first coined the term 'battery' to describe a system of charged plates in 1749 [51], however the first chemical battery was not constructed until 1800 when Alessandro Volta invented the voltaic pile [52]. This consisted of an alternating stack of copper and zinc discs, separated by layers of salt water, and was able to deliver electrical currents to circuits, albeit for short periods of time. Due to batteries being constructed from multiple components, all of which require some compatibility with every other component, there have been only relatively few improvements to the construction and operation of batteries since their initial creation. Fortunately, there have been some significant milestones over the past three centuries which have allowed the development of modern batteries and technologies.

Lithium (from the Greek 'lithos' meaning 'stone') was the third element to form, coming into existence a mere five minutes after the Big Bang [53, 54]. The first lithium-containing mineral to be discovered was petalite ($LiAlSi_4O_{10}$) in 1800, with its lithium content determined in 1817 by Johan August Arfvedson [55,56]. William Thomas Brande then first isolated lithium metal by applying a voltaic pile to lithium oxide in 1821 [55]. This came over a decade later and utilised a different method to what Sir Humphry Davy used to isolate sodium, potassium, and many of the Group II elements [57]. The work of Brande thus gave access to the metal on the periodic table with the lowest atomic number, the lowest atomic mass, and hence the lowest density.

In 1860, Gaston Planté developed the first battery that could be recharged by passing a reverse current through it [58, 59]. This utilised Nicolas Gautherot's observations from 1801, where wires used in electrolysis experiments provided a small 'secondary' current, even after the main battery had been disconnected. Planté's early 'lead-acid' design consisted of two sheets of lead, separated by rubber strips, and rolled into a spiral. Whilst the next century offered several

improvements to the lead-acid battery, such as the lattice suggested by Camille Alphonse Faure and the gel electrolytes first used in the 1920s and 1930s, lead-acid batteries have comparatively low energy-densities to modern rechargeable batteries. Nevertheless, they still remain a major battery system, largely due to their low cost, light weight, high power density, and ability to supply high surge currents, and have found particular use in starting automotive engines.

In 1913, Lewis and Keyes began investigating the electrochemical properties of metallic lithium, and determined its $\mathrm{Li^+ + e^- \rightarrow Li}$ redox potential to be -3.04 V versus the standard hydrogen electrode [60]. In 1958, William Harris examined the solubility of various salts [61] in different electrolytes, including cyclic esters, molten salts, and inorganic lithium salt ($LiClO_4$) dissolved in propylene carbonate. It was observed that the formation of a passivation layer was capable of preventing a direct chemical reaction between lithium and the electrolyte while still allowing for ionic transport across it [56].

The promise of lithium metal, having a low density, a low redox level, and a passivation layer being able to protect the electrolyte from its high reactivity, prompted research into the use of lithium in lithium-ion batteries as energy storage devices [56]. Within a decade, there were numerous primary lithium-ion batteries available. A CuF_2|Li battery was developed by NASA in 1965 [62], a lithium-sulfur dioxide Li|SO_2 cathode became commercially available in 1969 [63, 64], Matsushita commercialised a lithium–polycarbon monofluoride Li|$(CF_x)_n$ cell in 1970 [65, 66], and lithium–manganese oxide (Li|MnO_2) batteries were commercialised by Sanyo in 1975 [56]. Though these offered 3 V lithium-ion cells, many of which are still used in devices today, they were primary cells and needed to be discarded after a single use: there was still the need for cells which could be recharged and reused.

The use of intercalation electrodes, that is, electrodes with a layered structure which allow the ‘insertion’ of lithium ions in between the sheets, for use in lithium cells was first proposed by Whittingham in 1976 [35]. Whittingham then investigated the electrical energy storage and intercalation chemistry of layered TiS_2 [67], following which Exxon, a multinational gas and oil corporation, tried to commercialise a TiS_2 battery [68, 69]. However, due to the sensitivity of TiS_2 to mois-

ture (releasing H_2S gas on contact with water), the inclusion of a dangerous, shock-sensitive electrolyte, and the use of metallic lithium, device manufacture was found to be expensive and complex. As such, the development of Whittingham's lithium-titanium disulfide battery was discontinued by Exxon [69].

In the early 1980s, working in separate groups, researchers Ned A. Godshall [70], and Koichi Mizushima and John B. Goodenough [71, 72] began looking at a material related to TiS_2: lithium cobalt oxide. Goodenough looked at a range of layered materials, and was able to experimentally verify both the superior stability of transition metal oxides over their sulfide counterparts during intercalation reactions, and their higher operating voltages. In an investigation of a variety of layered transition metal oxides, Li_aCoO_2 was identified as the best candidate for a cathodic material, able to have its lithium content reduced to from $\mathrm{a} = 1$ to $\mathrm{a} = 0.067$ during a charging voltage of 4 V [55, 71–73]. This provided a high-voltage, high capacity cathode that was more stable than its predecessors.

Throughout the investigation of materials for cathodes for rechargeable lithium ion batteries, metallic lithium anodes had been used. Unfortunately, metallic lithium is prone to dendrite formation [74, 75], which can cause short-circuiting of the cell and spontaneous combustion when in contact with oxygen, and large volumetric expansion [76]. Both of these properties raised concerns over the safety of its use. In the late 1980s, Moli Energy, a Canadian technology company, was even required to issue a total recall of their $Li|MoS_2$ cells used in mobile phones due to reports of battery fires [55]. As such, there was a serious need for a safe alternative to the lithium metal anode.

In 1983, Yazami found that a soft-carbon, graphitic electrode was able to demonstrate reversible lithium intercalation and had promise as the anode of lithium ion batteries [77]. With this anode, in 1985 Yoshino was able to create the first prototype of a secondary cell, composed of a $LiCoO_2$ cathode and carbon-based anode, that was small and light, demonstrated excellent cyclability, and offered a high energy density [78].

Using the design developed by Yoshino, Sony commercialised a lithium ion battery in 1991 [79], and a joint venture between Asashi Kasei Co. and Toshiba

produced a battery in 1992 [69]. Many companies were quick to utilise these small, light, and resilient devices, which were able to provide energy densities of 200 WhL^{-1} and 80 $Whkg^{-1}$ when charged to 4.1 V.

The works discussed above resulted in the commercialisation of lithium-ion batteries to such a scale that they are an integral part of modern life, being used in the vast majority of portable electronic devices across the globe. Together, these works also earned Goodenough, Yazami, and Yoshino the 2012 IEEE Medal for Environmental and Safety Technologies [80], and earned Goodenough, Whittingham, and Yoshino the 2019 Nobel Prize in Chemistry for their contributions towards the development of lithium-ion batteries [81].

Since the development of the rechargeable lithium-ion battery, there has been much work put into further development of battery technology [69]. Many other materials have been considered as cathodes, with $LiNi_xMn_yCo_{1-x-y}O_2$ (NMC), $LiNi_xCo_yAl_{1-x-y}O_2$ (NCA), and their variants [41, 82–86], several phosphates [36, 38, 40], and spinel oxides such as Mn_2O_4 [87] each offering high voltages. In an attempt to achieve capacities greater than those available when using graphite, materials such as silicon [88], lithium titanate [89], and other metal oxides being considered [90, 91] for the anode. Intercalant species other than lithium have also been investigated: following the success of lithium, other Group I metals have been investigated for intercalation batteries. Multivalent Group II elements, zinc, and aluminium, have also been considered, with each offering their own viable successes in recent years.

1.4 Outline

This work considers a theoretical investigation into the viability of atomically thin, layered materials for use as electrodes in intercalation batteries. In particular, we investigate the viability of transition-metal dichalcogenides, a group of layered materials similar to graphite. This thesis will predict the voltages associated with the intercalation and de-intercalation of ions into transition metal dichalcogenide (TMDC) materials, as would be seen as the significant features in common

electrochemical tests. It will also indicate the ability of intercalant ions to diffuse through the structures, and identify any intercalation-induced phase transitions in them. Further, it explains how the open-circuit voltage profiles and lithium diffusion barriers change for composite materials, how the stability changes upon superlatticing, and overall the potential such structures have for future battery development.

In the next Chapter, we will discuss the methods used throughout this thesis, providing a discussion and derivation of the fundamental principles and underlying theory of *ab initio* density functional theory, the tool with which we have explored the electronic, energetic, and structural properties of the materials in question. Chapter 3 provides the results of a high-throughput investigation into the properties of the TMDC family, a group of materials that has received much attention in a wide range of applications. Here, we focus on their suitability for intercalation electrodes (when intercalated with either lithium or magnesium) by determining their voltage profiles, thermodynamic phase diagrams, volumetric expansion, and their electronic structure, all of which are vital for characterising successful electrode materials. Chapter 4 discusses how the elastic properties of the TMDCs can be controlled through ion intercalation. This is of particular interest in a time where the demand for flexible electronics is on the rise, but is also vital for the modelling of material fracture during cell cycling. Chapter 5 provides a closer look into layered ScS_2, a material that is highlighted as a particularly promising cathode in Chapter 3, extending its study to intercalation with sodium and potassium, as well as the lithium and magnesium. Along with the methods outlined in Chapter 3 and Chapter 4, we also employ random structure search techniques, and consider the dynamic stability. We predict a stable intercalation electrode that can provide capacities that are competitive with current market leaders. Chapter 6 extends the investigation presented in Chapter 3 to TMDC superlattices. These are formed by making use of the layered structure of TMDCs, with superlattices consisting of alternating material layers, allowing us to utilise not only the properties of the component materials but also the novel physics that can arise from the interface between them. Finally, this thesis is then summarised, and a discussion of ways to take this work forward is presented.

Chapter 2

Methods

"Reality is frequently inaccurate"

Douglas Adams, 1980

2.1 Introduction

In the previous Chapter, we introduced the idea of using materials for energy storage applications. For atomic-scale investigations of such materials, we must first be able to accurately describe their geometric structure. Once we have established the structure, we can then begin our assessment of materials for applications: we can determine key energetic properties such as the intercalation voltage, and investigations of the electronic structure can provide insight into whether electronic conduction limits electrode function. We can also quantify functional limits through thermodynamic phase diagrams by identifying where decomposition into other compounds occurs, or through analysis of the phonon band structure to determine limits of the dynamic stability.

To carry out such an investigation into a material, however, we must first have a firm understanding of the fundamental physics that governs it at the atomic level. In this Chapter, we will summarise the core principles of quantum mechanics and solid-state physics necessary for discussions of crystalline solids. We will then examine some methods commonly used to investigate our chosen family

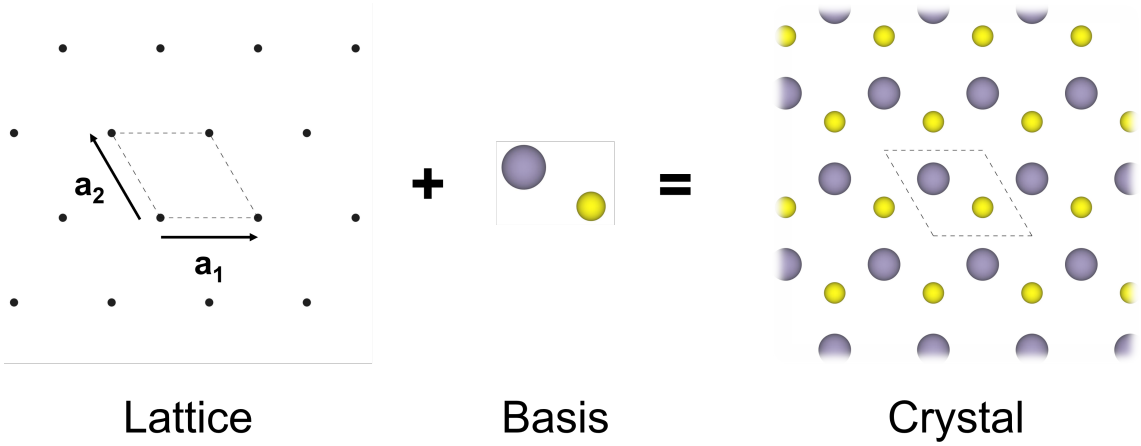

Figure 2.1: Diagram showing how a periodic lattice of points (black dots), the associated primitive lattice vectors $\mathbf{a}_1$ and $\mathbf{a}_2$, and an atomic basis (purple and yellow circles) can be used to generate a periodic crystal. The primitive unit cell is indicated with dashed lines.

of materials, methods which provide the backbone for the majority of the work presented in this thesis.

2.2 Crystal Structure

In the study of crystalline solids, one key concept is that of the crystal lattice: an infinite array of equivalent points, periodically repeated such that their arrangement and orientation remain unchanged, regardless of the point from which the array is viewed. Due to this intrinsic periodicity, rather than considering the infinite array, we can instead utilise a primitive unit cell defined by a parallelepiped (in three dimensions) of three vectors. These primitive vectors, $\mathbf{a}_1$, $\mathbf{a}_2$, and $\mathbf{a}_3$, do not lie in the same plane, and any integer ($n_i = 0, 1, 2, \cdots$) combination of them will translate between equivalent points within the lattice,

$$\mathbf{T} = n_1\mathbf{a}_1 + n_2\mathbf{a}_2 + n_3\mathbf{a}_3 = \sum_i n_i\mathbf{a}_i, \tag{2.1}$$

known as a lattice translation vector. An example of a two dimensional primitive unit cell is shown in Figure 2.1, with the lattice points depicted as black dots, and the resultant unit cell indicated with dashed lines.

Though useful for discussions of crystalline solids, the lattice is a mathematical construct and does not contain any information about the crystal composition,

chemistry, or the properties it possesses. However, to each lattice point we can attribute an atom or collection of atoms that is also repeated infinitely throughout the solid. This is referred to as the 'atomic basis'. Together, the lattice and basis generate the entire crystal, and the relationship between each of these is shown in Figure 2.1.

2.2.1 Crystal Symmetries

It is often extremely useful to make use of any symmetries of a crystal, beyond the translational symmetry required by the lattice, and allow for classification of lattices and crystal structures. Symmetries such as mirror planes or rotational symmetry, which preserve the position of the point about which these symmetries can be seen, are termed point symmetries. A group of point symmetries is called a point group, and the group of lattices with the same set of point groups is called a lattice system. Depending on the relative lengths of the primitive lattice vectors, quantities called the lattice constants, and the angles between them, a (three dimensional) crystal can fall into one of seven different lattice systems: triclinic, monoclinic, orthorhombic, tetragonal, cubic, trigonal, and hexagonal. Some of these can be further divided into different lattice types (primitive, body-centred, face-centred, and base-centred) which results in 14 Bravais lattices [92]. We can also consider the symmetries of the basis atoms. There are 32 unique crystallographic point groups, and the combination of lattice types and unique point groups leads to the full 230 unique space groups, which provide a full description of the crystal symmetry.

2.2.2 Reciprocal Space and the Brillouin Zone

Along with the real-space lattice described above, another concept that is useful for discussions of material properties is the reciprocal lattice. Consider a general plane wave $\exp(i\mathbf{k}\cdot\mathbf{r})$. For a general wave vector **k**, the plane wave will not possess the same periodicity as the lattice. However, the set of all **k**-points, **G**, that do produce plane waves with the same periodicity define the reciprocal lattice. This

can be analytically understood by considering the periodicity of the real-space lattice: we require the plane wave at a point **r** to be equivalent to the plane wave at another point, separated from **r** by any translation vector **T** defined above. Thus,

$$\exp(i\mathbf{G}\cdot\mathbf{r}) = \exp\big(i\mathbf{G}\cdot(\mathbf{r}+\mathbf{T})\big), \tag{2.2}$$

which can be factored to give the requirement,

$$\exp(i\mathbf{G}\cdot\mathbf{T}) = 1. \tag{2.3}$$

This is satisfied for any $\mathbf{G}\cdot\mathbf{T} = n\times 2\pi$, with integer n.

As this must hold for the lattice vectors themselves, we can write the reciprocal-lattice translation vector,

$$\mathbf{G} = m_1\mathbf{a}_1^* + m_2\mathbf{a}_2^* + m_3\mathbf{a}_3^* = \sum_i m_i\mathbf{a}_i^*, \tag{2.4}$$

in terms of reciprocal space lattice vectors $\mathbf{a}_1^*$, $\mathbf{a}_2^*$, and $\mathbf{a}_3^*$. These can be determined from the real-space lattice vectors using,

$$\begin{aligned}
\mathbf{a}_1^* &= 2\pi\frac{\mathbf{a}_2\times\mathbf{a}_3}{\mathbf{a}_1\cdot(\mathbf{a}_2\times\mathbf{a}_3)},\\
\mathbf{a}_2^* &= 2\pi\frac{\mathbf{a}_3\times\mathbf{a}_1}{\mathbf{a}_2\cdot(\mathbf{a}_3\times\mathbf{a}_1)},\\
\mathbf{a}_3^* &= 2\pi\frac{\mathbf{a}_1\times\mathbf{a}_2}{\mathbf{a}_3\cdot(\mathbf{a}_1\times\mathbf{a}_2)},
\end{aligned} \tag{2.5}$$

from which it can easily be shown that $\mathbf{a}_i\cdot\mathbf{a}_j^* = 2\pi\delta_{ij}$.

The reciprocal lattice vectors construct a periodic lattice. By finding the Wigner-Seitz cell of this reciprocal lattice, we can identify the first Brillouin zone, the volume of which, Ω_{BZ}, is related to the volume of the real space unit cell, Ω_{Cell}, by,

$$\Omega_{\mathrm{BZ}} = \frac{(2\pi)^3}{\Omega_{\mathrm{Cell}}}. \tag{2.6}$$

As the Brillouin zone is constrained by the symmetries of the reciprocal lattice, we can define an irreducible Brillouin zone, which contains all of the unique points necessary for a description of the full Brillouin zone. If the reciprocal lattice has M point symmetries, the irreducible Brillouin zone will be a $\frac{1}{M}$ fraction of the full Brillouin zone.

2.3 Mathematics of Electronic Structure Calculations

2.3.1 The Schrödinger Equation

One of the most fundamental equations in quantum mechanics is the Schrödinger equation, solutions of which allow us to describe the temporal and spatial evolution of a quantum state. The time-independent Schrödinger equation is given by,

$$\hat{H}\Psi(\mathbf{r}) = -\frac{\hbar^2}{2m}\nabla^2\Psi(\mathbf{r}) + \hat{V}(\mathbf{r})\Psi(\mathbf{r}) = E\Psi(\mathbf{r}), \tag{2.7}$$

where $\hat{H}$ is the Hamiltonian of the system, and is the sum of a kinetic energy term and a potential energy term. The eigenfunction of the Hamiltonian, Ψ, is the wave function, a complex, single-valued, continuous function of spatial coordinate **r**, and has eigenvalue E equal to the energy of the state it describes.

Whilst analytical solutions to the Schrödinger equation have been determined for a select few quantum systems, obtaining the wave function is typically a very difficult task. This is in-part due to the range of forms the potential $\hat{V}$ can take, but more so because the inclusion of many-body terms (which are necessary for an accurate consideration of most quantum systems) result in repeated interactions. This often results in a wave function being impractical or even impossible to obtain. We shall see in the coming sections a range of methods that can be used to combat the difficulty of obtaining wave functions of many-body systems.

2.3.2 Born-Oppenheimer Approximation

For a crystalline system, the electronic and ionic wave functions are typically coupled. Whilst consideration of static ions allows use to write the total wave function as a product of the ionic and electronic wave functions, nuclear motion (for example, due to finite temperature) can be expected to result in changes that prevent such a convenient decoupling. One approach that is commonly used to simplify this problem for electronic structure calculations is the Born-Oppenheimer approximation. We leave a detailed discussion of this to Appendix A, which consid-

ers the energy associated with ionic motion to be a perturbation to the electronic Hamiltonian due to the comparatively larger masses and smaller velocities of ions compared to electrons. At zeroth order, we achieve the case of static ions. An expansion to second order shows that nuclear motion is harmonic and the electrons move adiabatically in a potential created by nuclei fixed to their equilibrium positions. Consequently, and most importantly for our discussions, the electronic and nuclear wave functions can be decoupled, thus allowing us to isolate the electronic Schrödinger equation,

$$\hat{H}\Psi(\mathbf{r}) = \big(\hat{T}_{el} + \hat{V}_{el-el} + \hat{V}_{el-ion} + \hat{V}_{ion-ion}\big)\Psi(\mathbf{r}) = E\Psi(\mathbf{r}). \tag{2.8}$$

Here, we have separated out the terms of the Hamiltonian corresponding to the electron kinetic energy ($\hat{T}_{el}$), the electron-electron interaction potential ($\hat{V}_{el-el}$), the electron-ion interaction potential ($\hat{V}_{el-ion}$), and the ion-ion interaction potential ($\hat{V}_{ion-ion}$).

2.3.3 Orthonormal Basis Functions

One method that is commonly employed to obtain solutions to the Schrödinger equation is to decompose the wave function into a linear combination of mutually orthogonal basis functions,

$$\Psi = \sum_i c_i b_i. \tag{2.9}$$

It is then an algebraic problem to optimise the expansion coefficients, c_i, of each basis function b_i. We start by defining a functional, $G[\Psi]$:

$$G[\Psi] = \langle\Psi|\,\hat{H}\,|\Psi\rangle - E\,\langle\Psi|\Psi\rangle\,, \tag{2.10}$$

and impose stationary conditions on this functional. We substitute our expansion of (in general infinite) N orthonormal functions into our definition of $G[\Psi]$, to get

$$\begin{aligned} G(c_1, \cdots, c_N) &= \sum_{ij} c_i^* c_j H_{ij} - E\sum_{ij} c_i^* c_j \delta_{ij} \\ &= \sum_{ij} c_i^* c_j (H_{ij} - E\delta_{ij}), \end{aligned} \tag{2.11}$$

with matrix elements of the (square matrix) Hamiltonian $H_{ij} = \langle b_i|\,\hat{H}\,|b_j\rangle$, and elements of the (diagonal square matrix) $E\delta_{ij} = E\,\langle b_i|b_j\rangle$. The Hermitian nature of the operator $\hat{H}$ means $H_{ji} = H_{ij}^*$.

Minimising G with respect to the expansion coefficients leads to $\frac{\partial G}{\partial c_i^*} = 0$, and we get,

$$\sum_j (H_{ij} - E\delta_{ij})c_j = 0. \tag{2.12}$$

A non-trivial solution exists if

$$\det |H_{ij} - E\delta_{ij}| = 0. \tag{2.13}$$

This is the secular equation, and can also be written as $\hat{H}\mathbf{c} = E\mathbf{c}$. This is an eigenvector equation, with N×N matrix $\hat{H}$ and vector **c** formed of coefficients c_i. We thus have N eigenvectors (one for each row in the matrix $\hat{H}$), and so the N solutions can be written as:

$$\Psi_k = \sum_i C_{ik} b_i, \tag{2.14}$$

with $k = 1, \cdots, N$, and C_{ik} the fundamental matrix. We must now consider an important property of C: the relation $\Psi_k = \sum_i C_{ik} b_i$ can be viewed as a transformation between a starting set of N basis functions, b_i, and a final set of N functions, Ψ_k, via transformation matrix C. Rather than trying to directly obtain a solution Ψ_k, our task is to instead determine the elements of C to construct Ψ from the basis functions. If starting functions b_i are orthonormal, then,

$$\begin{aligned} \int \Psi_l^* \Psi_k \, d\mathbf{r} &= \int \sum_{ij} C_{jl}^* b_j^* C_{ik} b_i \, d\mathbf{r} \\ \delta_{lk} &= \sum_{ij} C_{jl}^* C_{ik} \delta_{ji} = \sum_i C_{il}^* C_{ik}, \end{aligned} \tag{2.15}$$

or in matrix notation,

$$(C^{-1})_{ij} = C_{ij}^* \equiv C_{ij}^\dagger, \tag{2.16}$$

and the transformation matrix C is unitary.

If we now consider the effect of the transformation matrix on the Hamiltonian,

$$\begin{aligned} (C^{-1}\hat{H}C)_{kn} &= \sum_{ij} (C^{-1})_{ki} H_{ij} C_{jn} \\ &= \sum_i C_{ik}^* \sum_j H_{ij} C_{jn} \\ &= \sum_i C_{ik}^* E_n C_{in} \\ &= E_n \sum_i C_{ik}^* C_{in} \\ &= E_n \delta_{kn}, \end{aligned} \tag{2.17}$$

we demonstrate that transformation matrix C transforms $\hat{H}$ into a diagonal matrix, with N non-zero (diagonal) elements which are the eigenvalues of the system. Our eigenvalue problem is therefore changed to a search for a transformation matrix, which allows us to move from our original 'guess' basis to a new basis which diagonalises the Hamiltonian of the system.

2.3.4 Variational Method

Using the above construction of a wave function from a set of orthonormal basis functions, it is possible to obtain approximate solutions to the Schrödinger equation using the variational method. This is the foundation for many practical approaches to obtaining a solution to the Schrödinger equation in condensed matter physics. To emphasise the usefulness of the this method, we now consider the complete orthonormal set of eigenfunctions ψ_n of a Hamiltonian $\hat{H}$ with eigenvalues E_n:

$$\hat{H}\psi_n = E_n\psi_n. \tag{2.18}$$

The ground state of this system, labelled $n = 0$ with energy E_0, by definition is the lowest energy eigenstate of $\hat{H}$. We expand an arbitrary function Ψ using energy eigenfunctions ψ_n as the basis set,

$$\Psi = \sum_n c_n\psi_n. \tag{2.19}$$

Substituting equation (2.19) into the expression for the expectation value of $\hat{H}$,

$$\begin{aligned}\langle\hat{H}\rangle &= \int \Psi^*\hat{H}\Psi\, dV \\ &= \frac{\sum_n |c_n|^2 E_n}{\sum_n |c_n|^2} \\ &= E_0 + \frac{\sum_n |c_n|^2 (E_n - E_0)}{\sum_n |c_n|^2} \\ \langle\hat{H}\rangle &\geq E_0,\end{aligned} \tag{2.20}$$

with equality for the case where the wave function Ψ is exactly equal to the ground state wave function ψ_0. This simple result is incredibly useful: it tells us that the lowest eigenvalues found from this method will always be higher than or equal to the true ground state energy, with the function Ψ yielding for the expectation value

of energy an upper bound estimate for the energy of the ground state energy. If the ground state is initially unknown, an approximation to the ground state can be found simply by varying Ψ to minimise $\langle \hat{H} \rangle$. One can often identify a set of trial wave functions, for example molecular orbitals of isolated atoms, as starting points to this process. The properties associated with the ground state are of particular importance for electronic structure calculations, as we shall see in Section 2.5.1 and 2.5.2.

2.3.5 Periodic Boundary Conditions

In our above discussion of crystalline solids, we have emphasised the translational symmetry of the lattice, but are yet to use this feature. As each unit cell is indistinguishable from another, the background potential of the crystal, and the resultant wave function, should also possess the same periodicity. Bloch stated that such a wave function can be written as the product of a plane wave, $\exp(i\mathbf{k}\cdot\mathbf{r})$ and a function $u(\mathbf{r}) = u(\mathbf{r}+\mathbf{T})$ with the same periodicity as the lattice,

$$\Psi(\mathbf{r}) = \exp(i\mathbf{k}\cdot\mathbf{r})u(\mathbf{r}). \tag{2.21}$$

By considering a system consisting of $N_1 \times N_2 \times N_3$ unit cells we can impose the Born-von Karman cyclic boundary condition, and so the Bloch function must satisfy,

$$\Psi(\mathbf{r}) = \Psi(\mathbf{r}+N_1\mathbf{a}_1) = \Psi(\mathbf{r}+N_2\mathbf{a}_2) = \Psi(\mathbf{r}+N_3\mathbf{a}_3). \tag{2.22}$$

As the $u(\mathbf{r})$ by definition has the periodicity of the lattice, we must instead enforce the above periodicity on the plane wave component,

$$\exp\left(i\mathbf{k}\cdot(\mathbf{r}+N_1\mathbf{a}_1)\right) = \exp\left(i\mathbf{k}\cdot(\mathbf{r}+N_2\mathbf{a}_2)\right) = \exp\left(i\mathbf{k}\cdot(\mathbf{r}+N_3\mathbf{a}_3)\right) \tag{2.23}$$

which is achieved when,

$$\exp(i\mathbf{k}\cdot N_1\mathbf{a}_1) = \exp(i\mathbf{k}\cdot N_2\mathbf{a}_2) = \exp(i\mathbf{k}\cdot N_3\mathbf{a}_3) = 1. \tag{2.24}$$

The arguments of the exponentials must be equal to an integer number of 2π, and so we can conclude that the allowed values of $\mathbf{k}$ are,

$$\mathbf{k} = \frac{m_1}{N_1}\mathbf{a}_1^* + \frac{m_2}{N_2}\mathbf{a}_2^* + \frac{m_3}{N_3}\mathbf{a}_3^*, \tag{2.25}$$

with integers m_1, m_2, and m_3. For infinitely large systems, $N_1, N_2, N_3 \to \infty$ and the allowed values of $\mathbf{k}$ becomes a continuum.

2.3.6 Fourier Transform

If we consider a function $f(\mathbf{r})$ within a three-dimensional crystal, it must satisfy,

$$f(\mathbf{r}+\mathbf{T}) = f(\mathbf{r}), \tag{2.26}$$

where **T** is the translation vector defined in equation ((2.1)).

We can instead consider the Fourier transform of the periodic function $f(\mathbf{r})$, as a function of wave vector **k**,

$$f(\mathbf{k}) = \frac{1}{\Omega_{\text{Crystal}}} \int_{\text{Crystal}} f(\mathbf{r}) \exp(i\mathbf{k}\cdot\mathbf{r})\, d\mathbf{r}, \tag{2.27}$$

where the total volume of the crystal, Ω_{Crystal}, can be obtained from the product of the volume of a single unit cell, Ω_{Cell}, and the total number of unit cells in the crystal, N_{Cell}. Making use of the lattice periodicity, we can replace the above integral over the whole crystal with a sum of integrals over each unit cell,

$$\begin{aligned} f(\mathbf{k}) &= \frac{1}{N_{\text{Cell}}\Omega_{\text{Cell}}} \sum_{\mathbf{T}}^{N_{\text{Cell}}} \int_{\text{Cell}} f(\mathbf{r}+\mathbf{T}) \exp\left(i\mathbf{k}\cdot(\mathbf{r}+\mathbf{T})\right) d\mathbf{r} \\ &= \frac{1}{N_{\text{Cell}}\Omega_{\text{Cell}}} \sum_{\mathbf{T}}^{N_{\text{Cell}}} \exp(i\mathbf{k}\cdot\mathbf{T}) \int_{\text{Cell}} f(\mathbf{r}) \exp(i\mathbf{k}\cdot\mathbf{r})\, d\mathbf{r}. \end{aligned} \tag{2.28}$$

We can now utilise equation ((2.3)), and the fact that all other values of **k** lead to Fourier components equal to zero, to give the Fourier transform of the periodic function,

$$f(\mathbf{G}) = \frac{1}{\Omega_{\text{Cell}}} \int_{\text{Cell}} f(\mathbf{r}) \exp(i\mathbf{G}\cdot\mathbf{r})\, d\mathbf{r}. \tag{2.29}$$

The Fourier transform is thus given by the discrete set of $f(\mathbf{G})$, where **G** is defined by the periodicity of the reciprocal space cell. The original function $f(\mathbf{r})$ can then be reconstructed from these Fourier coefficients using,

$$f(\mathbf{r}) = \sum_{m} f(\mathbf{G}_m) \exp(i\mathbf{G}_m\cdot\mathbf{r}). \tag{2.30}$$

Using this result, we can begin to assess the periodic wave function: we first write the i^{th} Bloch function for a given **k**, but write the lattice-periodic function as

a Fourier expansion [93],

$$\begin{aligned}\Psi_{i,\mathbf{k}}(\mathbf{r}) &= \exp(i\mathbf{k}\cdot\mathbf{r})u_{i,\mathbf{k}}(\mathbf{r}) \\ &= \exp(i\mathbf{k}\cdot\mathbf{r})\sum_m c_{i,\mathbf{k}}(\mathbf{G}_m)\exp(i\mathbf{G}_m\cdot\mathbf{r}) \\ &= \sum_m c_{i,\mathbf{k}}(\mathbf{G}_m)\exp\left(i(\mathbf{G}_m+\mathbf{k})\cdot\mathbf{r}\right).\end{aligned} \tag{2.31}$$

Thus, we are able to construct a wave function with the periodicity of the lattice, able to be decomposed into a linear combination of orthonormal plane waves, the coefficients of which can be determined using variational methods.

In principle, the sum over all reciprocal lattice translation vectors would include all of the infinite possible $\mathbf{G}_m$. In practice, this is not a viable procedure to complete, and so a truncation of the sum is required. Fortunately, the Fourier components for large $|\mathbf{G}_m + \mathbf{k}|$ are small, and so it is reasonable to expect lower energy solutions to the Schrödinger equation to dominate. Clearly, the inclusion of more terms in the expansion should lead to more accurate results, however at the cost of more computational effort. A cutoff value of $\mathbf{G}$ at which to truncate is chosen by specifying a 'cut-off' energy, E_{cut},

$$E_{cut} = \frac{\hbar^2|\mathbf{G}_{cut}|^2}{2m}. \tag{2.32}$$

2.3.7 Electronic Band Structure

Since we have a wave function that is determined for each $\mathbf{k}$ separately, we should have a corresponding set of $\mathbf{k}$-specific eigenvalues. Of course, due to the periodicity of the reciprocal lattice, these eigenvalues and eigenstates are periodic with any reciprocal translation vector $\mathbf{G}$. In the limit of large volumes, the $\mathbf{k}$-points become a dense continuum, as was outlined above, and so the eigenvalues become continuous energy bands. For each $\mathbf{k}$, there are a discrete set of eigenstates ($i = 1, 2, \cdots$) which can be found through diagonalisation of the Hamiltonian. The positions of these bands relative to each other, the band curvature, band occupation, and many other descriptors, are all important for determining electronic properties.

2.4 Hartree-Fock

One of the first attempts to simplify the many-body problem was provided by Hartree. Within this, we consider a many-body electron system as a system of N_e non-interacting electron-like particles. This allows us to decouple the many-body wave function into a product of N_e independent single-particle 'spin-orbitals', ψ_i, called the Hartree product:

$$\Psi_{HP}(\mathbf{x}_1, \cdots, \mathbf{x}_{N_e}) = \psi_1(\mathbf{x}_1) \cdots \psi_{N_e}(\mathbf{x}_{N_e}) = \prod_{i=1}^{N_e} \psi_i(\mathbf{x}_i). \tag{2.33}$$

Here, $\mathbf{x}_i \equiv \{\mathbf{r}_i, \sigma_i\}$ describes the set of spatial $\mathbf{r}_i$ and spin σ_i coordinates of the i^{th} particle. In the absence of spin-orbit interaction, $\psi_i(\mathbf{r}_j)$ can be written as a product of a function of the spatial position, $\phi_i^{\sigma}(\mathbf{r}_j)$, and a function of the spin variable, $\alpha_i(\sigma_j)$.

One major flaw with this description is that it fails to describe the behaviour required by identical fermionic particles, where an exchange of two particles should result in a change in the sign of the wave function due to its antisymmetry. This is resolved by considering instead the Slater determinant of the single-particle wave functions:

$$\Psi_{HF}(\mathbf{x}_1, \cdots, \mathbf{x}_{N_e}) = \frac{1}{\sqrt{N_e!}} \begin{vmatrix} \psi_1(\mathbf{x}_1) & \cdots & \psi_1(\mathbf{x}_{N_e}) \\ \vdots & \ddots & \vdots \\ \psi_{N_e}(\mathbf{x}_1) & \cdots & \psi_{N_e}(\mathbf{x}_{N_e}) \end{vmatrix}. \tag{2.34}$$

The Slater determinant form then satisfies the antisymmetric requirement of the fermionic wave function. This can be checked by the exchange of two rows resulting in a change in the sign of Ψ due to properties of a determinant, or by the determinant equalling zero when two states are set equal to each other hence satisfying the Pauli exclusion principle.

Using the above form of the wave function for the many-electron system, we can now obtain a form for the energy by considering the expectation value of the Hamiltonian (in the following, we employ Hartree atomic units $\hbar = m_e = e = 4\pi/\epsilon_0 = 1$). We make use of the requirement that the spin-orbitals be linearly independent and for simplicity assume the Hamiltonian is diagonal in the spin basis $\sigma = |\uparrow\rangle ; |\downarrow\rangle$,

giving the Hartree-Fock energy,

$$\begin{aligned} E_{HF} &= \langle \Psi_{HF} | \, \hat{H}_{HF} \, | \Psi_{HF} \rangle \\ &= \sum_i \langle i | \, \hat{h} \, | i \rangle + \frac{1}{2} \sum_{i,j} \left(\langle i | \, \hat{V}_{ij} \, | j \rangle - \langle i | \, \hat{V}_{jj} \, | i \rangle \right) \end{aligned} \tag{2.35}$$

where $|i\rangle \equiv \psi_i$ has been used for brevity. The term $\langle i | \, \hat{h} \, | i \rangle$ is the single-electron energy given by,

$$\langle i | \, \hat{h} \, | i \rangle = \int \psi_i^*(\mathbf{x}_i) \Big[-\frac{1}{2} \nabla_i^2 - \sum_{\alpha}^{N_{ion}} \frac{Z_\alpha}{|\mathbf{r}_i - \mathbf{R}_\alpha|} \Big] \psi_i(\mathbf{x}_i) d\mathbf{x}_i, \tag{2.36}$$

and contains both the kinetic energy of a single electron and the energy due to external potential due to, for example, electron-ion interactions.

The second sum in equation (2.35) contains the effects of direct Coulombic electron-electron repulsion and electron exchange, both obtained with appropriate index choice in,

$$\langle i | \, \hat{V}_{jk} \, | l \rangle = \int \psi_i^*(\mathbf{x}_1) \psi_j(\mathbf{x}_1) V(\mathbf{x}_1 - \mathbf{x}_2) \psi_k^*(\mathbf{x}_2) \psi_l(\mathbf{x}_2) d\mathbf{x}_1 d\mathbf{x}_2. \tag{2.37}$$

Th element $\langle i | \, \hat{V}_{jk} \, | l \rangle$ describes the scattering of one particle from state j to state i, and another particle in state l to state k, due to the presence of a two-particle potential $V(\mathbf{x}_1 - \mathbf{x}_2)$. For two electron-like particles, we shall assume a Coulomb-like potential, $V(\mathbf{x}_1 - \mathbf{x}_2) = \frac{1}{|\mathbf{r}_i - \mathbf{r}_j|}$. Whilst equation (2.35) includes fictitious self-interaction term when $i = j$, the Coulomb and exchange terms are identical for $i = j$, so they cancel in the summation and any self-interaction is ignored.

In equation (2.35), we can see that the third term (electronic exchange) is to always lower the energy of the system. Hence, it can be interpreted for each electron as an interaction between the electron and a positively charged 'exchange hole' surrounding it, with the electronic charge associated with this 'hole' being redistributed (to preserve the charge of the whole system).

We then reach the Hartree-Fock equations,

$$\begin{aligned} &\Bigg[-\frac{1}{2} \nabla^2 + V_{ext} + \sum_j \int \psi_j^*(\mathbf{x}_j) \frac{1}{|\mathbf{r}_i - \mathbf{r}_j|} \psi_j(\mathbf{x}_j) d\mathbf{x}_j \\ &- \sum_j \int \psi_j^*(\mathbf{x}_j) \psi_i(\mathbf{x}_j) \frac{1}{|\mathbf{r}_i - \mathbf{r}_j|} \frac{\psi_j(\mathbf{x}_i)}{\psi_i(\mathbf{x}_i)} d\mathbf{x}_j \Bigg] \psi_i(\mathbf{x}_i) = \varepsilon_i \psi_i(\mathbf{x}_i), \end{aligned} \tag{2.38}$$

where the term in square brackets is the Fock operator, $\hat{F}$,

$$\hat{F} = \hat{h} + \hat{V}_H + \hat{V}_{ex}. \tag{2.39}$$

The first term is the single-electron Hamiltonian,

$$\hat{h} = -\frac{1}{2}\nabla^2 + V_{ext}, \tag{2.40}$$

the second is the Hartree operator (for electrons of the same spin [94]),

$$V_H(\mathbf{x}_i) = \sum_j \int \frac{|\psi_j(\mathbf{x}_j)|^2}{|\mathbf{r}_i - \mathbf{r}_j|} d\mathbf{x}_j. \tag{2.41}$$

and the third is the exchange operator,

$$V_{ex}(\mathbf{x}_i) = -\sum_j \frac{\psi_j(\mathbf{x}_i)}{\psi_i(\mathbf{x}_i)} \int \frac{\psi_j^*(\mathbf{x}_j)\psi_i(\mathbf{x}_j)}{|\mathbf{r}_i - \mathbf{r}_j|} d\mathbf{x}_j. \tag{2.42}$$

The Hartree-Fock approach aims to minimise the energy ε_i above with respect to all degrees of freedom of the spin-orbital $\psi_i(\mathbf{x}_i)$ whilst still satisfying the Slater determinant. However, it is largely limited to special cases like the homogeneous electron gas.

The Hartree-Fock approach has offered a lot of success, being able to provide an exact description of electronic exchange (Fermi correlation), which prevents two parallel-spin electrons from being found at the same point in space and includes the effects of exchanging two identical electrons. However, it does not account for the Coulomb correlation, which describes the correlation between the spatial position of electrons of opposite spin due to their Coulombic repulsion [94, 95]. Electronic exchange is often abbreviated to 'exchange' and Coulomb correlation to 'correlation'. We shall see in the next section that obtaining accurate descriptions of the exchange and correlation of electronic systems is the largest challenge faced in *ab initio* calculations of electronic structure, and considerable care must be taken in choosing an appropriate description.

2.5 *ab initio* Density Functional Theory

A solid is composed of a large number of electrons and nuclei, and to determine the electronic and energetic properties of a system a solution to the many-body

Schrödinger equation is required. Considering the large number of bodies involved, the mutual interactions between electrons and nuclei, and the dynamics of these individual particles, obtaining this solution is an extremely difficult task. Unlike Hartree-Fock or more sophisticated methods like many-body perturbation theory which are based on the wave function, density functional theory (DFT), as the name might suggest, considers the electronic charge density as the quantity of interest.

DFT is a principal tool used in the study of materials and calculation of electronic structure for both crystalline solids and single molecules. This first principles approach aims to make as few assumptions as possible, relying on the fundamentals of physics and quantum chemistry to achieve a complete description of a given material. In the following, we shall explore the core ideas and theories that go into building a successful DFT methodology. For brevity, we have not explicitly addressed spin in much of the following, however, an extension to include spin is possible and does not dramatically change the main proofs or conclusions presented. We will also make use of Hartree atomic units ($\hbar$ = m_e = e = $4\pi/\epsilon_0$ = 1) for similar reasons.

2.5.1 Hohenberg-Kohn Theorems

Consider an collection of an arbitrary number of electrons, in a large box, under the influence of an arbitrary external potential, $V_{\text{ext}}(\mathbf{r})$, and mutual Coulomb interaction (an 'inhomogeneous electron gas' [96]). The electronic Hamiltonian can be reduced to the form,

$$\hat{H}_{el} = \hat{T}_{el} + \hat{V}_{el-el} + \hat{V}_{ext}, \tag{2.43}$$

where $\hat{T}_{el}$ is the kinetic energy of the electrons, $\hat{V}_{el-el}$ is the interaction potential between electrons, and $\hat{V}_{ext}$ is an externally applied potential (for example, from nuclei) [96]. The density of particles, $n(\mathbf{r})$, is given by the expectation value of the

density operator $n(\mathbf{r}) = \sum_{i=1}^{N} \delta(\mathbf{r} - \mathbf{r}_i)$,

$$\begin{aligned} n(\mathbf{r}) &= \frac{\langle\psi|\,\hat{n}(\mathbf{r})\,|\psi\rangle}{\langle\psi|\psi\rangle} \\ &= N\,\frac{\int d\mathbf{r}_2, \cdots, d\mathbf{r}_N |\psi(\mathbf{r}, \mathbf{r}_2, \cdots, \mathbf{r}_N)|^2}{\int d\mathbf{r}_1, d\mathbf{r}_2, \cdots, d\mathbf{r}_N |\psi(\mathbf{r}_1, \mathbf{r}_2, \cdots, \mathbf{r}_N)|^2}. \end{aligned} \tag{2.44}$$

Note the numerator is not integrated over $d\mathbf{r}_1$, and the $\mathbf{r}_1$ in ψ is replaced by $\mathbf{r}$ to avoid carrying an unnecessary index throughout the following. This is the same as the normalisation condition,

$$\int d\mathbf{r}\; n(\mathbf{r}) = N \tag{2.45}$$

The total energy, E, is the expectation value of the Hamiltonian, given by

$$\begin{aligned} E &= \frac{\langle\psi|\,\hat{H}\,|\psi\rangle}{\langle\psi|\psi\rangle} \\ &= \langle\hat{T}_{el}\rangle + \langle\hat{V}_{el-el}\rangle + \int d\mathbf{r}\, V_{\text{ext}}(\mathbf{r}) n(\mathbf{r}), \end{aligned} \tag{2.46}$$

where the expectation of the external potential has been explicitly written as an integral over the density function.

The first of the Hohenberg-Kohn Theorems is: *For any system of interacting particles, in an external potential $V_{\text{ext}}(\boldsymbol{r})$, the potential is determined completely, except for an additive constant, by the ground state density, $n_0(\boldsymbol{r})$.*

Suppose now that there are two different external potentials, $V_{\text{ext}}^{(1)}(\mathbf{r})$ and $V_{\text{ext}}^{(2)}(\mathbf{r})$, which differ by more than an additive constant, but lead to the same ground state density $n_0(\mathbf{r})$. The two external potentials lead to two different Hamiltonians, $\hat{H}^{(1)}$ and $\hat{H}^{(2)}$, and different ground state wave functions, $\psi^{(1)}$ and $\psi^{(2)}$, hypothesized to have the same ground state density $n_0(\mathbf{r})$. Unless $V_{\text{ext}}^{(1)}(\mathbf{r}) - V_{\text{ext}}^{(2)}(\mathbf{r})$ is a constant, the two wave functions, $\psi^{(1)}$ and $\psi^{(2)}$, cannot be equal as they satisfy two different Schrödinger equations [96]. Since $\psi^{(2)}$ is not the ground state of $\hat{H}^{(1)}$, it follows,

$$E^{(1)} = \left\langle\psi^{(1)}\right|\hat{H}^{(1)}\left|\psi^{(1)}\right\rangle < \left\langle\psi^{(2)}\right|\hat{H}^{(1)}\left|\psi^{(2)}\right\rangle. \tag{2.47}$$

The last term in equation (2.47) can be written as,

$$\begin{aligned} \left\langle\psi^{(2)}\right|\hat{H}^{(1)}\left|\psi^{(2)}\right\rangle &= \left\langle\psi^{(2)}\right|\hat{H}^{(2)}\left|\psi^{(2)}\right\rangle + \left\langle\psi^{(2)}\right|(\hat{H}^{(1)} - \hat{H}^{(2)})\left|\psi^{(2)}\right\rangle \\ &= E^{(2)} + \int d\mathbf{r}\left[V_{\text{ext}}^{(2)}(\mathbf{r}) - V_{\text{ext}}^{(1)}(\mathbf{r})\right] n_0(\mathbf{r}). \end{aligned} \tag{2.48}$$

and so,

$$E^{(1)} < E^{(2)} + \int d\mathbf{r} \left[V_{\text{ext}}^{(1)}(\mathbf{r}) - V_{\text{ext}}^{(2)}(\mathbf{r})\right] n_0(\mathbf{r}). \tag{2.49}$$

If, however, we consider $E^{(2)}$ in the same way, we can find exactly the same equation, but with the superscripts (1) and (2) interchanged, resulting in,

$$E^{(2)} < E^{(1)} + \int d\mathbf{r} \left[V_{\text{ext}}^{(2)}(\mathbf{r}) - V_{\text{ext}}^{(1)}(\mathbf{r})\right] n_0(\mathbf{r}). \tag{2.50}$$

Adding equations (2.49) and (2.50) we get the contradictory inequality $E^{(1)} + E^{(2)} < E^{(2)} + E^{(1)}$. Therefore, different external potentials, differing by more than a constant, will always produce different densities. This confirms the first Theorem, in that the ground state particle density uniquely determines the external potential, to within a constant [93]: for any given ground state particle density there can only be one corresponding external potential. To be able to have a quantum theory based on density, the opposite must also be true, i.e. the external potential determines the resulting ground state density. A corollary of this is that since the Hamiltonian is fully determined, except for the constant shift in energy, the many-body wave functions for all states (ground and excited) are also determined, with the ground state being the one with the lowest energy. Hence, given a ground state density $n_0(\mathbf{r})$, all properties of the system are completely determined.

Whilst this result holds much promise, the original problem still remains: solving the many-body problem, with interacting electrons, moving in an external potential. Though the many-body ground state wave function is a unique functional of the ground state particle density, $\psi(\mathbf{r}_1, \mathbf{r}_2, \cdots, \mathbf{r}_N) \equiv \psi[n_0(\mathbf{r})]$, the functional is not known [94].

The second of the Hohenberg-Kohn Theorems is: *For any external potential* $V_{\text{ext}}(\mathbf{r})$*, there exists a universal functional for the energy,* $E[n(\mathbf{r})]$*, in terms of the particle density* $n(\mathbf{r})$*. For a given* $V_{\text{ext}}(\mathbf{r})$*, the exact ground state produces the global minimum in this energy functional, and the density* $n(\mathbf{r})$ *that minimises the functional is the exact ground state density,* $n_0(\mathbf{r})$*.*

We have seen that the external potential applied to a system is uniquely determined by $n(\mathbf{r})$. All other ground state properties of the system, such as kinetic

energy, are also uniquely determined by $n(\mathbf{r})$ once specified, and as such we can consider each as a functional of $n(\mathbf{r})$:

$$\begin{aligned} E_{HK}[n] &= T[n] + E_{el-el}[n] + \int d\mathbf{r}\, V_{\text{ext}}(\mathbf{r}) n(\mathbf{r}) \\ &\equiv F_{HK} + \int d\mathbf{r}\, V_{\text{ext}}(\mathbf{r}) n(\mathbf{r}), \end{aligned} \tag{2.51}$$

where we have neglected nuclei interactions. The functional F_{HK} includes all internal energy terms of the interacting electron system. These terms are of the same form for all systems consisting of electrons, regardless of the number of particles or external potential [96]. For different particles (e.g. different masses, interactions, etc.) there will be correspondingly different functionals. Note that the discussion so far applies irrespective of the level of interaction. For example, the case of 'non-interacting electrons', fermions with electronic mass but with no interactions between them. This idea will be useful when discussing the Kohn-Sham equations later [93].

Consider a system with ground state energy $n^{(1)}(\mathbf{r})$ and associated external potential $V_{\text{ext}}^{(1)}(\mathbf{r})$. In the unique ground state, $\psi^{(1)}$, the expectation value of the Hamiltonian is given by $E^{(1)} = E[n^{(1)}] = \left\langle \psi^{(1)} \right| \hat{H}^{(1)} \left| \psi^{(1)} \right\rangle$. Now consider a different state $\psi^{(2)}$, with particle density $n^{(2)}(\mathbf{r})$: $E^{(2)}$ is greater than $E^{(1)}$, as $E^{(1)}$ is the ground state energy. It follows that if the functional $F_{HK}[n]$ is known, one could find the ground state density and energy by minimising $E_{HK}[n]$ with respect to the particle density [94], as outlined by the second Theorem. Unfortunately it is not easy to minimise an unknown functional, as all we know at this time is that it exists. The complexity of determining the functional $F_{HK}[n]$, and hence $E_{HK}[n]$, arises from the description of the many-body electron interactions [96].

The variational property of the Hohenberg-Kohn functional is a direct consequence of the general variational principle in quantum mechanics. We have therefore demonstrated an algorithm by which it is possible to find the ground state: instead of solving the Schrödinger equation to find the 3N-dimensional wave function, we need to find a function of three spatial dimensions in the form of the charge density. The functional $E[n]$ is sufficient to determine the ground state energy and density. In general, excited states must be determined by other means [93].

2.5.2 Kohn-Sham Single-Particle Equations

The approach of Kohn and Sham [97] is to replace the complex many-body interacting system with a system that is a fictitious ensemble of non-interacting particles which is much easier to solve. The ansatz of Kohn and Sham assumes that the ground state density of the original system (with interactions) is equal to that of a chosen non-interacting system. This makes the particles independent of each other, leading to a series of single-particle equations that can, in principle, be solved. The construction of the auxiliary system is built upon two assumptions [93]:

1. The ground state density of the true many-body system can be represented by the ground state density of an auxiliary system of non-interacting particles. This is called 'non-interacting-V-representability'.

2. The Hamiltonian of the auxiliary system is chosen to have an independent-particle kinetic energy term and an effective local potential $V_{\text{eff}}(\mathbf{r})$, for particle at position $\mathbf{r}$.

The Hamiltonian for the auxiliary system is given by,

$$\hat{H}_{\text{aux}} = \hat{T}_s + \hat{V}_{\text{eff}}(\mathbf{r}), \tag{2.52}$$

where we have included the kinetic energy term for the Kohn-Sham electron-like particles, $\hat{T}_s$, and the effective potential $\hat{V}_{\text{eff}}(\mathbf{r})$ which includes the interactions which are not included in the auxiliary system. This set of single-particle Schrödinger-like equations is then satisfied by the Kohn-Sham orbital eigenstates $\phi_i(\mathbf{r})$:

$$\hat{H}_{\text{aux}}\,\phi_i(\mathbf{r}) = \epsilon_i \phi_i(\mathbf{r}). \tag{2.53}$$

These Kohn-Sham orbitals are required to reconstruct the particle density,

$$n(\mathbf{r}) = \sum_{i=1}^{N} |\phi_i(\mathbf{r})|^2, \tag{2.54}$$

with summation over occupied eigenstates.

The kinetic energy operator of the independent-particles is functionally the same as for the true electrons, but the resultant kinetic energy in general differs from that of the true electron kinetic energy, $T_s \neq T$,

$$T_s = -\frac{1}{2}\sum_{i=1}^{N}\int \phi_i^*(\mathbf{r})\nabla^2\phi_i(\mathbf{r})d\mathbf{r} \tag{2.55}$$

Writing the effective potential out explicitly, then, we can decompose it into the different contributions present in the real system,

$$\begin{aligned} V_{\text{eff}}[n(\mathbf{r})] &= \int V_{\text{ext}}(\mathbf{r})n(\mathbf{r})d\mathbf{r} + \frac{1}{2}\int \frac{n(\mathbf{r})n(\mathbf{r}')}{|\mathbf{r}-\mathbf{r}'|}d\mathbf{r}d\mathbf{r}' + E_{\text{xc}}[n(\mathbf{r})] \\ &= E_{\text{ext}}[n(\mathbf{r})] + E_H[n(\mathbf{r})] + E_{\text{xc}}[n(\mathbf{r})]. \end{aligned} \tag{2.56}$$

In this effective potential, we have included any present external potentials (such as those due to nuclei), $E_{\text{ext}}[n(\mathbf{r})]$, the Hartree energy relating to Coulombic interactions, $E_H[n(\mathbf{r})]$, and an extra term $E_{\text{xc}}[n(\mathbf{r})]$ which includes all of the complex many-body interactions between electrons. This final term, E_{xc}, is referred to as the 'exchange-correlation' energy, and will be discussed more in the next section.

Kohn and Sham demonstrated [97] that solving the above Schrödinger-like equations is equivalent to minimising the energy functional,

$$E_{\text{KS}}[n(\mathbf{r})] = T_s[n(\mathbf{r})] + E_{\text{ext}}[n(\mathbf{r})] + E_H[n(\mathbf{r})] + E_{\text{xc}}[n(\mathbf{r})] \tag{2.57}$$

with respect to the particle density, as is required by the Hohenberg-Kohn theorems. To do this minimisation, instead of varying the density $n(\mathbf{r})$ we vary the Kohn-Sham orbital wave function, $\phi_i(\mathbf{r})$,

$$\begin{aligned} \frac{\delta}{\delta\phi_i(\mathbf{r})}E_{KS}[n(\mathbf{r})] &= \frac{\delta}{\delta\phi_i^*(\mathbf{r})}E_{KS}[n(\mathbf{r})] \\ &= \frac{\delta T_s[\phi_i^*(\mathbf{r})]}{\delta\phi_i^*(\mathbf{r})} + \frac{\delta E_{\text{ext}}[n(\mathbf{r})]}{\delta\phi_i^*(\mathbf{r})} + \frac{\delta E_H[n(\mathbf{r})]}{\delta\phi_i^*(\mathbf{r})} + \frac{\delta E_{\text{xc}}[n(\mathbf{r})]}{\delta\phi_i^*(\mathbf{r})} \\ &= \frac{\delta T_s[\phi_i^*(\mathbf{r})]}{\delta\phi_i^*(\mathbf{r})} + \left[\frac{\delta E_{\text{ext}}[n(\mathbf{r})]}{\delta n(\mathbf{r})} + \frac{\delta E_H[n(\mathbf{r})]}{\delta n(\mathbf{r})} + \frac{\delta E_{\text{xc}}[n(\mathbf{r})]}{\delta n(\mathbf{r})}\right]\frac{\delta n(\mathbf{r})}{\delta\phi_i^*(\mathbf{r})} \\ &= 0. \end{aligned} \tag{2.58}$$

The choice to vary of the wave function over the density is due to the term T_s being explicitly dependent on the orbitals through equation (2.55) and,

$$\frac{\delta T_s}{\delta\phi_i^*(\mathbf{r})} = -\frac{1}{2}\sum_{i=1}^{N}\nabla^2\phi_i(\mathbf{r}) \tag{2.59}$$

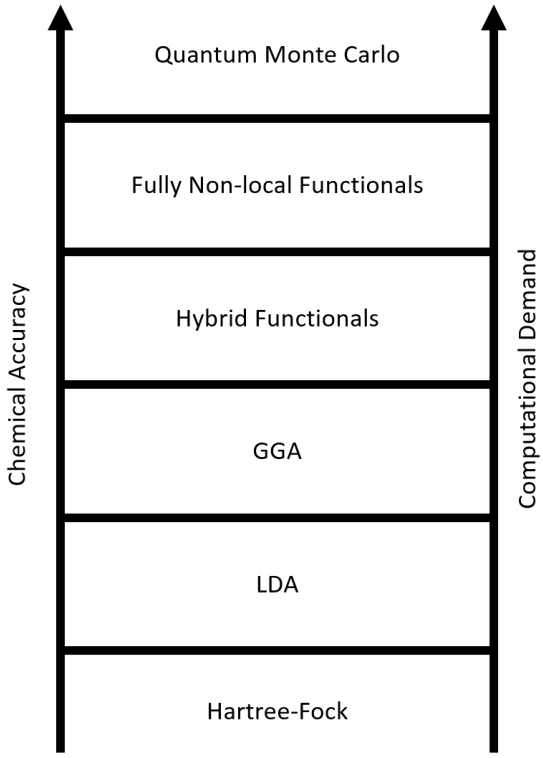

Figure 2.2: Jacob's Ladder of DFT, indicating the relative chemical accuracy and cost of different methods used for many-body problems.

and the dependence of the density on the Kohn-Sham wave function through equation (2.54) and,

$$\frac{\delta n(\mathbf{r})}{\delta \phi_i^*(\mathbf{r}')} = \phi_i(\mathbf{r})\delta(\mathbf{r} - \mathbf{r}'). \tag{2.60}$$

As a consequence of the Kohn-Sham approximation, we are thus able to replace a real system consisting of many interacting particles with an simplified system with no interactions. To account for the lack of interactions that would be present in a real system (and hence are required for any realistic description) we introduce an effective 'exchange-correlation' potential. Solving the single particle Kohn-Sham equations using variational methods then allows us to find the ground state density and energy in theory exactly [98, 99], but in practice is limited by the accuracy of this exchange-correlation functional.

2.5.3 Exchange-Correlation Functionals

We mentioned in Section 2.5.2 the 'exchange-correlation' correction term to the energy of the non-interacting electron system, $E_{\mathrm{xc}}[n(\mathbf{r})]$. This comes about from us mapping one N-body problem onto N one-body problems. Within this corrective term, all of the information of the complex many-body interactions between electrons is held: "*our ignorance is hidden there*". This term has been shown to exist, and have a functional dependence on the particle density, $n(\mathbf{r})$, however this functional dependence is essentially unknowable [100]. One of the first attempts to model these functionals was made by means of Monte Carlo methods applied to the uniform electron-gas, for a range of densities, and then paramaterised to yield density functionals. It is important to keep in mind that all practically used functionals are approximations. Their benefit, however, comes from the reduction in computational effort when compared to calculating an exact solution.

Due to the variety of chemical environments, from strong covalent bonds found in isolated organic molecules to metals and ionic crystals, no functional currently exists that can accurately describe all properties of interest for all materials, though some inevitably prove more useful in a wider range of contexts than others. The range of functionals available has led to a 'Jacob's Ladder' of DFT, with the respective rungs of representing different levels of approximation. Each rung should be able to reproduce the results of lower rungs in appropriate limits, but also introduce more capabilities, better chemical accuracy, and a wider range of applicability, though these advantages usually come at the cost of computational effort. We present an example Jacob's Ladder in Figure 2.2, where we have included the Hartree-Fock method discussed in Section 2.4, the LDA, GGA, and hybrid functionals which will be discussed in the following, as well as fully non-local functionals and quantum Monte Carlo methods.

Local Density Approximation

The local density approximation (LDA) is the simplest functional for describing the exchange-correlation energy. This approximation assumes the electronic density of an inhomogeneous electron density is a slowly varying function in space, and

locally behaves like a homogeneous electron gas. To describe the homogeneous electron gas, then, N_e electrons are placed in a volume V, with a positive background charge to retain a neutral charge within the system. N and V are then taken to infinity in a manner than preserves a finite density $n = N_e/V$. In the following, we will also make use of the quantity, r_s, which is more commonly used in place of the density. This is defined as the radius of a sphere containing one electron on average,

$$n = \frac{N_e}{V} = \left(\frac{4\pi}{3} r_s^3\right)^{-1}. \tag{2.61}$$

The LDA proves very useful as the kinetic energy, electrostatic interaction energy, and the exchange energy of a homogeneous electron gas are all known. Further, the wave function is able to be expressed in terms of plane waves. The exchange-correlation energy, depending only on the electronic density at that point, is written as,

$$E_{\mathrm{xc}}^{\mathrm{LDA}}[n(\mathbf{r})] = \int n(\mathbf{r}) \epsilon_{\mathrm{xc}}^{LDA}[n(\mathbf{r})]\, d\mathbf{r}, \tag{2.62}$$

where we have used the corresponding energy per electron, $\epsilon_{\mathrm{xc}}^{LDA}$. The corresponding exchange-correlation potential can be expressed as,

$$\begin{aligned} V_{\mathrm{xc}}^{\mathrm{LDA}}[n(\mathbf{r})] &= \frac{d}{dn}\left\{ \epsilon_{\mathrm{xc}}^{LDA}[n(\mathbf{r})] n(\mathbf{r}) \right\} \\ &= \epsilon_{\mathrm{xc}}^{LDA} + n \frac{\partial \epsilon_{\mathrm{xc}}}{\partial n} \\ &= \epsilon_{\mathrm{xc}}^{LDA} - \frac{r_s}{3} \frac{d\epsilon_{\mathrm{xc}}^{LDA}}{dr_s}. \end{aligned} \tag{2.63}$$

This exchange-correlation energy is often linearly decomposed into exchange and correlation terms,

$$\begin{aligned} E_{\mathrm{xc}}[n(\mathbf{r})] &= E_{\mathrm{x}}[n(\mathbf{r})] + E_{\mathrm{c}}[n(\mathbf{r})] \\ &= \int n(\mathbf{r}) \epsilon_{\mathbf{x}}[n(\mathbf{r})]\, d\mathbf{r} + \int n(\mathbf{r}) \epsilon_{\mathrm{c}}[n(\mathbf{r})]\, d\mathbf{r}, \end{aligned} \tag{2.64}$$

so that expressions for the exchange and correlation energies are independently sought. Though the exchange term for the homogeneous electron gas is known analytically,

$$\epsilon_{\mathrm{x}}[n(\mathbf{r})] = -\frac{3}{4}\left(\frac{3}{\pi}\right)^{\frac{1}{3}} n(\mathbf{r})^{\frac{1}{3}}, \tag{2.65}$$

the correlation energy is only known for special cases of electron gases with high density (small r_s) [93, 101],

$$\epsilon_c(r_s) = A \ln r_s + B + r_s(C \ln r_s + D) + \cdots , \tag{2.66}$$

or low density (large r_s) [93, 102],

$$\epsilon_c(r_s) = \frac{a_1}{r_s} + \frac{a_2}{r_s^{\frac{3}{2}}} + \frac{a_3}{r_s^2} + \cdots . \tag{2.67}$$

Beyond these two limiting cases, different approximations of the correlation energy have consequently led to different forms of the LDA functional [103–105]. The LDA functional has been used for a generation in the materials science community, however it is not accurate for most chemical purposes. Some typical errors the LDA functional encounters include its over-binding of compounds, leading to higher binding energies, and an underestimation of lattice parameters.

Generalised Gradient Approximation

Functionals using the genaralised gradient approximation (GGA) contain the next term in the derivative expansion of the charge density, requiring information of both the density and the gradient of the density at that point. They have been shown to offer improvements to their LDA predecessors, offering improved total and atomisation energies [106–109], energy barriers and structural energy differences [110–114], and soften atomic bonding, correcting some LDA prediction [115]s. The exchange-correlation energy is given by,

$$E_{\mathrm{xc}}^{\mathrm{GGA}}[n(\mathbf{r})] = \int n(\mathbf{r}) \epsilon_{\mathrm{xc}}^{GGA}[n(\mathbf{r}), \nabla n(\mathbf{r})] \, d\mathbf{r}, \tag{2.68}$$

The exchange-correlation potentials take the form [93],

$$V_{\mathrm{xc}}^{\mathrm{GGA}}[n(\mathbf{r})] = \epsilon_{\mathrm{xc}}^{GGA} + n \frac{\partial \epsilon_{\mathrm{xc}}^{GGA}}{\partial n} - \nabla \left(n \frac{\partial \epsilon_{\mathrm{xc}}^{GGA}}{\partial \nabla n} \right). \tag{2.69}$$

Some commonly used GGA functionals include the Becke 1988 (B88) [116], Purdew-Wang 1991 (PW91) [106], Armiento-Mattsson 2005 (AC05) [117], and Wu-Cohen 2006 [118] variants. However, the majority of the work completed for this thesis has been carried out using the Perdew, Burke, and Ernzerhof [119, 120]

(PBE) form of the GGA functional. The PBE functional arose from the need for a functional that performed better than the available semi-empirical functionals, particularly for systems with delocalised electrons (such as in simple metals). It also improved upon the PW91 functional through a simpler derivation (hence easier understanding and application), relying on less parameter fitting, and provided a better recovery of LDA results [119].

For the PBE functional, we break the exchange-correlation energy into the exchange contribution and the correlation contribution. First, the exchange energy is given through a exchange-specific form of equation (2.68),

$$E_{\mathrm{x}}^{\mathrm{PBE}}[n(\mathbf{r})] = \int n(\mathbf{r})\epsilon_{\mathrm{x}}^{hom}[n(\mathbf{r})]F_{\mathrm{x}}\, d\mathbf{r}, \tag{2.70}$$

where $\epsilon_{\mathrm{x}}^{hom}$ is the exchange energy of the electron gas, and F_{x} is a dimensionless quantity given by,

$$F_{\mathrm{x}} = 1 + \kappa - \frac{\kappa}{1 + \frac{\mu s^2}{\kappa}}, \tag{2.71}$$

with $\kappa = 0.804$, $\mu = 0.220$, and s is a dimensionless gradient of the charge density given by $|\nabla n|/2k_F n$.

The correlation is then given by,

$$E_{\mathrm{c}}^{\mathrm{PBE}}[n(\mathbf{r})] = \int n(\mathbf{r})\left(\epsilon_{\mathrm{c}}^{hom}(r_s,\zeta) + H(r_s,\zeta,t)\right) d\mathbf{r}, \tag{2.72}$$

where r_s was defined above, $\zeta = (n^{\uparrow} - n^{\downarrow})/2$ is the spin polarisation, and t is another dimensionless gradient related to s. We now define $\phi = ((1+\zeta)^{2/3} + (1-\zeta)^{2/3})/2$, allowing us to write H as,

$$H = \frac{e^2}{a_0}\gamma\phi^3 \ln\left(1 + \frac{\beta}{\gamma}t^2\frac{1 + At^2}{1 + At^2 + A^2t^4}\right), \tag{2.73}$$

where A is given by,

$$A = \frac{\beta}{\gamma}\left[\exp\left(\frac{-\epsilon_{\mathrm{c}}^{hom}}{\gamma\phi^3\frac{e^2}{a_0}}\right)\right]^{-1}. \tag{2.74}$$

Since its release, the PBE functional has been used extensively within the materials science community for a range of materials, and is often used as a benchmark by which other functionals or methods are assessed [121–124]. At the time of writing, the original article discussing the PBE functional is one of the most cited papers ever, having over 130,000 citations [119, 125–127], highlighting its exhaustive use and wide-spread success.

Hybrid Functionals

Local and semi-local functionals such as those built upon LDA and GGA typically underestimate electronic band gaps, whereas the band gaps predicted using the Hartree-Fock method tend to be too large compared with experiment. We also saw in the above discussions that such semi-local functionals can lead to over-binding or under-binding of molecules. As a result, the mixing of the DFT and Hartree-Fock approaches was suggested by Becke in 1993 [128] as a method to more accurately describe molecular bonding. These 'hybrid' functionals typically build upon GGA functionals, providing a more accurate description of atomisation energies, bond lengths, and vibrational frequencies of most molecules [129]. The exact exchange energy is calculated using Hartree-Fock method, and this is mixed with the exchange energy calculated with a GGA functional. As GGA functionals only consider up to semi-local effects, hybrid functional calculations are typically more costly as the exact exchange is a non-local effect: the exchange interaction in insulators decays exponentially as a function of the band gap, and algebraically in metallic systems [130]. The mixing scheme is broadly achieved as follows:

$$E_{\mathrm{xc}}^{Hybrid} = \alpha E_{\mathrm{x}}^{HF} + (1-\alpha) E_{\mathrm{x}}^{DFT} + E_{\mathrm{c}}^{DFT}, \tag{2.75}$$

where $0 \leq \alpha \leq 1$ is a parameter to be decided (usually ~ 0.2), E_{c}^{DFT} is the correlation energy determined from DFT methods, and E_{x}^{HF} and E_{x}^{DFT} are the exchange energies obtained using Hartree-Fock and DFT methods, respectively. The apparent improvements that come from these functionals arise from the inclusion of a non-dynamical 'static correlation' effect which effectively delocalises the GGA exchange hole [130]. The choice of α is usually decided by comparing results from DFT to experiment; at this point the DFT calculation is no longer *ab initio*.

Some commonly used hybrid functionals include the B3LYP (Becke 3-parameter [109], Lee-Yang-Parr [131]) functional [132–134] and PBE0 [129]. Where hybrid functionals are used in this work, however, we shall employ the HSE06 functional proposed by Heyd, Scuseria and Ernzerhof [130, 135], which builds upon the GGA-PBE functional. This applies a screened Coloumb potential to the exchange interaction, thus screening the long-range part of the Hartree-Fock exchange.

As a result, there is mixing of exact exchange only for short-range interactions, allowing the exchange hole to be delocalised among the near neighbours of a reference point, but not beyond. The purpose of this screening was to avoid the divergence that arises at $k = 0$ in the Fourier transform of the Coulomb potential.

We split the Coulomb potential into a short-range (SR) and long-range (LR) interaction,

$$\frac{1}{r} = \frac{\mathrm{erfc}(\omega \mathrm{r})}{r} + \frac{\mathrm{erf}(\omega \mathrm{r})}{r}. \tag{2.76}$$

The first of these terms represents the SR interaction, and the second represents the LR interaction, with ω an adjustable parameter which governs the extent of the short-range interactions. Looking again at equation (2.75), specifying the PBE form of GGA, we have,

$$E_{\mathrm{xc}}^{Hybrid} = \alpha E_{\mathrm{x}}^{HF} + (1-\alpha) E_{\mathrm{x}}^{PBE} + E_{\mathrm{c}}^{PBE}. \tag{2.77}$$

We now specify the SR and LR interactions for each of these terms,

$$\begin{aligned} E_{\mathrm{xc}}^{Hybrid} = {} & \alpha E_{\mathrm{x}}^{HF,SR}(\omega) + \alpha E_{\mathrm{x}}^{HF,LR}(\omega) \\ & + (1-\alpha) E_{\mathrm{x}}^{PBE,SR}(\omega) + (1-\alpha) E_{\mathrm{x}}^{PBE,LR}(\omega) + E_{\mathrm{c}}^{PBE}. \end{aligned} \tag{2.78}$$

The authors of the functional found that the long-range exchange for HF and PBE contributions could be omitted as they are small and tend to cancel each other. Thus,

$$E_{\mathrm{xc}}^{Hybrid} = \alpha E_{\mathrm{x}}^{HF,SR}(\omega) + (1-\alpha) E_{\mathrm{x}}^{PBE,SR}(\omega) + E_{\mathrm{x}}^{PBE,LR}(\omega) + E_{\mathrm{c}}^{PBE}. \tag{2.79}$$

A value of $\alpha = 0.25$ is usually taken, as determined from perturbation theory [130]. When $\omega = 0$, the above expression is equivalent to the PBE0 functional, and asymptotically approaches PBE as $\omega \to \infty$. The authors found a value of $\omega = 0.106$ [135].

Hubbard-U Parameter

For many materials, the LDA approach provides a reliable description of the ground state electronic structure. However, the LDA and semilocal GGA functionals often fail to accurately describe systems with localized (strongly correlated)

or partially filled *d* or *f* shells, such as with transition metal oxides. This usually results in unrealistic one-electron energies or too small magnetic moments, for example, transition metal compounds like NiO experience a strong on-site Coulomb repulsion between the 3*d* electrons due to the narrow band width of the *d*-electrons, which is not described in a spin-polarised DFT treatment. In some cases this can be remedied by introducing on the *d* or *f* atom a strong intra-atomic interaction in a simplified (screened) Hartree-Fock like manner between electrons (E_U) as an on-site replacement of the semilocal functional. To account for the double-counting of the electron-electron interactions that are already present in a DFT functional, a double-counting correction term (E_{dc}) is also included:

$$E_{\mathrm{xc}}^{LDA/GGA+U} = E_{\mathrm{xc}}^{LDA/GGA} + E_U - E_{dc}. \tag{2.80}$$

This method is known as the DFT+U method.

The approach of Dudarev [136] is to account for the orbital degeneracy of *d*-shell electrons using a Hamiltonian of the form,

$$\hat{H} = \frac{U}{2} \sum_{m,m',\sigma} \hat{n}_{m,\sigma}\hat{n}_{m',-\sigma} + \frac{U-J}{2} \sum_{m\neq m',\sigma} \hat{n}_{m,\sigma}\hat{n}_{m',\sigma}. \tag{2.81}$$

Here, $\hat{n}_{m,\sigma} = \hat{a}^{\dagger}_{m,\sigma}\hat{a}_{m,\sigma}$ is the operator for the number of electrons occupying a particular site with magnetic quantum number m and spin σ. U is a spherically averaged Hubbard parameter which describes the electron-electron Coloumb repulsion, and gives the energy cost to place an extra electron on a particular site, $U = E(d^{n+1}) + E(d^{n-1}) - 2E(d^n)$. J is then a parameter representing the screened exchange energy. The first term in the above Hamiltonian describes the interaction between electrons of opposite spin, whilst the second term describes interaction between electrons of like spin. The corresponding $E_U(\hat{n})$ is then,

$$E_U = \frac{U}{2} \sum_{m,m',\sigma} n_{m,\sigma}n_{m',-\sigma} + \frac{U-J}{2} \sum_{m\neq m',\sigma} n_{m,\sigma}n_{m',\sigma}, \tag{2.82}$$

and the double-counting correction is,

$$E_{dc} = \frac{U}{2} \sum_{m,\sigma} n_{m,\sigma}(n_{m,\sigma}-1) - \frac{J}{2} \sum_{m,\sigma} n_{m,\sigma}\left(\frac{n_{m,\sigma}}{2} - 1\right). \tag{2.83}$$

We finally arrive at the functional correcting the DFT functional,

$$E^{LDA/GGA+U} = E^{LDA/GGA} + \frac{U-J}{2} \sum_{m,\sigma} (n_{m,\sigma} - n_{m,\sigma}^2), \tag{2.84}$$

where we see that, for positive $U - J$, the whole of the second term becomes a cost that drives the on-site occupancy to idempotency.

The DFT+U method provides a computationally less demanding approach to combating errors produced in DFT calculations compared to hybrid functionals. However, in practice the +U parameter is obtained either from a constrained DFT calculation, or used as a variable parameter, thus requiring comparison with experiment or higher level calculations.

In this thesis, we aim to explore a large family of materials in a predictive way. Unfortunately, not all of these materials have been explored within the literature, and so comparison with experiment/other theoretical works to determine appropriate values of +U is not always possible. Further, the size of the TMDC family means that determining the +U parameter for each system would be a demanding task. Consequently, we have not utilised the +U method in this work.

2.6 Computational Implementation

In the above section we have discussed the theoretical grounding for *ab initio* electronic structure calculations. However, in practice, other techniques can be utilised to reduce computational cost. Here, we discuss such techniques which have been employed in this work.

2.6.1 Pseudopotentials

It is well known that the core electrons are not particularly important for many of the physical properties of materials (e.g. ionisation, chemical bonding) and do not significantly change between free atoms and solids, especially when compared to the valence electrons. As such, we can utilise the 'frozen-core' or 'pseudopotential' method to effectively combine the core electrons and the ionic nucleus, replacing them with a weaker potential than that of the original system. This new 'pseudopotential' can be chosen to produce any important physical and mathematical properties of the original system.

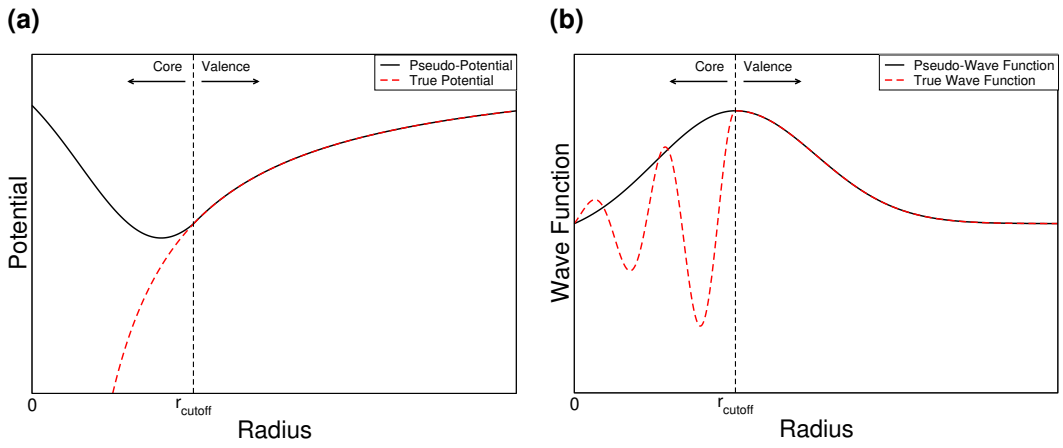

Figure 2.3: Comparison of the true (Coulomb) and a possible pseudo-pontential (2.3a), and a comparison of the true and pseudo-wave functions (2.3b). The core and valence regions have been indicated.

The value of utilising a pseudopotential instead of the true potential can be seen by considering the approach of the orthogonalised plane wave (OPW) method. We assume that the lowest n_{core} energy eigenvalues, E_c, and eigenfunctions, ψ_c, of the Hamiltonian (corresponding to the core states of the atom) are already known, and denote these states as,

$$\hat{H}\psi_c = E_c\psi_c \quad n = 1, 2, \cdots, n_{core}. \tag{2.85}$$

From here, we wish to obtain all other eigenvalues and eigenfunctions of the Hamiltonian, $\hat{H}$. To do this, we consider a transformation of the single-particle wave functions, ψ_i,

$$|\phi_i\rangle = |\psi_i\rangle - \sum_c \alpha_c |\psi_c\rangle . \tag{2.86}$$

Here, ψ_i is a smooth function which corresponds to a valence state i, and ψ_c corresponds to the core states bound to the atom [94]. Coefficients α_c are determined by enforcing that ϕ_i be orthogonal to all of the known eigenstates, ψ_c (i.e. $\langle\psi_c|\phi_i\rangle = 0$),

$$\begin{aligned} \langle\psi_{c'}|\phi_i\rangle &= \langle\psi_{c'}| \left[|\psi_i\rangle - \sum_c \alpha_c |\psi_c\rangle \right] \\ &= \langle\psi_{c'}|\psi_i\rangle - \sum_c \alpha_c \langle\psi_{c'}|\psi_c\rangle \\ 0 &= \langle\psi_{c'}|\psi_i\rangle - \alpha_{c'}, \end{aligned} \tag{2.87}$$

where we have made use of the orthogonality of the different core states. Thus, $\alpha_c = \langle\psi_c|\psi_i\rangle$.

We now consider $\langle\phi_j|\,\hat{H}\,|\phi_i\rangle$,

$$\begin{aligned}\langle\phi_j|\,\hat{H}\,|\phi_i\rangle &= \langle\phi_j|\,\hat{H}\Big[\,|\psi_i\rangle - \sum_c \alpha_c\,|\psi_c\rangle\,\Big] \\ &= \langle\psi_j|\,\Big[\hat{H} - \sum_c E_c\,|\psi_c\rangle\,\langle\psi_c|\,\Big]\,|\psi_i\rangle\,,\end{aligned} \tag{2.88}$$

where we have made use of the above expression for α_c and the required orthogonality $\langle\psi_c|\phi_i\rangle = 0$. We can perform a similar evaluation of $\langle\phi_j|\,E\,|\phi_i\rangle$,

$$\begin{aligned}\langle\phi_j|\,E\,|\phi_i\rangle &= \langle\phi_j|\,E\Big[\,|\psi_i\rangle - \sum_c \alpha_c\,|\psi_c\rangle\,\Big] \\ &= \langle\psi_j|\,\Big[E - E\sum_c |\psi_c\rangle\,\langle\psi_c|\,\Big]\,|\psi_i\rangle\,.\end{aligned} \tag{2.89}$$

Combining these two results, we get,

$$\begin{aligned}\langle\phi_j|\,\hat{H} - E\,|\phi_i\rangle &= \langle\phi_j|\,\hat{H}\,|\phi_i\rangle - \langle\phi_j|\,E\,|\phi_i\rangle \\ &= \langle\psi_j|\,\Big[\hat{H} - \sum_c E_c\,|\psi_c\rangle\,\langle\psi_c|\,\Big]\,|\psi_i\rangle - \langle\psi_j|\,\Big[E - E\sum_c |\psi_c\rangle\,\langle\psi_c|\,\Big]\,|\psi_i\rangle \\ &= \langle\psi_j|\,\Big[\hat{H} - E + \sum_c (E - E_c)\,|\psi_c\rangle\,\langle\psi_c|\,\Big]\,|\psi_i\rangle \\ &= \langle\psi_j|\,\Big[\hat{H}^{eff} - E\Big]\,|\psi_i\rangle\,.\end{aligned} \tag{2.90}$$

Solving the above secular equation requires,

$$\det|\,\langle\psi_j|\,\hat{H}^{(eff)}\,|\psi_i\rangle - E\delta_{ij}| = 0, \tag{2.91}$$

with effective (single-particle) Hamiltonian,

$$\begin{aligned}\hat{H}^{(eff)} &= \hat{H} + \sum_c (E - E_c)\,|\psi_c\rangle\,\langle\psi_c| \\ &= -\nabla^2 + V(\mathbf{r}) + \sum_c (E - E_c)\,|\psi_c\rangle\,\langle\psi_c|\,,\end{aligned} \tag{2.92}$$

where $-\nabla^2 + V(\mathbf{r})$ is the ordinary crystal Hamiltonian. The additional summation term is energy dependent and non-local, and can be qualitatively considered as a repulsive potential due to the presence of the core states: it takes a positive value, as the energy eigenvalue of each of the core states, E_c, is lower in energy than the valence state eignvalues, E [94]. This repulsive term acts to partially cancel the strong attractive potential within the core region, $V(\mathbf{r})$. Thus, the idea of the pseudopotential method is to consider an effective potential, which is smoother than the true potential of the core region, but identical to it outside of the core region.

Further, whilst Bloch's theorem states that the wave functions of electrons in solids can be expanded using a discrete set of plane waves, accurate descriptions of the wave functions for tightly bound core electrons require a large number of plane waves due to rapid oscillations. As the pseudopotential is smaller and smoother than the true potential, it reduces the number of plane waves required to describe the electronic wave function.

We schematically show the effect of using a pseudopotential in Figure 2.3. Beyond some given radius from the nucleus ($\mathrm{r_{cutoff}}$), the pseudopotential matches the true potential of the ion. However, for radii smaller than this cut-off there is a significant difference between the two potentials, arising from the grouping of the nucleus with the core electrons, as is shown in Figure 2.3a. In 2.3b we then see the effect of this pseudopotential on the wave function: beyond the cutoff radius, the true and pseudo-wave functions match, but we see a significant reduction in the number of oscillations within the core region.

We thus consider the system to be described by a collection of pseudo-valence electrons and pseudo-ionic cores. The pseudo-electrons experience exactly the same potential outside the ionic core as the original electrons, however the potential they experience within the core is significantly weaker [137, 138]. If no pseudopotential is used, and all of the electrons are to be explicitly considered, then the calculation is said to be an 'all-electron' calculation.

PAW Pseudopotentials

There exist a range of different types of pseudopotentials, such as ultrasoft (which require relatively few plane waves, but are empirically fit to experimental data) and norm-conserving (which ensure the norm of the pseudo-wave function is equal to the true wave function at the cutoff radius). Within this work, however, we have utilised pseudopotentials built upon the Projector Augmented Wave (PAW) method [139]. We first consider a transformation, T, which brings the pseudo-wave function, $\left|\tilde{\Psi}\right\rangle$, into the single particle Kohn-Sham wave function of the all-

electron case,

$$|\Psi\rangle = T\left|\tilde{\Psi}\right\rangle. \tag{2.93}$$

As we require that the pseudo-wave functions still reproduce the behaviour of the states outside of the core region, we write,

$$T = 1 + \sum_R T_R, \tag{2.94}$$

where T_R is non-zero only in the core region surrounding atom R.

It is useful to expand the pseudo-wave functions into pseudo-basis functions,

$$\begin{aligned}\left|\tilde{\Psi}\right\rangle &= \sum_i c_i \left|\tilde{\phi}_i\right\rangle \\ &= \sum_i \left\langle p_i \middle| \tilde{\Psi}\right\rangle \left|\tilde{\phi}_i\right\rangle \\ &= \sum_i \left|\tilde{\phi}_i\right\rangle \left\langle p_i \middle| \tilde{\Psi}\right\rangle,\end{aligned} \tag{2.95}$$

where we have written $c_i = \left\langle p_i \middle| \tilde{\Psi}\right\rangle$ in terms of the so-called 'projector functions', p_i. There is exactly one projector function for each pseudo-basis functions $\tilde{\phi}_i$. If we now replace $\left|\tilde{\Psi}\right\rangle$ with $\left|\tilde{\phi}_j\right\rangle$,

$$\left|\tilde{\phi}_j\right\rangle = \sum_i \left|\tilde{\phi}_i\right\rangle \left\langle p_i \middle| \tilde{\phi}_j\right\rangle, \tag{2.96}$$

which requires that $\left\langle p_i \middle| \tilde{\phi}_j\right\rangle = \delta_{ij}$.

Operating on the pseudo-wave function with the operator T, we get,

$$|\Psi\rangle = \sum_i \left(1 + \sum_R T_R\right) \left|\tilde{\phi}_i\right\rangle \left\langle p_i \middle| \tilde{\Psi}\right\rangle. \tag{2.97}$$

We also require that the transformation T transforms the pseudo-basis functions into the true basis functions, hence,

$$\begin{aligned}|\phi_j\rangle &= \sum_i \left(1 + \sum_R T_R\right) \left|\tilde{\phi}_i\right\rangle \left\langle p_i \middle| \tilde{\phi}_j\right\rangle \\ &= \sum_i \left(1 + \sum_R T_R\right) \left|\tilde{\phi}_i\right\rangle \delta_{ij} \\ &= \left(1 + \sum_R T_R\right) \left|\tilde{\phi}_j\right\rangle,\end{aligned} \tag{2.98}$$

which can be rearranged to get an expression for $\sum_R T_R$,

$$\sum_R T_R \left|\tilde{\phi}_j\right\rangle = |\phi_j\rangle - \left|\tilde{\phi}_j\right\rangle. \tag{2.99}$$

Right multiplying both sides with $\langle p_j|$,

$$\sum_R T_R \left|\tilde{\phi_j}\right\rangle \langle p_j| = (|\phi_j\rangle - \left|\tilde{\phi_j}\right\rangle) \langle p_j| \,. \tag{2.100}$$

Finally, this allows us to write our transformation as,

$$\begin{aligned} |\Psi\rangle &= T \left|\tilde{\Psi}\right\rangle \\ &= \sum_i \left(1 + \sum_R T_R\right) \left|\tilde{\phi_i}\right\rangle \left\langle p_i \middle| \tilde{\Psi}\right\rangle \\ &= \sum_i \left|\tilde{\phi_i}\right\rangle \left\langle p_i \middle| \tilde{\Psi}\right\rangle + \sum_i \sum_R T_R \left|\tilde{\phi_i}\right\rangle \left\langle p_i \middle| \tilde{\Psi}\right\rangle \\ &= \left[1 + \sum_i \left(|\phi_i\rangle - \left|\tilde{\phi_i}\right\rangle \right) \langle p_i| \right] \left|\tilde{\Psi}\right\rangle , \end{aligned} \tag{2.101}$$

giving,

$$T = 1 + \sum_i \left(|\phi_i\rangle - \left|\tilde{\phi_i}\right\rangle \right) \langle p_i| \,. \tag{2.102}$$

The transformation is therefore given by the set of all-electron basis functions $|\phi_i\rangle$, the set of pseudo-basis functions $\left|\tilde{\phi_i}\right\rangle$, and the set of projector functions $|p_i\rangle$.

We therefore have a method by which we can reduce the number of electrons needed to be explicitly evaluated in an electronic structure calculation by combining the nucleus and core electrons into an effective, pseudo-potential. Outside of the core region, the pseudo-basis wave functions are equal to the original all-electron basis functions. Within the core regions, they can be any smooth continuation, such as a linear combination of polynomials or Bessel functions.

2.6.2 Brillouin Zone Sampling

The evaluation of many important physical properties involves an integral over the first Brillouin zone. For instance, the particle density, $n(\mathbf{r})$,

$$n(\mathbf{r}) = \frac{1}{\Omega_{BZ}} \sum_i \int_{BZ} f_{i\mathbf{k}} |\psi_{i\mathbf{k}}(\mathbf{r})|^2 d\mathbf{k}, \tag{2.103}$$

for first Brillouin zone volume Ω_{BZ}, sum index i indicating the band index, Bloch vector $\mathbf{k}$, and occupation number of the state $i\mathbf{k}$ denoted by $f_{i\mathbf{k}}$. In fact, much of the work done in a DFT calculation reduces to an integral of the form,

$$G = \frac{1}{\Omega_{BZ}} \int_{BZ} g(\mathbf{k})\, d\mathbf{k}, \tag{2.104}$$

where integration is done only over the possible values of **k** in the first Brillouin zone.

For an infinite, periodic crystal, however, **k** is a continuous variable and hence there are an infinite number of **k**-points that need to be considered for evaluation of the arbitrary function $g(\mathbf{k})$. As this is not feasible to do with finite resources, a compromise is made: a discrete set of points is instead used. Equation (2.104) is then rewritten as,

$$G = \frac{1}{\Omega_{BZ}} \sum_{BZ} g(\mathbf{k})\, d\mathbf{k}. \tag{2.105}$$

The most commonly used process for Brillouin zone sampling was developed by Monkhorst and Pack [140], with the selected points being given by,

$$\mathbf{k}^{\text{sampled}}_{n_1,n_2,n_3} = \sum_{i=1}^{3} \frac{2n_i - N_i - 1}{2N_i} \mathbf{a}^*_i, \tag{2.106}$$

with the reciprocal lattice vectors $\mathbf{a}^*_i$, and $n_i = 1, 2, ..., N_i$. This gives a grid of $N_1 N_2 N_3$ uniformly spaced points. To use this method, all that needs to be specified is the number of **k**-points to be used in each direction of reciprocal space. If there are $N_{1,2,3}$ **k**-points used in each direction $(1, 2, 3)$ of reciprocal space, the calculation is specified as having a uniformly spaced $N_1 \times N_2 \times N_3$ **k**-point mesh, typically centered on the Γ point [137].

Irreducible Brillouin Zone

As equations of the form (2.104) can require a lot of computational effort, most DFT codes available make use of symmetries within the Brillouin zone to speed up calculations. These symmetries mean that the integrals do not need to be completed over the entire Brillouin zone, as some points are equivalent, and so we can replace our sum over the Brillouin zone with a weighted sum, weighting repeated **k**-points with some weighting function. For example, we reconsider the particle density, calculated using a sum over **k**-points,

$$n(\mathbf{r}) = \sum_{i\mathbf{k}} w_{\mathbf{k}} f_{i\mathbf{k}} |\psi_{i\mathbf{k}}(\mathbf{r})|^2, \tag{2.107}$$

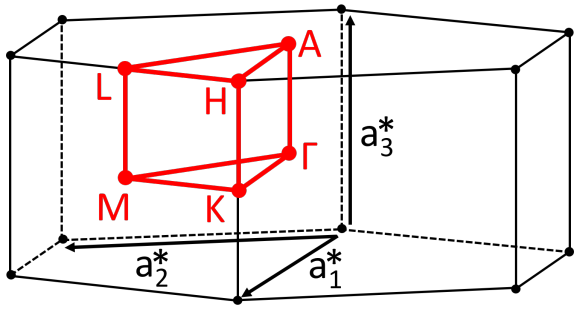

Figure 2.4: High symmetry points of the hexagonal Brillouin zone.

with weighting function $w_{\mathbf{k}}$. This weighting function corresponds to the probability of a chosen **k** being sampled, taking into account any equivalent points.

Points and Lines of High Symmetry

Though a uniform sampling of **k**-points is used for calculation of important material properties, visualisation of the electronic structure often relies on a sampling that is biased along lines between specific points. Due to the symmetry of the Brillouin zone, these points typically lie along the edge of irreducible Brillouin zone, and hence are referred to as points of high symmetry. We show in Figure 2.4 a schematic of the high symmetry points in the hexagonal (Figure 2.4) Brillouin zone [141], as this example of a Brillouin zone is discussed throughout this work.

2.6.3 Geometric Relaxation

Before the investigation into a material can begin, it is necessary for the geometric structure to be accurately determined, and so calculation of the forces on component ions is required. Further, knowledge of these ionic forces is fundamental to the working of nudged elastic band calculations, and strict force minimisation is necessary for obtaining phonon band structures. Here, we discuss the definition of ionic forces and how they can be obtained, and the scheme by which these forces have be minimised within this work.

Hellmann-Feynman Forces

The force, $\mathbf{F}_I$, on an ion, I, is given by,

$$\mathbf{F}_I = -\frac{dE}{d\mathbf{R}_I}, \tag{2.108}$$

where E is the total energy of the system, and $\mathbf{R}_I$ is the position of the ion I. As the ion moves, the wave functions must change to the self-consistent Kohn-Sham eigenstates corresponding to the new ionic position. These changes in the electronic wave functions, ψ_i, for state i, contribute to the force exerted on the ion. We show this by expanding the above total derivative,

$$\mathbf{F}_I = -\frac{\partial E}{\partial \mathbf{R}_I} - \sum_i \frac{\partial E_i}{\partial \psi_i}\frac{d\psi_i}{d\mathbf{R}_I} - \sum_i \frac{\partial E_i}{\partial \psi_i^*}\frac{d\psi_i^*}{d\mathbf{R}_I}. \tag{2.109}$$

However, we can show that the last two terms on the right cancel, by using $E = \int \sum_i \psi_i^* \hat{H} \psi_i \, dV$,

$$\begin{aligned}
-\sum_i \frac{\partial E_i}{\partial \psi_i}\frac{d\psi_i}{d\mathbf{R}_I} - \sum_i \frac{\partial E_i}{\partial \psi_i^*}\frac{d\psi_i^*}{d\mathbf{R}_I} &= -\int \sum_i \frac{\partial(\psi_i^* \hat{H}\psi_i)}{\partial \psi_i}\frac{d\psi_i}{d\mathbf{R}_I}\, dV - \int \sum_i \frac{\partial(\psi_i^* \hat{H}\psi_i)}{\partial \psi_i^*}\frac{d\psi_i^*}{d\mathbf{R}_I}\, dV \\
&= -\int \sum_i \psi_i^* E_i \frac{d\psi_i}{d\mathbf{R}_I}\, dV - \int \sum_i \psi_i E_i \frac{d\psi_i^*}{d\mathbf{R}_I}\, dV \\
&= -\sum_i E_i \int \psi_i^* \frac{d\psi_i}{d\mathbf{R}_I}\, dV - \sum_i E_i \int \psi_i \frac{d\psi_i^*}{d\mathbf{R}_I}\, dV \\
&= -\sum_i E_i \frac{d}{d\mathbf{R}_I} \int \psi_i^* \psi_i \, dV \\
&= 0,
\end{aligned} \tag{2.110}$$

due to the normalisation condition $\int \psi \, \psi^* \, dV = 1$, and hence,

$$\mathbf{F}_I = -\frac{\partial E}{\partial \mathbf{R}_I}. \tag{2.111}$$

This shows that when each ψ_i is an eigenstate of the Hamiltonian, the partial derivative of the Kohn-Sham total energy with respect to the position of a specified ion gives the force on the ion, akin to the classical definition of a force [95]. This result it often referred to as the Hellmann-Feynman theorem [142].

The Hellmann-Feynman theorem relies on the given wave functions, ψ_i, being eigenstates of the (Kohn-Sham) Hamiltonian, and so accurate forces can only be obtained when the wave functions are close to the exact eigenstate. Once

the forces and stresses have been obtained, atomic positions and the size and shape of the unit cell can be changed accordingly. Each time the geometry of the system is changed, however, the electronic eigenstates must be re-evaluated for the updated geometry in order to repeat the process. Repeating this process, moving the ions in the directions of the calculated forces, will reduce the total energy of the system and the Hellmann-Feynman forces acting on the atoms. That is, until the Hellmann-Feynman forces are decreased to a point where they are smaller than the errors in the forces, in which case movement of the ions may not necessarily decrease the total energy of the system [138].

Pulay Forces

In principle, there should be an extra term included in equation (2.109) to consider the derivative of the basis set, ϕ, with respect to the position of the ion, of the form $\frac{\partial \phi}{\partial \mathbf{R}_I}$. This extra contribution is called the Pulay force [143], and, if it is not calculated, provides further error in the value of the Hellmann-Feynman forces [138].

The derivative of any orbital with no dependence on the ionic positions (such as plane waves) with respect to the atomic position is zero, and hence the Hellmann-Feynman forces will be exactly equal to that given above. This is another advantage of using a plane wave basis set over a basis set comprised of atomic orbitals. If the Pulay force does not vanish, the resultant error will be independent of how close the electronic configuration is to its ground state. Moving an ion in the direction of the Hellmann-Feynman force can then increase the total energy of the system, and significantly more computational effort is required to find a local energy minimum [138].

Conjugate Gradient

In mathematics, the conjugate gradient method is an algorithm to obtain the solution for systems of linear equations, often implemented as an iterative algorithm. However, it can also be used to solve unconstrained problems of optimisation, for

example energy minimisation. For geometric relaxations completed for the work presented in this thesis, the conjugate gradient method is employed, and so we present a discussion of it here.

Consider a quadratic function F in a space of variables $\{x_i\} \equiv \mathbf{x}$, given by,

$$F(\mathbf{x}) = \frac{1}{2}\mathbf{x} \cdot \mathbf{H} \cdot \mathbf{x}, \tag{2.112}$$

with the Hessian matrix $\mathbf{H}$ describing the system. The challenge we face is, for such a given multidimensional space, to find a way of efficiently moving from some coordinate $\mathbf{x}$ to a minimum described by $\mathbf{x}^*$.

The simplest method by which we can achieve this minimisation is through the 'steepest descent' algorithm. For the n^{th} iterative step, we define the gradient $\mathbf{g}$ at $\mathbf{x}^n$ as,

$$\mathbf{g}(\mathbf{x}^n) = -\left.\frac{\partial F}{\partial \mathbf{x}}\right|_{\mathbf{x}=\mathbf{x}^n} = -\mathbf{H} \cdot \mathbf{x}^n. \tag{2.113}$$

To move towards the minimum, a new set of coordinates is obtained using $\mathbf{x}^{n+1} = \mathbf{x}^n + \alpha^n \mathbf{g}^n$. A series of such steps to consecutive coordinates $\mathbf{x}^{n+2}, \mathbf{x}^{n+3}, \mathbf{x}^{n+4}, \cdots$ can be taken. However, this method does not move directly towards the minimum, suffering from a version of Zeno's paradox such that the minimum is never reached exactly.

A more efficient, faster method to reach the minimum can instead be achieved through a 'conjugate gradient' descent, taking into account not only the gradient of the current coordinate set, but also the gradients at previous points. Analogous to the steepest descent approach, the new coordinate is given by,

$$\mathbf{x}^{n+1} = \mathbf{x}^n + \alpha^n \mathbf{d}^n, \tag{2.114}$$

where $\mathbf{d}^n$ is the change in coordinates from the n^{th} step.

The first step is the same as steepest descent, using $\mathbf{x}^1 = \mathbf{x}^0 + \alpha^0 \mathbf{d}^0$ where $\mathbf{d}^0 = \mathbf{g}^0$. However, for subsequent steps a slightly different approach can be taken. If minimisation along $\mathbf{d}^n$ is carried out effectively, the gradient at $\mathbf{x}^{n+1}$ along $\mathbf{d}^n$ should be zero,

$$\mathbf{d}^n \cdot \mathbf{g}(\mathbf{x}^{n+1}) = 0. \tag{2.115}$$

The best choice for the $n+1^{th}$ step is then to move in a direction where the change in gradient $\Delta\mathbf{g}^{n+1}$ along the previous direction $\mathbf{d}^n$ is zero, i.e.,

$$\mathbf{d}^n \cdot \Delta\mathbf{g}^{n+1} = 0. \tag{2.116}$$

Using the gradients of two consecutive points, $\mathbf{g}(\mathbf{x}^{n+1})$ and $\mathbf{g}(\mathbf{x}^{n+2})$, we can find this change in the gradient as we move along the direction $\mathbf{d}^{n+1}$ to be,

$$\begin{aligned} \Delta\mathbf{g}^{n+1} &= \mathbf{g}(\mathbf{x}^{n+2}) - \mathbf{g}(\mathbf{x}^{n+1}) \\ &= -\mathbf{H} \cdot (\mathbf{x}^{n+2} - \mathbf{x}^{n+1}) \\ &= -\alpha^{n+1}\mathbf{H} \cdot \mathbf{d}^{n+1}, \end{aligned} \tag{2.117}$$

where we have used equations (2.113) and (2.114). We now see that the condition given by equation (2.116) is satisfied if the inner product,

$$\mathbf{d}^n \cdot \mathbf{H} \cdot \mathbf{d}^{n+1} = 0, \tag{2.118}$$

holds. For such a condition, $\mathbf{d}^n$ and $\mathbf{d}^{n+1}$ are mutually conjugate vectors with respect to $\mathbf{H}$, hence the naming of this method. Further, if this condition is satisfied at each step, the conjugate condition is maintained for every step,

$$\mathbf{d}^{n'} \cdot \mathbf{H} \cdot \mathbf{d}^n = 0, \quad \text{for all } n' < n. \tag{2.119}$$

It can be useful to describe the new, conjugate direction in terms of quantities that are easily accessible, in particular the gradient at the current coordinate, and the direction of the previous step,

$$\mathbf{d}^{n+1} = \mathbf{g}(\mathbf{x}^{n+1}) + \gamma^{n+1}\mathbf{d}^n, \tag{2.120}$$

where γ is determined through,

$$\gamma^{n+1} = \frac{\mathbf{g}^{n+1} \cdot \mathbf{g}^{n+1}}{\mathbf{g}^n \cdot \mathbf{g}^n}, \tag{2.121}$$

with the special case of $\gamma^1 = 0$ (as was used with the steepest descent method).

Though the conjugate gradient method is well suited to problems involving quadratic functions, it can be extended to functions of higher dependency as with electronic structure calculations. To do so, the conjugate directions are defined as above, but a line minimisation is carried out for the particular non-linear functional being addressed.

2.6.4 Bader Charge Analysis

The charges on atomic species in molecules or solids are not observables, and therefore are not well defined within quantum mechanics. Common approaches assign charge through the orbitals, such as with Lowdin or Mulliken charge analysis. However, these require a basis set that is centred on atoms, allowing for the charge of the basis function to be assigned to its associated atom. For plane wave basis sets, this is not possible as the plane waves are not associated with any particular atom within the system. In such cases, it seems reasonable that the electronic charge density, which is obtainable from electronic structure calculations, would be able to offer some way to assign these charges instead.

A method by which the charge density is used to assign charge proposed by Bader [144] relies on its spatial variation, exhibiting maxima at the positions of the nuclei and minima between. Determination of the gradient of the charge density, $\nabla\rho(\mathbf{r})$, allows us to describe the nuclei as attractors of this gradient vector field in all three dimensions, with the field lines extending to infinity. Hence, we can partition the total space of a system into a set of separate basins, with basins being the open region of space traversed by all of the trajectories of $\nabla\rho(\mathbf{r})$ which terminate on a given ion, and (usually) the associated ion. We can define the surface S bounding this basin Ω with the boundary condition,

$$\nabla\rho(\mathbf{r}) \cdot \mathbf{n}(\mathbf{r}) = 0 \quad \text{for all} \;\; \mathbf{r} \in S(\Omega, \mathbf{r}), \tag{2.122}$$

demanding that for a given charge density, $\rho(\mathbf{r})$, the dot product of its gradient with the surface normal $\mathbf{n}(\mathbf{r})$ (i.e. the flux in the gradient vector field) should vanish at every point on the surface. Such regions that satisfy this condition are called Bader regions [145].

Common implementations of this method involve finding the critical points where $\nabla\rho(\mathbf{r}) = 0$ to construct the surfaces of zero-flux, integration over which gives the contained charge. Though many approaches have been used to refine the implementation of this method, they still typically suffer from high computational demand, complexity, and convergence issues. An alternative approach has been presented [145] in which an explicit representation of the dividing surfaces is not used and no attempt is made to locate stationary points of the charge density.

This makes the approach more robust than many alternatives, and is more applicable to systems where the boundary surfaces are difficult to obtain. Instead, to determine which of these grid points belong to a given Bader region, a path of steepest ascent is defined for each point on the charge density grid, terminating on a point of maximal charge. Points which share the same point of maximal charge are then members of the same Bader region. The total electronic charge within a Bader region can then be approximated by the sum over the grid points within the region.

There have been several developments to this algorithm, focused around better assignment of charge near the surfaces of Bader regions [146–148]. More recently, a weighting method has been suggested [149], which introduces a weight to the integrand of the charge integration to smooth out the grid-based partition. This weighting, which varies between 0 and 1, is determined from the total integral of flux of trajectories from a given grid volume into adjacent grid volumes. Though this scales quadratically, compared to the linear scaling of previous methods, it dramatically improves upon integration accuracy.

Bader charge analysis is used at several points throughout this thesis to offer insight into the transfer of charge that arises from material combination, or through the intercalation of foreign ions into a host material.

2.6.5 van der Waals Corrections

One drawback to all commonly-used functionals which utilise GGA (including hybrid functionals) is the lack of description of long-range electron correlations that are responsible for van der Waals (vdW) forces. Such interactions between atoms and molecules are vital for accurate descriptions of organic compounds [150], the noble gases [151,152], and, importantly for the work presented here, layered vdW materials.

Of the methods available for vdW corrections, the DFT-D method has been tested most thoroughly, being applied to thousands of chemically-different systems. This is an empirical method, whereby a corrective dispersion potential is added to the

energy obtained using DFT methods. This potential can be written as [153–155],

$$E_{\text{disp}} = -\sum_{AB} \sum_{n=6,8,10,\ldots} s_n \frac{C_{AB,n}}{r_{AB}^n} f_{d,n}(r_{AB}), \tag{2.123}$$

where the first sum is over all pairings of two atoms AB in the system, $C_{AB,n}$ gives the averaged (isotropic) n^{th}-order dispersion coefficient (orders $n = 6, 8, 10, ...$) for atom pair AB, and r_{AB} is their internuclear distance. s_n are scaling factors to ensure the correct asymptotic behaviour, and $f_{d,n}(r_{AB})$ are damping functions to avoid singularities for small r_{AB}.

In this work, we use the Grimme-D3 correction [155] specifically, as atom pair-specific dispersion coefficients are explicitly computed and so it is less empirical than other DFT-D approaches, it provides consistent descriptions of the first 94 elements, and achieves close agreement with other high-accuracy methods. The correction is given by,

$$E_{\text{disp}} = -\sum_{AB} \left(f_{d,6}(r_{AB}) \frac{C_{6,AB}}{r_{AB}^6} + f_{d,8}(r_{AB}) \frac{C_{8,AB}}{r_{AB}^8} \right). \tag{2.124}$$

Here, the coefficients $C_{n,AB}$ are geometry-dependent, adjusted on the basis of the local coordination number. This dispersion correction is added to the total energy, potential, and hence interatomic forces, allowing for lattice relaxations to be performed with vdW interactions included.

2.7 Nudged Elastic Band

The nudged elastic band (NEB) method is a popular tool used for mapping out the potential energy surface (PES) of ionic diffusion in solids, providing an efficient method for finding reaction barriers between given initial and final states. The energy barrier between two different ionic configurations is determined by constructing a series of equivalent ‘images’ of the structure of interest, but with distortions that are intermediate to the initial and final states. Allowing for ionic relaxation of any of these distorted images would then reproduce one of the minimum points. To prevent this, a spring-like interaction between adjacent images is added to ensure continuity of the path, mimicking an elastic band.

An essential feature of the NEB method is the projection of forces both parallel and perpendicular to the path tangent. This ensures that the true force does not alter the distribution of images along the path, and that the spring forces do not interfere with convergence of the elastic band to the path [156]. It is therefore necessary to estimate the tangent to the path at each image for each iteration of a minimisation. The component of the total force perpendicular to the tangent is equal to the component of the true force that is perpendicular to the local tangent, and so the PES does not interfere with the distribution of images. The component of the total force that is parallel to the tangent is then taken from the parallel component of the elastic force, and so the elastic force is only required to maintain image spacing. This force projection is referred to as 'nudging'.

An elastic band with $N+1$ total images can be denoted with $[\mathbf{R}_0, \mathbf{R}_1, \mathbf{R}_2, \cdots, \mathbf{R}_N]$. The points $\mathbf{R}_0$ and $\mathbf{R}_N$ correspond to the initial and final configurations, respectively, and are fixed points on the PES. The total force acting on the i^{th} of $N-1$ intermediate images is found using,

$$\mathbf{F}_i^{tot} = \mathbf{F}_i^{spring}\big|_{\parallel} - \nabla E(\mathbf{R}_i)\big|_{\perp}. \tag{2.125}$$

This involves the sum of the tangent-perpendicular component of the true force, and tangent-parallel component of the force due to the fictitious elastic band. $\nabla E(\mathbf{R}_i)\big|_{\perp}$ is given by,

$$\nabla E(\mathbf{R}_i)\big|_{\perp} = \nabla E(\mathbf{R}_i) - \nabla E(\mathbf{R}_i) \cdot \hat{\tau}_i, \tag{2.126}$$

where E is the energy of the system, and $\hat{\tau}_i$ is the normalised local tangent at image i. The normalised local tangent is calculated from $\hat{\tau}_i = \frac{\tau_i}{|\tau_i|}$, where [157],

$$\tau_i, = \frac{\mathbf{R}_i - \mathbf{R}_{i-1}}{|\mathbf{R}_i - \mathbf{R}_{i-1}|} + \frac{\mathbf{R}_{i+1} - \mathbf{R}_i}{|\mathbf{R}_{i+1} - \mathbf{R}_i|}. \tag{2.127}$$

The spring force is then given by,

$$\mathbf{F}_i^{spring}\big|_{\parallel} = k\big(|\mathbf{R}_{i+1} - \mathbf{R}_i| - |\mathbf{R}_i - \mathbf{R}_{i-1}|\big)\hat{\tau}_i, \tag{2.128}$$

with spring constant k. Once the total force on an image is obtained, optimisation algorithms can be used to move the images according the direction of the force. Issues can arise when the parallel component of the total image force is large compared to the perpendicular component, and careful choice of tangent vector

must be made to avoid the appearance of kinks along the path and corner-cutting. However, a discussion of these is not necessary for a working understanding of the NEB method, but have been presented elsewhere [157].

Due to the discrete sampling of images with the NEB method, the energy of PES saddle points between end images needs to be obtained by interpolation. However, except for very fortunate image samplings, this interpolation can be inaccurate. The climbing image nudged elastic band (CI-NEB) method [156] offers a small modification to the NEB method, retaining the information of the shape of the PES whilst also achieving a rigorous convergence of saddle points, at the cost of relatively little added computational effort.

After some initial NEB calculations, the image with the highest energy is identified, $i_{\max}$. For this image, the total force is given by the true force due to the PES, but with the path-parallel component inverted,

$$\begin{aligned} \mathbf{F}^{tot}_{i_{\max}} &= -\nabla E(\mathbf{R}_{i_{\max}})\big|_{\perp} + \nabla E(\mathbf{R}_{i_{\max}})\big|_{\parallel} \\ &= -\nabla E(\mathbf{R}_{i_{\max}}) + 2\nabla E(\mathbf{R}_{i_{\max}})\big|_{\parallel} \end{aligned} \tag{2.129}$$

From this we see that the $i_{\max}$ image is not affected by the spring force at all, but is moved along the path in the direction of increasing energy. Once the CI-NEB calculation converges, the climbing image will be at the saddle point (a maximum along the particular path) and all other images will have followed it such that they give good description of the PES around the saddle point.

2.8 Phonons and Lattice Dynamics

The potential, V, experienced by an atom within a crystal lattice can be expanded as a Taylor series in atomic displacement vector,

$$V = V_0 + \sum_{l\sigma}\sum_{\alpha} \frac{\partial V}{\partial u_\alpha(l\sigma)} u_\alpha(l\sigma) + \frac{1}{2}\sum_{l\sigma l'\sigma'}\sum_{\alpha\beta} \frac{\partial^2 V}{\partial u_\alpha(l\sigma)\partial u_\beta(l'\sigma')} u_\alpha(l\sigma)u_\beta(l'\sigma') + O(u^3). \tag{2.130}$$

Here, the vector $u_\alpha(l\sigma)$ gives the displacement of atom σ in unit cell l with polarisation α. The first term is the equilibrium potential, and the second term is identically zero as the equilibrium configuration is defined where the forces $\frac{\partial V}{\partial u_\alpha(l\sigma)}$

are zero. The third term then describes a harmonic potential, and higher order terms $O(u^3)$ describe anharmonic effects. When one approaches the problem of crystal dynamics, N atoms are usually considered to be connected by harmonic springs which result in a linear combination of $3N$ modes of vibration, with any anharmonic terms usually being treated as perturbations. Whilst anharmonic terms can be important in some materials, the associated force constants are difficult to evaluate from first principles and also require the consideration of coupling between phonons (yet another many-body problem). As such, we shall omit third order terms in the following discussion, and work entirely within the domain of the harmonic approximation.

We can define a matrix of second-order inter-atomic force constants, the elements of which being given by,

$$\Phi_{\alpha\beta}(l\sigma, l'\sigma') = \frac{\partial^2 V}{\partial u_\alpha(l\sigma)\partial u_\beta(l'\sigma')}. \tag{2.131}$$

We can then produce the equations of motion for a 3D-crystal of atomic masses M_σ within the harmonic approximation,

$$M_\sigma \ddot{u}_\alpha(l\sigma) = -\sum_{l'\sigma'\beta} \Phi_{\alpha\beta}(l\sigma, l'\sigma')u_\beta(l'\sigma'), \tag{2.132}$$

which can be solved with displacement vector,

$$u_\alpha(l\sigma) = \frac{1}{\sqrt{M_\sigma}} \sum_q U_\alpha(\mathbf{q}\sigma) \exp\left[i(\mathbf{q}\cdot\mathbf{r} - \omega t)\right]. \tag{2.133}$$

Here, **r** is the position vector to unit cell l and t is time. Making this substitution of the displacement vector into the equation of motion gives,

$$\omega^2 U_\alpha(\mathbf{q}\sigma) = \sum_{l'\sigma'\beta} \frac{1}{\sqrt{M_\sigma M_{\sigma'}}} \Phi_{\alpha\beta}(l\sigma, l'\sigma') \exp\left[i(\mathbf{q}\cdot(\mathbf{r'} - \mathbf{r}) - \omega t)\right] U_\beta(\mathbf{q}\sigma'), \tag{2.134}$$

where we have dropped the summation over **q** to provide the expression for a single **q**-point.

We now make use of the translational symmetry of the crystal, and hence the translational invariance of $\Phi_{\alpha\beta}(l\sigma, l'\sigma')$. If we translate the system by $-l$, we require,

$$\Phi_{\alpha\beta}(0\sigma, (l'-l)\sigma') = \Phi_{\alpha\beta}(l\sigma, l'\sigma'). \tag{2.135}$$

This allows us to rewrite our above result from the equation of motion,

$$\begin{aligned}\omega^2 U_\alpha(\mathbf{q}\sigma) &= \sum_{\sigma'\beta} \frac{1}{\sqrt{M_\sigma M_{\sigma'}}} \sum_{l'} \Phi_{\alpha\beta}(0\sigma, l'\sigma') \exp\left[i(\mathbf{q}\cdot\mathbf{r}' - \omega t)\right] U_\beta(\mathbf{q}\sigma') \\ &= \sum_{\sigma'\beta} D_{\alpha\beta}(\sigma\sigma'|\mathbf{q}) U_\beta(\mathbf{q}\sigma'),\end{aligned} \tag{2.136}$$

and we have introduced the elements of the dynamical matrix for a fixed value of **q**,

$$D_{\alpha\beta}(\sigma\sigma'|\mathbf{q}) = \frac{1}{\sqrt{M_\sigma M_{\sigma'}}} \sum_{l'} \Phi_{\alpha\beta}(0\sigma, l'\sigma') \exp\left[i(\mathbf{q}\cdot\mathbf{r}' - \omega t)\right]. \tag{2.137}$$

Non-trivial solutions can be found by evaluating the secular equation,

$$\det\left|D_{\alpha\beta}(\sigma\sigma'|\mathbf{q}) - \omega^2 \delta_{\alpha,\beta}\delta_{\sigma,\sigma'}\right| = 0. \tag{2.138}$$

We can combine the atomic (σ) and directional (α) indices since α can only take one of the three values corresponding to the three spatial directions, and so we instead use σ_α. With this, for each of the eigenvalues $\omega^2_{\mathbf{q}s}$ corresponding to a specific **q**-point and band/polarisation branch s, we can write the eigenvector of the dynamical matrix as,

$$\begin{aligned}\mathbf{U}(\mathbf{q}s) = \Big(&U(\mathbf{q}s1_x), U(\mathbf{q}s1_y), U(\mathbf{q}s1_z), \cdots, U(\mathbf{q}s\sigma_x), U(\mathbf{q}s\sigma_y), U(\mathbf{q}s\sigma_z), \\ &\cdots, U(\mathbf{q}sN_x), U(\mathbf{q}sN_y), U(\mathbf{q}sN_z)\Big).\end{aligned} \tag{2.139}$$

This has dimensions of 3N (three degrees of freedom for each of the N atoms in the basis) with each element giving the amplitude of the displacement for each of those atoms in each of the directions, allowing us to write equation (2.136) as,

$$D(\mathbf{q}s)\mathbf{U}(\mathbf{q}s) = \omega^2_{\mathbf{q}s}\mathbf{U}(\mathbf{q}s). \tag{2.140}$$

From the above discussions, it is now clear that to find the phonon frequencies $\omega_{\mathbf{q}s}$ of a material characterised by a set of force constants the dynamical matrix must be diagonalised, with the square of the phonon frequencies being the eigenvalues of the dynamical matrix. For a given **q**-point, calculating the $3N$ frequencies allows the construction of the phonon band structure, analogous to the construction of electronic band structures described in Section 2.3.7. However, a negative eigenvalue would correspond to an imaginary phonon frequency, which, when substituted into a displacement with a plane wave form as was used

above, would result in motion with no restoring force and indicates a crystal is not dynamically stable. The only remaining challenge is to determine the form of the dynamical matrix, which depends on the second-order interatomic force constants, $\Phi_{\alpha\beta}(0\sigma, l'\sigma')$.

2.8.1 *Ab initio* Approaches to Lattice Dynamics

If we consider a phonon mode (characterised by a plane wave with wave vector **q**) propagating through a crystal, the ionic cores will oscillate about their equilibrium positions with a definite displacement pattern. The electron cloud will respond quickly to this displacement, as within the adiabatic approximation. Taking a snapshot of this oscillation, it is possible to consider the system in a new crystal structure arising from the distortion of the phonon. This new crystal structure will be closely related to the original, possessing the same translational symmetry, but will have a lower symmetry and a higher total energy.

If $E_{tot}(0)$ and $E_{tot}(u)$ are the total energy of the undistorted and distorted structures, respectively, then the frequency of the 'frozen phonon' is defined by,

$$\frac{1}{2}\omega^2 \sum_{\sigma} M_\sigma |\mathbf{u}_\sigma|^2 = E_{tot}(u) - E_{tot}(0). \tag{2.141}$$

Alternatively, the phonon frequency can be obtained from the force equation,

$$\mathbf{F}_\sigma = -\sum_{\sigma'} \Phi(0\sigma, l'\sigma')\mathbf{u}_{\sigma'}, \tag{2.142}$$

where the left hand side represents the harmonic contribution to the force on atom σ, and $\Phi(0\sigma, l'\sigma')$ is the force constant matrix. Though the frozen phonon mode can be calculated using either of these approaches, the force method has some advantages over using the energy. Firstly, fewer distorted geometries are required to determine the dynamical matrix than with the energy approach. Secondly, the energy differences associated with the distortions are typically very small compared to the total energies, whereas the changes in the forces are of the same order of magnitude as the forces themselves, and so a higher numerical accuracy is attainable [158].

In practice, supercells of a fully geometry-relaxed structure are used to consider a set of unique finite atomic displacements, allowing calculation of the force con-

Species	Included Electrons	Species	Included Electrons
Li	$1s^2 2s^1$ (3)	Mn	$3p^6 3d^6 4s^1$ (13)
Na	$2p^6 3s^1$ (7)	Re	$5d^6 6s^1$ (7)
K	$3p^6 4s^1$ (7)	Fe	$3d^7 4s^1$ (8)
Mg	$2p^6 3s^2$ (8)	Ru	$4s^2 4p^6 4d^7 5s^1$ (16)
S	$3s^2 3p^4$ (6)	Os	$5d^7 6s^1$ (8)
Se	$4s^2 4p^4$ (6)	Co	$3d^8 4s^1$ (9)
Te	$5s^2 5p^4$ (6)	Rh	$4d^8 5s^1$ (9)
Sc	$3d^2 4s^1$ (3)	Ir	$5d^8 6s^1$ (9)
Y	$4s^2 4p^6 4d^2$ (10)	Ni	$3d^9 4s^1$ (10)
Ti	$3p^6 3d^3 4s^1$ (10)	Pd	$4d^9 5s^1$ (10)
Zr	$4s^2 4p^6 4d^3$ (11)	Pt	$5d^9 6s^1$ (10)
Hf	$5d^3 6s^1$ (4)	Cu	$3d^{10} 4s^1$ (11)
V	$3d^4 4s^1$ (5)	Ag	$4d^{10} 5s^1$ (11)
Nb	$4s^2 4p^6 4d^4 5s^1$ (13)	Au	$5d^{10} 6s^1$ (11)
Ta	$5d^4 6s^1$ (5)	Ge	$3d^{10} 4s^2 4p^2$ (14)
Cr	$3s^2 4s^1 4p^6 4d^5$ (14)	Sn	$4d^{10} 5s^2 5p^2$ (14)
Mo	$4d^5 5s^1$ (6)	Pb	$5d^{10} 6s^2 6p^2$ (14)
W	$5d^5 6s^1$ (6)		

Table 2.1: Electronic configurations of electrons modelled for different species considered in this thesis.

stants using first principles calculations. In typical DFT calculations, the atomic forces within a supercell are obtained by a small additional computation from the converged Kohn–Sham orbitals. In this work, we use the Phonopy [159, 160] for generation of the supercells and unique displacements, interfaced with VASP, allowing the calculation of phonon band structures.

2.9 Summary

In this thesis, first principles calculations, within the framework of density functional theory, were performed using the Vienna Ab initio Simulation Package (VASP) [161–164]. Unless otherwise specified, the Perdew-Burke-Ernzerhof [119, 120] (PBE) form of the generalised gradient approximation was used to perform structural and electronic relaxations of the systems presented. The projector augmented wave (PAW) method [139] was used to describe the interaction between core and valence electrons, and in Table 2.1 the valence electrons explicitly considered for each species are presented. All other electrons were effectively contained within the used PAW-PBE pseudopotentials. A plane-wave basis set was chosen to model the electronic wave functions, and we demonstrate the convergence of the calculations with the plane wave energy cutoff in Appendix A. All **k**-point grids used for calculations were Γ-centred and generated using the Monkhorst-Pack scheme [140], with the exception of band structure calculations. A demonstration of the convergence of the calculations with the chosen **k**-point grids is presented in Appendix A. For band structures, specific **k**-points were chosen to follow routes along high-symmetry lines, between high-symmetry points of the Brillouin zone, and are indicated in the relevant figures. Geometric relaxation was achieved using the conjugate gradient algorithm, and electronic minimisation was achieved through a combination of blocked Davidson and RMM-DIIS iteration schemes. The finite displacement of ions was used to calculate phonon band dispersions using the frozen phonon supercell method employed by Phonopy [159, 160]. All figures in this thesis that depict ball and stick models of atomic structures, and the associated charge densities, were generated using the VESTA atomic structure visualisation package (VESTA 3). Further calculation details are included in the chapters where the relevant work is presented.

Chapter 3

Intercalation of TMDCs

"Lashing out the action, returning the reaction,
Weak are ripped and torn away,
Hypnotising power, crushing all that cower,
Battery is here to stay."

Metallica, 1986

3.1 Introduction

Lithium ion batteries, as a result of their high specific energy and capacity, have a vital role in sustainable energy storage, driven in recent years by the rising popularity of electric vehicles, flexible electronics, and the ever-increasing demand for more powerful portable devices. Unfortunately, battery technology has struggled to meet the demand from these areas of electronics meaning that, for example, most commercially available electric vehicles are currently limited to distances of 100 miles [165] and costs of $100-250 per stored kWh [166]. Reducing battery pack costs [167] to a target of $40-50 per stored kWh, improving flexibility [168, 169], or enhancing the electronic properties of materials are all aspects that would make electric cars and flexible devices more accessible to consumers, and would help facilitate the transition to renewable energy sources.

Beyond intercalation with lithium, other ionic species have also been considered. Group I elements (sodium [170] and potassium [171]) have very similar

chemistries to lithium and so offer an alternative that would require minimal modification to the existing infrastructure of lithium-ion batteries. Group II elements such as magnesium and calcium have also received attention as possible successors to lithium. Whilst these elements offer twice the number of valence electrons as their Group I neighbours, and hence twice the charge available for transfer, this larger charge leads to issues in the stability of the electrodes and electrolytes being used [172]. However, they have been shown to be safer due to non-dendritic metal deposition [173], and do not provoke environmental or socio-economic concerns from limited global distribution or the safety of its mining and use.

The electrodes are a crucial component of batteries, determining voltages, capacity, and cost. The anode is required to have a low voltage with respect to the redox level of the intercalant species (e.g. vs. Li/Li^+). A particularly successful material being graphite, with lithium intercalation occurring between 0.2 and 0.01 V vs. Li/Li^+. However, graphite suffers from a capacity being limited to LiC_6 (equivalent to 372 $mAhg^{-1}$) [43] and the low intercalation potential results in the decomposition of organic electrolytes. This has led to materials such as silicon [88], lithium titanate [89], and other metal oxide materials being considered [90,91]. Cathodes, on the other hand, need to offer high intercalation potentials typically in excess of 3 V. Following the success of $LiCoO_2$, many transition metal-based oxides have been investigated and have demonstrated their own successes. NMC, NCA, and their variants [41, 82–86], several phosphates [36, 38, 40], and spinel oxides such as Mn_2O_4 [87] have offered high voltages. Despite the numerous promising candidates for both anode and cathode materials, they each suffer from their individual short-comings, and so the exploration and investigation of other materials is still required.

Many electrode materials experience stresses arising from the intercalation of ions into their structure. These can be due to phase changes [174], ionic diffusion [175, 176], and volumetric expansion [177, 178], and can lead to the material 'fracturing', ultimately leading to structural degradation and device failure. Layered materials such as graphite [179–181], NMC [83, 86, 182], and the MXenes [183] show lower volume expansions [184] upon intercalation as they can more readily accept intercalants [35, 72] into their van der Waals gaps. This re-

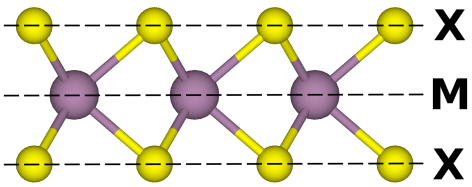

Figure 3.1: Side-on view showing an example structure of a single TMDC layer. The dashed lines indicate the planes of metal (M) and chacolgen (X) atoms, forming an 'atomic trilayer'.

duces the fracturing and structural degradation [185] that many electrode materials suffer from [186].

There are many metal chalcogenide materials which do offer the desired layered structure, and have also been shown to be electrochemically active and have shown good cyclability [187, 188]. One particularly diverse group of layered materials are the transition metal dichalcogenides (TMDCs) [189–191], with general formula MX_2. The presence of a transition metal M allows us to utilise the redox levels that have led to the successes of the transition metal oxides, the choice of chalcogen X means that electrolytes that are not oxygen-based (such as sulfur-based electrolytes) may now be a more viable option, and the different possible M-X pairings allow us to consider the wide range of properties that have been demonstrated within the TMDC family. In this Chapter, we consider the whole family of TMDC materials for use as intercalation electrodes in lithium-ion and magnesium-ion batteries.

3.2 Background

3.2.1 Atomic Structure

Each TMDC layer consists of three atomic planes, having a hexagonally-packed plane of metal atoms sandwiched between two planes of chalcogen atoms (X-M-X), sometimes described as an 'atomic trilayer' structure. An example of such a structure is shown in Figure 3.1. The structure of the individual sheets is main-

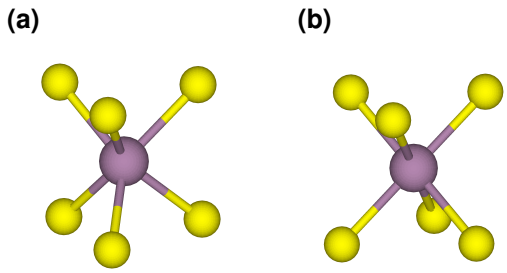

Figure 3.2: The possible coordination states for the metal atom within a TMDC sheet to exhibit. (a) shows the hexagonal coordination state with trigonal prismatic symmetry (denoted 'H'). (b) shows the octahedral coordination state with anti-trigonal prismatic symmetry (denoted 'T').

tained by intra-layer, covalent M-X bonds with *p*-*d* hybridisation [192], whilst the sheets are coupled to each other by weak van der Waals forces [193].

The metal atoms in a TMDC structure typically exhibit one of two different coordination states, or 'polymorphs', with the chalcogen atoms. The first of these is the hexagonal coordination state with trigonal prismatic symmetry (denoted 'H', and shown in Figure 3.2a). The second is the octahedral coordination state with anti-trigonal prismatic symmetry (denoted 'T', and shown in Figure 3.2b). As Figure 3.2 shows, the metal atom in each of the coordination states is bonded to six chalcogen atoms. The bonding of the H-coordinated structure is symmetric through a horizontal mirror-plane (passing through the plane of metal atoms), whereas for T-coordination there is a 60° rotation of one of the chalcogen planes resulting in an inversion symmetry (about the metal atom). The coordination state exhibited by a TMDC is largely governed by the d-electron count on the transition metal. For example, Group IV TMDCs are all in the T-phase, Group V demonstrate both the T- and H-phases, and Group VI are commonly in the H-phase [189, 194–196].

Due to the structure of individual layers, TMDCs are capable of exhibiting different stacking polytypes depending on the positing of the atoms in one TMDC layer with respect to the atoms in another. To highlight this, Figure 3.3 shows the stacking arrangement for T-phase and three arrangements for two layers of H-phase TMDC. As we can see from Figure 3.3, the chalcogen and metal atoms can be in one of three positions, and we describe the layer by which of these

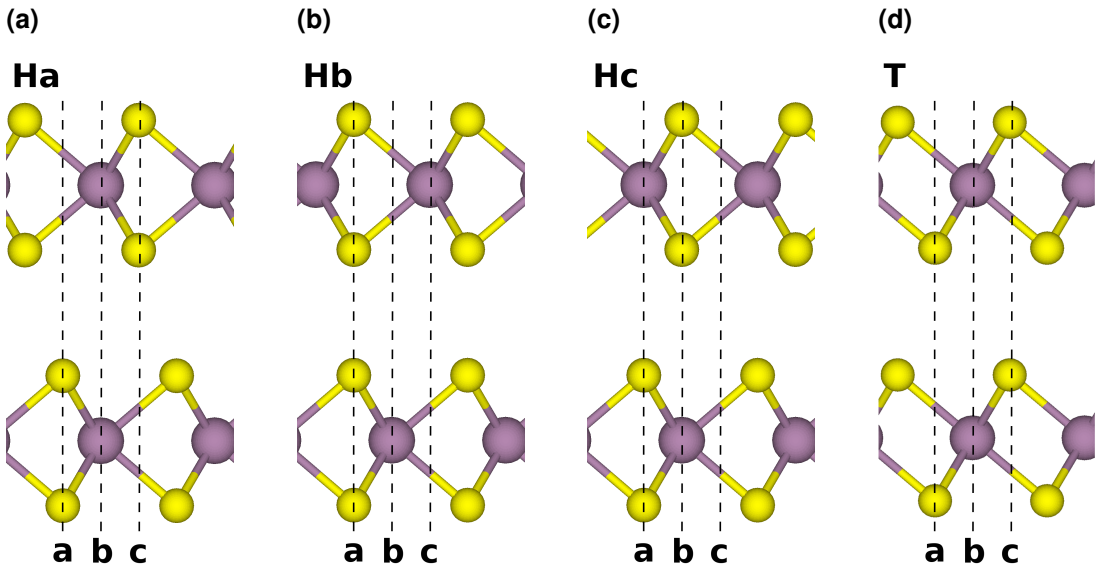

Figure 3.3: Side-views showing the different stacking arrangements for two layers of H-phase and T-phase TMDCs. Vertical dashed lines indicate the three positions that the metal and chalcogen atoms can occupy, and are denoted 'a', 'b' and 'c'. The stacking arrangements are then shown for the Ha-phase (3.3a) described by AbA CbC, for the Hb-phase (3.3b) described by AbA AcA, and the Hc-phase (3.3c) described by AbA BaB. The stacking arrangement for the T-phase is also shown (3.3d), which is described by AbC AbC.

sites are occupied by the atoms of the sheet. We use capital letters to specify the position of the chalcogen atoms, and lower case letters to specify the position of the transition metal atom. For example, the Ha-phase is described by AbA CbC (cholcogen atoms in the 'A' positions in the lower layer, and the 'C' positions in the upper layer, with transition metal atoms in the 'b' position in both layers). Similarly, the Hb-phase is described by AbA AcA, the Hc-phase is described by AbA BaB, and the T-phase is described by AbC AbC.

This discussion of the stacking polytypes highlights a difference between each of the Ha-, Hb-, and Hc-phases, and the T-phase: the H-phases require a specification of the position of six atoms over two layers, whereas the T-phase is specified by three atoms as there is a repeated unit. If there are two layers within a unit cell/stacking sequence, as in the case of the H-phases discussed above, then the structure can be totally described as the 2Ha-, 2Hb-, or 2Hc-phase. Conversely, the T-phase above only has a single layer in its unit cell, and thus is described as the 1T-phase. Therefore, we can include the number of layers in a unit cell, the

coordination of the transition metal with the chalcogen atoms, and any specific stacking in a concise manner. When referring to a TMDC we will denote them as, for example, 2Hc-MX_2 where applicable, thus including the size of the unit cell, the coordination state between the M and X atoms, the stacking arrangement of the layers, and the constituent species.

Though the layered structure is not always observed, with many MX_2 compounds exhibiting a pyrite or marcasite phase, and the intercalated MX_2 compositions exhibiting a chalcopyrite or spinel phase [197, 198], various techniques can be employed to encourage the growth of the layered structure, such as through careful choice of a substrate, the use of specific growth conditions, or specific techniques [199, 200].

For each of the phases presented, the hexagonal packing of the metal atoms within the single TMDC sheets results in the primitive cell, and hence the lattice, being hexagonal. In this work, we choose the (wide angle) lattice vectors of the real lattice to be,

$$\begin{aligned} \mathbf{a}_1 &= a\,\hat{x} \\ \mathbf{a}_2 &= -\frac{1}{2}a\,\hat{x} + \frac{\sqrt{3}}{2}a\,\hat{y} \\ \mathbf{a}_3 &= c\hat{z}. \end{aligned} \tag{3.1}$$

The corresponding reciprocal lattice vectors for the hexagonal real-space lattice vectors given above are then,

$$\begin{aligned} \mathbf{a}_1^* &= \frac{2\pi}{a}\left(\hat{x} + \frac{1}{\sqrt{3}}\hat{y}\right) \\ \mathbf{a}_2^* &= \frac{2\pi}{a}\left(\frac{2}{\sqrt{3}}\hat{y}\right) \\ \mathbf{a}_3^* &= \frac{2\pi}{c}\,\hat{z}. \end{aligned} \tag{3.2}$$

Due to the three-fold axis of rotational symmetry of the basis compared to the six-fold axis of the lattice, the crystal is instead classified with trigonal symmetry. In particular, we find space group number 164 to be the most relevant for this work, so we consider this more closely. The point symmetries include a three-fold rotation axis, three two-fold rotation axes perpendicular to the three-fold axis, and mirror planes whose normals are perpendicular to the three-fold rotation axis.

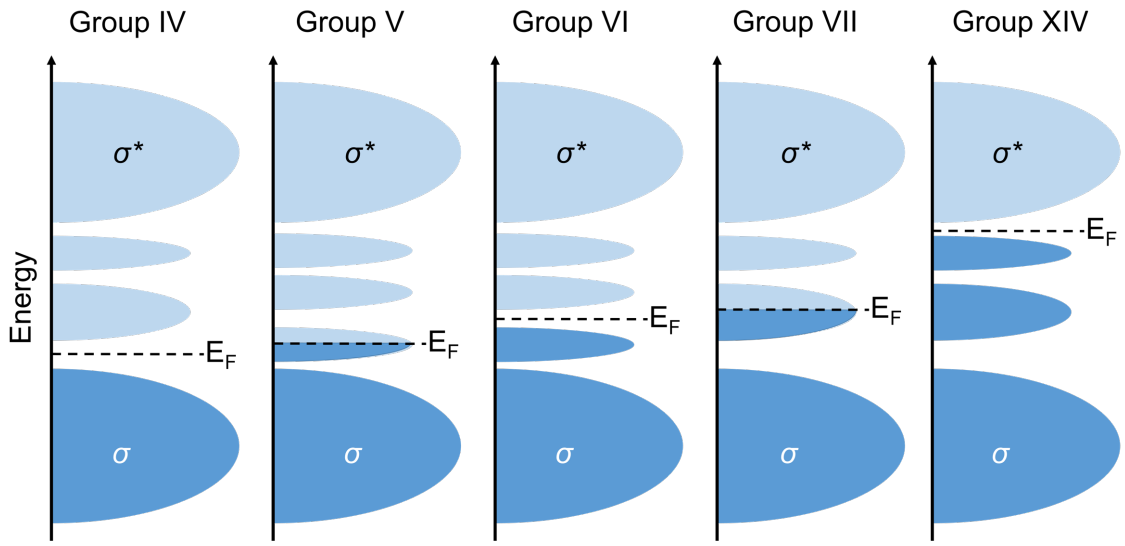

Figure 3.4: Qualitative schematic highlighting the ideal progressive filling of *d* orbitals that are located within the bandgap between bonding (σ) and anti-bonding (σ^*) states in group IV, V, VI, VII and XIV TMDCs. The Fermi energy is denoted E_F. Dark blue regions indicate filled states, and light blue regions indicate unfilled states.

3.2.2 Electronic Structure

In contrast to most transition metal complexes, where bonding occurs between lone pairs of electrons on ligands and the empty orbitals of the transition metal, in layered TMDCs the metal atoms provide four electrons to the chalcogen species to form filled bonding states (σ) and unfilled anti-bonding states (σ^*). Within the gap between the bonding and anti-bonding states are the non-bonding M atom *d*-bands. As the Group of the transition metal is increased, the number of electrons on the transition metal increases, and thus the unoccupied non-bonding *d*-bands are progressively filled. This is highlighted in Figure 3.4. When the bands are partially filled and the Fermi level lies within a band, such as for Groups V and VII in Figure 3.4, the material will exhibit metallic behaviour. Conversely, when the bands are completely filled, the Fermi level lies within a band gap, such as for Groups IV, VI and X in Figure 3.4, and the material will exhibit semiconducting or insulating behaviour [189].

T-phase TMDCs have D_{3d} symmetry, and form degenerate d_{z^2,x^2-y^2} and degenerate $d_{xy,yz,zx}$ orbitals. This leads to the non-bonding *d*-bands splitting into two orbitals, with the $d_{xy,yz,zx}$ orbitals lower in energy than the d_{z^2,x^2-y^2} orbitals. H-

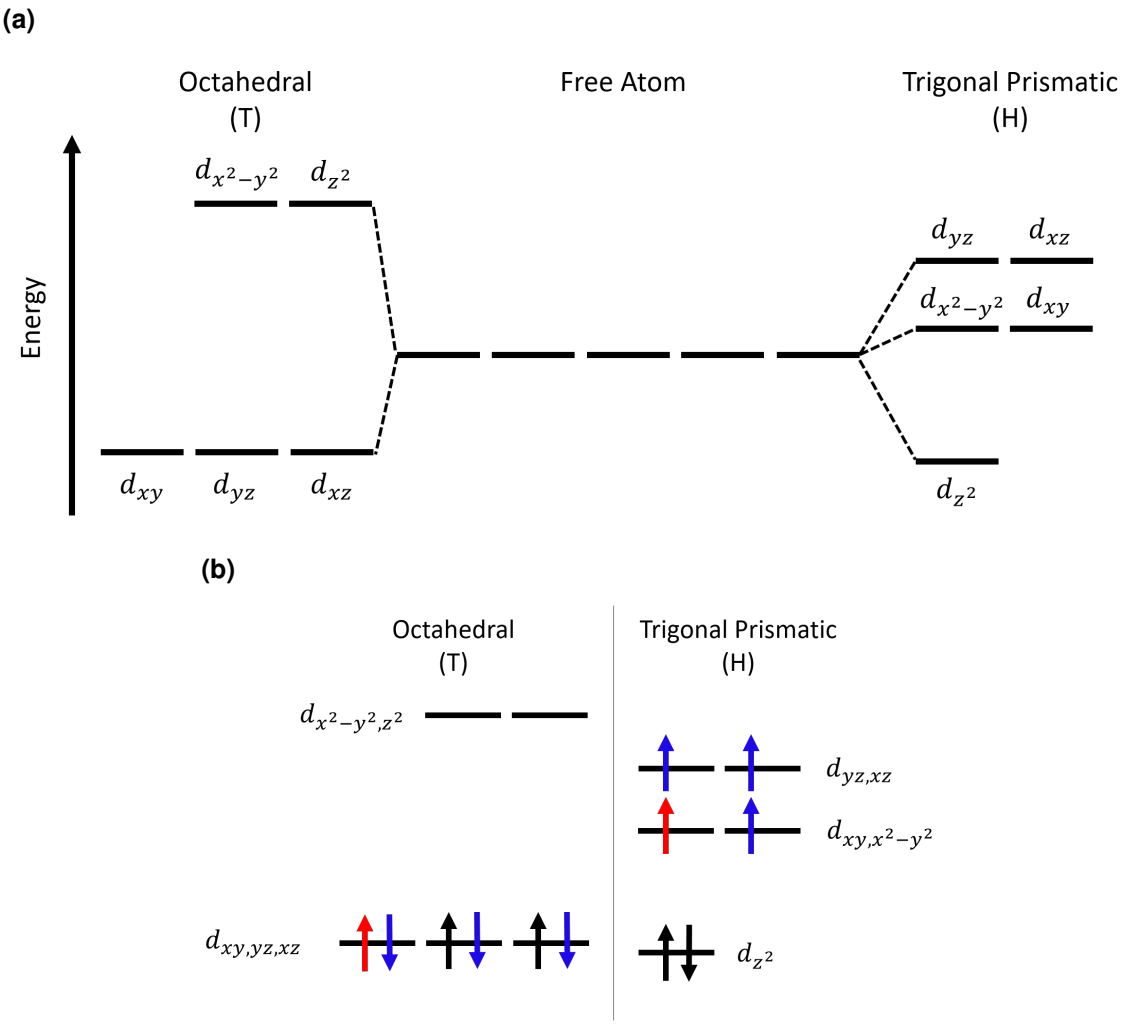

Figure 3.5: 3.5a presents a crystal field diagram showing the energy of transition metal *d* states in a free atom, and in the octahedral (T) and trigonal prismatic (H) coordination states of a TMDC. 3.5b then shows the *d*-electron configuration for Group VI TMDCs (black) and the effect of adding further *d*-electrons is indicated with red and blue arrows.

phase TMDCs have D_{3h} symmetry, and form three sets of degenerate orbitals: d_{z^2}, $d_{x^2-y^2,xy}$ and $d_{yz,zx}$, in increasing energy order. These can be seen in Figure 3.5a [201].

In Figure 3.5b we show an example of the electronic configuration in a Group VI TMDC such as MoS_2 [202, 203], comparing the octahedral and trigonal prismatic coordination states. The two *d* electrons remaining on the transition metal in the TMDC are represented with black arrows. In the trigonal prismatic coordination, the d_{z^2} orbital is doubly filled and all other orbitals are empty, whereas in the octahedral coordination state two of the degenerate d_{xy}, d_{yz}, and d_{xz} orbitals are singly filled. Comparing these, the sum of the electron energies in the T-phase is

greater than the sum of the electron energies in the H-phase, and so Group VI TMDCs can be expected to (and do) exhibit the H-phase.

If the group of the transition metal is increased, however, additional *d* electrons will be present. This is indicated in Figure 3.5b with the red arrow denoting a single additional electron, corresponding to a Group VII TMDC. For the T-phase, this single additional electron occupies the remaining low-energy degenerate state, whereas in the H-phase it must begin to fill the higher energy $d_{x^2-y^2}$ or d_{xy} states. The result of this is that the sum of electron energies in the T-phase is now lower than the sum of the electron energies in the H-phase. There is now an energetic preference for the TMDC to exhibit the T-phase as has been observed experimentally, where MoS_2 shows a reduced favourability to exhibit the H-phase as the concentration of nickel and/or cobalt dopants (and hence the number of *d* electrons) is increased [204].

Due to the large energy difference between the $d_{xy,yz,zx}$ orbitals and d_{z^2,x^2-y^2} in the T-phase, further occupation of the *d* states (corresponding to Group VIII, IX, and X TMDCs) would result in the $d_{xy,yz,zx}$ states being doubly filled. This would be lower in energy than the equivalent filling of the $d_{x^2-y^2,xy}$ and $d_{yz,zx}$ in the H-phase, and so the T-phase is preferred for higher Group TMDCs. We indicate this with the additional blue arrows in Figure 3.5b. It is worth noting that the specific filling order of the high energy H-phase states will depend on the energy separation between $d_{x^2-y^2,xy}$ and $d_{yz,zx}$, though this does not affect our conclusions.

Upon changing the chalcogen species, however, the effect on the electronic structure of the is much smaller than the effect of changing the transition-metal species. With increased atomic number of the chalcogen atom, the *d*-bands begin to broaden, resulting in smaller band gap [189].

3.2.3 Intercalation of TMDCs

Many members of the TMDC family and their intercalated structures have already received a lot of attention, being the subject of intense study over the last few decades [35, 205–207]. The mechanism for the reaction of lithium intercalation

into layered TMDCs is generally accepted to be,

$$\mathrm{MX_2} + a\mathrm{Li} \leftrightarrow \mathrm{Li}_a\mathrm{MX_2}, \tag{3.3}$$

with typical ranges of $0 < a < 1$. TiS_2 was identified as early as the 1970s [67,208] for showing a lithium-intercalation voltage of 2 V and a reversible capacity of 240 $mAhg^{-1}$. However, due to the sensitivity of TiS_2 to moisture (releasing H_2S gas on contact with water), the inclusion of a dangerous, shock-sensitive electrolyte, and the use of metallic lithium, device manufacture was found to be expensive and complex. Nonetheless, it inspired works of magnesium intercalation into TiS_2 [209, 210], and prompted investigations into the Zr [211–214] and Hf [211, 215] analogues. The large inter-layer spacing in VS_2 has been shown to allow rapid insertion and extraction of alkali-metal intercalants [216], and recently it was proposed for magnesium-based cathodes, delivering a reversible discharge capacity of 235 $mAhg^{-1}$ [217]. The Nb- and Ta-based materials [211] have been intercalated to similar levels, but their heavier masses result in lower theoretical capacities below 170 $mAhg^{-1}$. Of course, the ubiquitous MoS_2 [218–223] is a favourite within the study of layered materials and has been the subject of many of its own investigations, demonstrating an intercalation voltage of 2 V with a capacity of 167 $mAhg^{-1}$. This material, along with some others, can exhibit multiple TMDC phases, and has been observed to undergo transitions between them with intercalation [224, 225]. Other materials, such as CrS_2 [226, 227] and ScS_2 [228, 229], are not stable without intercalants, though it is possible to synthesise them in their intercalated forms. ScS_2 in particular has recently been suggested as a promising electrode [230], promising an ideal cathode voltage of 4.5 V and a reversible capacity of 183 $mAhg^{-1}$ and will be the subject of Chapter 5.

Though the above intercalation reaction appears relatively simple, there are many ways for the intercalants to arrange within the host material. The staging of lithium and how it distributes evenly across layers in graphite has been identified and explored in numerous studies. Recent works have identified a similar staging in MoS_2, but with lithium filling the structure in a layer-by-layer manner [225, 231, 232]. Lithium intercalation into SnS_2, on the other hand, has been shown to proceed by a two-phase reaction, forming a SnS_2|$LiSnS_2$ boundary, initiated by nucleation of the $LiSnS_2$ composition [233].

As we discussed above, the number of *d*-electrons plays an important role in both the resultant geometric structure and the electronic properties of TMDCs. It can be expected, then, that upon the intercalation of a foreign species which can donate or accept electrons to/from the host, the effective number of *d*-electrons in the TMDC changes, which would result in corresponding geometric and/or electronic structure changes. Indeed, this has been observed for the intercalation of alkali metals into TMDCs, where the alkali metal donates an electron to the host TMDC structure. Most famously, the transformation of 2H-MoS_2 to 1T-MoS_2 [222], but also the irreversible transition from 2H-$NbSe_2$ to distorted 2H'-$NbSe_2$ [50] and the transformation of 1T-TaS_2 to 2H-TaS_2 [234], with lithium intercalation are all well documented. For intermediate intercalant concentrations, charge donation to a single host transition metal would encourage local distortion, whilst the structure of the surrounding TMDC structure would retain its initial geometry.

For several of these materials, however, the intercalation capacity is dictated by the formation of the Li_2S (or equivalent) compound, a conversion product which can result in the irreversible loss or amorphisaton of the layered TMDC structure [225]. For lithium intercalation, a typical conversion reaction is,

$$\mathrm{Li}_a\mathrm{MX}_2 + (4-a)\mathrm{Li} \rightarrow \mathrm{M} + 2\mathrm{Li}_2\mathrm{X}. \tag{3.4}$$

The post-transition metal sulfide SnS_2, for example, has also been the subject of many studies [233, 235–243], however it has been shown to readily undergo conversion to Li_2S and elemental tin. These conversion reactions allow for further cell charging, facilitated by subsequent reactions involving Li_2S or lithium polysulfides to elemental lithium and sulfur [219, 244], as has utilised in lithium-sulfur batteries. However, they result in the loss of the ideal layered structure and the deposition of the inert metal species of the host material. As a result, the volumetric expansion can reach as high as 80%, resulting in large mechanical stresses and rapid device failure. We can therefore consider the formation of these conversion products the limit to intercalation, such that identifying and improving the intercalant concentration that these reactions occur is a key challenge for investigation.

Intercalation with other species will have a different but equivalent conversion-reaction equations, depending on the nature of the intercalant. Other Group I elements (such as sodium and potassium) have similar chemistry to that of lithium,

and so the reactions and products are analogous (i.e. Na_2X or K_2X). Group II intercalants such as beryllium and magnesium, however, possess twice as many valence electrons, and so they exhibit different chemical behaviour. Whilst intercalation into TMDCs or other layered materials can occur in the same manner, conversion reactions result in different products (MgS instead of Li_2S, for example). Typically, the breakdown of Li_aMX_2 into Li_2X occurs at some point $0 < a < 1$, as has been observed for MoS_2 [220, 223] and WS_2 [244].

Recent works have looked at improving many of the properties offered by these materials, with the aim of extending device operation, increasing the intercalant capacities, and improving operating voltages. Dimension reduction [245–247] provides greater surface area and thus a higher surface reactivity, allowing for faster ionic and electronic transport. To a similar effect, morphology control [218, 248, 249] and composite formation [216, 250–255], particularly through the inclusion of graphitic carbon or other layered materials, has been used to improve electrical and ionic conductivity, provide mechanical support, and ultimately improve the resultant capacity. Coating and encapsulation has been used to protect both the electrolyte and electrode from mutual decomposition, stabilisation of surfaces and prevention of reactions between the electrolyte and the electrode surface [256]. Finally, doping and functionalisation [257, 258] can improve chemical and thermal stability, and allow for some control of the operating voltage [230]. However, to understand the improvements that arise from each of these methods, an understanding of the fundamental electrochemical properties of the bulk structures is first needed. Properties such as the volumetric expansion, the intercalation voltage, and the intercalation capacity need to be established in a consistent manner as these are vital for discussions of electrode materials. Further, much of this family is yet to be investigated, meaning there are still many materials that could offer ideal voltages or higher capacities, or alternatively demonstrate other properties that could be advantageous to a wide range of other applications.

3.3 Computational Details

In this work, first principles techniques based on density functional theory were used to determine structural, energetic, and electronic properties of layered MX_2 materials intercalated with varying levels of either lithium or magnesium. These calculations were performed using the Vienna *Ab initio* Simulation Package (VASP) [161–164]. The projector augmented wave method [139] was used to describe the interaction between core and valence electrons, and a plane-wave basis set was used with an energy cutoff of 700 eV. The valence electrons included for each species are indicated in Table 2.1. vdW interactions have been addressed using the zero damping DFT-D3 method of Grimme [155].

This study focuses on 1T-phase TMDCs, as many of the TMDCs exhibit the 1T-phase [194–196, 205]. Not only are they known to have superior electrical conductivities over their 2Hc-phase counterparts [259], making them better suited to electrode application, but alternative phases often undergo a phase transition to the T-phase under intercalation [260, 261]. However, the Hc-phase is found to be important for several TMDCs. As such, comparisons have been made with the 2Hc-phase for such TMDCs, as is discussed later in the Chapter. Though transition metal dichalcogenide compounds can exhibit a wide range of different structural phases beyond the layered structures considered here [197], we focus on the T- and Hc-phases to utilise their ideal layered structures.

For comparisons of intercalant site and of the T- and Hc-phases, primitive cells of each of the TMDCs were used. However, for a more thorough consideration of these materials with finer sampling of intercalant concentrations, supercells of $(2 \times 2 \times 1)$ and $(2 \times 2 \times 2)$ unit cells of 2Hc- and 1T-phase MX_2, respectively, were generated and structurally relaxed. This corresponds to 24 atoms, eight MX_2 formula units, and two TMDC layers in the supercells. These were then used as the bulk unit cells into which lithium and magnesium were intercalated for evaluation of voltages and thermodynamic stability.

All structural relaxations (allowing for both ionic and unit cell optimisation) were completed using the Perdew-Burke-Ernzerhof (PBE) [119] functional form of the generalised gradient approximation (GGA), and converged to a force tolerance

of 0.01 eV/Å, while electronic self-consistency was considered to an accuracy of 10^{-7} eV. Monkhorst-Pack grids [140] of k-points equivalent to a $6\times6\times6$ grid in the supercells are used throughout. Upon intercalation, local charge transfer leads to local electric fields within the structure, making it impossible to align the electronic structures of pristine and intercalated materials using typical means of core-state alignment [262] or with respect to the vacuum level [262–264]. Instead, we have qualitatively aligned to the high-energy occupied states of the unintercalated superlattice at Γ, allowing us to comment on the relative position of the Fermi level. To account for the inaccurate calculation of exchange in GGA functionals, the HSE06 hybrid functional [130, 135, 265] has also been used for a selection of systems. For these systems, geometric relaxations were performed on the primitive cell to the same force and energy tolerance as used with the PBE functional, though a coarser k-point grid was used due to the increased computational cost of the hybrid functional.

Climbing-image nudged elastic band (CI-NEB) methods, as employed in VASP, were used to consider transition states for intercalant diffusion through the system [156, 157] (using the PBE functional). This method uses a series of interpolated 'images' along a specified path to determine the activation energies for diffusion. For these calculations, we formed 2×2 bilayers of selected TMDCs and fixed the positions of the transition metal species with intercalant species occupying high-coordination sites. CI-NEB relaxations were considered to a force tolerance of 0.01 eV/Å per atom, electronic self-consistency was considered to an accuracy of 10^{-7} eV, and Monkhorst-Pack grids of $6\times6\times1$ k-points were used. Five images were considered along the reaction route.

3.4 Methods for Material Evaluation

When assessing a material for its suitability as an electrode material, there are many key properties that need to be determined. Quantities such as the volumetric expansion and electronic band gaps can be directly obtained from DFT calculations, however there are many other properties that need careful attention. The intercalation voltage gives a measure of the energy associated with interca-

lation of a given ion and hence the energy storage, whereas the intercalation capacity gives a limit on how much of a given intercalant can be introduced to a host material before secondary reactions that degrade the material occur. Here, we outline how we approach these challenges using a first principles approach.

3.4.1 Calculation of Voltage

For a given state of charge, a, the potential difference in the open circuit, $V_{OC}(a)$, can be calculated from the difference between the chemical potential of lithium in the cathode, $\mu_{\mathrm{Li}}^{Cathode}(a)$, and in the anode, $\mu_{\mathrm{Li}}^{Anode}(a)$, divided by the total charge transfer, ze, where z is the valency of the intercalant ion ($z = 1$ in the case of lithium, $z = 2$ for magnesium) and e is the elementary charge [266],

$$V_{OC}(a) = -\frac{\mu_{\mathrm{Li}}^{Cathode}(a) - \mu_{\mathrm{Li}}^{Anode}(a)}{ze}. \tag{3.5}$$

As we are assuming a lithium anode (see the previous discussion in Section 1.3.1 regarding the half-cell potential), we can replace the second term in the numerator with μ_{Li}^{0}, which is the chemical potential of lithium under standard conditions, equivalent to the energy of a single lithium atom when in its bulk form. However, assessing the chemical potential of a given element in a specific cathode compound is not a trivial task. Instead, we now consider the change in electrical energy, ΔE, from discharging a cathode between two charge states, $q_2 > q_1$,

$$\Delta E = \int_{q_1}^{q_2} V_{OC}(a)\, dq = -\int_{q_1}^{q_2} \frac{\mu_{\mathrm{Li}}^{Cathode}(a) - \mu_{\mathrm{Li}}^{0}}{ze}\, dq. \tag{3.6}$$

If we assume that all transferred charge is due to the lithium, we are able to write $dq = ze\, da$, and so,

$$\begin{aligned}
\Delta E &= -\int_{a_1}^{a_2} \mu_{\mathrm{Li}}^{Cathode}(a) - \mu_{\mathrm{Li}}^{0}\, da \\
&= -\left[\int_{a_1}^{a_2} \mu_{\mathrm{Li}}^{Cathode}(a)\, da - \int_{a_1}^{a_2} \mu_{\mathrm{Li}}^{0}\, da\right] \\
&= -\left[G(\mathrm{Li}_{a_2}\mathrm{MX}_2) - G(\mathrm{Li}_{a_1}\mathrm{MX}_2) - (a_2 - a_1)\mu_{\mathrm{Li}}^{0}\right] \\
&= -\Delta G,
\end{aligned} \tag{3.7}$$

which is simply the change in the Gibbs free energy of the host material. This then allows us to write the average voltage between two different lithium contents

as,

$$V_{OC} = -\frac{dG}{dq} \approx -\frac{\Delta G}{\Delta q} = -\frac{G(\mathrm{Li}_{a_2}\mathrm{MX}_2) - \left[G(\mathrm{Li}_{a_1}\mathrm{MX}_2) + (a_2 - a_1)\mu^0_{\mathrm{Li}}\right]}{(a_2 - a_1)ze}, \tag{3.8}$$

in terms of the Gibbs free energy at different lithium contents, which are much more accessible quantities. We make a further approximation,

$$V_{OC} = -\frac{E_{\mathrm{Li}_{a_2}\mathrm{MX}_2} - \left[E_{\mathrm{Li}_{a_1}\mathrm{MX}_2} + (a_2 - a_1)E_{\mathrm{Li}}\right]}{(a_2 - a_1) \times ze}, \tag{3.9}$$

where we have replaced the Gibbs free energy of a given compound with the total energy, $E_{\mathrm{Li}_a\mathrm{MX}_2}$, as is obtained using DFT methods. We do this as the pressure-volume, and vibrational entropy contributions are known to be negligible in transition metal oxide and chalcogenide materials [266–268].

Whilst we can evaluate the total energy for different levels of intercalation, the true lowest energy for a specific intercalant concentration might not be achievable for the unit cell size being modelled within a DFT framework. Instead, a combination of different concentrations (the total concentration equalling the target concentration) might instead be preferred, as has been observed for some materials including SnS_2 [233, 239, 269, 270]. For example, whilst we have evaluated the energy for a supercell containing four lithium atoms, a lower energy might instead be obtained by the average of a cell with no lithium in and cell with eight lithium atoms. In cases like this, the intercalated structure would have a phase separation, with fully intercalated regions and completely empty regions instead of a homogeneous lithium distribution. This simple example can be extended to include other components and different numbers of components, which can have dramatic effects on the resulting voltage profiles. In the following short discussion we shall make use of notation whereby the true energy (allowing for phase separations) is written as $E'_n = \sum_{m=0}^{8} c_m E_m$, in terms of the energy obtained from DFT for a given composition $E_m \equiv E_{\mathrm{Li}\frac{m}{8}\mathrm{MX}_2}$.

We can easily visualise this phase separation by consideration of the convex hull: Figure 3.6a presents the convex hull for $\mathrm{Li}_a\mathrm{MoS}_2$ using the formation energy calculated with,

$$E_{form} = E_{\mathrm{Li}_a\mathrm{MoS}_2} - \left[aE_{\mathrm{LiMoS}_2} + (1 - a)E_{\mathrm{MoS}_2}\right]. \tag{3.10}$$

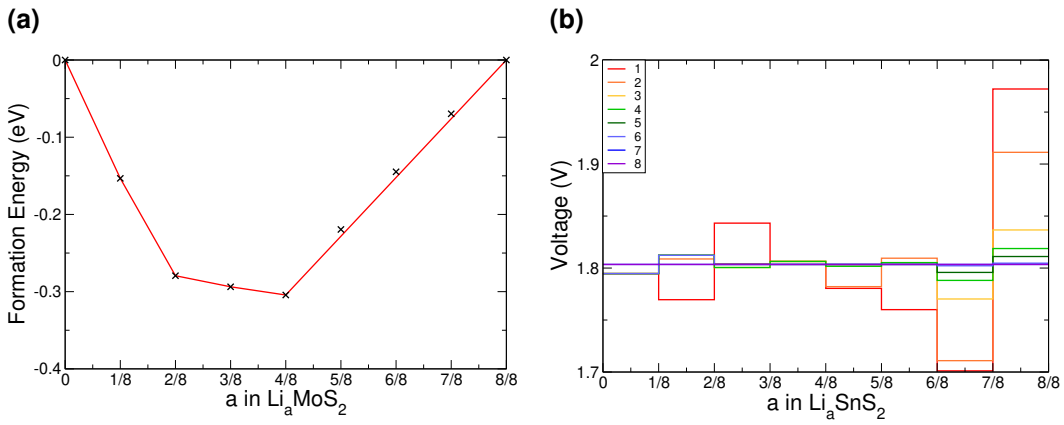

Figure 3.6: The convex hull for Li_aMoS_2 is shown in 3.6a, and the effect on the resultant voltage (for Li_aSnS_2) from changing the maximum number allowed for any c_m involved in calculating the lowest energy E'_n for a given lithium concentration is given in 3.6b.

Whilst the formation energies lie on the hull for $0 \leq a \leq \frac{4}{8}$ $(0 \leq m \leq 4)$, for concentrations of $a = \frac{5}{8}, \frac{6}{8}, \frac{7}{8}$ $(m = 5, 6, 7)$ they lie above it, and so a combination of the energies $E_{\mathrm{Li}\frac{4}{8}\mathrm{MoS_2}}$ and $E_{\mathrm{LiMoS_2}}$ are required.

This is also shown for SnS_2 in Figure 3.6, where the effect of the number of components included is highlighted. The point at which the voltage profile becomes constant or decreasing with lithium concentration gives the correct profile. As shown in Figure 3.6, the voltage for SnS_2 is constant across the intercalation range. This is due to the fact that, for each of the concentrations, it is energetically preferred for the lithium to separate into regions with no lithium (with an energy of E_0) and regions that are fully intercalated (with and energy of E_8). For example, the lowest energy for $Li_{\frac{1}{8}}SnS_2$ is given by $E'_1 = (\frac{7}{8}E_0 + \frac{1}{8}E_8) < E_1$, and the lowest energy for $Li_{\frac{2}{8}}SnS_2$ is given by $E'_2 = (\frac{6}{8}E_0 + \frac{2}{8}E_8) < E_2$. As the difference between consecutive concentrations is a constant $\Delta E = \frac{1}{8}(E_8 - E_0)$, the voltage is also constant across the range.

3.4.2 Thermodynamic Phase Diagrams

The stability of TMDCs with intercalation depends heavily on how favourable the formation of secondary products is, for example Li_2X or MgX. Generally, these conversion products are not desired for intercalation electrodes as they indicate

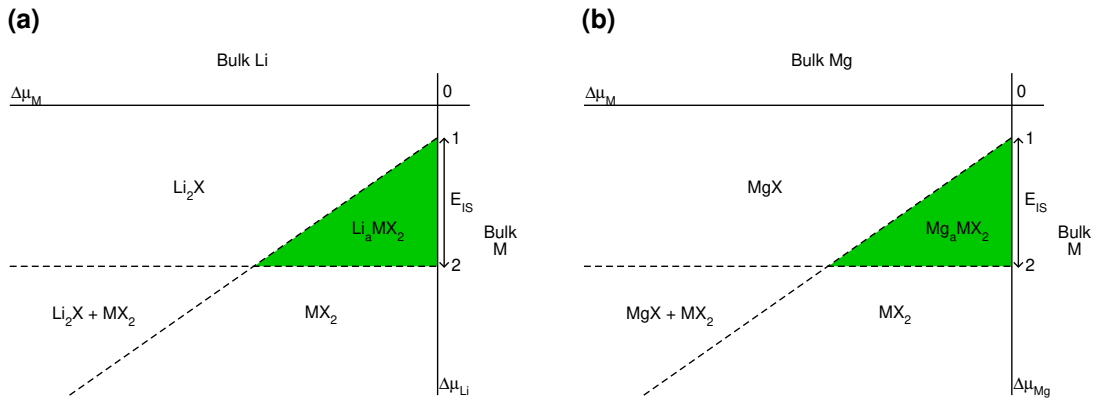

Figure 3.7: Schematic phase diagrams for lithium (3.7a) and magnesium (3.7b) intercalated TMDCs, constructed using equations (3.19)-(3.20) and (3.23).

the loss of the layered TMDC structure, and limits the reversibility of cell charging. By assessing the relative stability of these conversion products against the intercalated phases, one can construct phase diagrams indicating the viability of the intercalated structure at different intercalation capacities [271]. We can then determine the maximum intercalant capacity that can be reached, and hence the reversible charge capacity, a key metric for assessing the viability of electrode materials. For an arbitrary TMDC material, MX_2, when intercalated with lithium, Li_aMX_2, we define the Gibbs free energy of formation of relevant products:

$$\Delta G(\mathrm{Li}_a\mathrm{MX}_2) = E(\mathrm{Li}_a\mathrm{MX}_2) - [a\mu^0_{\mathrm{Li}} + \mu^0_{\mathrm{M}} + 2\mu^0_{\mathrm{X}}], \tag{3.11}$$

$$\Delta G(\mathrm{MX}_2) = E(\mathrm{MX}_2) - [\mu^0_{\mathrm{M}} + 2\mu^0_{\mathrm{X}}], \tag{3.12}$$

and,

$$\Delta G(\mathrm{Li}_2\mathrm{X}) = E(\mathrm{Li}_2\mathrm{X}) - [2\mu^0_{\mathrm{Li}} + \mu^0_{\mathrm{X}}]. \tag{3.13}$$

Here, $\Delta G(\mathrm{A})$ gives the Gibbs free energy of formation of the compound A, $E(\mathrm{A})$ gives the energy of the compound A, and $\mu^0_{\mathrm{B}} = E(\mathrm{B})$ gives the chemical potential of elemental species B when it is in its elemental bulk structure.

The thermodynamic equilibrium condition requires,

$$\Delta G(\mathrm{Li}_a\mathrm{MX}_2) = a\Delta\mu_{\mathrm{Li}} + \Delta\mu_{\mathrm{M}} + 2\Delta\mu_{\mathrm{X}}, \tag{3.14}$$

where we have used the notation $\Delta\mu_{\mathrm{B}} = \mu_{\mathrm{B}} - \mu^0_{\mathrm{B}}$, with μ_{B} being the chemical potential of elemental species B in Li_aMX_2. This simply states that the energy of

the intercalated compound is the sum of the chemical potentials of the constituent atoms. Rearranging the thermodynamic equilibrium condition gives,

$$\Delta\mu_{\mathrm{X}} = \frac{1}{2}\big\{\Delta G(\mathrm{Li_aMX_2}) - [a\Delta\mu_{\mathrm{Li}} + \Delta\mu_{\mathrm{M}}]\big\}. \tag{3.15}$$

We require that MX_2, Li_2X, and the bulk forms of the component elements do not form. Therefore,

$$\Delta\mu_{\mathrm{M}} + 2\Delta\mu_{\mathrm{X}} \leq \Delta G(\mathrm{MX_2}), \tag{3.16}$$

$$2\Delta\mu_{\mathrm{Li}} + \Delta\mu_{\mathrm{X}} \leq \Delta G(\mathrm{Li_2X}), \tag{3.17}$$

and,

$$\Delta\mu_{\mathrm{Li,M,X}} \leq 0. \tag{3.18}$$

Substituting (3.15) into (3.16) and rearranging,

$$\frac{1}{a}\big\{\Delta G(\mathrm{Li_aMX_2}) - \Delta G(\mathrm{MX_2})\big\} \leq \Delta\mu_{\mathrm{Li}}. \tag{3.19}$$

This then gives the thermodynamic limit on the lithium chemical potential such that the intercalation of the TMDC is preferred to the pristine TMDC and bulk lithium.

We now substitute (3.15) into (3.17) which results in,

$$\Delta\mu_{\mathrm{Li}} \leq \frac{1}{4-a}\big[2\Delta G(\mathrm{Li_2X}) - \Delta G(\mathrm{Li}_a\mathrm{MX_2}) + \Delta\mu_{\mathrm{M}}\big], \tag{3.20}$$

which is then the thermodynamic limit on the chemical potential of the lithium so that the conversion-reaction product Li_2X do not form. Thus, we have two equations describing the boundary conditions for the chemical potential of lithium, dependent on formation energies of the relevant products, and the chemical potentials of the relevant metals.

We can equally consider the magnesium-compounds, and the limits on the chemical potential of magnesium. We start by defining the Gibbs free energy of formation of MgX,

$$\Delta G(\mathrm{MgX}) = E(\mathrm{MgX}) - [\mu^0_{\mathrm{Mg}} + \mu^0_{\mathrm{X}}] \tag{3.21}$$

Analogous to the condition (3.17),

$$\Delta\mu_{\mathrm{Mg}} + \Delta\mu_{\mathrm{X}} \leq \Delta G(\mathrm{MgX}), \tag{3.22}$$

which can be combined with the magnesium equivalent of (3.15), to get,

$$\Delta\mu_{\mathrm{Mg}} \leq \frac{1}{2-a}\big[2\Delta G(\mathrm{MgX}) - \Delta G(\mathrm{Mg_aMX_2}) + \Delta\mu_{\mathrm{M}}\big]. \tag{3.23}$$

It should be noted, by considering the equations (3.11)-(3.13) and (3.21), that the limiting conditions are independent of μ^0_{X},and hence $\Delta\mu_{\mathrm{X}}$. As a result, the phase diagrams are only dependent on the chemical potentials of lithium and the relevant metal, $\Delta\mu_{\mathrm{Li,Mg,M}}$.

Using equations (3.18)-(3.20) and (3.23), we can construct thermodynamic phase diagrams with the purpose of estimating the intercalation capacity. Schematics of such phase diagrams are shown in Figure 3.7. We restrict ourselves to the negative-negative quadrant to ensure that the elemental bulks do not form. Above the diagonal line, labelled "1", the experimentally observed Li_2S (or equivalent) crystal is favoured, as opposed to the intercalated TMDC. Below the horizontal line, labelled "2", the pristine MX_2 structure is preferred to intercalation. The result of this is that intercalation is favoured for chemical potential combinations that sit within the shaded region indicated in Figure 3.7. Outside of this window, however, the secondary products (as indicated in the figure) are favourable to form. Though a transition to these is not guaranteed, the intercalated TMDC sstructure becomes meta-stable. Whilst other compounds could have their respective boundaries determined to be included in these phase diagrams, such as Li_2X_2 or MX, these first require the disintegration of the Li_aMX_2 material into Li_2X and/or elemental bulks. Hence, we only consider the limits outlined above.

We can quantitatively compare the phase diagrams for the different concentrations considered by evaluating the difference between the intercepts of lines '1' and '2' with the vertical $\Delta\mu_{\mathrm{Li}}$-axis. We define this as,

$$E^{\mathrm{Li}}_{IS} = \Delta\mu^{(1)}_{\mathrm{Li}}(\Delta\mu_{\mathrm{M}} = 0) - \Delta\mu^{(2)}_{\mathrm{Li}}(\Delta\mu_{\mathrm{M}} = 0), \tag{3.24}$$

where $\Delta\mu^{(1/2)}_{\mathrm{Li}}(\Delta\mu_{\mathrm{M}} = 0)$ is the value of the boundary line $1/2$ at the point where $\Delta\mu_{\mathrm{M}} = 0$. Alternatively, using (3.19) and (3.20), E_{IS} can be expressed as,

$$E^{\mathrm{Li}}_{IS} = \frac{2}{4-a}\Delta G(\mathrm{Li_2X}) + \frac{1}{a}\Delta G(\mathrm{MX_2}) - \frac{4}{4a-a^2}\Delta G(\mathrm{Li_aMX_2}), \tag{3.25}$$

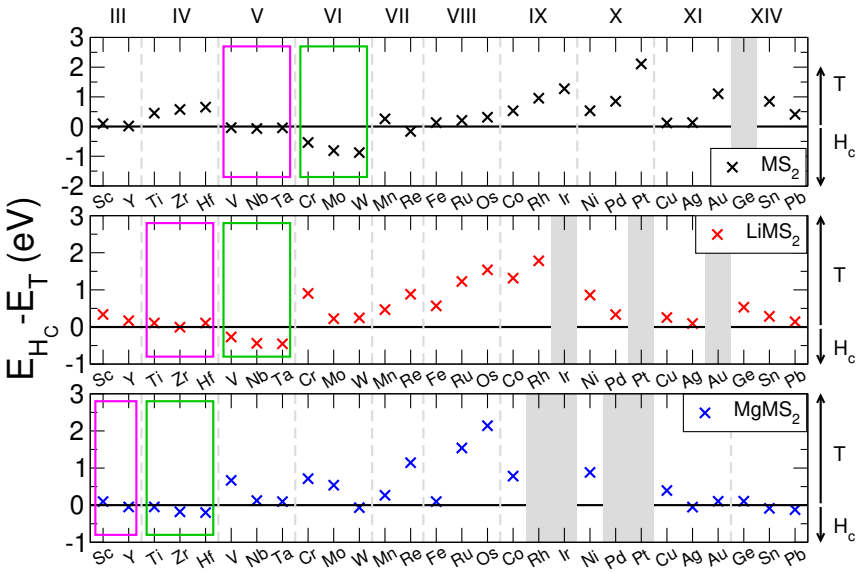

Figure 3.8: Comparison of the TMDC T- and Hc-phase energies in the pristine bulk and intercalated forms, for the sulfide materials. Positive values indicate a more favourable T-phase, whereas negative values indicate a more favourable Hc-phase. Group V-like behaviour is tracked with the magenta boxes, and Group VI-like behaviour is tracked with the green boxes.

in terms of the relevant formation Gibbs free energy values. Each of these free energy formation values should be negative for them to be thermodynamically stable with respect to their atomic constituents. When the value of E_{IS}^{Li} is negative, the first two terms dominate, and line '1' intercepts below line '2' so no stability region exists. When the value of E_{IS} is positive, however, $\Delta G(\mathrm{Li}_a\mathrm{MX}_2)$ dominates and the intercalated MX_2 material is stable. For magnesium intercalation, we have an equivalent expression using,

$$E_{IS}^{\mathrm{Mg}} = \Delta\mu_{\mathrm{Mg}}^{(1)}(\Delta\mu_{\mathrm{M}} = 0) - \Delta\mu_{\mathrm{Mg}}^{(2)}(\Delta\mu_{\mathrm{M}} = 0), \tag{3.26}$$

resulting in,

$$E_{IS}^{\mathrm{Mg}} = \frac{2}{2-a}\Delta G(\mathrm{MgX}) + \frac{1}{a}\Delta G(\mathrm{MX}_2) - \frac{2}{2a-a^2}\Delta G(\mathrm{Mg_aMX}_2). \tag{3.27}$$

3.5 Determination of Structure

As we discussed in Section 3.2.1, the family of TMDCs have been shown to exhibit multiple polymorphs of the layered structure, most commonly the 1T-phase

and 2Hc-phase [195, 196]. The phase a TMDC exhibits is largely determined by the number of transition metal *d*-electrons. As the phase of the host TMDC material can have some effect on the operating voltage, material stability, and hence the overall energy capacity, it is important that the correct phase be determined first.

We evaluate the energetic ordering of these phases in the pristine bulk by taking the difference between the Hc-phase energy (E_{H_c}) and the T-phase energy (E_T). The results of this are presented in Figure 3.8 for the TMDC sulfides, where positive values indicate a more favourable T-phase and negative values indicate a more favourable Hc-phase. Equivalent data for the selenide and telluride materials is presented in Appendix B. We find that most of the TMDCs prefer the T-phase, with the exception of those composed of Group V and Group VI transition metals which prefer to exhibit the Hc-phase, agreeing with many other works [195, 196, 259].

Some materials are susceptible to more significant structural changes, and do not exhibit a layered structure. $LiAuS_2$, $LiPtS_2$, $LiPtSe_2$, $MgPdS_2$, $MgPtS_2$, and $MgPtSe_2$ each structurally relaxed from the H-phase into a structure that does not resemble that of a layered TMDC, and so these have also not been included. For others, geometric relaxation transformed the intercalated structure from the H-phase into the T-phase, and so a quantitative comparison between the two structures was not able to be made, though we are able to comment that the T-phase is lower in energy than the H-phase. As such, these points, which included $LiIrS_2$, $MgGeSe_2$, $MgRhS_2$, $MgIrS_2$, and $MgRhSe_2$, have also been omitted.

Upon intercalation, charge donation from the intercalated species increases the effective number of *d*-electrons on the transition metal, and so the effective transition metal Group is increased. This can result in a phase transition between the two phases, as has been demonstrated by many materials, but most notably by MoS_2 [225, 261]. With lithium intercalation, we note that the electron count of Group VI metal sulfides has effectively increased by one, resulting in them being 'Group VII-like' and reproducing the H $\rightarrow$ T transition seen in MoS_2 [261]. When Group V materials are intercalated with lithium the extra electron results in 'Group VI-like' behaviour (with the H phase being preferred), and upon magne-

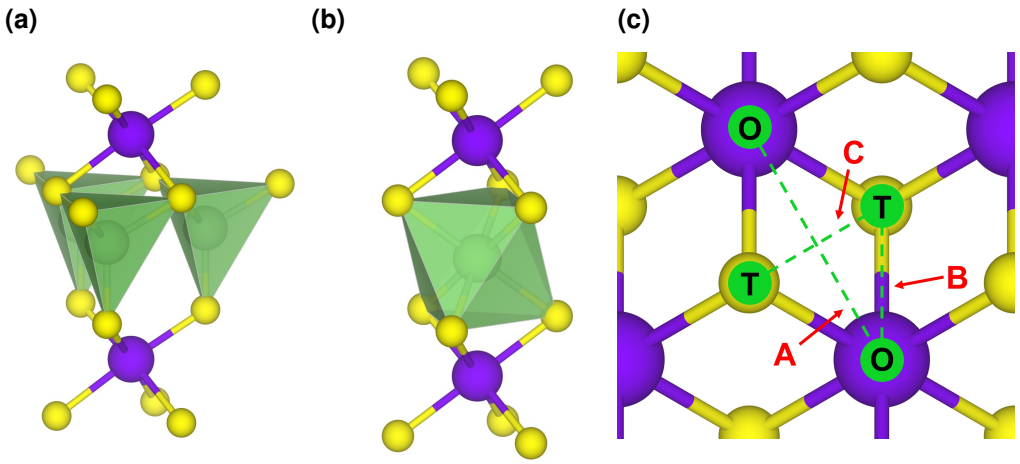

Figure 3.9: Tetrahedral (3.9a) and octahedral (3.9b) coordination of an intercalant with sulfur in an intercalated TMDC. 3.9c shows the different routes considered for the CI-NEB calculations.

sium intercalation the Group IV materials become 'Group VI-like'. This behaviour, and the favourability of the Hc-phase over the T-phase, is indicated with the green boxes in Figure 3.8. We see that the pristine Group V materials show little difference in energy between the T- and Hc-phases (with $E_{H_c} - E_T$ being close to 0 eV). When intercalated with lithium, the Group IV materials lose their clear preference for the T-phase and become 'Group V-like', as do the Group III materials when intercalated with magnesium. This progression of Group V behaviour is indicated with the magenta boxes in Figure 3.8. From these results we conclude that (i) the T-phase is the preferred phase in the pristine, lithium-intercalated, and magnesium-intercalated forms for most of the TMDCs considered in this work, with the exception of those materials composed of early transition metals, and (ii) the additional electrons from lithium causes Group VI TMDCs to undergo a H$\rightarrow$T transition, and similarly the addition electrons from magnesium causes Group IV TMDCs to undergo a T$\rightarrow$H transition. We therefore also consider the Hc-phase TMDCs only for the Group IV, V, and VI transition metals.

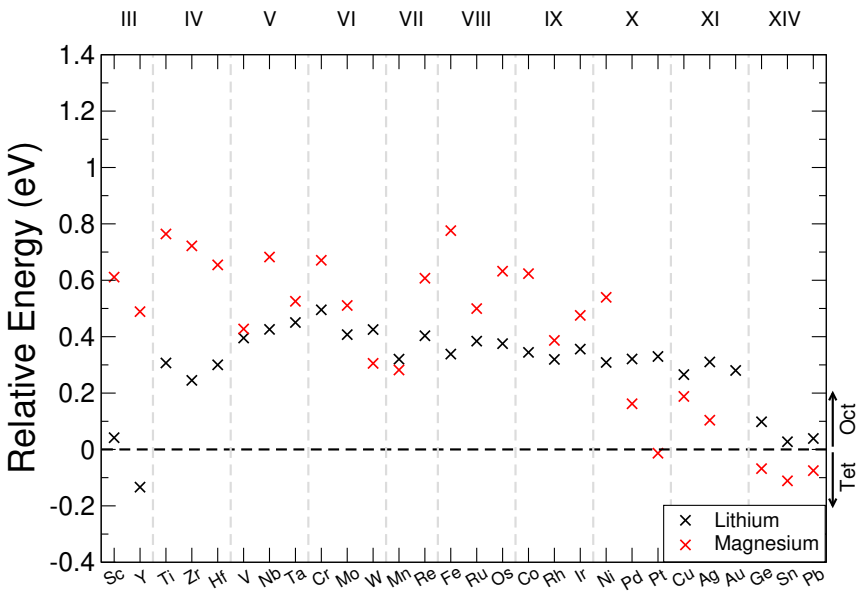

Figure 3.10: Relative energy of the tetrahedral intercalation site compared to the octahedral intercalation site for the sulfide TMDCs. Data for lithium intercalation is presented in black, and data for magnesium intercalation is presented in red.

3.6 Intercalation Site

Before assessing the intercalation properties of a host material, and hence its suitability for electrode applications, it is important to first determine the correct intercalation site within it. The two sites often considered in investigations of intercalated TMDCs are the octahedrally coordinated site and the tetrahedrally coordinated site directly above the chalcogen. Whilst the octahedrally coordinated site has been shown to be the preferred site for many TMDC-like structures intercalated with lithium [82, 272–274] and magnesium [210, 274], for consistency, we examine this here. First, we compare the relative energy from intercalation into each of these sites of the primitive cell for both lithium and magnesium intercalation, the results of which are presented in Figure 3.10. We focus on the sulfide materials here, but equivalent data for the selenide and telluride materials is presented in Appendix B. For most of the TMDCs, we find that the tetrahedrally coordinated site (Figure 3.9a) is higher in energy than the octahedrally coordinated site (Figure 3.9b) by $\sim$0.5 eV. This is due to the octahedral site having a higher coordination between the intercalant and chalcogen species than the tetrahedral site. We do identify some exceptions, such as $LiYS_2$, $LiYSe_2$, $MgWSe_2$, $MgAuSe_2$, and $MgGeSe_2$, where the tetrahedral site is lower in energy, though

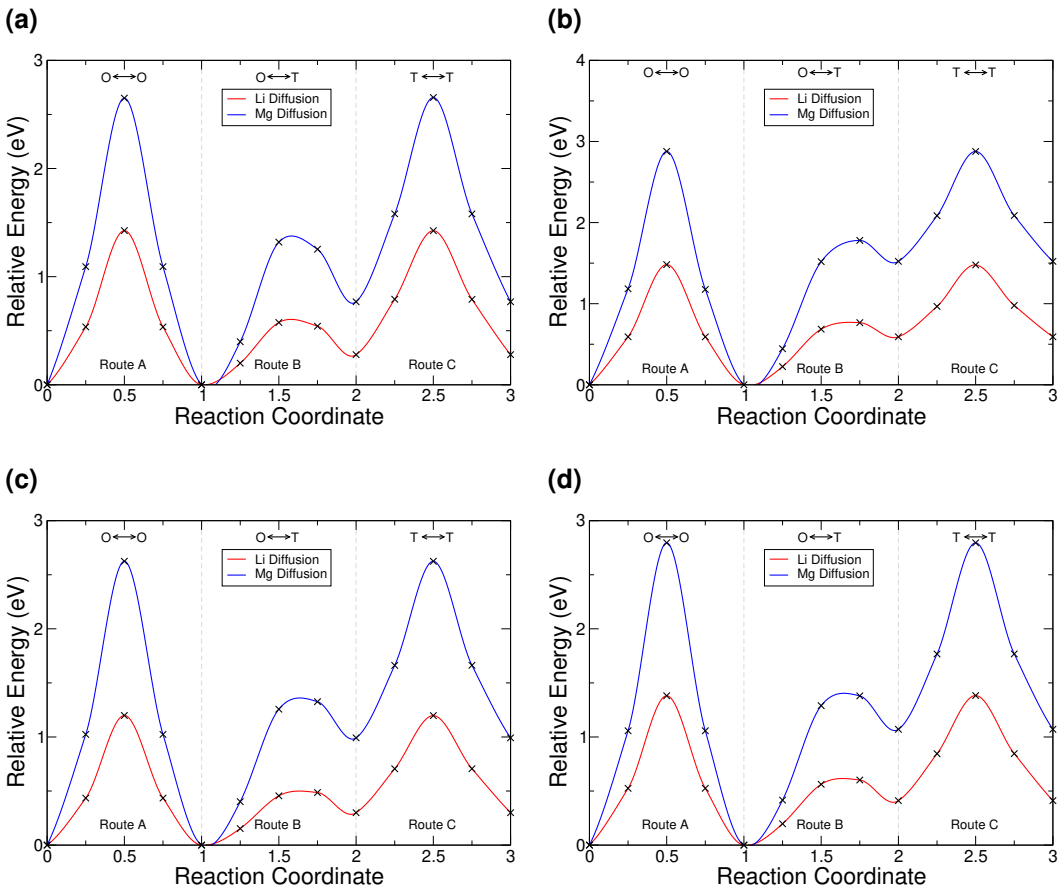

Figure 3.11: Nudged elastic band diffusion barriers for ScS_2 (3.11a), TiS_2 (3.11b), ZrS_2 (3.11c), and $ZrSe_2$ (3.11d). Octahedral (O) and tetrahedral (T) sites are indicated. Data for lithium diffusion is shown in red, and in blue for magnesium intercalation.

a closer investigation of these (using larger unit cells and hence intermediate intercalant concentrations) show a transition in favourability of the two sites: for concentrations of a in Li_aMX_2 and Mg_aMX_2 greater than 0.5 the tetrahedral site is indeed energetically preferred, but for concentrations lower than 0.5 the octahedral is preferred. Thus, if these TMDC materials are intercalated from MX_2, the octahedral site will be occupied first, and promote further filling of octahedral sites as more intercalants are added.

Whilst these high-symmetry, high-coordination intercalation sites are frequently considered for investigations of intercalation into TMDCs, we have also performed nudged elastic band (NEB) calculations between these sites on selected systems, to confirm that there are no lower-energy sites within these materials. The three routes investigated are a) between two octahedrally-coordinated (O) sites, depicted by Route A in Figure 3.9c, b) between one octahedrally-coordinated site

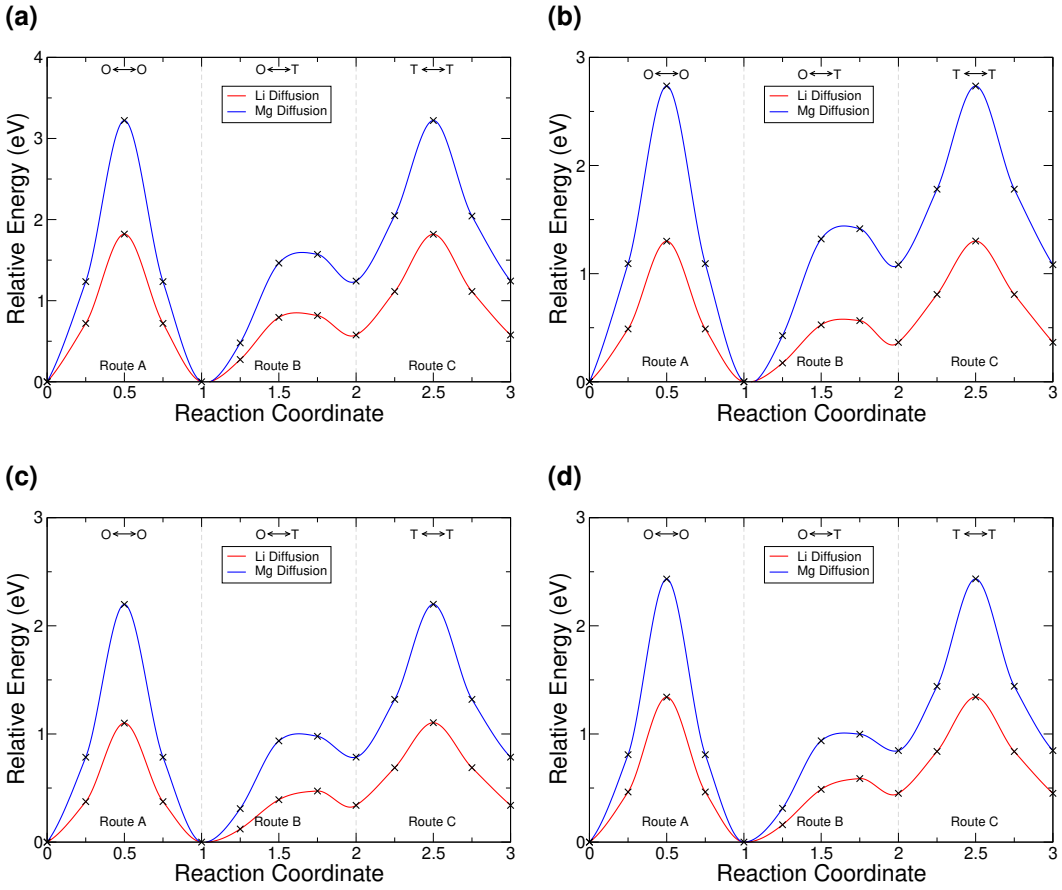

Figure 3.12: Nudged elastic band diffusion barriers for $ZrTe_2$ (3.12a), HfS_2 (3.12b), SnS_2 (3.12c), and $SnSe_2$ (3.12d). Octahedral (O) and tetrahedral (T) sites are indicated. Data for lithium diffusion is shown in red, and in blue for magnesium intercalation.

and one tetrahedrally-coordinated (T) site, depicted by Route B, and c) between two tetrahedrally-coordinated sites, depicted by Route C. We have considered a selection of TMDC materials (ScS_2, TiS_2, ZrS_2, $ZrSe_2$, $ZrTe_2$, HfS_2, SnS_2, and $SnSe_2$) for this investigation. We have not performed an exhaustive investigation into the diffusion barriers of every TMDC material due to the dependency of results on the calculation details. As a result of the periodic boundary conditions used here, we have here fixed the positions of the host transition metal atoms throughout the CI-NEB calculation, as the diffusion of a single ion should only cause local distortions and not cause the macroscopic expansion of whole TMDC sheets. Restriction of the out-of-plane expansion results in the barriers we have determined being over-estimations [210]. As such, our use of the CI-NEB is focused on determination of intercalation site.

For both lithium and magnesium intercalation, we find that the octahedrally- and

tetrahedrally-coordinated sites commonly used for investigations of intercalated TMDCs are local minima within the layer, and find no other minima. As such, these are the only candidates for intercalation sites. Each of the materials also show that the octahedrally-coordinated site is lower in energy that the tetrahedral, due to a higher Li-S coordination and a larger volume for intercalation [191], agreeing with the above discussion. Hence, we conclude that the octahedral site is the correct site for ion intercalation, which is in agreement with other TMDC investigations [191, 233, 272, 273].

These CI-NEB results also allow us to comment on the diffusion properties of intercalants in such layered materials. As the rate of diffusion is determined through an Arrhenius equation, the height of the activation barriers is a key parameter for characterizing electrode materials. For each of the materials considered, we see that, whilst Route A offers the most direct path between two octahedral sites, diffusion along Route B has a lower activation energy. We also find that magnesium diffusion is subject to higher barriers for each of the three routes considered. This can be attributed to the higher ionic charge: the larger positive charge of the intercalant and the larger negative charge of the host chalcogen produce stronger Coulombic interactions than those for lithium intercalation. Separation of these oppositely-charged species throughout diffusion therefore requires more energy, and thus a larger barrier to diffusion. For example, in $SnSe_2$, the diffusion barrier along Route A is 1.34 eV for lithium and 2.43 eV for magnesium. The lowest diffusion barrier is actually found along Route B, where the barriers are 0.59 eV and 1.01 eV for lithium and magnesium, respectively. This agrees with other works on TMDC intercalation [205, 210, 226]. Diffusion of both lithium and magnesium would therefore occur at a higher rate along Route B than along Route A.

From the results presented here, it is clear that the preferred site of intercalation is the octahedrally-coordinated site above the transition metal of the host material. As such, we use this site for the following study. For the $2 \times 2 \times 2$ supercells used in this work, there are eight different sites available for intercalation (indexed a - h in Figure 3.13) and 23 unique intercalant configurations for intercalation, listed in Table 3.1. Each of these configurations has been considered.

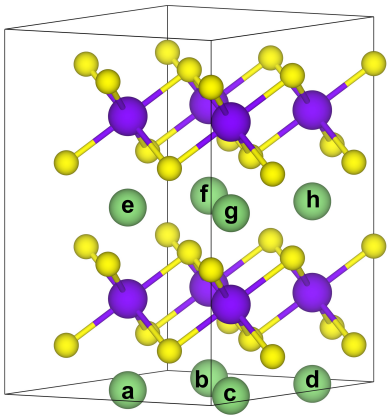

Figure 3.13: The different intercalation sites available in the supercells of T-phase TMDCs considered in this work.

3.7 Charge Analysis

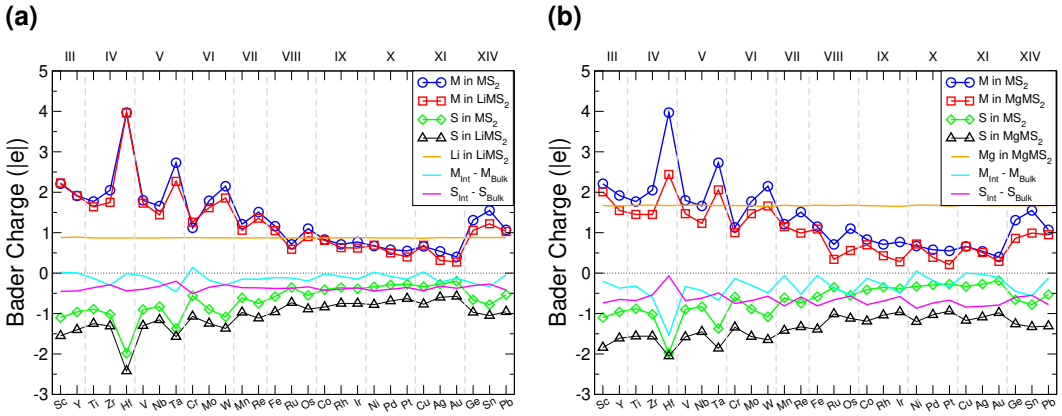

Figure 3.14: Bader charges for the metal, sulfur, lithium, and magnesium atoms in the bulk, $LiMS_2$, and $MgMS_2$ structures. Blue circles correspond to the metal atom (M) in the bulk MS_2 structure, red squares correspond to M atom in the intercalated structure, green diamonds correspond to the sulfur atom (S) in the bulk MS_2 structure, black triangles correspond to S atom in the intercalated structure, and the orange line indicates the charge of the intercalated species in the intercalated structure. The data for the lithium-intercalated sulfides are presented in Figure 3.14a, and the magnesium-intercalated data is presented Figure 3.14b.

Charge transfer from the intercalant species to the host material is the fundamental mechanism for energy storage in electrode materials, and the distribution of charge within the material can affect how the structure transforms during intercalation, dictating the resultant volumetric expansion. It is therefore important to consider both the magnitude and direction of any charge transfer. To this end,

No. Li Atoms	Sites Filled	No. Li Atoms	Sites Filled
0	-	4	adeh
1	a	4	adfg
2	ab	4	adfh
2	ae	5	abcde
2	af	5	abcef
2	ah	5	abceh
3	abc	6	abcdef
3	abe	6	abcefg
3	bce	6	abdefg
4	abcd	6	bcdefg
4	abce	7	abcdefg
4	abch	8	abcdefgh

Table 3.1: Table showing the 24 different intercalation configurations (including the un-intercalated) considered for the intercalation of MX_2 materials for nine different lithium concentrations.

we utilise two different approaches for assessing charge transfer: Bader charge analysis, and evaluation of differences in the charge density.

Bader charge analysis [144–147, 149] was performed on both the pristine TMDCs and the fully intercalated ($LiMX_2$ and $MgMX_2$) TMDCs, and the average charges of the M, X, Li, and Mg atoms are all displayed in Figure 3.14 for the TMDC sulfides. Firstly, we note that the charge of the intercalant ion in an intercalated TMDC structure maintains an almost constant value, independent of the host material. Lithium maintains a charge of of $+0.86$ (± 0.02) |e| across all TMDCs considered, agreeing with Bader charges reported for the same materials with the chalcopyrite structure [198] and in graphite [275]. For magnesium intercalation, the magnesium ion maintains a charge of $+1.63$ $(^{+0.05}_{-0.07})$ |e| across the materials considered. On average, the magnesium ions posses a charge 1.89 times greater than that of the intercalated lithium, close to the double valency of the magnesium ion.

Generally, the M species has a small reduction in its charge after intercalation,

as indicated by the cyan line in Figure 3.14. There is a larger reduction for magnesium intercalation than there is for lithium intercalation, demonstrating that the reduction in the charge of the metal arises from the intercalant. This charge transfer to the metal species is increased as the atomic number of the chalcogen increases, due to the greater number of electrons already present and hence the reduced electronegativity of the chalcogen. There is a greater transfer of electronic charge to the chalcogen species compared to the charge transferred to the metal, as indicated by the magenta line in Figure 3.14. As the chalcogen species is both closer to the intercalant and more electronegative than the metal species, this is unsurprising. Again, there is a greater charge transfer to the chalcogen species with magnesium intercalation than with lithium intercalation. We identify a gradual decrease in the absolute charge on both the transition metal and chalcogen in the intercalated states, as the Group of the transition metal is increased, which has also been noted for the chalcopyrite structure [198]. Selenide and telluride data show the same trends, which are presented in Appendix B.

Above, we have only considered the Bader charges of the extremes of intercalation (the MX_2, $LiMX_2$, and $MgMX_2$ compositions). Of course, during cycling of a cell, intermediate concentrations will be achieved, potentially resulting in different charges on the component ions to those at each end of the intercalation range. To investigate the charges each ionic species can explore, we present in Figure 3.15 and Figure 3.16 the charges exhibited by ions in selected TMDCs, across each of the 24 intercalant configurations considered in this work. Straight-line connections between the MX_2 and $LiMX_2$/$MgMX_2$ compositions have been included as visual aid.

We present the results for the intercalated ZrX_2 materials in Figure 3.15, and for NbS_2, GeS_2, and SnS_2 in Figure 3.16. The first thing of note is the uniform charge exhibited by both lithium and magnesium intercalants. This follows the constant charge exhibited by both intercalants regardless of which host material they are introduced to. Of the TMDCs considered, the transition metals all closely follow the linear trend suggested, with very little spread. On the other hand, the chalcogens follow the linear line fairly well but present a much larger spread in charges. This greater spread seen for the chalcogen is to be expected, as the

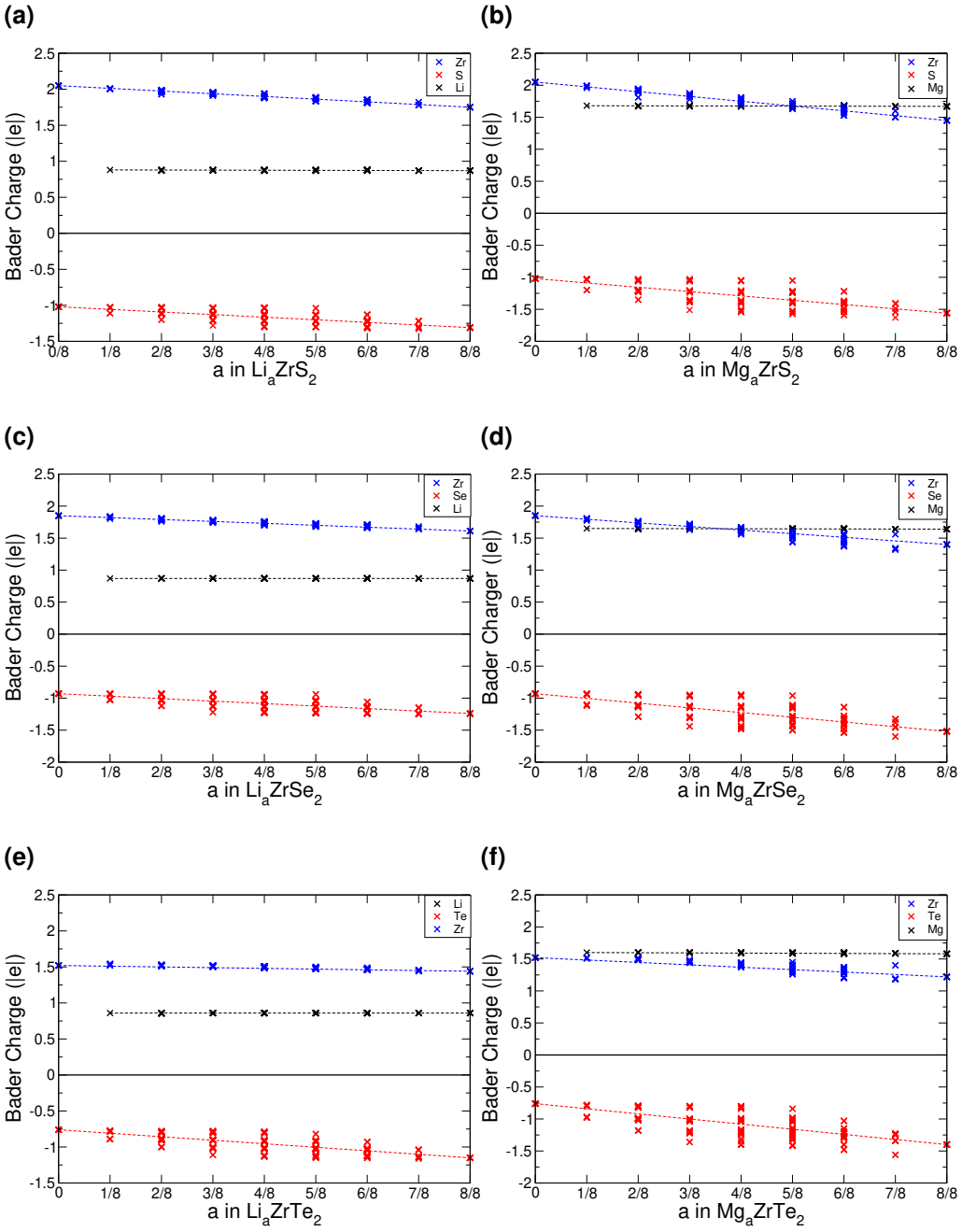

Figure 3.15: Bader charges for lithium-intercalated ZrS_2 (3.15a), $ZrSe_2$ (3.15c), and $ZrTe_2$ (3.15e) across the different intercalant concentrations and configurations considered. Similarly, the Bader charges of magnesium-intercalated ZrS_2 (3.15b), $ZrSe_2$ (3.15d), and $ZrTe_2$ (3.15f) are also shown. Dashed lines connecting the initial and final charges have also been included as visual aid.

ions are closest to the intercalant ions and receive most of the donated electronic charge.

Beyond Bader charge analysis, an alternative evaluation of the charge transfer can be achieved by analysing the differences in the charge density before and

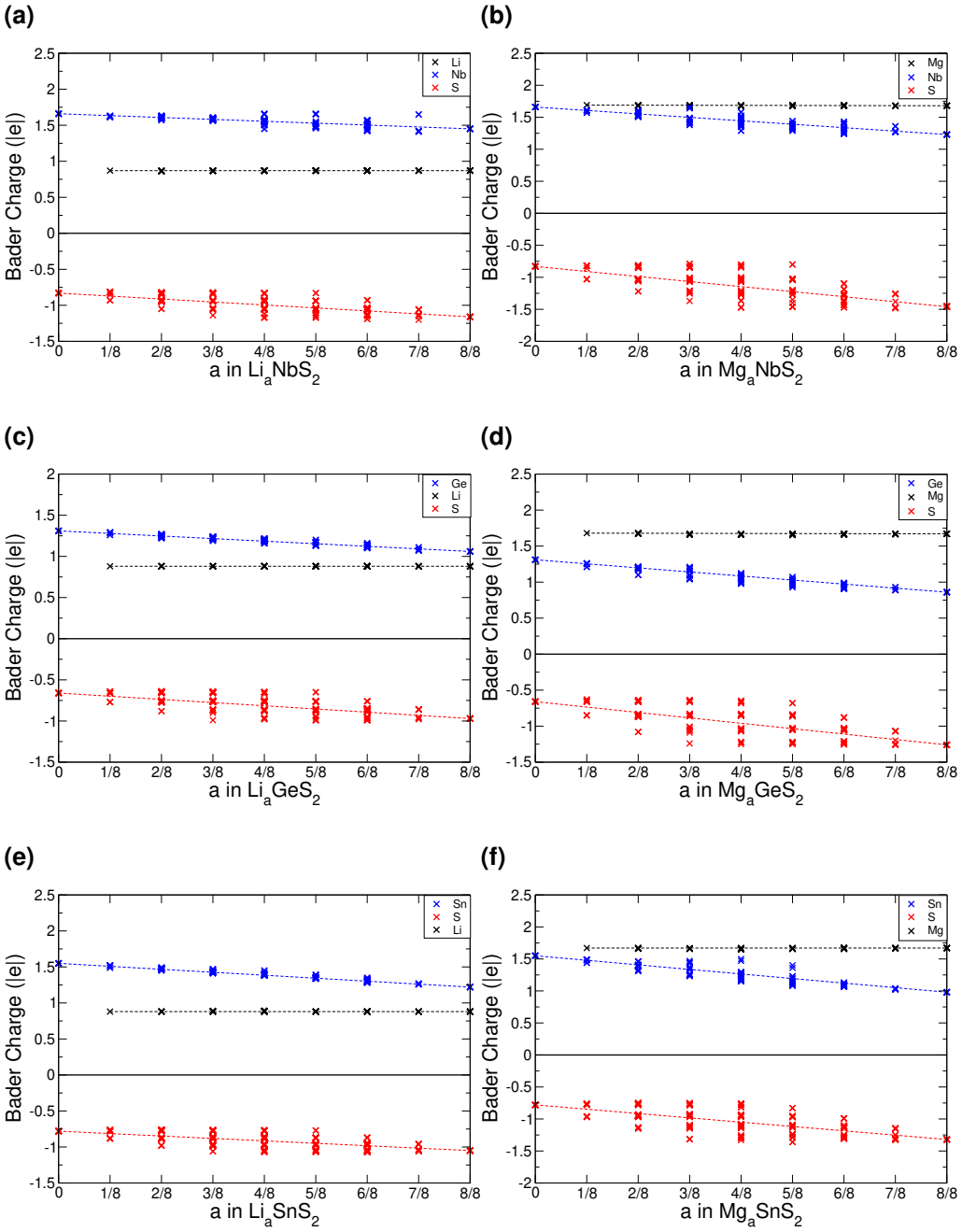

Figure 3.16: Bader charges for lithium-intercalated NbS_2 (3.16a), GeS_2 (3.16c), and SnS_2 (3.16e) across the different intercalant concentrations and configurations considered. Similarly, the Bader charges of magnesium-intercalated NbS_2 (3.16b), GeS_2 (3.16d), and SnS_2 (3.16f) are also shown. Dashed lines connecting the initial and final charges have also been included as visual aid.

after intercalation. Keeping the positions of the ions the same as in the intercalated material, the electronic charge densities were obtained. By comparing the charge density of the full structure with those of the TMDC and lithium (or magnesium) [276], i.e. $\Delta\rho = \rho_{\mathrm{LiMX_2}} - [\rho_{\mathrm{Li}} + \rho_{\mathrm{MX_2}}]$, it is possible to comment on the

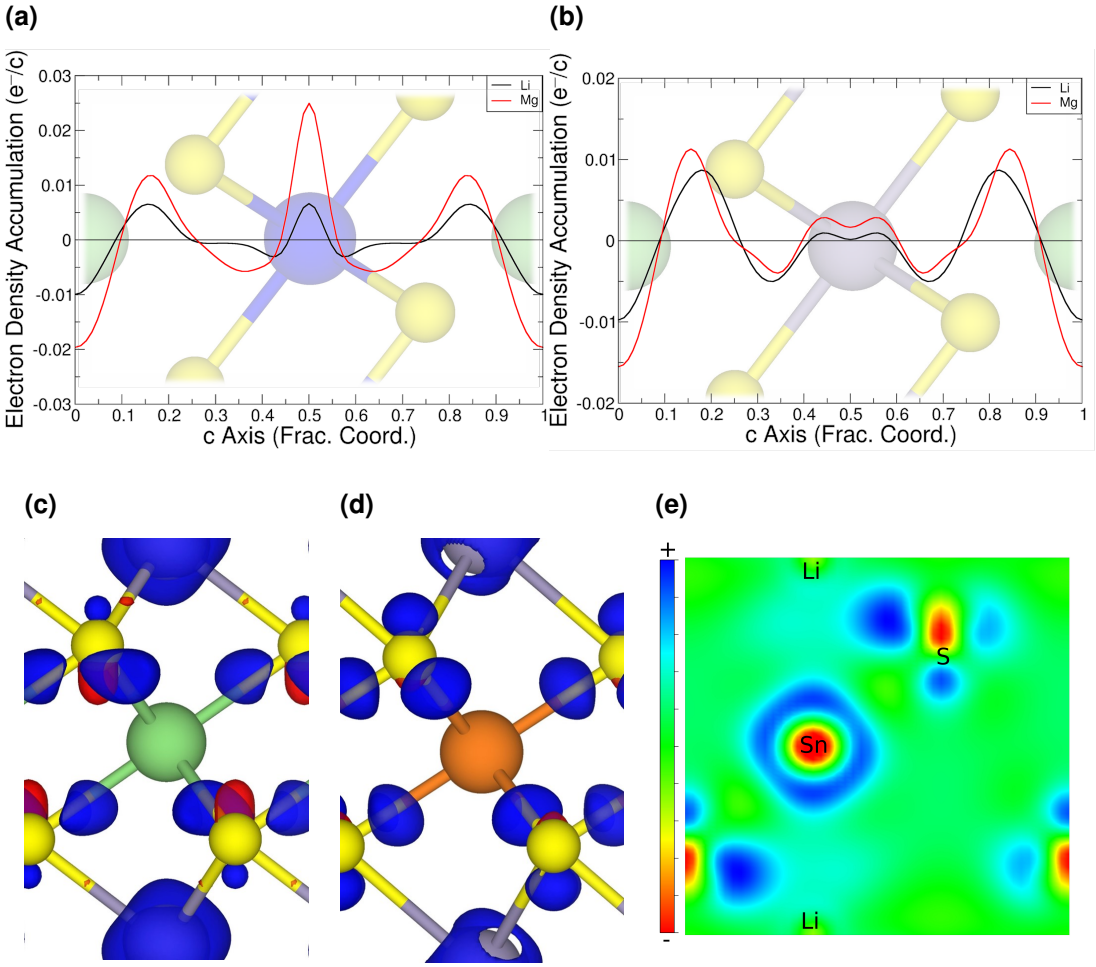

Figure 3.17: The planar-average of $\Delta\rho = \rho_{\mathrm{LiMX_2}} - [\rho_{\mathrm{Li}} + \rho_{\mathrm{MXS_2}}]$ for intercalants Li (black) and Mg (red) for intercalated ZrS_2 (3.17a) and SnS_2 (3.17b). Positive values correspond to regions of electron accumulation, and negative values correspond to regions of electron depletion. The corresponding structure is overlayed on these plots. The 3D visualisation of this charge transfer in SnS_2 is shown in 3.17c and 3.17d for lithium (isosurface 3.0 $me^-/Å^3$) and magnesium (isosurface 5.8 $me^-/Å^3$) intercalation, respectively. 3.17e shows a 2D slice through the (1 1 0) plane of the $LiSnS_2$ charge-difference distribution. Red isosurfaces show electron depletion and blue isosurfaces show electron accumulation.

charge transfer upon intercalation. An example is shown in Figure 3.17, where we present the planar-averaged values of $\Delta\rho$ for ZrS_2 (3.17a) and SnS_2 (3.17b), which are representative of the TMDC materials. In these, the metal species of the host TMDC (blue, purple) is positioned at $c = 0.5$, the host chalcogens (yellow) are at $c = 0.25$ and $c = 0.75$, and the intercalant species (green) is at $c = 0$ with its periodic image at $c = 1$. We can see there is significant electron depletion from

the location of intercalant ($c = 0, 1$), which is to be expected as the intercalated species donate their valence electrons to the host material. These donated electrons are shown to be partially donated into the Li-S and Mg-S bonding regions. These extra electrons in the vicinity of the chalcogen species repel the electrons that are present in the M-X bond closer to the metal of the host/reduce the number of electrons required for donation from the metal to the chalcogen. Hence we observe negative $\Delta\rho$ values in the ranges $c = 0.3 - 0.4$ and $c = 0.6 - 0.7$, and the positive values of $\Delta\rho$ on the metal site itself. This agrees with the reduction in Sn and Zr Bader charges presented above. This is further supported with the 3D visualisations of the charge transfer, presented in 3.17c and 3.17d for lithium and magnesium intercalation into SnS_2. The isosurfaces chosen are the determined by the ratio of intercalant Bader charges ($\frac{q_{Mg}}{q_{Li}} = \frac{1.67}{0.86}$). Figure 3.17e shows a 2D slice through the (1 1 0) plane of the $LiSnS_2$ charge-difference distribution, passing through the tin, sulfur, and lithium atoms. In each of the 3D and 2D visualisations, red isosurfaces show electron depletion and blue isosurfaces show electron accumulation. Finally, we note the increased charge transfer, both with the planar-averaged charge transfer plots and the 3D visualisation, for magnesium intercalation compared to lithium. Due to the double valency this is to be expected, and is in line with the results of the Bader analysis.

3.8 Volumetric Expansion

For intercalation electrodes, it is important to consider the volumetric expansion that arises from the intercalation of ions, as significant expansion during cycling can result in degradation of the electrode material, ultimately leading to device failure. We therefore present in Figure 3.18a and Figure 3.18b the volumetric expansion associated with lithium and magnesium intercalation, respectively. This is calculated using $\% = \frac{V - V_0}{V_0} \times 100$, for fully intercalated ($LiMX_2$ and $MgMX_2$) volume V and volume of the unintercalated structure V_0.

We note that as the transition metal Group increases, there is a larger volume expansion upon intercalation, with the Group III, IV, and V metal TMDC sulfides not exceeding 15% expansion with lithium intercalation. ZrS_2 and HfS_2

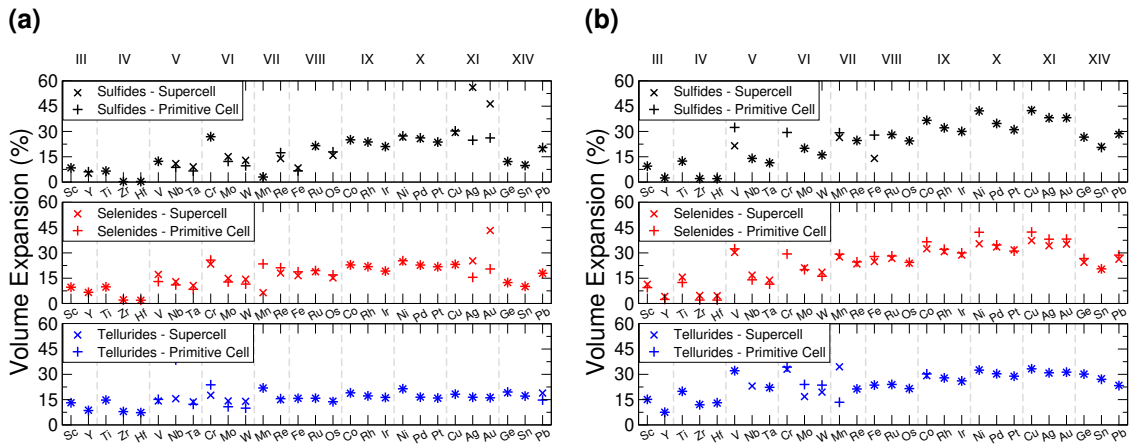

Figure 3.18: Total percentage volume expansion is presented for lithium (3.18a) and magnesium (3.18b) intercalation, calculated using $\% = \frac{V-V_0}{V_0} \times 100$. In each of these, sulfide data is presented in black (top), selenide data is presented in red (middle), and telluride data is presented in blue (bottom).

in particular demonstrate expansions of less than 1%. These expansions are comparable to many market leaders which posses a layered structure, including $LiCoO_2$ [277, 278] (2-3.25%), NMC [279] (8.44%), and graphite [280] (13.2%). Conversely, Group IX, X, and XI metal TMDC sulfides undergo expansions over 20%. We see the volume expansion of all of the TMDCs remaining below 60%, with most materials remaining below 30%. Whilst these are larger than expansions demonstrated by other layered materials, they remain exceptionally low compared to many materials that have been considered for electrode applications, such as tin [281] (300%) and silicon [282] (380%). Across the family of TMDCs the expansion that arises from magnesium intercalation is comparable to that with lithium intercalation, and considering the ionic radii of both lithium and magnesium, this is not surprising.

Looking at the expansion of the **a**- and **c**-lattice vectors can not only be useful for determining the origin of the volume expansion, but also for the pairing of materials in superlattice structures. We present in Appendix B the lattice constants for each of the TMDCs without an intercalant, when intercalated with lithium, and when intercalated with magnesium. With intercalation, most TMDCs show an out-of-plane lattice expansion. For Group III-VIII, this expansion remains below $\sim$15%, with some TMDCs showing out-of-plane contraction with magnesium intercalation. Later Groups, however, demonstrate expansions exceeding 15%,

reaching as high as 45%. This expansion is shown to be due to a lengthening of the M-X bond, and an increase in the vertical separation between chalcogens on opposing sides of the vdW gap. For lithium intercalation, most of the TMDCs exhibit in-plane lattice expansion of 5-10%, with a few of the early-transition metal TMDCs surprisingly contracting. We notice greater expansion of the in-plane lattice constants with magnesium intercalation, with some TMDC tellurides exhibiting expansions close to 20%.

Unintercalated structures show a large spread in the in-plane lattice constants, but upon intercalation the spread in lattice constants of the TMDCs is reduced. To highlight this, the TMDC with the largest lattice constant of the pristine T-phase sulfides is shown to be YS_2 with $\mathrm{a} = 4.07$ Å and the smallest lattice constant is CrS_2 with $\mathrm{a} = 3.04$ Å, giving a range of 1.03 Å. However, upon intercalation to $LiMS_2$ the largest lattice constant is PbS_2 with $\mathrm{a} = 3.84$ Å and the smallest is WS_2 with $\mathrm{a} = 3.24$ Å. This gives a smaller range of 0.60 Å. Similarly, upon intercalation with magnesium to $MgMS_2$ the largest lattice constant is PbS_2 with $\mathrm{a} = 3.86$ Å and the smallest is WS_2 with $\mathrm{a} = 3.27$ Å, giving a range of 0.61 Å. Clearly, the largest lattice constant is reduced and the smallest lattice constant is increased. This is likely due to the intercalated ions straining the TMDCs such that the nearest-neighbour distance of the intercalated species is close to the nearest-neighbour distance in the bulk form of the intercalant.

Along with the changes in lattice vectors and volume of these materials, there are also small changes to the atomic structure of the host material. Upon intercalation, we typically see an increase in the in-plane metal-metal distance, following the increase of the in-plane lattice constants, and a smaller increase in the metal-chalcogen bond length. These increases are more significant for the magnesium intercalant than they are for lithium. We also note a vertical stretching/contraction of the TMDC sheets: this is identified by both an increase/decrease in the vertical separation between the transition metal and nearest six chalcogen ions, and by an increase/decrease in the vertical separation between intralayer chalcogen ions on opposing basal planes of a TMDC layer. The bond length between the magnesium and the chalcogen species is found to be longer than the bond length between lithium and the chalcogen species. Further details of ionic geometry is

given in Appendix B.

3.9 Voltages

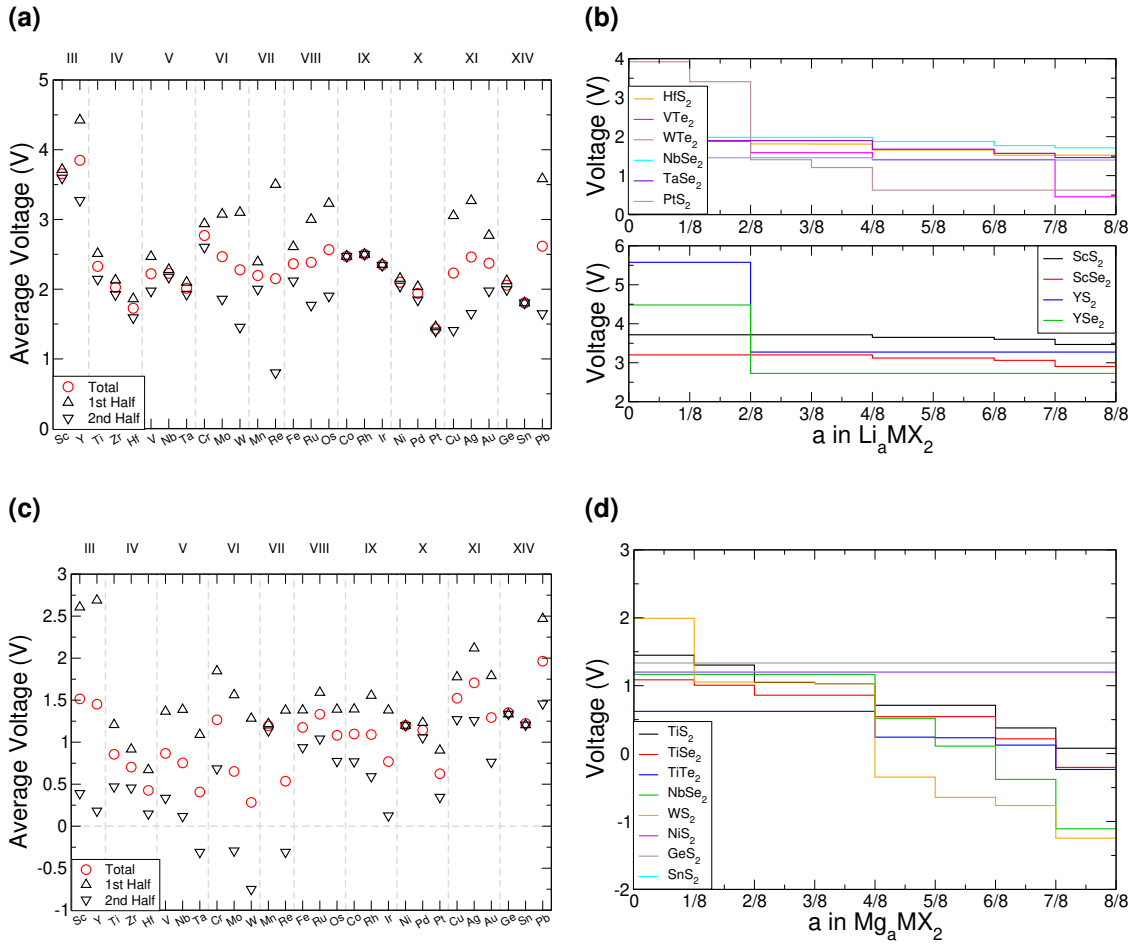

Figure 3.19: Intercalation voltages for TMDC materials intercalated with lithium and magnesium. The average lithium and magnesium intercalation voltages for the TMDC sulfides are given in 3.19a, and 3.19c, respectively. The average voltage obtained from intercalaton between MX_2 and $LiMX_2$ is presented as red crosses, the average voltage obtained from intercalaton between MX_2 and $Li_{0.5}MX_2$ is presented as black upward-pointing triangles, and the average voltage obtained from intercalaton between $Li_{0.5}MX_2$ and $LiMX_2$ is presented as black downward-pointing triangles. 3.19b and 3.19d give specific examples of the variation of intercalation potential with lithium and magnesium content, respectively.

One of the fundamental properties used to evaluate a particular material for its application as an electrode is the voltage. This gives the energy associated with intercalation with a given intercalant ion, allows for easy comparison of different

materials, and determines whether a material is best suited for a cathode (high voltage) or an anode (low voltage). Using equation (3.9) the intercalation potential vs. Li/Li^+ can be obtained for a range of intercalant concentrations. In Figure 3.19a we present the supercell average voltages for the TMDC sulfides with lithium intercalation. The average voltage is obtained by taking the average across the intercalation range, equivalent to $\mathrm{V_{av}} = \frac{E_8-(E_0+8E_{Li})}{8}$. We have also indicated the average potential for the first half of the intercalation range ($0 < a < 0.5$) and the average potential for the second half ($0.5 < a < 1$). Equivalent data for the selenide and telluride materials are presented in Appendix B. Comparing these values, we see a clear reduction in the average voltage as the atomic number of the chalcogen species is increased. In general, most of the sulfide (selenide|telluride) values lie in the $2 - 2.5$ V ($1.5 - 2$ V|$1 - 1.5$ V) range.

Anode materials should have well-defined voltage plateaus lower than 2 V vs. Li/Li^+, ideally in the range 0.5-1.5 V [283]. Based solely on this, telluride materials appear best suited with most voltages being around 1.5 V. We highlight this with VTe_2 and WTe_2 in Figure 3.19b, which have average voltages of 1.46 V and 1.56 V, respectively. However, the voltage profiles of these materials vary significantly across the concentration range. Other telluride materials offer the low voltages ideal for anodes but with a more plateau-like voltage profile, such as those composed of the Group IV, X, and XIV metals, each varying by less than 0.5 V. Unfortunately, the atomic mass of tellurium is much larger than sulfur and selenium, the other chalcogen species used in TMDC materials, which would significantly increase the mass of an electrode host-material, and thus reduce the gravimetric capacity. Though there are fewer sulfide and selenide materials that have ideal voltage profiles for anodes, there are still many (such as HfS_2, PtS_2, $NbSe_2$, and $TaSe_2$ as shown in Figure 3.19b) which also have relatively flat voltages below 2 V. Conversely, cathode materials should possess much higher voltages, with current cathodes offering voltages above 3 V [284]. We demonstrate this in Figure 3.19b with scandium and yttrium sulfide and selenide materials, which are seen to have voltages exceeding 3 V (in the case of the selenides) and 3.5 V (in the case of the sulfides). The promise of ScS_2 will be discussed further in Chapter 5.

In a similar manner we consider magnesium intercalation, with equation (3.9) allowing us to obtain the average magnesium intercalation potentials vs. Mg/Mg^{2+}. We present the results for the TMDC sulfides in Figure 3.19c, with selenide and telluride data being presented in Appendix B. Due to the double valency of magnesium, one can expect different intercalation behaviours to manifest in the profiles of the TMDCs, corresponding to different changes to the oxidation state of the host material. At a concentration of $a = 0.5$, the two electrons from each of the magnesium ions are donated to the host material, with one electron effectively being donated to each MX_2 unit. Past $a = 0.5$, further electron donation results in another change to the oxidation states of the MX_2 unit.

As was observed for lithium intercalation, we note the reduction in intercalation potential with increased atomic number of the chalcogen species, and highlight it in Figure 3.19d with the TiX_2 materials: TiS_2 has an average voltage of 0.86 V, $TiSe_2$ a voltage of 0.61 V, and $TiTe_2$ a voltage of 0.37 V. For most of the TMDCs, there is a significant drop in the magnesium intercalation potential for the second half of the intercalation range. This is dramatically shown with WS_2, where the initial intercalation potential is 1.99 V and the final intercalation potential is -1.24 V, demonstrating a drop of over 3 V. We observe that TMDCs composed of early-transition metals have a greater range in the magnesium intercalation voltage than the late-transition metals/post-transition metals. There are some of the materials which show very little change to the intercalation potential, with NiS_2, GeS_2 and SnS_2 each varying by 0 V. These are presented in Figure 3.19d. This constant voltage is due to the fact that, for each of the concentrations, it is energetically preferred for the magnesium to separate into regions with no magnesium (with an energy of E_0) and regions that are fully intercalated (with and energy of E_8). For example, the lowest energy for $\mathrm{Mg}_{\frac{1}{8}}\mathrm{SnS}_2$ is given by $E_1' = \frac{7}{8}E_0 + \frac{1}{8}E_8$, and the lowest energy for $\mathrm{Mg}_{\frac{2}{8}}\mathrm{SnS}_2$ is given by $E_2' = \frac{6}{8}E_0 + \frac{2}{8}E_8$. As the difference between consecutive concentrations is a constant $\Delta E = \frac{1}{8}E_8 - \frac{1}{8}E_0$, the voltage is also constant across the range. Further discussion of such clustering or phase separation is presented in the next section.

For magnesium intercalation, none of the TMDCs achieve voltages greater than 3 V, and so do not offer much promise as cathode materials. However, many of

them have voltages below 1.5 V, indicating their potential as anode materials. Further, we can highlight those materials with little difference between the two stages of their intercalation to ensure we have a well-defined voltage plateau [283]. However, we do not need to rule out those materials with a large difference between the two stages. Due to the double valency of magnesium, the total charge transferred from the magnesium in either the range $0 < a < 0.5$ or $0.5 < a < 1$, and hence the total energy stored, is comparable to the charge transferred across the full $0 < a < 1$ range using lithium intercalation. As such, in situations where the there is a large difference between the two charging stages, we can utilise just part of the intercalation range. For example, TMDCs composed of the Group III, IV, and V metals show voltages below 0.5 V in the range $0.5 < a < 1$, which is ideal for anodes.

The results presented here find good agreement with many experimental works. In particular, we see good agreement between the 2-2.5 V intercalation voltage identified for $LiTiS_2$ [67, 205, 208], and the 1.6-1.9 V intercalation voltage of $LiZrS_2$ [212, 214]. The intercalation voltage of T-MoS_2 has been identified in the range 1.9-2.5 V which agrees with the results we have presented [218, 222], and we reproduce the 1.8 V intercalation potential seen for intercalation of SnS_2 [233, 239]. Of course, many transition metal dichalcogenide compounds do not typically exhibit the layered structure that has been considered in this work [197], most commonly the pyrite structure as for FeS_2 [285], MnS_2, and CoS_2. Comparison with experiment with such materials is therefore not appropriate.

3.10 Clustering

We can comment on whether it is preferred for intercalants to intercalate a single vdW gap or to distribute across multiple layers. This is presented in Figure 3.20, where we focus on the $Li_{0.5}MX_2$ (3.20a) and $Mg_{0.5}MX_2$ (3.20b) intercalant concentration as an indicator, and used the indexing outlined in Figure 3.13 and Table 3.1. We indicate where intercalants spread evenly throughout the host structure with orange-shaded regions, and indicate where intercalants completely fill a single layer before occupying adjacent layers with the green-shaded regions.

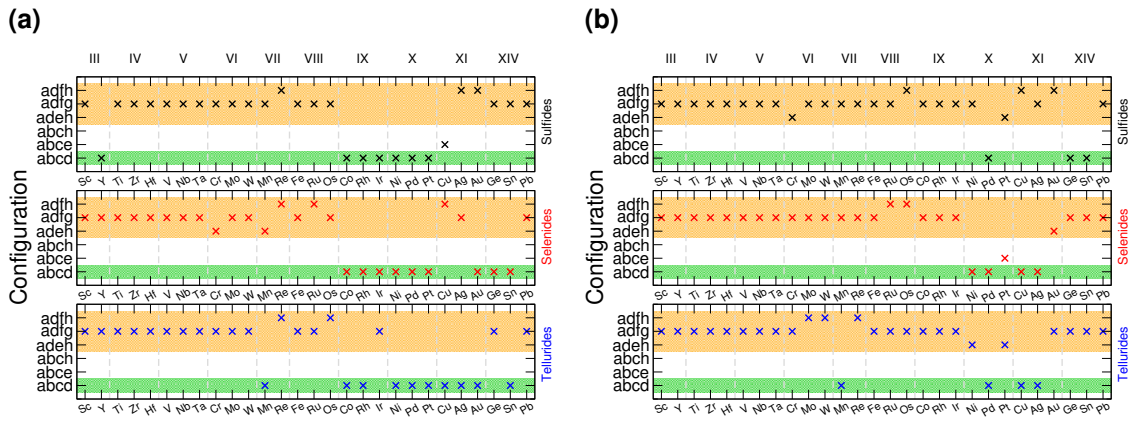

Figure 3.20: Graphs indicating which intercalant configuration at $Li_{0.5}MX_2$ (3.20a) and $Mg_{0.5}MX_2$ (3.20b) is the lowest in energy. Indexing is used following Figure 3.13 and Table 3.1. The orange-shaded regions indicate intercalants spread evenly throughout the host structure, and the green-shaded regions indicate intercalants fill a single layer before intercalation of a second layer begins.

For lithium intercalation, most TMDCs have lithium spread evenly throughout the host [286], with the exception of Group IX and X TMDCs. There is then an even stronger preference for even-distribution of magnesium. This preference for intercalants to be distributed evenly throughout the host can be explained with a simple argument of minimising Coulombic repulsion between intercalant ions.

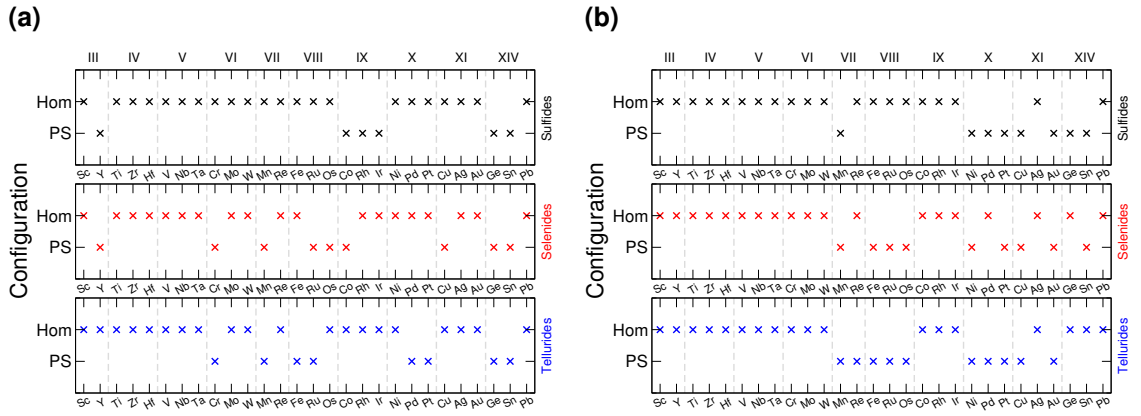

Figure 3.21: Graphs depicting whether TMDCs are intercalated homogeneously (Hom) or whether there is domain/phase separation (PS). Results for lithium-intercalated TMDCs are presented in 3.21a, and those for magnesium-intercalated TMDCs are presented in 3.21b.

As mentioned in the above discussion on how we obtain the intercalation voltage, it is possible for intercalants to separate into domains of different concentrations,

beyond the configurations presented in Figure 3.20. For example, rather than have each cell of a crystal intercalated to $Li_{0.5}MX_2$, it may be preferred for domain/phase separation into Li_0MX_2 and Li_1MX_2, as has been demonstrated with $LiSnS_2$. We again consider the $Li_{0.5}MX_2$ and $Mg_{0.5}MX_2$ concentrations as an indicator for this separation, and present the results in Figure 3.21. Most materials show homogeneous (Hom) filling, and would follow the intercalant configuration presented in Figure 3.20. However, many materials show a phase separation (PS) into domains of different intercalant concentrations, for example (but not limited to) Li_0MX_2 and Li_1MX_2.

3.11 Thermodynamic Stability

Using equations (3.18)-(3.20), we are able to construct thermodynamic phase diagrams to evaluate the thermodynamic stability of the intercalated structures against conversion, which would result in the loss of the layered structure. By determining the intercalant concentration that leads to the loss of the window of stability on the phase diagram, we can obtain the limit on the reversible intercalation charge capacity, an important property for any electrode material. Figure 3.22 presents the values of E_{IS} (given by equations (3.25) and (3.27)) for both lithium and magnesium intercalation of the TMDCs, for a range of intercalation concentrations. Positive values of E_{IS} indicate an intercalated TMDC structure is stable against conversion, and from the range of concentrations over which E_{IS} remains positive, we have determined the specific charge capacity of each material. These values (in $mAhg^{-1}$) have been included in Figure 3.22.

Figure 3.22a presents the values of E_{IS} for lithium intercalation of the sulfides, with specific examples being highlighted in Figure 3.22b. Equivalent figures are presented in Appendix B for the selenide and telluride materials. In general, we see a reduction in the stability of the TMDCs as the concentration of lithium is increased. The size of this effect varies across the periodic table, with the TMDCs composed of the central Group VI, VII, and VIII metals showing the largest variation. This is highlighted with WS_2 in Figure 3.22b, where E_{IS} drops from 2.42 eV at a concentration of $Li_{0.125}WS_2$, to 2.23 eV at a concentration of $Li_{0.25}WS_2$, to

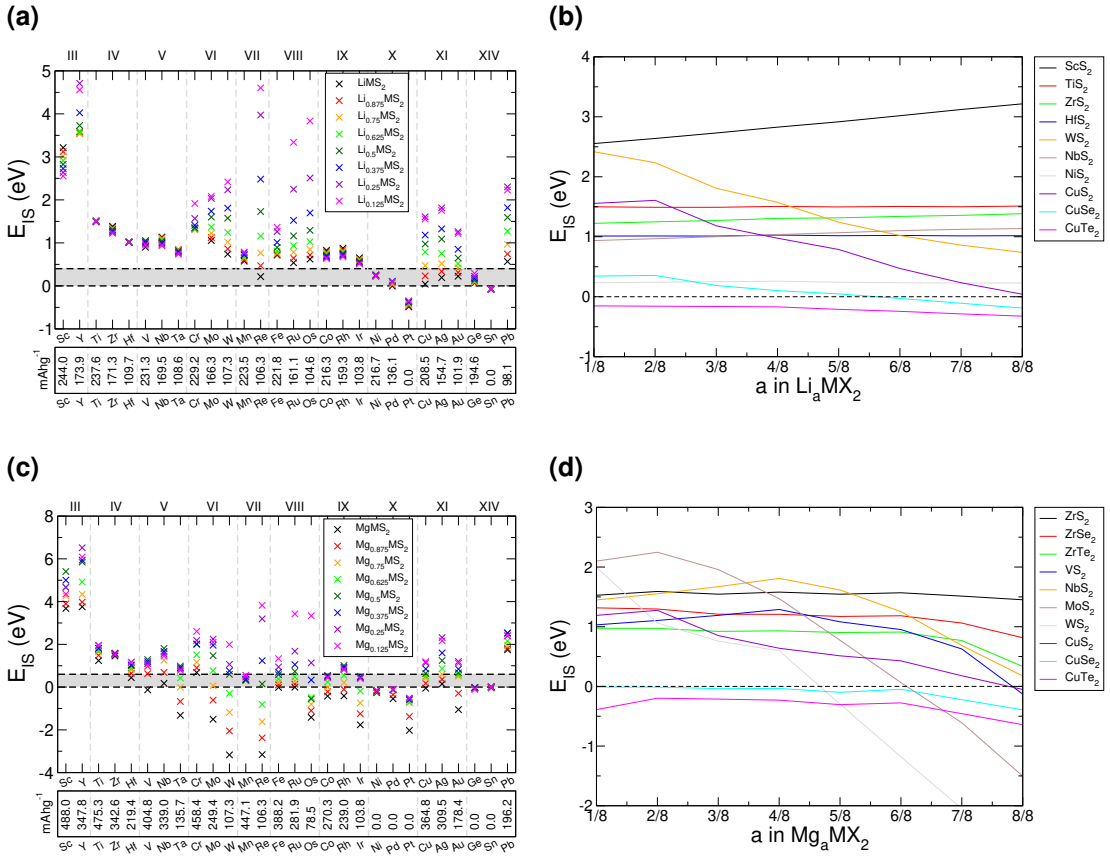

Figure 3.22: E_{IS} values for each of the TMDC sulfides intercalated with different concentrations of lithium (3.22a) and magnesium (3.22c). The resultant gravimetric charge capacities in mAhg^{-1} (as determined from the range over which E_{IS} is positive) are also presented at the bottom of each of the figures. 3.22b and 3.22d give specific examples of the variation of E_{IS} with lithium and magnesium content, respectively.

1.57 eV at a concentration of $Li_{0.5}WS_2$, finally to 0.74 eV at a concentration of $LiWS_2$. However, those TMDCs composed of metals from Groups IV, V, IX, and X having a relatively constant values of E_{IS}. For example, as shown in Figure 3.22b, TiS_2 demonstrates a constant $E_{IS} = 1.51$ eV at both $LiTiS_2$ and $Li_{0.125}TiS_2$, HfS_2 has a minor decrease from 1.02 eV ($LiHfS_2$) to 1.01 eV ($Li_{0.125}HfS_2$), and for NiS_2 it retains the same value of $E_{IS} = 0.23$ eV. Whilst most TMDCs are shown to destabilise with increased lithium content, we do highlight in Figure 3.22b some examples that prove exceptions, such as ScS_2, ZrS_2, and NbS_2, whose values of E_{IS} increase with lithium content.

With increasing atomic number of the chalcogen species, there is a gradual reduction in the stability (indicated by a reduction in E_{IS}). This is shown best with the Group XI TMDCs (CuX_2, AgX_2, and AuX_2), where the sulfides are sta-

ble across the concentration range investigated, the selenides become unstable when the lithium concentration exceeds $a = 0.5$, but none of the tellurides are stable for any of the intercalant concentrations. The data for the CuX_2 materials is presented in Figure 3.22b to highlight this. This can be explained with the reduced electronegativity for larger atomic numbers, as the greater number of electrons already present at the chalcogen site lowers the favourability of additional electrons being donated. There is no easily-identifiable trend seen for changing the transition metal species, however, with some Groups showing an increase in E_{IS} as the atomic number of the transition metal is increased (e.g. Groups III and VIII) and some showing a decrease (e.g. Groups IV and X).

Overall, the Group III (Sc, Y), IV (Ti, Zr, Hf), V (V, Nb, Ta), and VI (Cr, Mo, W) materials offer the greatest stability, which is unsurprising given that these materials have been investigated the most thoroughly over the past 50 years. However, we also highlight the Group VIII (Fe, Ru, Os) and IX (Co, Rh, Ir) sulfides as potential lithium-intercalation materials as they show stability over the intercalation range considered here.

For magnesium intercalation we see similar results, as shown in Figure 3.22c for the sulfides, with specific examples are presented in Figure 3.22d. The selenide and telluride results are also presented in Appendix B. We typically see a reduction in the stability with increased magnesium concentration. Again, we highlight this with WS_2, where E_{IS} drops from 1.99 eV at a concentration of $Mg_{0.125}WS_2$, to 1.06 eV at a concentration of $Mg_{0.25}WS_2$, to 0.60 eV at a concentration of $Mg_{0.5}WS_2$, finally to -3.17 eV at a concentration of $MgWS_2$. We note this large reduction in E_{IS} between intercalation concentrations of $a = 0.5$ and $a = 1$, which is greater than what was demonstrated for lithium intercalation. This is also seen for other materials, including VS_2, NbS_2, and MoS_2, as shown in Figure 3.22d. We attribute this large reduction to the second donated electron from the magnesium: the electrons donated in the range $0 \leq \ a \leq 0.5$ with magnesium intercalation stimulate the same transition in oxidation state as that of the electrons donated in the range $0 \leq a \leq 1$ with lithium intercalation. Any further charge donation triggers different changes in oxidation state, as more than one electron is then being donated to each of the MX_2 units. However, despite this larger drop

for greater magnesium concentrations, many of the TMDCs still possess positive values of E_{IS}, including TMDCs containing Group III, IV, or V metals. As with lithium intercalation, we note a gradual reduction in stability of the TMDCs as the atomic number of the chalcogen species is increased, and demonstrate this with both the ZrX_2 and CuX_2 TMDCs in Figure 3.22d. Despite these causes for stability reduction, however, there still remain several TMDCs that are predicted to be resilient with magnesium intercalation: The Group III (Sc, Y), IV (Ti, Zr, Hf), and V (V, Nb, Ta) sulfides again offer the greatest stability to intercalation. Though many of the other materials show a susceptibility to conversion with intercalation, the Group VIII (Fe, Ru, Os) and IX (Co, Rh, Ir) sulfides offer stability over a significant intercalant concentration range ($0 < a < 0.5$), which corresponds to significant charge transfer when noting the double valency of magnesium.

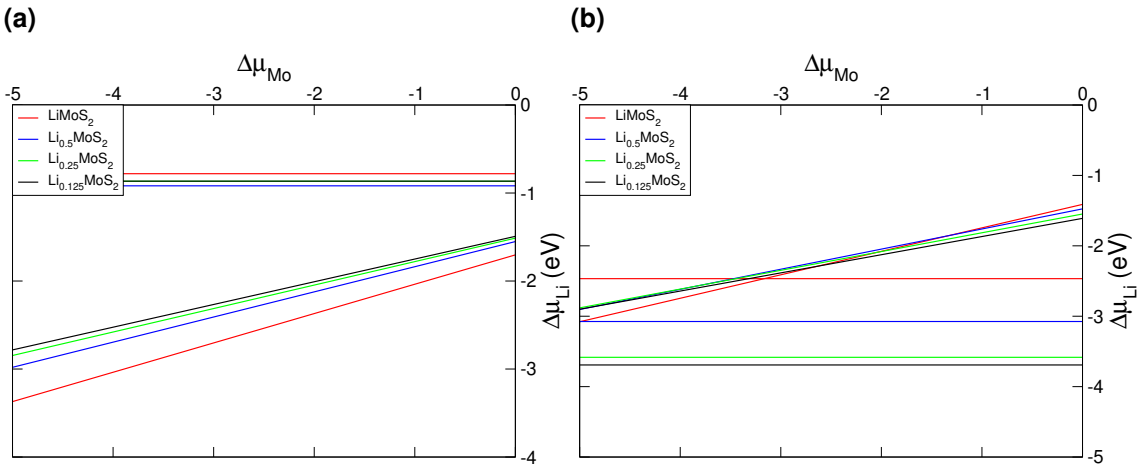

Figure 3.23: 3.23a shows the phase diagram for intercalated 2H-MoS_2 and 3.23b shows the phase diagram for intercalated 1T-MoS_2, for varying lithium concentrations.

Comparing our results here with experimental studies we find good agreement, particularly for the Group IV TMDCs. For each of the Group IV dichalcogenides, we find a positive value of E_{IS}, indicating their stability against conversion. Experimentally, TiS_2 has been shown to be stable over a range of lithium concentrations up to $a = 1$ in Li_aTiS_2, as have the ZrX_2 and HfX_2 materials [211, 226]. SnS_2 is shown here to have a negative E_{IS}, indicating it is not stable to intercalation and hence susceptible to conversion. This agrees with experimental works [236–239] where SnS_2 is observed to readily undergo conversion reactions to Li_2S or an alloy of Sn and Li. We are also able to show the Hc-MoS_2 $\rightarrow$ T-MoS_2 transition arising from lithium intercalation. It has been widely reported that, upon interca-

lation with lithium, 2H-MoS_2 undergoes a phase transition to 1T-MoS_2. Within the phase diagrams, this presents itself as the 2H-MoS_2 having no window of stability for the intercalated structure, with a negative value of E_{IS}. The 1T-MoS_2 phase, however, has a value of $E_{IS} = 1.055$ eV. These are shown in Figure 3.23a and Figure 3.23b, respectively. As such, the intercalated layered structure must convert to the T-phase, otherwise the decomposition into Li_2S becomes energetically favourable.

Whilst some works have achieved intercalant contents greater than $a = 1$, such as with Li_2VSe_2 [211], Li_3TiS_2 [287], and $Li_{3.48}NbSe_2$ [26], we have not investigated beyond this limit here. However, we have shown for these cases that E_{IS} remains positive with lithium concentration, with values of $E_{IS} = 0.63$ eV, $E_{IS} = 1.51$ eV, and $E_{IS} = 0.70$ eV for $LiVSe_2$, $LiTiS_2$, and $LiNbSe_2$, respectively. These positive values, therefore, still allow for further intercalation towards the concentrations that have been observed experimentally.

It should also be noted that we have not considered the effects of surface formation or how microscopic morphology can play a role. Experimental works have shown that lithium deposition onto the surface of these TMDC materials can lead to conversion even for TMDCs that are stable to intercalation [194, 288], and first principles methods have been used to confirm that the formation of a surface can reduce the size of the stability window [271], therefore reducing E_{IS} and making these materials more susceptible to conversion reactions.

The values of E_{IS} presented here are only for the geometrically relaxed structure where the intercalant occupies the lowest-energy intercalation site. Of course, during the cycling of the electrode an intercalant is expected to occupy not only higher-energy intercalation sites, but also intermediate points (e.g. along Routes A, B and C in Figure 3.9c). As such, the host material will undergo local distortions that will increase its energetic state, and hence reduce the corresponding stability indicated by E_{IS}. However, accurate mapping of the energy space for intercalant diffusion remains a challenge due to current limits on cell sizes. Further, obtaining a sufficient number of interpolated CI-NEB images at different intercalant concentrations for each of the TMDCs would be computationally demanding. As such, we use the difference in energy between the intercalant occupying the octahderal

and tetrahedral sites rather than the activation barrier height. We rationalise this further by considering the coordination between the intercalant and chalcogen species which is reduced for intermediate positions and so limits the available ions for conversion to the appropriate Li_2X or MgX compound. Finally, the time scales associated with an intercalant ion being in an intermediate position are significantly shorter than the time scales associated with occupation of an octahedral or a tetrahedral site.

The difference in energy between lithium in the octahedral and tetrahedral sites is approximately 0.4 eV across each of the TMDCs, whereas it is typically slightly higher at 0.6 eV for magnesium (see Section 3.6). Whilst there are examples of both higher and lower energies, we can use these typical values as a further limit on E_{IS}, indicated by the shaded region in Figure 3.22c. For lithium intercalation, only a few of the sulfides are affected by this new limit, with the fully intercalated ReS_2 becoming susceptible to conversion, along with the Group X, XI, and XIV materials. However, there is a more dramatic consequence for magnesium intercalation due to the second donated electron. Almost all of the TMDC sulfides demonstrate a reduction in their capacity, arising from the higher magnesium concentrations being falling within the new limit on E_{IS}.

3.11.1 Formation Energy vs. Intercalant Binding Energy

An alternative but equivalent way to assess the stability of a TMDC material against conversion is to consider the two contributions to the material stability: the formation energy of the pristine TMDC material and the binding energy of the intercalant with the host material [271]. These two quantities are more commonly used for first-principles material evaluation. The TMDC formation energy is given by,

$$\Delta G(\mathrm{MX_2}) = E(\mathrm{MX_2}) - [E(\mathrm{M}) + 2E(\mathrm{X})]. \tag{3.28}$$

The formation energy describes the energy required to form a material from the constituent elements, and so gives an indication of the strength of the M-X bond. The more negative a value of $\Delta G(\mathrm{MX_2})$ the stronger the M-X bond, and hence the more resistant the TMDC is to conversion. Similarly, the intercalant binding

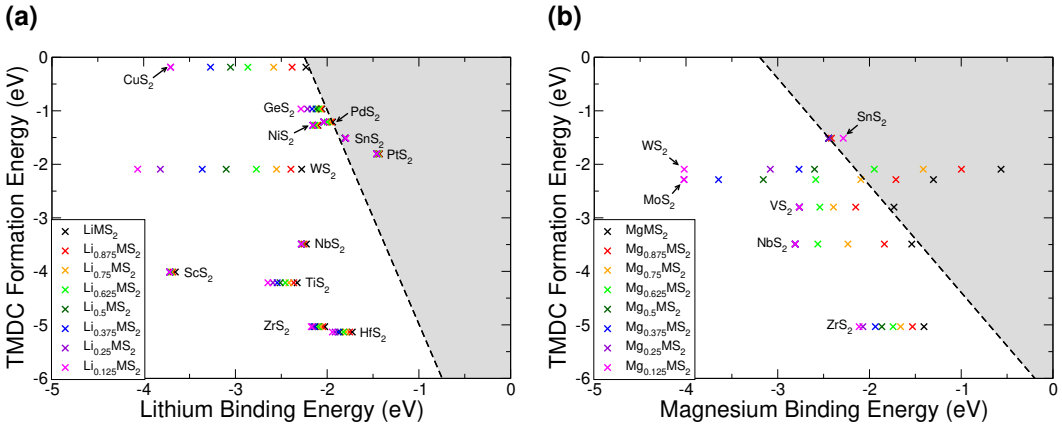

Figure 3.24: Comparison of TMDC formation energy (equation (3.28)) and intercalant binding energy (equation (3.29)) for different intercalant concentrations of selected TMDCs. 3.24a and 3.24b present results for lithium and magnesium intercalation, respectively. The shaded region indicates where conversion is energetically favourable, equivalent to negative values of E_{IS}.

energy is given by,

$$E_b = E(\mathrm{Li}_a\mathrm{MX}_2) - [E(\mathrm{MX}_2) + aE(\mathrm{Li})] \tag{3.29}$$

(or equivalent for magnesium). This then gives the energy required to add some quantity a of an intercalant to the host TMDC, again with negative values signifying a more favourable intercalation reaction, hence indicating the strength of the interaction between intercalant and TMDC. To resist the conversion reaction, a TMDC should possess a large (negative) formation energy, large (negative) intercalant binding energy, or ideally both.

In terms of the above two quantities, we can determine the limits of stability, which are,

$$\begin{aligned} \Delta G(\mathrm{MX}_2) + 4E_b &\leq 2\Delta G(\mathrm{Li}_2\mathrm{X}) \\ \Delta G(\mathrm{MX}_2) + 2E_b &\leq 2\Delta G(\mathrm{MgX}). \end{aligned} \tag{3.30}$$

which requires the formation energy of the TMDC and the intercalant binding energy to be lower that the formation energy of the appropriate conversion product ($\Delta G(\mathrm{Li}_2\mathrm{X})$ or $\Delta G(\mathrm{MgX})$). In Figure 3.24a we plot the TMDC formation energy against the lithium binding energy, and also indicate the boundary described by equation (3.30). Here, it is now easy to see that materials that possess a negative value of E_{IS} and are unstable against intercalation (such as PdS_2, SnS_2, or

$CuTe_2$) are those with low TMDC formation energy and low lithium binding energy.

3.12 HSE06 Hybrid Functional

Whilst we have shown good agreement with experiment, validating our choice of functional, previous studies have shown that the choice of functional can lead to differences in predictions for properties important to electrode materials [289, 290]. To account for the inaccurate calculation of exchange in GGA functionals such as PBE, and to evaluate the differences that can arise from choice of functional, the HSE06 hybrid functional [130, 135, 265] has used for a selection of systems. Due to the higher computational cost of this functional compared to PBE, a smaller system was considered: the primitive unit cell of each of the 1T-TMDCs was used and intercalated with a single lithium atom. This corresponds to a lithium concentration equivalent to eight lithium atoms in the supercell system. Clearly, the primitive and supercell systems significantly differ in size, and so, to ensure that a comparison is made with an equivalently sized system, PBE calculations were also performed on the primitive cell with a single lithium intercalated per cell. For both the HSE and PBE calculations, geometric relaxations were converged to less than 0.01 eV/Å per atom, and electronic self-consistency is considered to an accuracy of 10^{-7} eV. Monkhorst-Pack k-point grids [140] of $6\times6\times6$ and $12\times12\times12$ were used for the HSE and PBE calculations, respectively.

The comparison of the PBE and HSE06 functionals are presented in Figure 3.25 for selected lithium-intercalated TMDCs, with further presentation of results provided in Appendix B. In general, we identify an increase in both the voltage and E_{IS} using the HSE06 functional compared to PBE. For example, the $LiTiS_2$ voltage is increased by 0.17 V, the $LiMoS_2$ voltage is increased by 0.25 V, and the $LiIrS_2$ voltage is increased by 0.58 V compared to the PBE functional. This increase in intercalation voltage with use of a hybrid functional (as well as with using GGA+U corrections) has been shown for a range of transition metal oxides commonly used as electrode materials [289, 290]. We also note, in general, a larger effect on the voltage for heavier chalcogen species, as shown with the MoX_2 series of TMDCs: the telluride material has a larger voltage increase (1.03 V) than

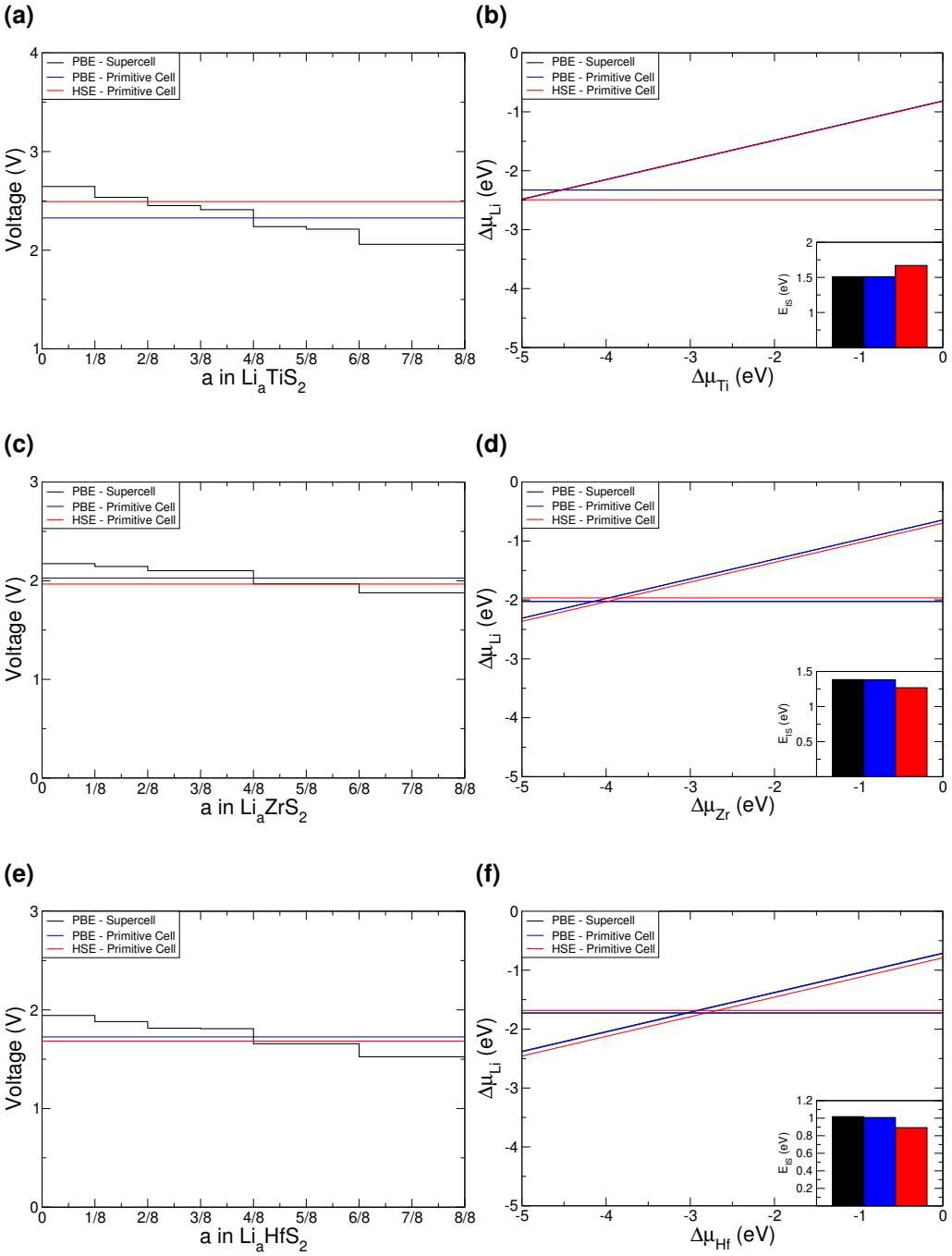

Figure 3.25: Comparison of results using the PBE and HSE06 functionals. 3.25a, 3.25c, and 3.25e present the voltages for TiS_2, ZrS_2, and HfS_2, respectively. 3.25b, 3.25d, and 3.25f present the phase diagrams for TiS_2, ZrS_2, and HfS_2, respectively. The insets show the values of E_{IS}.

the selenide (0.46 V), which has a larger increase than the sulfide (0.25 V).

The exceptions to this include the voltages of SnS_2 (reduced by 0.14 V), ZrS_2 (reduced by 0.06 V), and HfS_2 (reduced by 0.04 V). Further, there is also a reduction in E_{IS} for these materials due to lowering of the diagonal line described by

TMDC	PBE Supercell Average Voltage (V)	PBE Primitive Cell Voltage (V)	HSE Primitive Cell Voltage (V)
ScS_2	3.655	3.655	4.231
YS_2	3.559	3.559	4.108
TiS_2	2.327	2.327	2.493
ZrS_2	2.027	2.027	1.966
HfS_2	1.726	1.726	1.684
MoS_2	2.466	1.814	2.066
IrS_2	2.348	2.348	2.922
$MoSe_2$	2.039	1.285	1.748
$MoTe_2$	1.597	0.820	1.849

Table 3.2: Summary of average TMDC lithium intercalation voltages, using the HSE06 functional for the primitive unit cells. PBE results using the supercell and primitive cell have been reproduced for easy comparison.

equation (3.20), corresponding to the boundary between the intercalated TMDC and the Li_2X crystal. Similarly, there is a raising of the horizontal line described by equation (3.19), which describes the boundary between the intercalated and pristine TMDC structures. As such, the intercalated compound is reduced in favourability compared to both the pristine structure, and the conversion product Li_2X. By looking at the phase diagrams for the MoX_2 materials (see Appendix B) we also note that as the chalcogen is varied down the group, the horizontal line is shifted further downwards. In Table 3.2 and Table 3.3 we present numerical values comparing HSE06 and PBE results. As we have achieved good agreement with experiment using the PBE functional, however, we have not performed an exhaustive study using the HSE06 alternative.

We also consider the difference in volumetric expansion. Using the PBE (HSE06) functional the expansion for SnS_2 is 9.81% (9.92%), for ZrS_2 it is 0.28% (-0.40%), and for HfS_2 it is 0.32% (-0.24%). Again, the differences between the two functionals are very small.

TMDC	PBE Supercell E_{IS} (eV)	PBE Primitive Cell E_{IS} (eV)	HSE Primitive Cell E_{IS} (eV)
ScS_2	3.22	3.22	3.81
YS_2	3.58	3.20	3.78
TiS_2	1.51	1.51	1.67
ZrS_2	1.38	1.38	1.27
HfS_2	1.02	1.02	0.89
MoS_2	1.05	0.19	0.30
IrS_2	0.65	0.65	1.28
SnS_2	-0.09	-0.09	-0.42
$MoSe_2$	0.53	-0.48	-0.11
$MoTe_2$	0.10	-0.93	0.21

Table 3.3: Summary of average E_{IS} values for lithium intercalation of TMDCs, using the HSE06 functional for the primitive unit cells. PBE results using the supercell and primitive cell have been reproduced for easy comparison.

3.13 Discussion of Hc-Phase TMDCs.

We here present data for those TMDCs where the Hc-phase was preferred to the T-phase at some point over the intercalation range. We present the average intercalation voltages in Figure 3.26a, where we note some slight changes to the intercalation voltages, with the Hc-phase voltages being higher that the T-phase for Group IV TMDCs, and lower in the Hc-phase than the T-phase for the Group VI TMDCs. There is a mix for the Group V TMDCs.

We present in Figure 3.26 the evolution of E_{IS} with lithium (Figure 3.26b) and magnesium (Figure 3.26c) intercalant concentration in H-phase TMDC sulfides. More significantly, we note some large differences in the stability characterised through E_{IS}, though we see the same general trends as are observed in the T-phase: With increased lithium intercalation, the Group IV and V TMDCs retain a relatively constant value of E_{IS}, and the Group VI TMDCs show a drop in stability for higher concentrations. With magnesium intercalation, we again notice the drop in stability for intercalation concentration greater than $a = 0.5$

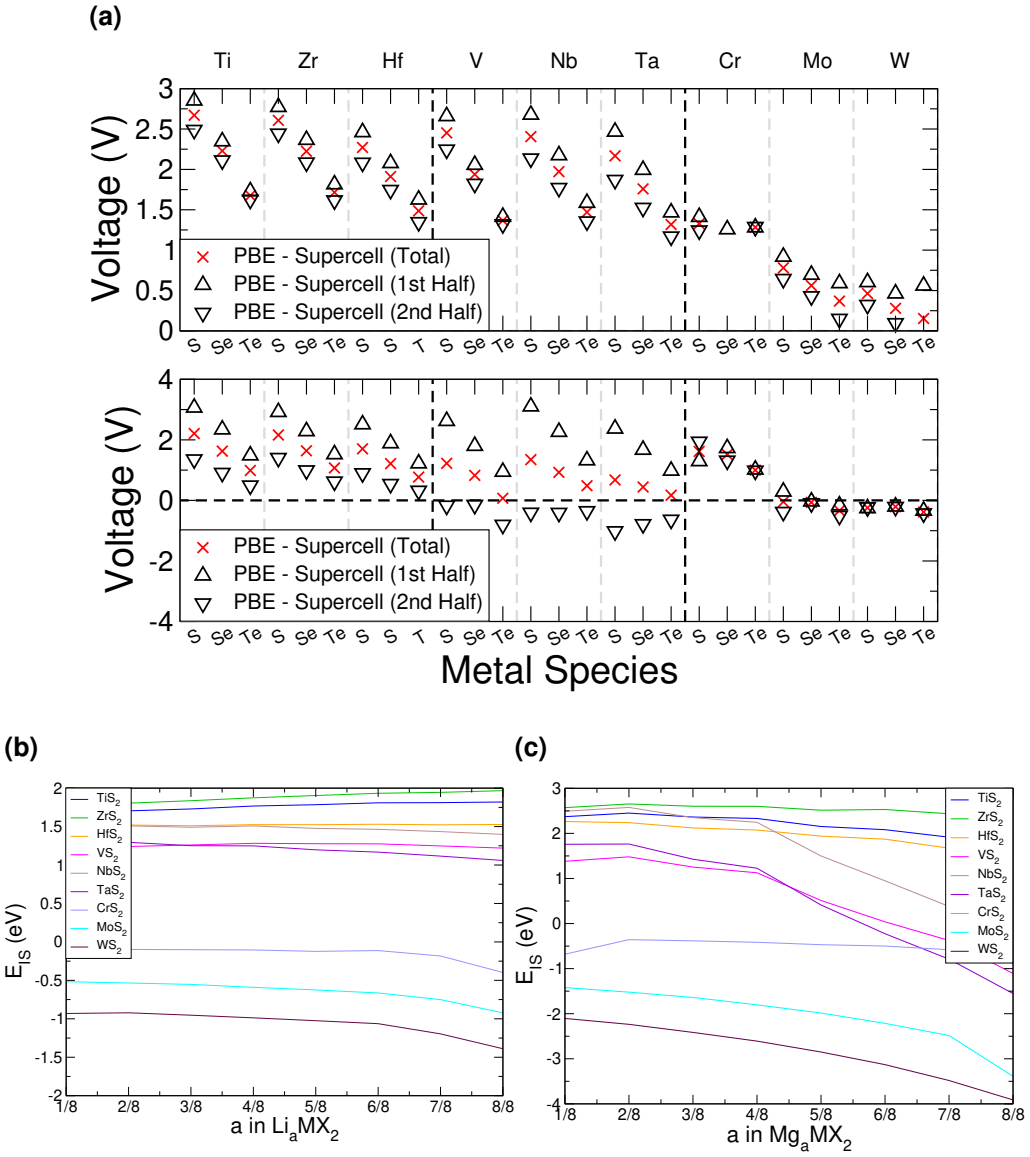

Figure 3.26: H-phase intercalation voltages (3.26a) and values of E_{IS} for lithium (3.26b) and magnesium (3.26c) intercalation into H-phase TMDCs.

attributed to the double valency of magnesium. The Group IV materials remain stable across the range of concentrations, as do the Group V materials for concentrations lower than $a = 0.5$. Beyond this intercalant concentration they become unstable. The MoX_2 and WX_2 materials show no positive values of E_{IS}, but as their T-phase counterparts do, this is a manifestation of the H→T transition. For each of the TMDCs considered here, the heavier chalcogens show reduced stability and hence a higher susceptibility to conversion reactions.

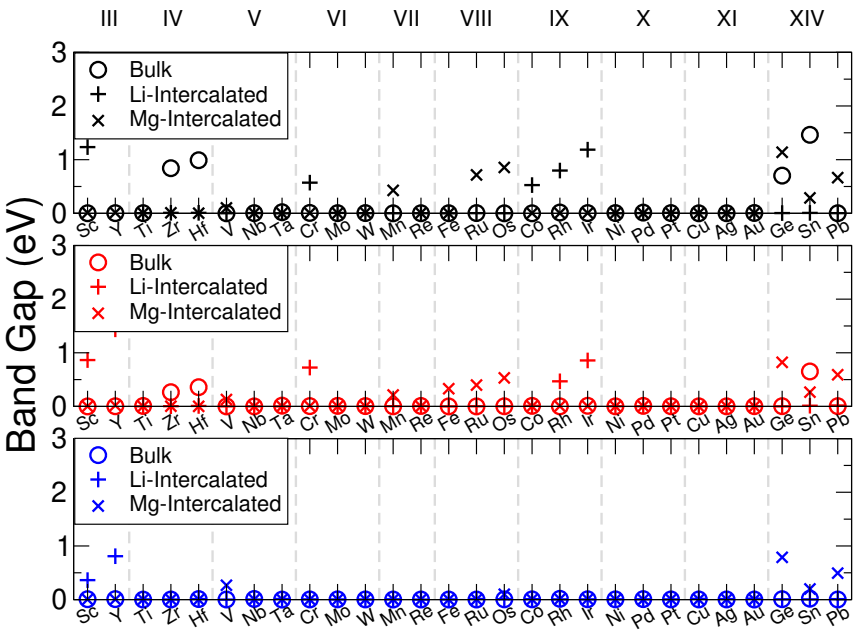

Figure 3.27: Electronic band gap sizes for pristine bulk (circles), lithium-intercalated (pluses), and magnesium-intercalated (crosses) TMDCs. Sulfide data is in black (top), selenide data is in red (middle), and telluride data is in blue (bottom).

3.14 Electronic Structure

One of the attractive features of the TMDC family is the wide range of electronic properties that have been reported [189, 190, 291]. For electrodes, it is desirable for the host material to be conductive so that the compensating electrons can more easily conduct throughout the host material, and to remove the need for additives such as graphitic carbon. However, upon the addition of intercalant species it can be expected that the electronic structure and properties are modified. As it is desirable for this conductive nature to endure across the range of intercalation, we here present the changes to the electronic structure with intercalation.

We present in Figure 3.27 the electronic band gaps for each of the pristine, lithium-intercalated, and magnesium-intercalated materials. It is clear to see that the vast majority possess no band gap, and so should be electronically conductive. This agrees with previous works which have established the increased conductivity of T-phase TMDCs over their H-phase counterparts. This is ideal for electrode applications where the conduction of electrons is required. However, TMDCs composed of Group III, VII, IX, and XIV metals undergo transitions be-

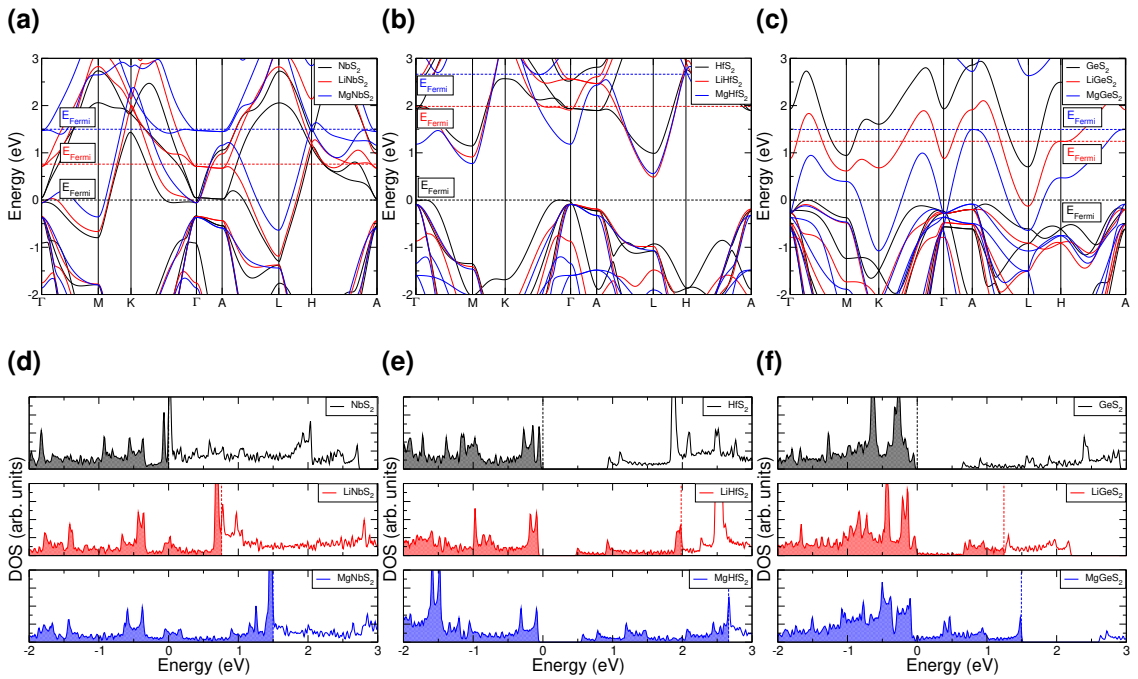

Figure 3.28: Electronic band structures and density of states (DOS) for pristine and intercalated TMDCs. NbS_2 data is presented in 3.28a and 3.28d, HfS_2 in 3.28b and 3.28e, and GeS_2 in 3.28c and 3.28f. MX_2 data is presented in black, $LiMX_2$ data in red, and $MgMX_2$ data in blue. Each has been aligned with high energy occupied states of the pristine MX_2 material. The energy of the highest occupied state ($\mathrm{E_{Fermi}}$) is indicated with dashed lines.

tween conducting and semiconducting/insulating states, and so conductive additives would be necessary to facilitate charge transfer. In fact, we identify four different cases describing how the electronic structure can change with intercalation: either the TMDC i) retains a conductive nature with intercalation, ii) undergoes a semiconductor-to-conductor transition, iii) undergoes a conductor-to-semiconductor transition, or iv) possesses an insulating nature before intercalation and at the $a = 1$ intercalation level. We highlight some examples of these in Figure 3.28, where the electronic band structures and associated density of states (DOS) are presented.

We track the shift in the position of the Fermi level with intercalation by alignment of the band structures of the pristine, lithium-intercalated, and magnesium-intercalated structures. Alignment of electronic band structures is usually achieved either through alignment of core states [262] or through alignment with respect to the vacuum level [262–264]. However, charge transfer upon intercalation (as

shall be discussed later) leads to local electric dipoles that shift the position of even deep core states, and so core alignment is not appropriate. Alignment with respect to the vacuum level, on the other hand, requires the inclusion of a vacuum region within the system. To maintain stoichiometry, one surface would need to consist of intercalant ions and the opposite layer should be a bare TMDC layer, which naturally leads to large electric fields across the vacuum region. To avoid these large electric fields, both surfaces should be symmetrically equivalent, but this then breaks the stoichiometry of the compound in question. As such, we have instead chosen to qualitatively align the high-energy occupied states of the pristine and intercalated structures at Γ, allowing us to comment on the position of the Fermi level.

For materials such as NbS_2, the Fermi level lies in the middle of a band, as shown in see Figure 3.28a and 3.28d. The addition of lithium donates electronic charge to the host, and so the Fermi level rises accordingly. Similarly, with magnesium intercalation the Fermi level rises but by a greater amount due to the larger electronic charge that is donated to the host. We note some small changes to the positions and shape of the individual bands due to local electric fields arising from charge transfer (as was shown in Figure 3.17), which can be identified by considering the bands positions at Γ. Otherwise, the general features of the bands can easily be tracked. No new bands, which would be associated with the intercalant species, are introduced into the regions presented. For materials such as HfS_2 which undergo a transition from a semiconducting to conducting, we see much the same behaviour, with the addition of a larger jump in the position of the Fermi level due to the presence of the host band gap. Once this band gap has been overcome, however, population of the conduction band states can occur and a conducting nature is achieved (see Figure 3.28b and 3.28e). Conversely, ScS_2 is an example of a material which loses its conductive nature once fully intercalated, further discussion of this has been presented elsewhere [230]. In this situation, the addition of electrons fills states until the next band gap is reached. Finally, in Figure 3.28c and 3.28f we highlight an example of a material which is an insulator before intercalation, becomes conducting under intercalation with lithium (or partial intercalation with magnesium), but once fully intercalated with magnesium recovers a band gap. The cause of this is the gradual downwards shift in the

position of the GeS_2 conduction band that is dispersive across the energy range 1 eV to 3 eV. Once intercalated with lithium, this band becomes partially occupied and is reduced in energy by $\sim$1 eV at Γ. When intercalated with magnesium, the band is fully occupied and we see a further energy drop of $\sim$1 eV at Γ. This ability to control both the material conductivity and position of the Fermi level through intercalation could be useful in a range of applications.

By decomposing the DOS into contributions from the different ionic orbitals (see Appendix B), we find that TMDCs composed of main-block transition metals have conduction bands dominated by the *d*-orbital of the metal, with a significantly smaller contribution from the *p*-orbitals of the chalcogen. For TMDCs composed of Group XIV metals, however, the conduction band is instead composed of metal *s*-orbitals and chalcogen *p*-orbitals. The contributions from these states are almost equal, with the chalcogen contributing slightly more. This difference in the character of the conduction band is likely the origin for the difference of its behaviour under intercalation, (as demonstrated for GeS_2 in Figure 3.28c and 3.28f).

We emphasise that these electronic band structures (and the corresponding band gaps) were obtained using the PBE functional. Use of a hybrid functional would likely increase the band gaps of those materials that are semiconducting, and could also introduce a band gap into some materials that are metallic. Whilst the PBE functional is known to underestimate band gaps, previous work has suggested that hybrid functionals over-estimate the band gap for TMDC materials [292].

Finally, in Figure 3.28, we have only shown materials that do no have spin-split electronic structures. We present in Figure 3.29 the magnetic moments (per formula unit) for each of the TMDCs in their pristine and their $a = 1$ intercalated structures. We find that magnetic moments are only presented by TMDCs composed of central block transition metals (Groups V to X). Of these, the largest moments are shown by the top row transitions metals V, Cr, and Mn when their TMDCs are intercalated with magnesium, and when their tellurides are intercalated with lithium.

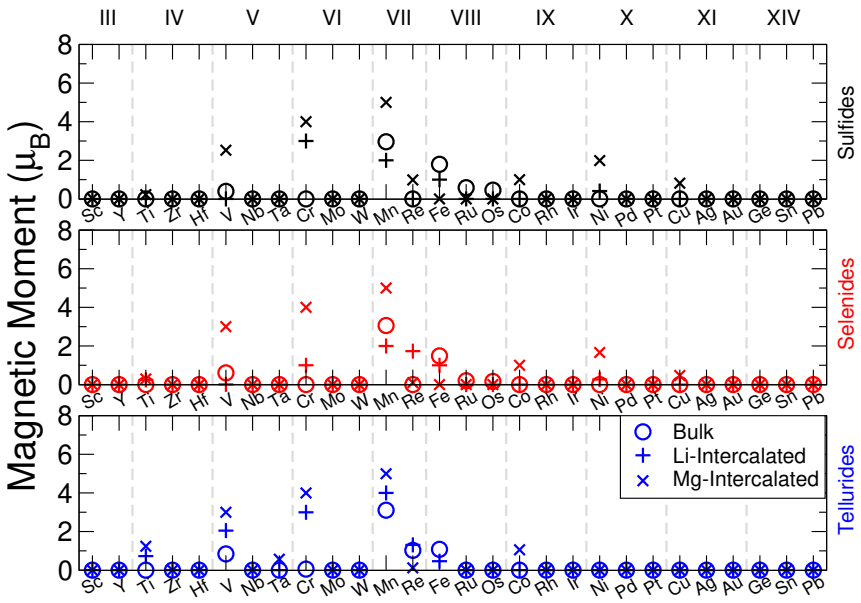

Figure 3.29: Magnetic moment (per formula unit) of the different TMDCs explored. The sulfides (top), selenides (middle), and telluride (bottom) materials are included, with the results for lithium-intercalated structures presented with pluses, and magnesium-intercalated presented with crosses.

3.15 Summary

In the evaluation of any given electrode material, there are many metrics that need to be considered to determine the promise of that material, and we have presented here the results of an investigation of lithium- and magnesium-intercalation into each of the layered transition metal dichalcogenides, as indicated in Figure 3.30. By comparing the two polymorphs of the layered TMDC structures, we have shown that the T-phase is typically the preferred phase. However, phase changes can be induced with intercalation, particularly for the Group IV, V, and VI materials. The layered phase of the TMDCs is ideal for intercalation due to the presence of vdW gaps, providing natural space for intercalation with minimal need for volumetric expansion. All of the TMDCs present expansions lower than 60%, with many of the early transition metal structures expanding by less than 15%. Most of this expansion comes from an increase in the out-of-plane lattice constant, though we also identify minor changes to the in-plane structure.

Using thermodynamic phase diagrams, we evaluate the stability of intercalated TMDCs to conversion reactions and thus provide an estimate of the reversible

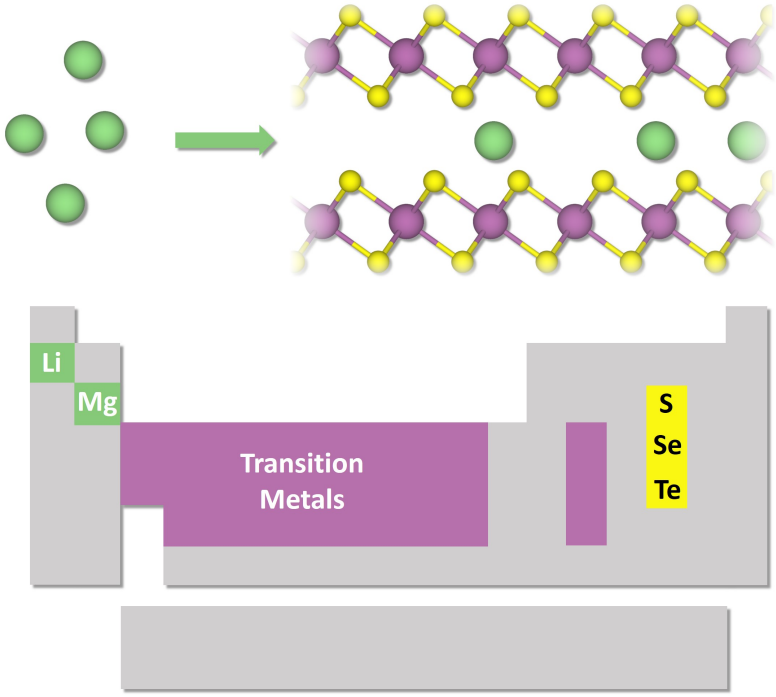

Figure 3.30: Summary of the work presented in this Chapter.

capacity. We find that most TMDCs are stable with lithium intercalation, though this stability is reduced for magnesium intercalation due to the extra charge of the intercalant. Compounds composed of heavier chalcogens also suffer a reduction in stability due to the reduced electronegativity of the chalcogen leading to a reduction in the M-X bonding strength. From the range over which the materials are stable, we determine the gravimetric charge density, and find that many of the Period IV transition metal sulfides offer capacities in excess of 200 mAhg^{-1} with lithium intercalation, and over 400 mAhg^{-1} with magnesium intercalation. These materials have shown a range of voltage profiles as well. For lithium intercalation, sulfide materials offer the largest voltages (in the range of $2 - 2.5$ V), with a gradual decrease as the mass of the chalcogen is increased. There is further reduction in the voltage for intercalation with magnesium, with most materials offering voltages lower than $\sim$1.5 V, and a significant spread across the range of magnesium concentration.

We find that most of the TMDCs retain a conductive nature across the range of intercalant concentrations considered, though some materials do become insulating at concentrations of $a = 1$ in Li_aMX_2 or Mg_aMX_2. Many key features of the band structure can be easily tracked with the inclusion of intercalants, and there

is a gradual shift upwards of the Fermi level due to the charge that is donated to the host material. The Group XIV materials do deviate from this behaviour slightly, but we can attribute this to the difference in character of the conduction band compared to main-block TMDCs.

In general, we find that the TMDC sulfides are the best for lithium intercalation, and we highlight the Group IV, V, and VI in particular for their low volumetric expansion, moderate intercalation voltages, and high stability against conversion reactions. We also highlight ScS_2 and YS_2 as promising cathode materials, which offer high voltages close to 4 V, and high intercalation stability allowing for theoretical capacities of 243.99 $mAhg^{-1}$ and 173.91 $mAhg^{-1}$, respectively. Finally, we suggest that the Group VIII and IX materials are also worthy of further investigation. For magnesium intercalation, we again show that the early transition metals offer the best performance as anodes, but also show that many other materials show ideal voltages and sufficient thermodynamic stability over a significant concentration range. The comprehensive and consistent study here shows both the promise of the TMDCs as electrodes and provides a repository of data for future studies of these materials.

In the following Chapter, we shall extend the above study to investigate the elastic properties of the TMDCs and how they change with intercalation. Not only are these elastic properties useful for microscopic modelling of electrode materials, but they are important role for considering materials in flexible electronics.

Chapter 4

Elastic Properties of Intercalated TMDCs

"Your suit can stretch as far as you can without injuring yourself, and still retain its shape. Virtually indestructible, yet it breathes like Egyptian cotton."

Edna E. Mode, The Incredibles, 2004

4.1 Introduction

Layered van der Waals (vdW) materials have been the subject of intense study over the past few decades due to the wide range of electronic, optical, and chemical properties they can exhibit. This is further enhanced by the ability to tune these properties through layer control and defect engineering, resulting in them being utilised across a wide range of applications. Besides the optical and electronic properties that are typically of direct practical interest, other fundamental properties such as the mechanical behaviour are also important for all industrial applications. However, very few investigations have been carried out to explore such mechanical behaviour. Nevertheless, due to the presence of a vdW gap, the mechanical properties of layered materials are highly anisotropic [293], making them interesting candidates for thermoelectric [294, 295], superconducting [296, 297], and piezoelectric [298–300] applications.

As we saw in the previous Chapter, one application in which the layered vdW materials have found particular success is as intercalation electrodes. Conventional materials experience stresses arising from the intercalation of ions into their structure due to phase changes [301–303], ionic diffusion [304], and volumetric expansion [305]. These lead to material 'fracturing', ultimately resulting in structural degradation and device failure. However, the intrinsic interlayer spacings within vdW materials allow for easy storage and transport of ions during cell cycling [35, 72], resulting in relatively low volumetric expansions [184]. As such, many vdW materials, such as the NMC variants [83, 86, 182], graphite [179–181], MXenes [183], and the TMDCs have each been the subject of many studies in recent years. Unfortunately, despite their ideal layered nature, vdW materials are not totally immune from the intercalant-related stresses, and can suffer from limited lifetimes because of this.

Several models based on solid-state diffusion and continuum mechanics have been developed to investigate stresses in electrodes associated with ionic diffusion [306–312], and have been applied to graphite. However, these rely on quantities describing the mechanical and elastic behaviour of the material, such as the Young's modulus, Poisson ratio, or elements of the elastic tensor. Though the elastic properties of several materials have been explored using experimental and theoretical methods, many quantities are typically absent from literature as experimental investigations into these mechanical properties are difficult to perform. Consequently, such investigations of intercalated materials are often restricted to the limits of intercalation: For example, the elastic properties of lithium-intercalated graphite have been explored using ultrasonic resonance and neutron scattering techniques [313–316], and though data is available for the pure graphite and Li_6C compositions, little is known about the elastic properties for intermediate concentrations. Even recent techniques such as nanoindentation limit studies of vdW materials to samples of a few layers [317–323], raising issues of resolving vdW adhesion to substrate materials [324]. Further, reported elastic properties of bulk TMDC samples are typically dominated by defects at grain boundaries and existing cracks, which have been studies using molecular dynamics simulations [325–327], but are not intrinsic to the material [323].

In the absence of such experimental data, then, approximations and assumptions must be made. For unintercalated materials, extrapolation from the elastic properties of chemically or structurally related materials has been suggested [328,329], though this requires an in-depth investigation of at least one related structure and calibrations for non-linear properties are needed. For the evolution of elastic properties with increased intercalant concentration, on the other hand, one approach is to assume the elastic moduli and components of the elasticity tensor are independent of intercalant concentration, whereas another is to assume a linear trend between the initial and final charge states [275,277]. Clearly, an investigation into the fundamental elastic behaviour of these materials is required: Not only will this further our understanding of the elastic properties of layered materials and how these change with the loss of the vdW spacing, but will also provide necessary quantities for continuum models.

In this Chapter, we report on a theoretical modelling of the mechanical properties of TMDC layers, with a focus on their properties for use as electrode materials in lithium and magnesium ion cells. From the calculated elastic tensor we derive many key elastic quantities, including the bulk and shear moduli, and commonly-considered elastic ratios. We also comment on the elastic anisotropy using the universal anisotropy metric and the angular Young's modulus.

4.2 Background

4.2.1 The Strain Tensor

We define the position of a point in a body as **r**, with the components x_i in some coordinate system (e.g. $x_1 = x$, $x_2 = y$, and $x_3 = z$). Under a deformation, every point within the body is (in general) displaced to **r'** (with components x_i'). The displacement which transforms **r** into **r'** is then given by the displacement vector **u** = **r'** − **r**, with components $u_i = x_i' - x_i$. The coordinates of the final vector (x_i') depend upon the coordinates of the initial vector (x_i), hence the components of the displacement vector (u_i) are a function of x_i [330].

Let us now consider two different points within the body which are very close together, separated by a vector described by dx_i of length $dl^2 = \sum_i dx_i^2$. After the deformation, the two points are now separated by the vector $dx_i' = dx_i + du_i$, of length $dl'^2 = \sum_i x_i'^2$. For brevity we will drop the explicit summation, allowing us to write $dl^2 = dx_i^2$ and $dl'^2 = dx_i'^2 = (dx_i + du_i)^2$. Expanding this, we get,

$$\begin{aligned} dl'^2 &= dx_i^2 + 2dx_i du_i + du_i^2 \\ &= dl^2 + 2dx_i du_i + du_i^2. \end{aligned} \tag{4.1}$$

Substituting $du_i = (\frac{\partial u_i}{\partial x_k})dx_k$ we get,

$$dl'^2 = dl^2 + 2\frac{\partial u_i}{\partial x_k}dx_i dx_k + \frac{\partial u_i}{\partial x_k}\frac{\partial u_i}{\partial x_l}dx_k dx_l. \tag{4.2}$$

As summation over i and k in the second term extends the same range, we can write the second term in its explicitly symmetric form,

$$\frac{\partial u_i}{\partial x_k}dx_i dx_k = \frac{1}{2}\left(\frac{\partial u_i}{\partial x_k} + \frac{\partial u_k}{\partial x_i}\right)dx_i dx_k. \tag{4.3}$$

For the final term in equation (4.2), we swap the dummy indices i and l (to match the $dx_i dx_k$ of the second term), giving,

$$\frac{\partial u_i}{\partial x_k}\frac{\partial u_i}{\partial x_l}dx_k dx_l = \frac{\partial u_l}{\partial x_k}\frac{\partial u_l}{\partial x_i}dx_i dx_k. \tag{4.4}$$

We can now write the element dl' as,

$$\begin{aligned} dl'^2 &= dl^2 + 2 \cdot \frac{1}{2}\left(\frac{\partial u_i}{\partial x_k} + \frac{\partial u_k}{\partial x_i}\right)dx_i dx_k + \frac{\partial u_l}{\partial x_k}\frac{\partial u_l}{\partial x_i}dx_i dx_k \\ &= dl^2 + 2\epsilon_{ik}dx_i dx_k, \end{aligned} \tag{4.5}$$

where we have used the tensor ϵ_{ik}, defined as,

$$\epsilon_{ik} = \frac{1}{2}\left(\frac{\partial u_i}{\partial x_k} + \frac{\partial u_k}{\partial x_i} + \frac{\partial u_l}{\partial x_k}\frac{\partial u_l}{\partial x_i}\right). \tag{4.6}$$

The tensor ϵ_{ik} is the strain tensor, and we see from its definition that it is symmetric with swap of index, $\epsilon_{ik} = \epsilon_{ki}$. As such, we can choose coordinate axes called the principal axes of the tensor so that the tensor is diagonalised at a given point, and the leading diagonal terms (labelled $\epsilon_{11} = \epsilon^{(1)}$, $\epsilon_{22} = \epsilon^{(2)}$, and $\epsilon_{33} = \epsilon^{(3)}$) are all non-zero. Once diagonalised, the element dl' becomes,

$$\begin{aligned} dl'^2 &= (\delta_{ik} + 2\epsilon_{ik})dx_i dx_k \\ &= (1 + 2\epsilon^{(1)})dx_1^2 + (1 + 2\epsilon^{(2)})dx_2^2 + (1 + 2\epsilon^{(3)})dx_3^2. \end{aligned} \tag{4.7}$$

From this, we see that the strain on an element volume may be treated as three independent strains in three mutually perpendicular directions (the principal axes of the tensor).

Except for special cases (such as thin rods and thing plates) a deformation results in only a small displacement vector, meaning that u_i and its derivatives are small. We can therefore afford to ignore the third term of the strain tensor as it is second-order small due to the product of two derivatives. Hence, we reach the strain tensor for small deformations,

$$\epsilon_{ik} = \frac{1}{2}\left(\frac{\partial u_i}{\partial x_k} + \frac{\partial u_k}{\partial x_i}\right). \tag{4.8}$$

4.2.2 The Stress Tensor

We can expand the internal energy E of a crystal with respect to the strain tensor as,

$$\begin{aligned} E(V_0, \{\epsilon_{mn}\}) &= E_0(V_0) + \frac{1}{2}\sum_{ij}\left(\frac{\partial E}{\partial \epsilon_{ij}}\right)\epsilon_{ij} + \frac{1}{2}\sum_{ijkl}\left(\frac{\partial^2 E}{\partial \epsilon_{ij}\partial \epsilon_{kl}}\right)\epsilon_{ij}\epsilon_{kl} + ... \\ &= E_0(V_0) + V_0 \cdot \frac{1}{V_0}\sum_{ij}\left(\frac{\partial E}{\partial \epsilon_{ij}}\right)\epsilon_{ij} + V_0 \cdot \frac{1}{V_0}\cdot\frac{1}{2}\sum_{ijkl}\left(\frac{\partial^2 E}{\partial \epsilon_{ij}\partial \epsilon_{kl}}\right)\epsilon_{ij}\epsilon_{kl} + ... \\ &= E_0(V_0) + V_0\sum_{ij}\sigma_{ij}\epsilon_{ij} + \frac{V_0}{2}\sum_{ijkl}C_{ijkl}\epsilon_{ij}\epsilon_{kl} + ... \end{aligned} \tag{4.9}$$

where we have defined the stress tensor,

$$\sigma_{ij} = \frac{1}{V_0}\left(\frac{\partial E(V_0, \{\epsilon_{mn}\})}{\partial \epsilon_{ij}}\right)_{\epsilon=0}, \tag{4.10}$$

and the second-order adiabatic elastic constants,

$$C_{ijkl} = \frac{1}{V_0}\left(\frac{\partial^2 E(V_0, \{\epsilon_{mn}\})}{\partial \epsilon_{ij}\partial \epsilon_{kl}}\right)_{\epsilon=0}, \tag{4.11}$$

with the equilibrium volume being given by V_0. It can be shown that the stress and strain tensors are linearly related by a multiplicative constant equal to an appropriate elastic constant, similar to Hooke's law,

$$\sigma_{ij} = C_{ijkl}\,\epsilon_{kl}. \tag{4.12}$$

The elements C_{ijkl} construct a tensor called the 'elastic tensor' or 'stiffness tensor'. The above Hooke's law relation can be inverted, however, and rewritten in terms of elements of the compliance tensor, S_{ijkl},

$$\epsilon_{ij} = S_{ijkl}\,\sigma_{kl}. \tag{4.13}$$

The compliance tensor is the inverse of the elastic tensor, $\mathbf{S} = \mathbf{C}^{-1}$, so has the same symmetries.

4.2.3 The Elastic Tensor

We can define a strain energy density function, w, as,

$$\sigma_{ij} = \frac{\partial w}{\partial \epsilon_{ij}}. \tag{4.14}$$

If the material is not only elastic but also obeys a linear stress-strain relation, as given by Hooke's law (equation (4.12)), then we can write the strain energy density function in quadratic form,

$$w = \frac{1}{2}\,C_{ijkl}\,\epsilon_{ij}\,\epsilon_{kl}. \tag{4.15}$$

The elastic tensor consists of the 81 elastic constants (three for each of the i, j, k, and l indices). Considering the symmetry of the stress tensor (with indices ij), we can say $C_{ijkl} = C_{jikl}$, which reduces the number of elastic constants to 54 (six for ij, and three for each of the indices k and l). Similarly, we can consider the symmetry of the strain tensor (with indices kl) to note that $C_{ijkl} = C_{ijlk}$, and further reduce the number of elastic constants to 36. These symmetries are called the minor symmetries. Finally, we notice that the strain energy density function, as given in equation (4.15), should be unchanged by swapping ij and kl so $C_{ijkl} = C_{klij}$. This major symmetry then reduces the number of unique elastic constants to 21.

It is convenient to make use of the tensor-symmetries established above to use Voigt notation instead of the indices $ijkl$. In Voigt notation, we contract pairs of Cartesian indices into a single integer: $xx \to 1$, $yy \to 2$, $zz \to 3$, $yz/zy \to 4$, $xz/zx \to 5$, and $xy/yx \to 6$. We now simplify the various expressions outlined

above. The elastic energy is now given as,

$$E(V_0, \{\epsilon_m\}) = E(V_0) + V_0 \sum_i \sigma_i \epsilon_i + \frac{V_0}{2} \sum_{ij} c_{ij} \epsilon_i \epsilon_j + ... \tag{4.16}$$

the stress tensor as,

$$\sigma_i = \frac{1}{V_0} \left(\frac{\partial E(V_0, \{\epsilon_m\})}{\partial \epsilon_i} \right)_{\epsilon=0}, \tag{4.17}$$

and elastic constants as,

$$c_{ij} = \frac{1}{V_0} \left(\frac{\partial^2 E(V_0, \{\epsilon_m\})}{\partial \epsilon_i \partial \epsilon_j} \right)_{\epsilon=0}. \tag{4.18}$$

These c_{ij} elastic constants construct a 6×6 'elastic matrix' (six for each of the i and j indices). The elastic matrix $\mathbf{c}$ and its elements c_{ij} are closely related to the elastic tensor $\mathbf{C}$ and its elements C_{ijkl}, however they are subtly different due to the reduction of Hooke's law from tensor form to matrix form. A similar construction of a compliance matrix can also be completed, which is the inverse of the elastic matrix. Within this Chapter, we will primarily utilise the elements of the elastic matrix.

4.2.4 Elastic Stability

Within the harmonic approximation, a crystalline structure (in the absence of any external load) is considered stable if all phonon modes have positive frequencies for all wave vectors, so-called dynamic stability. It also required that the change in elastic energy (given by the quadratic term in equation (4.16)) is always positive ($E > 0$, for all $\epsilon \neq 0$), which is called the elastic stability criterion. This latter condition is equivalent to the following necessary stability conditions for an unstressed crystal,

1. The elastic matrix (given by c_{ij}) is definite positive (symmetric and real).
2. All eigenvalues of the elastic matrix are positive.
3. All leading principal minors of the elastic matrix (determinants of its upper-left k by k sub-matrix, with $1 \leq k \leq 6$) are positive. This is known as Sylvester's Criterion.

4. An arbitrary set of minors of the elastic matrix are all positive.

From these conditions, we can also deduce further necessary (but not sufficient) conditions. For example, the condition on the principal minors implies that all diagonal elements are positive ($c_{ii} > 0$, for all i), though this is not strong enough to ensure stability. Another is that $(c_{ij})^2 < c_{ii}c_{jj}$ for all i, j.

4.2.5 Polycrstalline Elastic Moduli

From the elastic matrix, various elastic properties are able to be determined. It is unlikely that fabricated samples of a given material will be a perfect crystal with a single crystal orientation, instead consisting of many domains with different alignments. However, from the elastic matrix, we are able to determine average values of the various elastic constants and elastic moduli of a polycrystalline sample. The bulk and shear moduli of these polycrystalline materials can be calculated from the single crystal elastic matrix [331, 332], though there are different schemes by which we can do this. Upper bounds of bulk modulus (B_V) and shear modulus (G_V) can be found using the Voigt scheme [333, 334],

$$\begin{aligned} B_V =& \frac{1}{9}\big[(c_{11} + c_{22} + c_{33}) + 2(c_{12} + c_{23} + c_{31})\big] \\ G_V =& \frac{1}{15}\big[(c_{11} + c_{22} + c_{33}) - (c_{12} + c_{23} + c_{31}) \\ & + 3(c_{44} + c_{55} + c_{66})\big]. \end{aligned} \tag{4.19}$$

An alternative method by which we can evaluate the bulk and shear moduli utilises the elements of the compliance matrix (the inverse of the elastic matrix). This can be achieved using the Reuss scheme [333, 334] to obtain the lower bounds B_R and G_R,

$$\begin{aligned} \frac{1}{B_R} =& (s_{11} + s_{22} + s_{33}) + 2(s_{12} + s_{23} + s_{31}) \\ \frac{1}{G_R} =& \frac{1}{15}\big[4(s_{11} + s_{22} + s_{33}) - 4(s_{12} + s_{23} + s_{31}) \\ & + 3(s_{44} + s_{55} + s_{66})\big]. \end{aligned} \tag{4.20}$$

The results of the Voigt and Reuss schemes can be combined in the Voigt-Reuss-Hill scheme [333, 334], where an average of the upper (V) and lower (R) bounds

is taken,

$$\begin{aligned} B_{VRH} &= \frac{B_V + B_R}{2} \\ G_{VRH} &= \frac{G_V + G_R}{2}. \end{aligned} \tag{4.21}$$

Once the bulk and shear moduli have been determined, the polycrystalline Young's modulus, Y, can also be obtained:

$$Y = \frac{9BG}{3B + G} \tag{4.22}$$

Two other quantities that can be useful for describing the elastic nature of a material are the, the Poisson ratio, ν, and the Pugh ratio, R, each given by,

$$\begin{aligned} \nu &= \frac{3B - 2G}{2(3B + G)} \\ R &= \frac{B}{G}. \end{aligned} \tag{4.23}$$

As a general guide, Poisson ratios greater than 0.26 indicate a material will be ductile, whereas it will be brittle for ratios smaller than 0.26. Similarly, Pugh ratios greater than 1.75 indicate that a material will be ductile, whereas for ratios lower than 1.75 the material is expected to be brittle [279, 331, 335, 336].

4.2.6 Elastic Anisotropy

In only relatively few cases is the elastic response of a single crystal isotropic, and given the layered nature of the compounds under consideration, the expectation is that many will exhibit a signficant degree of anisotropy [293]. We can evaluate the extent of this anisotropy using a universal elastic anisotropy index, A^U, using the Voigt and Reuss moduli discussed above [337],

$$A^U = 5\frac{G_V}{G_R} + \frac{B_V}{B_R} - 6 \geq 0. \tag{4.24}$$

This takes a minimal value of zero when the single crystal is locally isotropic. Departure from this minimal value gives a measure of the single crystal anisotropy, accounting for both the shear and bulk contributions. This can be interpreted as a generalization of the Zener anisotropy index, whereby, instead of taking the ratios of individual stiffness constants to define the anisotropy, all stiffness constants have been taken into account by considering the matrix nature of elastic stiffness [337].

The anisotropic Young's modulus of a general crystal class can be calculated from the compliance tensor [338], starting from,

$$\frac{1}{Y} = \sum_{m=1}^{3}\sum_{n=1}^{3}\sum_{p=1}^{3}\sum_{q=1}^{3} S_{mnpq} l_m l_n l_p l_q, \tag{4.25}$$

where S_{mnpq} is an element of the compliance tensor, and each of the l_i is an element of the unit vector,

$$\hat{\mathbf{l}} = \begin{pmatrix} l_1 \\ l_2 \\ l_3 \end{pmatrix} = \begin{pmatrix} \sin\theta\,\cos\phi \\ \sin\theta\,\sin\phi \\ \cos\theta \end{pmatrix} \tag{4.26}$$

with directional cosines l_1, l_2, and l_3. We have used the Euler angles θ (angle from the z axis) and ϕ (angle in the x-y plane from the x axis). For trigonal crystals, equation (4.25) reduces to,

$$\begin{aligned} \frac{1}{Y} &= s_{11}\left(l_1^4 + l_2^4\right) + \left(2s_{12} + s_{66}\right)\left(l_1^2 l_2^2\right) + \left(2s_{13} + s_{44}\right)\left(l_3^2\right)\left(l_1^2 + l_2^2\right) \\ &\quad + 2s_{14}\left(2l_1^2 l_2 l_3 - l_2^3 l_3\right) + s_{33}\left(l_3^4\right) \\ &= s_{11}\sin^4\theta + \frac{1}{4}\left(s_{13} + s_{44}\right)\sin^2 2\theta + s_{33}\cos^4\theta \\ &\quad + 2s_{14}\sin^3\theta\left(2\sin\phi\cos^2\phi - \sin^3\phi\cos\phi\right), \end{aligned} \tag{4.27}$$

where we have used the elements of the compliance matrix, s_{ij}, and the relation $s_{66} = 2(s_{11} - s_{12})$. This expression for anisotropic Y is equal to the expression for hexagonal systems [339] when the element s_{14} is equal to zero.

4.3 Computational Details

In this work, first principles techniques based on density functional theory were used to determine the elastic properties of layered MX_2 materials, as well as their lithium- and magnesium-intercalated structures. These calculations were performed using the Vienna Ab initio Simulation Package (VASP) [161–164]. The valence electrons included for each species are those presented in Table 2.1. The projector augmented wave method [139] was used to describe the interaction between core and valence electrons, and a plane-wave basis set was used with an energy cutoff of 700 eV. Van der Waals interactions have been addressed using the zero damping DFT-D3 method [155].

This study focuses on 1T-phase TMDCs, as many of the TMDCs exhibit the 1T-phase [194–196, 205] and in the previous Chapter we highlighted the preference for the T-phase structure with intercalation. Individual TMDC sheets are held together by covalent M-X bonds with *p-d* hybridisation [192], whilst the sheets are coupled to each other by weak van der Waals forces [193]. Intercalant ions were introduced into the vdW spacing, choosing the octahedrally-coordinated site above the metal atom of the host structure as this has been shown in the previous Chapter to be the lowest in energy. Initial structural relaxations (allowing for both ionic and unit cell optimisation) to determine the geometry were completed using the Perdew-Burke-Ernzerhof (PBE) [119] functional form of the generalised gradient approximation (GGA). These were converged to a force tolerance of 0.0001 eV/Å per atom, electronic self-consistency was considered to an accuracy of 10^{-8} eV, using a Monkhorst-Pack [140] k-point grids of $12 \times 12 \times 12$.

Due to the small changes in energy that can be involved, the elements of the elastic tensor can be sensitive to the sampling of reciprocal space [277]. For the primitive unit cells considered, Monkhorst-Pack k-point grids of $18 \times 18 \times 18$ were used, and for the $2 \times 2 \times 2$ supercells comparable grids of $9 \times 9 \times 9$. These correspond to k-point densities of 17496 per reciprocal atom (pra) in the pristine systems, and 23328 pra in the intercalated systems. These values are comparable values to those used in databases such as the Materials Project [340, 341], and in similar studies of other layered materials [275, 279, 293, 342, 343].

The limited number of studies into the elastic properties of the TMDCs and how they change with intercalation make it difficult to check the accuracy of our calculations with other first principles works, investigations using other theoretical approaches, and with experimental works. We have therefore performed a separate study into graphite and $LiCoO_2$ (for which there are several works in the literature) to determine the reliability of our results, which we present in Appendix C. We conclude that **k**-point grids of $18 \times 18 \times 18$ for the primitive unit cells of the TMDCs are sufficient for accurate descriptions of the elastic response (compared to other theoretical approaches and experimental works), and convergence against more dense grids.

Many works have shown that choice of functional can lead to differences in pre-

dictions for properties important to electrode materials [289,290]. Previous works have found that use of hybrid functionals such as HSE06 demonstrate a change of $\sim 5\%$ in the matrix elements and elastic values in monolayers of CaFI [344] and CaFCl [345] compared to GGA method, and a change of $\sim 10\%$ for $BiAlO_3$ [346]. Compared to GGA functionals, +U corrections have been shown to reduce the elements of the elastic tensor and produce small deviations in some elastic properties for $CuInTe_2$ [347], and increase elastic constants in $FePO_4$ [348] resulting in an increase in the bulk and shear moduli. +U has also been shown to produce little change to the values obtained for $LiFePO_4$ [348]. The functionals rVV10 and VdW-DF2 have produced similar values to the PBE functional [349] for bulk and monolayer MoS_2, with no significant improvement to the matrix elements or elastic constants compared to the values obtained using experimental methods.

Computational studies [350, 351] on 2H-MoS_2 have also been used to compare results obtained with different levels of exchange-correlation approximation to those obtained experimentally. For example, the c_{11} element is found to have an experimental value of 238 GPa which is reproduced with HSE methods, but underestimated at 211 GPa using a GGA functional. However, other elements of the elastic matrix are more accurately calculated using GGA than with HSE, though these typically fall within $\sim 10\%$ of experiment. There is also a spread in values for any given method (for example, between different calculations using GGA), suggesting that other aspects of a first principles calculation offer more significant changes to elastic results than the level of exchange-correlation approximation employed. Finally, we have also performed a limited study on the elastic properties of graphite and $LiCoO_2$ using the PBE functional. This is outlined in Appendix C, where we find close agreement with experimental results, improving on LDA and other GGA results in the case of graphite, and improving on LDA, other GGA, and HSE results in the case of $LiCoO_2$.

In this work we have chosen to use the PBE functional for three reasons: (i) the increased computational cost of using hybrid functionals; (ii) the lack of experimental results for many of the materials considered necessary for accurate choice of +U corrections, and (iii) the relatively small changes to the elastic properties that arise from these methods. For evaluation of the elastic matrix symmetry,

elements are considered to be equal if they fall within 0.01 GPa.

As transition metal compounds allow for the possibility of unpaired electrons in *d* and *f* orbitals, all calculations have been performed allowing for optimisation of collinear spin-polarization without specifying any initial spin configuration, or the inclusion of spin-orbit (SO) effects. Given the possible complexity of magnetic ordering in TMDCs, there can be many local minima in the potential energy surface, and the global minimum might not be easily identifiable. This ambiguity increases the risk of drawing incorrect conclusions from SO calculations. Further, despite the additional cost and time, calculations including SO may not yield significantly distinct properties compared to simpler calculations.

In the case of the TMDCs, numerous prior studies have already examined the influence of SO effects on their electronic structure. Typically, the SO interaction can be thought of as a modulation on the electronic structure. Specifically for elastic properties, some previous works have compared results of transition-metal containing compounds obtained with and without the SO interaction. Small ($\sim$1%) change in c_{11} and c_{12} when doping $Ni_{24}Al_7$ with transition metals, and the effect is a lot less significant compared to that arising from the inclusion of spin [352]. There is also a small ($\sim$5%) change in the in-plane elastic constants of monolayers of HfSSe, and no change in the HfS_2 and $HfSe_2$ equivalents [353]. One material composed of Period V and VI elements, YPtBi, shows an increase in c_{11}, c_{12} and c_{44} by $\sim$10% with the inclusion of SO [354]. However, we consider this change to be at the extreme end due to the high content of heavy elements compared to the TMDCs considered in this work.

4.4 Methods for Evaluation of Elastic Properties

4.4.1 Single Crystal Bulk Modulus

The single-crystal bulk modulus was evaluated by uniformly expanding and compressing the three lattice vectors in $\pm$1% intervals and allowing for ionic relaxation. The five lowest-energy points (0%, $\pm$1%, $\pm$2%) were then used to fit a

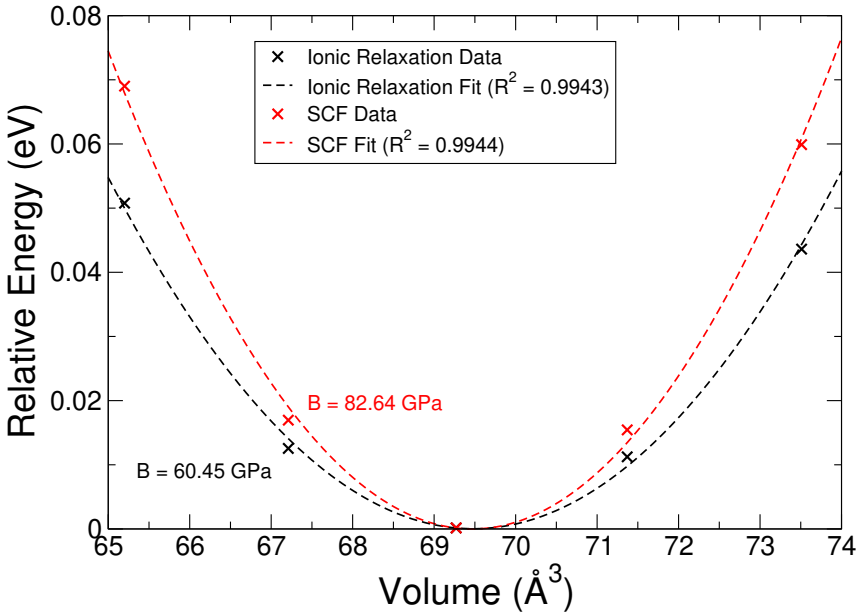

Figure 4.1: An example plot showing the variation in the relative energy of lithium-intercalated ScS_2 with volume expansion and compression.

quadratic relation between the system energy and the cell volume, as we show in Figure 4.1. Almost all R^2 values of these fits exceed $R^2 = 0.99$. We find that most of the fits show R^2 values greater than 0.99. Of those that fall below this value, seven (MoS_2, ReS_2, $ScSe_2$, VTe_2, $NbTe_2$, $LiVTe_2$, and $MgMnTe_2$) are in the range $R^2 = 0.98 - 0.99$. A further eleven fall below $R^2 = 0.98$, but these are either found to be elastically unstable (such as $LiMnSe_2$, $MgMnS_2$, and $MgCrSe_2$, see Section 4.6) or demonstrate a range of magnetic moments at different strains (such as $MnSe_2$, $OsSe_2$, $CrTe_2$, $LiCrTe_2$, $LiMnTe_2$, $LiVSe_2$, and $MgMnSe_2$) hence making a quadratic fit inappropriate. However, for consistency, we have maintained this approach whilst highlighting the issues arising from these magnetic considerations.

The second order derivative of each of the fits was used for determination of the single-crystal bulk modulus B_S, as given by,

$$B_S = V_0 \frac{\partial^2 E}{\partial V^2}, \tag{4.28}$$

where E is the energy, V is volume, and V_0 is the volume at zero pressure. Though further extensions beyond the $\pm 2\%$ could have been considered, the energy-strain profiles tend to deviate from a parabolic curve for larger strains [355, 356].

4.4.2 Elastic Matrices

The elastic and internal strain tensors were computed from the second order derivatives of the total energy with respect to the position of the ions and changes to the size and shape of the unit cell, as employed in VASP. For evaluation of the elastic matrix symmetry, elements are considered to be equal if they fall within 0.01 GPa. Near all of the TMDCs in their pristine, lithium-intercalated, and magnesium-intercalated forms are found to be trigonal with space group number 164 (space group P$\bar{3}$m1 and point group $\bar{3}$2/m), with the exception of $LiCrS_2$. This space group number was found to be the most prevalent in a recent study of vdW layered structures, and was also frequently observed for the related ionic structures [293]. For such trigonal crystal systems, the elastic matrix has the form,

$$\begin{pmatrix} c_{11} & c_{12} & c_{13} & c_{14} & & \\ \cdot & c_{11} & c_{13} & -c_{14} & & \\ \cdot & \cdot & c_{33} & & & \\ \cdot & \cdot & & c_{44} & & \\ & & & & c_{44} & c_{14} \\ & & & & \cdot & c_{66} \end{pmatrix}, \tag{4.29}$$

where empty elements are equal to zero. There are thus only six independent elastic constants due to the symmetry constraints and the relation $c_{66} = \frac{1}{2}(c_{11} - c_{12})$. The above matrix takes the form of a hexagonal crystal system when the element c_{14} is equal to zero [357]. We have evaluated the elastic matrix for the considered materials, as this is the fundamental object for the following discussions.

In the previous Chapter, we assessed the thermodynamic stability of the intercalated TMDCs, finding most to be stable with the inclusion of lithium or small amounts of magnesium. Whilst the mechanical stability of a material is usually evaluated by identifying the presence of any imaginary ($\omega^2 < 0$) phonon modes, calculation of full phonon dispersions are not conducive to broad investigations such as this. However, as these instabilities occur for long wavelength modes ($\mathbf{q} \to 0$), we can instead utilise the Born stability criteria to assess stability from the elastic tensor [293, 358]. This is because the elastic tensor is derived from the linear approximation of the stress-strain relationship, and so the components

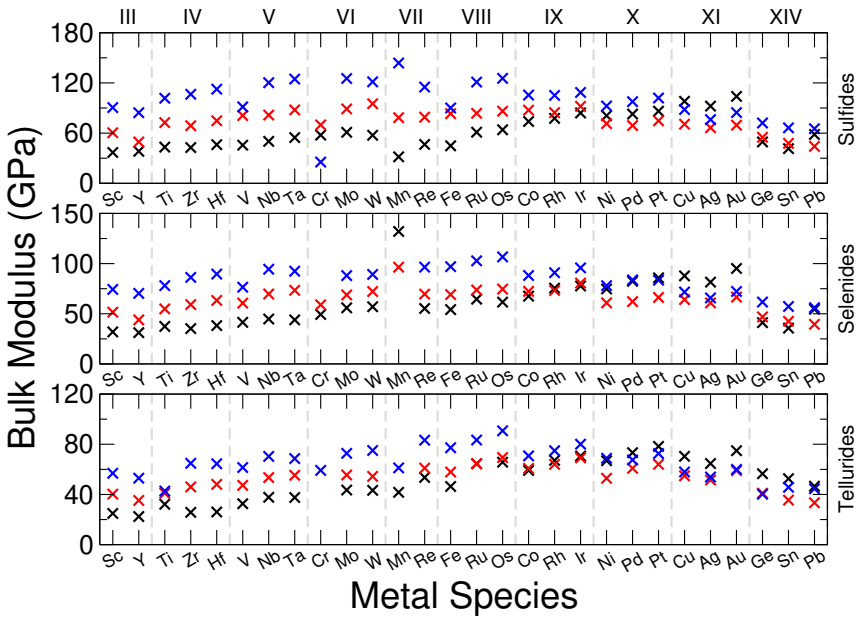

Figure 4.2: Single crystal bulk modulus values for the pristine, unintercalated structures are presented in black, lithium-intercalated in red, and magnesium-intercalated in blue. The top shows the sulfide data, the middle shows the selenide data, and the bottom shows the telluride data.

are related to the dispersion curves for low energy acoustic phonons [293]. The elastic stability conditions have been outlined elsewhere for different crystal systems [357], which for trigonal crystals are,

$$\begin{aligned} &(a) \quad c_{11} > |c_{12}| \\ &(b) \quad c_{44} > 0 \\ &(c) \quad c_{13}^2 < \frac{1}{2} c_{33}(c_{11} + c_{12}) \\ &(d) \quad c_{14}^2 < \frac{1}{2} c_{44}(c_{11} - c_{12}) = c_{44} c_{66} \end{aligned} \tag{4.30}$$

which can be determined through calculating the leading principal minors of the elastic matrix, and requiring that they are all positive (Sylvester's criterion).

4.5 Single Crystal Bulk Modulus

The single-crystal bulk modulus can be obtained using equation (4.28), and we present the results of this in Figure 4.2 for the pristine and intercalated systems. For the pristine structures, we see a gradual increase in the bulk modulus as the Group of the metal composing the host TMDC increases. Using the TMDC

sulfides as an example to highlight this, there is an increase from 36.86 GPa (ScS_2) to 103.92 GPa (AuS_2). Though there is a general linear trend between these points, the central transition metal Groups VII and VIII drop below this. A closer look at the magnetic configuration of these materials, however, reveals a change in the spin state for different strains. Being able to utilise this spin degree of freedom allows for further energy minimisation in these materials and so they can achieve a lower bulk modulus, and also highlights the potential to utilise these materials for their magnetoelastic properties.

With intercalation, we notice a general increase in the bulk modulus. For example, with lithium intercalation, the bulk modulus of TiS_2 increases from 43.24 GPa to 72.60 GPa in $LiTiS_2$, and for magnesium intercalation it increases to 101.72 GPa. This increase in the bulk modulus is observed for most materials, specifically for those composed of transition metals in Groups III to VIII. This can be understood by an increase in the bonding strength between TMDC layers, facilitated by the introduction of the ionic intercalants, and the consequent formation of ionic bonds between the intercalant and the TMDC layers. We note a surprising change in this trend for later transition metals: For Group IX compounds, the bulk modulus of the magnesium-intercalated structure remains the largest. However, the values for the pristine and lithium-intercalated compounds are near equal, with relatively small (~ 10 GPa) differences between them, and there are some cases where the lithium-intercalated bulk modulus is smaller than that of the pristine material, such as with $CoSe_2$ ($\mathrm{B} = 67.58$ GPa) and $LiCoSe_2$ ($\mathrm{B} = 72.31$ GPa). For Group X compounds, this evolves to the bulk modulus of magnesium-intercalated compounds being comparable with the pristine compounds, and for Group XI materials the bulk modulus of the pristine structures is higher than that of the corresponding intercalated compounds. With few exceptions, we also identify a reduction in the bulk modulus with increased mass of the chalcogen, in line with increased formation energy [359] and hence weaker bonding.

Changing the chalcogen species results in comparable changes to those arising from a change in the transition metal. We note a general decrease in the bulk modulus as the atomic number of the chalcogen is increased. For example, the pristine TiX_2 materials offer a bulk modulus of 43.24 GPa (sulfide), 37.42 GPa

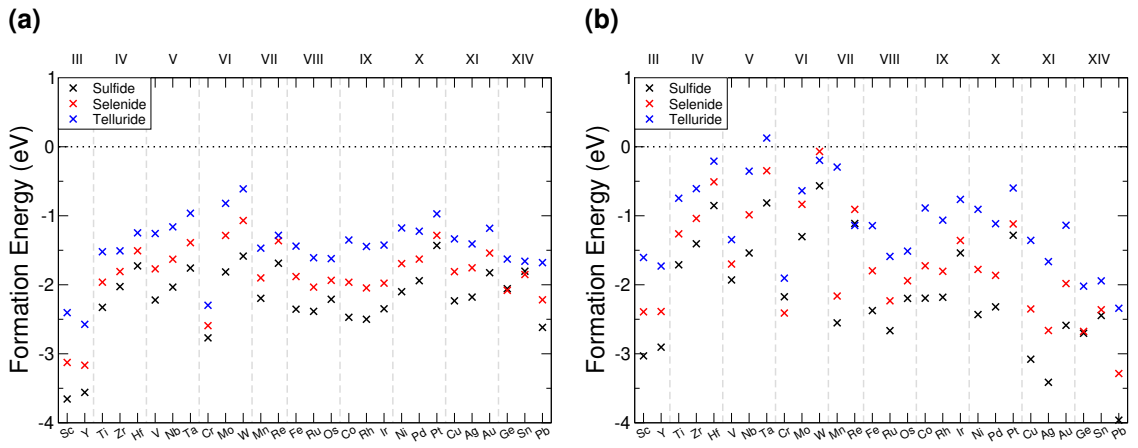

Figure 4.3: The formation energy (per formula unit) described by equation (4.31) is presented in 4.3a for lithium and in 4.3b for magnesium. Negative values of formation energy indicate intercalation is favourable. In each, sulfide data is presented in black, selenide data is presented in red, and telluride data is presented in blue.

(selenide), and 32.17 GPa (telluride). To explain this, we consider the formation energy of the intercalated TMDC as a metric to assess the stability of a host TMDC with intercalation. This is given by,

$$E_{\text{form}} = E_{\text{LiMX}_2} - \left[E_{\text{MX}_2} + E_{\text{Li}}\right], \tag{4.31}$$

where E_{MX_2} is the energy of the pristine bulk MX_2 structure, E_{LiMX_2} is the energy of the intercalation MX_2 structure, and E_{Li} is the energy of a lithium atom as found in bulk. An equivalent expression can be written for magnesium intercalated TMDCs. We present in Figure 4.3a and Figure 4.3b the formation energy (per formula unit) for the lithium-intercalated and magnesium-intercalated TMDCs, respectively. We see that all TMDCs (with the exception of magnesium-intercalated $TaTe_2$) show negative formation energies, and therefore intercalation is energetically favourable.

As the atomic number of the chalcogen is increased, the formation energy of TMDC layers similarly increases [359], highlighting TMDC formation is less favourable. This reduction in favourability is an indication of a weakened bonding. It has also previously been shown that there is a reduction in the (2D) Young's modulus with increased formation energy [360], hence we can conclude that the reduction in the bulk modulus as the chalcogen is changed S$\rightarrow$Se$\rightarrow$Te can be attributed to a weakening of the TMDC bonding. Likewise, there is a change in the bulk modu-

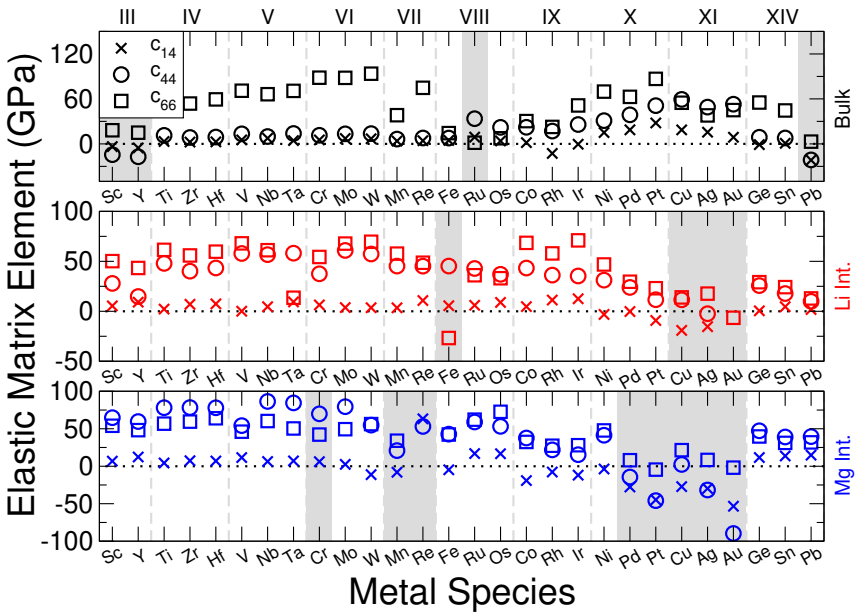

Figure 4.4: Elements of the elastic matrix, c_{14}, c_{44}, and c_{66}, for the sulfide TMDC materials. Data shows pristine bulk (black), lithium-intercalated (red), and magnesium-intercalated (blue) data. Materials which are not elastically stable are indicated with shaded regions.

lus with change in chalcogen species. For example, the $LiTiX_2$ materials the bulk modulus is 72.60 GPa (sulfide), 54.85 GPa (selenide), and 40.97 GPa (telluride), and for the $MgTiX_2$ compounds it is 101.72 GPa (sulfide), 78.07 GPa (selenide), and 42.72 GPa (telluride). We see a similar increase in the formation energy for the intercalated TMDC structures, and so the above discussion using the weakened bonding to explain this reduction holds.

4.6 Elastic Stability

Evaluating the above elastic stability conditions for each of the materials presented, we find that of the 252 materials considered, 212 are elastically stable. In the following presentation of results, regardless of which criteria are violated, we also include data for the elastically unstable materials, but shade their data ranges to identify them. For the pristine materials, we find that twelve materials break the elastic stability equations outlined in equation (4.30). We find that all twelve break condition (d), and of these eight break condition (b). Three materials break condition (a), and one breaks condition (c). For lithium-intercalated TMDCs, there

are nine materials which break the stability conditions: five break condition (a), four break condition (b), three break condition (c), and eight break condition (d). For magnesium-intercalated TMDCs, nineteen materials which break the stability conditions: six break condition (a), eleven break condition (b), five break condition (c), and sixteen break condition (d). The conditions broken by each material are summarised in Appendix C.

We note that conditions (b) and (d) are most commonly broken by materials that are not elastically stable. These conditions can both be related to the element c_{44}, and so we conclude that the largest source of instability arise from the response to shear deformations. For the sulfide materials, we present in Figure 4.4 the elements of the elastic matrix, c_{14}, c_{44}, and c_{66}, which are present in the stability conditions. It is now clear to see the cases which typically lead to elastic instability in these materials: negative values of either the element c_{44} (as with ScS_2, YS_2, and PbS_2) or the element c_{66} (as with $LiFeS_2$). These would both result in negative quantities on the right hand side of stability condition (d).

Materials composed of the central Mn, Re, and Fe metals frequently break the stability conditions. These materials have magnetic moments that deserve close attention. Although we have allowed for different (collinear) spin configurations in the following presentation of results, a more careful consideration of their spin configurations might remove the elastic instabilities shown here. With the introduction of an intercalant, we find that many late-transition metal TMDCs lose their elastic stability. However, we do identify some materials, such as ScS_2 and YS_2, where the introduction of an intercalant results in an elastically stable compound. Finally, we find that twenty two selenide materials break stability conditions, which is more than the sulfide (fifteen) or telluride (eleven) materials. However, overall the same trends (in terms of which conditions are broken most frequently) are seen across TMDCs composed of different chalcogen atoms.

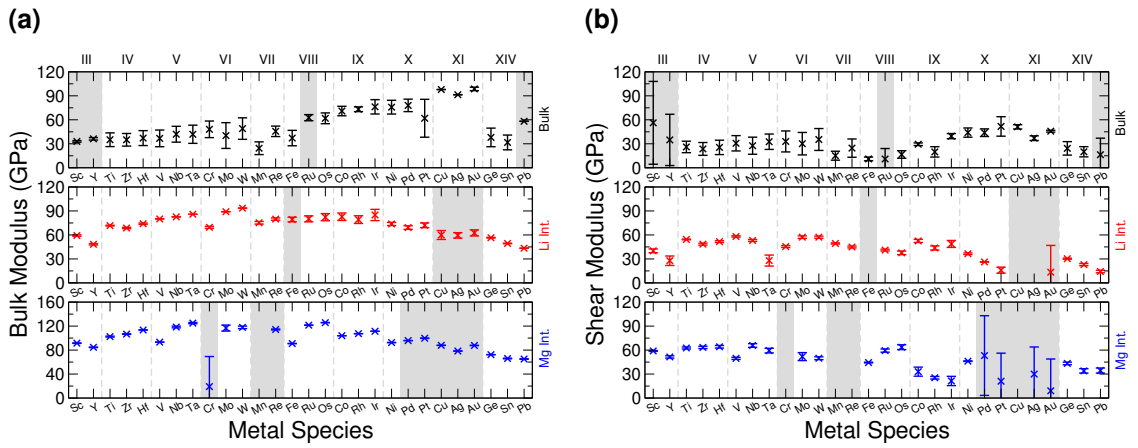

Figure 4.5: Bulk modulus (4.5a) and shear modulus (4.5b) for sulfide TMDC materials. Values calculated using the VRH scheme are presented with crosses, and the corresponding Reuss and Voigt results are presented as error bars. Data for the pristine bulk, lithium-intercalated, and magnesium-intercalated structures is presented in black, red, and blue, respectively. Materials which are not elastically stable are indicated with shaded regions.

4.7 Polycrystalline Properties

4.7.1 Elastic Moduli

In Figure 4.5a we present the polycrystalline bulk modulus for each of the sulfide TMDCs in the pristine bulk (black), lithium-intercalated (red), and magnesium-intercalated (blue) forms. We have included values using each of the Voigt, Reuss, and VRH schemes where values calculated using the VRH scheme are presented with crosses, and the corresponding Reuss and Voigt results are presented as error bars. This shows the range in values that can be obtained using the different schemes. Equivalent data for the selenide and telluride materials is presented in Appendix C. For the pristine bulk structures, we note a gradual increase in the bulk modulus as the Group of the transition metal is increased from III (Sc, Y) to XI (Cu, Ag, Au), for each of the chalcogen species. We highlight this with the VRH values of the sulfide materials. The bulk modulus is found to be 32.92 GPa for ScS_2, which increases to 36.76 GPa for VS_2, to 48.09 GPa for CrS_2, to 70.96 GPa for CoS_2, to 75.79 GPa for NiS_2, to 97.85 GPa for CuS_2, demonstrating a range of 65 GPa. However, this range is reduced upon intercala-

ton: the bulk modulus for lithium-intercalated sulfides ranges between 43.42 GPa ($LiPbS_2$) and 93.54 GPa ($LiWS_2$), a difference of 50.12 GPa, and the bulk modulus for magnesium-intercalated sulfides ranges between 65.04 GPa ($MgPbS_2$) and 125.80 GPa ($MgOsS_2$), showing a difference of 60.76 GPa. These values also highlight that intercalation moves the maximal values of bulk modulus away from the late-transition metals (Group XI) towards the Groups in the middle of the transition metal block, (VI to VIII). The intercalant, therefore, acts to level out the bulk modulus of these materials.

We note some exceptions to the upward trend exhibited by the pristine materials, and point out the drop in bulk modulus for the Group VII and Group VIII sulfides. For TMDCs composed of these transition metals we see that the magnetic state changes by as much as 0.2 μ_B per unit cell across the unique distortions made. This spin degree of freedom is not utilised in the other TMDCs, and allows for further energy minimisation (and hence a lower bulk modulus). This is in line with results presented elsewhere [361], where magnetic materials with larger magnetic moments typically showed a lower bulk modulus than those with a zero magnetic moment. We also notice a drop for the Group XIV metals, where we have determined a value of 37.98 GPa for GeS_2, though these are post-transition metal materials, and the difference in behaviour from main-block transition metals is not surprising. Beyond these exceptions, however, the general upwards trend is evident in Figure 4.5a for the sulfides, and for the selenide, and telluride materials presented in Appendix C.

For the selenide and telluride materials, the bulk modulus follows the same trends as those shown by the sulfides. However, we do note a general reduction in the bulk modulus. For example, the Voigt-Reuss-Hill values for TiX_2 compounds decreases from 35.07 GPa (sulfide), to 28.95 GPa (selenide), to 22.60 GPa (telluride). For the lithium-intercalated $LiTiX_2$ structures this reduction is again seen, decreasing from 71.64 GPa (sulfide), to 57.23 GPa (selenide), to 40.27 GPa (telluride), as well as for the magnesium-intercalated $MgTiX_2$ structures, with values of 102.47 GPa (sulfide), 80.41 GPa (selenide), and 39.88 GPa (telluride). This is in line with what was seen for the single-crystal bulk modulus discussed above, which was rationalised with the reduction in TMDC bonding strength.

Using the different schemes (Voigt, Reuss, VRH) we can obtain different estimates for the elastic moduli. For the pristine systems, there is a large spread between the Voigt and Reuss values of bulk modulus. We find that these values are closer for the materials composed of larger chalcogen species: using the WX_2 materials as an example, the difference between the bulk modulus using the Voigt and Reuss schemes are 26.94 GPa, 17.24 GPa, and 5.03 GPa for the WS_2, WSe_2, and WTe_2 materials, respectively. Once intercalated, this difference between the Voigt and Reuss values is decreased (for example, to 0.04 GPa for $LiWS_2$ and to 2.09 GPa for $MgWS_2$).

In Figure 4.5b we show the polycrystalline shear modulus for the sulfide materials, with the equivalent selenide and telluride data presented in Appendix C. For the pristine materials (black) the shear modulus shows a general increase with increasing Group number, from 23.56 GPa (ZrS_2) to 51.69 (PtS_2) for the sulfides in the VRH scheme. Again, the central transition metals (Groups VII to IX) fall below this trend by utilising their spin state during deformation. There is then a further, but small, reduction for the Group XI materials. Finally, the Group XIV materials shown the lowest values of shear modulus, for example with values of 20.00 GPa, 16.94 GPa, and 7.54 GPa for SnS_2, $SnSe_2$, and $SnTe_2$, respectively. We present the equivalent selenide and telluride shear modulus data in Appendix C. However, for the pristine materials, we note a less dramatic change as the chalcogen species is changed. Using the TiX_2 materials to highlight this, the Voigt-Reuss-Hill values of shear modulus are 26.03 GPa (sulfide), to 20.36 GPa (selenide), to 20.95 GPa (telluride). The similarity in these values is likely due to the weak vdW interaction coupling different MX_2 layers.

We also identify a spread in the shear moduli using the different (Voigt, Reuss, VRH) schemes, larger than the spread that was present for the bulk modulus. Whilst this spread is typically reduced with the inclusion of an intercalant, many materials, such as the magnesium-intercalated Group XI materials, have a greater spread than their pristine counterparts. However, we explain this through consideration of the elastic stability: From equations (4.19) and (4.20) we can see that the polycrystalline bulk modulus does not depend on the c_{44} element of the elastic tensor (which we determined above to be the cause of the elastic instability

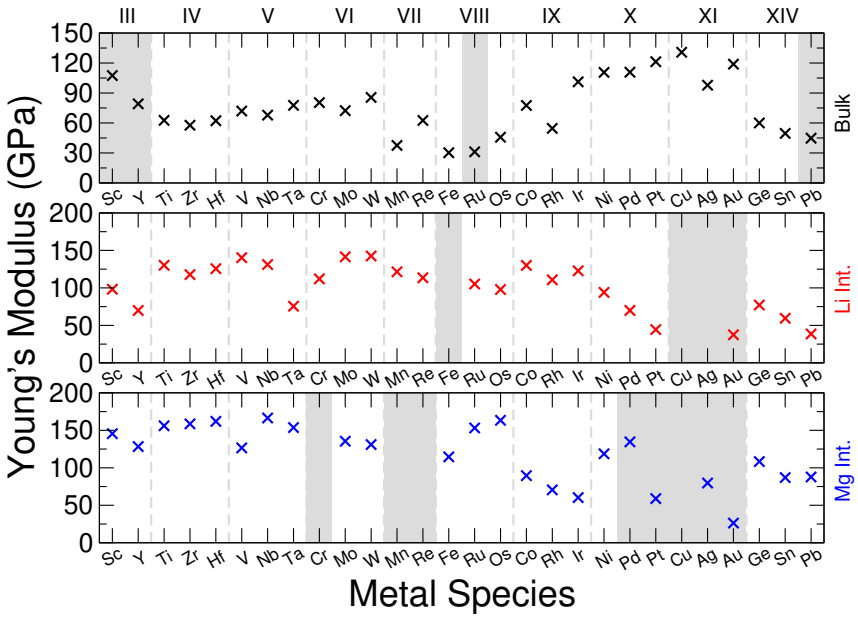

Figure 4.6: Voigt-Reuss-Hill values of Young's modulus for sulfide TMDC materials. Data for the pristine bulk, lithium-intercalated, and magnesium-intercalated structures is presented in black, red, and blue, respectively. Materials which are not elastically stable are indicated with shaded regions.

present in these materials). As such, it would be expected that the values of bulk modulus be relatively well behaved regardless of the elastic stability. However, the dependence of the polycrystalline shear modulus on the c_{44} element results in the anomalous values of the shear modulus. We highlight this with the magnesium-intercalated compounds: whilst equivalent materials that are elastically stable show very little variation in shear modulus between the different schemes, elastic instability leads to dramatic differences. The Group XI TMDCs (CuX_2, AgX_2, AuX_2), for example, show differences in excess of 100 GPa and some unphysical negative values when intercalated with magnesium.

The spread in bulk and shear moduli will propagate into the elastic properties that are determined from B and G, as can be seen from equations (4.22)-(4.23). In the following, we present only the results of the VRH scheme for clarity and brevity.

4.7.2 Young's Modulus

We can obtain values for the polycrystalline Young's modulus using the above values of bulk and shear moduli. We present these in Figure 4.6 for the sulfide TMDCs. For the pristine bulk structures, we see a roughly linear trend upwards as the Group of the transition metal is increased, similar the behaviour of the bulk modulus (see equation 4.22). There are some exception to this, including the Group III TMDC sulfides which are elastically unstable, and the Group XIV TMDC sulfides which show a drop due to the corresponding drop in the bulk modulus arising from the difference in chemical character of the metal compared to the main transition block. We also note that TMDCs composed of metals from Groups VII-IX also fall below this trend, but we again ascribe this to the ease with which these TMDCs change their spin state. Of the pristine sulfides, FeS_2 has the lowest Young's modulus of 30.21 GPa, and CuS_2 has the highest with 130.73 GPa. Due to the range in values for the bulk and shear moduli using the different Voigt/Reuss/Hill schemes, there is a corresponding spread in the obtained values for the Young's modulus. Upon intercalation, there is in general a small increase in the Young's modulus, with a larger increase with magnesium intercalation that with lithium intercalation.

With changing chalcogen species, we find that TMDC composed of chalcogens with higher atomic number show a general reduction in the polycrystalline Young's modulus. Using the ZrX_2 materials to highlight this, the Young's modulus (using the Voigt-Reuss-Hill scheme) reduces from 57.73 GPa (ZrS_2), to 51.82 GPa ($ZrSe_2$), to 44.17 GPa ($ZrTe_2$). Above, we discussed how the increase in formation energy with S$\rightarrow$Se$\rightarrow$Te [359] is an indication of a weakened bonding, and that an increased formation energy has led to a corresponding decrease to the (2D) Young's modulus for similarly layered structures [360]. In fact, it has previously been reported that a reduction in the charge transfer between the metal and chalcogen atoms leads to a reduction in the (2D) Young's modulus of ultra-thin TMDCs [323]. We do stress, however, that due to the sensitivity of the Young's modulus on the bulk and shear values through equation (4.22) and the choice of scheme used to calculate them, there are several examples of TMDCs which break this trend, though not by much. Further details of the values obtained using

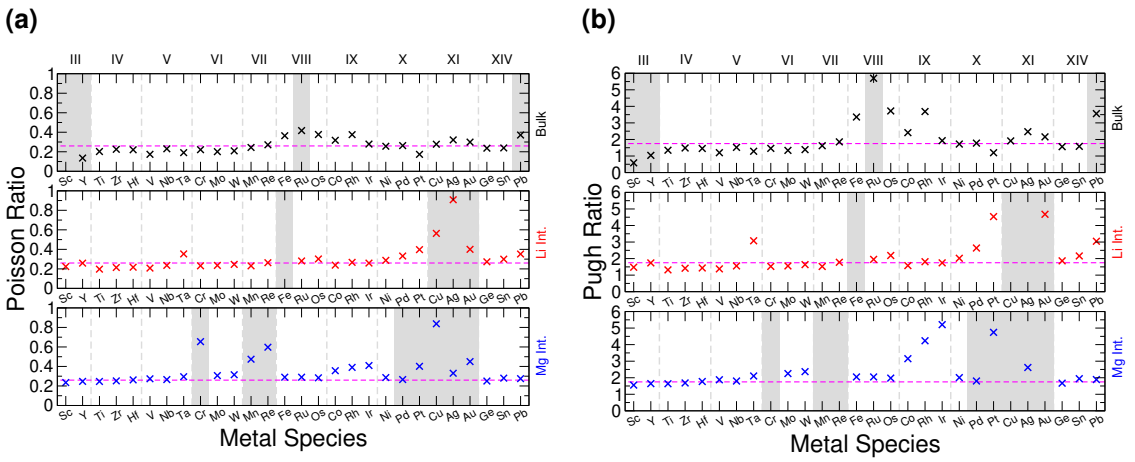

Figure 4.7: Voigt-Reuss-Hill values of Poisson ratio (4.7a) and Pugh ratio (4.7b) for sulfide TMDC materials. Data for the pristine bulk, lithium-intercalated, and magnesium-intercalated structures is presented in black, red, and blue, respectively. A Poisson ratio of 0.26 and a Pugh ratio of 1.75 are indicated with horizontal dashed lines. Materials which are not elastically stable are indicated with shaded regions.

the different schemes and equivalent data for the selenide and telluride materials are presented in Appendix C.

4.7.3 Elastic Ductility

We can assess the ductility of a material using equation (4.23), which describes two commonly used elastic ratios. We present in Figure 4.7 the Poisson and Pugh rations for the pristine and intercalated sulfide materials, where a Poisson ratio of 0.26 and a Pugh ratio of 1.75 are indicated with horizontal dashed lines. Above these limits, materials are described as ductile, where as ratios lower than these limits indicate brittle materials. Equivalent data is presented in Appendix C for the selenide and telluride materials.

We find that for the unintercalated structures, the materials composed of Group III-VI transition metals show Poisson and Pugh ratios that lie below the respective limits, indicating they are brittle in nature. With lithium intercalation, each group displays a slightly different response: Group III show an increase in the elastic ratios, however their pristine structures are elastically unstable and so a direct comparison with the intercalated structures is not appropriate. The Group IV sul-

fides show a stiffening (reduction in Poisson and Pugh ratios), the selenides retain a similar stiffness/ductility, and the tellurides show an increased ductility (increase in Poisson and Pugh ratios). The Group V materials become more ductile, and the Group VI materials experience little change to their ductility. With magnesium intercalation, we see a universal increase in the material ratios, though, with each of these early-Group TMDCs showing an increased ductility. For materials composed of later transition metals, most exhibit a higher ductility and lie above the Poisson and Pugh criteria. For both lithium and magnesium intercalation, Group VII to IX materials show a shift towards the brittle/ductile limit, but the Group X and XI materials show increase Poisson and Pugh ratios. We do highlight, however, that the intercalated Group XI TMDCs are not elastically stable. Compared to the changes that arise with choice of transition metal, we notice very little difference arising with choice of chalcogen, with most changes being within 0.05 (Poisson ratio) and 0.2 (Pugh ratio) of each other.

4.8 Elastic Anisotropy

4.8.1 Comparison of Elastic Matrix Elements

To assess the anisotropic elastic response, we present in Figure 4.8 a comparison between the c_{11} and c_{33} elements of the sulfide TMDCs (selenide and telluride data is presented in Appendix C). These elements correspond to in-plane and out-of-plane stretching, respectively. For the pristine structures, we identify a much larger value of c_{11} compared to c_{33}, demonstrating the much stronger covalent M-X bonding present in-plane and the significantly weaker vdW bonding between consecutive TMDC layers. With the introduction of an intercalant, though, the difference between these elements is reduced. With lithium intercalation, materials composed of early transition metals (Groups III to VI) have comparable values of c_{11} and c_{33}. For materials composed of metals from Groups VIII to X, there is still a significant difference between these values. For example, the values of c_{11} and c_{33} for $LiTiS_2$ are 160.33 GPa and 129.00 GPa respectively, for $LiCoS_2$ these are 196.89 GPa and 103.13 GPa. However, with magnesium intercalation, we see a

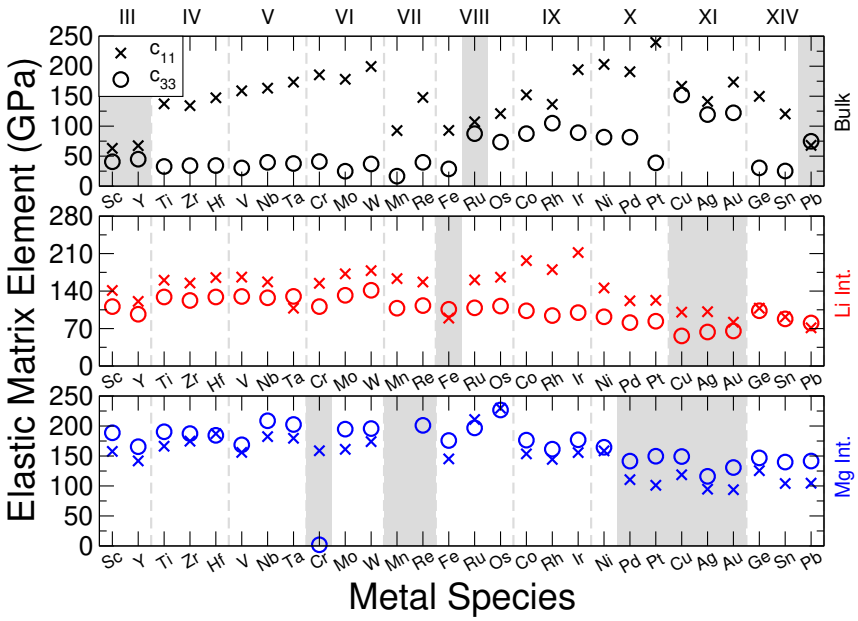

Figure 4.8: Elements of the elastic matrix, c_{11} and c_{33}, for the sulfide TMDC materials. Data for the pristine bulk, lithium-intercalated, and magnesium-intercalated structures is presented in black, red, and blue, respectively. Materials which are not elastically stable are indicated with shaded regions.

further increase in the values of c_{33} such that many of them are greater than the corresponding c_{11} element. For the selenides and tellurides, we typically see a reduction in the values of c_{11} and c_{33} as the chalcogen mass is increased, though some deviations are present for c_{33}. However, we see the same trends that are present for the sulfide materials which arise with changing the transition metal and with intercalation with lithium or magnesium.

4.8.2 Universal Anisotropy

We can further assess the anisotropy by determining the universal anisotropy index, A^U, as given by equation (4.24). We present these values in Figure 4.9a for the sulfide materials (equivalent data for the selenide and telluride TMDCs is shown in Appendix C). A value of $A^U = 0$ indicates a locally isotropic material, and deviation from this indicates a larger degree of anisotropy. The results of elastic instability is highlighted here, with materials which are not elastically stable show negative values of A^U. For the pristine crystals there is a wide range in the obtained anisotropies: many materials, such as the Group IV-VII sulfides, having

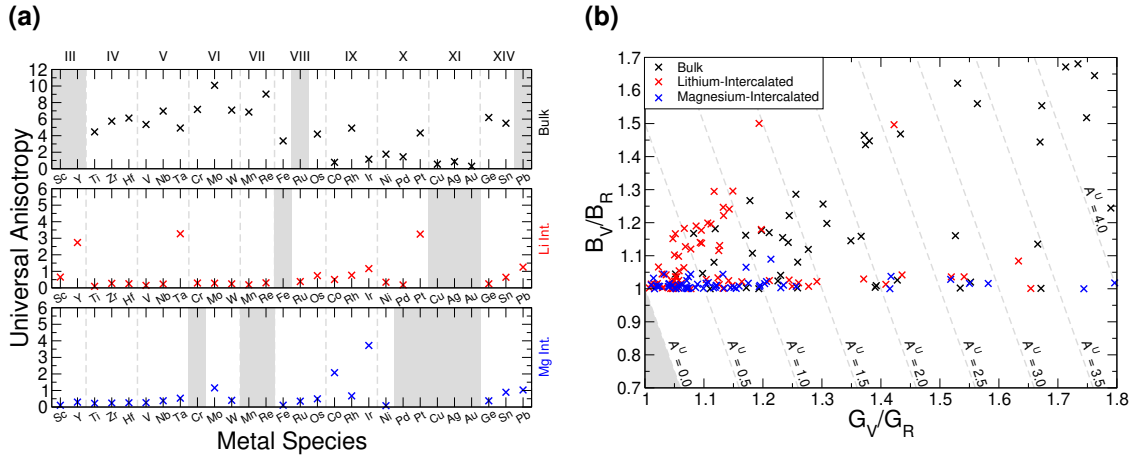

Figure 4.9: Universal anisotropy values for the sulfide TMDC materials in shown in 4.9a, where data for the pristine bulk, lithium-intercalated, and magnesium-intercalated structures is presented in black, red, and blue, respectively. Arrows with labels indicate values that lie outside of the plotted range. Materials which are not elastically stable are indicated with shaded regions. 4.9b shows the elastic anisotropy diagram, with data for all materials included.

values in the range $A^U = 6 - 12$. There are even some values even exceeding 12, such as $ScTe_2$ and $CrTe_2$, though there are very few of these. This was to be expected due to the difference between the nature of the in-plane and out-of-plane bonding. Surprisingly, despite this difference in bonding, there are many pristine materials, such as the Group XI sulfides and $GeTe_2$, possessing values of A^U less than unity which indicates materials that are close to isotropic.

With intercalation, there is then a dramatic reduction in the elastic anisotropy of the TMDCs: Figure 4.9a shows that almost all of the intercalated systems possess anisotropy indices less than unity, with very few exceeding even 2, and this extends to the selenide and telluride materials. This follows other works which have compared the anisotropy between vdW and ionic materials [293]. It is not surprising that the anisotropy of these layered materials is reduced with intercalation: the presence of the van der Waals gap results in a large difference between the in-plane and out-of-plane bonding, and hence the restoring forces to any elastic deformation. The inclusion of an intercalant removes this van der Waals gap and introduces a large positive charge between the negatively charged chalcogen species (as we saw in Chapter 3), and so a significant change in the elastic properties is to be expected. However, as the two intercalants considered in this work

are metals and possess positive charges once intercalated, they are qualitatively very similar to the metals constituting the host structure, and so the out-of-plane bonding becomes comparable to the in-plane bonding, demonstrating a similar elastic response.

Using the ratios of the Voigt and Reuss values of bulk and shear moduli we can construct an elastic anisotropy diagram (EAD), which is presented in Figure 4.9b. The advantages of such a diagram have previously been described elsewhere [337], but we briefly outline them here: we see from Figure 4.9b that the $\frac{B_V}{B_R} < 1$ and $\frac{G_V}{G_R} < 1$ regions are inadmissible, and the included lines of constant anisotropy (which have a slope of -5) highlight that changes in $\frac{G_V}{G_R}$ have a greater influence on crystal elasticity than an equivalent change in $\frac{B_V}{B_R}$. Cubic crystals have been shown to cluster along the line given by $\frac{B_V}{B_R} = 1$, and so other materials that lay along this line are elastically similar to cubic crystals, despite their trigonal symmetry. As locally isotropic materials appear closer to the $\frac{G_V}{G_R} = 1, \frac{B_V}{B_R} = 1$ point than those that are not locally isotropic, we see that the main effect of intercalation is to reduce the anisotropy of the TMDC family, as was shown with Figure 4.9a. Many of the pristine TMDCs are scattered across the EAD away from the $\frac{G_V}{G_R} = 1, \frac{B_V}{B_R} = 1$ point, but after intercalation there is a significant shift of all points towards $\frac{G_V}{G_R} = 1, \frac{B_V}{B_R} = 1$.

4.8.3 Anisotropic Young's Modulus

We can further assess the anisotropy of these materials by making use of equations (4.25) and (4.27) to determine the angular dependence of the anisotropic Young's modulus. We present in Figure 4.10a the angular Young's modulus for pristine TiS_2, where it is clear to see the relatively high in-plane Young's modulus (~ 120 GPa) compared to the out-of-plane Young's modulus (~ 40 GPa). This large disparity arises from the stronger covalent in-plane bonding compared to the weaker vdW bonding present between layers. Equivalent figures for the lithium- (Figure 4.10b) and magnesium-intercalated (Figure 4.10c) TiS_2 structures, where we see a dramatic change with the included intercalants. For lithium intercalation, we see an increase in the in-plane Young's modulus to ~ 145 GPa, and a more

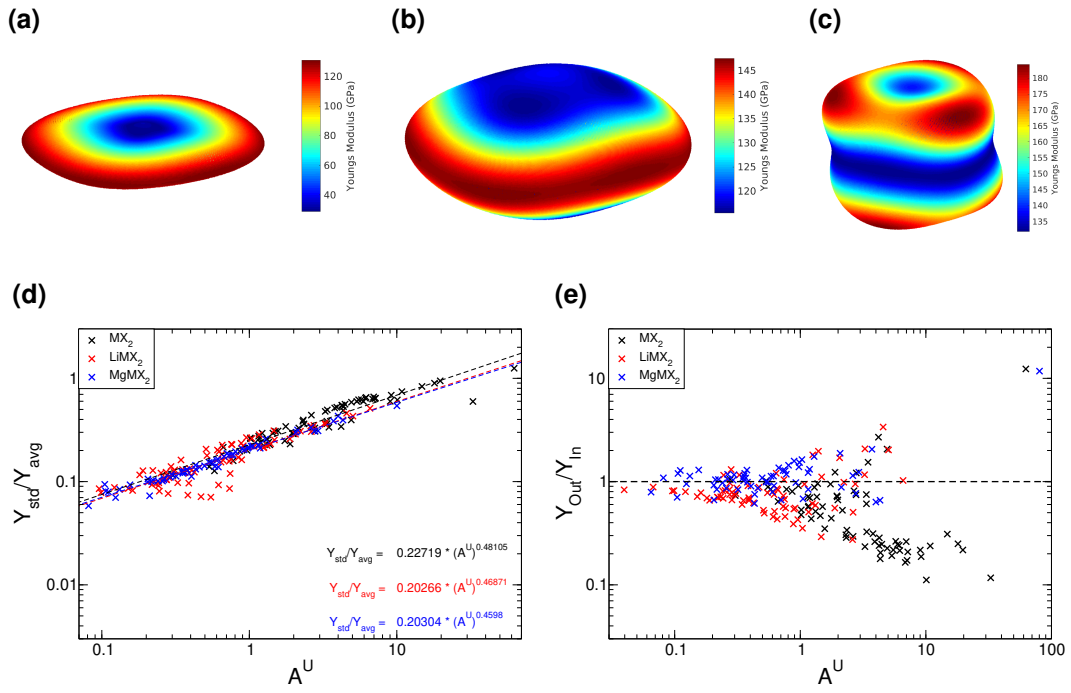

Figure 4.10: Three-dimensional heat maps showing the angular-dependent Young's modulus for TiS_2 (4.10a), $LiTiS_2$ (4.10b), and $MgTiS_2$ (4.10c). Scatter plots show the relative standard deviation of the Young's modulus as a function of anisotropy index A^U (4.10d), and the variation in the ratio of the out-of-plane and in-plane Young's modulus with A^U. In these, we include data for each of the structures considered.

dramatic increase in the vertical Young's modulus to ~ 120 GPa. We see a similar effect for magnesium intercalation, with the in-plane Young's modulus increased to ~ 140 GPa and the out-of-plane similarly increased to ~ 145 GPa. This shows the effect of coupling between layers through intercalation, and that the donated electron can increase the strength of the in-plane bonding, as has been seen for the covalent strengthening of bonds through introduction of extra electrons in other systems [362]. We also note the Young's modulus along the direction of the Ti-S bond is particularly high, reaching values of 180 GPa. Similar figures for other TMDCs are presented in Appendix C, where we find a very similar evolution of the Young's modulus with intercalation.

Similar figures for other TMDCs are presented in Appendix C, where we find a very similar evolution of the Young's modulus with intercalation. In particular, we have included equivalent data for $TiSe_2$ and its intercalated structures for comparison with TiS_2 shown in Figure 4.10. Aside from a global reduction of about 40 GPa due to the reduced bonding of the selenide TMDC compared to the sulfide

equivalents, as was discussed above, the general shape shown in Figure 4.10 is reproduced. Specifically when intercalated with lithium, we see the increase in the Young's modulus out-of-plane, resulting in a more isotropic Young's modulus similar to what is shown in Figure 4.10b. When intercalated with magnesium, we see the extremes in Young's modulus along the Ti-Se bonds, and the comparable Young's modulus in-plane and out-of-plane (coloured blue), similar to what is shown in Figure 4.10c.

A broader investigation of the Young's modulus can be achieved by comparing the relative variation of the Young's modulus over a large, evenly-distributed set of angles with the universal anisotropy. We present this in Figure 4.10d, where, by fitting with guidelines given in the figure, we find that these slopes are close to the $E_{std}/E_{avg} \propto (A^U)^{0.5}$ determined elsewhere [293]. Similarly, we present the ratio of out-of-plane and in-plane Young's modulus against the anisotropy metric. The pristine structures (black) show the largest deviation from the constant $Y_{Out}/Y_{In} = 1$ line of equivalence, in most cases dropping below it due to the significant difference between the weak out-of-plane vdW bonding to the strong in-plane covalent bonding. With the addition of lithium (red), there is a general movement of these materials upwards, towards the $Y_{Out}/Y_{In} = 1$ line, and hence show a reduction in the anisotropy. However, they again fall below the constant line, indicating that the in-plane bonding is much stronger than out-of-plane. Finally, for magnesium intercalation (blue) we see a further shift upwards and a reduction in the anisotropy. Many of the magnesium-intercalated compounds fall on the line of equivalence, showing that the magnesium intercalant facilitates bonding between layers that is similar in strength to those in-plane. In fact, many of the magnesium-intercalated structures (as well as some lithium-intercalated) demonstrate bonding out-of-plane that is stronger than bonding in-plane. For large A^U, there is little trend Y_{Out}/Y_{In}, as has been shown in a broader study of layered materials [293].

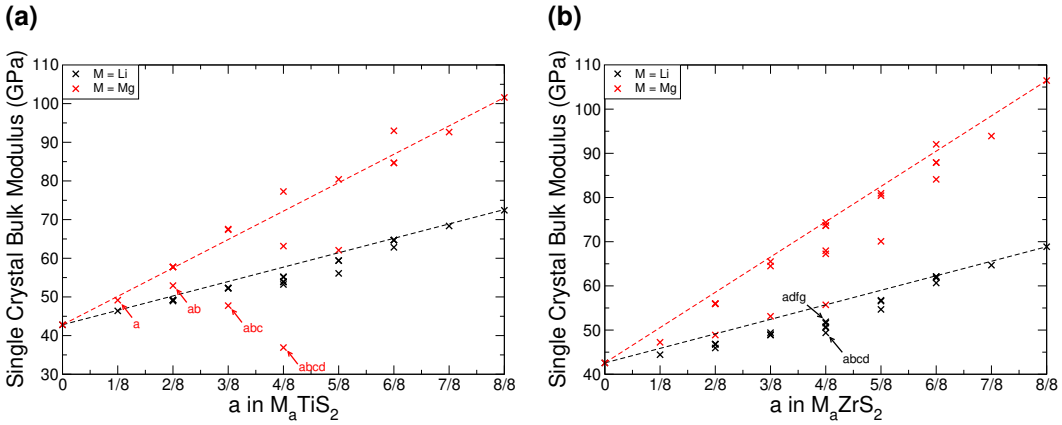

Figure 4.11: Variation of the single crystal bulk modulus with intercalant concentration for TiS_2 (4.11a) and ZrS_2 (4.11b). Data for both lithium and magnesium intercalation is presented. A straight line (dashed) connecting the bulk modulus of pristine and fully-intercalated structures has been included for visual aid.

4.9 Dependence on Intercalant Concentration

So far, we have only considered the limiting cases of pristine bulk TMDCs and their fully intercalated $LiMX_2$ and $MgMX_2$ forms. However, it is possible to intercalate these materials by intermediate amounts through control of precursor or by limiting the discharge voltage in a half-cell arrangement. The elastic properties of similarly layered materials graphite and $LiCoO_2$ have been shown to be linearly dependent on the concentration of an intercalant species [275, 277], which suggests the possibility of tuning the elastic properties of the TMDCs by controlling the level to which they are intercalated. Due to the larger cell sizes required for a finer sampling of intercalant concentration, and hence larger computational cost, we have investigated TiS_2 and ZrS_2 and their intercalated forms for closer study.

We present the single-crystal bulk modulus for lithium- and magnesium-intercalated TiS_2 in Figure 4.11a, and the equivalent ZrS_2 structures in Figure 4.11b. For visual aid, we have included the linear trend suggested previously with dashed lines. With increased lithium intercalation we find the single-crystal bulk modulus falls slightly below the linear, with the largest deviation being at the $Li_{0.5}TiS_2$ and $Li_{0.5}ZrS_2$ compositions. As we show for $Li_{0.5}ZrS_2$ in Figure 4.11b, the smallest values arise from intercalation into a single vdW spacing (labelled abcd) as such intercalant arrangement retains an uninterrupted, weakly-bonded vdW re-

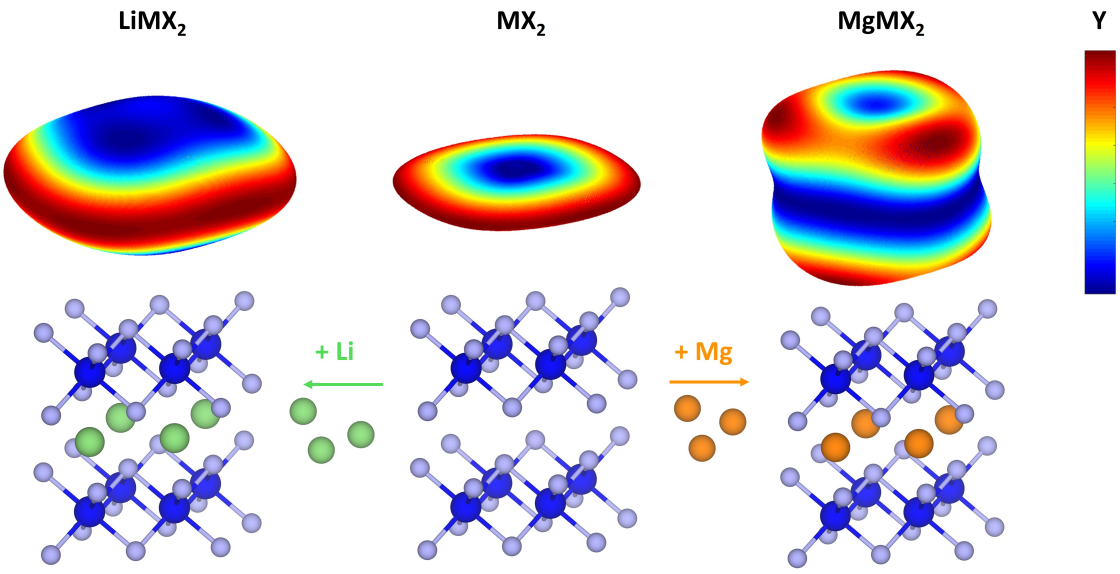

Figure 4.12: Summary of the key results presented in this Chapter.

gion. The largest bulk modulus is then achieved with a uniform distribution of lithium across the vdW layers (labelled adfg), hence coupling each of the TMDC layers with an intercalant.

For magnesium intercalation, we identify a more significant deviation from the linear trend than was seen for lithium intercalation. The intercalant configurations which display the lowest bulk modulus are again those where a single vdW spacing is filled (as has been indicated by labels a, ab, abc, and abcd in Figure 4.11a) and more equal filling between the layers results in higher values of bulk modulus. However, comparing the energies for these different configurations show that the filling of a single layer is the least energetically favourable, and more homogeneous filling is preferred. As such, we would still expect the bulk modulus to vary roughly linearly between the start and end of intercalation in an experimental investigation, for both lithium- and magnesium-intercalated materials. Regardless, this does indicate the importance of considering intermediate intercalant concentrations, as there can be a wide range in elastic properties between different intercalant arrangements for a given concentration, and hence significant deviations from the linear trend that is often assumed.

4.10 Summary

In this Chapter, we have presented a first-principles study into the elastic behaviour of layered TMDCs and their intercalated structures. The elastic properties of materials are important for all industrial applications, and are particularly important for modelling electrodes beyond the atomic scale. We have determined the elastic matrices, allowing us to evaluate key properties including the bulk, shear, and Young's moduli, and show that there is a general increase in these quantities with intercalation. Commonly used elastic ratios which describe the ductility of a material have also been calculated, allowing us to conclude that the pristine materials are brittle, but become more ductile with the addition of lithium or magnesium. The anisotropy of these materials was also assessed using a combination of the universal anisotropy metric and a direct calculation of the angular dependence of the Young's modulus. These showed that the pristine van der Waals materials possess a high degree of anisotropy, which is to be expected given the relatively weak interactions across the vdW spacing in the pristine structures. However, this anisotropy is reduced with the introduction of a positively charged intercalant. This general stiffening and reduction in anisotropy of TMDC materials with intercalation is schematically indicated in Figure 4.12. Finally, for selected systems we have also explored intermediate intercalant concentrations, and conclude that, whilst linear extrapolation of elastic properties between the limits of intercalation may be suitable in some situations, different intercalant configurations or the use of multivalent intercalant species can cause significant deviations from this.

This work builds upon the work of the previous Chapter which investigated the energetic and electronic properties of intercalated TMDCs. The elastic properties of materials are important for all industrial applications, and are particularly important for modelling electrodes beyond the atomic scale. The work presented here therefore allows for further investigation into the layered TMDCs as electrode materials. In the next Chapter, we explore one particular layered TMDC material that has offered promise as an electrode in this and the previous Chapter: ScS_2.

Chapter 5

Intercalation of Scandium Disulfide

"Scandium, the unsung hero of the periodic table, embodies both strength and versatility. Like a hidden gem, it quietly empowers innovation, sparking a brilliant cascade of possibilities."

ChatGPT, 2023

5.1 Introduction

In Chapter 3, we investigated the family of TMDCs for intercalation lithium- and magnesium-ion batteries. We were able to show that their layered structure did indeed limit the volumetric expansion due to intercalation when compared to typical 3D-materials. We were able to determine their intercalation voltages, and show that many of them were thermodynamically stable, and commented on their reversible intercalation capacities. However, of the whole family, one material stood out as a particularly promising cathode material: ScS_2.

In this Chapter, we present a focused investigation into the layered ScS_2 material for intercalation electrodes, extending the previous study to intercalation with lithium, sodium, potassium, and magnesium. We begin with a detailed discussion of scandium-based materials, and highlight the few works that have considered layered ScS_2 as an intercalation electrode. After outlining the calculation details used in this work, we then present the results of our investigation. First, we determine the ground state structure of intercalated ScS_2 to indeed be layered, using

a combination of random structure search and by explicitly considering the structures of analogous compounds. The layered structure is then investigated for key electrode properties such as the volumetric expansion, voltage, and the capacity, along with other material properties such as the electronic structure and the elastic behaviour. Once we have established the promise of the ScS_2, we try to push the limits of it by intercalating beyond the $LiScS_2$ limit, and through substitutional metal mixing.

5.2 Background

As the demand for rechargeable batteries rises, the need for both better and a wider range of cathode materials rises with it. Whereas for anodes there are a wealth of materials available and the key challenge is competing with the abundance of hard carbons, for cathodes the range of materials is much lower with leading contenders being the phosphates [36,38,40], the ubiquitous NMC and its variants [41,82–86], and spinel oxides such as $LiMn_2O_4$ [87].

For intercalation electrodes, layered materials such as the TMDCs [189–191], NMC [83,182], and the MXenes [183] are highly attractive as their van der Waals gaps allow for low diffusion barriers and hence fast intercalant transport. Recent works have started to note the potential of scandium, where the doping of metal oxides with scandium has been shown to increase particle size without affecting the crystal structure [363], provide a comparable capacity whilst improve cycling stability [363,364], and significantly lower the surface energy of nanoparticles [365]. With these clear structural and energetic improvements, as well as the fact that scandium is one of the lightest available metals, it raises the question as to how good scandium-based materials themselves would perform as electrode materials.

Transition metal oxides have been widely investigated and used for intercalation cathodes as they display high voltages and capacities. Lithium scandium dioxide ($LiScO_2$) has been experimentally verified to exist in only one form, a fractional cationic ordered rock-salt structure, with the $I4_1/amd$ space group [366,367]. This

is similar to the anatase structure of TiO_2 but with lithium filling the void spaces. However, this material was found to have poor ionic conductivity, requiring substitutional doping with transition metals in place of the scandium atoms [367]. This lack of ionic conductivity therefore prevents its exploitation as a cathode material. Alternative, layered structures of the oxide have therefore been considered [368, 369], but are unfeasible as the structure is energetically unfavourable compared to the rock-salt phase.

Layered sulfides are closely related to the oxides, and have the added benefit of being compatible with sulfide electrolytes. Sulfide electrolytes are chemically unstable with high-voltage oxides due to the difference in electronegativity of oxygen and sulfur [198]. Thus, scandium-sulfide materials could offer the optimal properties for cathodes whilst allowing the use of sulfide-electrolytes. The bulk properties of the TMDC T- and H-phases of ScS_2 have been shown to be conducting [370], however, the monolayer form of the H-phase is insulating [192, 370, 371]. Bulk forms of $LiScS_2$, $NaScS_2$, and $KScS_2$ have all been synthesised [228, 229], and were found to have the layered α-$NaFeO_2$ structure with space group $R\bar{3}M$. Unfortunately, theoretical investigations of this structure have been limited to monolayers [247, 372], and though these have suggested high capacities of over 400 $mAhg^{-1}$ with lithium intercalation, monolayers are significantly more difficult to synthesise compared to their bulk counterpart, and do not provide an accurate representation of the dimensions of electrodes being utilised in functional devices. To the best of our knowledge there are currently no studies investigating the potential of bulk ScS_2 for electrodes, and so the questions of how well the bulk material would perform as an intercalation electrode remains.

5.3 Computational Details

In this work, first principles techniques based on density functional theory were used to determine structural and energetic properties of layered scandium disulfide (ScS_2) intercalated with varying levels of lithium, sodium, potassium, and magnesium. These calculations were done using the Vienna Ab initio Simulation

Package (VASP) [161–164]. The valence electrons included for each species were Sc $3d^2 4s^1$, S $3s^2 3p^4$, Li $1s^2 2s^1$, Na $2p^6 3s^1$, K $3p^6 4s^1$, and Mg $2p^6 3s^2$. All other electrons were effectively contained within the used pseudopotentials. The projector augmented wave method [139] was used to describe the interaction between core and valence electrons, and a plane-wave basis set was used with an energy cutoff of 700 eV. Van der Waals interactions have been addressed using the zero damping DFT-D3 method of Grimme [155].

Three different phases of the ScS_2 structure were considered: the T-phase, the Hc-phase [195, 196], and the α-$NaFeO_2$-like [228, 229] structure which is here referred to as the α-phase. The T- and α-phases have the same in-plane structure but differ in the relative stacking of layers (as shown in Figure 5.1) leading to the α-structure containing three ScS_2 layers in the primitive unit cell, compared to the one in the primitive unit cell of T-ScS_2. The Hc-phase has a different layer structure, and possesses two layers of ScS_2 in its primitive unit cell. To consider intercalation with the different species, supercells of $(2 \times 2 \times 2)$, $(2 \times 2 \times 1)$, and $(2 \times 2 \times 1)$ were used for the T-, Hc-, and α-phases, respectively. These supercells provided eight different intercalation sites for the T- and Hc- phases, and twelve sites for the α-phase. These allowed for various filling configurations, as was seen in Chapter 3, each of which was explored. Whilst other phases are possible for the TMDCs, such as 3R and distorted T structures, their intercalation environments are similar to that of the T-, Hc-phase, or α-phases, and so have not been explicitly considered here. It was found through two different methods that the favoured intercalation site in all three phases of ScS_2 is the octahedrally-coordinated site. Consequently, this site has been used in the following study.

All structural relaxations were completed using the Perdew-Burke-Ernzerhof (PBE) [119] functional form of the generalised gradient approximation (GGA), using the conjugate gradient algorithm and converged to a force tolerance of 0.01 eV/Å per atom, while electronic self-consistency is considered to an accuracy of 10^{-7} eV. Of these, only the most energetically favourable structures at each level of intercalant concentration were considered. To account for the inaccurate calculation of exchange in GGA functionals, the HSE06 hybrid functional [130, 135, 265] was also used for a selection of systems. Monkhorst-Pack grids [140] of k-points

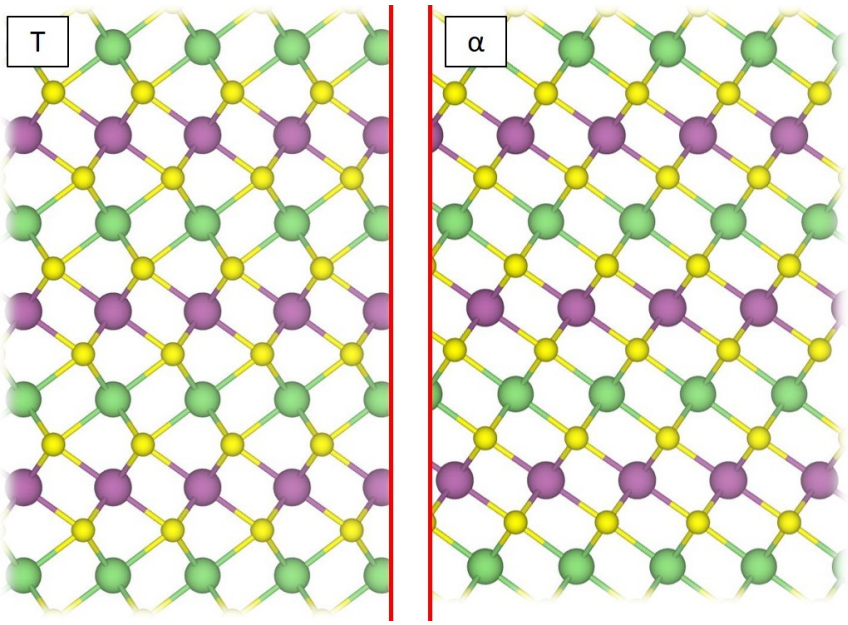

Figure 5.1: Comparison of the T-phase (left) and α-phase (right) of $LiScS_2$.

equivalent to a $6 \times 6 \times 6$ grid in the supercells are used throughout.

Phonon band structures were obtained using the frozen-phonon method employed with Phonopy [159]. For these, the primitive unit cells of the pristine and intercalated structures were geometrically relaxed to a force tolerance of 0.0001 eV/Å per atom, and electronic convergence of 10^{-8} eV. From these, the unique displacements were generated in supercells of $6 \times 6 \times 1$. Elastic properties were determined using these primitive cell for the pristine and interalated T-phase and α-phase ScS_2. The elastic and internal strain tensors were computed from the second order derivatives of the total energy with respect to the position of the ions and changes to the size and shape of the unit cell, as employed in VASP. From the elastic tensor, various elastic moduli were also computed.

One possible method commonly used to modify the properties of electrodes is through the introduction of other elements, in particular substitution with transition metals [373–375] or lithium [87]. We consider the substitution of these metals in place of the scandium, which can be achieved through additional precursor materials. For low quantities of alternative metals this results in a substitutional doping [82], and for higher concentrations this results in metal mixing akin to how cobalt in lithium cobalt oxide is replaced with nickel and manganese in NMC. Seeing the effects of doping and metal mixing in other materials, it offers the natural question as to whether it can be employed to enhance the properties of

ScS_2. Here, we consider the metals Co, Cr, Fe, Hf, Mn, Nb, Ni, Sn, Ta, Ti, V, and Zr for this substitution, which were chosen to ensure a sufficient spread of species from across the transition metal block. We have also considered lithium as substitutions could occur during synthesis or cycling.

Due to the number of possible concentrations (and the configurations of each of those concentrations) available for metal mixing in the α-phase, we have limited this part of our study to the T-phase. Different concentrations of substitutions were considered, with all unique configurations being considered for each concentration of mixed metals. For $Sc_{1-x}M_xS_2$, concentrations of $\frac{0}{8} \leq x \leq \frac{8}{8}$ in increments of $\frac{1}{8}$ were considered, with $x = \frac{0}{8} = 0$ corresponding to the ScS_2 composition and $x = \frac{8}{8} = 1$ corresponding to the MS_2 composition. The configurations of mixing used are equivalent to the different configurations used for lithium intercalation, with the same indexing being used for the metal species instead of the intercalated lithium. Once the $Sc_{1-x}M_xS_2$ compound is synthesised, the metal species M becomes 'locked' in the host structure due to bonding with the sulfur atoms. It is thus more difficult for the metal species to reconfigure into a lower energy configuration than it would be for intercalated species such as lithium. As such, we consider a random configuration of metal mixing by taking the average of the different configurations considered.

5.3.1 RAFFLE

The pseudoRandom Approach For Finding Local Energetic minima (RAFFLE) has been developed in a similar manner to the approaches postulated by AIRSS [376], CALYPSO [377, 378], CrySPY [379], and GASP [380] in the field of structure search. RAFFLE draws from said previous methodologies by repeatedly sampling the structure space in question in order to approach a heuristic convergence to the energy landscape of prospective new structures.

The beginning of any RAFFLE exploration consists of determining the stoichiometries of interest; taking ScS_2 with intercalant lithium as an example, the $Sc : S : Li$ ratios of interest are $1 : 2 : (0-1)$, with non integer lithium fractions corresponding to larger supercells. This suite of stoichiometries provides a basis for structural

generation; in this case, the fully intercalated picture (e.g. a ratio of $1:2:1$) is considered to explicitly explore the structures with a stoichiometry equal to that of the fully-intercalated layered structure.

The process behind any structure search is to generate random structures, and then rank them using a suitable metric. In the case of RAFFLE we use formation energy per atom. The process for generating the random structures is as follows: Our first stage begins with a volume estimation, which is estimated from a packing fraction approach. This range is adjusted by $\pm 50\%$ to allow for different packing radii in compounds as opposed to elemental bulk. The unit cells are then constructed by randomly varying the ratios between the six unit cell defining parameters (a, b, c, α, β, γ), with a skewed normal distribution designed to prevent extremely small angles and lattice constants (i.e. below the atomic radii).

Atoms are placed within the resultant unit cell according to a set of 2-, 3-, and 4-body distribution functions. These functions are initially populated with structural information from databases such as the Materials Project [340], but as the data set grows to encompass relaxed structures, these structures are encoded into the distribution functions according to their relative energetic favorability; those which are more stable contribute their distributions more heavily to future generations. The essence of the methodology is distilled as follows: replicating the pseudo-local favourable chemistry of atoms leads to more energetically stable structures, thus a set of descriptors of local chemistry must be obtained that is sufficient to replicate key features inversely. The expansion to i^{th}-body could be continued arbitrarily far, but from an anecdotal standpoint 3-body (angular) is simply not sufficient and 5-body would be more expensive than is practical, thus 4-body is a determined to be a suitable compromise. Utilising algorithms designed to place atoms in sensible locations, all the atoms are placed sequentially within the cell, according to the positions which maximise similarity between the seeded distribution functions and that of the new structure.

Once the structure is generated, the unit cell is relaxed using standard methodologies employed in this thesis. Relaxed structures are characterised and their distributions are added to the distribution functions mentioned above. This process is repeated until the apparent ground state structure has been repeated

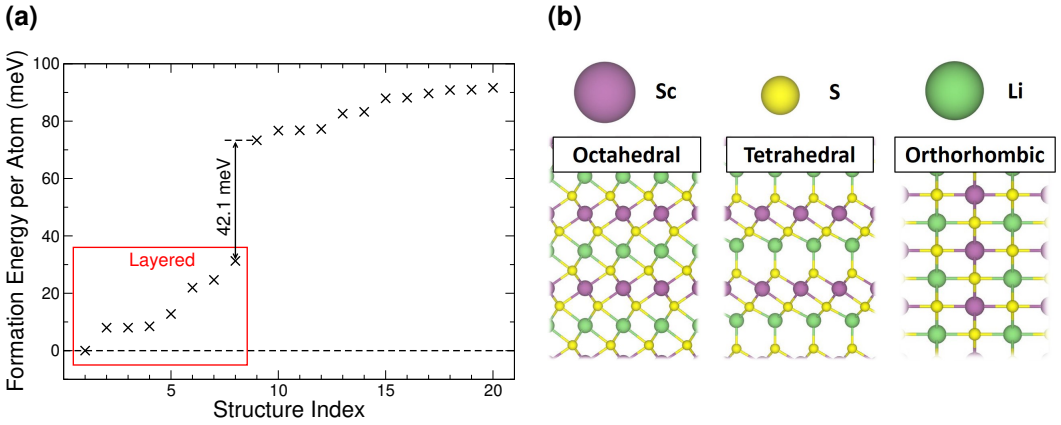

Figure 5.2: 5.2a presents the calculated formation energies per atom for the 20 lowest-energy structures of $LiScS_2$ found using the RAFFLE structural prediction algorithm. The results have been shifted such that the lowest-energy structure has a formation energy of 0 eV/atom. The typical structures obtained from this search are presented 5.2b, with the layered structures having octahedral or tetrahedral coordination, and the non-layered structure being orthorhombic.

several times, and the lowest ranked structures are then considered to be the found structures. We have here limited our calculations to small unit cells of up to 16 atoms.

5.4 Determination of Structure

5.4.1 RAFFLE Structure Search

We first explore the phase space of $LiScS_2$ using our random structure search RAFFLE. Of the over 800 structures generated and structurally relaxed, the energies of the 20 lowest-energy systems are presented in Figure 5.2a. Of these, the eight lowest-energy systems are are all T-phase structures possessing hexagonal symmetry, with the differences in energy arising from different coordination of the lithium with the ScS_2 layers, relative shifts of the ScS_2 layers, and small structural fluctuations arising from the tolerances of the search. These are indicated in 5.2b, where the structures with octahedrally-coordinated lithium are lower in energy [191,233,272,273] than the equivalent systems with tetrahedrally-

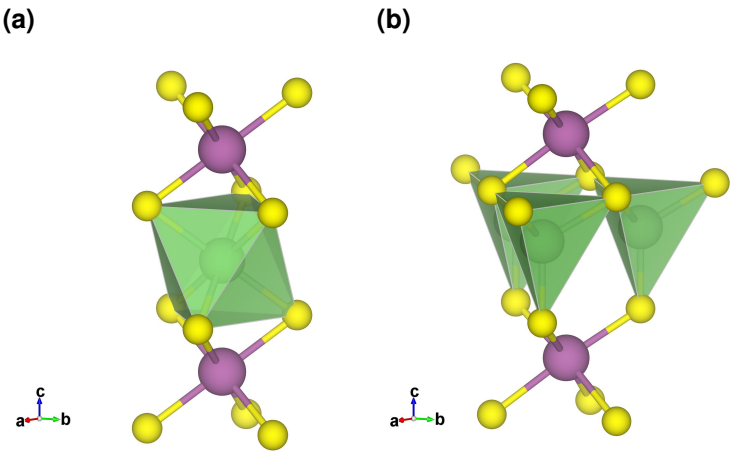

Figure 5.3: Octahedral (5.3a) and tetrahedral (5.3b) coorindation of an intercalant with sulfur in intercalated ScS_2.

Phase	Relative Energy of Intercalation Site	
	Octahedral (eV)	Tetrahedral (eV)
T	0	0.04
Hc	0	0.31
Tp	0	0.38

Table 5.1: Relative energies for the different Li intercalation sites considered for T-, Hc-, and α-ScS_2 phases.

coordinated lithium due to the higher coordination between lithium and sulfur. There is then a large jump of 42.1 meV per atom to the next group of structures, which have orthorhombic unit cells. As this energy exceeds typical values associated with thermal energy, we conclude that the layered structure will preferentially form.

5.4.2 Intercalation Site

The results of the structure search show that layered structures are the most favourable, and so we we explicitly investigate them further. As with all partially heuristic methods of structure searching, the result is never guaranteed to be the true ground state. So, to ensure that we do not limit our investigation to the results of the random structure search, further layered polymorphs of intercalated ScS_2

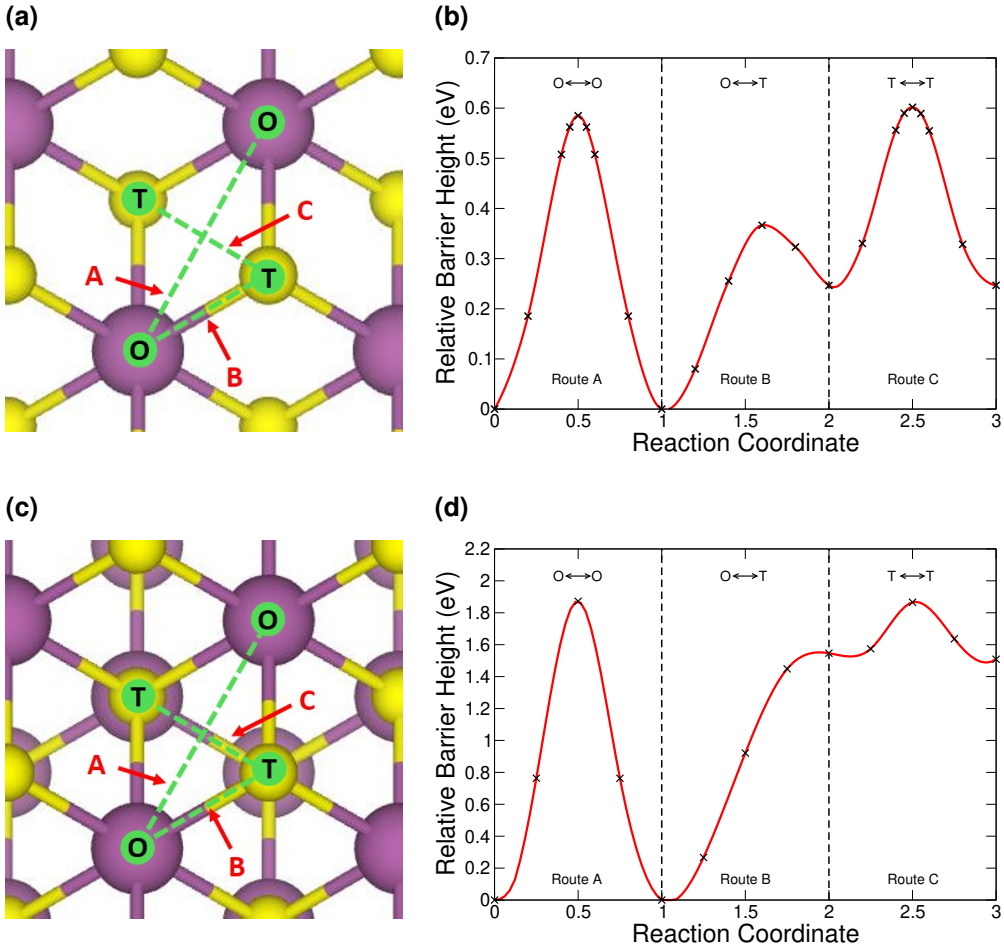

Figure 5.4: Nudged elastic band results used to determine site of intercalation. The routes through T-ScS_2 are presented in 5.4a, and the resultant barrier is shown in 5.4b. Similarly, 5.4c shows the routes through α-ScS_2, resulting in the barriers presented in 5.4d. The intercalation sites these routes are between, the octahedrally coordinated (O) and tetrahedrally coordinated (T), are also indicated.

were also considered. Specifically, we focused on the TMDC 1T-phase (following the results of the random structure search), the TMDC 2Hc-phase, and the α-ScS_2 phase (following experimental evidence [228, 229]).

We first determine the preferred site of intercalation into the three different ScS_2 polymorphs using two different methods. The first method was by intercalating at known interacalation sites for other TMDC structures in the literature [191, 233, 272, 273, 381]. For the T- and H-phases, the intercalation sites considered were the octahedrally coordinated site above the scandium atom, and the tetrahedrally coordinated site above the chalcogen atom. These are depicted in Figure 5.3. For α-ScS_2, the sites considered also have octahedral and tetrahedral coordination,

but their positions with respect to the scandium atom are different due to the shift of the layers. Geometric relaxations were performed on these to obtain the relative energy of the two sites. The data for this is presented in Table 5.1, where for all three phases it can be seen that the octahedral site is lowest in energy (due to the higher Li-S coordination).

To ensure a more thorough exploration of the potential intercalation sites, climbing-image nudged elastic band (CI-NEB) calculations, as employed in VASP, were used to consider transition states for lithium diffusion through the system [156, 157] (using the PBE functional). These CI-NEB calculations were performed along three different routes between two intercalation sites in bilayer systems with fixed positions of the scandium atoms, for each of the phases considered, using lithium as the intercalant. The specific sites considered were the octahedrally-coordinated (O) and the tetrahedrally coordinated (T) discussed above. The CI-NEB routes between two equivalent O sites (Route A), between adjacent O and T sites (Route B) and between two equivalent T sites (Route C) were considered, and are shown in Figure 5.4a for the T-phase and Figure 5.4c for the α-phase. The results of the CI-NEB calculation are then presented in 5.4b and 5.4d, and again show that the most favourable intercalation site for each of the phases is the octahedral-coordination (O) site. This is in agreement with other TMDC works [191, 233, 272, 273], as well as the results of the structure search.

We are also able to comment on the diffusion properties of intercalants in ScS_2. As the rate of diffusion follows an Arrhenius equation, the height of the activation barriers is a key parameter for characterizing electrode materials. For both T- and α-phases we see that, whilst Route A offers the most direct path between two octahedral sites, diffusion along Route B has a lower activation energy. Route A in the T-phase demonstrates a barrier height of 0.58 eV, and 0.37 eV along Route B (and 0.12 eV in the reverse direction). These compare very well with the 0.67 eV and 0.34 eV see for lithium diffusion along monolayer T-ScS_2 [247]. We see the same for the α-phase ScS_2, though we do note significantly larger barriers of 1.87 eV along Route A and 1.55 eV along Route B (0.01 eV in the reverse direction). These larger barriers are partially caused by the particular method (fixing the scandium positions) used for generating these CI-NEB barriers. However a

No. Intercalant Ions	Sites Filled	No. Intercalant Ions	Sites Filled
0	-	8	bcegijkl
1	a	8	bcehijkl
4	abcd	8	bcfgijkl
4	abce	8	cdefhijk
4	abch	8	cdefhijl
4	abei	8	cdefhikl
4	abfi	8	cdefhjkl
4	abgi	8	cdeghjkl
4	abgj	8	cdfghjkl
4	abgk	8	defgijkl
4	abgl	8	dfghijkl
4	adeh	8	efghijkl
4	adfg	11	abcdefghijk
4	adfg	12	abcdefghijkl

Table 5.2: Different intercalation configurations considered for α phase.

more significant cause is due to the relative layer shift seen for the α-phase compared to the T-phase resulting in an 'interlocking' of layers, and hence a sulfur of one layer protrudes into the void space of the next. Thus we see a larger barrier to ionic movement.

5.4.3 Intercalation Configuration

As stated above, the T-, Hc-, and α-phases of ScS_2 have been considered, with supercells of $(2 \times 2 \times 2)$ for the T-phase, $(2 \times 2 \times 1)$ for the Hc-phase, and $(2 \times 2 \times 1)$ for the α-phase being used for intercalation. For these supercell sizes, there were many symmetrically equivalent octahderal sites available for intercalation. For the T- and Hc-phases there are eight different intercalation sites (indexed a-h), and for the α-phase there are twelve different intercalation sites (indexed a-l). These sites are indicated with the green spheres in Figure 5.5. These different intercalation sites allow various symmetrically-unique configurations of intercalants which were

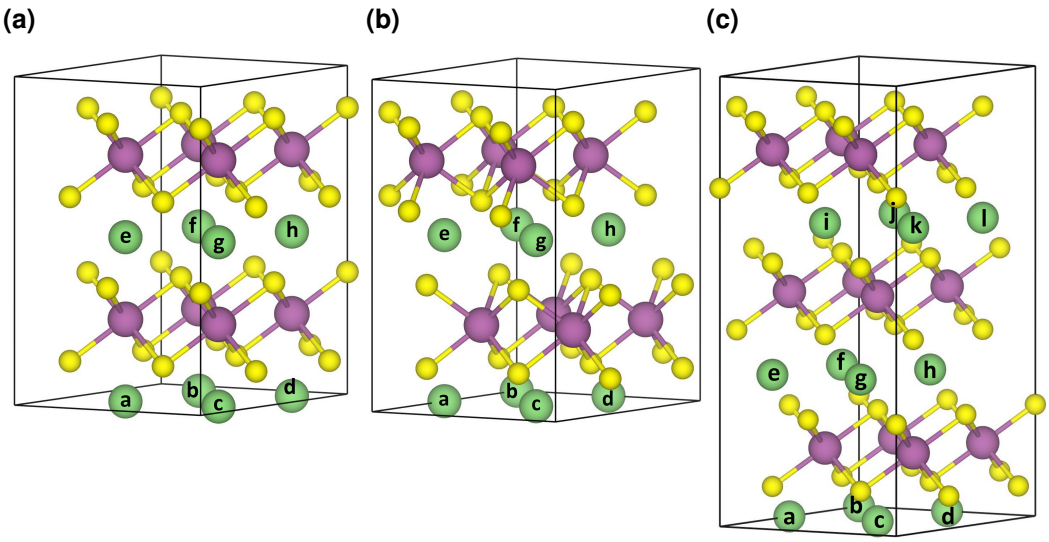

Figure 5.5: The different intercalation sites available in the supercells of T- (5.5a), Hc- (5.5b), and α-ScS_2 (5.5c) considered in this work.

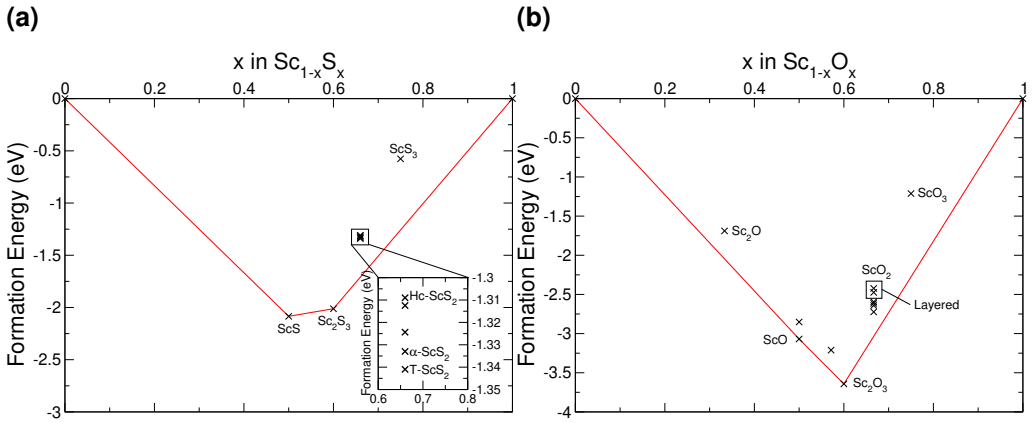

Figure 5.6: Convex hulls for Sc-S (5.6a) and Sc-O (5.6b) compounds.

each explored for obtaining the intercalation voltage. These configurations are presented in Table 3.1 for the T- and Hc-phases, and in Table 5.2 for α-phases, where the sites occupied with an intercalant are indicated with the letters (a-h) and (a-l). Due to the number of intercalation sites (and hence the number of intercalation configurations) for the α-phase, we have performed a more limited investigation across the intercalation range.

5.4.4 Convex Hull for Sc-S and Sc-O Compounds

So far, we have concluded that the intercalated form of ScS_2 is layered, we have highlighted the T-, Hc, and α-phases for explicit investigation, and have determined that the preferred sites for ionic intercalation are those with octahedral coordination. However, we are also interested in the structure of ScS_2 when the intercalants are removed, and so we have investigated a range of Sc-S stoichiometries to determine the stability of ScS_2. As the data available within literature and on databases such as the ICSD and Materials Project [340] for scandium-sulfide compounds is fairly limited, we have also used the structures of scandium-oxide analogues. The results of this are presented in the convex hull shown in Figure 5.6a. For the composition ScS_2, the layered structures are most favourable, with the T-structure again being shown to be the lowest in energy. However, it lies 0.37 eV above the convex hull, and a mixture of Sc_2S_3 and S would be preferred.

Figure 5.6b presents the generated convex hull for compounds of scandium and oxygen with different stoichiometries, where we note that the compounds with stoichiometry ScO_2 do not lie on the hull. Furthermore, the layered structures are the least energetically favourable of the structures considered for that composition, lying 0.62 eV above the hull. Of the structures investigated for the ScO_2 composition, the lowest energy belongs to the monoclinic structure similar to that of Baddeleyite. Clearly, the layered ScO_2 structure would be prone to form the monoclinic structure instead, or a decomposition reaction $2ScO_2 \rightarrow Sc_2O_3 + \frac{1}{2}O_2$.

5.5 Comparison of Intercalated Phases

Having determined the layered TMDC phases to be of primary interest for intercalated ScS_2, we now compare the different polymorphs with intercalant concentration. We present in Figure 5.7a the energies (per formula unit) of each of the considered phases of Li_aScS_2. This allows for easy comparison of the different phases and indicates which phases are energetically preferred for different intercalation concentrations. For visual aid we have included a linear fit, which allows

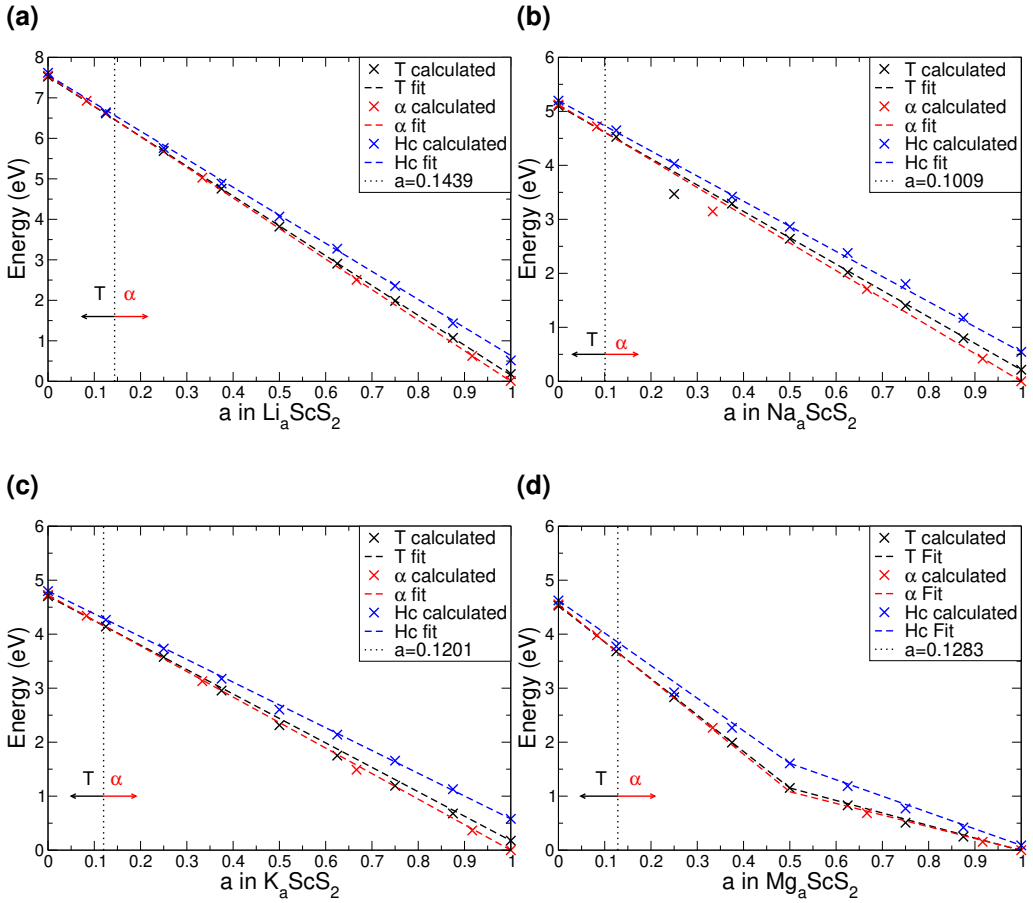

Figure 5.7: Relative energy per formula unit of T, α and Hc phases of M_aScS_2 ($M = Li, Na, K, Mg$) for a range of concentrations a. 5.7a shows the data for Li_aScS_2, 5.7b shows the data for Na_aScS_2, 5.7c shows the data for K_aScS_2, and 5.7d shows the data for Mg_aScS_2. Linear fits have been presented in each as visual aid to identify the crossing points.

us to determine that the T-phase is the lowest in energy for low intercalant concentrations ($a < 0.15$ in Li_aScS_2), whereas for higher concentrations the α-phase is preferred.

Whilst we have not performed the RAFFLE structure search for ScS_2 intercalated the other intercalants considered, due to the similar chemistry (for the Group I intercalants Na and K) and ionic size (for the Group II intercalant Mg), we argue that similar conclusions about the layered structure would be reached. However, to compare the relative energies of the different phases of ScS_2 intercalated with the different intercalants, and hence determine the polymorph that is energetically preferred, we also present in Figure 5.7 energy per formula unit for each of the considered phases. For visual aid we have again included a linear fits to the

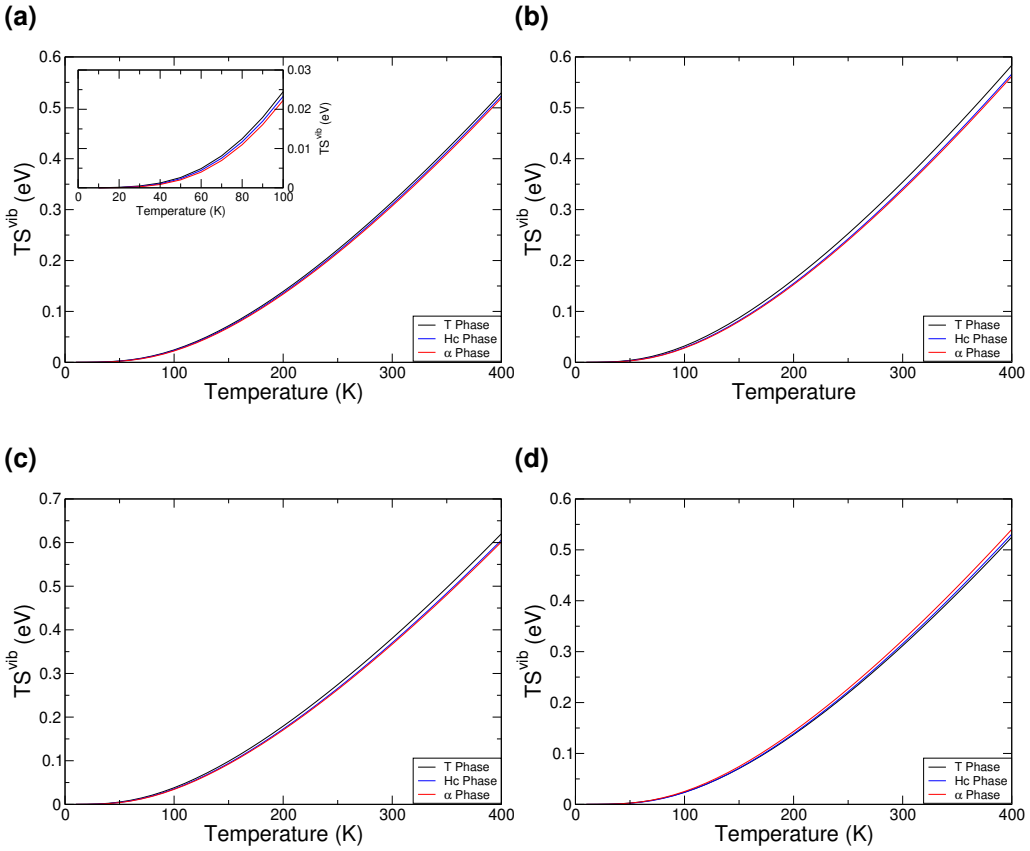

Figure 5.8: Corrections to the total energy that would arise from finite-temperature lattice vibrations in intercalated ScS_2. The figures presented are for $LiScS_2$ (5.8a), $NaScS_2$ (5.8b), $KScS_2$ (5.8c), and $MgScS_2$ (5.8d).

Na, and K intercalated systems. For each of these, we can determine that the T-phase is the lowest in energy for low intercalant concentrations ($\mathrm{a} < 0.15$ in M_aScS_2, M = Na, K), whereas for higher concentrations the α-phase is preferred. These boundaries are indicated in each of the Figures 5.7b for Na, and 5.7c for K with vertical dashed lines. However, the double valency of magnesium results in two changes to the oxidation state of the host material. This can be seen with the change in gradient of the line from $0 < \mathrm{a} < 0.5$ and $0.5 < \mathrm{a} < 1$. It is noted that for all of the phases and each of the intercalants, the Hc-phase of ScS_2 is always the highest in energy, hence we focus on the T- and α-phases for the remainder of this Chapter. Thus, we see the same results for the beyond-lithium intercalant species as we did for lithium.

5.5.1 Dynamic Corrections

In most scenarios, the total internal energy obtained from DFT calculations is useful for comparisons for different phases of the same material, but it is not able to account for dynamic effects such as zero-point energy (ZPE) motion and vibrations due to finite temperature. To include these dynamic effects we instead use,

$$U^{Dyanmic} = U^{DFT} + U^{ZPE} - TS^{vib}, \tag{5.1}$$

where U^{DFT} is the energy obtained from the DFT calculation (presented in Figure 5.7), U^{ZPE} is the energy associated with the zero-point motion of the lattice, and TS^{vib} is the energy from finite temperature vibrations. The last two of these terms are given by,

$$U^{ZPE} = \sum_{\nu,\mathbf{q}} \frac{1}{2}\hbar\omega_{\nu,\mathbf{q}}, \tag{5.2}$$

and,

$$S^{vib} = \frac{1}{2T}\left[\sum_{\nu,\mathbf{q}} \hbar\omega_{\nu,\mathbf{q}} \coth\left(\frac{\hbar\omega_{\nu,\mathbf{q}}}{2k_BT}\right)\right] - k_B\left[\sum_{\nu,\mathbf{q}} \ln\left(2\sinh\left(\frac{\hbar\omega_{\nu,\mathbf{q}}}{2k_BT}\right)\right)\right]. \tag{5.3}$$

The origins of these expressions are presented in Appendix D

The size of the TS^{vib} corrections are presented in Figure 5.8 for each of the phases intercalated with each of the intercalants, and the values of U^{ZPE}, $TS^{vib}(T = 400\ \mathrm{K})$, and the resultant correction ($U^{ZPE} - TS^{vib}(T = 400\ \mathrm{K})$) are presented in Table 5.3. The values of $\omega_{\nu,\mathbf{q}}$ were obtained from the phonon band structures presented below. For each of the Group I intercalants, the T-phase has the largest TS^{vib} value whilst the α-phase has the smallest. The ordering is reversed for magnesium intercalation. Interestingly, the corrections that arise from considering these dynamic effects for each phase are all of the order of 0.7 eV, with minor

Intercalant	Phase	U^{ZPE} (eV)	$TS^{vib}(T = 400\ \mathrm{K})$ (eV)	Correction (eV)
Li	T	0.174	0.529	-0.355
Li	Hc	0.176	0.523	-0.347
Li	α	0.176	0.519	-0.343
Na	T	0.154	0.584	-0.430
Na	Hc	0.158	0.566	-0.408
Na	α	0.159	0.562	-0.403
K	T	0.142	0.620	-0.478
K	Hc	0.146	0.606	-0.460
K	α	0.146	0.601	-0.455
Mg	T	0.175	0.525	-0.350
Mg	Hc	0.170	0.531	-0.355
Mg	α	0.168	0.540	-0.372

Table 5.3: Dynamics corrections to the total energy of intercalated ScS_2. U^{ZPE} is the zero-point energy calculated using equation (5.2), and $TS^{vib}(T = 400\ \mathrm{K})$ is the energy arising from finite-temperature vibrations calculated using equation (5.3) at a temperature of $T = 400\ \mathrm{K}$.

variation (< 0.02 eV) for each of the intercalants. As a result, the ordering of the intercalated phases presented in Figure 5.7 is not affected by the inclusion of these additional terms, and so these corrections have not been included in the proceeding discussions of results.

5.5.2 Lattice Constants

The real-space lattice constants for the different phases of ScS_2, intercalated with the different intercalants, obtained using the PBE and HSE06 functionals in this work are presented in Table 5.4. Where possible, lattice constants found within the literature have also been presented. With the PBE functional, we see that the calculated values for the in-plane lattice constants for Group I-intercalated α-ScS_2 are in very good agreement with the experimental values, being within 1%. The out-of-plane lattice constants deviate from the experimental values slightly more,

Material	a (Å)	c (Å)	c/a	Source
T-$LiScS_2$	3.610	6.135	1.699	This work (PBE)
Hc-$LiScS_2$	3.569	12.409	3.477	This work (PBE)
α-$LiScS_2$	3.652	17.910	4.904	This work (PBE)
α-$LiScS_2$	3.641	17.841	4.901	This work (HSE)
$LiScS_2$	3.687	18.318	4.968	van Dijk [228]
T-$NaScS_2$	3.694	6.736	1.824	This work (PBE)
Hc-$NaScS_2$	3.638	13.553	3.725	This work (PBE)
α-$NaScS_2$	3.732	19.467	5.216	This work (PBE)
α-$NaScS_2$	3.717	19.382	5.214	This work (PBE)
$NaScS_2$	3.751	19.744	5.264	van Dijk [228]
T-$KScS_2$	3.774	7.432	1.969	This work (PBE)
Hc-$KScS_2$	3.701	15.151	4.093	This work (PBE)
α-$KScS_2$	3.800	21.806	5.738	This work (PBE)
α-$KScS_2$	3.787	21.735	5.740	This work (HSE)
$KScS_2$	3.814	21.726	5.697	Havlak [229]
$KScS_2$	3.811	21.719	5.700	Havlak [229]
T-$MgScS_2$	3.598	6.234	1.733	This work (PBE)
Hc-$MgScS_2$	3.584	12.621	3.522	This work (PBE)
α-$MgScS_2$	3.612	18.491	5.119	This work (PBE)
α-$MgScS_2$	3.592	18.372	5.115	This work (HSE)

Table 5.4: Lattice constants of the different phases of ScS_2 intercalated with different species.

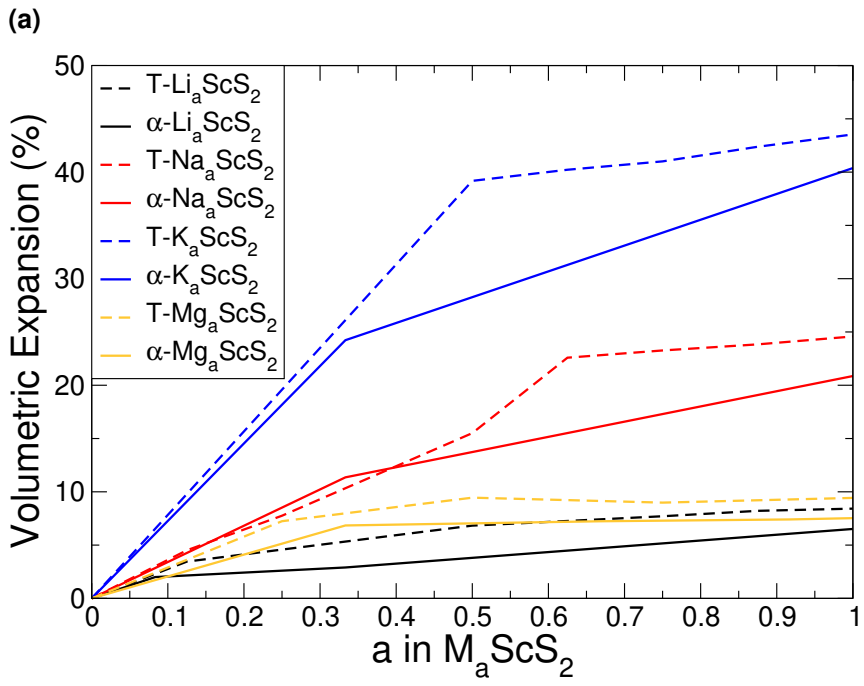

Figure 5.9: 5.9a shows the percentage volume change ($\% = 100 \times \frac{V-V_0}{V_0}$) of T-$ScS_2$ and α-ScS_2 caused by intercalation.

but still remain within 2.5%. The use of the HSE06 hybrid functional produces lattice constants of intercalated α-ScS_2 that differ from those of the PBE functional by less than 1%, reducing both the a and c lattice constants.

5.6 Volumetric Expansion

For intercalation electrodes, the volume change of ScS_2 upon cycling needs to remain suitably small to prevent material fracturing and improve device lifetime. Figure 5.9a shows the volumetric expansion that arises in T-ScS_2 and α-ScS_2 upon intercalation. This is given as a percentage of the unintercalated bulk material volume, using $\% = 100 \times \frac{V-V_0}{V_0}$, where V_0 is the volume of the unintercalated bulk material. From the figure, we see that as the size of the intercalant is increased from Li to Na to K, the expansion increased by a larger percentage accordingly: the volume change from intercalating with lithium to $LiScS_2$ is 6.51%, which is comparable to the 8% observed for NMC [279]. However, for $NaScS_2$ the expansion exceeds 20%, and for $KScS_2$ is exceeds 40%. Interestingly, intercalation with magnesium leads to a volume expansion of 7.53%, comparable to that

Phase	Intercalant Species	Charge of Sc (|e|)	Charge of S (|e|)	Charge of Intercalant (|e|)
T	-	2.21	-1.11	-
	Li	2.23	-1.55	0.88
	Na	2.23	-1.54	0.85
	K	2.23	-1.51	0.79
	Mg	2.01	-1.84	1.67
Hc	-	2.19	-1.10	-
	Li	2.21	-1.55	0.88
	Na	2.22	-1.53	0.85
	K	2.20	-1.50	0.78
	Mg	1.95	-1.82	1.69
α	-	2.21	-1.11	-
	Li	2.23	-1.56	0.88
	Na	2.23	-1.54	0.85
	K	2.23	-1.51	0.80
	Mg	2.02	-1.85	1.69

Table 5.5: Bader charge values of species in pristine and fully-intercalated ScS_2, for the different phases considered in this work.

arising from intercalation with lithium, which is due to the larger nuclear charge on the Mg resulting in a reduced ionic radius.

5.7 Charge Analysis

Before assessing the key electrode properties of ScS_2, it will be useful to first discuss the charge transfer upon intercalation, as charge transfer is ultimately the source of the energy storage in electrodes. We first do this with Bader charge analysis, the data for which is presented in Table 5.5. We note that the intercalant charge remains unchanged with intercalation into the different phases of ScS_2, highlighted best with lithium which possesses a charge of 0.88 |e| in each of the phases. Between the different intercalants, though, there is a more significant

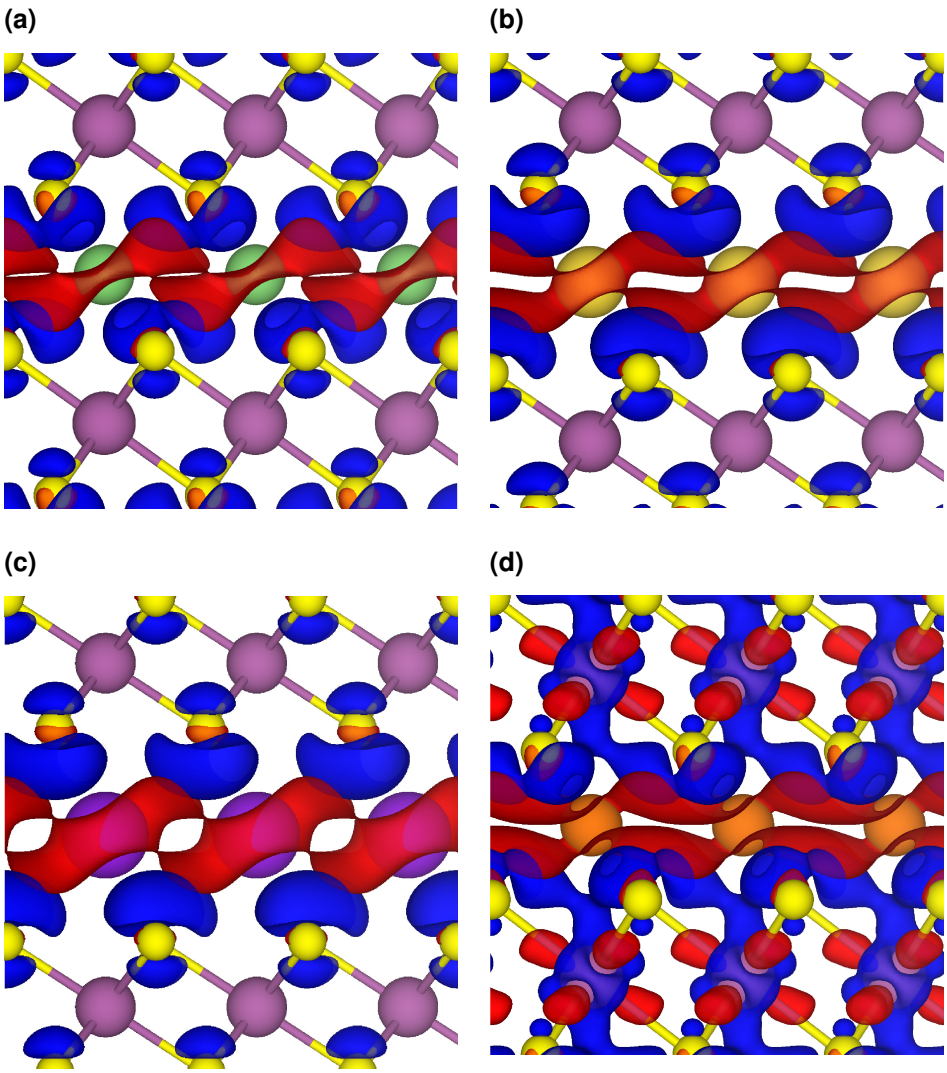

Figure 5.10: The charge difference plots arising from intercalation of T-ScS_2 obtained using $\Delta\rho = \rho_{MScS_2} - [\rho_M + \rho_{ScS_2}]$ for intercalants M = Li (5.10a), Na (5.10b), K (5.10c) and Mg (5.10d). In these, red isosurfaces show electron depletion and blue isosurfaces show electron accumulation. The ScS_2 layers are shown with purple and yellow atoms.

difference. In α-ScS_2, the charge on lithium is 0.88 |e|, the charge on sodium is 0.85 |e|, and the charge on potassium is 0.80 |e|. Magnesium, being a Group II element, possesses twice the valence electrons as its Group I neighbour of sodium. It is therefore unsurprising to see that magnesium possesses a charge of 1.69 |e|, twice the charge of sodium.

To evaluate charge transfer between intercalant ions and the host ScS_2 more rigorously, the geometrically-relaxed intercalated structures were separated into the host ScS_2 and the intercalant ions. Retaining the size and shape of the unit cell, and keeping the positions of the ions the same as in the intercalated material,

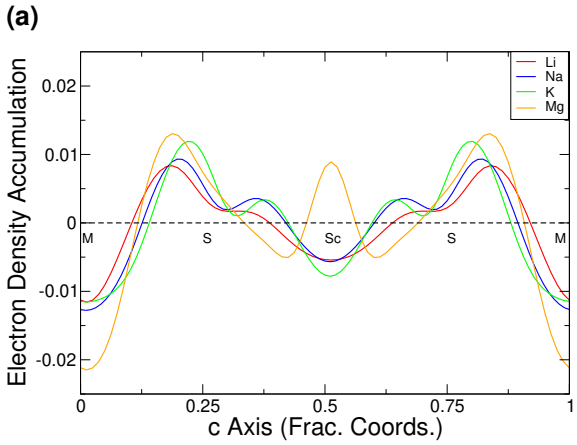

Figure 5.11: The planar-average of $\Delta\rho = \rho_{\mathrm{MScS_2}} - [\rho_{\mathrm{M}} + \rho_{\mathrm{ScS_2}}]$ for intercalants M = Li (red), Na (blue), K (green) and Mg (orange). Positive values correspond to regions of electron accumulation, and negative values correspond to regions of electron depletion. The black dashed line indicates zero change. Labels indicating the positions of the constituent atoms have also been included, where the repeated 'M' label shows the periodicity of the cell.

the electronic charge densities were obtained. By comparing the charge density of the full structure with those of the ScS_2 structure and the intercalant [276], i.e. $\Delta\rho = \rho_{\mathrm{MScS_2}} - [\rho_{\mathrm{M}} + \rho_{\mathrm{ScS_2}}]$, it is possible to comment on the charge transfer upon intercalation. This is shown in Figure 5.10 for the T-phase of ScS_2 intercalated with each of lithium, sodium, potassium, and magnesium, and the planar average values are presented in Figure 5.11.

For each of the Group I intercalants, it is clear to see in Figure 5.10 the loss of electronic charge from the intercalant into a bond with the sulfur atom, shown with the red (depletion) regions around the intercalant, and the blue (accumulation) regions. This is further highlighted with the planer-averaged values of Figure 5.11, where we notice the peaks in the electron density accumulation around $\mathrm{c} = 0.2$ and $\mathrm{c} = 0.8$. We also notice a further transfer of charge from the scandium to the sulfur-scandium bonding. For magnesium, we see a larger loss of electronic charge from the magnesium, corresponding to approximately double that of the Group I intercalants, as would be expected. This charge can again be seen to collect in the intercalant-sulfur bonding region. However, upon magnesium intercalation the scandium appears to gain electrons from the scandium-sulfur bonding region, opposite to what was seen for the Group I intercalants.

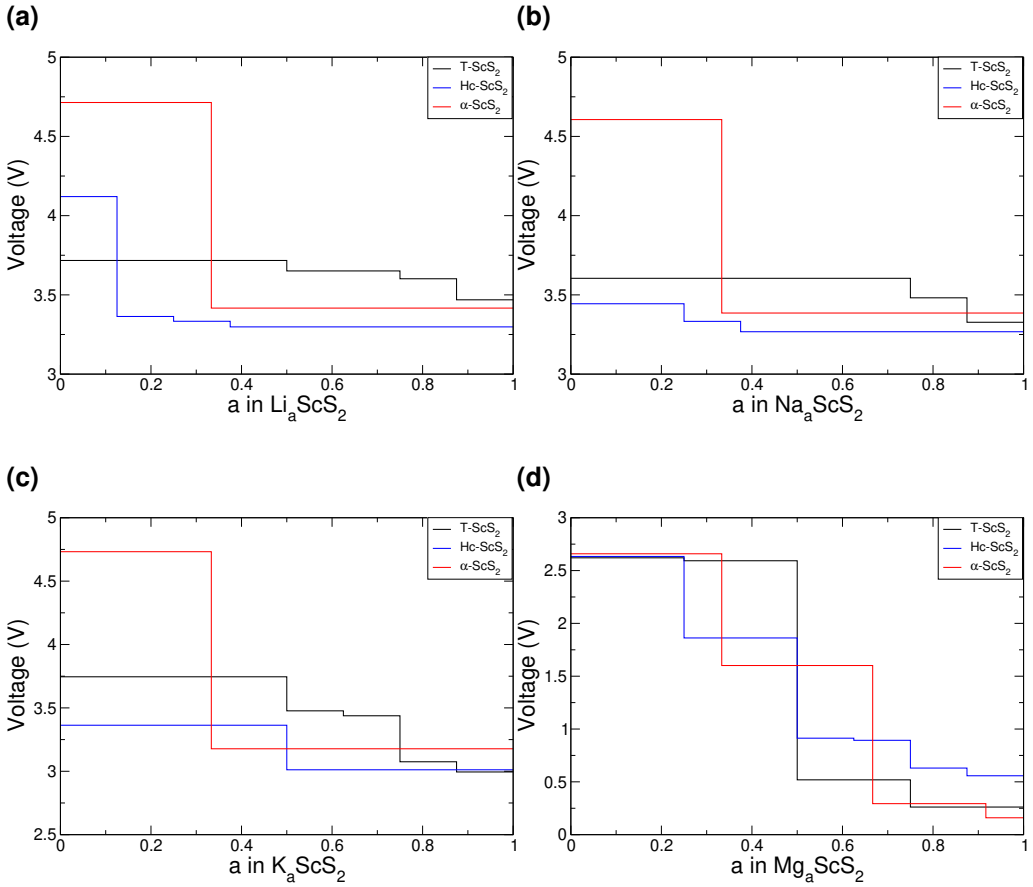

Figure 5.12: Intercalation voltages obtained when ScS_2 is intercalated with lithium (5.12a), sodium (5.12b), potassium (5.12c), and magnesium (5.12d).

5.8 Voltages of ScS_2 Cathodes

ScS_2 has several properties which are attractive as a cathode. First, in Figure 5.12 we present the voltage profiles for each of the phases, with each of the considered intercalants. For α-ScS_2 intercalated with Group I metals, our calculations show that the voltages at low levels of intercalation reach above 4.5 V. As the concentration of the intercalant increases, the decrease in voltage across the range explored is less than 1.5 V, and so the final voltage remains above 3 V. The α-phase shows for Li, Na and K no change in the voltage for concentrations of $a > 0.4$. Increasing the atomic number of the Group I intercalant results in a small decrease in the average intercalation voltage: Whilst for Li intercalation the average voltage is 3.977 V, this drops to 3.874 V for Na, and to 3.799 V for K. This drop in voltage is due to the reduced charge transfer from the intercalated species to the host material, as is shown through the Bader charge analysis pre-

sented above, where the lithium charge is 0.88 |e|, the sodium charge is 0.85 |e|, and the potassium charge is 0.80 |e|.

For the other phases of intercalated ScS_2, we see that there is much less variation in the voltage compared to that for the α-phase for each of the intercalated species, with the profiles being demonstrating smaller drops as the concentration is increased. For lithium intercalation, the average intercalation potentials are 3.655 V, 3.414 V, and 3.977 V for the T-, Hc-, and α-phases, respectively. Similarly, the voltages for sodium intercalation are 3.554 V (T), 3.320 V (Hc), and 3.874 V (α), and for potassium intercalation the voltages are 3.496 V (T), 3.187 V (Hc), and 3.799 V (α). These show that the voltages of the α-phase are greater than those for the T-phase, which are greater than the Hc-phase, and that the voltage obtained from T-ScS_2 is about 0.3 V lower than that obtained from the equivalent α-ScS_2 structure for each of the intercalants. As the structures of the individual ScS_2 layers are the same in each of the T- and α-phases, the increase in output voltage must be due to the change in bonding environment arising from the relative shift in the ScS_2 layers. However, for Li, Na and K, irrespective of phase the voltages remain above 3 V for all concentrations considered.

For magnesium intercalation the voltage behaviour is different from that of the Group I elements. The average voltage is 1.474 V for α-ScS_2, but changes considerably by 2.5 V across the range. This is due to the double valency of magnesium allowing for two changes in oxidation state of the host material. This behaviour is also present in the T- and Hc-phases. All phases, when fully intercalated ($\mathrm{a} = 1$), decrease to voltages below 0.6 V. The voltages of the T-phase and Hc-phase are 1.499 V and 1.498 V respectively, where we see the ordering of the phases is different to what is observed for the Group I intercalants, and the differences between each of the voltages is much lower ($\sim$0.03 V).

5.9 Thermodynamic Stability of ScS_2 Cathodes

One can construct thermodynamic phase diagrams in terms of the chemical potentials of scandium and the intercalated species to determine the stability of

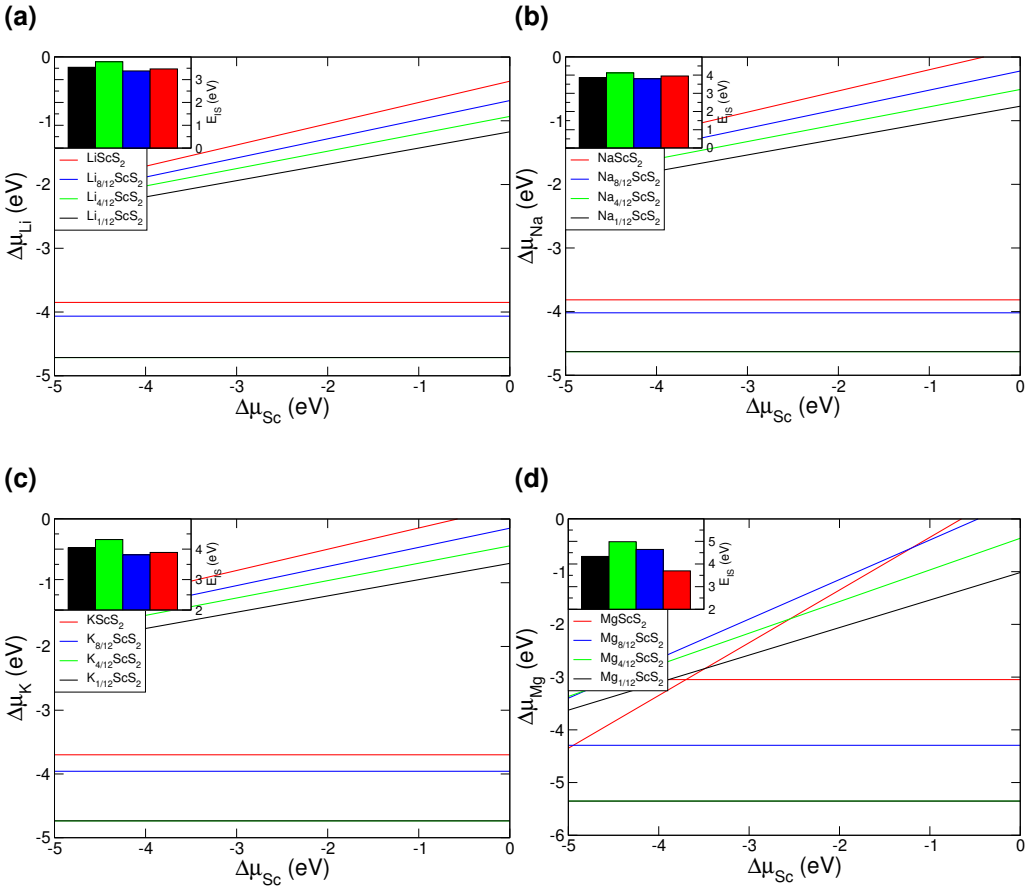

Figure 5.13: 5.13a, 5.13b, 5.13c, and 5.13d show the phase diagrams for α-ScS_2 intercalated with different concentrations of Li, Na, K and Mg, respectively. The insets show the corresponding values of E_{IS}.

the intercalated structure against undesirable conversion reactions, as outlined in Chapter 3. We use this to evaluate the capacity of the material, reasoning that the formation of Li_2S (or equivalent product) will result in irreversible loss of the layered structure and hence cyclability.

The phase diagrams for α-ScS_2 intercalated with each of the intercalants are presented in Figure 5.13, and the resultant values of E_{IS} for each of the intercalants is presented in the insets. It is clear to see that, for the range of intercalation concentrations presented here, ScS_2 has a sizeable window of stability with E_{IS} values in excess of 3 eV, much greater than equivalent values for the other TMDCs (as shown in Chapter 3). This means that ScS_2 has a total capacity of 243.99 $mAhg^{-1}$ at full intercalation for the Group I intercalants, and a capacity of 487.98 $mAhg^{-1}$ when intercalated with magnesium.

Phase	Intercalant	a in M_aScS_2	Old E_{IS} (eV)	Intercept (eV)	New E_{IS} (eV)
α	Na	$\frac{12}{12}$	3.949	0.134	3.815
α	K	$\frac{12}{12}$	3.891	0.192	3.699
α	Mg	$\frac{12}{12}$	3.698	0.651	3.047
α	Mg	$\frac{8}{12}$	4.644	0.350	4.293
T	Na	$\frac{8}{8}$	3.637	0.082	3.554
T	K	$\frac{8}{8}$	3.629	0.133	3.496
T	Mg	$\frac{8}{8}$	3.690	0.659	3.031
T	Mg	$\frac{4}{8}$	5.415	0.168	5.247
Hc	Na	$\frac{8}{8}$	3.592	0.562	3.030

Table 5.6: Adjusted values of E_{IS} taking into account the boundary described by equation 4 in the main article. New value of E_{IS} obtained from $E_{IS}^{New} = E_{IS}^{Old} - \text{Intercept}$.

For the Group I intercalants, E_{IS} remains relatively unchanged with intercalant concentration, but we note that the thermodynamic stability behaviour for magnesium intercalation is different. It has very favourable energetics for low intercalation, but for higher concentrations E_{IS} dramatically reduces. This arises from a significant upward shift of the phase boundary between ScS_2 and Mg_aScS_2, given by the magnesium-equivalent of equation (3.19). This behaviour is not dependent on the phase of the ScS_2, and can be seen in the equivalent phase diagrams (presented in Appendix D) for the intercalation stability of T-ScS_2 (Figure D.1) and Hc-ScS_2 (Figure D.2). This is due to the double valency of magnesium compared to the Group I metals, resulting in a different orbital being filled, and hence a second redox transition being stimulated with the second electron.

5.9.1 Additional Considerations for E_{IS}

The definition of E_{IS} above does not account for the limits imposed by the bulk species. The lines defined by equations (3.20) and (3.23), and presented in Figure 5.13, may cross above $\Delta\mu_M = 0$. This violates the condition given by equation (3.18) requiring that the elemental bulk form of the intercalant species does not

form. As such, the values of E_{IS} presented in the inset of Figure 5.13 are optimistic and require correction. These adjusted values are presented in Table 5.6. It is clear to see that the corrected values of E_{IS} are still remarkably large, and so the conclusions presented above hold.

5.10 Dynamic Stability

The thermodynamic phase diagrams presented in the previous section allowed us to determine the range of concentrations for which the intercalated materials are stable against conversion reactions. However, it is also important to assess whether these materials are dynamically stable by considering their phonon modes. Figure 5.14 presents the phonon band structures for pristine α-ScS_2, and α-ScS_2 intercalated with lithium. As can be seen, the fully intercalated structure is phonon-stable, whereas for bulk α-ScS_2, it is clear to see the presence of imaginary phonon modes in the Γ-M path of the Brillouin zone which result in dynamic instability. The motions associated with imaginary modes at -1.16 THz (-38.7 cm^{-1}) correspond to longitudinal in-plane oscillations of the ScS_2 sheets, as indicated in Figure 5.14b. This behaviour holds for Na, K, and Mg intercalated into ScS_2.

By comparing the phonon band structures for the different intercalants, similar features can be seen for the Group I metals. The key difference between them being a reduction in frequency of the optical bands. This is highlighted at the zone centre, with the highest optical band having frequency of 12.19 THz (406.49 cm^{-1}) for lithium intercalation, 11.52 THz (384.12 cm^{-1}) for sodium interalation, and 11.10 THz (370.21 cm^{-1}) for potassium intercalation. This reduction amounts to $\sim$0.5 THz between each. There is a significant change in the phonon band structure for magnesium intercalation, however, with the resulting phonon bands being much less dispersive than those of the Group I intercalants.

Our results show that $LiScS_2$ is phonon stable, and at some point, as the concentration of lithium is decreased, the phonon-stability is lost. The evaluation of the phonon band structures for intermediate lithium concentrations (Figure 5.15)

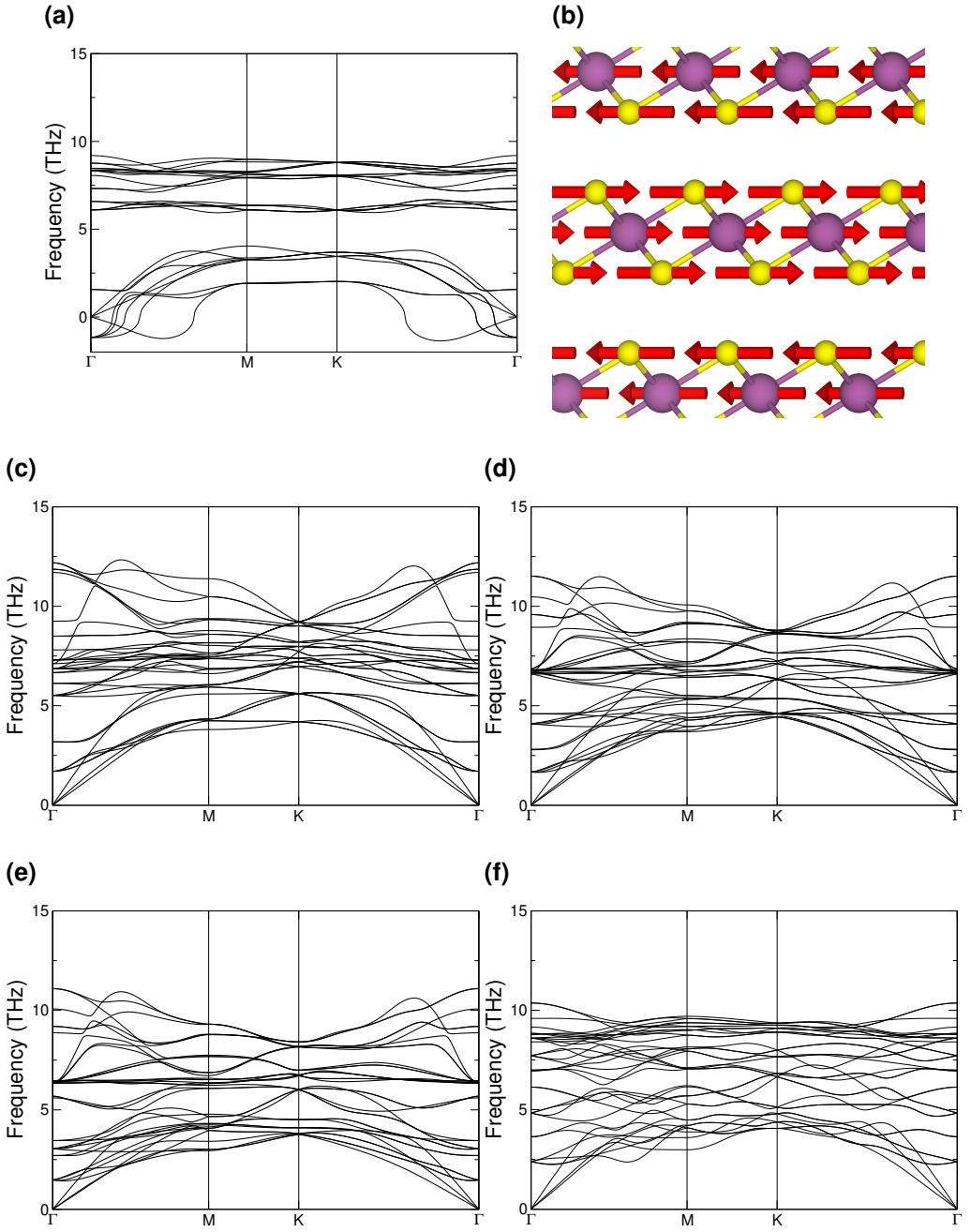

Figure 5.14: Phonon band structures for pristine α-ScS_2, and α-ScS_2 intercalated with different metal species. 5.14a shows the phonon band structure for pristine bulk α-ScS_2, with 5.14b showing the atomic structure and motions associated with the imaginary modes at Γ. Similarly, the band structures for $LiScS_2$, $NaScS_2$, $KScS_2$, and $MgScS_2$ are shown in 5.14c, 5.14d, 5.14e, and 5.14f respectively.

allows us to determine the lowest concentration of lithium we can access before the intercalated layered structure becomes dynamically unstable. For the α-phase, the instability is also seen up to and including $Li_{\frac{2}{12}}ScS_2$. Similarly for T-ScS_2, $Li_{\frac{1}{8}}ScS_2$ is unstable whereas $Li_{\frac{2}{8}}ScS_2$ is not. We can therefore conclude

that the lowest concentration of lithium that can be reached (corresponding to the depth of discharge and hence the maximum reversible capacity) in ScS_2 lies in the range $0.125 < \mathrm{a} < 0.25$. Taking the range of intercalation to be $0.25 < \mathrm{a} < 1$, corresponding to 75% of the theoretical capacity, this gives a charge capacity of 182.99 mAhg^{-1}, which is comparable to the $\sim$200 mAhg^{-1} of other materials [36, 38, 40, 41, 82–86]. The 75% of the maximum capacity compares well with the 60%-80% available in NMC materials [83].

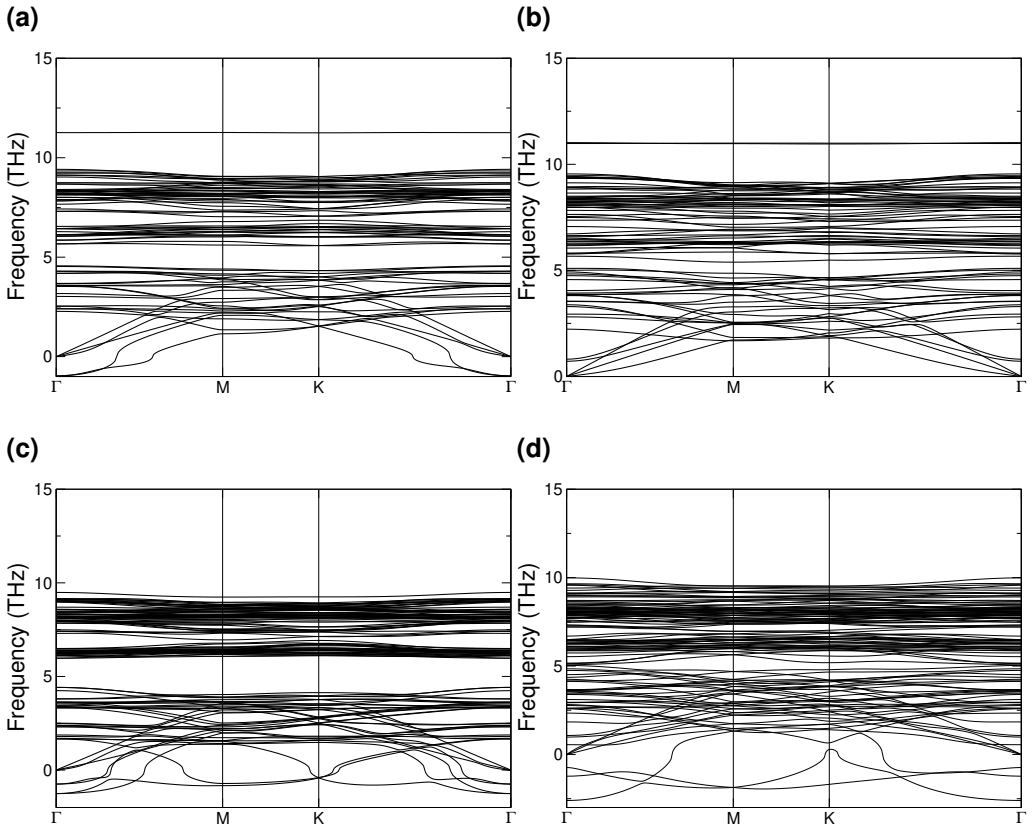

Figure 5.15: Phonon band structures for T-ScS_2 intercalated to $Li_{\frac{1}{8}}ScS_2$ (5.15a) and $Li_{\frac{2}{8}}ScS_2$ (5.15b), and for α-ScS_2 intercalated to $Li_{\frac{1}{12}}ScS_2$ (5.15c), and $Li_{\frac{2}{12}}ScS_2$ (5.15d).

5.11 Elastic Properties

For stable intercalation cycling it is desirable for the electrode material to be resistant to the associated stresses. However, to evaluate the various elastic properties of a material, we first need to obtain the elastic tensor. Using the elements of the elastic tensor, the bulk (B) and shear (G) moduli can be determined, from which many other elastic properties can be determined [279]. Upper bounds of

these quantities, denoted B_V and G_V, can be found using the Voigt scheme (see (4.19)), with the bulk modulus being given by,

$$\begin{aligned} B_V &= \frac{1}{9}\big[(c_{11}+c_{22}+c_{33})+2(c_{12}+c_{23}+c_{31})\big] \\ G_V &= \frac{1}{15}\big[(c_{11}+c_{22}+c_{33})-(c_{12}+c_{23}+c_{31})+3(c_{44}+c_{55}+c_{66})\big]. \end{aligned} \tag{5.4}$$

From these, the Young's modulus, Y, the Poisson ratio, ν, and the Pugh ratio, R, can be obtained:

$$\begin{aligned} \mathrm{Y} &= \frac{9\mathrm{BG}}{3\mathrm{B}+\mathrm{G}} \\ \nu &= \frac{3\mathrm{B}-2\mathrm{G}}{2(3\mathrm{B}+\mathrm{G})} \\ \mathrm{R} &= \frac{\mathrm{B}}{\mathrm{G}}. \end{aligned} \tag{5.5}$$

5.11.1 Elastic Tensor

Both the pristine and intercalated α-ScS_2 found to be rhombohedral with space group number 164 (space group P$\overline{3}$m1 and point group $\overline{3}$m). Rhombohedral crystals have elastic tensors of the form,

$$\begin{pmatrix} c_{11} & c_{12} & c_{13} & c_{14} & & \\ \cdot & c_{11} & c_{13} & -c_{14} & & \\ \cdot & \cdot & c_{33} & & & \\ \cdot & \cdot & & c_{44} & & \\ & & & & c_{44} & c_{14} \\ & & & & \cdot & c_{66} \end{pmatrix}, \tag{5.6}$$

with six independent elastic constants due to the symmetry constraints and the relation $c_{66} = \frac{1}{2}(c_{11} - c_{12})$. To ensure elastic stability, there are certain conditions that are necessary to be met [357], as we outlined in equation (4.30).

We find the elastic tensor (with elements in units of GPa) of the pristine α-ScS_2 structure to be,

Intercalant	Space Group	c_{11} (GPa)	c_{12} (GPa)	c_{13} (GPa)	c_{33} (GPa)	c_{44} (GPa)	c_{14} (GPa)	c_{66} (GPa)
Li	164	142.65	36.93	32.74	112.61	34.11	-1.07	52.87
Na	164	125.28	32.81	32.32	98.58	35.57	7.95	46.23
K	164	101.36	28.46	29.46	103.76	32.45	10.56	36.45
Mg	164	165.39	49.00	58.22	158.47	68.70	17.48	58.20

Table 5.7: Elements of the elastic matrix, c_{ij} in units of GPa, of α-$MScS_2$ (M = Li, Na, K, Mg).

$$\begin{pmatrix} 69.64 & 36.67 & 27.91 & 7.78 & 0.00 & 0.00 \\ & 69.64 & 27.91 & -7.78 & 0.00 & 0.00 \\ & & 17.38 & 0.00 & 0.00 & 0.00 \\ & & & -25.85 & 0.00 & 0.00 \\ & & & & -25.85 & 7.78 \\ & & & & & 16.48 \end{pmatrix}, \tag{5.7}$$

which does not meet conditions (b) and (d), due to the negative values of the c_{44} elements. This elastic instability is also seen for the T-phase structure, and demonstrates again that the pristine ScS_2 is not stable. This places a limit on lowest intercalant concentration that could be accessed in a practical setup, to avoid this instability.

In Table 5.7 we present the non-zero elements of the eleastic matrix for the fully intercalated α-ScS_2 structure. The elements of each of these satisfies the imposed elastic condition listed above, and so we conclude that they are each elastically stable.

5.11.2 Elastic Constants

From the elastic tensors presented above, the elastic properties can be determined. We present in Figure 5.16 the bulk and shear moduli, as calculated using the Voigt upper bound method, and the corresponding Young's modulus for the

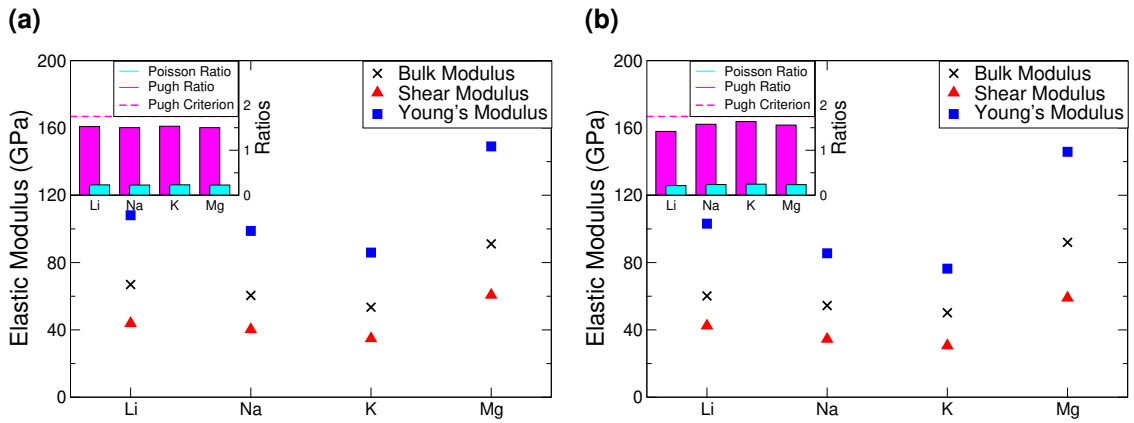

Figure 5.16: Elastic properties of α-ScS_2 (5.16a) and T-ScS_2 (5.16b) in its intercalated forms. The bulk and shear moduli were calculated using the upper-bound Voigt scheme.

α- and T-phases of ScS_2. We present only the data for the intercalated structures and omit the results for the pristine structure due to the elastic instability arising from the negative values of the c_{44} elements.

For the Group I intercalants, as the nuclear mass increases we identify a gradual decrease in each of the elastic moduli. However, we note that magnesium intercalation results in a higher stiffness. For intercalation with Group I intercalants, the α-phase demonstrates a reduction in the bulk modulus from 66.77 GPa (Li) to 60.45 GPa (Na) to 53.47 GPa (K). However, intercalation with magnesium produces a bulk modulus of 91.12 GPa. This trend is also seen with the T-phase structure. The shear modulus similarly drops from 43.92 GPa (Li) to 40.25 GPa (Na) to 34.88 GPa (K), and then increases to 60.71 GPa (Mg), as does the Young's modulus, from 108.12 GPa (Li) to 98.82 GPa (Na) to 85.94 GPa (K), and then increases to 149.02 GPa (Mg).

We rationalise the above results using Bader charge analysis (as will be presented later): as the atomic number of the Group I intercalant is increased, the ionic charges on the intercalant and the chalcogen are reduced (closer to zero). This results in a smaller Coulombic attraction between the layers, and so less energy is required to stretch the material. For intercalation with magnesium, whilst the binding energy of magnesium with the ScS_2 host is lower, the higher charge of the intercalant species results in significantly higher Coulomb forces and thus a stiffer system. Comparing between the elastic properties of both the intercalated

α- and T-phases of ScS_2, we find that the behaviour with changing intercalant holds for both forms.

A key metric for assessing the elasticity of a material is the Pugh ratio, given as the ratio of the bulk modulus and shear modulus, which can be used as an indicator of how ductile or brittle a material is. For Pugh ratios greater than 1.75 materials are usually considered ductile, whereas ratios of less than 1.75 are considered brittle. Similarly, Poisson ratios greater than 0.26 indicate a material will be ductile, whereas it will be brittle for ratios smaller than 0.26 [279, 335]. The inset of Figure 5.16 presents both the Poisson and Pugh ratios. The Poisson ratio for each if the intercalated ScS_2 structures is 0.23, just below the 0.26 limit. We can also see that the Pugh ratios are well below 1.75. It has been indicated previously [277, 279] that the change in the elastic moduli as a function of concentration is near linear. As such, these materials could be expected to become more ductile as the concentration of the intercalants are decreased. Compared to other layered materials, such as $LiCoO_2$ and graphite [277], ScS_2 and its intercalated forms are much more ductile, and so are more attractive for use in flexible electronics.

5.12 Electronic Structure

As many electrode materials require conductive additives (such as graphitic carbon) to allow for electronic conduction during cycling of a cell, determining the material electronic structure is also necessary. In Figure 5.17 we present the electronic band structure and orbital-decomposed density of states (DOS) for pristine ScS_2 (Figure 5.17a and Figure 5.17b), $LiScS_2$ (Figure 5.17c and Figure 5.17d), and $MgScS_2$ (Figure 5.17e and Figure 5.17f). Equivalent electronic structure data for $NaScS_2$ and $KScS_2$ are qualitatively similar to $LiScS_2$, and so have not been explicitly presented here.

In the unintercalated form, α-ScS_2 is shown to have a metallic nature with a Fermi level intersecting a band. This metallic nature is also seen for the T- and Hc-phases, and is also seen using the HSE06 functional, which is capable of in-

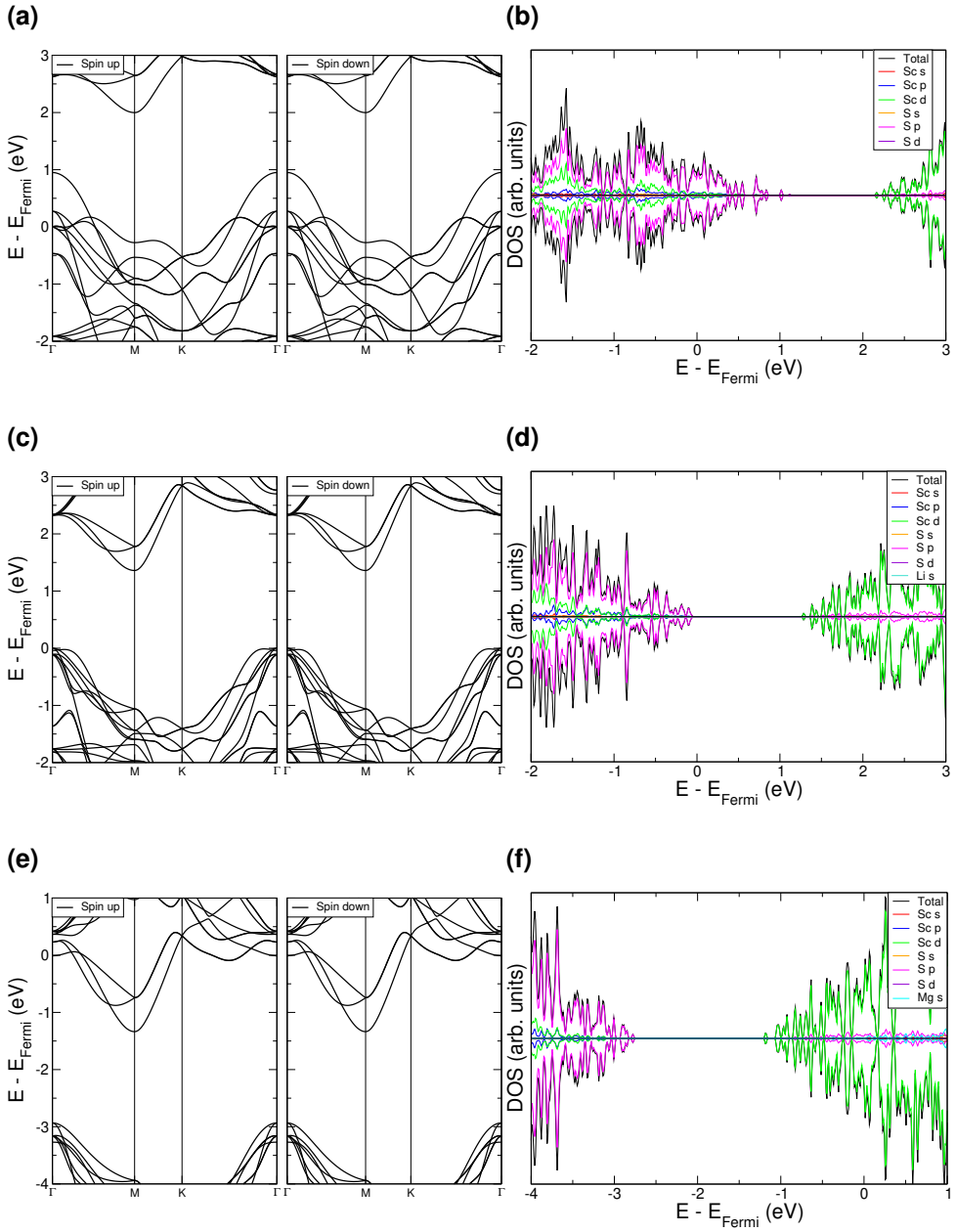

Figure 5.17: Electronic band structure (5.17a, 5.17c, and 5.17e) and orbital-decomposed density of states (5.17b, 5.17d, and 5.17f) for α-ScS_2 compounds. Pristine bulk data is presented in 5.17a and 5.17b, data for $LiScS_2$ is presented in 5.17c and 5.17d, and data for $MgScS_2$ is presented in 5.17e and 5.17f. In each, all data has been normalised such that the highest occupied state (E_{Fermi}) is set to 0 eV.

troducing band gaps into metallic systems. This is ideal for electrode materials, as it means that conductive additives are not necessary to facilitate the electron conduction. From the orbital-projected density of states, it can be seen that the valence bands of each of the phases are dominated by sulfur *p*-states and the conduction bands are dominated by scandium *d*-states.

Equivalent data for the intercalated ScS_2 structures show that the addition of the Group I intercalants provides electrons, filling the previously unoccupied sulfur *p*-orbitals, shifting the Fermi level (located mid-band in ScS_2) upwards. This is also shown with the charge analysis presented above. Upon intercalation to the point of $MScS_2$ with Group I metals, the intercalated structure develops a semiconducting nature with an occupied valence band separated from the conduction band by an moderate PBE-functional band gap of size $\sim$1 eV. Specifically for $LiScS_2$, the PBE band gap is 1.36 eV and the HSE06 band gap is 2.32 eV, though we note from previous work that the HSE06 functional can overestimate the band gap of TMDC structures [292]. This gives a limit on the intercalation potential obtainable for practical uses: the insulating nature at this point would inhibit electronic conduction during cycling, and any intercalation past this point would require ScS_2 to be mixed with conductive additives to account for the insulating behaviour.

Magnesium intercalated into ScS_2 has different conducting behaviour compared to the Group I elements, due to its double valency, as shown in Figure 5.17e and Figure 5.17f. Whilst the unintercalated system is conducting, intercalating to $Mg_{0.5}ScS_2$ fills the unoccupied sulfur *p*-orbitals and results in the structure losing its conductive nature, possessing a band gap of over 1.5 eV using the PBE functional. This would provide a practical limit during cycling, and would require conductive additives to be used to help facilitate intercalation past this point. However, past this the added magnesium provides electrons that begin to fill the unoccupied scandium *d*-states above the band gap.

5.13 HSE06 Results

It is important to make a careful choice of exchange-correlation functional in first-principles calculations, as it can lead to discrepancies in the electronic structure [264, 382] and material energetics [289, 290, 383]. Here, we compare our PBE results with those obtained from the HSE06 functional for a limited number of cases to determine the sensitivity of the results to functional choice. With the use of the HSE06 hybrid functional, we note the intercalation voltage is significantly increased to 4.440 V (Li), 4.420 V (Na), 3.953 V (K), and 1.719 V (Mg). These

Material	Voltage (V)	Intercalation Capacity ($mAhg^{-1}$)	Volume Change (%)
$LiScS_2$	3.977	182.99	6.51
$LiCoO_2$	3.9–4.7 [42]	190-215 [42]	3.25 [278]
NMC	2.85-3.41 [41]	160-189 [41]	8.44 [279]
$LiFePO_4$	3.5 [36,38,40]	95 [36], 140.9 [38], 156 [40]	6.81 [384]
$LiMn_2O_4$	4.13, 4.25 [37], 3.9, 4.1 [39]	111.5 [385], 106.3 [37], 105.2 [39]	4.7 [386]

Table 5.8: Comparison table of key lithium-ion electrode properties for ScS_2 and other presently practiced electrode materials. Data for $LiScS_2$ was obtained in this work.

are higher than the PBE voltages by 0.463 V, 0.546 V, 0.154 V, and 0.245 V, respectively. However, the voltage ordering is maintained and thus both functionals indicate that the ScS_2 would be very suitable for a cathode material.

We also note differences in the constructed phase diagrams, and hence the values of E_{IS}. We find that the diagonal line, corresponding to the boundary between the intercalated ScS_2 and the Li_2S crystal, remains relatively unchanged. The discrepancy between the phase diagrams using the HSE06 and PBE functionals, therefore, arises from the modification to the horizontal line, corresponding to the boundary between the intercalated and pristine ScS_2 structure. Across each of the phases and intercalants presented here, the amount that the horizontal line is modified with the use of HSE06 varies, though it is consistently shifted downwards (hence increasing the region of stability). However, these results do not change the main conclusions of the Chapter, nor invalidate the potential of ScS_2 as a cathode material. Graphical representations of the voltage profiles and phase diagrams using the HSE06 are presented in Appendix D.

5.14 Extending ScS_2

Of the intercalant metals presented, lithium is the smallest and lightest, presents the highest (average) voltage of nearly 4 V, and has the lowest volumetric expansion. As such, lithium is identified as the best ion for ScS_2 to be used as an inter-

calation electrode. We summarise the key electrode properties in Table 5.8, along with the properties of other presently practiced electrode materials for lithium-ion batteries, where it is clear to see that ScS_2 offers a serious competitor to these materials. Below, we focus on lithium for exploring intercalation beyond the $LiScS_2$ composition, the usual limit considered for intercalation of TMDC materials, and for considering the effect of substitution of different transition metals for the scandium site in ScS_2.

5.14.1 Intercalation Beyond a=1

The intercalated $LiScS_2$ structures show both dynamic stability (with no imaginary phonon modes) and thermodynamic stability against conversion (with positive values of E_{IS}), and so the question as to the maximum possible lithium capacity still remains. As each of the octahedral sites is occupied at $LiScS_2$, any further addition of lithium results in the occupation of the tetrahedrally-coordinated sites. For the supercell sizes considered, the first step of intercalation past $LiScS_2$ resulted in a stoichiometry of $Li_{\frac{13}{12}}ScS_2$. As this compound still possesses a sizeable value of $E_{IS} = 3.209$ eV, it is still remarkably stable against conversion reactions and demonstrates a robustness in this material to lithium intercalation beyond the usual limit considered for layered materials. However, there is a dramatic decrease in the intercalation voltage (with respect to the $LiScS_2$ structure) to 0.436 V, which indicates a clear cutoff in the practical uses for ScS_2 as a cathode material. With further intercalation the value of E_{IS} drops, reaching a value of -0.735 eV at Li_2ScS_2. At these relatively high lithium concentrations the large repulsion between these positively charged ions results in the intercalated structure being destabilised and becoming more susceptible to conversion.

5.14.2 Metal Mixing

One possible method commonly used to modify the properties of electrodes is through the introduction of other elements (M), in particular transition metals [373, 374] or with excessive lithium [87], resulting in the $LiSc_{1-x}M_xS_2$ compound. We

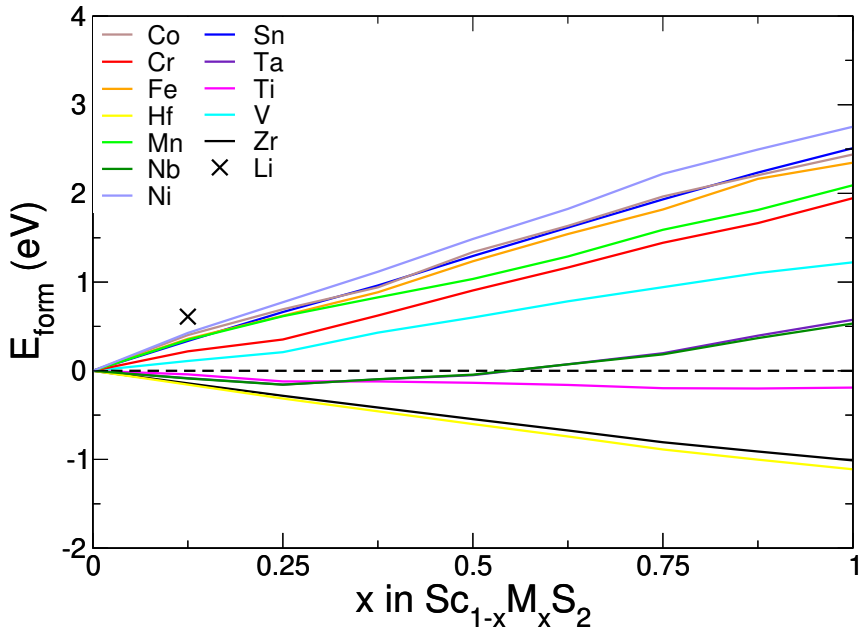

Figure 5.18: Formation energy of substituting scandium with different metal species, calculated with equation (5.8).

first consider the formation energy of metal mixing for a range of metal species, using,

$$E_{form} = \left[E(\mathrm{Sc_{1-x}M_xS_2}) + \mathrm{x}E(\mathrm{Sc})\right] - \left[E(\mathrm{ScS_2}) + \mathrm{x}E(\mathrm{M})\right]. \tag{5.8}$$

This gives an indication of the cost to do the metal substitution, with positive values corresponding to unfavourable swaps, and therefore a cost in energy.

Our results, presented in Figure 5.18, show that for low concentrations ($\mathrm{x} < 0.25$), the energetic cost is low or even negative, with lithium showing the highest formation energy of 0.61 eV at $\mathrm{x} = 0.125$. The Group IV metals (Ti, Zr and Hf) have negative formation energies, and so it is energetically favourable to perform this substitution. We also see negative values of E_{form} for Group V elements Nb and Ta for mixing values of $\mathrm{x} < 0.5$, whilst the other metals considered here (and $\mathrm{x} > 0.5$ for Nb and Ta) demonstrate positive values of formation energy.

In Figure 5.19a, we show the variation in voltage as scandium is substituted for different metals. For each of the transition metals, it is clear to see a reduction in the intercalation potential as the proportion of scandium is reduced. The exception to this is demonstrated with lithium where, for a mixing concentration of

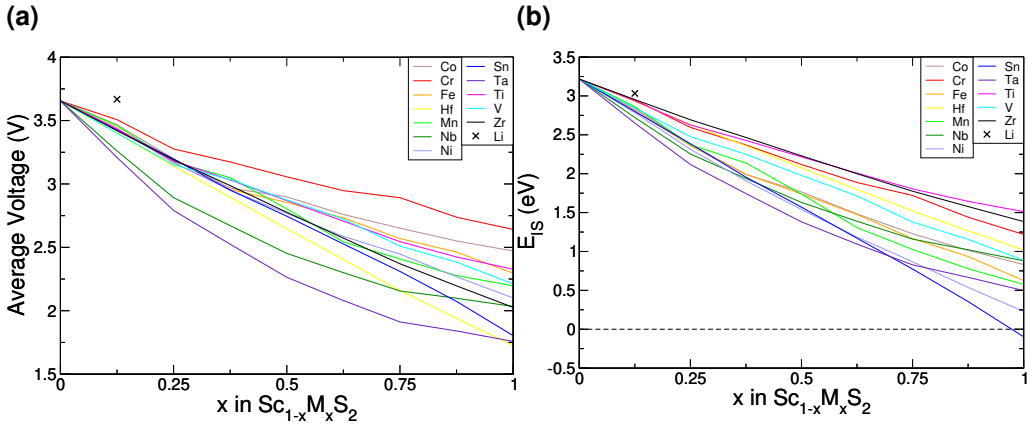

Figure 5.19: Energetic results for metal mixing in T-ScS_2. 5.19a gives the average voltage for various metal mixing, calculated by taking the difference between the fully intercalated ($LiSc_{1-x}M_xS_2$) and pristine structures ($Sc_{1-x}M_xS_2$), and 5.19b gives the obtained values of E_{IS}.

$x = 0.125$, the average voltage is increased past the 3.655 V of ScS_2 to 3.668 V. The values of E_{IS} (at full lithium intercalation) for transition metal mixing demonstrate a similar trend, as shown in Figure 5.19b.

In general, the voltage and E_{IS} values for the mixed materials falls below the weighted average of the two component materials. The greatest difference from the weighted average result is most dramatically show with $Sc_{0.5}Ta_{0.5}S_2$. For voltage, the average of the two components is 2.706 V, whereas the actual voltage obtained is 2.264 V. Similarly for the value of E_{IS}, the average of the ScS_2 and TaS_2 materials is 1.857 eV, whereas the value obtained is 1.381 eV. With changing metal composition, one might expect that the resulting values of voltage and E_{IS} would lie on a straight line connecting the respective values at $x = 0$ and $x = 1$. However, there is a varying amount of deviation from this expected linear trend for different metal species mixed. For example, the voltage and E_{IS} values for Hf (yellow), Sn (dark blue), and Zr (black) appear to follow very closely to a linear trend, whereas the trends of the other metals considered are much more convex. The convex shape is highlighted best with Ta (purple data), where there is a clear deviation from the straight line that would connect the ScS_2 and TaS_2 limits.

The energetic cost of formation of ScS_2 can be reduced by the inclusion of other

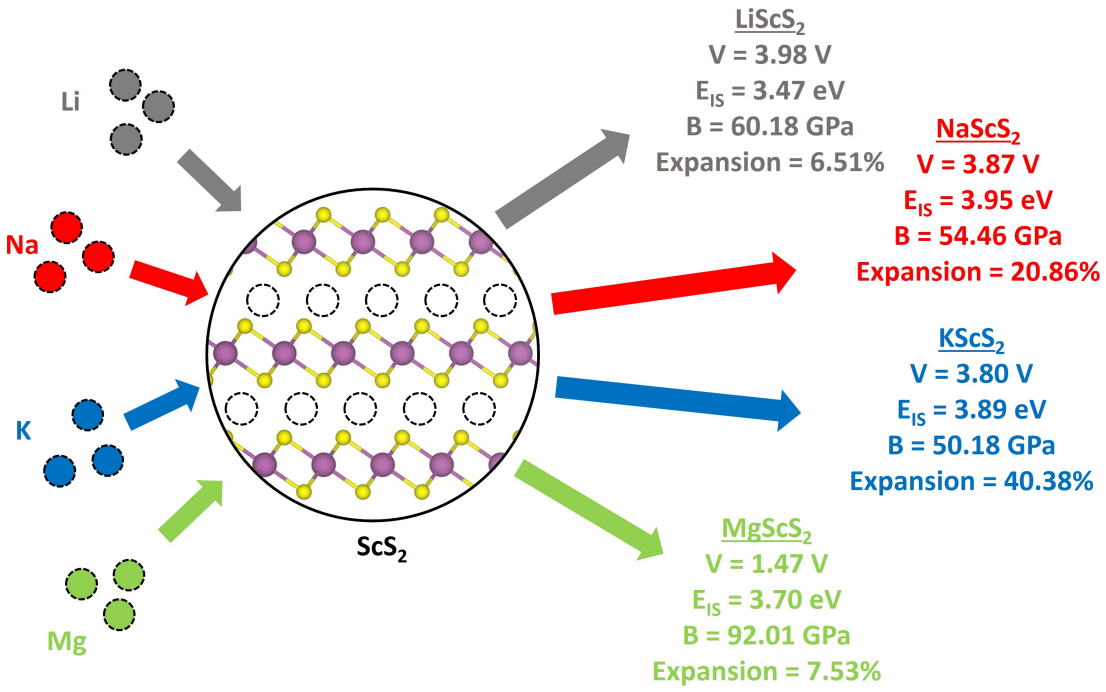

Figure 5.20: Summary of the key results presented in this Chapter.

metals, $Sc_{1-x}M_xS_2$. However, we see that this results in both a decrease in the obtainable voltage and a decrease in the thermodynamic stability indicated by E_{IS}. Whilst the mixing of these systems reduces the suitability of ScS_2 as a cathode, the mixing of scandium into other materials for cathodes could be highly beneficial, increasing their voltages or improving their stability. In particular, the transition metal oxides currently being utilised and explored as cathode materials, such as the NMC variants, could benefit from the inclusion of scandium into their structures, though further investigation is required to assess this.

5.15 Summary

In this Chapter, we have presented a thorough first-principles study into the performance of layered ScS_2 as a potential cathode electrode material. We have applied a random structure search to demonstrate that the ground state phase for the intercalated material is a layered structure, agreeing with experimental studies and supporting its use as an electrode. From this, different layered-phases of the material were investigated and intercalated with different metal species. It was found that the T- and α-phases to be energetically preferred, though they are not

dynamically stable (determined through analysis of the phonon band structures) for low intercalation concentrations. The lowest achievable intercalant concentration is thus determined to be $\mathrm{a} = 0.25$, and so a capacity corresponding to 75% of the theoretical capacity is predicted, corresponding to a charge capacity of 182.99 mAhg^{-1}.

For Group I intercalants, ScS_2 is found to have a high voltage of nearly 3.5 V which is ideal for cathodes. Whilst this is reduced to 1.5 V for intercalation with magnesium (a Group II metal), the double valency offers a larger range of charge transfer and hence a comparable energy density. This low voltage also offers some promise for an anode. Thermodynamic phase diagrams were constructed to evaluate the stability of the layered ScS_2 material against the conversion reaction forming Li_2S (or equivalent compound), a reaction commonly seen for TMDC sulfides when intercalated. ScS_2 was found to have a remarkably large window of stability, particularly when compared to the related TMDC materials. Beyond this, ScS_2 was shown to have a Fermi level which lies within a band, indicating a conductive nature that is convenient for device cycling. It also has a low volumetric expansion (below 10%) when intercalated with lithium or magnesium, something that is essential for extended device lifetime. These results are summarised in Figure 5.20.

To explore methods that could offer some improvement to the core properties of ScS_2 material, we also considered metal mixing (substitutionally swapping out scandium atoms with transition metal elements, similar to what is done with NMC). With mixing of other metals, we find a gradual drop in both the voltage and the size of the phase diagram window of stability which suggests that this would be detrimental to the performance of a ScS_2 electrode. However, this does highlight the potential advantage scandium could provide if mixed into other layered systems such as the layered transition metal oxides.

So far, we have assessed various properties of individual layered TMDC materials for use as electrodes in Li-ion and beyond-Li-ion batteries. This Chapter highlighted that ScS_2 in particular shows potential as a cathode material for lithium-ion batteries, with theoretical estimates of the capacity comparable with NMC and similar materials. We hope that our study encourages further develop-

ment of this material for lithium-ion batteries. In the following Chapter, we extend the study of TMDCs to consider how the formation of their superlattices modifies their properties.

Chapter 6

Intercalation of TMDC Superlattices

"No, actually it's a highly sophisticated inter-locking brick system."

The Man Upstairs, The Lego Movie, 2014

6.1 Introduction

Following the work of Whittingham [35,67] and Goodenough [71,72] in the 1970s and 1980s, and more recently the success of Novoselov and Geim [179–181] and their isolation of graphene, materials which possess a layered structure have received a lot of attention for energy storage. Materials such as NMC and its variants [41,82–86], and the MXenes [183,387–389] all demonstrate ideal electrode properties, and we have seen in previous Chapters the promise of TMDC materials. This is largely owing to the fact that their intrinsic structures posses van der Waals gaps provides natural channels for intercalated ions to occupy and travel through during the cycling of a cell. However, many of these materials are still plagued by slow charging rates and low capacities [171], and we saw in Chapter 3 that many TMDCs offer voltages that lie outside of ideal anode/cathode ranges and are susceptible to conversion reactions.

One clear extension to these layered materials can be achieved through the formation of superlattices and heterostructures, consisting of layers of different materials akin to stacking Lego bricks on top of each other (see Figure 6.1). This

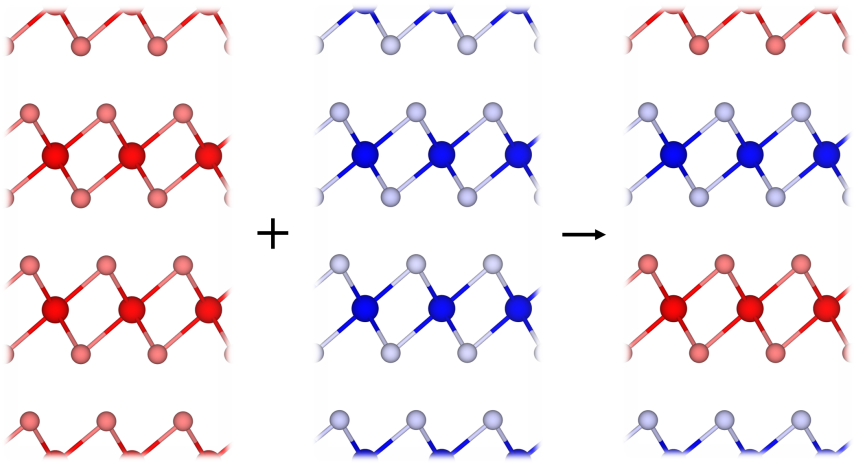

Figure 6.1: Schematic showing the 1:1 pairing of two lattice-matched TMDCs to form a superlattice.

not only allows for utilisation of both the properties of the component materials, but also the novel physics that can arise from their interface. Being able to design composite materials with specific properties, perfectly suited for specific functions, might be considered a trivial task considering the range of materials we have at our disposal. Unfortunately, combining different materials to form a composite in a way that either preserves the desired properties of the constituents or utilises the new physics that arises from their combination remains a challenge in materials science, and currently has no universal solution. However, the development of techniques such as molecular beam epitaxy, chemical vapour deposition [390], liquid exfoliation [391], and nucleation growth [392] allow for monolayer control of materials synthesis [190, 393, 394], and has led to many investigations into the properties of such materials in recent years.

In this Chapter, we report on a theoretical modelling of TMDC superlattices, with a focus on their properties for use as electrode materials in Li- and Mg-ion cells. We present the material voltage profiles, showing how these change between single constituents and compounds, and also discuss how the thermodynamic stability of these materials upon intercalation can be used as a way to estimate the charge storage capacity. We also discuss other properties that are important for possible electrode materials, such as the volumetric expansion that arises from intercalation, changes to the mechanical and elastic properties, and the resultant electronic structure which is important for efficient electronic conduction. This allows us to offer insight into how careful choice of materials in a superlattice can

be used to improve these materials for electrode applications.

6.2 Background

With heterostructure or superlattice formation, the resultant electronic structure is typically of the most interest, and has most widely been determined using Anderson's rule [395–397], which states that band alignment depends purely on the relative positions of the constituent work functions/hole affinities. Though very few experimental investigations validated this approach for 3D systems (due to the presence of broken/reorganised bonds), more recent explorations of weakly interacting 2D materials have allowed for a development in the understanding of band alignment in such systems. Whilst Anderson's rule has been shown to be an accurate model for predicting the electronic structure of heterostructures constructed of 2D materials, some works have shown that effects such as strain and orbital hybridisation must also be accounted for [264, 398–400].

There has already been some interest in utilising heterostructures for energy-storage applications [401–406]. Of course, graphitic carbon has been used as a popular additive to many TMDCs, such as with MoS_2 [404, 407] and SnS_2 [238, 256, 408], but beyond this many other pairings have also been considered. Experimental investigations into the intercalation of TMDC superlattices have shown improvements to the cyclability [254], and first-principles studies have found a reduction in diffusion barriers and reduced volumetric expansions [213, 215]. Hence, there is clearly great potential in using superlattice formation to enhance the performance of TMDCs for intercalation electrodes whilst preserving their favourable properties. Unfortunately, due to the immense number of possible combinations no study can be exhaustive, and previous works have been limited to a few select cases of heterostructures or superlattices. Nevertheless, a comprehensive study of TMDCs and their composites is needed to better understand how superlattice formation can enhance electrode properties, offer insight into heterostructures and superlattices composed of similarly layered materials, and to allow us to fully exploit these superlattice materials.

6.3 Computational Details

In this work, first principles techniques based on density functional theory were used to determine structural and energetic properties of superlattice structures composed of vertically stacked layered MX_2 materials, and to evaluate how these properties change when intercalated with varying levels of lithium or magnesium. This build upon the results of Chapter 3 which focused on the performance of individual TMDCs as intercalation electrodes.

We focus on superlattices with 1T-phase TMDC components as we determined in Chapter 3 that these are generally the preferred phase in their pristine and intercalated forms. Whilst other phases [195,196] are possible for the TMDCs, such as 3R and the α-$NaFeO_2$-like structure, their intercalation environments are similar to that of the 1T-phase, and so only the 1T-phase is considered. To investigate a range of superlattices based on TMDCs, we paired various TMDC materials with a second lattice-matched TMDC in a 1:1 match, as shown in Figure 6.1. To be considered 'lattice-matched', the two MX_2-materials are required to have a lattice constant within 5% of each other. Whilst the pairing of non-lattice matched MX_2-materials could be considered, there is a much larger combination space to investigate. Phenomena such as Moiré rotation effects [409–411], consideration of relative in-plane translations of the two atomic layers [196], and rippling [412,413] are each deserving of a study of their own. Further to this, analysis of the effects of edge formation [414–416] and the investigation of defects [291] would also be required for a thorough description of a material in a working electrode. However, none of these can be explored until the fundamental properties of the core superlattices have been established. As such, we limit our investigation to pristine bulk superlattices formed through combinations of aligned MX_2-materials with similar in-place lattice constants, with the addition of $MoS_2|SnS_2$ which shows strains between 5% and 10%. Further details of the material pairings, including the resultant strain and the formation energy are presented in Appendix E.

To achieve a finer sampling of intercalant concentrations than would be accessible through consideration of only the primitive unit cells, supercells consisting of $(2 \times 2 \times 2)$ unit cells were used for the individual TMDC materials and supercells

consisting of $(2\times2\times1)$ unit cells were used for the superlattice structures. Each of these corresponds to 24 atoms, eight MX_2 formula units, and two TMDC layers. These were then used as the bulk unit cells into which lithium and magnesium were intercalated for evaluation of voltages and thermodynamic stability, giving us access to intercalant concentrations equivalent to $Li_{\frac{1}{8}}MX_2$ and $Mg_{\frac{1}{8}}MX_2$.

We determine the preferred site of intercalation to be those with octahedral coordination, further discussion of which is presented in the Supplementary Material. Using the supercell sizes described above, we thus have access to eight potential octahedrally-coordinated intercalation sites, which allow for 24 potential intercalant filling configurations. Each of these has been explored, and combinations of different concentrations have been used to emulate clustering effects [233, 239, 269, 270]. Further details of these are presented in the Supplementary Material. For a given intercalant concentration, the configuration that results in the lowest energy structure is used for evaluation of key electrode properties, such as calculation of the intercalation voltage and assessment of the thermodynamic stability.

The calculations performed here employed the Vienna Ab initio Simulation Package (VASP) [161–164]. The valence electrons included for each species are indicated Table 2.1. The projector augmented wave method [139] was used to describe the interaction between core and valence electrons, and a plane-wave basis set was used with an energy cutoff of 700 eV. All structural relaxations were completed using the Perdew-Burke-Ernzerhof (PBE) [119] functional form of the generalised gradient approximation (GGA), and converged to a force tolerance of 0.01 $\mathrm{eV/Å}$ per atom, while electronic self-consistency is considered to an accuracy of 10^{-7} eV. Monkhorst-Pack grids [140] of k-points equivalent to a $6\times6\times6$ grid in the supercells are used throughout, and we have allowed for optimisation of collinear spin. Van der Waals interactions have been addressed using the zero damping DFT-D3 method of Grimme [155]. Upon intercalation, local charge transfer leads to local electric fields within the structure, making it impossible to align the electronic structures of pristine and intercalated materials using typical means of core-state alignment [262] or with respect to the vacuum level [262–264]. Instead, we have qualitatively aligned to the high-energy occu-

pied states of the unintercalated superlattice at Γ, allowing us to comment on the relative position of the Fermi level.

6.4 Methods for Material Evaluation

6.4.1 Intercalation Voltage

To compare different levels of lithium-intercalated superlattice (SL = $MX_2M'X_2'$) the voltage, V, can be calculated using,

$$V = -\frac{E_{\mathrm{Li}_{b_2}\mathrm{SL}} - \left[E_{\mathrm{Li}_{b_1}\mathrm{SL}} + (b_2 - b_1)E_{\mathrm{Li}}\right]}{(b_2 - b_1) \times ze}, \tag{6.1}$$

for total lithium content $b_2 > b_1$, and energy of the superlattice structure with b intercalant atoms per SL formula unit $E_{\mathrm{Li}_b\mathrm{SL}}$. In this work, we consider values of $0 \leq b \leq 2$, with $b = 2$ corresponding to one intercalant ion per metal atom of the host structure. z is the valency of the intercalant ($z = 1$ for the case of lithium, $z = 2$ for magnesium) and E_{Li} is the energy of a lithium atom as found in bulk. Each occurrence of Li should be replaced with an equivalent Mg for magnesium intercalation.

6.4.2 Thermodynamic Phase Diagrams

For an arbitrary superlattice consisting of two lattice-matched TMDC materials (SL = $MX_2M'X_2'$) when intercalated with b lithium (Li_bSL) we define the Gibbs free energy of formation of relevant products:

$$\Delta G(\mathrm{Li}_b\mathrm{SL}) = E(\mathrm{Li}_b\mathrm{SL}) - [b\mu^0_{\mathrm{Li}} + \mu^0_{\mathrm{M}} + \mu^0_{\mathrm{M}'} + 2\mu^0_{\mathrm{X}} + 2\mu^0_{\mathrm{X}'}], \tag{6.2}$$

$$\Delta G(\mathrm{SL}) = E(\mathrm{SL}) - [\mu^0_{\mathrm{M}} + \mu^0_{\mathrm{M}'} + 2\mu^0_{\mathrm{X}} + 2\mu^0_{\mathrm{X}'}], \tag{6.3}$$

$$\Delta G(\mathrm{Li}_2\mathrm{X}) = E(\mathrm{Li}_2\mathrm{X}) - [2\mu^0_{\mathrm{Li}} + \mu^0_{\mathrm{X}}], \tag{6.4}$$

and,

$$\Delta G(\mathrm{Li_2X'}) = E(\mathrm{Li_2X'}) - [2\mu^0_{\mathrm{Li}} + \mu^0_{\mathrm{X'}}]. \tag{6.5}$$

We have again used $\Delta G(A)$ to denote the Gibbs free energy of formation of the compound A, $E(A)$ gives the energy of the compound A, and $\mu^0_B = E(B)$ gives the chemical potential of elemental species B when it is in its elemental bulk structure.

The thermodynamic equilibrium condition requires,

$$\Delta G(\mathrm{Li}_b\mathrm{SL}) = b\Delta\mu_{\mathrm{Li}} + \Delta\mu_{\mathrm{M}} + \Delta\mu_{\mathrm{M'}} + 2\Delta\mu_{\mathrm{X}} + 2\Delta\mu_{\mathrm{X'}}, \tag{6.6}$$

where we have used the notation $\Delta\mu_B = \mu_B - \mu^0_B$, with μ_B being the chemical potential of elemental species B in Li_bSL. This simply states that the energy of the superlattice structure is the sum of the chemical potentials of the constituent atoms. Rearranging the thermodynamic equilibrium condition gives,

$$\Delta\mu_{\mathrm{X}} + \Delta\mu_{\mathrm{X'}} = \frac{1}{2}\big\{\Delta G(\mathrm{Li}_b\mathrm{SL}) - [b\Delta\mu_{\mathrm{Li}} + \Delta\mu_{\mathrm{M}} + \Delta\mu_{\mathrm{M'}}]\big\}. \tag{6.7}$$

We require that $\mathrm{Li_2X}$, $\mathrm{Li_2X'}$, SL, and the bulk forms of the component elements do not form. For superlattices in particular, it is unreasonable to assume that the layered structure would be obtained upon reversal of the conversion reaction. Therefore,

$$\Delta\mu_{\mathrm{M}} + \Delta\mu_{\mathrm{M'}} + 2\Delta\mu_{\mathrm{X}} + 2\Delta\mu_{\mathrm{X'}} \leq \Delta G(\mathrm{SL}), \tag{6.8}$$

$$2\Delta\mu_{\mathrm{Li}} + \Delta\mu_{\mathrm{X}} \leq \Delta G(\mathrm{Li_2X}), \tag{6.9}$$

$$2\Delta\mu_{\mathrm{Li}} + \Delta\mu_{\mathrm{X'}} \leq \Delta G(\mathrm{Li_2X'}), \tag{6.10}$$

and,

$$\Delta\mu_{\mathrm{Li,M,M',X,X'}} \leq 0. \tag{6.11}$$

Substituting (6.7) into (6.8) and rearranging,

$$\frac{1}{b}\big\{\Delta G(\mathrm{Li}_b\mathrm{SL}) - \Delta G(\mathrm{SL})\big\} \leq \Delta\mu^{(2)}_{\mathrm{Li}}. \tag{6.12}$$

This then gives the thermodynamic limit on the lithium chemical potential such that the intercalation of the superlattice is preferred to the pristine superlattice and bulk lithium. We now add equations (6.9) and (6.10) to get,

$$4\Delta\mu_{Li} \leq \Delta G(\mathrm{Li_2X}) + \Delta G(\mathrm{Li_2X'}) - \Delta\mu_X - \Delta\mu_{X'}, \tag{6.13}$$

and make use of equation (6.7) to get,

$$\Delta\mu_{Li}^{(1)} \leq \frac{1}{8-b}\big[2\Delta G(\mathrm{Li_2X}) + 2\Delta G(\mathrm{Li_2X'}) - \Delta G(\mathrm{Li_bSL}) + \Delta\mu_M + \Delta\mu_{M'}\big]. \tag{6.14}$$

We now have two equations describing the boundary conditions for the chemical potential of lithium, given $\Delta\mu_{Li}^{(1)}$ and $\Delta\mu_{Li}^{(2)}$. These each define a plane, analogous to the one-dimensional boundaries for individual TMDCs, giving the thermodynamic limits on the chemical potential of the lithium so that the conversion-reaction products Li_2X and Li_2X' do not form.

For the case where the two component TMDCs are the same (i.e. M = M′, X = X′ and $b = 2a$), these simplify to:

$$\Delta\mu_{\mathrm{Li}}^{(1)} \leq \frac{1}{4-a}\big[2\Delta G(\mathrm{Li_2X}) - \Delta G(\mathrm{Li}_a\mathrm{MX_2}) + \Delta\mu_{\mathrm{M}}\big], \tag{6.15}$$

and,

$$\frac{1}{a}\big[\Delta G(\mathrm{Li}_a\mathrm{MX_2}) - \Delta G(\mathrm{MX_2})\big] \leq \Delta\mu_{\mathrm{Li}}^{(2)}, \tag{6.16}$$

which are equations (3.19) and (3.20) presented in Chapter 3.

It should be noted, by considering the equations (6.2)-(6.5), that the limiting conditions are also independent of $\mu^0_{\mathrm{X,X'}}$, and hence $\Delta\mu_{\mathrm{X,X'}}$. As a result, the phase diagrams are only dependent on the chemical potentials of lithium and the relevant metals, $\Delta\mu_{\mathrm{Li,M,M'}}$.

Using equations (6.11), (6.12) and (6.14), we can construct thermodynamic phase diagrams. A schematic of such a phase diagram is shown in Figure 6.2, which can be viewed as a three-dimensional extension of the two-dimensional equivalent presented in Chapter 3. We again restrict ourselves to the negative-negative quadrant to ensure that the elemental bulks do not form. Above the diagonal plane, coloured red in Figure 6.2, the experimentally observed Li_2S crystal (or equivalent chalcogen) is favoured, as opposed to the intercalated superlattice.

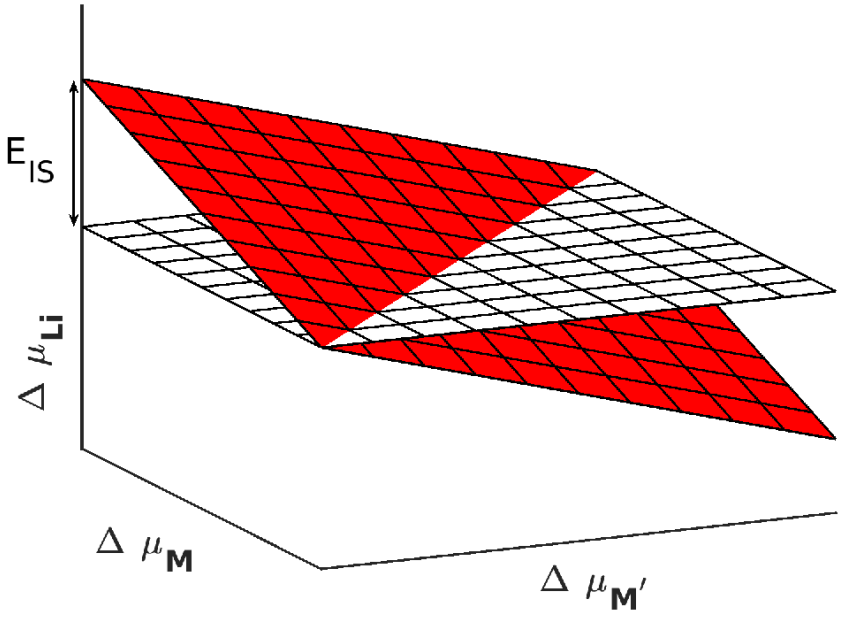

Figure 6.2: Schematic indicating the phase diagrams constructed for the superlattice structures. This is a 3D-equivalent of those presented in Figure 3.7, with the planes being described by equation (6.12) and (6.14).

Below the horizontal plane, coloured white in Figure 6.2, the pristine superlattice structure is preferred to intercalation. As with the phase diagrams of Chapter 3, this results in a window of stability. Outside of this window, the secondary products are favourable to form. Though a transition to these is not guaranteed, the intercalated superlattice structure becomes meta-stable. Whilst other compounds could have their respective boundaries determined to be included in these phase diagrams, such as Li_2X_2 or MX, these first require the disintegration of the intercalated superlattice material into Li_2X, MgX, and/or elemental bulks. Hence, we only consider the limits outlined above.

To quantitatively compare the phase diagrams for the different concentrations considered, we can evaluate the difference between the intercepts of the two planes with the $\Delta\mu_{\mathrm{Li}}$-axis. E_{IS} is then defined as,

$$E_{IS}^{\mathrm{Li}} = \Delta\mu_{\mathrm{Li}}^{(1)}(\Delta\mu_{\mathrm{M,M'}} = 0) - \Delta\mu_{\mathrm{Li}}^{(2)}(\Delta\mu_{\mathrm{M,M'}} = 0). \tag{6.17}$$

where $\Delta\mu_{\mathrm{Li}}^{(1/2)}(\Delta\mu_{\mathrm{M,M'}} = 0)$ is the value of the boundary plane $1/2$ at the point where $\Delta\mu_{\mathrm{M,M'}} = 0$. Using (6.14) and (6.12), this can be written in terms of the relevant values for formation Gibbs free energy,

$$E_{IS}^{\mathrm{Li}} = \frac{2}{8-b}\left[\Delta G(\mathrm{Li_2X}) + \Delta G(\mathrm{Li_2X'})\right] + \frac{1}{b}\Delta G(\mathrm{SL}) - \frac{8}{8b-b^2}\Delta G(\mathrm{Li}_b\mathrm{SL}). \tag{6.18}$$

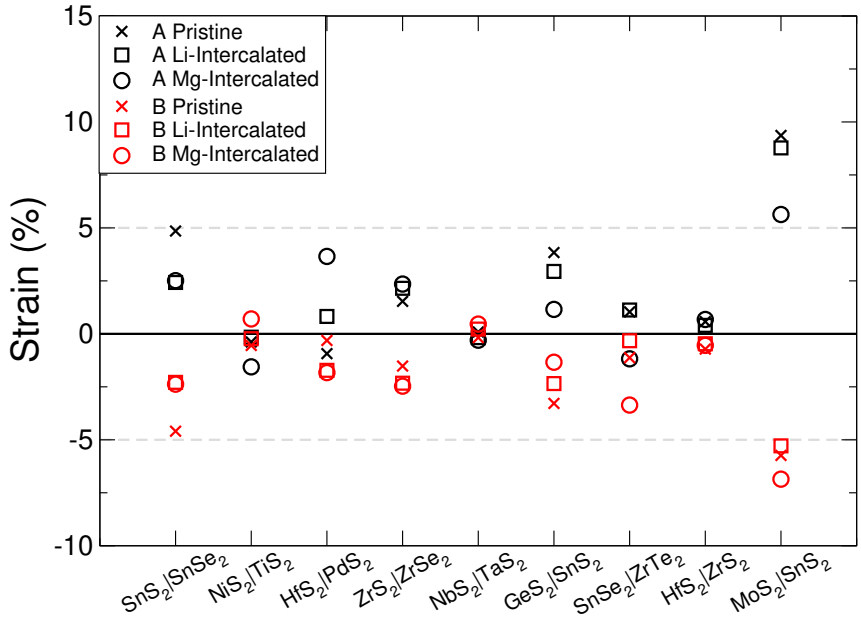

Figure 6.3: Resultant strains on the component TMDCs when combined in the superlattice structure. For a superlattice of the form $MX_2|M'X'_2 = A|B$, the strain on A is given as $\% = \frac{a_{SL}^{P/I} - a_A^{P/I}}{a_A^{P/I}} \times 100$.

For magnesium intercalation, we have the equivalent expression,

$$E_{IS}^{\mathrm{Mg}} = \frac{2}{4-b}\left[\Delta G(\mathrm{MgX}) + \Delta G(\mathrm{MgX'})\right] + \frac{1}{b}\Delta G(\mathrm{SL}) - \frac{4}{4b-b^2}\Delta G(\mathrm{Mg}_b\mathrm{SL}). \tag{6.19}$$

6.4.3 Lattice Matching

To minimise the strain on each of the component materials comprising a superlattice, a close matching of each of the respective in-plane lattice constants is required. Here, we evaluate how well-matched different pairings are when combined in a superlattice. We focus on selected systems $SnS_2|SnSe_2$, $NiS_2|TiS_2$, $HfS_2|PdS_2$, $ZrS_2|ZrSe_2$, $NbS_2|TaS_2$, $GeS_2|SnS_2$, $SnSe_2|ZrTe_2$, $HfS_2|ZrS_2$, and $MoS_2|SnS_2$. Details of other superlattices considered in this work are presented in Appendix E. In Figure 6.3 we see the percentage strain on the pristine TMDCs when at the lattice constant of the formed superlattice without intercalants. For component A (with lattice constant a_A^P) strained to the lattice constant of the superlattice (a_{SL}^P), the strain is calculated using $\% = \frac{a_{SL}^P - a_A^P}{a_A^P} \times 100$. Similarly, we also present the percentage strain on the intercalated TMDCs when at the lattice constant of the intercalated superlattice. For component A of lattice constant a_A^I

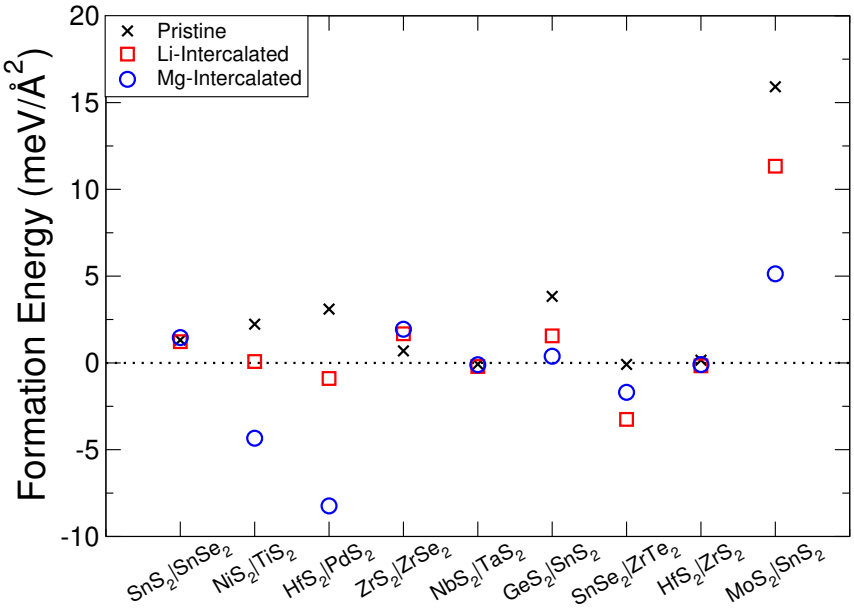

Figure 6.4: Formation energy of pristine and intercalated superlattice formation from the pristine and intercalated components. Calculated using $E_{form} = [E_{SL}^{P/I} - (E_A^{P/I} + E_B^{P/I})]/S$.

strained to the lattice constant a_{SL}^I, the strain is calculated using $\% = \frac{a_{SL}^I - a_A^I}{a_A^I} \times 100$. With the exception of MoS_2|SnS_2, all TMDCs show strains of less than 5%, indicating that the paired systems are well lattice-matched. The MoS_2|SnS_2 pairing has been included to see if larger values of strain have significant effects on the determined properties of superlattices.

6.4.4 Formation Energy

We evaluate the energy (per formula unit) required to form the superlattice, in both the pristine and intercalated systems. This has been calculated using $E_{form} = [E_{SL}^{P/I} - (E_A^{P/I} + E_B^{P/I})]/S$, with interface surface area S, energies of the superlattice, $E_{SL}^{P/I}$, and component TMDC materials, $E_A^{P/I}$ and $E_B^{P/I}$. Positive values of E_{form} indicate superlattices where it costs energy to combine the components, whereas negative values indicate superlattices in which it is energetically preferred for the components to be combined rather than exist as their respective bulk materials. These results are presented in Figure 6.4. Formation energies for most of the systems are small (remaining below 5 meV/Å^2), with several structures demonstrating negative formation energy. We generally see that systems

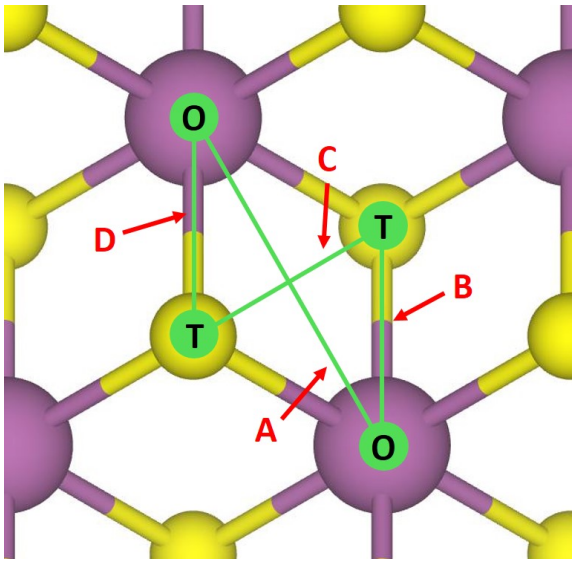

Figure 6.5: Different NEB routes (A, B, C, D) considered, between different octahedral (denoted 'O') and tetrahedral (denoted 'T') sites.

with lower strains result in more favourable formation energies, resulting in the most strained system ($MoS_2|SnS_2$) demonstrating the highest formation energy. Interestingly, the formation energy is reduced with the introduction of an intercalant, as highlighted with the $NiS_2|TiS_2$ system which has a formation energy of 2.23 meV/Å^2, which is reduced to 0.08 meV/Å^2 with lithium intercalation, and to -4.34 meV/Å^2 with magnesium intercalation.

6.5 Diffusion

We have performed climbing-image nudged elastic band (CI-NEB) calculations on each of the selected superlattice structures, along the routes indicated in Figure 6.5. In Figure 6.6 we show the results for lithium and magnesium intercalation into the $SnS_2|SnSe_2$ superlattice, with the equivalent results for the component TMDCs for easy comparison. Due to the global minimum of the intercalation site with octahedral coordination, we confirm the preference for intercalation into the octahedrally coordinated (O) site over the site with tetrahedral coordination (T), as was shown for the TMDCs in Chapter 3. We are also able to show that the preferred diffusion path for lithium and magnesium between two of these O sites is via a T site. This is due to the significantly smaller barrier than the one that arises from diffusion directly between two adjacent O sites.

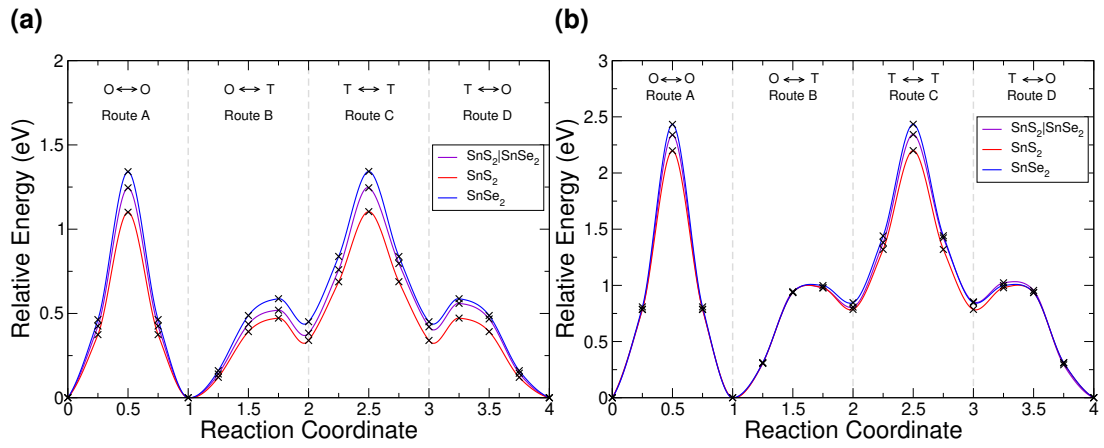

Figure 6.6: Nudged elastic band diffusion barriers for lithium (6.6a) and magnesium (6.6b) along unique routes in $SnS_2|SnSe_2$ (purple), SnS_2 (red), and $SnSe_2$ (blue). In the individual TMDCs, Route B and Route D are equivalent.

Generally, we note that the diffusion barrier for the superlattice is intermediate to the barriers arising from the component TMDCs. For example, the barrier to lithium (magnesium) diffusion along Route A is 1.25 eV (2.34 eV) in the superlattice, whereas it is 1.10 eV (2.20 eV) in SnS_2 and 1.34 eV (2.43 eV) in $SnSe_2$. Along Route B these values are 0.52 eV (1.00 eV) in the superlattice, 0.47 eV (1.00 eV) in SnS_2, and 0.59 eV (1.01 eV) in $SnSe_2$. Similarly along Route C these values are is 0.56 eV (1.03 eV) in the superlattice, 0.47 eV (1.00 eV) in SnS_2, and 0.59 eV (1.01 eV) in $SnSe_2$. In a single TMDC, diffusion Routes B and D are equivalent, and hence the diffusion barriers are identical. Due to the chemical and structural similarity of SnS_2 and $SnSe_2$, Routes B and D are very similar in Figure 6.6. However, other pairings which involve more dissimilar TMDCs demonstrate a greater asymmetry between these routes, the results of which we include in Appendix E.

Using the results of the CI-NEB calculations, we can also comment on the ionic rates of diffusion through the superlattices. We first note from Figure 6.6 that, whilst the T-site is higher in energy, the barrier between an O- and T-site is lower than the barrier between two O-sites. As to the rate of diffusion is governed by an Arrhenius equation, these asymmetries can lead to a significant bias to diffusion along different routes. Due to the exponential dependence on the diffusion barrier in the Arrhenius rate, the rate of diffusion through a superlattice (with the barrier being approximately the average of the two components) is lower than the aver-

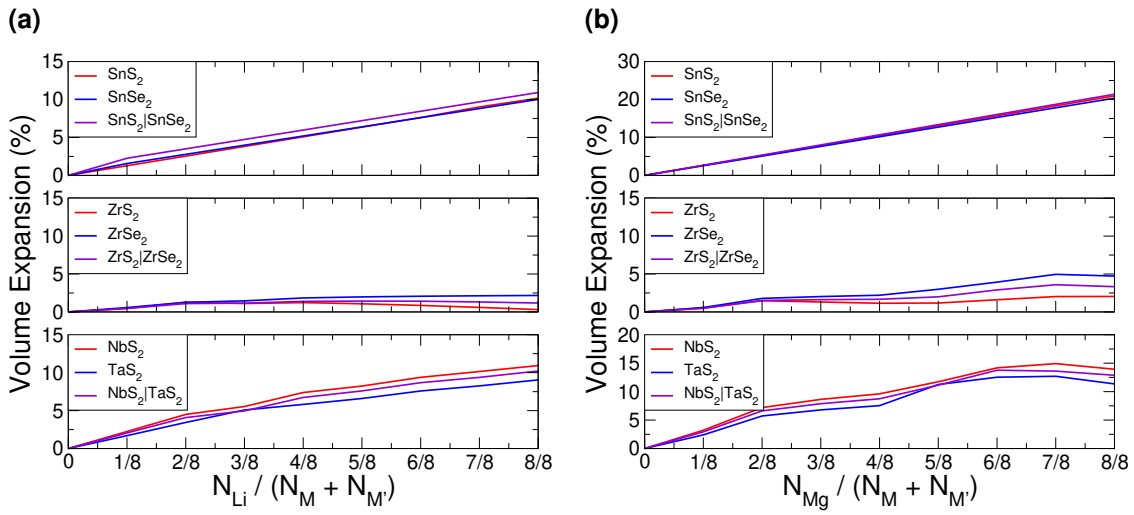

Figure 6.7: Volume expansion with intercalation for the selected TMDC superlattices, calculated with respect to the unintercalated structures using $\% = \frac{V-V_0}{V_0} \times 100$. Figure 6.7a presents the data for lithium intercalation, and Figure 6.7b presents the data for magnesium intercalation. In each of these, the x-axis gives the number of intercalant ions ($N_{Li/Mg}$) per metal atoms of the host structure ($N_M + N_{M'}$).

age of the rates of the two components, but faster than the rate of the component with the largest barrier.

6.6 Volumetric Expansion

One important metric for assessing the promise of a material for electrode applications is the volumetric expansion arising from intercalation. We calculate this expansion with respect to the unintercalated structure, using $\% = \frac{V-V_0}{V_0} \times 100$ for initial volume V_0 and final volume V. Importantly for electrode applications, we show that there is minimal volumetric expansion with intercalation of these superlattices, and highlight this with some examples inFigure 6.7. When intercalated with lithium (magnesium), we see that the $SnS_2|SnSe_2$ superlattice has a total volumetric expansion of 10.9% (21.4%), for $ZrS_2|ZrSe_2$ we see a total expansion of 1.8% (3.3%), and for $NbS_2|TaS_2$ we see a total expansion of 10.2% (12.9%). Thus, the minimal expansion demonstrated by layered materials holds upon formation of the superlattice, with most superlattices expanding by less than 20% (30%). These values compare well with other layered materials that have

demonstrated success as intercalation electrodes, including $LiCoO_2$ [277, 278] (2-3.25%), NMC [279] (8.44%), and graphite [280] (13.2%), as well as the $< 30\%$ seen for the TMDCs in general.

We note the surprising reduction in volume expansion of ZrS_2 as lithium content increases beyond $a = \frac{4}{8}$, and this behaviour extends to the superlattice structure. The same can be seen as magnesium content increases beyond $a = \frac{2}{8}$ (corresponding to the same amount of charge transfer to the host structure as $a = \frac{4}{8}$ of lithium), though the volume increases again for larger intercalant concentrations. We also notice in Figure 6.7b a larger increase in the volume for SnS_2 and TaS_2 with magnesium intercalation beyond $a = \frac{4}{8}$, and this behaviour carries over to the corresponding superlattices.

A closer evaluation shows that, for lithium intercalation, the volumetric expansions of the superlattices fall within 2% of the mean of the volumetric expansion for the relevant components. Thus, if the superlattice volumetric expansion were to be estimated by calculating the mean of the volumetric expansion arising in the component TMDCs, we could expect the result to deviate by up to a 2% error from what is observed in the actual superlattice. This close agreement is not surprising considering the vdW gaps between MX_2 layers.

We note a larger expansion upon magnesium intercalation than with lithium intercalation, and attribute this to the greater charge donation from magnesium than with lithium. This can be seen in Figure 6.7. For example, $SnS_2|SnSe_2$ expands by 10.69% when half-intercalated with magnesium, and 10.92% when fully-intercalated with lithium (hence having similar levels of charge donation). Similarly, $ZrS_2|ZrSe_2$ expands by 1.67% when half-intercalated with magnesium and by 1.18% when fully-intercalated with lithium, and $NbS_2|TaS_2$ expands by 8.74% when half-intercalated with magnesium and by 10.21% when fully-intercalated with lithium. We rationalise this as the chalcogen species in the intercalated structures have larger negative charges, and the metal species have smaller positive charges. Consequently, there is a reduced attraction between the M and X species but an increased repulsion between X species. This leads to a 'stretching' of the MX_2 layers along the c-axis. Comparable results are also seen for the other superlattices considered, further details of which are presented in Appendix E.

We note a larger expansion upon magnesium intercalation than with lithium intercalation, and attribute this to the greater charge donation from magnesium than with lithium. The chalcogen species in the intercalated structures have larger negative charges, and the metal species have smaller positive charges, and so there is a reduced attraction between the M and X species but an increased repulsion between X species. This leads to a 'stretching' of the MX_2 layers along the c-axis. Comparable results are also seen for the other superlattices considered. Further details of the volumetric expansion, along with comparisons to the component materials, are presented in Appendix E.

6.7 Voltages

In Figure 6.8, we present the voltage profiles and thermodynamic stability (indicated by E_{IS}) of the highlighted superlattices with lithium and magnesium intercalation. For easy comparison, we have also included the results of the relevant individual TMDCs which were presented in our previous work. In general, we find that the intercalation voltage of the formed superlattice is an intermediate of the profiles of the component materials. We highlight this best with lithium intercalation into the SnS_2|$SnSe_2$ superlattice: SnS_2 is shown to have a flat voltage profile at 1.80 V, and $SnSe_2$ has a flat voltage of 1.85 V, with a minor step at the start of intercalation ($0 < \mathrm{a} < 1$) of 1.89 V. The superlattice then shows an almost flat voltage of 1.83 V, intermediate in value to the those of the components in both shape and magnitude. It also presents the minor step at the start of the intercalation range with a value of 1.84 V, which is intermediate to the constant voltage of 1.80 V of SnS_2 and the 1.89 V shown by $SnSe_2$. We show a similar result for the NbS_2|TaS_2 superlattice with lithium intercalation, where the more distinct features of the NbS_2 and TaS_2 components are reproduced, maintaining the intermediate voltage profile.

For intercalation with magnesium, the same result is observed. We highlight this with the SnS_2|$SnSe_2$ and GeS_2|SnS_2 structures, again showing how the flat voltage profiles of the components result in a similarly flat voltage profile in the superlattices, and also show that the dramatic drop in voltage for high magnesium

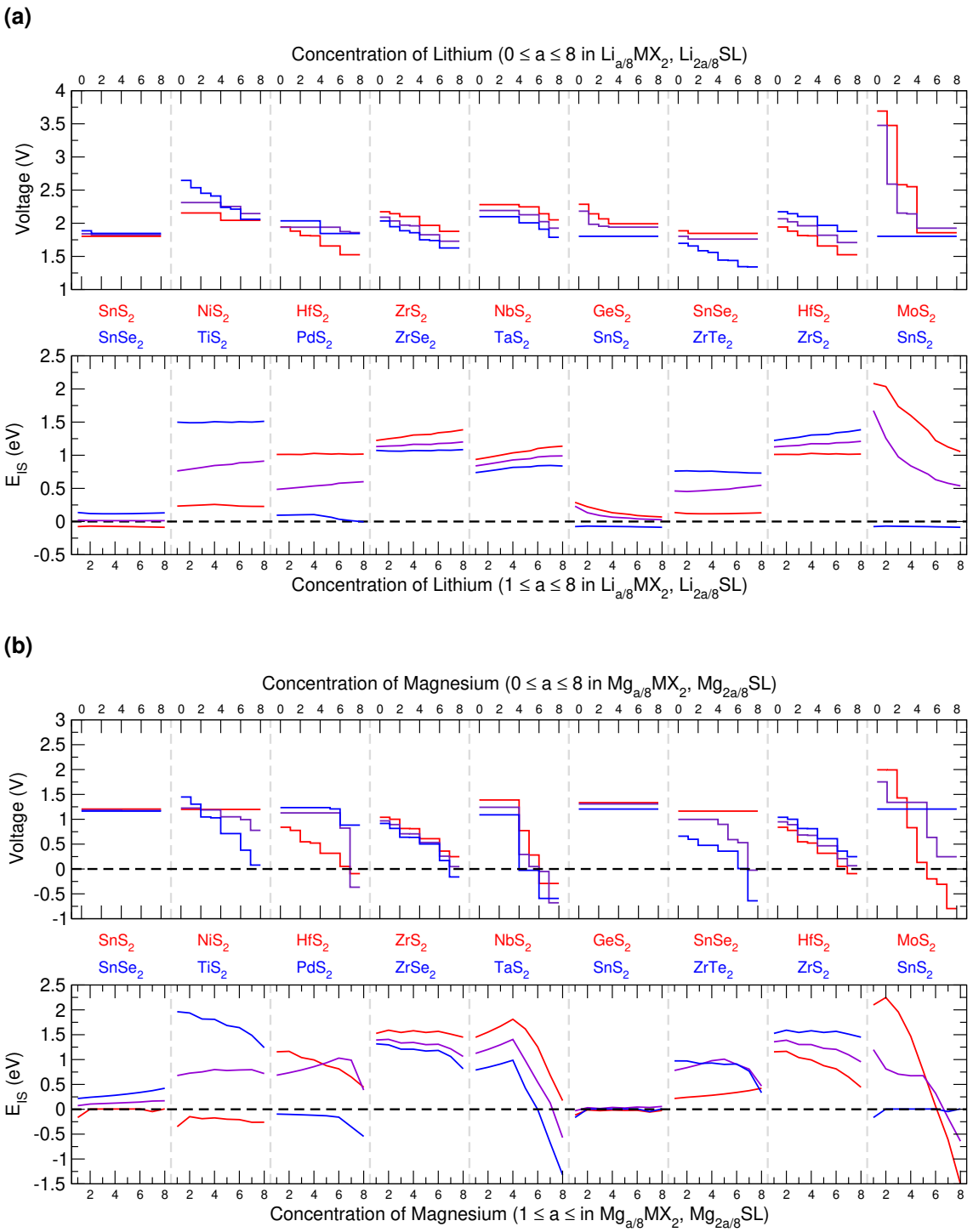

Figure 6.8: Intercalation voltages and E_{IS} for selected superlattices. 6.8a presents the results for lithium intercalation, and 6.8b presents the results for magnesium intercalation. In each of these, the top shows the voltage profile, and the bottom shows the variation of E_{IS} with intercalation. Superlattice data is presented in purple, and the data for the component materials is color-coded in red or blue.

concentrations in $ZrTe_2$ produces a similar drop in the voltage for high magnesium concentrations in the $SnSe_2|ZrTe_2$ superlattice. This $SnSe_2|ZrTe_2$ superlat-

tice also suggests an exciting use of superlatticing: whereas the drop seen for $ZrTe_2$ reaches a voltage of -0.64 V, the voltage drop demonstrated by the superlattice reaches a value of -0.02 V. Although this value is still negative, it suggests that the inclusion of the $SnSe_2$, a material which retains a constant voltage across the concentration range, limits the drop shown by the superlattice. The $HfS_2|ZrS_2$ further supports this: though the HfS_2 component shows a negative voltage at high concentrations, the superlattice retains a positive value due to the inclusion of the ZrS_2. This effect has been observed before, both using first principles methods [191] and experimentally [254].

Whilst there are some materials that deviate from this with voltages profiles that extend beyond the bounds of the component materials, such as with the lithium-intercalated $NiS_2|TiS_2$ and $MoS_2|SnS_2$, and the magnesium-intercalated $NbS_2|TaS_2$ and $MoS_2|SnS_2$, these deviations do not remove the underlying shape of the component materials. Further, comparing the average voltages of the superlattice with those of the components highlights that taking a simple average of the component materials is a reliable method to predict the voltage of the formed superlattice. These comparisons, along with the results of 41 other superlattice structures which show the same result are presented in Appendix E.

As mentioned above, electrode materials should ideally have a well-defined voltage [283], and so, based only on the voltage profiles in Figure 6.8a, pairings such as $MoS_2|SnS_2$ can be ruled out as a promising electrode material for lithium ion batteries. As one of the components has a large variation in the voltage, in this case MoS_2, the resultant voltage for the superlattice can also be expected to have large variation. Similarly, the magnesium-intercalation voltage profiles of $NbS_2|TaS_2$, $SnSe_2|ZrTe_2$, and $MoS_2|SnS_2$ vary significantly across the magnesium concentration range, due to the large variation of one or both of the component TMDCs. However, this does also suggest that a large variation seen for a TMDC can be reduced by pairing with a TMDC with a constant voltage profile. For example, TiS_2 varies by 0.59 V from across the concentration range considered here. However, when paired with NiS_2 (which varies by 0.11 V), the variation of the resultant $NiS_2|TiS_2$ superlattice is 0.17 V. Therefore, if a particular TMDC is desirable for use as an electrode, but possesses a voltage which varies

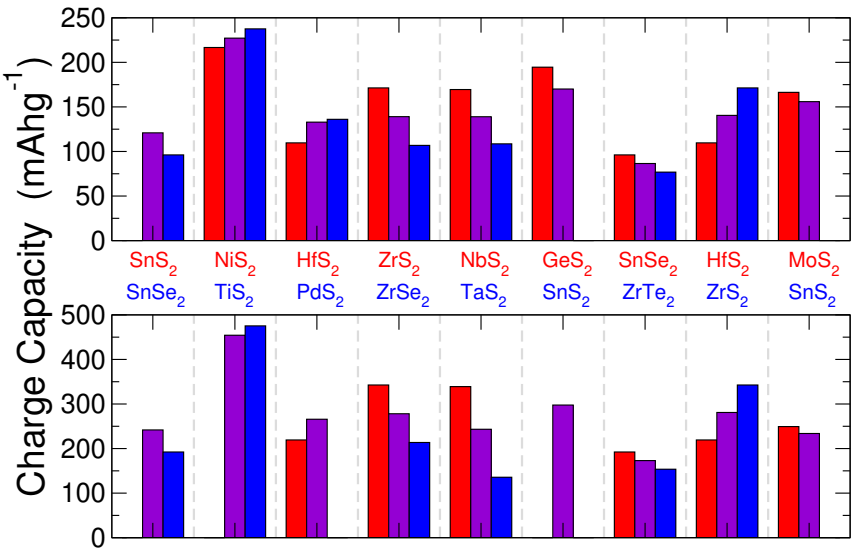

Figure 6.9: Reversible gravimetric charge capacity of selected superlattices and their component TMDCs for lithium (top) and magnesium (bottom) intercalation. Superlattice results are presented in purple, and the corresponding results for component materials are presented in red and blue. Missing bars indicate materials with zero reversible capacity.

significantly, its voltage could be 'pinned' by pairing it with a suitable partner.

The intercalation voltage of anode materials should be lower than 2 V, ideally in the range 0.5-1.5 V [283], and for cathode materials it should exceed 3 V [284]. As the pairing of two TMDCs results in a voltage that is intermediate to them both, it would only be sensible to combine materials that are energetically alike. For anodes two TMDCs with low voltages should be combined, and for cathodes two TMDCs with high voltages should be combined. If a low voltage TMDC (e.g. SnS_2 with a voltage of 1.80 V) were to be combined with a high voltage TMDC (e.g. ScS_2 with a voltage of 3.66 V [230]), the voltage of the superlattice (e.g. 2.69 V, see Appendix E) would be poor for both anode and cathode applications.

6.8 Thermodynamic Stability

The values of E_{IS} for a range of intercalant concentrations within the superlattices are also shown in Figure 6.8a and Figure 6.8b. As was demonstrated with the evolution of the intercalation voltage with concentration, the evolution of E_{IS}

with intercalant concentration follows a trend that is an intermediate of the two component materials, and the value of E_{IS} of a superlattice at a given concentration is well approximated by calculating the average of the component materials. This suggests that, as E_{IS} is an indicator of the thermodynamic stability of a given TMDC against conversion, a highly stable material (characterised by a high, positive value of E_{IS}) can be paired with a material that is susceptible to conversion (characterised by a low or negative value of E_{IS}) to make a superlattice that is also resistant to conversion. This is shown with pairings $SnS_2|SnSe_2$, $GeS_2|SnS_2$, and $MoS_2|SnS_2$ with lithium intercalation. In each of these, SnS_2 is the component with a negative value of E_{IS} across the range of lithium concentration. However, the formed superlattices have positive values of E_{IS}, indicating the stability that has arisen from the inclusion of a thermodynamically stable component. We see the same result of a conversion-resistant component stabilising a conversion-susceptible component with pairings $NiS_2|TiS_2$ and $HfS_2|PdS_2$ for magnesium intercalation.

The importance of this result is further highlighted by consideration of the gravimetric charge capacity, a quantity that is crucial for characterising a material for electrode applications. We have used the range over which E_{IS} has a positive value to calculate the reversible gravimetric charge capacities for each of the superlattice structures, which are presented in Figure 6.9, along with the capacity of the component materials for easy comparison (see Chapter 3). Aside from the improvements in stability, we can also expect improvements in the capacity simply due to the inclusion of a lighter material. For example, hafnium is a Period-VI element and so the specific capacity of 109.7 $mAhg^{-1}$ for lithium intercalation (219.4 $mAhg^{-1}$ for magnesium intercalation) is relatively low despite it possessing positive values of E_{IS} across the intercalation range. However, combining with a TMDC composed of a lighter transition metal, such as ZrS_2 in $HfS_2|ZrS_2$, increases this to 140.5 $mAhg^{-1}$ (281.0 $mAhg^{-1}$). Further, superlattice formation can in some cases provide a reversible charge capacity that is better than either of the components. This is highlighted with the intercalation of $SnS_2|SnSe_2$: SnS_2 is shown to be susceptible to conversion reactions, and so the capacity is zero. However, combination with $SnSe_2$ (which possesses a positive E_{IS} for both intercalants) results in a capacity of 120.9 $mAhg^{-1}$ (241.8 $mAhg^{-1}$). We can therefore

improve not just the voltage (through 'pinning') and thermodynamic stability (by increasing E_{IS}) of a TMDC through superlatticing, but also the gravimetric charge capacity.

6.9 Elastic Properties

Here we present the elastic properties of the superlattices that we highlight. We find each to possess a trigonal symmetry, and so the only unique non-zero elements are c_{11}, c_{12}, c_{13}, c_{33}, c_{44}, c_{14}, and c_{66}. We find that most of the pristine, lithium-intercalated, and magnesium-intercalated structures are elastically stable, by assessing the Born stability criteria outlined in Chapter 4 However, we find that magnesium-intercalated $HfS_2|PdS_2$ is elastically unstable, breaking the same conditions that are broken by magnesium-intercalated PdS_2. Further, magnesium-intercalated $MoS_2|SnS_2$ is also found to be elastically unstable (breaking the requirements of $c_{11} > |c_{12}|$ and $c_{14}^2 < \frac{1}{2}c_{44}(c_{11} - c_{12}) = c_{44}c_{66}$) despite neither of its components being elastically unstable. This could be due to the larger strain on each of these systems ($> 5\%$) compared to the other superlattices.

In Table 6.1, we present the polycrystalline bulk (B), shear (G), and Young's (Y) moduli for each of the superlattice structures. We also include the Poisson (ν) and Pugh (R) elastic ratios which are commonly used to describe the ductility of a material. A ductile material typically has a Poisson ratio greater than 0.26, and Pugh ratios greater than 1.75. Each of these quantities has been calculated using the elastic matrices presented above and the Voigt-Reuss-Hill average scheme. With the exception of $SnS_2|SnSe_2$, we find that the bulk modulus of the superlattice is increased with the introduction of an intercalant, with a larger increase seen for lithium than for magnesium intercalation.

A|B	Intercalant	B (GPa)	G (GPa)	Y (GPa)	ν	R
SnS_2|$SnSe_2$	-	96.73	30.53	82.87	0.36	3.17
	Li	44.51	19.26	50.49	0.31	2.31
	Mg	61.31	31.11	79.82	0.28	1.97
NiS_2|TiS_2	-	45.67	31.27	76.38	0.22	1.46
	Li	54.78	41.29	99.00	0.20	1.33
	Mg	97.12	49.21	126.31	0.28	1.97
HfS_2|PdS_2	-	38.37	26.24	64.10	0.22	1.46
	Li	65.02	32.81	84.26	0.28	1.98
	Mg*	79.24	-16.55	-53.38	0.61	-4.79
ZrS_2|$ZrSe_2$	-	33.08	22.67	55.36	0.22	1.46
	Li	63.04	43.43	105.95	0.22	1.45
	Mg	95.56	53.11	134.42	0.27	1.80
NbS_2|TaS_2	-	42.39	27.02	66.86	0.24	1.57
	Li	85.55	48.11	121.54	0.26	1.78
	Mg	121.46	62.82	160.74	0.28	1.93
GeS_2|SnS_2	-	34.30	20.93	52.19	0.25	1.64
	Li	49.38	17.14	46.08	0.34	2.88
	Mg	69.08	38.39	97.17	0.27	1.80
$SnSe_2$|$ZrTe_2$	-	26.61	16.13	40.27	0.25	1.65
	Li	39.45	23.94	59.73	0.25	1.65
	Mg	47.38	10.67	29.76	0.40	4.44
HfS_2|ZrS_2	-	36.05	24.68	60.29	0.22	1.46
	Li	70.61	47.71	116.82	0.22	1.48
	Mg	109.82	62.36	157.31	0.26	1.76
MoS_2|SnS_2	-	37.94	26.89	65.25	0.21	1.41
	Li	64.14	35.48	89.86	0.27	1.81
	Mg*	76.57	3.21	9.48	0.48	23.89

Table 6.1: Elastic properties for each of the pristine and intercalated superlattices highlighted in this Chapter. These have been calculated using the Voigt-Reuss-Hill average scheme. Materials marked with an asterisk (*) are elastically unstable.

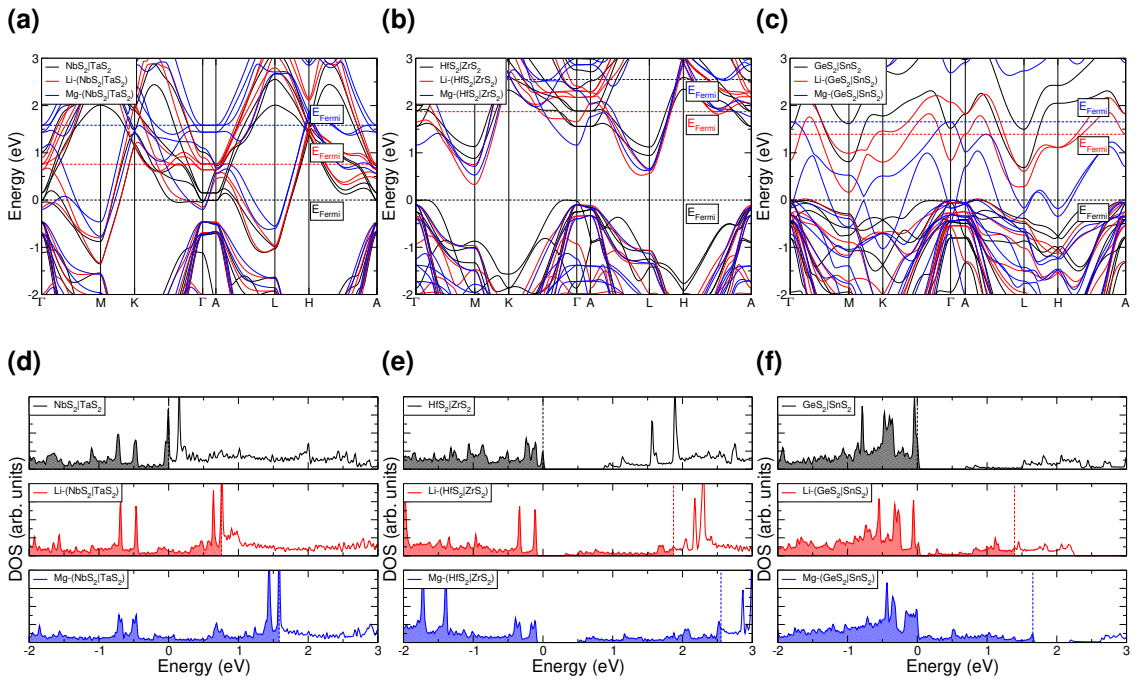

Figure 6.10: Electronic band structures and density of states (DOS) for pristine and intercalated superlattice structures. $NbS_2|TaS_2$ data is presented in 6.10a and 6.10d, $HfS_2|ZrS_2$ in 6.10b and 6.10e, and $GeS_2|SnS_2$ in 6.10c and 6.10f. Pristine data is presented in black, data for lithium-intercalated structures in red, and data for magnesium-intercalated structures in blue. Each has been aligned with high energy occupied states of the pristine superlattice material. The energy of the Fermi level ($\mathrm{E_{Fermi}}$) is indicated with dashed lines.

6.10 Electronic Structure

One of the main reasons the TMDCs have received a lot of attention in recent years is for the wide range of electronic properties the family can exhibit, and their superlattices/heterotructures have been of further interest for the electronic physics that can arise from the combination of two materials [264, 400]. For electrode applications, materials with an electronically-conductive nature are preferred so that compensating electrons from an external circuit can balance the positively-charged lithium/magnesium ions. However, the introduction of ionic species into the host structure dramatically changes the nature of inter-layer bonding, and consequent changes to the electronic structure can be expected. Here, we investigate how the electronic structure of superlattice structures change with intercalation.

We find that the electronic structure of a superlattice can crudely be obtained by superimposing the electronic structures of the constituent TMDC materials. As a result, combining TMDCs which offer a relative type II band alignment (staggered gap) results in a superlattice with a band gap that is smaller than either of the components, and combination of a metallic TMDC with a TMDC which possesses a band gap results in a superlattice that is also metallic. Though exact band gap values can be sensitive to the choice of functional and the level of strain induced from lattice matching, this observation agrees with many previous works [264] and shows that construction of a superlattice provides a simple method through which the electrical conductivity can be improved.

The introduction of ionic species into the host structure dramatically changes the nature of inter-layer bonding, however, and consequent changes to the electronic structure can be expected. Here, we investigate how the electronic structure of superlattice structures change with intercalation. In Figure 6.10 we present the electronic band structures and corresponding density of states (DOS) for $NbS_2|TaS_2$ (6.10a and 6.10d), $HfS_2|ZrS_2$ (6.10b and 6.10e), and $GeS_2|SnS_2$ (6.10c and 6.10f). These show the electronic structure for the unintercalated superlattices, along with the limit of lithium and magnesium intercalation corresponding to one intercalant per metal atom in the host supercell. Due to the presence of intercalants and local charge transfer leading to local electric fields, it is not possible to align these band structures using typical means of core-state alignment [262] or with respect to the vacuum level [262–264]. Instead, we have qualitatively aligned to the high-energy occupied states of the unintercalated superlattice at Γ, allowing us to comment on the relative position of the Fermi level.

We identify several broad groups describing what happens with the electronic behaviour: the superlattice either i) retains a conductive nature with intercalation, ii) undergoes a transition from semiconductor to conductor, iii) possesses an insulating nature before intercalation and at the $b = 2$ intercalation level, or iv) undergoes a transition from conductor to semiconductor. The superlattice $NbS_2|TaS_2$ is an example of group i), possessing no band gap at the start and end of intercalation. We can see from Figure 6.10a that this is due to the Fermi lying in the middle of a linear band that extends from -0.5 eV at M to 2.5 eV between K and Γ. Elec-

trons that are transferred from the intercalants to the host then simply occupy the unoccupied states in this band, and so the Fermi level progressively rises. Due to the greater charge transfer with magnesium, the Fermi level is raised to a higher level than with lithium. For $HfS_2|ZrS_2$, an example of group ii), we see a very similar behaviour, but the presence of an initial band gap means that there is a much larger initial jump in the position of the Fermi. However, the continuous range of bands beyond this allows for a gradual rise in the Fermi level as was seen for group i). This is presented in Figure 6.10b. Figure 6.10c then shows the electronic structure for the $GeS_2|SnS_2$ superlattice and its intercalated forms, where we see the pristine structure possesses a band gap of ~ 0.6 eV. Upon lithium intercalation, the Fermi shifts to intersect the two lowest-energy unoccupied states of the pristine structure, becoming metallic as with a type ii) material. However, intercalation with magnesium (and, it is expected, further intercalation with lithium), these states become fully occupied, and the Fermi level then sits at the bottom of a further band gap.

As there is minimal change to the electronic structure of component TMDCs upon formation of a superlattice/heterostructure [264, 400], the behaviour of superlattices described above is very similar to what has been observed for the component materials.

6.11 Charge Analysis

We compare the Bader charges for the lithium-intercalated (Figure 6.11a) and magnesium-intercalated (Figure 6.11b) systems. Surprisingly, whilst there is more charge transfer than is seen with the pristine systems, this remains relatively small. However, some systems, for example lithium-intercalated $NbS_2|TaS_2$ and magnesium-intercalated $HfS_2|PdS_2$, show significant charge transfer between the component layers. The intercalants themselves maintain almost constant charges, as has been shown for intercalation into the individual TMDCs. Across the different superlattices, the charge of lithium varies between $0.87-0.88$, and magnesium varies between $1.65-1.67$. Specific values are presented in Appendix E.

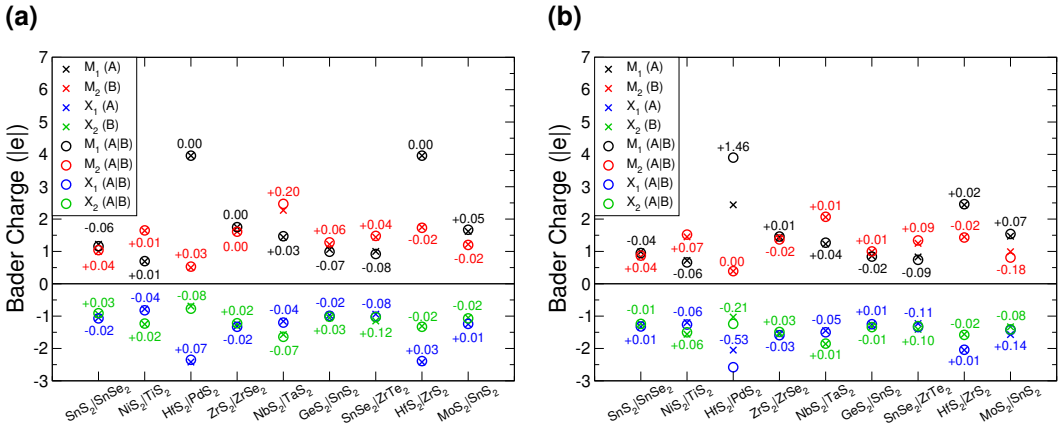

Figure 6.11: Bader charges for the different metal and chalcogen species in superlattices and the relevant component TMDCs, when intercalated with lithium (6.11a) and magnesium (6.11b). The included numbers indicate the difference in charge between the superlattice and individual TMDC components, $Q^{SL} - Q^{TMDC}$.

To supplement the results of the Bader charge analysis, we have also considered the differences in the charge density arising from intercalation: Whilst maintaining the positions of the constituent atoms, the electronic charge densities were obtained, and compared using $\Delta\rho = \rho_{\mathrm{LiSL}} - [\rho_{\mathrm{Li}} + \rho_{\mathrm{SL}}]$. We present in Figure 6.12 the planar-averaged values of $\Delta\rho$ for the $SnS_2|SnSe_2$ superlattice intercalated with lithium (Figure 6.12a) and magnesium (Figure 6.12b). The results for the component SnS_2 and $SnSe_2$ structures have also been included.

For $SnS_2|SnSe_2$, the tin atoms (purple) are positioned at $c = 0.25$ and $c = 0.75$, the chalcogen (yellow sulfur, green selenium) atoms are positioned at c values ± 0.125 either side of these, and the intercalant species (orange) are positioned at $c = 0$ (periodic image at $c = 1$) and $c = 0.5$. For both lithium and magnesium, we see significant electron depletion from the intercalant regions (at $c = 0, 0.5, 1$) as these species donate electrons to the parent superlattice structure. This charge is seen to accumulate in the bonding regions between chalcogen and intercalant. Due to this additional charge on the chalcogen species, the electrons used in the M-X bond are able to redistribute back to the host metal. This is seen with a depletion of electronic charge between the metal and chalcogen ($c = 0.15 - 0.20, c = 0.30 - 0.35, c = 0.65 - 0.70, c = 0.80 - 0.85$), and by a charge donation to the metal. We find that charge transfer to each of the layers in the superlattice closely matches the charge transfer seen for the respective TMDC on its own. For example, with

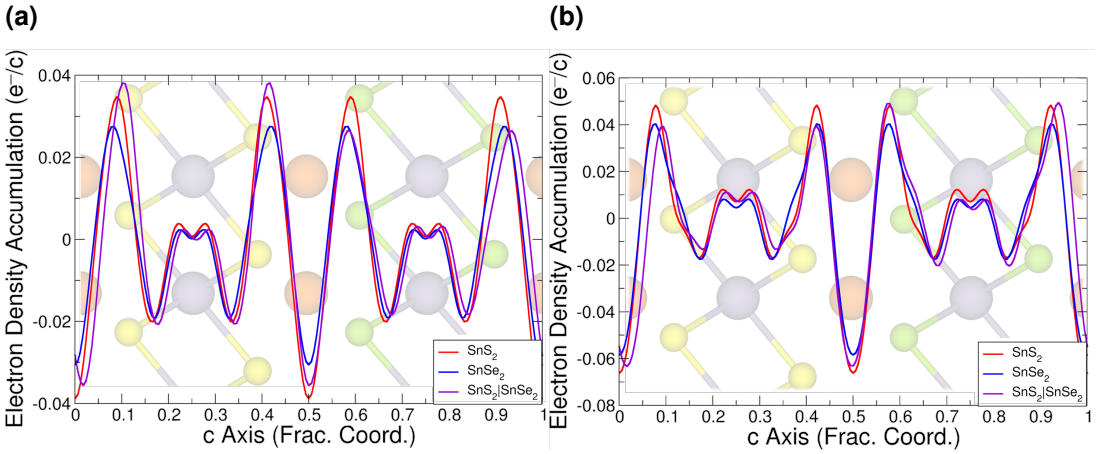

Figure 6.12: The planar-average of $\Delta\rho = \rho_{\mathrm{LiSL}} - [\rho_{\mathrm{Li}} + \rho_{\mathrm{SL}}]$ for the $SnS_2|SnSe_2$ superlattice (and the component materials) intercalated with lithium (6.12a) and magnesium (6.12b). Positive values correspond to regions of electron accumulation, and negative values correspond to regions of electron depletion. The corresponding structure is overlayed on these plots, with purple tin atoms, yellow sulfur, green selenium, and orange intercalant.

magnesium intercalation, the charge transfer from the intercalated magnesium to the SnS_2 layer of the superlattice (Figure 6.12b, purple line, $c = 0 - 0.5$) very closely resembles the profile of charge transfer seen for magnesium intercalation into SnS_2 (same figure, red line).

We continue our discussion of charge analysis in Figure 6.13a and Figure 6.13b, which depict 3D visualisations of this charge transfer for lithium and magnesium intercalation, respectively. The isosurfaces chosen are the chosen by the ratio of intercalant Bader charges ($\frac{q_{Mg}}{q_{Li}} = \frac{1.65}{0.88}$). In Figure 6.13c, we further show a 2D slice through this charge difference along the (1 1 0) plane, passing through host metal atoms, chalcogen atoms, and the intercalated lithium. In each of these 2D and 3D visualisations, red isosurfaces show electron depletion and blue isosurfaces show electron accumulation. These offer further detail of the structure of the charge transfer, and show the similarity for both lithium and magnesium intercalation. We find a very similar results to those presented in the above discussion for the other superlattices, examples of which have been presented in Appendix E.

As the charge transfer upon formation of the superlattice remains small, and the charge transfer that follows the inclusion of an intercalant mirrors the transfer that

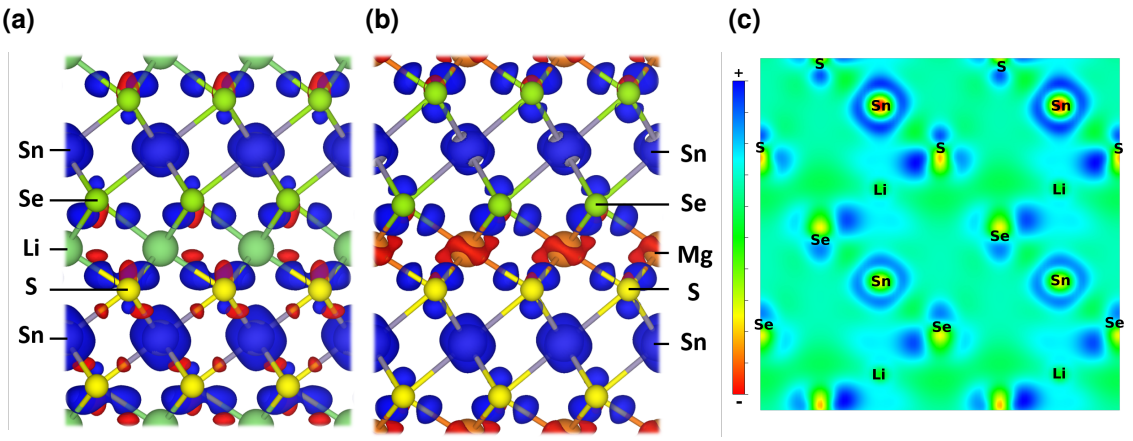

Figure 6.13: The 3D visualisation of this charge transfer in $SnS_2|SnSe_2$ is shown in 6.13a and 6.13b for lithium (isosurface 2.5 $me^{-}/Å^3$) and magnesium (isosurface 4.7 $me^{-}/Å^3$) intercalation, respectively. 6.13c shows a 2D slice through the (1 1 0) plane of the Li-($SnS_2|SnSe_2$) charge-difference distribution. Red isosurfaces show electron depletion and blue isosurfaces show electron accumulation.

arises in each of the constituent TMDC layers, it is therefore clear as to why the superlattice energetics (i.e. the intercalation voltage and the stability metric of E_{IS}) take on intermediate values to those of the component TMDCs.

6.12 Summary

In this Chapter, we have presented the results of an investigation of intercalation into transition metal dichalcogenide superlattices with both lithium and magnesium. Though we established the electrode properties of the individual TMDCs in Chapter 3, the question remained as to how these properties would change when combined, as indicated by Figure 6.14. Such composite materials have received much attention in recent years due to the advent of synthesis methods allowing for nanoscale control. We have therefore extended the work of Chapter 3 to explicitly consider such structures.

The volumetric expansion, electronic structure, intercalation voltages, and thermodynamic stability determined through phase diagrams have all been considered as the information they provide is essential for the consideration of materials for use as an electrode. Upon formation of a superlattice, we find that many of

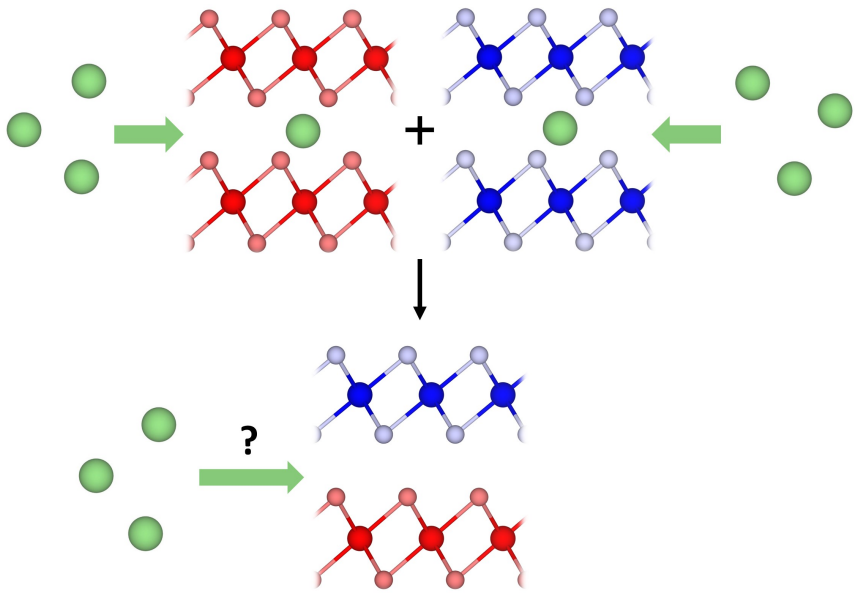

Figure 6.14: Summary of the work presented in this Chapter.

these properties can be well approximated through consideration of the equivalent property for the component layers. For example, if the superlattice volumetric expansion were to be estimated by calculating the mean of the volumetric expansion arising in the component TMDCs, we could expect the result to deviate by up to a 2% error from what is observed in the actual superlattice, and the voltage profiles of the component materials provide bounds to the voltage profile exhibited by the constructed superlattice. Further, the unoccupied states of the host material are progressively filled with the addition of an intercalant, which follows the behaviour observed with the individual TMDCs. Most interestingly, the formation of superlattices allows for many improvements to component materials: formation of a superlattice results in a reduction of the electronic band gap, improving electronic conductivity; conversion-resistant materials can be used to increase the stability of conversion-susceptible materials, extending their cyclability and lifetime; and materials can be chosen such that the overall voltage can be tuned towards specific values.

The conclusions presented in this Chapter should also extend to other layered materials. In particular, the layered transition metal oxides offer a group of materials that are very closely related to the TMDCs used to construct the superlattices here, and have already demonstrated success as electrodes. Using the ideas used here, however, they could have their voltages tuned, their intercalation

stability improved, and ultimately have an increased energy storage capacity.

Chapter 7

Outlook

"I have only made this letter longer because I have not had the time to make it shorter."

Blaise Pascal, 1657

7.1 Summary

In this work, *ab initio* density functional theory methods have been used to assess the suitability of layered transition metal dichalcogenides and their superlattices as intercalation electrodes in lithium-ion and beyond-lithium-ion batteries. Chapter 1 provided the key methods of energy storage and how these have been utilised in technology and society thus far, with particular focus being given to the function and development of modern intercalation batteries. In Chapter 2 we then outlined the core physics and mathematical tools often used in electronic structure calculations, and provided a more focused discussion of the first principles methods utilised throughout this thesis.

Whilst numerous studies have shown that layered materials (and in particular, the TMDCs) offer much promise as rechargeable intercalation electrodes, with large electrochemically active surface areas, high capacities, and good cycling stability, much of the family is yet to be explored. There was a clear need for a comprehensive study of the key electrode properties, such as the volume expansion, the voltage, and the reversible intercalation capacity. With this in mind, in Chapter 3 we

presented a first principles investigation of lithium- and magnesium-intercalation into each of the layered transition metal dichalcogenides to explore such these metrics. Comparison of the two commonly observed layered TMDC polymorphs showed that the T-phase is typically the preferred phase, but that phase changes could be induced with intercalation, particularly for the Group IV, V, and VI materials. We were able to demonstrate that the layered structure ensured generally low volume expansions, and characterised the intercalation voltage profile for each of the materials. Using thermodynamic phase diagrams, constructed around the stability of the host against conversion reactions, we were able to provide an estimate of the reversible capacity, a key indicator for the energy storage and the lifetime. We showed that most TMDCs are stable with lithium intercalation, though this stability is reduced for magnesium intercalation due to the extra charge of the intercalant. Assessment of the material electronic structures showed that most of the TMDCs retain a conductive nature across the range of intercalant concentrations considered, though some materials do become insulating at concentrations of $a = 1$ in Li_aMX_2 or Mg_aMX_2.

We identified TMDC sulfides to be the best in general for lithium intercalation, highlighting the Group IV, V, and VI in particular for their low volumetric expansion, moderate intercalation voltages, and high stability against conversion reactions. In particular, ScS_2 and YS_2 were identified as promising cathode materials, offering high voltages close to 4 V and high intercalation stability allowing for theoretical capacities of 243.99 $mAhg^{-1}$ and 173.91 $mAhg^{-1}$, respectively. Finally, we also suggested that the Group VIII and IX materials are also worthy of further investigation. For magnesium intercalation, we demonstrated that the early transition metals offer the best performance as anodes, but also show that many other materials show ideal voltages and sufficient thermodynamic stability over a significant concentration range.

In Chapter 4, we extended the work of Chapter 3 to explore the elastic and mechanical properties of the TMDCs. Such properties play an important role in many industrial applications, but are particularly important for the cycling of electrodes in a working cell. We therefore presented a first-principles study into the elastic behaviour of layered TMDCs and their lithium- or magnesium-intercalated struc-

tures. Assessment of the elastic matrices allow us to evaluate key properties such as the bulk, shear, and Young's moduli. These showed a general increase with the addition of an intercalant species, though TMDCs composed of late-Group transition metals break this trend. We also assessed elastic ratios which describe the ductility of a material, allowing us to conclude that the pristine materials are brittle, but become more ductile with the addition of lithium or magnesium. The anisotropy of these materials was also assessed using a combination of the universal anisotropy metric and a direct calculation of the angular dependence of the Young's modulus. The pristine van der Waals materials demonstrated a high degree of anisotropy due to their relatively weak interactions across the vdW spacing, but the introduction of an ion within the vdW region reduced this anisotropy. Finally, we have also explored intermediate intercalant concentrations on elastic properties for selected systems, where we conclude that different intercalant configurations or the use of multivalent intercalant species can cause significant deviations from commonly-used linear extrapolations.

The growing demand for high efficiency portable batteries has prompted a deeper exploration for alternative cathode materials. From the results of Chapter 3 and Chapter 4, we highlighted ScS_2 as a particularly promising cathode candidate. Due to low Earth abundance, scandium has not received much attention, however its low atomic mass makes it ideal for high gravimetric capacity electrodes. In Chapter 5 we performed a comprehensive first-principles study to assess the performance of layered ScS_2 as a potential cathode for lithium-ion and beyond-lithium-ion batteries. We explored the configuration space of ScS_2 and its intercalated compounds using a mix of machine learning and *ab initio* techniques, finding the ground state geometry to be layered in nature. This layered structure is found to have a high voltage, reaching above 4.5 V for Group I intercalants, ideal volume expansions below 10% for lithium and magnesium intercalation, is electronically conductive, and is ductile once intercalated. Of the intercalants considered, we find that lithium is the best choice for cathode applications, for which we have used a combination of thermodynamic phase diagrams, *ab intio* phonon calculations, and evaluation of the elastic tensor to conclude that ScS_2 possesses a reversible capacity of 182.99 $mAhg^{-1}$, on par with current state of the art cathode materials such as $LiCoO_2$, NMC, and NCA. Finally, we substitute foreign metal

species into the ScS_2 material to determine their effect on key cathode properties, but find that these are overall detrimental to the performance of ScS_2. This does, however, highlight the potential for improvement if scandium were mixed into other layered systems such as the layered transition metal oxides.

Following the work of the previous Chapters, we presented in Chapter 6 a first principles investigation of the properties of superlattices made from transition metal dichalcogenides for use as electrodes in lithium-ion and magnesium-ion batteries. From of a study of 50 pairings, we were able to show that, in general, the volumetric expansion, intercalation voltages, and thermodynamic stability of vdW superlattice structures can be well approximated with the average value of the equivalent property for the component layers. Further, we were also able to show that the band gap can be reduced, improving the electronic conductivity. Thus, we conclude that superlattice formation can be used to improve material properties through tuning of intercalation voltages towards specific values, and by increasing the stability of conversion-susceptible materials. For example, we demonstrate how pairing SnS_2 with systems such as MoS_2 can change it from a conversion to an intercalation material, thus opening it up for use in intercalation electrodes.

7.2 Future Work

Many of the points and ideas presented in this thesis warrant further investigation. The work presented in Chapter 3 considered the 'perfect' TMDC structures. Of course, when fabricated and when cycled in real devices such perfect structures are not always guaranteed. Indeed, defects such as vacancies or impurities can be present and could offer some modification to the material operation. Whilst the effects of these defects on, for example, the voltage and volumetric expansion could be expected to be small, they could reduce the structural and chemical stability of a TMDC such that it degrades/degrades quicker with repeated cycling. Before utilisation of any material presented in the study, then, a thorough investigation of likely and possible defects and how the electrode properties can change should be completed. In a similar vein, the formation of a surface (as would be

required when constructing a finite electrode) should also be considered. Such surfaces could also be investigated for use with a complimentary electrolyte or with a resulting solid-electrolyte interphase. Though possible to complete such investigations using the first principles methods used in this thesis, methods beyond DFT would likely be more appropriate due to the inclusion of organics and/or ionic liquids.

The motivation behind Chapter 4 was to allow for study of materials using methods based on solid-state diffusion and continuum mechanics. We therefore hope for the results presented in the Chapter to be used in models beyond the atomic scale. The work in this Chapter looked at the mechanical properties of these materials and how they change with intercalation. An alternative approach to complete such an investigation would be through the study of the material phonon band structures. We commented that this has not been done in an exhaustive manner here because of the higher computational demand, however such a study would be interesting for comparison to the result obtained here. Further, it would allow for further development into the thermal conductivity of these materials and how this evolves with intercalation. Not only is this another crucial assessment that should be made for the cycling of electrode materials, but would also be of interest for other areas of materials science and energy materials, such as for the thermoelectrics community.

Whilst scandium dioxide does not exhibit the layered structure, in Chapter 5 we suggested the mixing of scandium into transition metal oxides that are layered to modify the voltage, stability, and other electrode properties, similar to what has been done with the mixing of nickel, manganese, and cobalt in NMC compounds. As scandium disulfide was shown to offer many desirable properties, and we see a smooth evolution of these properties with metal mixing, we proposed that the mixing of scandium into the transition metal oxides may be able to benefit to other materials that have successfully performed as cathode materials. However, the primary extension for the work presented in Chapter 5 is through experimental verification.

In Chapter 6 we only considered vertical superlattices. However, there has been recent interest in the formation of lateral heterotstructures and Janus structure,

where the chemical composition changes within a single TMDC layer. Other layered materials beyond the TMDCs should also be investigated with the conclusions of Chapter 6 in mind, to verify whether the same 'averaging' rule extends to other materials, and whether the properties of such materials can be similarly optimised. Though we expect these trends to extend to other layered materials, the question as to whether this rule is broken and the physics around that could be of interest to those interested in layered materials and their composites. We have also only considered superlattices consisting of lattice-matched materials. Due to the vdW interactions between layers, this is not a restriction in reality, with lattice mismatches being allowed and can result in Moiré structures. Such structures are also worth exploring, where we expect a minor modification to the averaging rule as the relative intercalant concentrations would be different for two component materials.

Appendix A

Supplementary Information to Chapter 2

A.1 Born-Oppenheimer Approximation

Here, we present a more detailed discussion of the origins and validity of the Born-Oppenheimer approximation. If we consider the many body problem discussed above, we have a system of electrons and nuclei. For brevity in the following, we will denote the set of nuclear coordinates $\{\mathbf{R}\}$ as X, and the set of electronic coordinates $\{\mathbf{r}\}$ as x. Due to the much larger masses, and hence much lower speeds, of the nuclei, the associated kinetic energy of the nuclei is much smaller than the kinetic energy associated with the electrons. As such, we can consider the reduced Hamiltonian $\hat{H}_0$ for electrons for fixed nuclei, $\hat{H}_0$,

$$\hat{H}_0 = \hat{T}_{el} + \hat{V}_{el-el} + \hat{V}_{el-ion} + \hat{V}_{ion-ion}, \tag{A.1}$$

where we have separated out the terms of the Hamiltonian corresponding to the electron kinetic energy ($\hat{T}_{el}$), the electron-electron interaction potential ($\hat{V}_{el-el}$), the electron-ion interaction potential ($\hat{V}_{el-ion}$), and the ion-ion interaction potential ($\hat{V}_{ion-ion}$) as in Chapter 2. The actual Hamiltonian of the system can then be written as $\hat{H} = \hat{H}_0 + \hat{T}_{ion}$, for which solutions can be found by considering the ionic kinetic energy $\hat{T}_{ion}$ a perturbation (so long as it is small) upon the Hamiltonian $\hat{H}_0$.

For a perturbative approach, we use the expansion parameter $\kappa = (\frac{m}{M_0})^{\frac{1}{4}}$ [417–

419], for electronic mass m and nuclear reference mass M_0, which can be either the average mass of the nuclear system, or any one of the nuclear masses. This will be useful later on, when we consider the kinetic energy term for the ions as a perturbation. If we let

$$\hat{H}_1 = \sum_I \frac{M_0}{M_I} \frac{\hat{\mathbf{P}}_I^2}{2m}, \tag{A.2}$$

for ionic index I, then,

$$\hat{T}_{ion} = \kappa^4 \hat{H}_1 = -\sum_I \frac{\hbar^2}{2M_I} \frac{\partial^2}{\partial X^2}, \tag{A.3}$$

with

$$\hat{H}_1 = -\sum_I \frac{M_0}{M_I} \frac{\hbar^2}{2m} \frac{\partial^2}{\partial X^2}, \tag{A.4}$$

and the total Hamiltonian has the form,

$$\hat{H} = \hat{H}_0 + \kappa^4 \hat{H}_1. \tag{A.5}$$

The Schrödinger equation for the total system is,

$$(\hat{H}_0 + \kappa^4 \hat{H}_1 - \epsilon)\Psi = 0. \tag{A.6}$$

As $\kappa \to 0$, we recover the Schrödinger equation representing the electronic motion for stationary nuclei. We replace ϵ with E to highlight this, giving,

$$(\hat{H}_0 - E)\,\psi(x; X) = 0. \tag{A.7}$$

We assume that this eigenvalue problem is solved, with electronic eigenfunctions ψ that depend parametrically upon nuclear coordinates [419]. We can further specify the n^{th} eigenvalue, E_n^0, corresponding to n^{th} normalised eigenfunction ψ_n, where n is understood to be the electronic quantum number [417–419],

$$(\hat{H}_0 - E_n(X))\,\psi_n(x; X) = 0. \tag{A.8}$$

Here we assume that E_n is a non-degenerate eigenvalue, and the dependence of E_n on X is explicitely written. Whilst this may be an inaccurate assumption to make for physical systems, we are only concerned with the approximate procedure, and will not consider possible degeneracies [417, 418].

If we consider functions ψ_n to be known for a certain nuclear configuration, X^0, we can make the assumption that nuclear motion is confined to small deviations

from X^0 to solve the exact equation (A.6). This assumption, justified by its success [417, 418], can be expressed as,

$$X - X^0 = \kappa u. \tag{A.9}$$

Replacing X^0 with $X = X^0 + \kappa u$, and differentiating $E_n(X)$ with respect to κ, we obtain the expansion,

$$E_n(X^0 + \kappa u) = E_n^{(0)} + \kappa E_n^{(1)} + \kappa^2 E_n^{(2)} + \cdots, \tag{A.10}$$

where the coefficients of the powers of κ are homogeneous polynomials in u,

$$\begin{aligned} E_n^{(0)} &= E_n(X^0), \\ E_n^{(1)} &= \sum_i u_i \frac{\partial E_n}{\partial X_i}, \\ E_n^{(2)} &= \frac{1}{2} \sum_{ij} u_i u_j \frac{\partial^2 E_n}{\partial X_i \partial X_j}, \\ &\cdots \end{aligned} \tag{A.11}$$

Similarly expanding ψ_n and reduced Hamiltonian $\hat{H}_0$ we get,

$$\begin{aligned} \psi_n(X^0 + \kappa u) &= \psi_n^{(0)} + \kappa \psi_n^{(1)} + \kappa^2 \psi_n^{(2)} + \cdots \\ \hat{H}_0(X^0 + \kappa u) &= \hat{H}_0^{(0)} + \kappa \hat{H}_0^{(1)} + \kappa^2 \hat{H}_0^{(2)} + \cdots. \end{aligned} \tag{A.12}$$

We notice that $E_n^{(0)}$ is independent of u, $E_n^{(1)}$ is linear in u, $E_n^{(2)}$ is quadratic in u, and so on.

Combining equations (A.10) and (A.12) with equation (A.8) we get,

$$\Big[(\hat{H}_0^{(0)} + \kappa \hat{H}_0^{(1)} + \kappa^2 \hat{H}_0^{(2)} + \cdots) - (E_n^{(0)} + \kappa E_n^{(1)} + \kappa^2 E_n^{(2)} + \cdots)\Big](\psi_n^{(0)} + \kappa \psi_n^{(1)} + \kappa^2 \psi_n^{(2)} + \cdots) = 0, \tag{A.13}$$

and equating the coefficients for the same powers of κ, we obtain:

$$\begin{aligned} &(a) \quad (\hat{H}_0^{(0)} - E_n^{(0)})\psi_n^{(0)} = 0, \\ &(b) \quad (\hat{H}_0^{(0)} - E_n^{(0)})\psi_n^{(1)} = -(\hat{H}_0^{(1)} - E_n^{(1)})\psi_n^{(0)}, \\ &(c) \quad (\hat{H}_0^{(0)} - E_n^{(0)})\psi_n^{(2)} = -(\hat{H}_0^{(1)} - E_n^{(1)})\psi_n^{(1)} - (\hat{H}_0^{(2)} - E_n^{(2)})\psi_n^{(0)}, \\ &\cdots \end{aligned} \tag{A.14}$$

To solve the exact equation (A.6), we use the expansions (it can be shown that $E_n^{(0)} = \epsilon_n^{(0)}$ [419]),

$$\begin{aligned} \epsilon_n &= E_n^{(0)} + \kappa \epsilon_n^{(1)} + \kappa^2 \epsilon_n^{(2)} + \cdots, \\ \Psi_n &= \Psi_n^{(0)} + \kappa \Psi_n^{(1)} + \kappa^2 \Psi_n^{(2)} + \cdots. \end{aligned} \tag{A.15}$$

By noting that $\frac{\partial}{\partial X} = \frac{1}{\kappa}\frac{\partial}{\partial u}$, we can rewrite the perturbation,

$$\hat{T}_{ion} = \kappa^4 \hat{H}_1 = \kappa^2 \hat{H}_1^{(2)}, \tag{A.16}$$

with,

$$\hat{H}_1^{(2)} = -\sum_I \frac{M_0}{M_I}\frac{\hbar^2}{2m}\frac{\partial^2}{\partial u^2}, \tag{A.17}$$

which shows that the kinetic energy of the nuclei only contributes a term of order κ^2 to the Hamiltonian. Thus, combining this with the reduced Hamiltonian, we obtain the full Hamiltonian $\hat{H}$:

$$\hat{H}(X^0 + \kappa u) = \hat{H}_0^{(0)} + \kappa \hat{H}_0^{(1)} + \kappa^2(\hat{H}_0^{(2)} + \hat{H}_1^{(2)}) + \cdots, \tag{A.18}$$

We combine equations (A.15) and (A.18) with equation (A.6) and compare coefficients for powers of κ, as we did for the reduced system, to get the set of equations:

$$\begin{aligned}
&(a) \quad (\hat{H}_0^{(0)} - E_n^{(0)})\Psi_n^{(0)} = 0, \\
&(b) \quad (\hat{H}_0^{(0)} - E_n^{(0)})\Psi_n^{(1)} = -(\hat{H}_0^{(1)} - \epsilon_n^{(1)})\Psi_n^{(0)}, \\
&(c) \quad (\hat{H}_0^{(0)} - E_n^{(0)})\Psi_n^{(2)} = -(\hat{H}_0^{(1)} - \epsilon_n^{(1)})\Psi_n^{(1)} - (\hat{H}_0^{(2)} + \hat{H}_1^{(2)} - \epsilon_n^{(2)})\Psi_n^{(0)}. \\
&\cdots
\end{aligned} \tag{A.19}$$

A.1.1 Zeroth and First Order: Equilibrium of Nuclei

As $\hat{H}_0^{(i)}$ are operators with respect to electronic coordinates, we can multiply the solutions $\psi_n^{(0)}$ by an arbitrary function in u (to be determined by higher order equations), allowing us to determine general solutions. It follows from equation (A.19a) that the normalised eigenfunction $\Psi_n^{(0)}$ is a general solution of the zeroth order equation, with eignevalue $E_n^{(0)} = E_n(X^0)$ and general form [417–419]:

$$\Psi_n^{(0)} = \chi_n^{(0)}(u)\,\psi_n^{(0)}(x; X^0), \tag{A.20}$$

with arbitrary function of ionic coordinates $\chi_n^{(0)}(u)$. At this point, we are able to separate the electronic wave function from the arbitrary function coupling the electrons to the nuclear cores. However, we will consider higher order terms.

Equation (A.19b), $(\hat{H}_0^{(0)} - E_n^{(0)})\Psi_n^{(1)} = -(\hat{H}_0^{(1)} - \epsilon_n^{(1)})\Psi_n^{(0)}$, is a linear inhomogeneous differential equation with respect to x. The solubility condition requires that the

right hand side be orthogonal to the solution, $\psi_n^{(0)}$, of the homogeneous equation. As such,

$$\begin{aligned}
&\int \psi_n^{(0)}(x;X^0)\,(\hat{H}_0^{(1)}-\epsilon_n^{(1)})\,\Psi_n^{(0)}(x,u)\,dx \\
&=\chi^{(0)}(u)\int \psi_n^{(0)}(x;X^0)\,(\hat{H}_0^{(1)}-\epsilon_n^{(1)})\,\psi_n^{(0)}(x;X^0)\,dx \\
&=\chi^{(0)}(u)\left\{(\hat{H}_0^{(1)})_{nn}-\epsilon_n^{(1)}\right\} \\
&=0.
\end{aligned} \tag{A.21}$$

where $(\hat{H}_0^{(1)})_{nn}$ is the diagonal matrix element of the operator $\hat{H}_0^{(1)}$. Born and Oppenheimer [417, 418] showed that we require $(\hat{H}_0^{(1)})_{nn}=\epsilon_n^{(1)}=0$. Using equation (A.11), we thus get,

$$(\hat{H}_0^{(1)})_{nn}=\epsilon_n^{(1)}=\sum_i u_i\frac{\partial\epsilon_n}{\partial X_i}. \tag{A.22}$$

We therefore require that the set of ionic coordinates X_i correspond to an extremal value of the energy $\epsilon_n(X)$.

If we now compare equations (A.14) and (A.19), with $\epsilon_n^{(1)}=0$ substituted,

$$\begin{aligned}
(\hat{H}_0^{(0)}-E_n^{(0)})\psi_n^{(1)}&=-\hat{H}_0^{(1)}\psi_n^{(0)} \\
(\hat{H}_0^{(0)}-E_n^{(0)})\Psi_n^{(1)}&=-\hat{H}_0^{(1)}\Psi_n^{(0)},
\end{aligned} \tag{A.23}$$

we see that $\Psi_n^{(1)}=\chi_n^{(0)}\psi_n^{(1)}$ is a solution. To this, we may add a solution, $\psi_n^{(0)}$, of the homogeneous equation, multiplied by an arbitrary function of nuclear coordinates, $\chi_n^{(1)}(u)$, resulting in the general solution,

$$\Psi_n^{(1)}(x,u)=\chi_n^{(0)}(u)\,\psi_n^{(1)}(x;u)+\chi_n^{(1)}(u)\,\psi_n^{(0)}(x). \tag{A.24}$$

A.1.2 Second and Third Order: Nuclear Vibrations

To consider higher order approximations, we substitute equations (A.20) and (A.24) into equation (A.19c), giving,

$$(\hat{H}_0^{(0)}-E_n^{(0)})\Psi_n^{(2)}=-\hat{H}_0^{(1)}\left[\chi_n^{(0)}\,\psi_n^{(1)}+\chi_n^{(1)}\,\psi_n^{(0)}\right]-(\hat{H}_0^{(2)}+\hat{H}_1^{(2)}-\epsilon_n^{(2)})\chi_n^{(0)}\,\psi_n^{(0)}. \tag{A.25}$$

Multiplying reduced-system equation[1] (A.14b) by $\chi_n^{(1)}$ gives:

$$(\hat{H}_0^{(0)}-E_n^{(0)})\chi_n^{(1)}\psi_n^{(1)}=-\hat{H}_0^{(1)}\chi_n^{(1)}\psi_n^{(0)}, \tag{A.26}$$

[1] Recalling that $\hat{H}_0^{(i)}$ does not operate on u.

and multiplying reduced-system equation[1] (A.14c) by $\chi_n^{(0)}$ gives:

$$(\hat{H}_0^{(0)} - E_n^{(0)})\chi_n^{(0)}\psi_n^{(2)} = -\hat{H}_0^{(1)}\chi_n^{(0)}\psi_n^{(1)} - (\hat{H}_0^{(2)} - E_n^{(2)})\chi_n^{(0)}\psi_n^{(0)}. \tag{A.27}$$

Subtracting these from equation (A.25) then gives,

$$(\hat{H}_0^{(0)} - E_n^{(0)})\left[\Psi_n^{(2)} - \chi_n^{(1)}\psi_n^{(1)} - \chi_n^{(0)}\psi_n^{(2)}\right] = -(\hat{H}_1^{(2)} + E_n^{(2)} - \epsilon_n^{(2)})\chi_n^{(0)}\,\psi_n^{(0)}. \tag{A.28}$$

Again, the solubility condition for this requires,

$$(\hat{H}_1^{(2)} + E_n^{(2)} - \epsilon_n^{(2)})\chi_n^{(0)} = 0, \tag{A.29}$$

hence,

$$(\hat{H}_0^{(0)} - E_n^{(0)})\left[\Psi_n^{(2)} - \chi_n^{(1)}\psi_n^{(1)} - \chi_n^{(0)}\psi_n^{(2)}\right] = 0. \tag{A.30}$$

Equation (A.29) represents the equation for nuclear motion, and shows that the ions move with kinetic energy $\kappa^2\hat{H}_1^{(2)}$ (from equation (A.16)), in an effective potential $\kappa^2 E_n^{(2)}$ due to electrons. This effective potential, $E_n^{(2)}$, is the clamped ion energy of the system, often referred to as the 'Born-Oppenheimer energy surface', and is the ground state energy of a system of interacting electrons moving in a field of fixed nuclei [420]. As mentioned previously, the function $E_n^{(2)}$ is a quadratic function of nuclear coordinate u (see equation (A.11)), and so the above equation leads to harmonic vibrations of the nuclei. As such, this is called the harmonic approximation [419]. Within this approximation, the wave function is only given to zeroth order: this is given by the product of the zeroth order nuclear wave function, $\chi_n^{(0)}$, and the zeroth order electronic wave function, $\psi_n^{(0)}$.

The harmonic approximation provides a simple description for the motions of a system: electrons move as though they are in the presence of fixed nuclei, and the nuclei move in an effective potential of quadratic form. However, many important properties of crystals are not described by the harmonic approximation, and a discussion of such properties requires higher levels of approximation.

Comparing equation (A.30) with the general second order equation, (A.19c), we see that,

$$\Psi_n^{(2)} - \chi_n^{(1)}\psi_n^{(1)} - \chi_n^{(0)}\psi_n^{(2)} = \chi_n^{(2)}\psi_n^{(0)}, \tag{A.31}$$

hence,

$$\Psi_n^{(2)} = \chi_n^{(1)}\psi_n^{(1)} + \chi_n^{(0)}\psi_n^{(2)} + \chi_n^{(2)}\psi_n^{(0)}, \tag{A.32}$$

where $\chi_n^{(2)}$ is a function of u. If we collect our expressions for $\Psi_n^{(0)}$, $\Psi_n^{(1)}$ and $\Psi_n^{(2)}$ in equation (A.15),

$$\begin{aligned}\Psi_n &= (\chi_n^{(0)}\,\psi_n^{(0)}) + \kappa(\chi_n^{(0)}\,\psi_n^{(1)} + \chi_n^{(1)}\,\psi_n^{(0)}) + \kappa^2(\chi_n^{(1)}\psi_n^{(1)} + \chi_n^{(0)}\psi_n^{(2)} + \chi_n^{(2)}\psi_n^{(0)}) + \cdots \\ &= \psi_n^{(0)}(\chi_n^{(0)} + \kappa\chi_n^{(1)} + \kappa^2\chi_n^{(2)}) + \kappa\psi_n^{(1)}(\chi_n^{(0)} + \kappa\chi_n^{(1)}) + \kappa^2\psi_n^{(2)}\chi_n^{(0)} + \cdots .\end{aligned} \tag{A.33}$$

We can rewrite this wave function, to the same order of accuracy [419], as,

$$\Psi_n = \left[\chi_n^{(0)}(u) + \kappa\chi_n^{(1)}(u) + \kappa^2\chi_n^{(2)}(u)\right]\psi_n(x;u). \tag{A.34}$$

The above wave function can be easily interpreted: the term in braces describes the nuclei, with small harmonic motions, and $\psi_n(x;u)$ describes the electrons, moving as though the nuclei were fixed in their instantaneous positions [419]. In this case, the electrons are said to move adiabatically with the nuclear motion. This assumes that, whilst the electronic wave functions and the energy of the state might change, electrons remain in the same state as the nuclei move: the electronic states are deformed with nuclear motion, but the electrons remain in their initial states [93]. Terminating the approximation here, we see that we have been able to write the wave function as the product of electronic and ionic wave functions, with ionic wave function depending on the positions of the ions, and the electronic wave function having a continuous dependence on the static ionic configuration. This allows us to separate out the electronic Schrödinger equation [94]:

$$\hat{H}_{el} = \hat{T}_{el}(\mathbf{r}) + \hat{V}_{el-el}(\mathbf{r}) + \hat{V}_{el-ion}(\mathbf{r},\mathbf{R}), \tag{A.35}$$

which is an eigenvalue equation for the electrons only. Thus, we can separate the electrons from the nuclei, and only consider the electronic Schrödinger equation.

This is referred to as the 'adiabatic approximation', a phrase regularly used interchangeably with 'Born-Oppenheimer approximation' as it is the most common termination of the Born-Oppenheimer expansion considered. Higher order terms can be considered, and result in electronic motion that is not adiabatic. The Born-Oppenheimer approximation is sufficient for most purposes, however it may begin

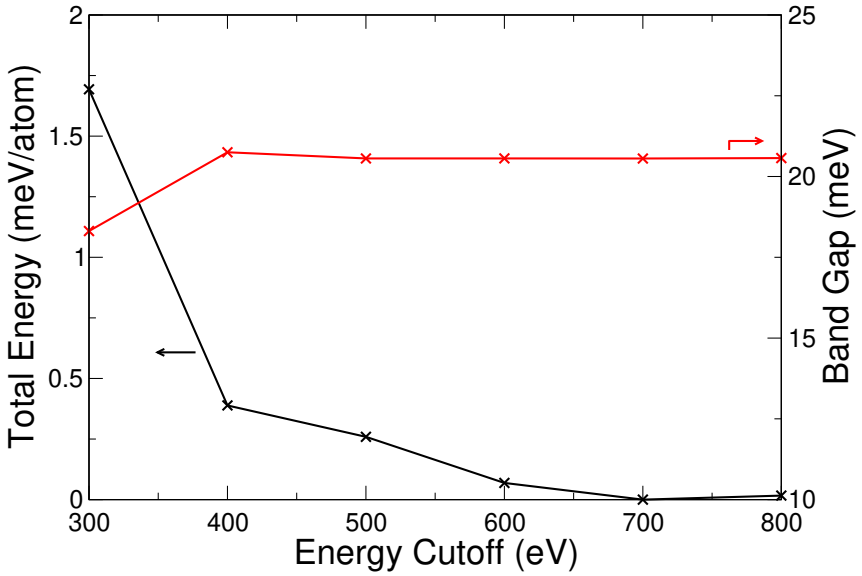

Figure A.1: Convergence of TiS_2 properties with cutoff energy.

to break down when two or more solutions of the Schrödinger equation are close in energy.

The third order wave function has the form,

$$\Psi_n^{(3)}(x,u) = \chi_n^{(0)}(u)\,\psi_n^{(3)}(x;u) + \chi_n^{(1)}(u)\,\psi_n^{(2)}(x;u) + \chi_n^{(2)}(u)\,\psi_n^{(1)}(x;u) + \chi_n^{(3)}(u)\,\psi_n^{(0)}(x) + F(x,u), \tag{A.36}$$

as given in references [417–419]. Here, $F(x,u)$ is an involved factor of x and u. This level of approximation, and indeed considering higher order terms, takes us beyond the simple model of harmonic motion in the adiabatic approximation. Whilst higher order terms are required for the accurate discussion of some crystal properties, most crystal properties can at least be understood with the supposition that the nuclei move within a potential, akin to that discussed in equation (A.29) [419].

A.2 Convergence Testing

In Chapter 2, we commented that the size of basis sets and the density of **k**-point grids can affect the results of electronic structure calculations. Larger basis sets should allow for a better description of electronic wave functions, allowing for lower energy states to be achieved (see Section 2.3.4). Similarly, the number of

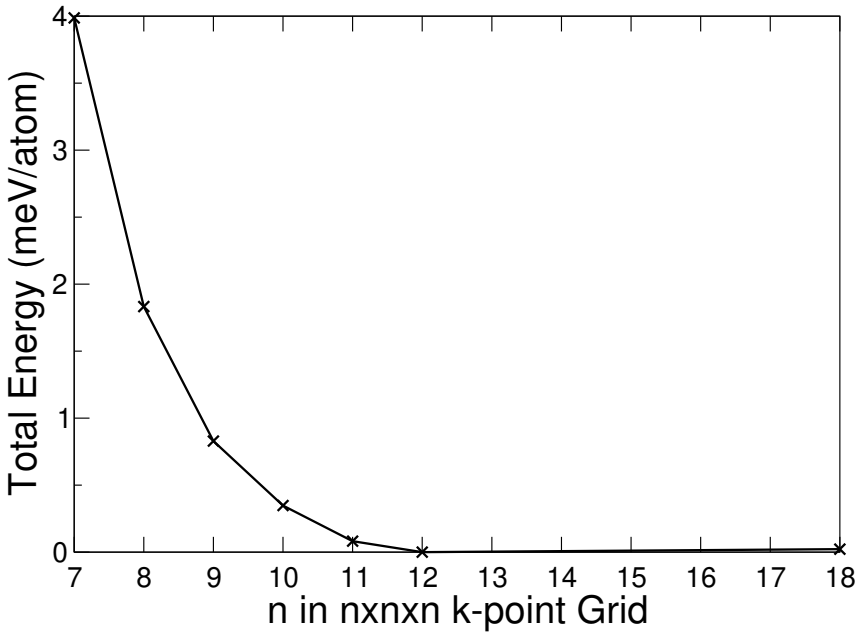

Figure A.2: Convergence of TiS_2 properties with **k**-point sampling.

k-points is also important for sums involved in the calculation of electronic properties (see Section 2.6.2). However, whilst infinitely large basis sets or infinitely dense **k**-point grids would produce precise results, we are limited in practice by the time it takes to complete a calculation and the computational hardware that is required. A trade-off must therefore be made, reducing calculation accuracy (small basis sets or coarser grids) to allow for reasonable use of resources. To assess this trade-off, we here present a small investigation into the convergence of our results. Such convergence testing is particularly important for broad studies such as those presented in the Chapters of this thesis. Previous works [421] have assessed the accuracy of VASP calculations, finding results to be within 0.6 meV per atom of all-electron calculations. We therefore consider a calculation to be converged if the increase of a computational parameter results in an improvement to the total energy of less than 1 meV. Due to the number of materials investigated and the calculations performed, it is not viable to check the convergence of results for every system considered. Instead, we have assessed a small subset of materials to determine appropriate cutoff energies (hence the size of the basis set) and the **k**-point grids for the remainder of the materials investigated. We have selected TiS_2 for a case study.

In Figure A.1, we demonstrate the convergence of the plane wave cutoff energy through assessment of the total energy and the resulting band gap. We present

the resulting total energy per atom of TiS_2, normalised so that the lowest energy obtained (at a cutoff energy of 700 eV). We see that with increasing cutoff energy, the energy is reduced, highlighting the improved description of the wave function attainable with a larger basis set. Increasing the cutoff energy from 600 eV to 700 eV there is a minimal reduction in energy of less than 0.07 meV per atom. Increasing from 700 eV to 800 eV, we actually see a small increase in energy of less than 0.02 meV per atom. As the larger basis set includes all of the basis functions used in the smaller basis set, the inclusion of any other basis functions should allow a reduction in the total energy. This increase therefore shows that we are now limited by other computational errors that are beyond our control, and inclusion of more basis functions will only serve to increase computational time and cost. We also show convergence of the electronic band gap with cutoff energy in Figure A.1. We see that there is minimal change to the band gap beyond a cutoff energy of 500 eV.

In Figure A.2, we similarly assess the convergence of the **k**-point grid through the total energy. As the sampling of the Brillouin zone is increased, we see a dramatic drop in the total energy for coarse grids. However, increasing the grids from $11 \times 11 \times 11$ to $12 \times 12 \times 12$ results in a small energy decrease of 0.08 meV per atom. Increasing the sampling to grids of $18 \times 18 \times 18$ leads to a small energy increase of 0.02 meV per atom, similar to what was seen for increasing the cutoff energy from 700 eV to 800 eV. This shows that we again in the domain where other computational errors become more significant, and so finer grids only serve to increase computational cost with no improvement in accuracy.

From the above discussion, we conclude that a plane wave basis set cutoff energy of 700 eV and a **k**-point grid of $12 \times 12 \times 12$ in the primitive unit cell are suitable for the calculations performed in this thesis. They show good convergence, achieving results that are comparable to larger sets and finer grids, offer improvement to smaller basis sets and coarser grids, and allow for other materials requiring larger sets or finer grids.

Appendix B

Supplementary Information to Chapter 3

B.1 Bader Charges for Selenide and Telluride Materials

In Chapter 3, we analysed the ionic charges in the sulfide TMDCs and how they changed with intercalation. In Figure B.1, we present the equivalent results for the selenide and telluride materials.

B.2 Geometry

In Section 3.8, we presented the volumetric expansion of the TMDCs with intercalation, and briefly commented on the broad changes to the unit cells and ionic geometry that are seen with intercalation. Here, we develop on these comments, and present data relevant to the geometric changes.

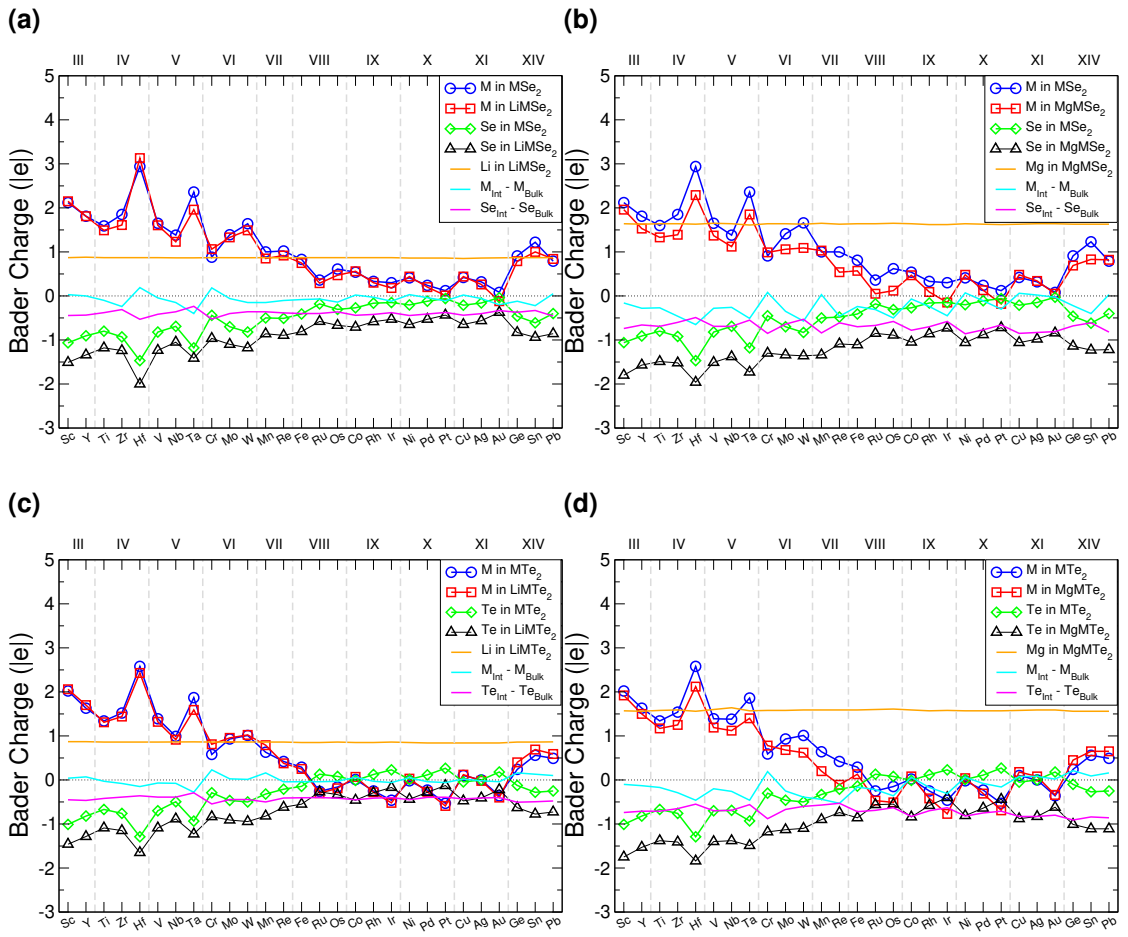

Figure B.1: Bader charges for the metal, chalcogen, and intercalant atoms in the bulk, $LiMX_2$, and $MgMX_2$ selenide and telluride structures. Blue circles correspond to the metal atom (M) in the bulk MX_2 structure, red squares correspond to M atom in the intercalated structure, green diamonds correspond to the chalcogen atom (S) in the bulk MX_2 structure, black triangles correspond to X atom in the intercalated structure, and the orange line indicates the charge of the intercalated species in the intercalated structure. The data for the lithium- and magnesium-intercalated selenides are presented in B.1a and B.1b, and the data for the lithium- and magnesium-intercalated tellurides are presented in B.1c and B.1d.

B.2.1 Lattice

In Figure B.2a we present the in-plane lattice constants for the pristine (black), lithium-intercalated (red), and magnesium-intercalated (blue) structures. In general, we see an increase of the in-plane lattice constant with intercalation. This is emphasised in Figures B.2b and B.2c, where we show the resultant percentage expansion of the in-plane lattice constant due to lithium (B.2b) and magnesium

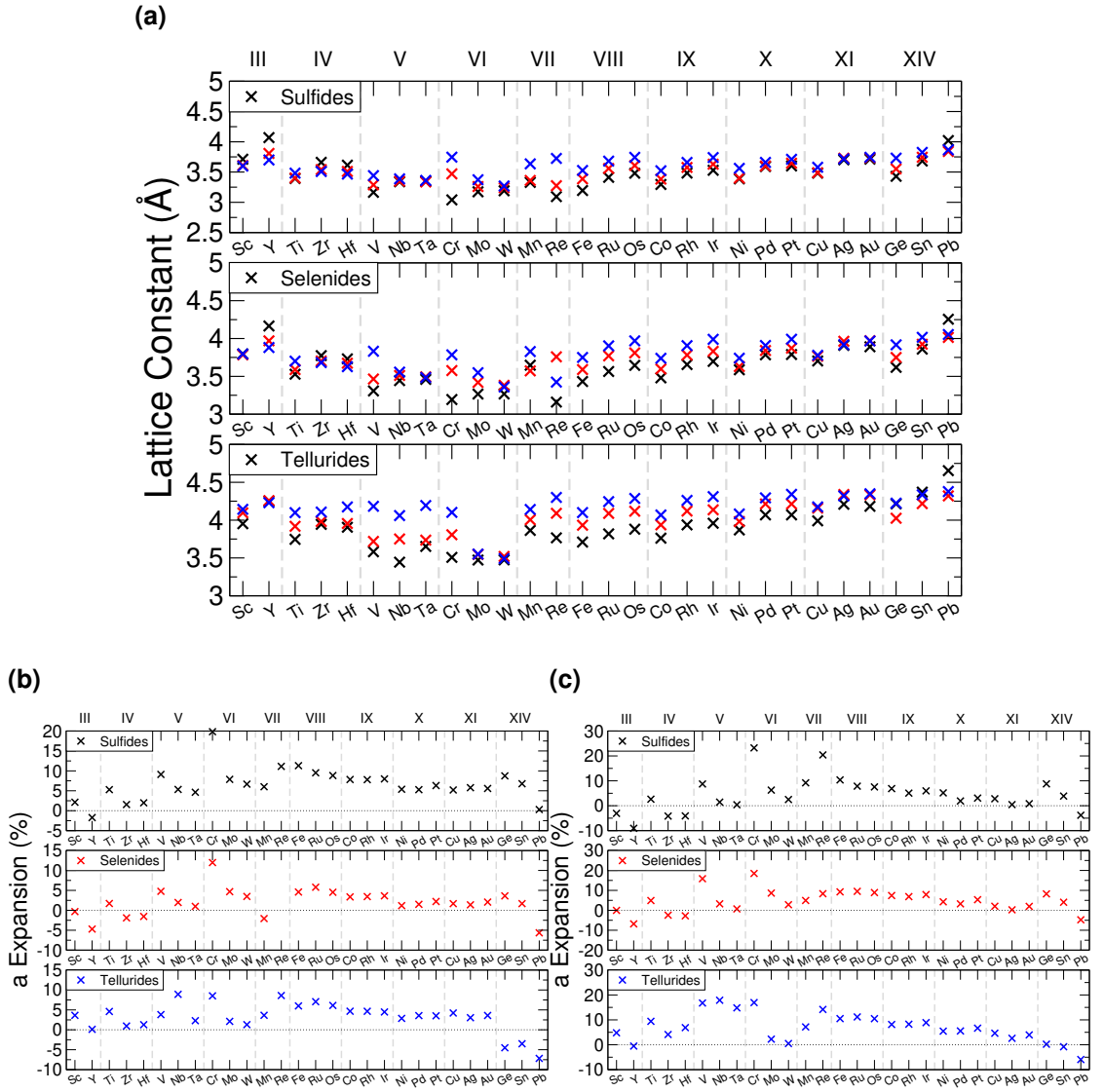

Figure B.2: In-plane lattice constants for the pristine (black), lithium-intercalated (red), and magnesium-intercalated (blue) TMDCs. Sulfide data is presented in the top, selenide data is presented in the middle, and telluride data is presented in the bottom. The percentage expansion is then presented in B.2b for lithium intercalation, and in B.2c for magnesium intercalation.

(B.2c) intercalation. There is a larger percentage expansion for TMDCs composed of transition metals from Period IV, but this is simply due to the smaller initial lattice constant of the unintercalated structures. For lithium intercalation, most of the TMDCs exhibit in-plane lattice expansion of 5 - 10%, and there are larger expansions under intercalation with magnesium. Somewhat surprisingly, we identify a contraction of the sulfides and selenides paired with Group IV and V metals. Overall, however, we show that most of these materials demonstrate in-plane expansions within $\pm$10%, which is ideal for electrode applications.

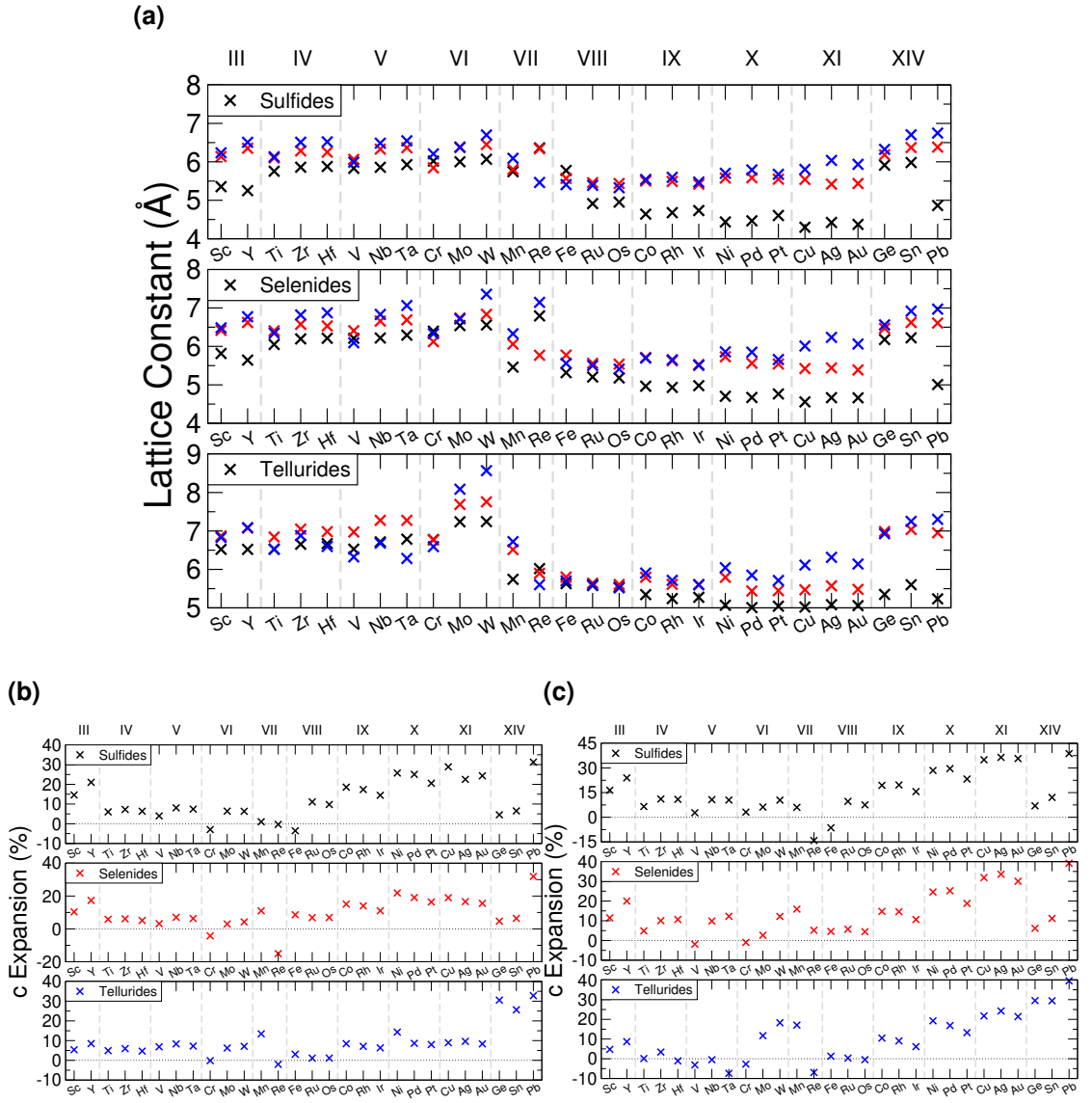

Figure B.3: Out-of-plane lattice constants for the pristine (black), lithium-intercalated (red), and magnesium-intercalated (blue) TMDCs. Sulfide data is presented in the top, selenide data is presented in the middle, and telluride data is presented in the bottom. The percentage expansion is then presented in B.3b for lithium intercalation, and in B.3c for magnesium intercalation.

As intercalation into the vdW gap changes the nature of the out-of-plane bonding, changes to the out-of-plane lattice constant can be expected. We present in Figure B.3a the out-of-plane lattice constants for the pristine (black), lithium-intercalated (red), and magnesium-intercalated (blue) structures. For TMDC sulfides, and materials composed of transition metals in Groups III to VII, and XIV, we see a large expansion ($\sim$20%) of the lattice constant with intercalation. However, for transition metals in Groups VIII to XI there is either a very small (<5%) expansion or a contraction of the out-of-plane lattice. We indicate this with the

percentage expansions in Figure B.3b (lithium intercalation) and in Figure B.3c (magnesium intercalation).

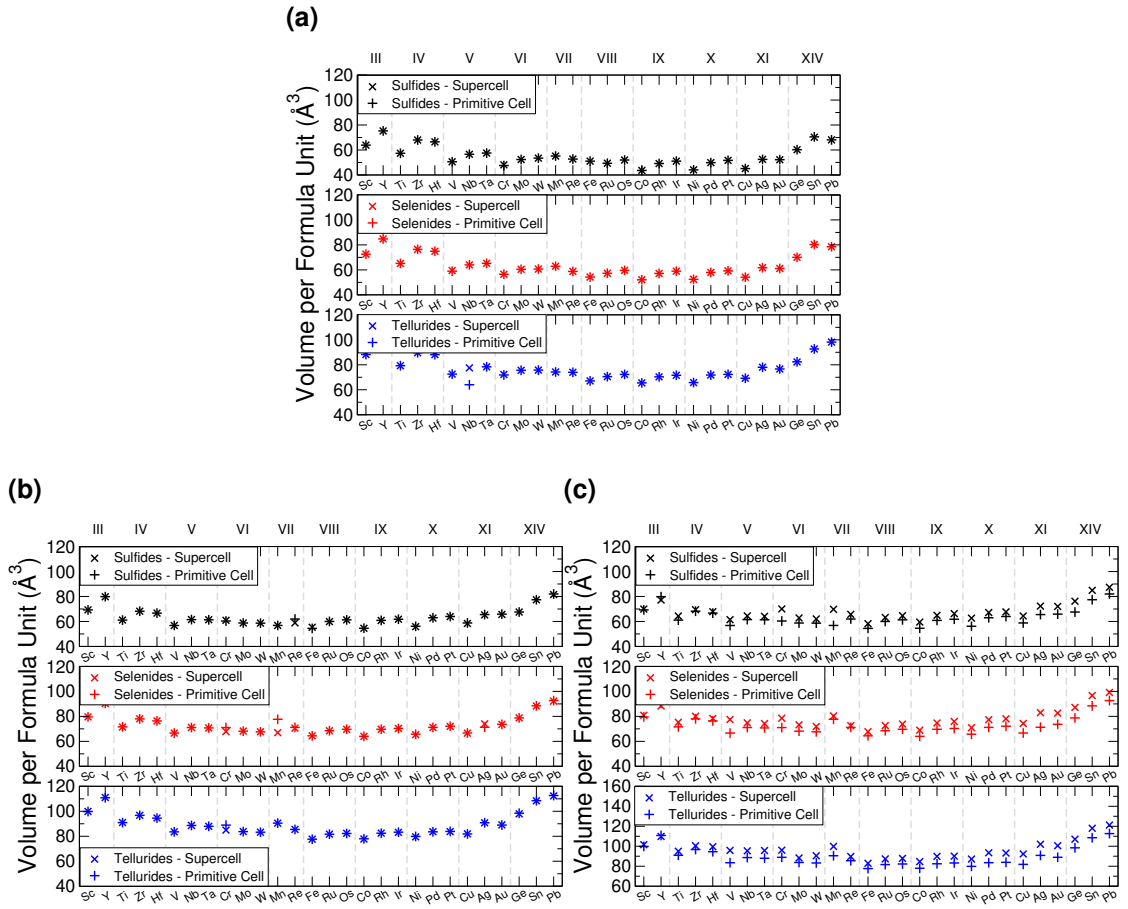

Figure B.4: Volumes of pristine (B.4a), lithium-intercalated (B.4b) and magnesium-intercalated (B.4c) TMDCs. In each of these, sulfide data is presented in black (top), selenide data is presented in red (middle), and telluride data is presented in blue (bottom).

In Figure B.4, we then present the formula unit volumes of the pristine (Figure B.4a), lithium-intercalated (Figure B.4b), and magnesium-intercalated (Figure B.4c) structures. We have included the volumes for the primitive and supercell ($2 \times 2 \times 2$), used for determining the volumetric expansion presented in the main article.

B.2.2 Ions

We indicate our labelling of the different ionic distances for the following discussion in Figure B.5. This includes the in-plane metal-metal distance (d_{MM}), the

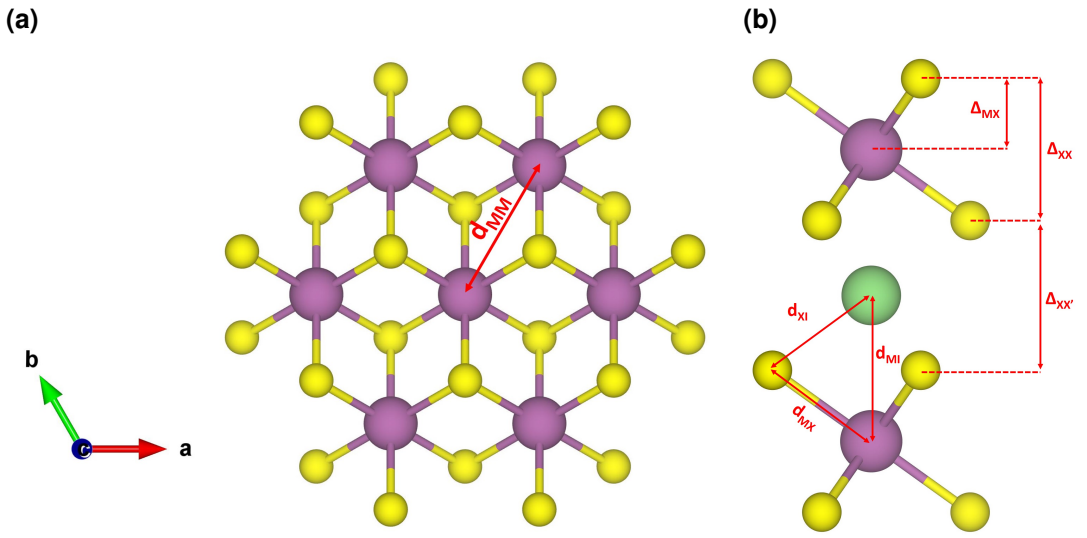

Figure B.5: Labels used for discussions of TMDC geometry. B.5a shows a 'top-down' view of the TMDC basal plane, and B.5b shows a side-view of the TMDC structure.

bond length/distance between the host transition metal and the chalcogen (d_{MX}), the bond length/distance between the host chalcogen of the host and the intercalant species (d_{XI}), and the distance between the host transition metal and the intercalant (d_{MI}). We also consider the vertical separation of the host transition metal and chalcogen (Δ_{MX}), the vertical separation between chalcogen atoms on opposing sides of a TMDC sheet (Δ_{XX}), and the vertical separation between chalcogen species on opposing sides of the vdW gap ($\Delta_{XX'}$).

Above, we commented on a general expansion of the in-plane lattice constant under intercalation. This leads to an increase in the distance between transition metal atoms within a layer of the host TMDC material, as is shown in Figure B.6a. The exceptions to this are the sulfide and selenide materials composed of Group IV and V metals, which demonstrated a small contraction of the in-plane structure, and here show a shortening of the M-M distance.

The distances between the host transition metal and chalcogen ions are shown in Figure B.6b. We identify a slight lengthening of the metal-chalcogen bond length when an intercalant is introduced to the TMDC structure. We attribute this to the significant charge donation from the intercalant to the host material, and a Coulombic attraction between the chalcogen and intercalant species. For the selenide and telluride materials in particular, the M-X bond length is approximately

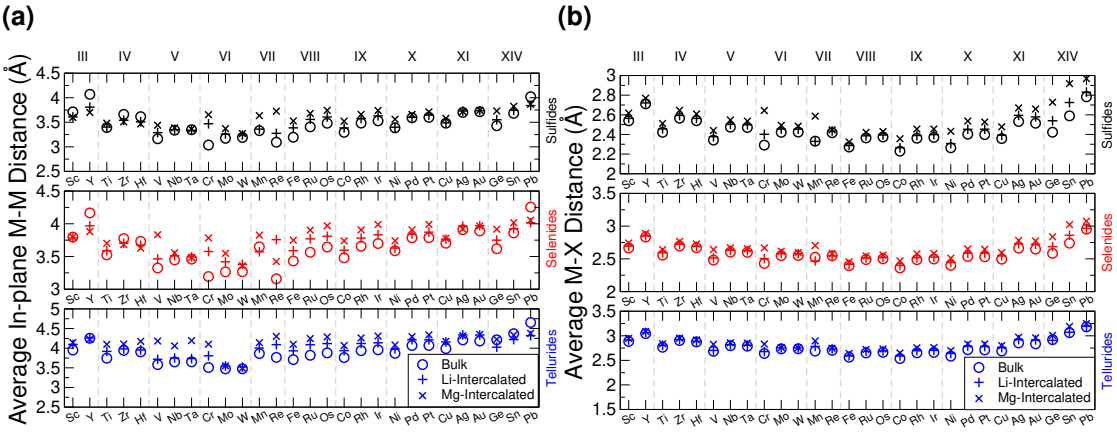

Figure B.6: Characteristic distances of the host TMDC materials. B.6a presents the values of d_{MM}, and B.6b presents the values of d_{MX}. The sulfides (top), selenides (middle), and telluride (bottom) materials are included, with the results for the pristine bulk structures presented with circles, lithium-intercalated presented with pluses, and magnesium-intercalated presented with crosses.

the same with both lithium and magnesium intercalation.

Above, we saw the general expansion of the **c** lattice vector with intercalation, and here aim to offer some insight into this expansion. In Figure B.7a we show the vertical separation between chalcogen species on opposing sides of the vdW spacing ($\Delta_{XX'}$). This gives an indication of the separation between consecutive TMDC layers, where we see a clear increase in this separation (with the exception of the Cr, Mn, Re, Ge, and Sn materials, for which there is little change). The expansion is to be expected from the introduction of an intercalant as it dramatically changes the nature of the out-of-plane bonding.

We similarly show in Figure B.7b the vertical separation between intralayer chalcogen species of the same TMDC sheet but on opposing basal planes (Δ_{XX}): This gives a measure of the thickness of each TMDC sheet. Groups III-IV, X-XI, and XIV all show a vertical stretching of the TMDC layer with intercalation, with magnesium intercalation resulting in a greater stretching than lithium intercalation. Groups V and VI show a mixture of expansion and contraction. Groups VII-IX, finally, show a contraction, with magnesium intercalation again showing the most dramatic change.

A closer look at the M-X bonding is revealed in Figure B.7c, where we show

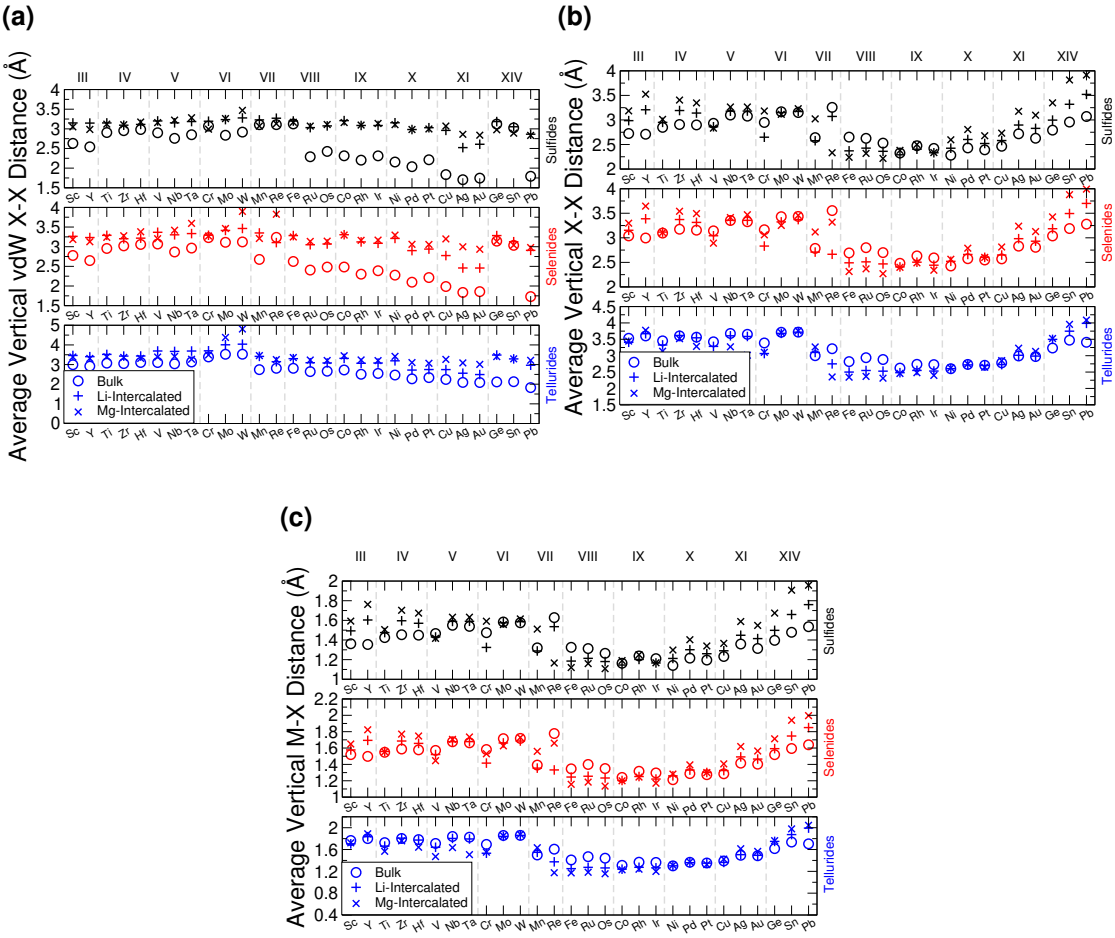

Figure B.7: Characteristic distances of the host TMDC materials. B.7c presents the values of Δ_{MX}, B.7b presents the values of Δ_{XX}, and B.7a presents the values of $\Delta_{\mathrm{XX'}}$. The sulfides (top), selenides (middle), and telluride (bottom) materials are included, with the results for the pristine bulk structures presented with circles, lithium-intercalated presented with pluses, and magnesium-intercalated presented with crosses.

the vertical separation between the metal atom and its nearest six coordinated chalcogens. This is another useful descriptor for the thickness of a TMDC layer. We identify the same trends with Δ_{MX} as we did for Δ_{XX}, with Groups III-IV, X-XI, and XIV all show a vertical stretching of the TMDC layer with intercalation, with magnesium intercalation resulting in a greater stretching than lithium intercalation; Groups V and VI show a mixture of expansion and contraction; and Groups VII-IX show a contraction. In each of these, magnesium intercalation again results in the most dramatic changes to the structure. We also note the more significant effect the intercalant has on the sulfides compared with heavier chalcogens. In particular, the Group III, IV, X, XI, and XIV tellurides all show minimal changes to Δ_{MX} which are pronounced in the case of the sulfides. Whilst

we saw a very uniform changes to the length of the M-X bond (as was discussed above in Figure B.6b), there is a much more varied behaviour for the vertical separation between the M and X species. This results in a wide range of bonding angles.

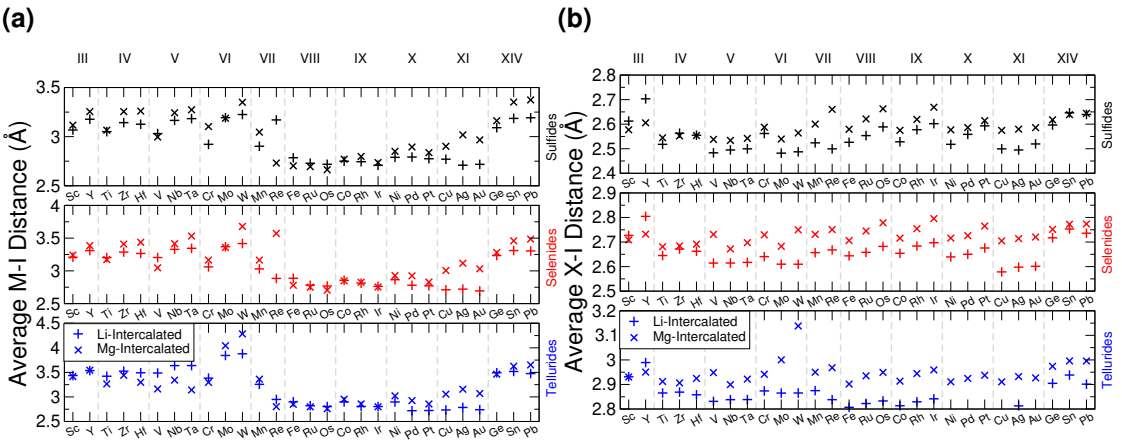

Figure B.8: Characteristic distances of the host TMDC materials. The sulfides (top), selenides (middle), and telluride (bottom) materials are included, with the results for lithium-intercalated structures presented with pluses, and magnesium-intercalated presented with crosses.

In Figure B.8 we show the distances between the host transition metal and the intercalant (Figure B.8a), d_{MI}, and the distance between the intercalant and the nearest six chalcogens of the host material (Figure B.8b), d_{XI}.

B.3 Selenide and Telluride Data

In Chapter 3, we presented results of the sulfide TMDCs and their properties when intercalated. Here, we present the equivalent results for the selenide and telluride materials. In Figure B.9 we compare the T- and Hc-phase energies in the pristine and intercalated TMDC forms, as we did for the sulfides in Figure 3.8. In Figure B.10 we compare the octahedrally-coordinated and tetrahedrally-coordinated intercalation sites, like was presented in Figure 3.10. Presenting the energetic results, then, we see the intercalation voltages in Figure B.11 (analogous to Figure 3.19) and the thermodynamic stability indicated by E_{IS} in Figure B.12 (analogous to Figure 3.22). Overall, these results offer the same trends demonstrated

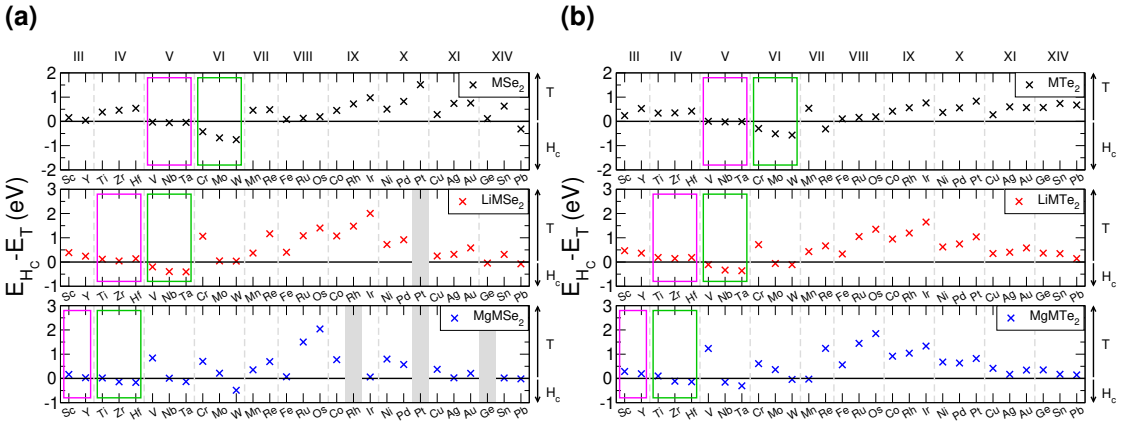

Figure B.9: Comparison of the TMDC T- and Hc-phase energies in the pristine bulk and intercalated forms, for the selenide (B.9a) and telluride (B.9b) TMDCs. Positive values indicate a more favourable T-phase, whereas negative values indicate a more favourable Hc-phase. Group V-like behaviour is tracked with the magenta boxes, and Group VI-like behaviour is tracked with the green boxes.

by the sulfide materials, and so the conclusions of Chapter 3 hold.

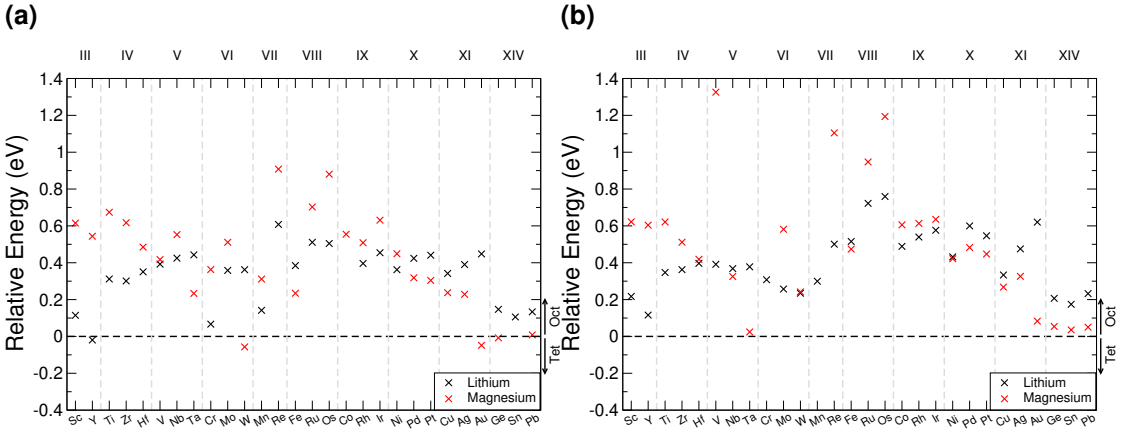

Figure B.10: Relative energy of the tetrahedral intercalation site compared to the octahedral intercalation site for the selenides (B.10a) and tellurides (B.10b). Data for lithium intercalation is presented in black, and data for magnesium intercalation is presented in red.

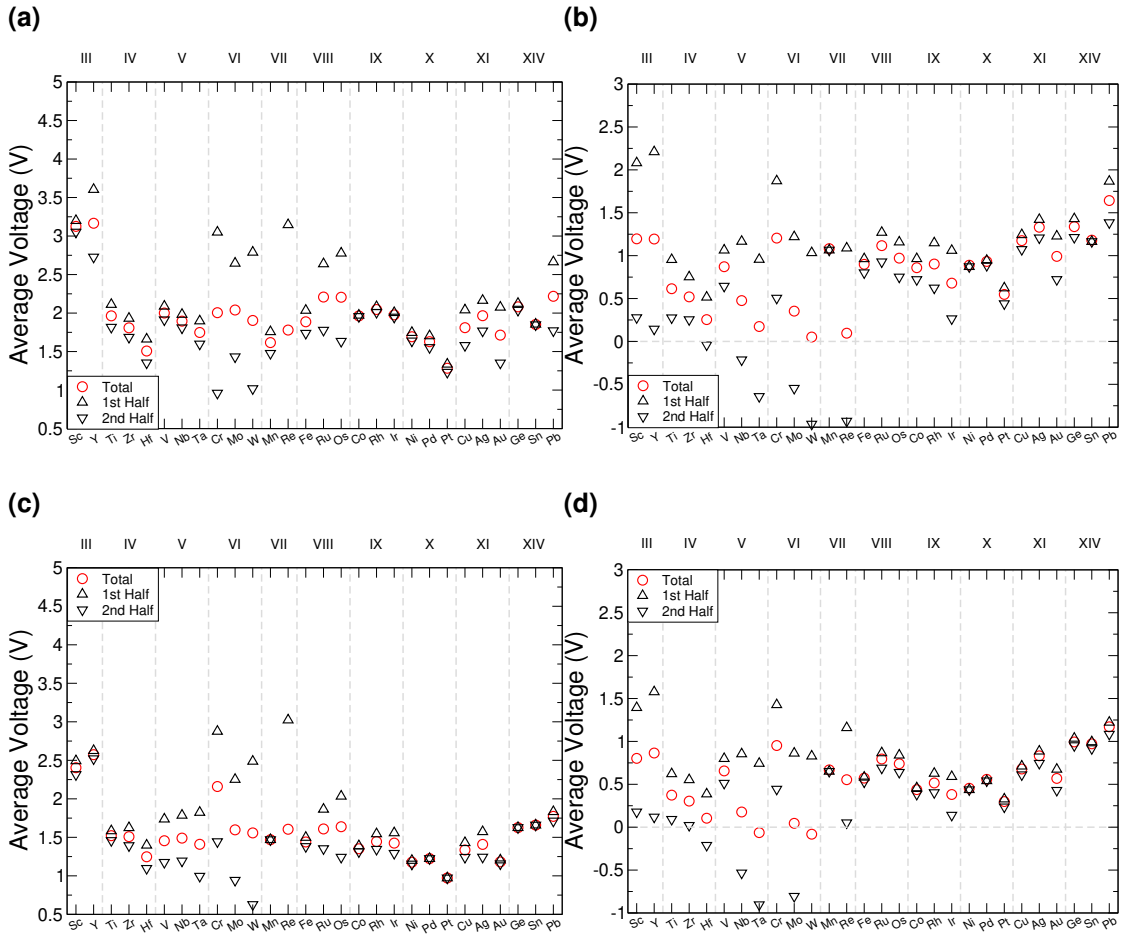

Figure B.11: Average intercalation voltages for each of the TMDC selenide and telluride materials when intercalated with lithium and magnesium. The average lithium intercalation voltages are given in B.11a and B.11c for the selenides and tellurides, respectively. Equivalent data for the magnesium intercalation voltages are given in B.11b, and B.11d for the selenides and tellurides, respectively.

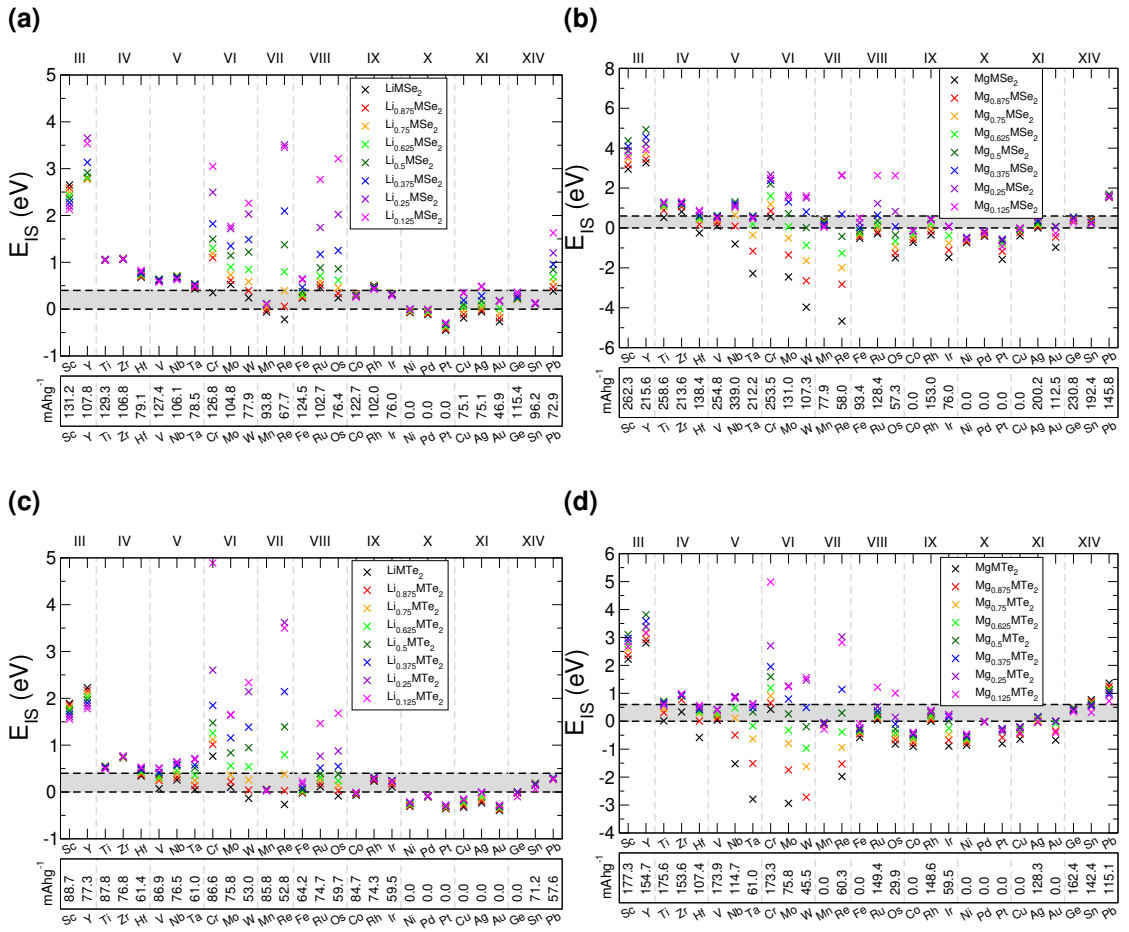

Figure B.12: Average E_{IS} values for each of the TMDCs intercalated with lithium and magnesium. B.12a and B.12c present the values of E_{IS} for the selenides and tellurides intercalated with lithium, respectively. B.12b and B.12d present the values of E_{IS} for the selenides and tellurides intercalated with magnesium, respectively. The reversible intercalation capacity, determined from the range over which E_{IS} remains positive, is given at the bottom of each figure in mAhg^{-1}.

B.4 HSE06 Results

As we discussed in Section 3.12, the choice of functional can have a significant effect on the results, particularly for materials composed of transition metal elements. Using a limited investigation into these materials using the HSE06 hybrid functional we have assessed the effect of changing the functional. We present the voltage profiles and phase diagrams for the MoX_2 materials in Figure B.13, and for SnS_2, ScS_2, and IrS_2 in Figure B.13.

B.5 H-Phase Data

We here the value of a in Li_aMX_2 at which the T- and Hc-phases are equal in energy, determined by using linear fits between the MX_2 and $LiMX_2$ compounds. For the Group IV TMDCs, the transition is from T-phase to Hc-phase, for Group V TMDCs the crossover indicates the T-Hc phase transition, with negative values indicating that the T phase is never favourable, and for the Group VI TMDCs the transition is from Hc-phase to T-phase for increasing a. For magnesium to Mg_aMX_2, this single linear fit is not sufficient as there are two behaviours arising from the double valency of the magnesium intercalant. We instead extrapolate a linear fit between the unintercalated MX_2 and $Mg_{0.5}MX_2$ compounds, with the charge transferred in $Mg_{0.5}MX_2$ corresponding to the full charge transfer of $LiMX_2$ due to the double valency of magnesium, and a second fit between the $Mg_{0.5}MX_2$ and $MgMX_2$ points. We identify that the Group IV TMDCs undergo T- to H-phase transitions, whereas the Group V and VI TMDCs undergo H- to T-transitions. $MgVTe_2$ does not transition (indicated by the negative crossover value), remaining in the T-phase throughout.

B.6 Orbital-Projected Density of States

In Chapter 3, we commented on the nature of the valence and conduction bands in terms of their orbital character. In Figure B.15 we present the orbital-projected

	Crossover		Average Voltage (V)		E_{IS} (eV)	
TMDC	Li	Mg	Li	Mg	Li	Mg
TiS_2	1.311	0.877	2.671	1.088	1.820	1.785
ZrS_2	0.991	0.608	2.608	1.063	1.967	2.384
HfS_2	1.196	0.648	2.272	0.835	1.527	1.495
VS_2	-0.164	0.268	2.452	0.596	1.220	-1.107
NbS_2	-0.378	0.817	2.406	0.657	1.399	-0.140
TaS_2	-0.282	0.782	2.168	0.321	1.059	-1.552
CrS_2	0.372	0.258	1.327	0.792	-0.397	-0.675
MoS_2	0.481	0.283	0.780	-0.039	-0.923	-3.388
WS_2	0.483	0.945	0.462	-0.138	-1.389	-3.913

Table B.1: Data for intercalated H-phase TMDC sulfides, including the intercalant concentration for phase crossover (a in Li_aMS_2 or Mg_aMS_2), average intercalation voltage, and E_{IS} values at $a = 1$.

	Crossover		Average Voltage (V)		E_{IS} (eV)	
TMDC	Li	Mg	Li	Mg	Li	Mg
$TiSe_2$	1.435	1.052	2.229	0.797	1.274	0.872
$ZrSe_2$	1.104	0.690	2.225	0.802	1.488	1.555
$HfSe_2$	1.337	0.719	1.912	0.590	1.040	0.617
VSe_2	0.482	0.082	1.939	0.396	0.560	-1.708
$NbSe_2$	-0.628	0.474	1.972	0.446	0.817	-0.871
$TaSe_2$	-3.305	0.716	1.759	0.205		
$CrSe_2$	0.035	0.293	-10.184	0.743	-15.759	-0.786
$MoSe_2$	0.459	0.270	0.561	-0.049	-1.219	-3.318
WSe_2	0.463	0.738	0.279	-0.121	-1.675	-3.844

Table B.2: Data for intercalated H-phase TMDC selenides, including the intercalant concentration for phase crossover (a in Li_aMSe_2 or Mg_aMSe_2), average intercalation voltage, and E_{IS} values at $a = 1$.

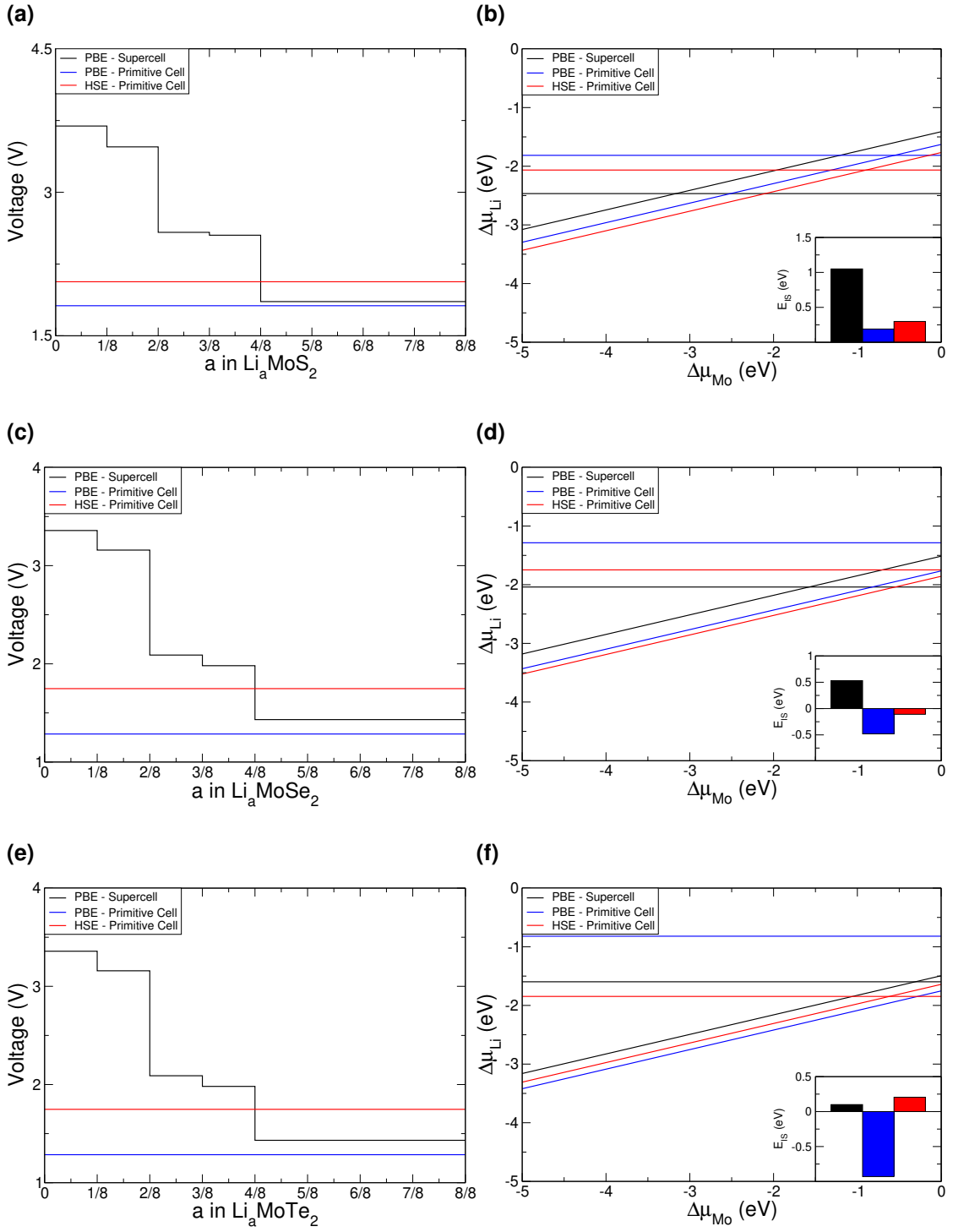

Figure B.13: Comparison of results using the PBE and HSE06 functionals. B.13a, B.13c, and B.13e present the voltages for MoS_2, $MoSe_2$, and $MoTe_2$, respectively. B.13b, B.13d, and B.13f present the phase diagrams for MoS_2, $MoSe_2$, and $MoTe_2$, respectively. The insets show the values of E_{IS}.

density of states for the selection of materials that were highlighted in the main article, i.e. NbS_2, HfS_2, and GeS_2. From these, it is clear to see the dominant *p*-character of the valence band (indicated by the magenta) of all three materials.

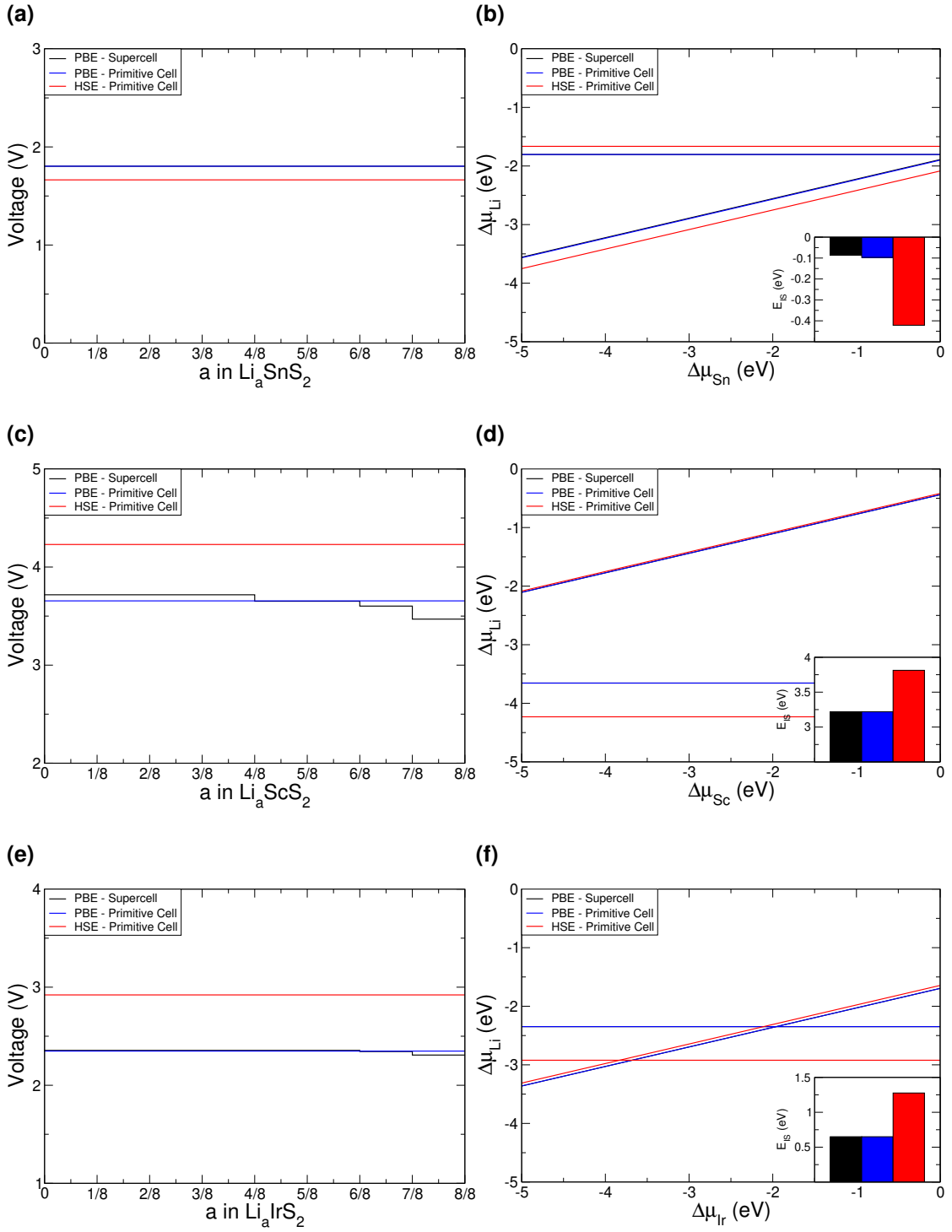

Figure B.14: Comparison of results using the PBE and HSE06 functionals. B.14a, B.14c, and B.14e present the voltages for SnS_2, ScS_2, and IrS_2, respectively. B.14b, B.14d, and B.14f present the phase diagrams for SnS_2, ScS_2, and IrS_2, respectively. The insets show the values of E_{IS}.

For the NbS_2 and HfS_2 materials, it is clear to see the *d*-character of the conduction band (indicated by green). However, GeS_2 does not show this *d*-character of the conduction bands, instead presenting further *p*-character due to the position

	Crossover		Average Voltage (V)		E_{IS} (eV)	
TMDC	Li	Mg	Li	Mg	Li	Mg
$TiTe_2$	2.208	1.364	1.676	0.477	0.641	0.156
$ZrTe_2$	1.701	0.791	1.715	0.520	0.890	0.913
$HfTe_2$	1.770	0.803	1.486	0.369	0.521	0.119
VTe_2	-0.033	-0.004	1.367	0.018	-0.051	-2.520
$NbTe_2$	1.178	0.775	1.470	0.225	0.238	-1.239
$TaTe_2$	0.080	0.731	1.318	0.069		-2.187
$CrTe_2$	0.337	0.158	1.284	0.483	-0.304	-1.088
$MoTe_2$	0.416	0.923	0.369	-0.186	-1.364	-3.285
WTe_2	0.403	0.783	0.153	-0.209	-1.818	-3.875

Table B.3: Data for intercalated H-phase TMDC tellurides, including the intercalant concentration for phase crossover (a in Li_aMTe_2 or Mg_aMTe_2), average intercalation voltage, and E_{IS} values at $a = 1$.

of Ge within the *p*-block on the periodic table.

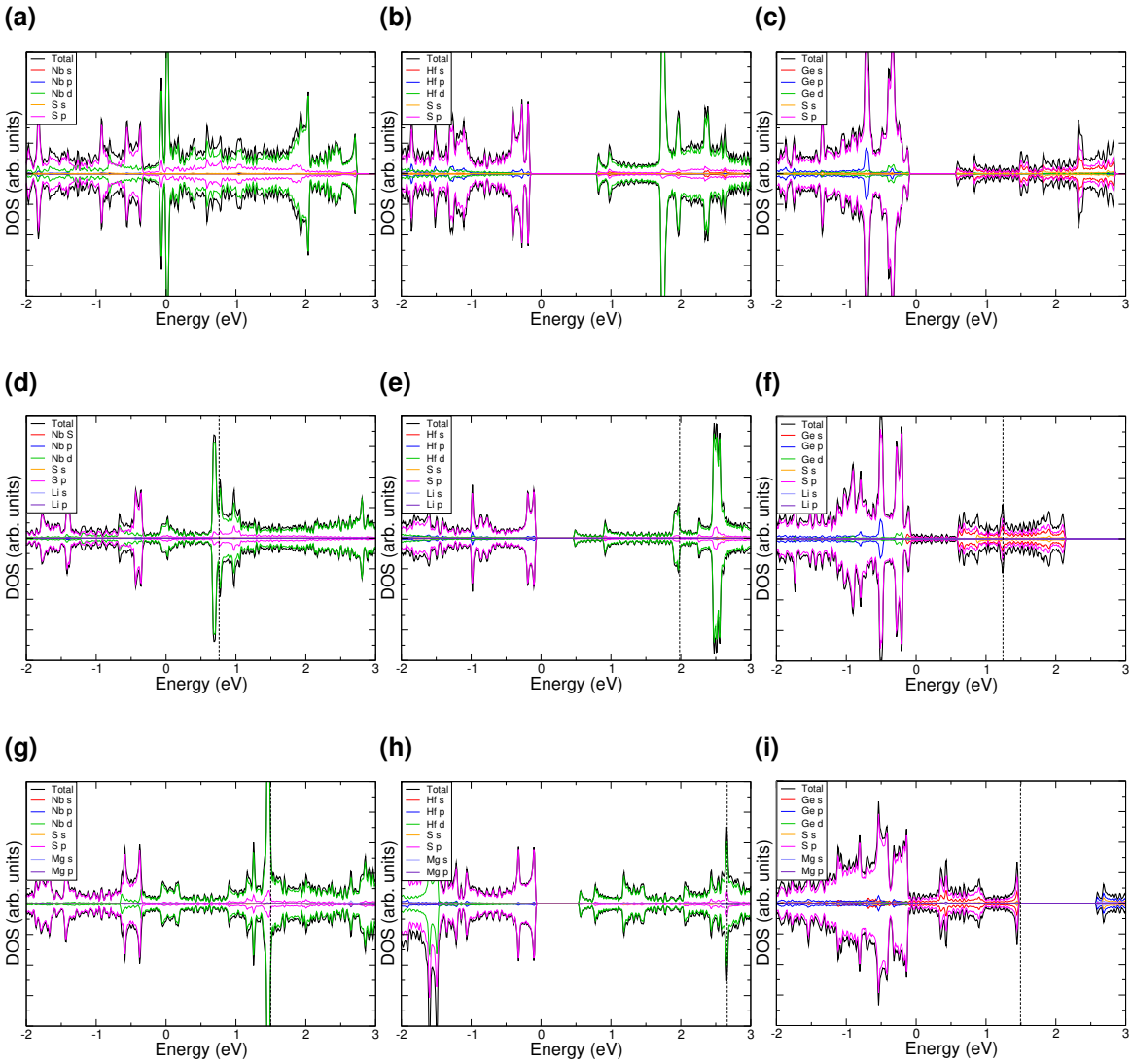

Figure B.15: Atomic-orbital decomposed density of states for selected materials, NbS_2 (B.15a, B.15d, and B.15g), HfS_2 (B.15b, B.15e, and B.15h), and GeS_2 (B.15c, B.15f, and B.15i). These have been aligned as the electronic structures presented in the main article have been.

Appendix C

Supplementary Information to Chapter 4

C.1 k-Point Convergence

C.1.1 Graphite Results

The elastic tensor for AB stacked graphite was calculated using k-point grids of $18 \times 18 \times 9$ (2,916 total, 185 irreducible), $24 \times 24 \times 12$ (6,912 total, 427 irreducible), and $30 \times 30 \times 15$ (13,500 total, 728 irreducible). More k-points are used in the grids compared to the TMDCs presented in the main article due to the smaller lattice constant of graphite. However, the density of k-points used for the study of graphite is comparable to the density of k-points used for the study of the TMDCs.

The elements of the tensor, along with values found within literature, are presented in Table C.1. As can be seen, for the tensor elements of c_{11}, c_{12}, c_{33}, and c_{66} the difference between the higher k-point grids considered and the experiment and other theoretical results is small. Disagreement between experiment and calculations is observed in the values of c_{13} and c_{44}. For c_{13} the range of theoretical data and the choice of approach presents a large range of values with the only measured value being provided by sonic scattering. Similarly, the c_{44} value shows a similar range. Critically, all the data presented shows that the minimum k-point

density required corresponds to the $24 \times 24 \times 12$ grid (which is similar to that we have adopted for the TMDCs). From these elastic tensor elements we can obtain several elastic properties, as given by the discussions of the main article. We present these in Table C.2, where we see close agreement with literature values.

Method	c_{11} (GPa)	c_{12} (GPa)	c_{13} (GPa)	c_{33} (GPa)	c_{44} (GPa)	c_{66} (GPa)
Our work $18 \times 18 \times 9$	1042.98	216.83	-2.99	32.32	-0.24	413.07
Our work $24 \times 24 \times 12$	1038.40	221.40	-2.98	32.37	1.45	408.50
Our work $30 \times 30 \times 15$	1051.02	208.75	-2.96	32.29	2.54	421.14
LDA [275]	1104.8	203.9	2.5	30.9	5.6	450.45
LDA [277]	1105	204	2.5	30.9	5.6	450
LDA [422]	1037.7(2.4)	180.8(1.6)	-12.4(0.3)	22.7(0.6)	1.2(0.5)	428.4
GGA-PBE [422]	1036.3(2.4)	170.3(1.4)	-12.4(0.2)	39.8(0.6)	3.3(0.5)	432.9
Lattice dynamics [423]	1211.3	275.5	0.59	36.79	4.18	468.0
Lattice dynamics [424]	1060	180	15	36.5	4.0	440
Lattice dynamics [425]	1130	354	-	37.4	4.4	388
Lattice dynamics [426]	1060	160	15	36.9	4.2	450
Sonic resonance [313, 427]	1060(20)	180(20)	15(5)	36.5(1.0)	4.0	440
Neutron scattering [428]	-	-	-	-	3.8(0.4)	-
Neutron scattering [429]	-	-	-	37.1(0.5)	-	-
Brillouin scattering [430]	-	-	-	-	5.05(0.35)	-

Table C.1: Comparison of graphite elastic matrix elements calculated in this work and obtained from literature. The numbers in parentheses are error estimates in GPa. Some elements not explicitly written in the provided sources have been included using $c_{66} = \frac{1}{2}(c_{11} - c_{12})$.

Method	Bulk Modulus (GPa)			Shear Modulus (GPa)			Young's Modulus (GPa)			Poisson Ratio			Pugh Ratio		
	V	R	H	V	R	H	V	R	H	V	R	H	V	R	H
Our work $18 \times 18 \times 9$	282.22	30.46	156.34	209.68	-0.60	104.54	504.18	-1.80	256.46	0.20	0.51	0.23	1.35	-50.96	1.50
Our work $24 \times 24 \times 12$	282.23	30.50	156.36	208.53	3.50	106.01	501.95	10.11	259.41	0.20	0.44	0.22	1.35	8.72	1.47
Our work $30 \times 30 \times 15$	282.22	30.43	156.33	214.01	6.01	110.01	512.49	16.91	267.32	0.20	0.41	0.21	1.32	5.07	1.42
LDA [275]	295.37	29.71	162.54	227.77	12.33	120.05	543.58	32.50	289.00	0.19	0.32	0.20	1.30	2.41	1.35
LDA [277]	295.43	29.71	162.57	227.80	12.33	120.07	543.67	32.50	289.04	0.19	0.32	2.41	1.30	2.41	1.35
LDA [422]	267.79	20.82	144.31	215.64	2.89	109.27	510.03	8.29	261.74	0.18	0.43	0.20	1.24	7.21	1.32
GGA-PBE [422]	267.04	35.72	151.38	219.05	7.76	113.40	516.04	21.71	272.23	0.18	0.40	0.20	1.22	4.60	1.33
Lattice dynamics [423]	334.75	35.11	184.93	240.77	9.63	125.20	582.62	26.46	306.44	0.21	0.37	0.22	1.39	3.65	1.48
Lattice dynamics [424]	286.28	35.76	161.02	219.37	9.21	114.29	524.21	25.45	277.27	0.19	0.38	0.21	1.31	3.88	1.41
Lattice dynamics [426]	281.88	36.12	159.00	222.81	9.64	116.22	529.03	26.56	280.36	0.19	0.38	0.21	1.27	3.75	1.39
Sonic resonance [313, 427]	286.28	35.76	161.02	219.37	9.21	114.29	524.21	25.45	277.27	0.19	0.38	0.21	1.31	3.88	1.41

Table C.2: Comparison of graphite elastic values calculated in this work and obtained from literature. Values have been calculated using the elements of the elastic matrix presented in Table C.1.

C.1.2 Lithium Cobalt Oxide Results

The elastic tensor for $LiCoO_2$ was calculated using k-point grids of $12 \times 12 \times 4$ (576 total, 164 irreducible), $18 \times 18 \times 6$ (1,944 total, 202 irreducible), and $24 \times 24 \times 8$ (4,608 total, 449 irreducible). Fewer k-points are used along the $\mathbf{k}_c$ direction compared to the TMDCs presented in the main article due to the larger lattice constant of $LiCoO_2$. However, the density of k-points used for the study of $LiCoO_2$ is comparable to the density of k-points used for the study of the TMDCs. The elements of the tensor, along with values found within literature, are presented in Table C.3. We then compare in Table C.4 various elastic values calculated in this work and presented in literature.

In contrast to graphite, for $LiCoO_2$ experimental values of many of the elastic elements could not be found. Thus we limit our comparison of the elements of the tensor to strict comparison with other calculations, as presented in Table C.3. As can be seen, for the tensor elements of c_{11}, c_{12},c_{13} c_{33}, c_{44}, and c_{66} the difference between the higher k-point grids considered and other theoretical first principle results is small. Disagreement between various methods arises in the value of c_{14}. In our results, the variation in c_{14} with k-point density is very small and whilst it captures the negative value shown in several works, the precise value is open to contention. Again, as noted for graphite, the data presented shows that the k-point density $18 \times 18 \times 6$ grid (which is similar to that we have adopted for the TMDCs) is more than sufficient. Given the natural structural comparisons between $LiCoO_2$ and the TMDCs this provides the basis for our k-point grid choice. From these elastic tensor elements we can obtain several elastic properties, as given by the discussions of the main article. We present these in Table C.4, where we see that our results demonstrate small deviations from the experimentally measured values, with the Reuss scheme generally being the closest to the experimentally derived values.

Method	c_{11} (GPa)	c_{12} (GPa)	c_{13} (GPa)	c_{33} (GPa)	c_{44} (GPa)	c_{14} (GPa)	c_{66} (GPa)
Our work $12 \times 12 \times 4$	362.10	107.44	72.00	227.92	60.13	-2.11	127.33
Our work $18 \times 18 \times 6$	359.68	106.27	70.33	225.70	58.65	-2.58	126.71
Our work $24 \times 24 \times 8$	362.03	107.37	71.90	227.78	60.12	-2.11	127.33
HSE [277]	422	106	62	239	68.1	0	158
Materials Project [431]	233	104	51	196	30	-46	65
PBE [432]	339.79	101.6	65.78	214.67	51.47	6.39	119.10
GULP [433]	596.4	199.4	133.5	375.2	124.1	-8.28	198.5
GULP [433]	569.9	185.2	87.8	313.8	68.0	-33.6	192.3

Table C.3: Comparison of $LiCoO_2$ elastic matrix elements calculated in this work and obtained from literature. Some elements not explicitly written in the provided sources have been included using $c_{66} = \frac{1}{2}(c_{11} - c_{12})$.

Method	Bulk Modulus (GPa)			Shear Modulus (GPa)			Young's Modulus (GPa)			Poisson Ratio			Pugh Ratio		
	V	R	H	V	R	H	V	R	H	V	R	H	V	R	H
Our work $12 \times 12 \times 4$	161.67	151.63	156.65	96.23	84.69	90.46	240.89	214.20	227.57	0.25	0.26	0.26	1.68	1.79	1.73
Our work $18 \times 18 \times 6$	159.88	149.79	154.83	95.34	83.33	89.34	238.60	210.89	224.78	0.25	0.27	0.26	1.68	1.80	1.73
Our work $24 \times 24 \times 8$	161.58	151.53	156.55	96.23	84.69	90.46	240.86	214.17	227.55	0.25	0.26	0.26	1.68	1.79	1.73
HSE [277]	171	156	163	115	98.6	107	283	244	264	0.22	0.24	0.23	1.48	1.58	1.53
LDA [434]	168.5 (EOS)			-	-	-	-	-	-	-	-	-	-	-	-
GGA [434]	142.9 (EOS)			-	-	-	-	-	-	-	-	-	-	-	-
Nanoindentation [435]	-			-			191 (10)			-			-		
Pulse echo [435]	-			80 (1)			198 (2)			0.24			-		
XRD [434]	149 (20)			-			-			-			-		
Nanoindentation [436]	-			-			174 (25)			-			-		

Table C.4: Comparison of $LiCoO_2$ elastic values calculated in this work and obtained from literature. The numbers in parentheses are error estimates. EOS indicates values calculated by fitting an equation of state, and not using the V/R/H methods.

C.2 Elastic Stability

In Table C.5, we highlight the materials which break one or more of the elastic stability conditions, along with the conditions that are broken. The elastic stability conditions have been outlined elsewhere for different crystal systems [357], which for trigonal crystals are,

$$\begin{aligned} &(a) \quad c_{11} > |c_{12}| \\ &(b) \quad c_{44} > 0 \\ &(c) \quad c_{13}^2 < \frac{1}{2} c_{33}(c_{11} + c_{12}) \\ &(d) \quad c_{14}^2 < \frac{1}{2} c_{44}(c_{11} - c_{12}) = c_{44} c_{66}, \end{aligned} \tag{C.1}$$

as given by equation (4.30).

MX_2	Conditions Broken	$LiMX_2$	Conditions Broken	$MgMX_2$	Conditions Broken
ScS_2	b d	$LiFeS_2$	a d	$MgCrS_2$	c
YS_2	b d	$LiCuS_2$	d	$MgMnS_2$	a c
RuS_2	d	$LiAgS_2$	b d	$MgPdS_2$	b d
PbS_2	b d	$LiAuS_2$	a b d	$MgPtS_2$	a b d
$ScSe_2$	b d	$LiMnSe_2$	a b c d	$MgCuS_2$	d
YSe_2	b d	$LiAuSe_2$	b d	$MgAgS_2$	b d
$FeSe_2$	a c d	$LiCrTe_2$	c	$MgAuS_2$	a b d
$RuSe_2$	d	$LiMnTe_2$	c	$MgCrSe_2$	a c d
$RhSe_2$	d	$LiReTe_2$	a d	$MgReSe_2$	a d
$PbSe_2$	a b d	$LiPbTe_2$	a d	$MgPdSe_2$	d
YTe_2	b d			$MgPtSe_2$	b d
$PdTe_2$	a b d			$MgCuSe_2$	b d
				$MgAgSe_2$	b d
				$MgAuSe_2$	b d
				$MgCrSe_2$	a c d
				$MgReSe_2$	a d
				$MgPdSe_2$	d
				$MgPtSe_2$	b d
				$MgCuSe_2$	b d
				$MgAgSe_2$	b d
				$MgAuSe_2$	b d
				$MgTaTe_2$	a c d
				$MgMnTe_2$	c
				$MgCuTe_2$	b d
				$MgAgTe_2$	b d
				$MgAuTe_2$	b d

Table C.5: Table indicated which materials are not elastically stable, and the stability conditions they break (given by equation (4.30)).

C.3 Elastic Quantities

In the main article, we highlighted the elastic properties of the sulfide materials. Here, we present the equivalent data for the analogous selenide and telluride materials. The bulk and shear moduli are shown in Figure C.1. The Hill values of bulk (B_{VRH}) and shear (G_{VRH}) moduli provide an intermediate to the Voigt upper limit and the Reuss lower limit. Many of the other elastic properties are derived from these values of bulk and shear moduli, and we only present those calculated from B_{VRH} and G_{VRH} in the main article for brevity and clarity of figures. In the following, we also include the values determined with the Voigt and Reuss schemes. Figure C.2 presents the Young's modulus, and Figure C.3 presents the elastic ratios indicating material ductility.

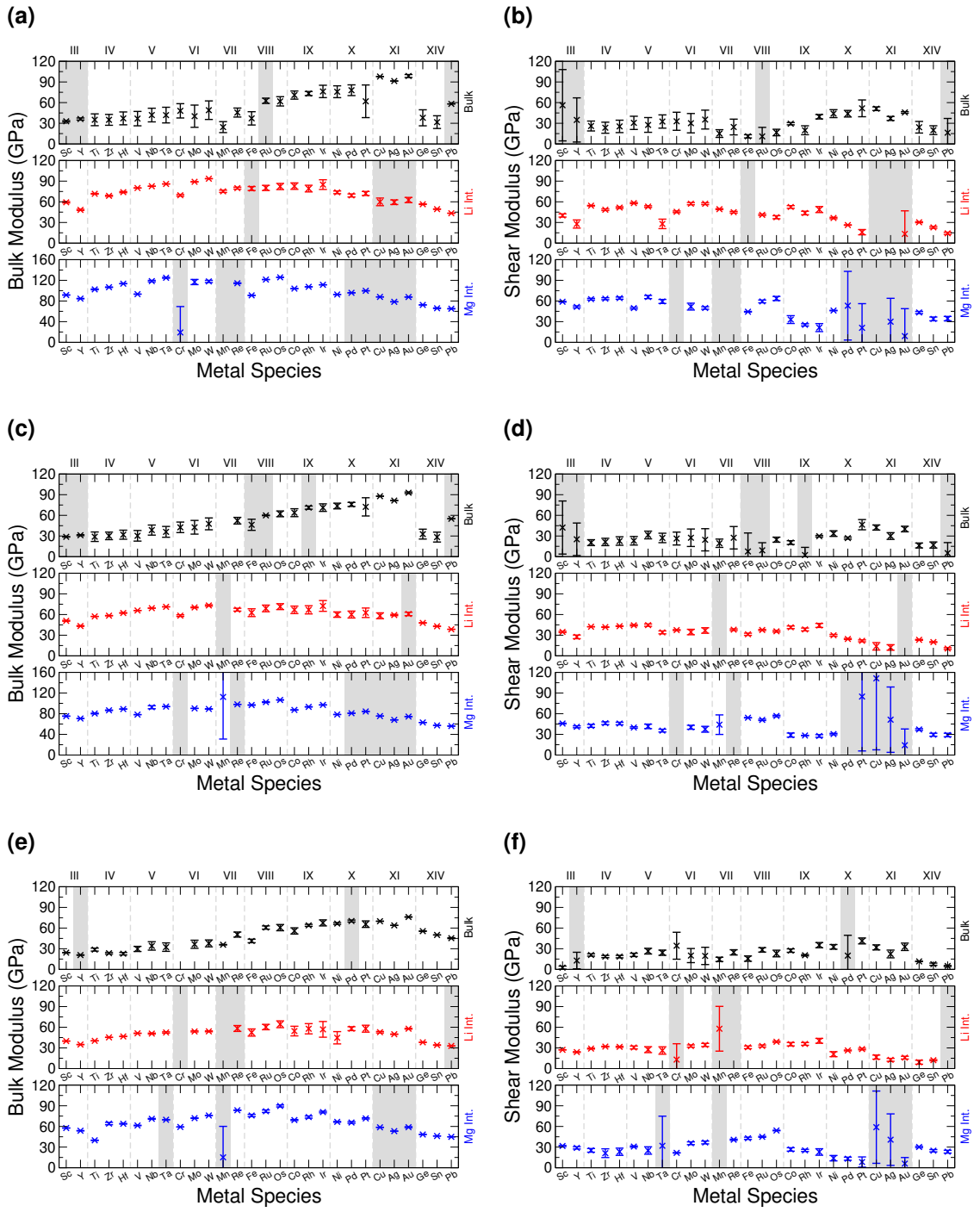

Figure C.1: Bulk modulus for sulfide (C.1a), selenide (C.1c), and telluride (C.1e) TMDC materials. We similarly show the shear modulus for sulfide (C.1b), selenide (C.1d), and telluride (C.1f) materials. Values calculated using the VRH scheme are presented with crosses, and the corresponding Reuss and Voigt results are presented as error bars. Data for the pristine bulk, lithium-intercalated, and magnesium-intercalated structures is presented in black, red, and blue, respectively. Materials which are not elastically stable are indicated with shaded regions.

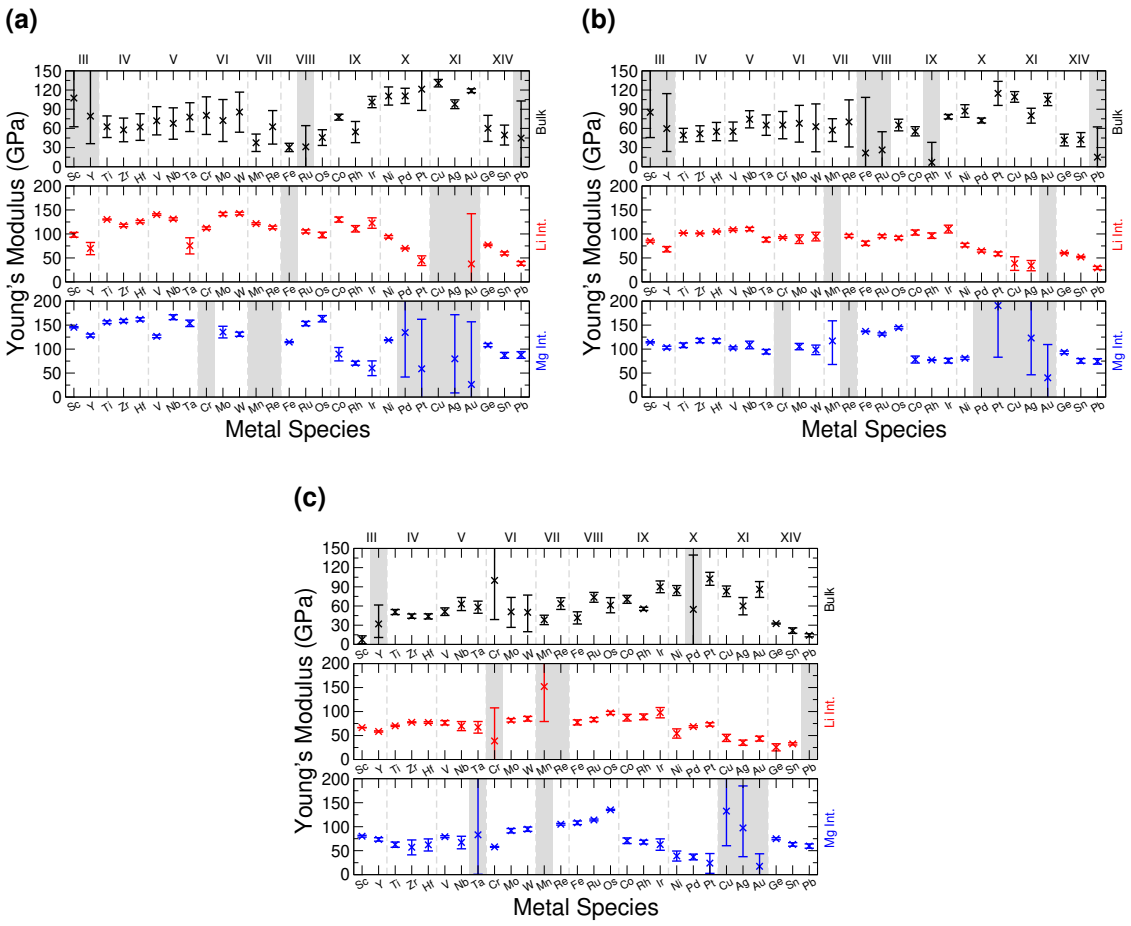

Figure C.2: Young's modulus for sulfide (C.2a), selenide (C.2b), and telluride (C.2c) TMDC materials. Values calculated using the VRH scheme are presented with crosses, and the corresponding Reuss and Voigt results are presented as error bars. Data for the pristine bulk, lithium-intercalated, and magnesium-intercalated structures is presented in black, red, and blue, respectively. Materials which are not elastically stable are indicated with shaded regions.

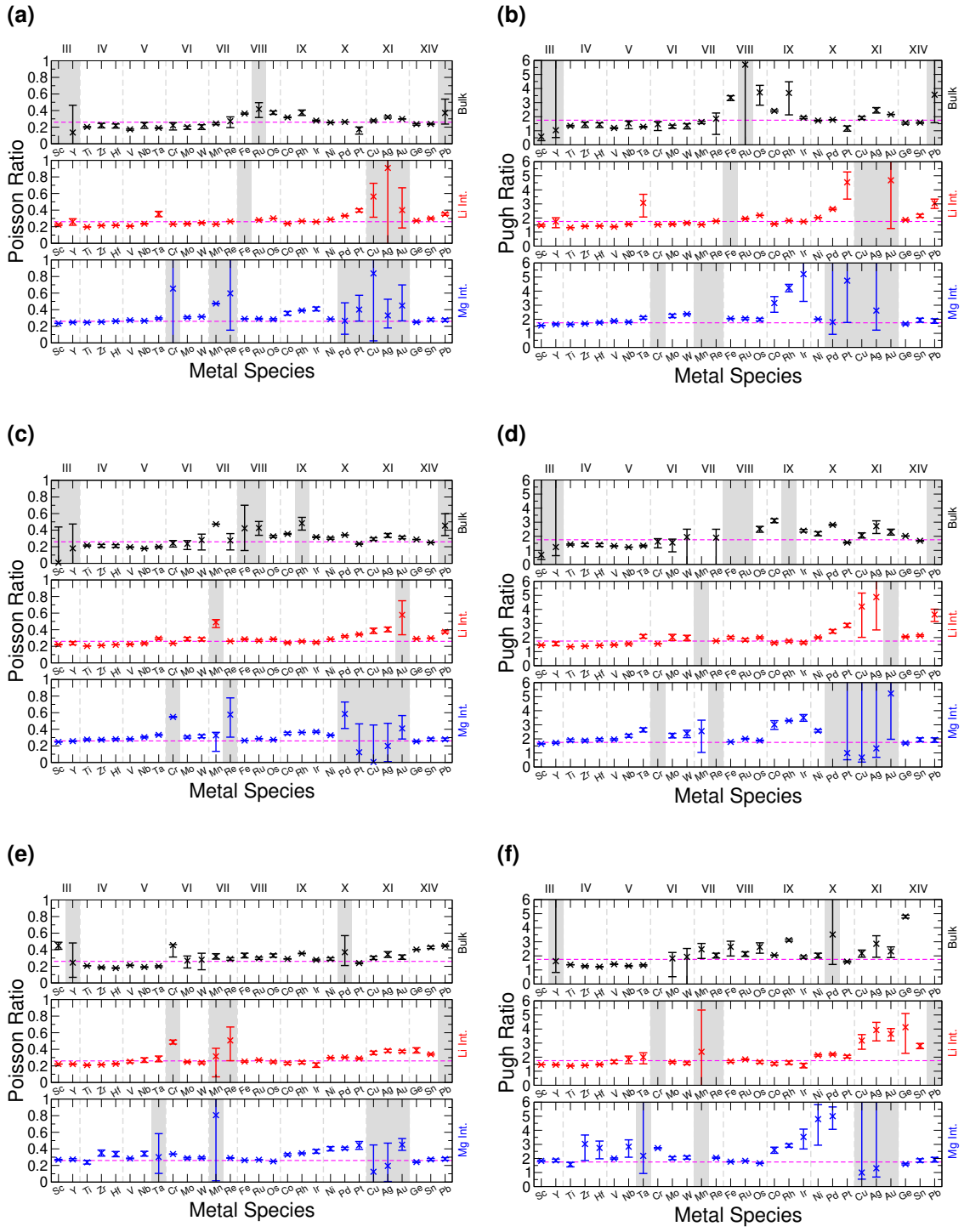

Figure C.3: Values of Poisson ratio for sulfides (C.3a), selenides (C.3c), and tellurides (C.3e), and Pugh ratio for sulfides (C.3b), selenides (C.3d), and tellurides (C.3f). Crosses indicate those calculated using the VRH scheme, and the corresponding Reuss and Voigt results are presented as error bars. Data for the pristine bulk, lithium-intercalated, and magnesium-intercalated structures is presented in black, red, and blue, respectively. A Poisson ratio of 0.26 and a Pugh ratio of 1.75 are indicated with horizontal dashed lines. Materials which are not elastically stable are indicated with shaded regions.

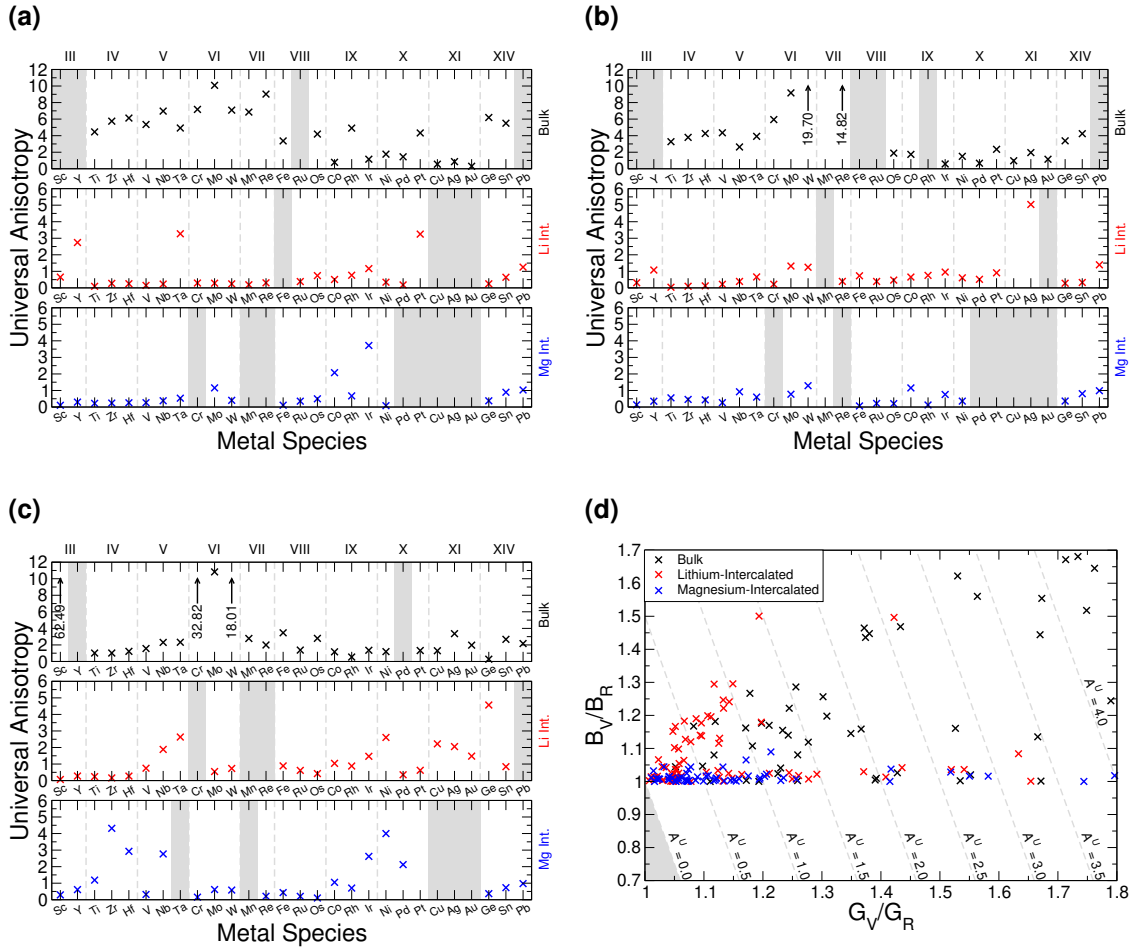

Figure C.4: Universal anisotropy values for the sulfide (C.4a), selenide (C.4b), and telluride (C.4c) materials, and data for the pristine bulk, lithium-intercalated, and magnesium-intercalated structures is presented in black, red, and blue, respectively. Arrows with labels indicate values that lie outside of the plotted range. Materials which are not elastically stable are indicated with shaded regions. C.4d shows the elastic anisotropy diagram, with data for all materials included.

C.4 Material Anisotropy

The universal anisotropy A^U is presented in Figure C.4, and the elastic constants c_{11} and c_{33} are shown in Figure C.5 for the sulfide, selenide, and telluride materials.

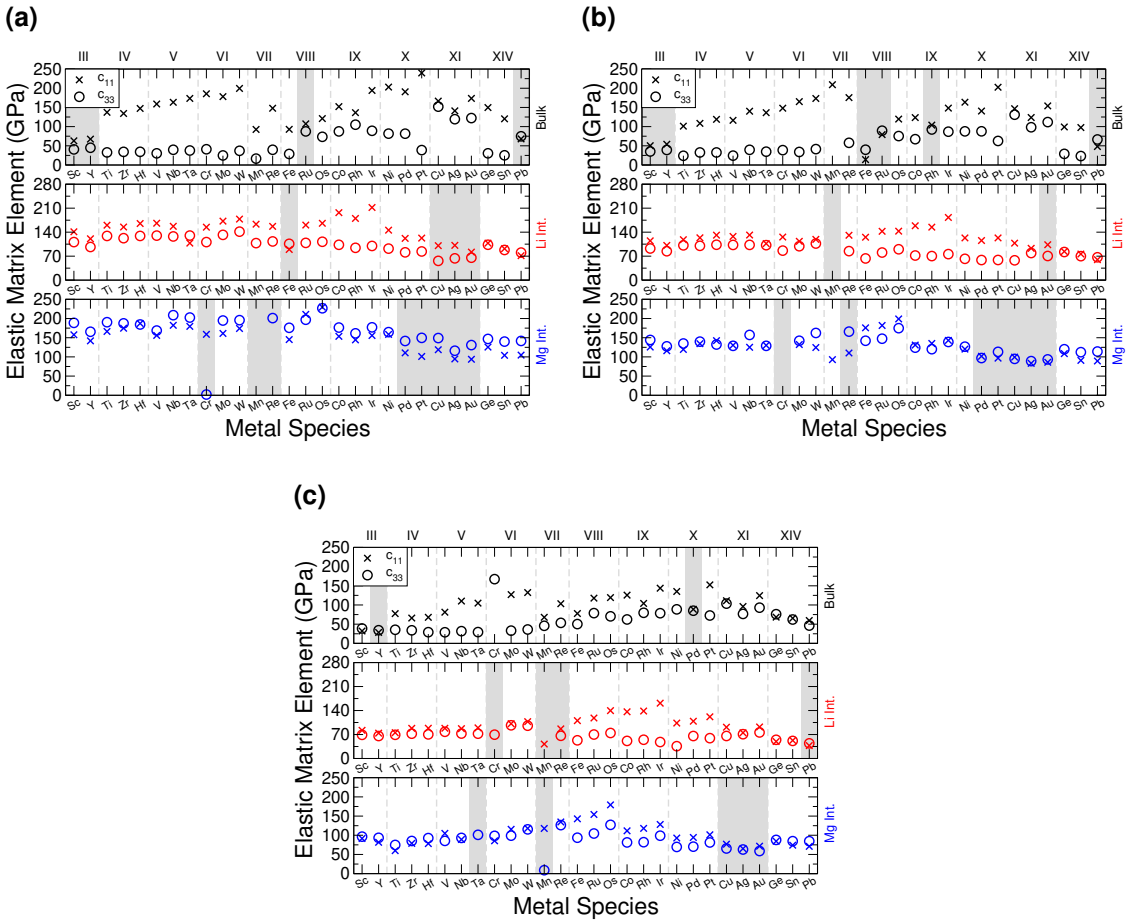

Figure C.5: Elements of the elastic matrix, c_{11} and c_{33}, for the sulfide (C.5a), selenide (C.5b), telluride (C.5c) TMDC materials. Data for the pristine bulk, lithium-intercalated, and magnesium-intercalated structures is presented in black, red, and blue, respectively. Materials which are not elastically stable are indicated with shaded regions.

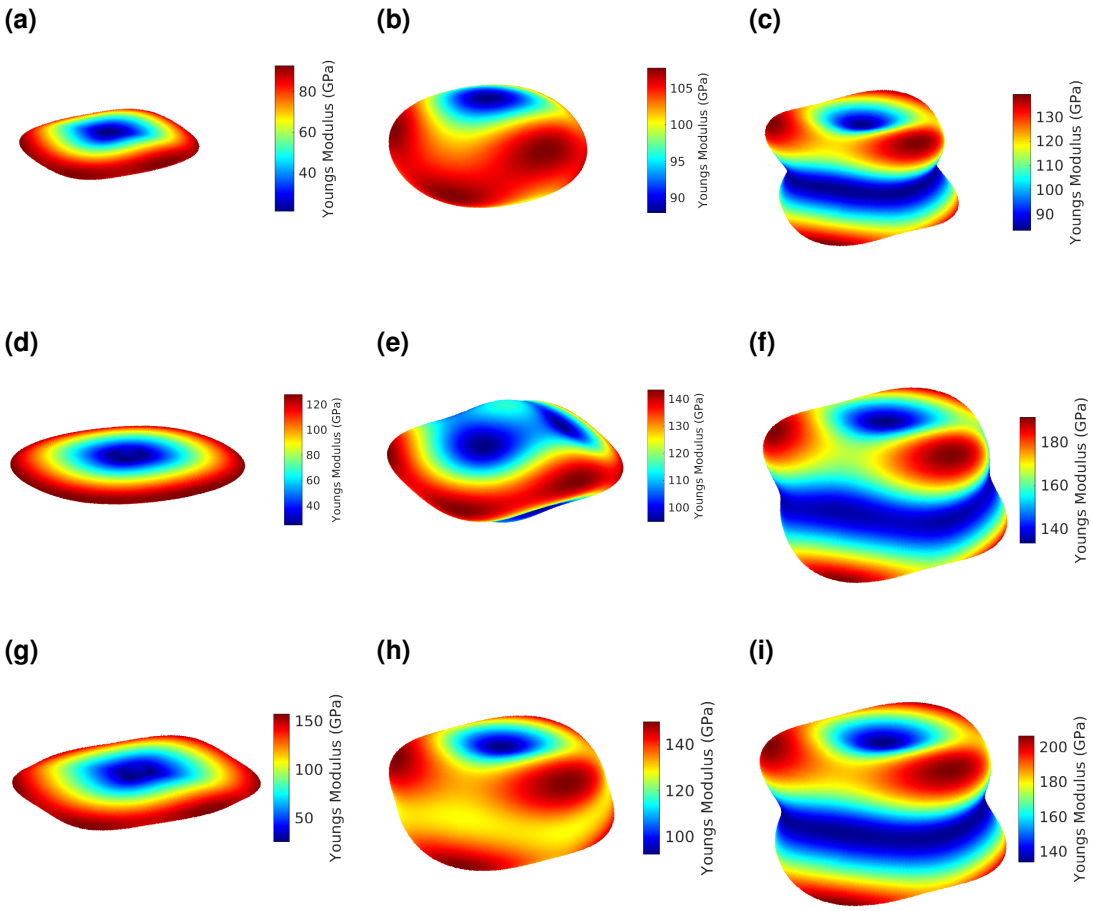

Figure C.6: Three-dimensional heat maps showing the angular-dependent Young's modulus for $TiSe_2$ (C.6a), $LiTiSe_2$ (C.6b), $MgTiSe_2$ (C.6c), ZrS_2 (C.6d), $LiZrS_2$ (C.6e), $MgZrS_2$ (C.6f), NbS_2 (C.6g), $LiNbS_2$ (C.6h), and $MgNbS_2$ (C.6i).

Anisotropic Young's Modulus

In Chapter 4, we presented the angular dependence of the Young's modulus for TiS_2, showing how this changed with lithium and magnesium intercalation. We include here similar graphics for several other TMDC materials. In Figure C.6 we show the anisotropic Young's modulus for $TiSe_2$, ZrS_2, and NbS_2, in their pristine and intercalated forms, and we show in Figure C.7 the anisotropic Young's modulus for MoS_2, WS_2, and SnS_2, in their pristine and intercalated forms.

In each of these, we see that the out-of-plane Young's modulus for the pristine structures is significantly smaller (with values below 50 GPa) than the in-plane Young's modulus (with values exceeding 100 GPa). Due to the strong in-plane covalent bonding and weak out-of-plane vdW bonding, this is to be expected.

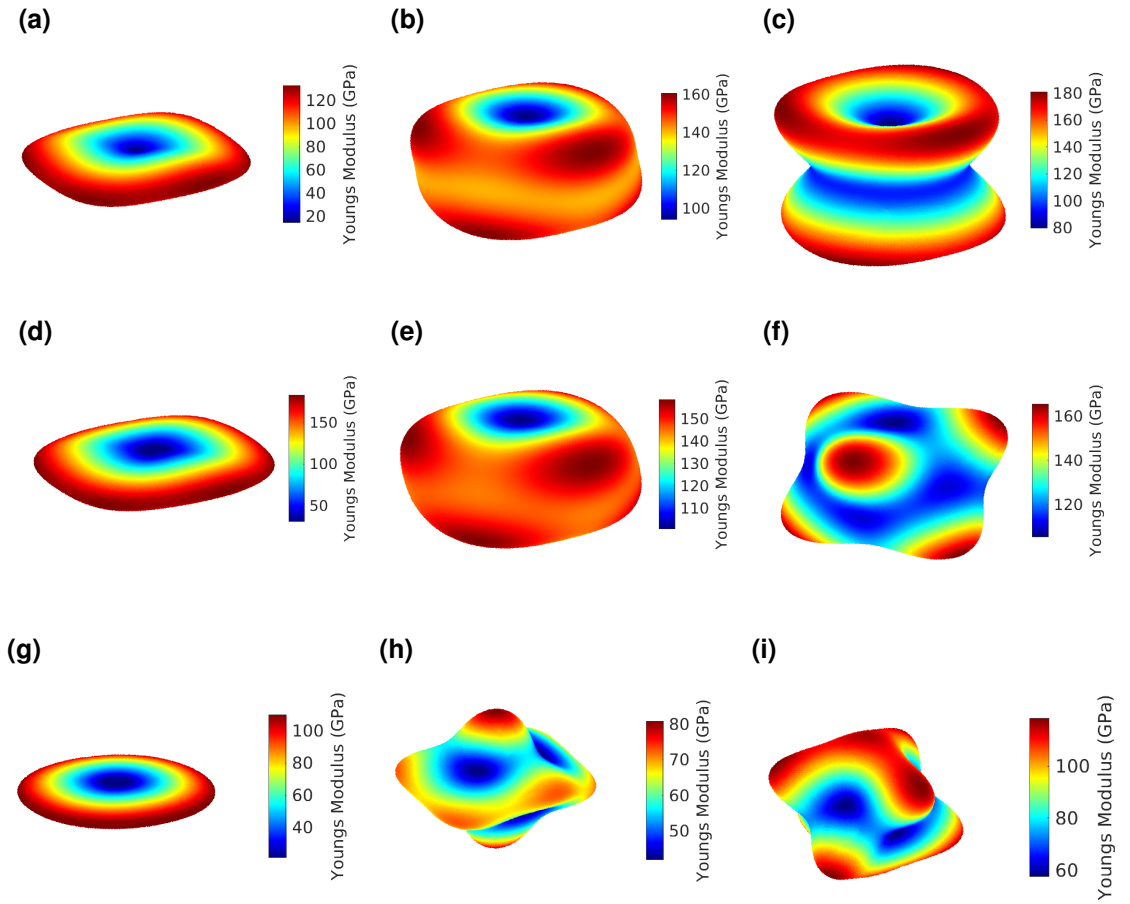

Figure C.7: Three-dimensional heat maps showing the angular-dependent Young's modulus for MoS_2 (C.7a), $LiMoS_2$ (C.7b), $MgMoS_2$ (C.7c), WS_2 (C.7d), $LiWS_2$ (C.7e), $MgWS_2$ (C.7f), SnS_2 (C.7g), $LiSnS_2$ (C.7h), and $MgSnS_2$ (C.7i).

With the introduction of lithium, there is an increase in the in-plane Young's modulus, but a more dramatic increase in the out-of-plane component. This indicates the strengthened bonding between consecutive TMDC layers, facilitated by the lithium ion. We see a similar effect with magnesium intercalation, but high Young's modulus values are achieved due to the larger charge transfer.

Appendix D

Supplementary Information to Chapter 5

D.1 Vibrational Entropy

Here, we outline the origin of the expressions for vibrational entropy, S_{vib}, as given in equation (5.3), which was used for the calculation of vibrational free energy $F_{vib} = TS_{vib}$. For a single harmonic oscillation of frequency $\omega_i = \frac{\epsilon_i}{\hbar}$, the partition function is given by,

$$\begin{aligned} Z_i &= \sum_{n=0}^{\infty} \exp\left(-\beta\left(n+\frac{1}{2}\right)\epsilon_i\right) \\ &= \exp\left(-\frac{1}{2}\beta\epsilon_i\right)\sum_{n}^{\infty}\exp(-\beta n\epsilon_i) \\ &= \exp\left(-\frac{1}{2}\beta\epsilon_i\right)\sum_{n}^{\infty}\exp(-\beta\epsilon_i)^n, \end{aligned} \tag{D.1}$$

where if we write $r = \exp(-\beta\epsilon_i) < 1$, we note that the above expression is a geometric series, $\sum_n^{\infty} r^n = \frac{1-r^{n+1}}{1-r}$ as $n \to \infty$, multiplied by a prefactor $\exp\left(-\frac{1}{2}\beta\epsilon_i\right)$. Hence, we can write,

$$Z_i = \frac{\exp\left(-\frac{1}{2}\beta\epsilon_i\right)}{1-\exp(-\beta\epsilon_i)}. \tag{D.2}$$

For a harmonic solid consisting of N atoms, we need to consider 3N independent harmonic oscillators. The partition function for such a system is given by the

product of the partition functions of the independent oscillators,

$$\begin{aligned} Z_N &= \prod_i^{3N} Z_i \\ &= \prod_i^{3N} \frac{\exp\left(-\frac{1}{2}\beta\epsilon_i\right)}{1-\exp(-\beta\epsilon_i)}. \end{aligned} \tag{D.3}$$

With the above partition function, we are now able to calculate the vibrational free energy due to phonons using $F = -k_B T \ln Z$, hence,

$$\begin{aligned} F_{vib} &= -k_B T \ln Z_N \\ &= -k_B T \ln \prod_i Z_i \\ &= -k_B T \sum_i \ln Z_i \\ &= -k_B T \sum_i \ln \frac{\exp\left(-\frac{1}{2}\beta\epsilon_i\right)}{1-\exp(-\beta\epsilon_i)} \\ &= -k_B T \left[\sum_i \ln \exp\left(-\frac{1}{2}\beta\epsilon_i\right) - \sum_i \ln\left(1-\exp(-\beta\epsilon_i)\right)\right] \\ &= -k_B T \left[\sum_i -\frac{1}{2}\beta\epsilon_i - \sum_i \ln\left(1-\exp(-\beta\epsilon_i)\right)\right] \\ &= \sum_i \frac{\epsilon_i}{2} + k_B T \sum_i \ln\left(1-\exp(-\beta\epsilon_i)\right). \end{aligned} \tag{D.4}$$

The first of these terms is the zero-point energy term, and the second is the term due to vibrations due to finite temperatures. The vibrational entropy (due to phonons) is then obtained by differentiating F_{vib} with respect to the temperature, T,

$$\begin{aligned} S_{vib} &= -\frac{dF_{vib}}{dT} \\ &= -\frac{d}{dT}\left[\sum_i \frac{\epsilon_i}{2} + k_B T \sum_i \ln\left(1-\exp(-\beta\epsilon_i)\right)\right] \\ &= \frac{d}{dT}\left[- k_B T \sum_i \ln\left(1-\exp(-\beta\epsilon_i)\right)\right] \\ &= k_B \sum_i \left[- \ln\left(1-\exp(-\beta\epsilon_i)\right) + \frac{\beta\epsilon_i}{\exp(\beta\epsilon_i)-1}\right] \\ S_{vib} &= \frac{1}{T}\sum_i \left[\epsilon_i \frac{1}{\exp(\beta\epsilon_i)-1}\right] - k_B\left[\sum_i \ln\left(1-\exp(-\beta\epsilon_i)\right)\right]. \end{aligned} \tag{D.5}$$

Using $\sinh x = \frac{\exp(x)-\exp(-x)}{2} = \frac{1-\exp(-2x)}{2\exp(-x)}$, we get,

$$\begin{aligned} 1-\exp(-\beta\epsilon_i) &= 2\sinh\left(\frac{\beta\epsilon_i}{2}\right)\exp\left(-\frac{\beta\epsilon_i}{2}\right) \\ \ln\Big(1-\exp(-\beta\epsilon_i)\Big) &= \ln\left(2\sinh\left(\frac{\beta\epsilon_i}{2}\right)\exp\left(-\frac{\beta\epsilon_i}{2}\right)\right) \\ &= \ln\left(2\sinh\left(\frac{\beta\epsilon_i}{2}\right)\right) + \ln\left(\exp\left(-\frac{\beta\epsilon_i}{2}\right)\right) \\ \ln\Big(1-\exp(-\beta\epsilon_i)\Big) &= \ln\left(2\sinh\left(\frac{\beta\epsilon_i}{2}\right)\right) - \frac{\beta\epsilon_i}{2}, \end{aligned} \tag{D.6}$$

which is the second term in the expression for S_{vib}. For the first term, we start with,

$$\begin{aligned} \frac{1}{\exp(\beta\epsilon_i)-1} &= \frac{\exp(-\beta\epsilon_i)}{1-\exp(-\beta\epsilon_i)} \\ &= \frac{\exp(-\beta\epsilon_i)}{2\sinh\left(\frac{\beta\epsilon_i}{2}\right)\exp\left(-\frac{\beta\epsilon_i}{2}\right)} \\ &= \frac{\exp\left(-\frac{\beta\epsilon_i}{2}\right)}{2\sinh\left(\frac{\beta\epsilon_i}{2}\right)}. \end{aligned} \tag{D.7}$$

Using $\exp(-x) = \cosh x - \sinh x$ and $\cosh(-x) = \cosh(x)$,

$$\begin{aligned} \frac{1}{\exp(\beta\epsilon_i)-1} &= \frac{\cosh\left(-\frac{\beta\epsilon_i}{2}\right) - \sinh\left(-\frac{\beta\epsilon_i}{2}\right)}{2\sinh\left(\frac{\beta\epsilon_i}{2}\right)} \\ &= \frac{\cosh\left(\frac{\beta\epsilon_i}{2}\right)}{2\sinh\left(\frac{\beta\epsilon_i}{2}\right)} - \frac{\sinh\left(-\frac{\beta\epsilon_i}{2}\right)}{2\sinh\left(\frac{\beta\epsilon_i}{2}\right)} \\ \frac{1}{\exp(\beta\epsilon_i)-1} &= \frac{1}{2}\coth\left(\frac{\beta\epsilon_i}{2}\right) - \frac{1}{2}, \end{aligned} \tag{D.8}$$

which is the first term in the expression for S_{vib}. Combining these, we get,

$$\begin{aligned} S_{vib} &= \frac{1}{T}\sum_i \left[\epsilon_i \frac{1}{\exp(\beta\epsilon_i)-1}\right] - k_B\left[\sum_i \ln\left(1-\exp(-\beta\epsilon_i)\right)\right] \\ &= \frac{1}{T}\sum_i \epsilon_i\left[\frac{1}{2}\coth\left(\frac{\beta\epsilon_i}{2}\right) - \frac{1}{2}\right] - k_B\left[\sum_i \ln\left(2\sinh\left(\frac{\beta\epsilon_i}{2}\right)\right) - \frac{\beta\epsilon_i}{2}\right] \\ &= \frac{1}{2T}\sum_i [\epsilon_i \coth\left(\frac{\beta\epsilon_i}{2}\right)] - k_B\left[\sum_i \ln\left(2\sinh\left(\frac{\beta\epsilon_i}{2}\right)\right)\right]. \end{aligned} \tag{D.9}$$

If we replace the oscillator energy ϵ_i with the energy of a phonon in band ν with wave vector $\mathbf{q}$, we get an alternative expression for the vibrational entropy in terms of sums over the individual phonon states,

$$S_{vib} = \frac{1}{2T}\left[\sum_{\nu,\mathbf{q}} \hbar\omega_{\nu,\mathbf{q}} \coth\left(\frac{\hbar\omega_{\nu,\mathbf{q}}}{2k_BT}\right)\right] - k_B\left[\sum_{\nu,\mathbf{q}} \ln\left(2\sinh\left(\frac{\hbar\omega_{\nu,\mathbf{q}}}{2k_BT}\right)\right)\right]. \tag{D.10}$$

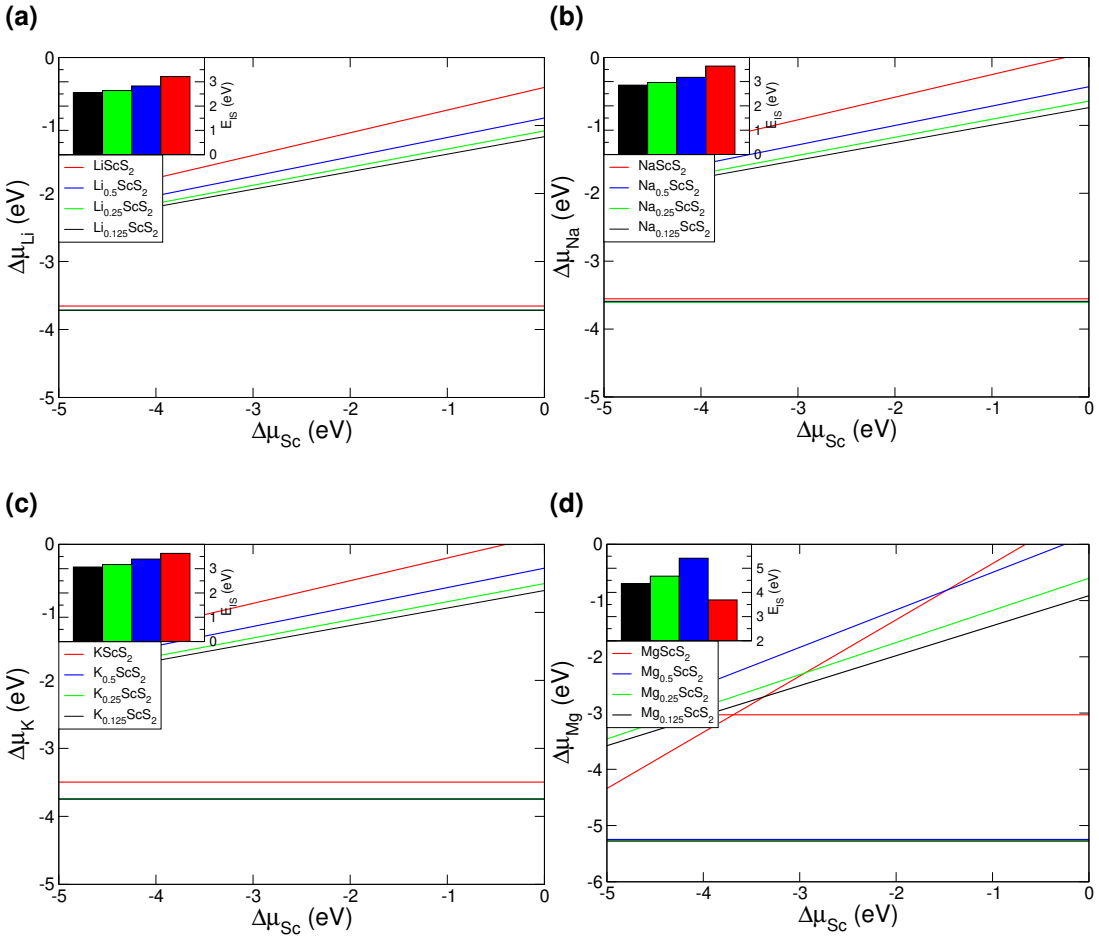

Figure D.1: D.1a, D.1b, D.1c, and D.1d show the phase diagrams for T-ScS_2 intercalated with different concentrations of Li, Na, K and Mg, respectively. The insets show the corresponding values of E_{IS}.

D.2 Phase Diagrams

In Chapter 5, we presented the phase diagrams for α-phase ScS_2 intercalated with the different ionic species, and how they evolved with intercalant concentration. Here, we present equivalent phase diagrams for the other phases of ScS_2, namely the T-phase (Figure D.1) and Hc-phase (Figure D.2). In these, we very similar behaviour as was demonstrated by the α-phase, but a reduced value of E_{IS} corresponding to the higher energy of these phases.

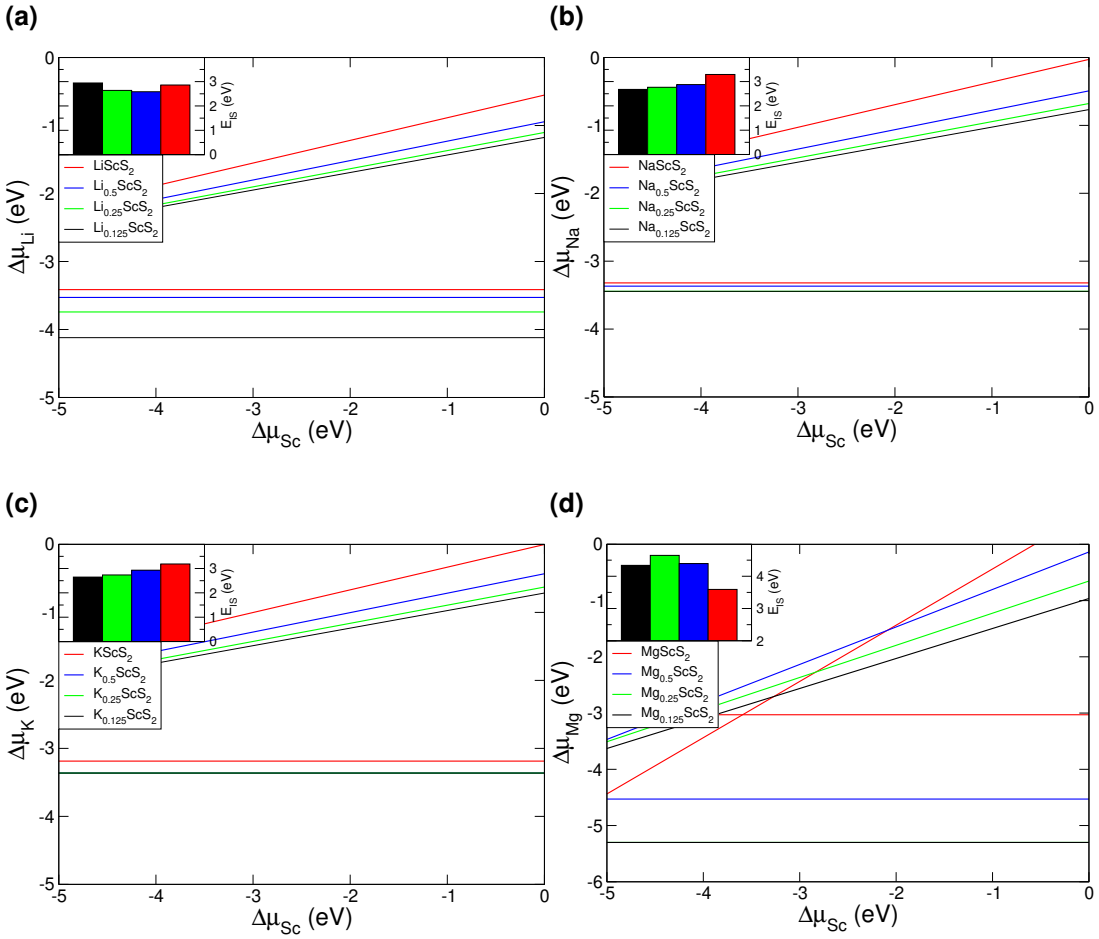

Figure D.2: D.2a, D.2b, D.2c, and D.2d show the phase diagrams for Hc-ScS_2 intercalated with different concentrations of Li, Na, K and Mg, respectively. The insets show the corresponding values of E_{IS}.

D.3 HSE06 Results

As we discussed in Chapter 5, the choice of exchange-correlation functional can lead to differences in predictions of material properties. Here, we present the voltages and phase diagrams for each of the TMDC phases considered, for each of the intercalants, making comparison between the PBE and HSE06 functionals. Figures for lithium-, sodium-, potatssium-, and magnesium-intercalated ScS_2 are presented in Figure D.3, Figure D.4, Figure D.5, and Figure D.6, respectively. With the use of the HSE06 hybrid functional, we note the intercalation voltage is significantly increased to 4.440 V (Li), 4.420 V (Na), 3.953 V (K), and 1.719 V (Mg). These are higher than the PBE voltages by 0.463 V, 0.546 V, 0.154 V, and 0.245 V, respectively. However, the voltage ordering is maintained and thus both

functionals indicate that the ScS_2 would be very suitable for a cathode material.

Consideration of the constructed phase diagrams also offers insight into the effect of using a different functional. We find that the diagonal line, corresponding to the boundary between the intercalated ScS_2 and the Li_2S (or equivalent) crystal, remains relatively unchanged. However, discrepancies between the phase diagrams arise from the modification to the horizontal line, corresponding to the boundary between the intercalated and pristine ScS_2 structures. Across each of the phases and intercalants considered, the amount that the horizontal line is modified with the use of HSE06 varies, though it is consistently shifted downwards (hence increasing the region of stability, and the corresponding value of E_{IS}). However, these results do not change the conclusions presented in Chapter 5, nor do they invalidate the potential of ScS_2 as a cathode material.

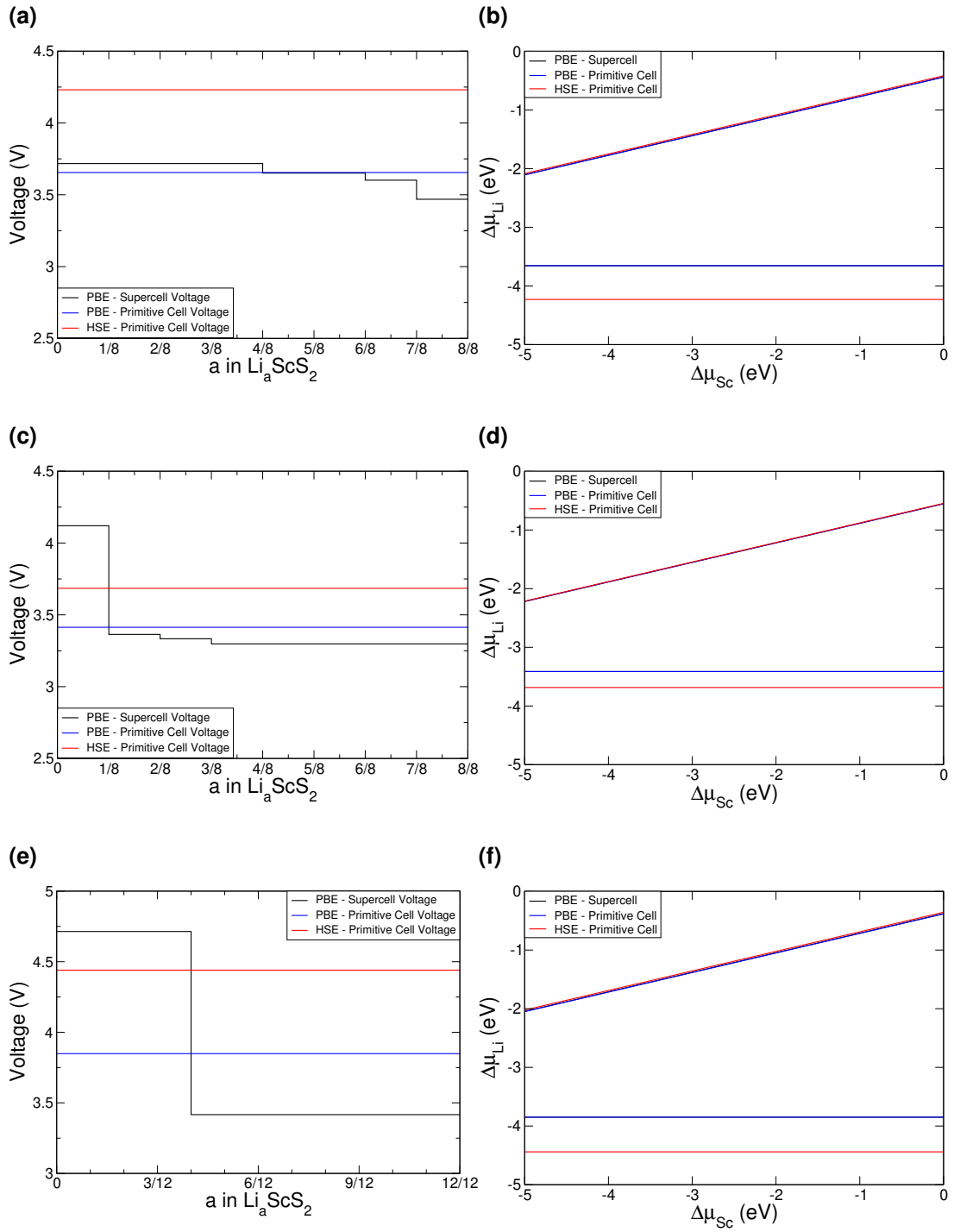

Figure D.3: Comparison of PBE and HSE06 results for the different phases of ScS_2 intercalated with Li. D.3a, D.3c, and D.3e show the comparison of intercalation potentials for T-, Hc-, and α-phases, respectively. D.3b, D.3d, and D.3f show the comparison of phase diagrams for T-, Hc-, and α-phases, respectively, for an intercalation concentration $LiScS_2$.

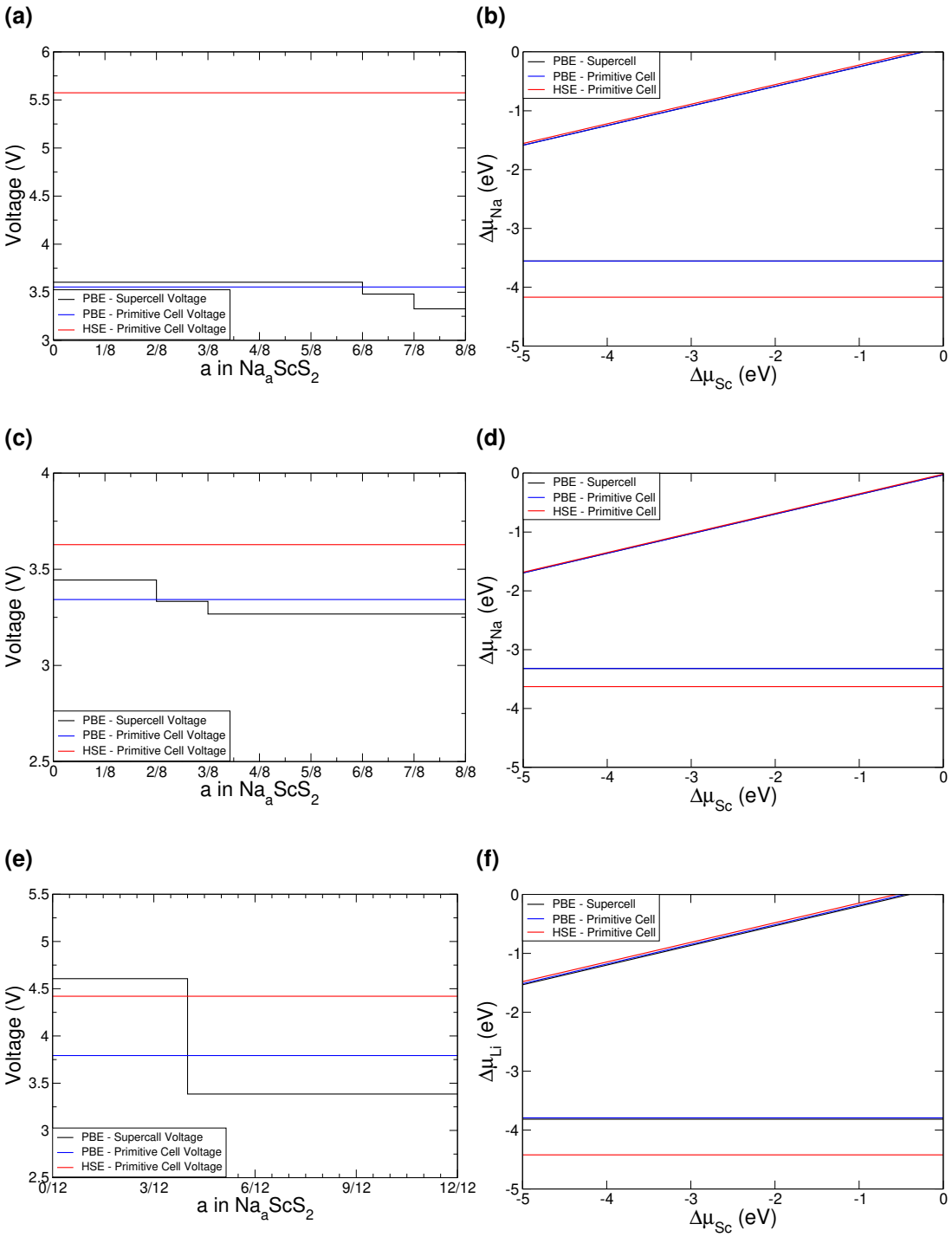

Figure D.4: Comparison of PBE and HSE06 results for the different phases of ScS_2 intercalated with Na. D.4a, D.4c, and D.4e show the comparison of intercalation potentials for T-, Hc-, and α-phases, respectively. D.4b, D.4d, and D.4f show the comparison of phase diagrams for T-, Hc-, and α-phases, respectively, for an intercalation concentration $NaScS_2$.

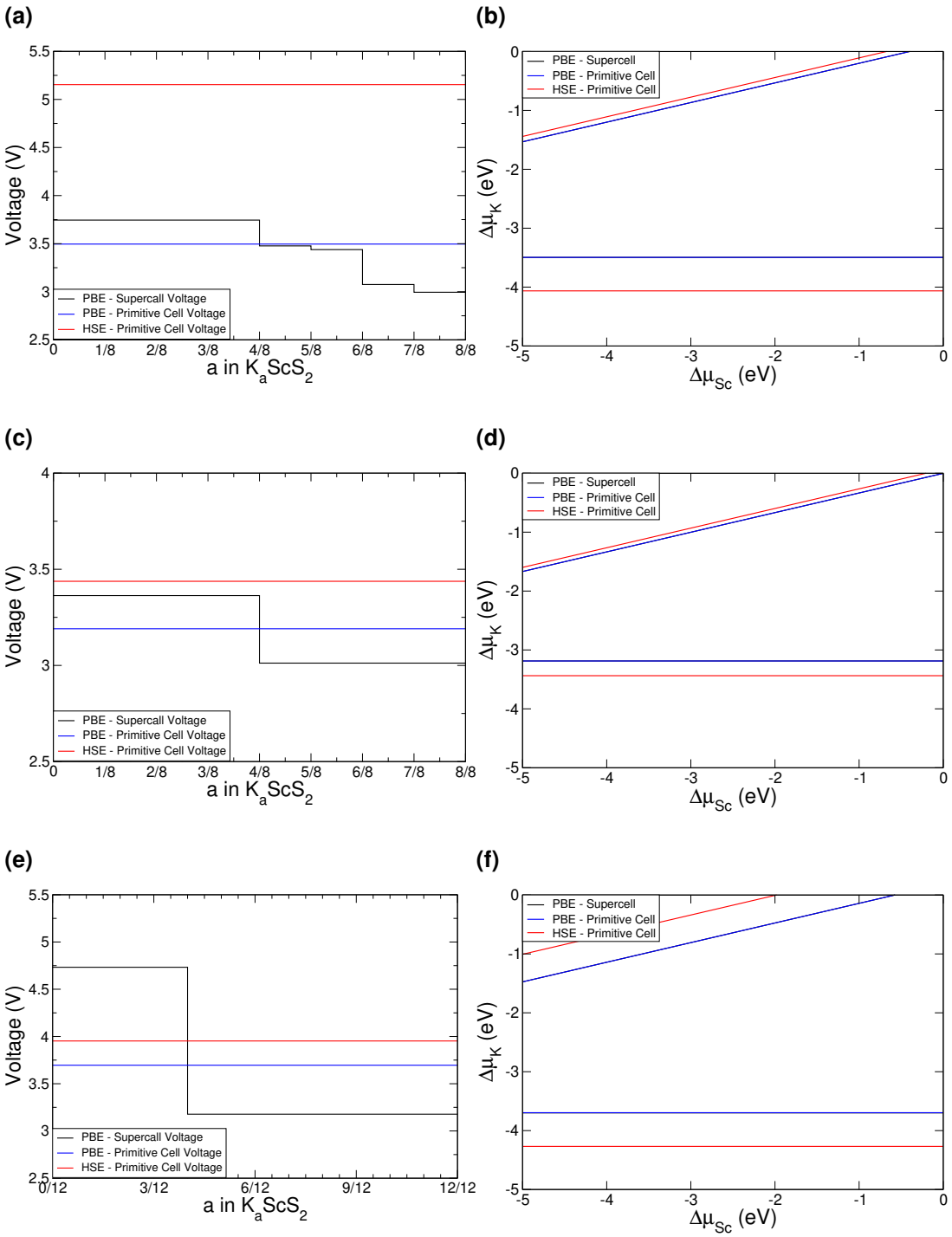

Figure D.5: Comparison of PBE and HSE06 results for the different phases of ScS_2 intercalated with K. D.5a, D.5c, and D.5e show the comparison of intercalation potentials for T-, Hc-, and α-phases, respectively. D.5b, D.5d, and D.5f show the comparison of phase diagrams for T-, Hc-, and α-phases, respectively, for an intercalation concentration $KScS_2$.

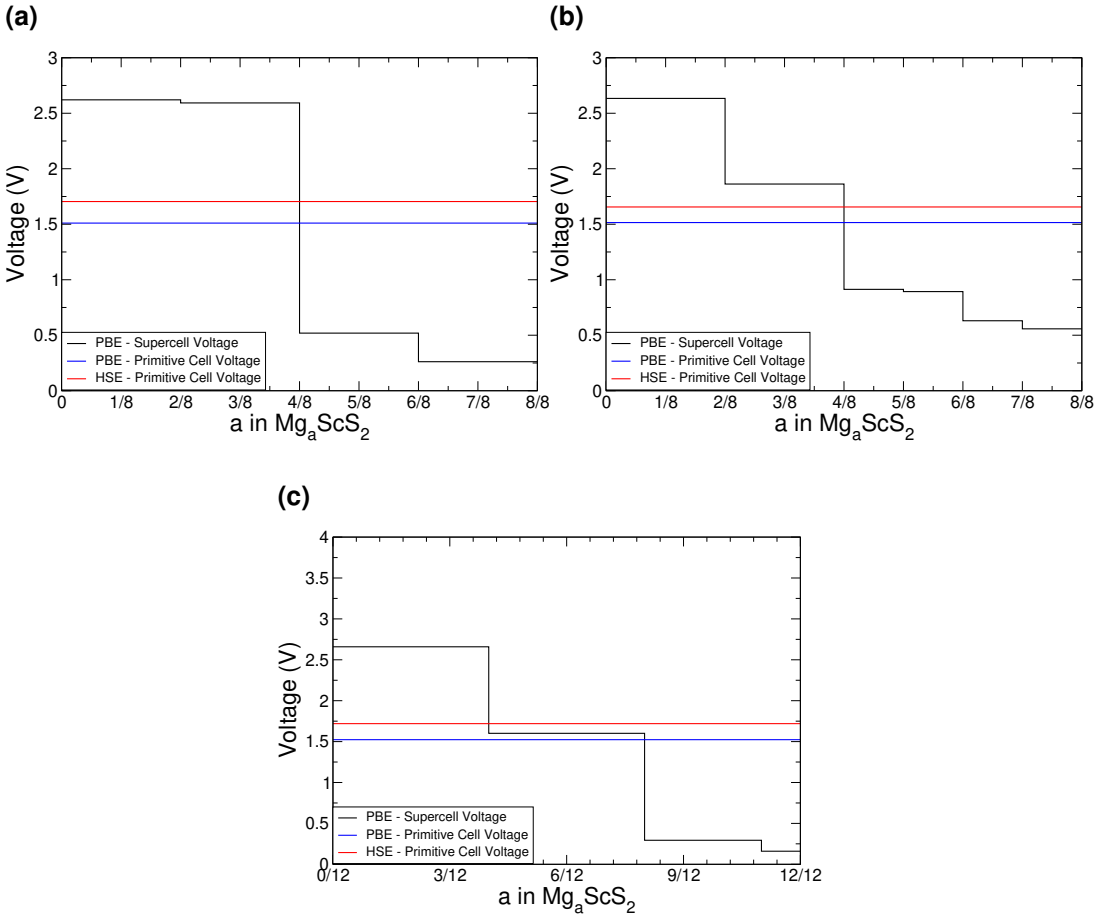

Figure D.6: Comparison of PBE and HSE06 results for the different phases of ScS_2 intercalated with Mg. D.6a, D.6b, and D.6c show the comparison of intercalation potentials for T-, Hc-, and α-phases, respectively.

Appendix E

Supplementary Information to Chapter 6

E.1 Diffusion Barriers

E.2 Volumetric Expansion

As we discussed in Chapter 6, the volumetric expansion that arises from intercalation is an important factor that must be considered for any potential electrode material. In Table E.1 and Table E.2 we show the volumetric expansion for the investigated superlattices as they are intercalated with lithium from $MX_2M'X_2$ to $Li_2MX_2M'X_2$. Similarly, Table E.3 and Table E.4 we show the volumetric expansion arising from magnesium intercalation. These have each been calculated using $\% = \frac{V-V_0}{V_0} \times 100$ for initial volume V_0 and final volume V. We have also included the corresponding expansions for the component TMDCs for easy comparison. From this, we conclude that the average volumetric expansion of the component TMDCs provides a good estimate for the volumetric expansion that arises in the formed superlattice.

Superlattice A|B	Superlattice Expansion (%)	Component A Expansion (%)	Component B Expansion (%)
CuS_2|OsS_2	24.87	29.39	15.81
CuS_2|RhS_2	28.18	29.39	23.70
GeS_2|SnS_2	11.15	12.15	10.17
GeS_2|$SnSe_2$	12.52	12.15	10.02
GeS_2|$TiSe_2$	11.86	12.15	9.74
$GeSe_2$|HfS_2	7.13	12.41	0.32
$GeSe_2$|$NiSe_2$	22.48	12.41	26.67
$GeSe_2$|$SnSe_2$	11.98	12.41	10.02
$GeSe_2$|$TaTe_2$	16.26	12.41	13.66
$GeSe_2$|$TiSe_2$	11.08	12.41	9.74
$GeSe_2$|$TiTe_2$	15.66	12.41	14.80
HfS_2|PdS_2	7.80	0.32	16.54
HfS_2|PtS_2	7.69	0.32	23.58
HfS_2|SnS_2	6.76	0.32	10.17
HfS_2|$SnSe_2$	6.26	0.32	10.02
HfS_2|ZrS_2	0.27	0.32	0.31
$HfTe_2$|$PbSe_2$	13.38	7.38	17.93
$HfTe_2$|$SnSe_2$	10.72	7.38	10.02
MoS_2|SnS_2	11.02	15.06	10.17
MoS_2|VS_2	12.04	15.06	12.26
MoS_2|WS_2	10.86	15.06	12.87
MoS_2|WSe_2	11.82	15.06	14.35
$MoTe_2$|OsS_2	19.36	14.22	15.81
NbS_2|TaS_2	7.86	10.93	9.04

Table E.1: Superlattice and component volumetric expansion for the considered superlattices intercalated with lithium.

Superlattice A|B	Superlattice Expansion (%)	Component A Expansion (%)	Component B Expansion (%)
NiS_2|SnS_2	11.55	26.67	10.17
NiS_2|TiS_2	14.79	26.67	6.61
$NiTe_2$|$PbSe_2$	20.13	21.35	17.93
$NiTe_2$|$SnSe_2$	20.44	21.35	10.02
OsS_2|RhS_2	21.27	15.81	23.70
$OsTe_2$|$SnSe_2$	18.12	14.08	10.02
PbS_2|$PbSe_2$	18.83	19.77	17.93
PbS_2|YS_2	13.89	19.77	5.21
$PbSe_2$|$SnTe_2$	17.77	17.93	17.30
$PbSe_2$|$ZrTe_2$	13.38	17.93	7.96
PtS_2|ZrS_2	8.07	23.58	0.31
ScS_2|SnS_2	10.76	8.42	10.17
ScS_2|$TiTe_2$	15.71	8.42	14.80
$ScTe_2$|$SnSe_2$	13.97	13.16	10.02
SnS_2|$SnSe_2$	10.92	10.17	10.02
SnS_2|$TiSe_2$	9.58	10.17	9.74
SnS_2|$TiTe_2$	12.44	10.17	14.80
SnS_2|ZrS_2	6.02	10.17	0.31
SnS_2|$ZrSe_2$	8.36	10.17	2.17
$SnSe_2$|$TiTe_2$	11.68	10.02	14.80
$SnSe_2$|$ZrTe_2$	10.92	10.02	7.96
VS_2|WS_2	11.00	12.26	12.87
ZrS_2|$ZrSe_2$	1.18	0.31	2.175

Table E.2: Superlattice and component volumetric expansion for the considered superlattices intercalated with lithium.

Superlattice A|B	Superlattice Expansion (%)	Component A Expansion (%)	Component B Expansion (%)
CuS_2|OsS_2	35.07	42.66	24.38
CuS_2|RhS_2	39.16	42.66	32.07
GeS_2|SnS_2	23.07	26.56	26.56
GeS_2|$SnSe_2$	23.20	26.56	24.40
GeS_2|$TiSe_2$	21.17	26.56	15.65
$GeSe_2$|HfS_2	13.11	24.40	2.01
$GeSe_2$|$NiSe_2$	33.91	24.40	35.42
$GeSe_2$|$SnSe_2$	22.80	24.40	24.40
$GeSe_2$|$TaTe_2$	24.39	24.40	22.08
$GeSe_2$|$TiSe_2$	19.81	24.40	15.65
$GeSe_2$|$TiTe_2$	24.03	24.40	19.84
HfS_2|PdS_2	14.18	2.01	34.62
HfS_2|PtS_2	12.86	2.01	30.95
HfS_2|SnS_2	15.27	2.01	26.56
HfS_2|$SnSe_2$	12.45	2.01	24.40
HfS_2|ZrS_2	1.92	2.01	2.04
$HfTe_2$|$PbSe_2$	20.03	12.98	26.27
$HfTe_2$|$SnSe_2$	21.81	12.98	24.40
MoS_2|SnS_2	20.36	19.95	26.56
MoS_2|VS_2	25.49	19.95	21.50
MoS_2|WS_2	17.81	19.95	15.97
MoS_2|WSe_2	18.56	19.95	18.57
$MoTe_2$|OsS_2	28.52	16.80	24.38
NbS_2|TaS_2	12.87	13.93	11.36

Table E.3: Superlattice and component volumetric expansion for the considered superlattices intercalated with magnesium.

Superlattice A|B	Superlattice Expansion (%)	Component A Expansion (%)	Component B Expansion (%)
NiS_2|SnS_2	21.64	42.10	26.56
NiS_2|TiS_2	23.32	42.10	12.21
$NiTe_2$|$PbSe_2$	30.34	32.62	26.27
$NiTe_2$|$SnSe_2$	30.44	32.62	24.40
OsS_2|RhS_2	29.32	24.38	32.07
$OsTe_2$|$SnSe_2$	27.87	21.50	24.40
PbS_2|$PbSe_2$	27.35	28.34	26.27
PbS_2|YS_2	17.76	28.34	2.51
$PbSe_2$|$SnTe_2$	26.88	26.27	27.37
$PbSe_2$|$ZrTe_2$	18.39	26.27	12.09
PtS_2|ZrS_2	13.06	30.95	2.04
ScS_2|SnS_2	18.11	9.43	26.56
ScS_2|$TiTe_2$	19.93	9.43	19.84
$ScTe_2$|$SnSe_2$	20.59	15.09	20.36
SnS_2|$SnSe_2$	21.39	26.56	20.36
SnS_2|$TiSe_2$	18.55	26.56	15.65
SnS_2|$TiTe_2$	23.55	26.56	19.84
SnS_2|ZrS_2	12.77	26.56	2.04
SnS_2|$ZrSe_2$	19.28	26.56	4.73
$SnSe_2$|$TiTe_2$	19.15	24.40	19.84
$SnSe_2$|$ZrTe_2$	17.15	24.40	12.09
VS_2|WS_2	19.12	21.50	15.97
ZrS_2|$ZrSe_2$	3.33	2.04	4.73

Table E.4: Superlattice and component volumetric expansion for the considered superlattices intercalated with magnesium.

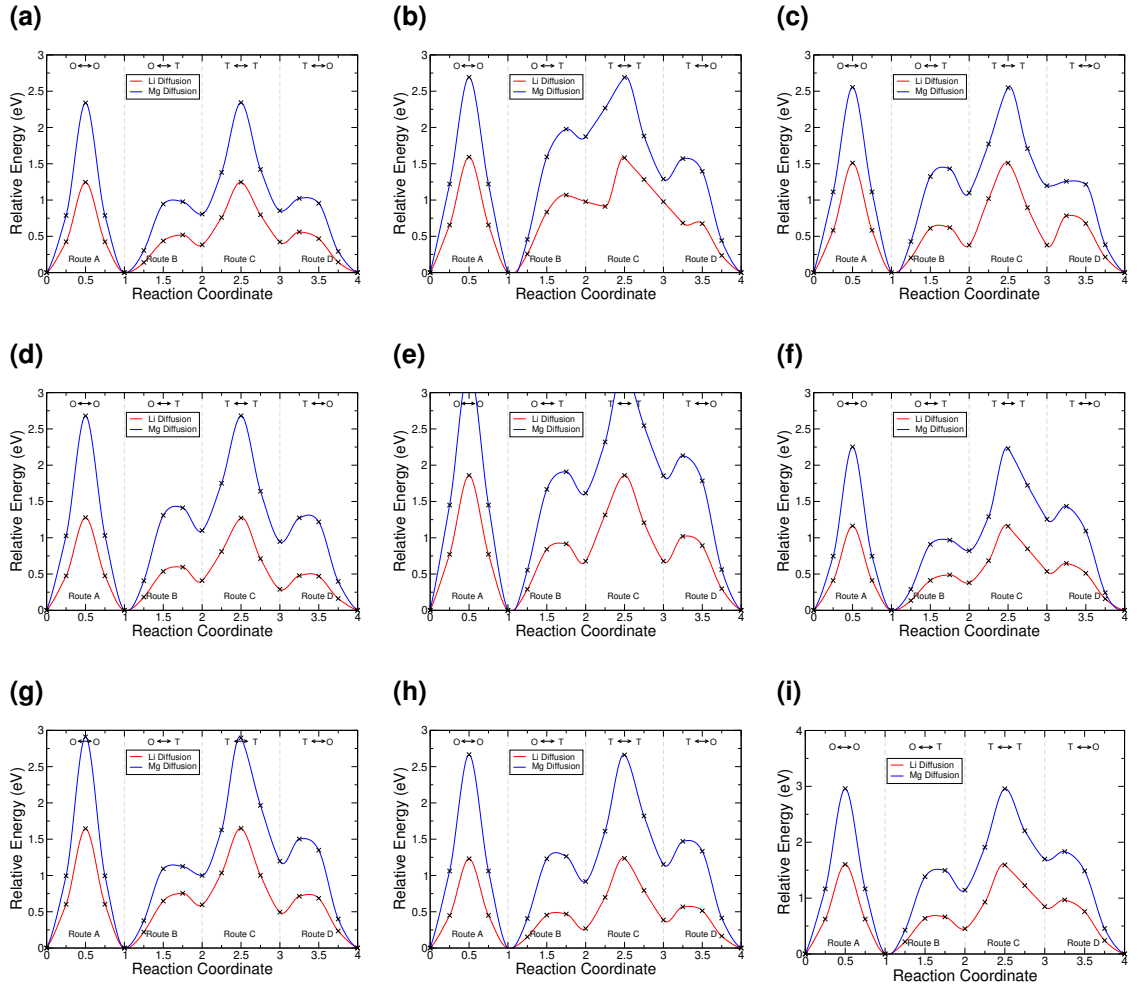

Figure E.1: Diffusion barrier heights calculated using the CI-NEB method for lithium and magnesium in the highlighted superlattice materials, $SnS_2|SnSe_2$ (E.1a), $NiS_2|TiS_2$ (E.1b), $HfS_2|PdS_2$ (E.1c), $ZrS_2|ZrSe_2$ (E.1d), $NbS_2|TaS_2$ (E.1e), $GeS_2|SnS_2$ (E.1f), $SnSe_2|ZrTe_2$ (E.1g), $HfS_2|ZrS_2$ (E.1h), and $MoS_2|SnS_2$ (E.1i).

E.3 Energetics

We here show and discuss the intercalation energetics for the superlattice structures. The average voltages (over the intercalant concentration range considered) and E_{IS} values (at intercalant concentrations of $Li_2MX_2M'X'_2$ and $Mg_2MX_2M'X'_2$) for the superlattices and the relevant components are presented in Table E.5 and Table E.6 for lithium intercalation, and in Table E.7 and Table E.8 for magnesium intercalation. In each of these, the component voltages and E_{IS} values are also presented for easy comparison with the superlattice value. The components in a given pairing have been ordered alphabetically, and then each pairing listed in the tables alphabetically.

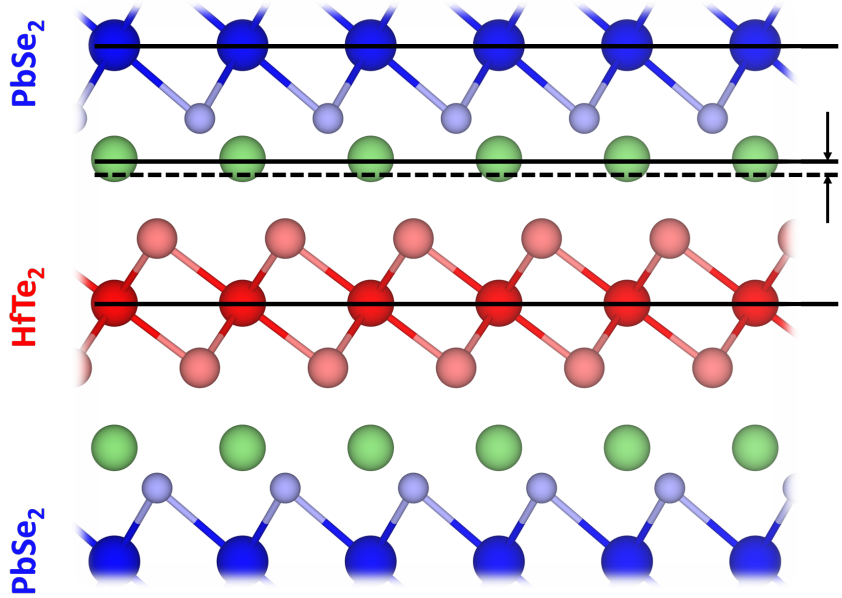

Figure E.2: Asymmetry of intercalant position in superlattices that display values of E_{IS} greater than their component TMDCs, using the lithium-intercalated $HfTe_2|PbSe_2$ as an example. Solid lines indicate the planes of atoms, dashed line indicates the mid-point within the vdW space.

We find that, for the further pairings considered, the average values of voltage and E_{IS} of the component materials provide bounds for the values exhibited by the superlattice, and the average of these values provides a good estimate. We do highlight some exceptions to this general rule, however.

For example, the values of E_{IS} for lithium-intercalated $HfTe_2|PbSe_2$, $HfTe_2|SnSe_2$, and $PbSe_2|ZrTe_2$, and magnesium-intercalated $CuS_2|RhS_2$, $SnS_2|TiTe_2$, and $SnSe_2|ZrTe_2$ exceed the values of the component materials. However, closer study of the geometry of these superlattices reveals a difference from their component TMDCs and the other superlattices: For most superlattices and component TMDCs, the intercalant species occupies a space in the vdW gap that close to half way between each of the neighbouring TMDC layers. However, for the exceptions listed above, the intercalant species is instead significantly closer to one of the component layers. For individual TMDCs this bias is not possible due to each layer being equivalent, and though there are some small deviations from the midpoint in other superlattices, these deviations are relatively small compared to the six exception highlight above. This is depicted in Figure E.2, where the position of the lithium ions within the vdW spacing of $HfTe_2|PbSe_2$ (indicated with a solid

line) lies away from the mid-point (indicated with a dashed line). This asymmetry is seen for each of the intercalant concentrations, and not just the $Li_2MX_2|M'X'_2$ and $Mg_2MX_2|M'X'_2$, though it becomes slightly more pronounced with higher intercalant concentrations.

E.4 Charge Analysis

The first consideration is of charge transfer changes during the formation of superlattices and during intercalation. Upon formation of a superlattice, and more importantly upon intercalation, there can be large charge transfers between the constituent atoms. The magnitude of this charge transfer and where the charge is transferred to/from plays an important role in determining how much energy is involved with forming a superlattice or intercalating a layered material. Numerical values are presented in Table E.9 - Table E.17.

E.4.1 Superlattice Formation

Upon formation of a superlattice (without the inclusion of any intercalant), we would expect minimal charge transfer between the component layers due to the presence of the vdW gap. In Figure E.3 we present the Bader charges of the species in the highlighted superlattices, along with the Bader charges of the species in the individual components. We find that the charges on both the metal and chalcogen species are largely preserved compared to their charges in the individual MX_2 components. For the pristine systems, Bader charges are shown in Figure E.3a, where the charges of the metal and chalcogen species are seen to be effectively unchanged between the individual pristine TMDCs and the superlattices. In fact, the largest difference between the component and superlattice is found to be 0.04 |e| in the $HfS_2|PdS_2$ system.

Superlattice A|B	Superlattice Voltage (V)	Component A Voltage (V)	Component B Voltage (V)	E_{IS}^{Li} Superlattice (eV)	E_{IS}^{Li} A (eV)	E_{IS}^{Li} B (eV)
CuS_2|OsS_2	2.41	2.23	2.57	0.29	0.04	0.62
CuS_2|RhS_2	2.42	2.23	2.50	0.50	0.04	0.88
GeS_2|$MoSe_2$	2.11	2.06	2.04	0.37	0.07	0.53
GeS_2|SnS_2	1.98	2.06	1.80	0.03	0.07	-0.09
GeS_2|$SnSe_2$	2.04	2.06	1.85	0.15	0.07	0.13
GeS_2|$TiSe_2$	2.06	2.06	1.96	0.62	0.07	1.05
$GeSe_2$|HfS_2	1.88	2.08	1.73	0.58	0.22	1.02
$GeSe_2$|$NiSe_2$	1.87	2.08	1.69	0.04	0.22	-0.08
$GeSe_2$|$SnSe_2$	2.01	2.08	1.85	0.21	0.22	0.13
$GeSe_2$|$TaTe_2$	1.76	2.08	1.41	0.17	0.22	0.05
$GeSe_2$|$TiSe_2$	2.03	2.08	1.96	0.64	0.22	1.05
$GeSe_2$|$TiTe_2$	1.87	2.08	1.52	0.48	0.22	0.55
HfS_2|PdS_2	1.92	1.73	1.94	0.60	1.02	-0.00
HfS_2|PtS_2	1.60	1.73	1.43	0.43	1.02	-0.49
HfS_2|SnS_2	1.75	1.73	1.80	0.45	1.02	-0.09
HfS_2|$SnSe_2$	1.68	1.73	1.85	0.41	1.02	0.13
HfS_2|ZrS_2	1.88	1.73	2.03	1.21	1.02	1.38
$HfTe_2$|$PbSe_2$	2.17	1.25	2.22	0.90	0.34	0.39
$HfTe_2$|$SnSe_2$	1.67	1.25	1.85	0.40	0.34	0.13
MoS_2|SnS_2	2.26	2.47	1.80	0.54	1.05	-0.09
MoS_2|VS_2	2.41	2.47	2.33	1.07	1.05	1.04
MoS_2|WS_2	2.39	2.47	2.28	0.92	1.05	0.74
MoS_2|WSe_2	1.86	2.47	1.90	0.22	1.05	0.24
$MoTe_2$|OsS_2	1.71	1.60	2.57	-0.11	0.10	0.62
NbS_2|TaS_2	2.12	2.23	2.01	0.99	1.14	0.84

Table E.5: Average voltage and E_{IS}^{Li} values (corresponding to $Li_2MX_2M'X'_2$) for considered superlattices. The values of the component TMDCs are also presented for easy comparison with the superlattice value.

Superlattice A|B	Superlattice Voltage (V)	Component A Voltage (V)	Component B Voltage (V)	E_{IS}^{Li} Superlattice (eV)	E_{IS}^{Li} A (eV)	E_{IS}^{Li} B (eV)
NiS_2|SnS_2	2.04	2.10	1.80	0.11	0.23	-0.09
NiS_2|TiS_2	2.26	2.10	2.33	0.91	0.23	1.51
$NiTe_2$|$PbSe_2$	1.82	1.18	2.22	0.24	-0.31	0.39
$NiTe_2$|$SnSe_2$	1.55	1.18	1.85	-0.04	-0.31	0.13
OsS_2|RhS_2	2.40	2.57	2.50	0.57	0.62	0.88
$OsTe_2$|$SnSe_2$	1.68	1.64	1.85	-0.06	-0.08	0.13
PbS_2|$PbSe_2$	2.41	2.62	2.22	0.46	0.57	0.39
PbS_2|YS_2	3.08	2.62	3.85	1.86	0.57	3.58
$PbSe_2$|$SnTe_2$	1.92	2.22	1.66	0.29	0.39	0.19
$PbSe_2$|$ZrTe_2$	2.23	2.22	1.51	1.01	0.39	0.73
PdS_2|PtS_2	1.73	1.94	1.43	-0.19	0.00	-0.49
PtS_2|ZrS_2	1.75	1.43	2.03	0.47	-0.49	1.38
ScS_2|SnS_2	2.69	3.66	1.80	1.52	3.22	-0.09
ScS_2|$TiTe_2$	2.28	3.66	1.52	1.55	3.22	0.55
$ScTe_2$|$SnSe_2$	2.11	2.40	1.85	0.98	1.89	0.13
SnS_2|$SnSe_2$	1.83	1.80	1.85	0.01	-0.09	0.13
SnS_2|$TiSe_2$	1.92	1.80	1.96	0.51	-0.09	1.05
SnS_2|$TiTe_2$	1.74	1.80	1.52	0.34	-0.09	0.55
SnS_2|ZrS_2	1.89	1.80	2.03	0.61	-0.09	1.38
SnS_2|$ZrSe_2$	1.87	1.80	1.81	0.58	-0.09	1.09
$SnSe_2$|$TiTe_2$	1.76	1.85	1.52	0.43	0.13	0.55
$SnSe_2$|$ZrSe_2$	1.83	1.85	1.81	0.60	0.13	1.09
$SnSe_2$|$ZrTe_2$	1.77	1.85	1.51	0.55	0.13	0.73
VS_2|WS_2	2.31	2.33	2.28	0.91	1.04	0.74
ZrS_2|$ZrSe_2$	1.90	2.03	1.81	1.20	1.38	1.09

Table E.6: Average voltage and E_{IS}^{Li} values (corresponding to $Li_2MX_2M'X'_2$) for considered superlattices. The values of the component TMDCs are also presented for easy comparison with the superlattice value.

Superlattice A|B	Superlattice Voltage (V)	Component A Voltage (V)	Component B Voltage (V)	E_{IS}^{Mg} Superlattice (eV)	E_{IS}^{Mg} A (eV)	E_{IS}^{Mg} B (eV)
CuS_2|OsS_2	1.49	1.54	1.10	-0.22	-0.05	-1.41
CuS_2|RhS_2	1.53	1.54	1.09	0.51	-0.05	-0.41
GeS_2|$MoSe_2$	0.85	1.35	0.35	-1.26	-0.02	-2.45
GeS_2|SnS_2	1.32	1.35	1.22	0.06	-0.02	0.01
GeS_2|$SnSe_2$	1.33	1.35	1.18	0.23	-0.02	0.42
GeS_2|$TiSe_2$	0.99	1.35	0.63	0.23	-0.02	0.52
$GeSe_2$|HfS_2	0.80	1.34	0.43	0.09	0.39	0.44
$GeSe_2$|$NiSe_2$	1.11	1.34	0.89	-0.19	0.39	-0.73
$GeSe_2$|$SnSe_2$	1.29	1.34	1.18	0.45	0.39	0.42
$GeSe_2$|$TaTe_2$	0.60	1.34	-0.06	-1.29	0.39	-2.79
$GeSe_2$|$TiSe_2$	0.99	1.34	0.63	0.49	0.39	0.52
$GeSe_2$|$TiTe_2$	0.84	1.34	0.37	0.17	0.39	0.01
HfS_2|PdS_2	0.92	0.43	1.16	0.39	0.44	-0.55
HfS_2|PtS_2	0.55	0.43	0.64	-0.76	0.44	-2.02
HfS_2|SnS_2	0.87	0.43	1.22	0.39	0.44	0.01
HfS_2|$SnSe_2$	0.80	0.43	1.18	0.36	0.44	0.42
HfS_2|ZrS_2	0.57	0.43	0.70	0.96	0.44	1.45
$HfTe_2$|$PbSe_2$	1.03	0.10	1.64	0.98	-0.58	1.57
$HfTe_2$|$SnSe_2$	0.71	0.10	1.18	0.19	-0.58	0.42
MoS_2|SnS_2	1.05	0.65	1.22	-0.64	-1.50	0.01
MoS_2|VS_2	0.77	0.65	0.87	-0.77	-1.50	-0.13
MoS_2|WS_2	0.46	0.65	0.28	-2.35	-1.50	-3.17
MoS_2|WSe_2	0.34	0.65	0.05	-2.80	-1.50	-3.97
$MoTe_2$|OsS_2	0.53	0.05	1.10	-2.27	-2.94	-1.41
NbS_2|TaS_2	0.59	0.77	0.41	-0.57	0.17	-1.32

Table E.7: Average voltage and E_{IS}^{Mg} values (corresponding to $Mg_2MX_2M'X'_2$) for considered superlattices. The values of the component TMDCs are also presented for easy comparison with the superlattice value.

Superlattice A|B	Superlattice Voltage (V)	Component A Voltage (V)	Component B Voltage (V)	E_{IS}^{Mg} Superlattice (eV)	E_{IS}^{Mg} A (eV)	E_{IS}^{Mg} B (eV)
NiS_2|SnS_2	1.28	1.22	1.22	-0.09	-0.26	0.01
NiS_2|TiS_2	1.10	1.22	0.86	0.72	-0.26	1.24
$NiTe_2$|$PbSe_2$	0.97	0.45	1.64	0.17	-0.86	1.57
$NiTe_2$|$SnSe_2$	0.79	0.45	1.18	-0.31	-0.86	0.42
OsS_2|RhS_2	1.07	1.10	1.09	-1.02	-1.41	-0.41
$OsTe_2$|$SnSe_2$	0.92	0.76	1.18	-0.40	-0.82	0.42
PbS_2|$PbSe_2$	1.80	1.98	1.64	1.60	1.75	1.57
PbS_2|YS_2	1.77	1.98	1.45	2.95	1.75	3.76
$PbSe_2$|$SnTe_2$	1.23	1.64	0.97	0.94	1.57	0.77
$PbSe_2$|$ZrTe_2$	1.08	1.64	0.30	1.25	1.57	0.33
PdS_2|PtS_2	0.94	1.14	0.63	-1.16	-0.55	-2.02
PtS_2|ZrS_2	0.67	0.64	0.70	-0.32	-2.02	1.45
ScS_2|SnS_2	1.38	1.52	1.22	1.92	3.68	0.01
ScS_2|$TiTe_2$	0.72	1.52	0.37	1.17	3.68	0.01
$ScTe_2$|$SnSe_2$	1.01	0.80	1.18	1.39	2.22	0.42
SnS_2|$SnSe_2$	1.20	1.22	1.18	0.17	0.01	0.42
SnS_2|$TiSe_2$	0.99	1.22	0.63	0.47	0.01	0.52
SnS_2|$TiTe_2$	0.86	1.22	0.37	0.24	0.01	0.01
SnS_2|ZrS_2	0.96	1.22	0.70	0.71	0.01	1.45
SnS_2|$ZrSe_2$	0.94	1.22	0.52	0.67	0.01	0.82
$SnSe_2$|$TiTe_2$	0.80	1.18	0.37	0.28	0.42	0.01
$SnSe_2$|$ZrSe_2$	0.83	1.18	0.52	0.52	0.42	0.82
$SnSe_2$|$ZrTe_2$	0.76	1.18	0.30	0.47	0.42	0.33
VS_2|WS_2	0.53	0.87	0.28	-1.82	-0.13	-3.17
ZrS_2|$ZrSe_2$	0.60	0.70	0.52	1.06	1.45	0.82

Table E.8: Average voltage and E_{IS}^{Mg} values (corresponding to $Mg_2MX_2M'X'_2$) for considered superlattices. The values of the component TMDCs are also presented for easy comparison with the superlattice value.

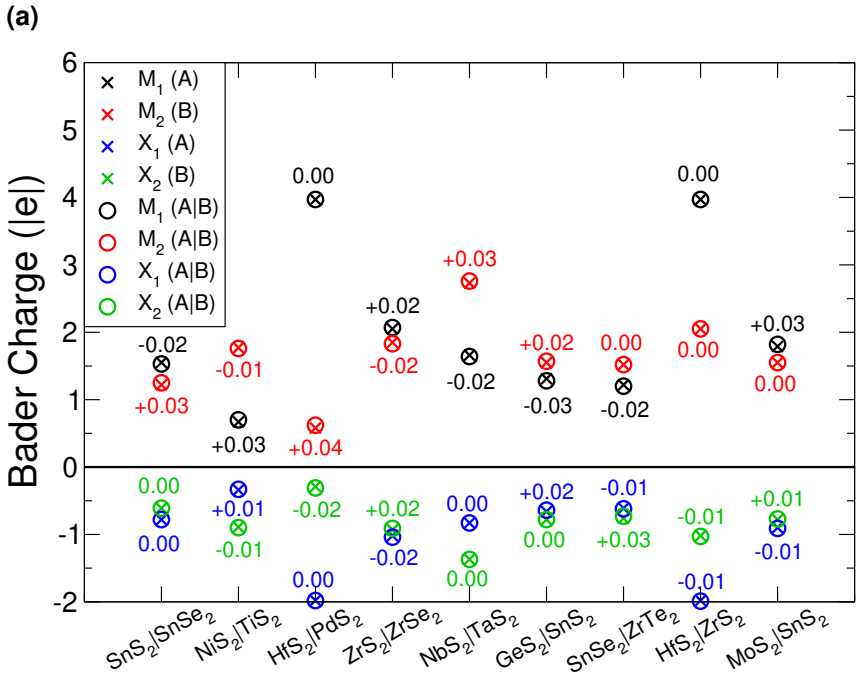

Figure E.3: Bader charges for the different metal and chalcogen species in the unintercalated pristine superlattices and the relevant component TMDCs. The included numbers indicate the difference in charge between the superlattice and individual TMDC components, $Q^{SL} - Q^{TMDC}$.

E.4.2 Intercalated Superlattices

We compare the Bader charges for the lithium-intercalated (Figure E.4a) and magnesium-intercalated (Figure E.4b) systems. Surprisingly, whilst there is more charge transfer than is seen with the pristine systems, this remains relatively small. However, some systems, for example lithium-intercalated $NbS_2|TaS_2$ and magnesium-intercalated $HfS_2|PdS_2$, show significant charge transfer between the component layers. The intercalants themselves maintain almost constant charges, as has been shown for intercalation into the individual TMDCs. Across the different superlattices, the charge of lithium varies between $0.87-0.88$, and magnesium varies between $1.65 - 1.67$.

E.4.3 Charge Tables

We present in Table E.9 - Table E.17 the numerical Bader charge values for each of the superlattice structures and their component TMDCs, each in their pristine

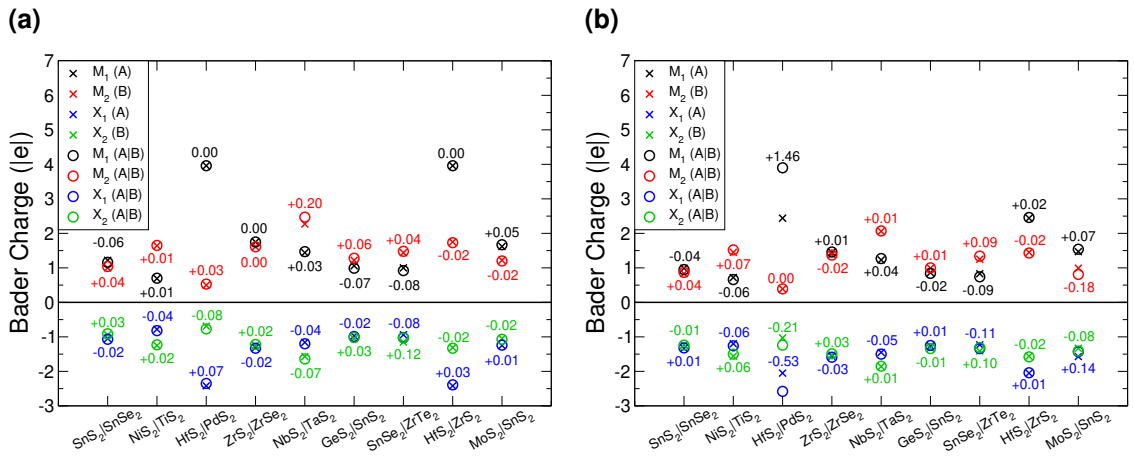

Figure E.4: Bader charges for the different metal and chalcogen species in superlattices and the relevant component TMDCs, when intercalated with lithium (E.4a) and magnesium (E.4b). The included numbers indicate the difference in charge between the superlattice and individual TMDC components, $Q^{SL} - Q^{TMDC}$.

and intercalated forms.

Species	Charge of species in bulk SnS_2 (|e|)	Charge of species in bulk $SnSe_2$ (|e|)	Charge of species in bulk superlattice (|e|)
Sn_1	1.55	-	1.53
S	-0.78	-	-0.78
Sn_2	-	1.22	1.25
Se	-	-0.61	-0.61
Species	Charge of species in intercalated $LiSnS_2$ (|e|)	Charge of species in intercalated $LiSnSe_2$ (|e|)	Charge of species in intercalated superlattice (|e|)
Sn_1	1.22	-	1.16
S	-1.05	-	-1.07
Sn_2	-	1.00	1.04
Se	-	-0.94	-0.91
Li	0.88	0.87	0.88
Species	Charge of species in intercalated $MgSnS_2$ (|e|)	Charge of species in intercalated $MgSnSe_2$ (|e|)	Charge of species in intercalated superlattice (|e|)
Sn_1	0.99	-	0.95
S	-1.33	-	-1.32
Sn_2	-	0.83	0.87
Se	-	-1.23	-1.24
Mg	1.67	1.63	1.65

Table E.9: Bader charge values for SnS_2, $SnSe_2$, and their superlattice.

Species	Charge of species in bulk NiS_2 (|e|)	Charge of species in bulk TiS_2 (|e|)	Charge of species in bulk superlattice (|e|)
Ni	0.67	-	0.70
S_1	-0.34	-	-0.33
Ti	-	1.77	1.76
S_2	-	-0.89	-0.90
Species	Charge of species in intercalated $LiNiS_2$ (|e|)	Charge of species in intercalated $LiTiS_2$ (|e|)	Charge of species in intercalated superlattice (|e|)
Ni	0.69	-	0.70
S_1	-0.78	-	-0.82
Ti	-	1.64	1.65
S_2	-	-1.25	-1.23
Li	0.87	0.87	0.87
Species	Charge of species in intercalated $MgNiS_2$ (|e|)	Charge of species in intercalated $MgTiS_2$ (|e|)	Charge of species in intercalated superlattice (|e|)
Ni	0.72	-	0.66
S_1	-1.20	-	-1.26
Ti	-	1.45	1.52
S_2	-	-1.56	-1.50
Mg	1.68	1.68	1.68

Table E.10: Bader charge values for NiS_2, TiS_2, and their superlattice.

Species	Charge of species in bulk HfS_2 (|e|)	Charge of species in bulk PdS_2 (|e|)	Charge of species in bulk superlattice (|e|)
Hf	3.97	-	3.97
S_1	-1.98	-	-1.98
Pd	-	0.58	0.62
S_2	-	-0.29	-0.31
Species	Charge of species in intercalated $LiHfS_2$ (|e|)	Charge of species in intercalated $LiPdS_2$ (|e|)	Charge of species in intercalated superlattice (|e|)
Hf	3.96	-	3.96
S_1	-2.42	-	-2.35
Pd	-	0.50	0.53
S_2	-	-0.69	-0.77
Li	0.87	0.87	0.87
Species	Charge of species in intercalated $MgHfS_2$ (|e|)	Charge of species in intercalated $MgPdS_2$ (|e|)	Charge of species in intercalated superlattice (|e|)
Hf	2.44	-	3.90
S_1	-2.05	-	-2.58
Pd	-	0.39	0.39
S_2	-	-1.03	-1.24
Mg	1.67	1.68	1.66

Table E.11: Bader charge values for HfS_2, PdS_2, and their superlattice.

Species	Charge of species in bulk ZrS_2 (|e|)	Charge of species in bulk $ZrSe_2$ (|e|)	Charge of species in bulk superlattice (|e|)
Zr_1	2.05	-	2.07
S	-1.02	-	-1.04
Zr_2	-	1.85	1.83
Se	-	-0.93	-0.91
Species	Charge of species in intercalated $LiZrS_2$ (|e|)	Charge of species in intercalated $LiZrSe_2$ (|e|)	Charge of species in intercalated superlattice (|e|)
Zr_1	1.75	-	1.75
S	-1.31	-	-1.33
Zr_2	-	1.61	1.61
Se	-	-1.24	-1.22
Li	0.87	0.87	0.87
Species	Charge of species in intercalated $MgZrS_2$ (|e|)	Charge of species in intercalated $MgZrSe_2$ (|e|)	Charge of species in intercalated superlattice (|e|)
Zr_1	1.45	-	1.46
S	-1.56	-	-1.59
Zr_2	-	1.39	1.37
Se	-	-1.52	-1.49
Mg	1.68	1.64	1.66

Table E.12: Bader charge values for ZrS_2, $ZrSe_2$, and their superlattice.

Species	Charge of species in bulk NbS_2 (|e|)	Charge of species in bulk TaS_2 (|e|)	Charge of species in bulk superlattice (|e|)
Nb	1.66	-	1.64
S_1	-0.83	-	-0.83
Ta	-	2.73	2.76
S_2	-	-1.37	-1.37
Species	Charge of species in intercalated $LiNbS_2$ (|e|)	Charge of species in intercalated $LiTaS_2$ (|e|)	Charge of species in intercalated superlattice (|e|)
Nb	1.44	-	1.47
S_1	-1.16	-	-1.20
Ta	-	2.27	2.47
S_2	-	-1.57	-1.64
Li	0.87	0.88	0.87
Species	Charge of species in intercalated $MgNbS_2$ (|e|)	Charge of species in intercalated $MgTaS_2$ (|e|)	Charge of species in intercalated superlattice (|e|)
Nb	1.23	-	1.27
S_1	-1.45	-	-1.50
Ta	-	2.06	2.07
S_2	-	-1.86	-1.85
Mg	1.68	1.67	1.67

Table E.13: Bader charge values for NbS_2, TaS_2, and their superlattice.

Species	Charge of species in bulk GeS_2 (|e|)	Charge of species in bulk SnS_2 (|e|)	Charge of species in bulk superlattice (|e|)
Ge	1.31	-	1.28
S_1	-0.66	-	-0.64
Sn	-	1.55	1.57
S_2	-	-0.78	-0.78
Species	Charge of species in intercalated $LiGeS_2$ (|e|)	Charge of species in intercalated $LiSnS_2$ (|e|)	Charge of species in intercalated superlattice (|e|)
Ge	1.06	-	0.99
S_1	-0.97	-	-0.99
Sn	-	1.22	1.28
S_2	-	-1.05	-1.02
Li	0.88	0.88	0.88
Species	Charge of species in intercalated $MgGeS_2$ (|e|)	Charge of species in intercalated $MgSnS_2$ (|e|)	Charge of species in intercalated superlattice (|e|)
Ge	0.86	-	0.84
S_1	-1.26	-	-1.25
Sn	-	0.99	1.00
S_2	-	-1.33	-1.34
Mg	1.67	1.67	1.67

Table E.14: Bader charge values for GeS_2, SnS_2, and their superlattice.

Species	Charge of species in bulk $SnSe_2$ (|e|)	Charge of species in bulk $ZrTe_2$ (|e|)	Charge of species in bulk superlattice (|e|)
Sn	1.22	-	1.20
Se	-0.61	-	-0.62
Zr	-	1.52	1.52
Te	-	-0.76	-0.73
Species	Charge of species in intercalated $LiSnSe_2$ (|e|)	Charge of species in intercalated $LiZrTe_2$ (|e|)	Charge of species in intercalated superlattice (|e|)
Sn	1.00	-	0.92
Se	-0.94	-	-1.02
Zr	-	1.44	1.48
Te	-	-1.15	-1.03
Li	0.87	0.86	0.87
Species	Charge of species in intercalated $MgSnSe_2$ (|e|)	Charge of species in intercalated $MgZrTe_2$ (|e|)	Charge of species in intercalated superlattice (|e|)
Sn	0.83	-	0.74
Se	-1.23	-	-1.34
Zr	-	1.25	1.34
Te	-	-1.41	-1.31
Mg	1.63	1.59	1.60

Table E.15: Bader charge values for $SnSe_2$, $ZrTe_2$, and their superlattice.

Species	Charge of species in bulk HfS_2 (|e|)	Charge of species in bulk ZrS_2 (|e|)	Charge of species in bulk superlattice (|e|)
Hf	3.97	-	3.97
S_1	-1.98	-	-1.99
Zr	-	2.05	2.05
S_2	-	-1.02	-1.03
Species	Charge of species in intercalated $LiHfS_2$ (|e|)	Charge of species in intercalated $LiZrS_2$ (|e|)	Charge of species in intercalated superlattice (|e|)
Hf	3.96	-	3.96
S_1	-2.42	-	-2.39
Zr	-	1.75	1.73
S_2	-	-1.31	-1.33
Li	0.87	0.87	0.87
Species	Charge of species in intercalated $LiHfS_2$ (|e|)	Charge of species in intercalated $LiZrS_2$ (|e|)	Charge of species in intercalated superlattice (|e|)
Hf	2.44	-	2.46
S_1	-2.05	-	-2.04
Zr	-	1.45	1.43
S_2	-	-1.56	-1.58
Mg	1.67	1.68	1.67

Table E.16: Bader charge values for HfS_2, ZrS_2, and their superlattice.

Species	Charge of species in bulk MoS_2 (|e|)	Charge of species in bulk SnS_2 (|e|)	Charge of species in bulk superlattice (|e|)
Mo	1.79	-	1.82
S_1	-0.90	-	-0.91
Sn	-	1.55	1.55
S_2	-	-0.78	-0.77
Species	Charge of species in intercalated $LiMoS_2$ (|e|)	Charge of species in intercalated $LiSnS_2$ (|e|)	Charge of species in intercalated superlattice (|e|)
Mo	1.62	-	1.67
S_1	-1.25	-	-1.24
Sn	-	1.22	1.20
S_2	-	-1.05	-1.07
Li	0.87	0.88	0.87
Species	Charge of species in intercalated $MgMoS_2$ (|e|)	Charge of species in intercalated $MgSnS_2$ (|e|)	Charge of species in intercalated superlattice (|e|)
Mo	1.47	-	1.54
S_1	-1.57	-	-1.43
Sn	-	0.99	0.81
S_2	-	-1.33	-1.41
Mg	1.67	1.67	1.67

Table E.17: Bader charge values for MoS_2, SnS_2, and their superlattice.

Bibliography

[1] R. G. Newell, D. Raimi, and G. Aldana. Global Energy Outlook 2019: The Next Generation of Energy. Technical Report July (2019).

[2] BP. BP Energy Outlook 2019 Edition. Technical report (2019).

[3] BP. BP Energy Outlook 2022 Edition. Technical report (2022).

[4] World Energy Outlook. Technical report (2022).

[5] United Nations Environment Programme. The Closing Window - Climate crisis calls for rapid transformation of societies. Technical report (2022).

[6] M. Lynas, B. Z. Houlton, and S. Perry. Greater than 99% consensus on human caused climate change in the peer-reviewed scientific literature. *Environmental Research Letters*, **16**, 11, (2021), p. 114005.

[7] Intergovernmental Panel on Climate Change. Climate Change 2022 - Mitigation of Climate Change - Full Report. Technical report (2022).

[8] B. Dunn, H. Kamath, and J.-M. Tarascon. Electrical Energy Storage for the Grid: A Battery of Choices. *Science*, **334**, 6058, (2011), pp. 928–935.

[9] D. M. Davies, M. G. Verde, O. Mnyshenko, Y. R. Chen, R. Rajeev, Y. S. Meng, and G. Elliott. Combined economic and technological evaluation of battery energy storage for grid applications. *Nature Energy*, **4**, 1, (2018), pp. 42–50.

[10] A. J. Bard and L. R. Faulkner. Electrochemical Methods: Fundamentals and Applications, (John Wiley and Sons Inc.2001), second edition. ISBN 978-0-471-04372-0.

[11] Y. Gogotsi and R. M. Penner. Energy Storage in Nanomaterials – Capacitive, Pseudocapacitive, or Battery-like? *ACS Nano*, **12**, 3, (2018), pp. 2081–2083.

[12] H. I. Becker. Low voltage electrolytic capacitor patent (1957).

[13] J. R. Miller. Perspective on electrochemical capacitor energy storage. *Applied Surface Science*, **460**, (2018), pp. 3–7.

[14] R. Kötz and M. Carlen. Principles and applications of electrochemical capacitors. *Electrochimica Acta*, **45**, 15-16, (2000), pp. 2483–2498.

[15] P. Simon and Y. Gogotsi. Perspectives for electrochemical capacitors and related devices. *Nature Materials*, **19**, 11, (2020), pp. 1151–1163.

[16] P. Simon and Y. Gogotsi. Materials for electrochemical capacitors. *Nature Materials*, **7**, 11, (2008), pp. 845–854.

[17] Y. Wang, Y. Song, and Y. Xia. Electrochemical capacitors: mechanism, materials, systems, characterization and applications. *Chemical Society Reviews*, **45**, 21, (2016), pp. 5925–5950.

[18] T. Starner. Powerful change. 1. Batteries and possible alternatives for the mobile market. *IEEE Pervasive Computing*, **2**, 4, (2003), pp. 86–88.

[19] S. Saxena, G. Sanchez, and M. Pecht. Batteries in Portable Electronic Devices: A User's Perspective. *IEEE Industrial Electronics Magazine*, **11**, 2, (2017), pp. 35–44.

[20] J. Tollefson. Car industry: Charging up the future. *Nature*, **456**, 7221, (2008), pp. 436–440.

[21] A. Wang, S. Kadam, H. Li, S. Shi, and Y. Qi. Review on modeling of the anode solid electrolyte interphase (SEI) for lithium-ion batteries. *npj Computational Materials*, **4**, 1, (2018), p. 15.

[22] Y. Tian, G. Zeng, A. Rutt, T. Shi, H. Kim, J. Wang, J. Koettgen, Y. Sun, B. Ouyang, T. Chen, Z. Lun, Z. Rong, K. Persson, and G. Ceder. Promises and Challenges of Next-Generation "Beyond Li-ion" Batteries for Electric

Vehicles and Grid Decarbonization. *Chemical Reviews*, **121**, 3, (2021), pp. 1623–1669.

[23] C.-X. Zu and H. Li. Thermodynamic analysis on energy densities of batteries. *Energy & Environmental Science*, **4**, 8, (2011), p. 2614.

[24] L. Chen, X. Fan, X. Ji, J. Chen, S. Hou, and C. Wang. High-Energy Li Metal Battery with Lithiated Host. *Joule*, **3**, 3, (2019), pp. 732–744.

[25] W. Liu, T. Placke, and K. Chau. Overview of batteries and battery management for electric vehicles. *Energy Reports*, **8**, (2022), pp. 4058–4084.

[26] E. Hitz, J. Wan, A. Patel, Y. Xu, L. Meshi, J. Dai, Y. Chen, A. Lu, A. V. Davydov, and L. Hu. Electrochemical Intercalation of Lithium Ions into $NbSe_2$ Nanosheets. *ACS Applied Materials & Interfaces*, **8**, 18, (2016), pp. 11390–11395.

[27] E. D. Hanson, L. M. Lilley, J. D. Cain, S. Hao, E. Palacios, K. Aydin, C. Wolverton, T. Meade, and V. P. Dravid. Phase engineering and optical properties of 2D $MoSe_2$: Promise and pitfalls. *Materials Chemistry and Physics*, **225**, July 2018, (2019), pp. 219–226.

[28] A. I. Smith, H. V. Wladkowski, Z. H. Hecht, Y. She, S. Kattel, P. I. Samarawickrama, S. R. Rich, J. R. Murphy, J. Tian, J. F. Ackerman, W. D. Rice, E. B. Hulley, and B. M. Leonard. Alkali Metal Intercalation and Reduction of Layered WO_2Cl_2. *Chemistry of Materials*, **32**, 24, (2020), pp. 10482–10488.

[29] T. C. Holgate, Y. Liu, D. Hitchcock, T. M. Tritt, and J. He. Thermoelectric Properties of Li-Intercalated $ZrSe_2$ Single Crystals. *Journal of Electronic Materials*, **42**, 7, (2013), pp. 1751–1755.

[30] T. Holgate, S. Zhu, M. Zhou, S. Bangarigadu-Sanasy, H. Kleinke, J. He, and T. Tritt. Thermoelectric transport properties of polycrystalline titanium diselenide co-intercalated with nickel and titanium using spark plasma sintering. *Journal of Solid State Chemistry*, **197**, (2013), pp. 273–278.

[31] A. Shkvarin, A. Titov, A. Merentsov, E. Shkvarina, M. Postnikov, I. Píš, S. Nappini, P. Agzamova, A. Volegov, and A. Titov. The crystal structure, chemical bonding, and magnetic properties of the intercalation compounds

Cr_xZrTe_2 (x = 0–0.3). *Materials Science and Engineering: B*, **270**, April, (2021), p. 115218.

[32] M. Kühne, F. Börrnert, S. Fecher, M. Ghorbani-Asl, J. Biskupek, D. Samuelis, A. V. Krasheninnikov, U. Kaiser, and J. H. Smet. Reversible superdense ordering of lithium between two graphene sheets. *Nature*, **564**, 7735, (2018), pp. 234–239.

[33] S. Zhou, W. Chen, J. Shi, G. Li, F. Pei, S. Liu, W. Ye, L. Xiao, M.-S. Wang, D. Wang, Y. Qiao, L. Huang, G.-L. Xu, H.-G. Liao, J.-F. Chen, K. Amine, and S.-G. Sun. Efficient diffusion of superdense lithium via atomic channels for dendrite-free lithium–metal batteries. *Energy & Environmental Science*, **15**, 1, (2022), pp. 196–205.

[34] The Nobel Prize in Chemistry 2019. URL https://www.nobelprize.org/prizes/chemistry/2019/summary/.

[35] M. S. Whittingham. The Role of Ternary Phases in Cathode Reactions. *Journal of The Electrochemical Society*, **123**, 3, (1976), pp. 315–320.

[36] A. S. Andersson. Thermal Stability of $LiFePO_4$-Based Cathodes. *Electrochemical and Solid-State Letters*, **3**, 2, (2000), p. 66.

[37] X. Li, Y. Xu, and C. Wang. Suppression of Jahn–Teller distortion of spinel $LiMn_2O_4$ cathode. *Journal of Alloys and Compounds*, **479**, 1-2, (2009), pp. 310–313.

[38] L. Liao, P. Zuo, Y. Ma, X. Chen, Y. An, Y. Gao, and G. Yin. Effects of temperature on charge/discharge behaviors of $LiFePO_4$ cathode for Li-ion batteries. *Electrochimica Acta*, **60**, (2012), pp. 269–273.

[39] Y. Liu, J. Lv, Y. Fei, X. Huo, and Y. Zhu. Improvement of storage performance of $LiMn_2O_4$/graphite battery with AlF_3-coated $LiMn_2O_4$. *Ionics*, **19**, 9, (2013), pp. 1241–1246.

[40] B. Lung-Hao Hu, F. Y. Wu, C. T. Lin, A. N. Khlobystov, and L. J. Li. Graphene-modified $LiFePO_4$ cathode for lithium ion battery beyond theoretical capacity. *Nature Communications*, **4**, 1, (2013), pp. 1–7.

[41] R. N. Ramesha, D. Bosubabu, M. G. Karthick Babu, and K. Ramesha. Tuning of Ni, Mn, and Co (NMC) content in 0.4($LiNi_xMn_yCo_zO_2$)·0.4(Li_2MnO_3) toward stable high-capacity lithium-rich cathode materials. *ACS Applied Energy Materials*, **3**, 11, (2020), pp. 10872–10881.

[42] Y. Lyu, X. Wu, K. Wang, Z. Feng, T. Cheng, Y. Liu, M. Wang, R. Chen, L. Xu, J. Zhou, Y. Lu, and B. Guo. An Overview on the Advances of $LiCoO_2$ Cathodes for Lithium-Ion Batteries. *Advanced Energy Materials*, **11**, 2, (2021), p. 2000982.

[43] J. Asenbauer, T. Eisenmann, M. Kuenzel, A. Kazzazi, Z. Chen, and D. Bresser. The success story of graphite as a lithium-ion anode material – fundamentals, remaining challenges, and recent developments including silicon (oxide) composites. *Sustainable Energy & Fuels*, **4**, 11, (2020), pp. 5387–5416.

[44] S. Yuan, K. Ding, X. Zeng, D. Bin, Y. Zhang, P. Dong, and Y. Wang. Advanced Nonflammable Organic Electrolyte Promises Safer Li-Metal Batteries: From Solvation Structure Perspectives. *Advanced Materials*, **35**, 13, (2023), pp. 1–25.

[45] A. Eftekhari, Y. Liu, and P. Chen. Different roles of ionic liquids in lithium batteries. *Journal of Power Sources*, **334**, (2016), pp. 221–239.

[46] A. Banerjee, X. Wang, C. Fang, E. A. Wu, and Y. S. Meng. Interfaces and Interphases in All-Solid-State Batteries with Inorganic Solid Electrolytes. *Chemical Reviews*, **120**, 14, (2020), pp. 6878–6933.

[47] J. B. Goodenough and Y. Kim. Challenges for Rechargeable Li Batteries. *Chemistry of Materials*, **22**, 3, (2010), pp. 587–603.

[48] J. Wang, R. Jia, Q. Huang, C. Pan, J. Zhu, H. Wang, C. Chen, Y. Zhang, Y. Yang, H. Song, F. Miao, and R. Huang. Vertical WS_2/SnS_2 van der Waals Heterostructure for Tunneling Transistors. *Scientific Reports*, **8**, 1, (2018), pp. 1–9.

[49] J. Guo, Y. Li, J. Meng, K. Pedersen, L. Gurevich, and D.-I. Stroe. Understanding the mechanism of capacity increase during early cycling of com-

mercial NMC/graphite lithium-ion batteries. *Journal of Energy Chemistry*, **74**, (2022), pp. 34–44.

[50] C. Peng, H. Lyu, L. Wu, T. Xiong, F. Xiong, Z. Liu, Q. An, and L. Mai. Lithium- and Magnesium-Storage Mechanisms of Novel Hexagonal $NbSe_2$. *ACS Applied Materials & Interfaces*, **10**, 43, (2018), pp. 36988–36995.

[51] A. Allerhand. Who invented the earliest capacitor bank ("battery" of leyden jars)? It's complicated. *Proceedings of the IEEE*, **106**, 3, (2018), pp. 496–503.

[52] Volta A. XVII. On the electricity excited by the mere contact of conducting substances of different kinds. In a letter from Mr. Alexander Volta, F. R. S. Professor of Natural Philosophy in the University of Pavia, to the Rt. Hon. Sir Joseph Banks, Bart. K.B. P. R. *Philosophical Transactions of the Royal Society of London*, **90**, (1800), pp. 403–431.

[53] S. Burles, K. M. Nollett, and M. S. Turner. Big-Bang Nucleosynthesis: Linking Inner Space and Outer Space.

[54] K. Xu. A Long Journey of Lithium: From the Big Bang to Our Smartphones. *Energy & Environmental Materials*, **2**, 4, (2019), pp. 229–233.

[55] M. Winter, B. Barnett, and K. Xu. Before Li Ion Batteries. *Chemical Reviews*, **118**, 23, (2018), pp. 11433–11456.

[56] M. V. Reddy, A. Mauger, C. M. Julien, A. Paolella, and K. Zaghib. Brief History of Early Lithium-Battery Development. *Materials*, **13**, 8, (2020), p. 1884.

[57] E. Katz. Electrochemical contributions: Sir Humphry Davy (1778–1829). *Electrochemical Science Advances*, **1**, 2, (2021), pp. 1–2.

[58] P. Ruetschi. Review on the lead—acid battery science and technology. *Journal of Power Sources*, **2**, 1, (1977), pp. 3–120.

[59] P. Kurzweil. Gaston Planté and his invention of the lead–acid battery—The genesis of the first practical rechargeable battery. *Journal of Power Sources*, **195**, 14, (2010), pp. 4424–4434.

[60] G. N. Lewis and F. G. Keyes. The Potential Of The Lithium Electrode. *Journal of the American Chemical Society*, **35**, 4, (1913), pp. 340–344.

[61] W. S. Harris. Electrochemical Studies in Cyclic Esters. Ph.D. thesis, Lawrence Livermore National Laboratory (LLNL), Livermore, CA (United States) (1958).

[62] S. G. Abens, W. C. Merz, and C. R. Walk. Development of high Energy Density Primary Batteries. Technical report, National Aeronautics and Space Administration (1967).

[63] W. F. Meyers, B. Bell, and J. W. Simmon. Electric current-producing cell with anydrous organic liquid electrolyte (1969).

[64] H. Park, H.-D. Lim, H.-K. Lim, W. M. Seong, S. Moon, Y. Ko, B. Lee, Y. Bae, H. Kim, and K. Kang. High-efficiency and high-power rechargeable lithium–sulfur dioxide batteries exploiting conventional carbonate-based electrolytes. *Nature Communications*, **8**, 1, (2017), p. 14989.

[65] N. Watanabe and M. Fukuda. Primary Cell for Electric Batteries (1970).

[66] Q. Zhang, K. J. Takeuchi, E. S. Takeuchi, and A. C. Marschilok. Progress towards high-power Li/CF_x batteries: electrode architectures using carbon nanotubes with CF_x. *Physical Chemistry Chemical Physics*, **17**, 35, (2015), pp. 22504–22518.

[67] M. S. Whittingham. Electrical Energy Storage and Intercalation Chemistry. *Science*, **192**, 4244, (1976), pp. 1126–1127.

[68] D. J. Eustace and B. M. L. Rao. Li/TiS_2 Current producing system (1983).

[69] M. Li, J. Lu, Z. Chen, and K. Amine. 30 Years of Lithium-Ion Batteries. *Advanced Materials*, **30**, 33, (2018), p. 1800561.

[70] N. Godshall, I. Raistrick, and R. Huggins. Thermodynamic investigations of ternary lithium-transition metal-oxygen cathode materials. *Materials Research Bulletin*, **15**, 5, (1980), pp. 561–570.

[71] K. Mizushima, P. Jones, P. Wiseman, and J. Goodenough. Li_xCoO_2 (0<x<-1): A new cathode material for batteries of high energy density (1980).

[72] K. Mizushima, P. C. Jones, P. J. Wiseman, and J. B. Goodenough. Li_xCoO_2 (0<x<1): A new cathode material for batteries of high energy density. *Solid State Ionics*, **3-4**, C, (1981), pp. 171–174.

[73] J. B. Goodenough and K. Mizuchima. Electrochemical Cell with New Fast Ion Conductors (1980).

[74] D. Aurbach, E. Zinigrad, Y. Cohen, and H. Teller. A short review of failure mechanisms of lithium metal and lithiated graphite anodes in liquid electrolyte solutions. *Solid State Ionics*, **148**, 3-4, (2002), pp. 405–416.

[75] X. Gao, Y.-N. Zhou, D. Han, J. Zhou, D. Zhou, W. Tang, and J. B. Goodenough. Thermodynamic Understanding of Li-Dendrite Formation. *Joule*, **4**, 9, (2020), pp. 1864–1879.

[76] Q. Wang, B. Liu, Y. Shen, J. Wu, Z. Zhao, C. Zhong, and W. Hu. Confronting the Challenges in Lithium Anodes for Lithium Metal Batteries. *Advanced Science*, **8**, 17, (2021), p. 2101111.

[77] R. Yazami and P. Touzain. A reversible graphite-lithium negative electrode for electrochemical generators. *Journal of Power Sources*, **9**, 3, (1983), pp. 365–371.

[78] A. Yoshino, K. Sanechika, and T. Nakajima. Secondary Battery (1987).

[79] Yamahira, Kato, and Anzai. Nonaqueous electrolyte secondary battery (1991).

[80] IEEE Medal for Environmental and Safety Technologies. URL https://ethw.org/IEEE_Medal_for_Environmental_and_Safety_Technologies#:~:text=2012%20%2D%20John%20Bannister%20Goodenough%2C%20Rachid,and%20for%20smartgrids%20incorporating%20renewables.%E2%80%9D.

[81] Nobel Prizes 2019. URL https://www.nobelprize.org/all-nobel-prizes-2019/.

[82] D. Y. Wan, Z. Y. Fan, Y. X. Dong, E. Baasanjav, H.-B. Jun, B. Jin, E. M. Jin, and S. M. Jeong. Effect of Metal (Mn, Ti) Doping on NCA Cathode Materials for Lithium Ion Batteries. *Journal of Nanomaterials*, **2018**, (2018), pp. 1–9.

[83] J. Kasnatscheew, S. Röser, M. Börner, and M. Winter. Do Increased Ni Contents in $LiNi_xMn_yCo_zO_2$ (NMC) Electrodes Decrease Structural and Thermal Stability of Li Ion Batteries? A Thorough Look by Consideration of the Li^+ Extraction Ratio. *ACS Applied Energy Materials*, **2**, 11, (2019), pp. 7733–7737.

[84] G. W. Nam, N. Y. Park, K. J. Park, J. Yang, J. Liu, S. C. Yoon, and K.-Y. Sun. Capacity Fading of Ni-Rich NCA Cathodes: Effect of Microcracking Extent. *ACS Energy Letters*, **4**, 12, (2019), pp. 2995–3001.

[85] W. Li, S. Lee, and A. Manthiram. High-Nickel NMA: A Cobalt-Free Alternative to NMC and NCA Cathodes for Lithium-Ion Batteries. *Advanced Materials*, **32**, 33, (2020), p. 2002718.

[86] N. D. Phillip, A. S. Westover, C. Daniel, and G. M. Veith. Structural Degradation of High Voltage Lithium Nickel Manganese Cobalt Oxide (NMC) Cathodes in Solid-State Batteries and Implications for Next Generation Energy Storage. *ACS Applied Energy Materials*, **3**, 2, (2020), pp. 1768–1774.

[87] H. Ji, J. Wu, Z. Cai, J. Liu, D. H. Kwon, H. Kim, A. Urban, J. K. Papp, E. Foley, Y. Tian, M. Balasubramanian, H. Kim, R. J. Clément, B. D. McCloskey, W. Yang, and G. Ceder. Ultrahigh power and energy density in partially ordered lithium-ion cathode materials. *Nature Energy*, **5**, 3, (2020), pp. 213–221.

[88] A. Franco Gonzalez, N.-h. Yang, and R.-s. Liu. Silicon Anode Design for Lithium-Ion Batteries: Progress and Perspectives. *The Journal of Physical Chemistry C*, **121**, 50, (2017), pp. 27775–27787.

[89] C. P. Sandhya, B. John, and C. Gouri. Lithium titanate as anode material for lithium-ion cells: a review. *Ionics*, **20**, 5, (2014), pp. 601–620.

[90] J. Jiang, Y. Li, J. Liu, and X. Huang. Building one-dimensional oxide nanostructure arrays on conductive metal substrates for lithium-ion battery anodes. *Nanoscale*, **3**, 1, (2011), pp. 45–58.

[91] A. R. Armstrong, C. Lyness, P. M. Panchmatia, M. S. Islam, and P. G. Bruce. The lithium intercalation process in the low-voltage lithium battery anode $Li_{1+x}V_{1-x}O_2$. *Nature Materials*, **10**, 3, (2011), pp. 223–229.

[92] C. Kittel. Introduction to Solid State Physics, (John Wiley and Sons Inc.2015), eighth edition. ISBN 978-81-265-3518-7.

[93] R. M. Martin. Electronic Structure: Basic Theory and Practical Methods, (Cambridge University Press2020), second edition. ISBN 978-1-108-42990-0.

[94] G. P. Srivastava. Theoretical Modelling of Semiconductor Surfaces, (World Scientific Publishing Co.1999).

[95] M. Weissbluth. Atoms and Molecules, (Academic Press, Inc.1978). ISBN 0-12-744452-1.

[96] P. Hohenberg and W. Kohn. Inhomogeneous Electron Gas. *Physical Review*, **136**, 3B, (1964), pp. 864–871.

[97] W. Kohn and L. J. Sham. Self-Consistent Equations Including Exchange and Correlation Effects. *Physical Review*, **140**, 4A, (1965), pp. A1133–A1138.

[98] R. G. Parr. Density Functional Theory. *Annual Review of Physical Chemistry*, **34**, (1983), pp. 631–656.

[99] K. Lejaeghere, G. Bihlmayer, T. Björkman, P. Blaha, S. Blügel, V. Blum, D. Caliste, I. E. Castelli, S. J. Clark, A. Dal Corso, S. de Gironcoli, T. Deutsch, J. K. Dewhurst, I. Di Marco, C. Draxl, M. Dułak, O. Eriksson, J. A. Flores-Livas, K. F. Garrity, L. Genovese, P. Giannozzi, M. Giantomassi, S. Goedecker, X. Gonze, O. Grånäs, E. K. U. Gross, A. Gulans, F. Gygi, D. R. Hamann, P. J. Hasnip, N. A. W. Holzwarth, D. Iuşan, D. B. Jochym, F. Jollet, D. Jones, G. Kresse, K. Koepernik, E. Küçükbenli, Y. O. Kvashnin, I. L. M. Locht, S. Lubeck, M. Marsman, N. Marzari, U. Nitzsche, L. Nordström, T. Ozaki, L. Paulatto, C. J. Pickard, W. Poelmans, M. I. J. Probert, K. Refson, M. Richter, G.-M. Rignanese, S. Saha, M. Scheffler, M. Schlipf, K. Schwarz, S. Sharma, F. Tavazza, P. Thunström, A. Tkatchenko, M. Torrent, D. Vanderbilt, M. J. van Setten, V. Van Speybroeck, J. M. Wills, J. R. Yates, G.-X. Zhang, and S. Cottenier. Reproducibility in density functional theory calculations of solids. *Science*, **351**, 6280.

[100] H. S. Yu, X. He, and D. G. Truhlar. MN15-L: A New Local Exchange-Correlation Functional for Kohn–Sham Density Functional Theory with Broad Accuracy for Atoms, Molecules, and Solids. *Journal of Chemical Theory and Computation*, **12**, 3, (2016), pp. 1280–1293.

[101] M. Gell-Mann and K. A. Brueckner. Correlation Energy of an Electron Gas at High Density. *Physical Review*, **106**, 2, (1957), pp. 364–368.

[102] W. J. Carr. Energy, Specific Heat, and Magnetic Properties of the Low-Density Electron Gas. *Physical Review*, **122**, 5, (1961), pp. 1437–1446.

[103] L. Hedin, B. I. Lundqvist, and S. Lundqvist. Local exchange-correlation potentials. *Solid State Communications*, **9**, 9, (1971), pp. 537–541.

[104] S. H. Vosko, L. Wilk, and M. Nusair. Accurate spin-dependent electron liquid correlation energies for local spin density calculations: a critical analysis. *Canadian Journal of Physics*, **58**, 8, (1980), pp. 1200–1211.

[105] J. P. Perdew and A. Zunger. Self-interaction correction to density-functional approximations for many-electron systems. *Physical Review B*, **23**, 10, (1981), pp. 5048–5079.

[106] J. P. Perdew, J. A. Chevary, S. H. Vosko, K. A. Jackson, M. R. Pederson, D. J. Singh, and C. Fiolhais. Atoms, molecules, solids, and surfaces: Applications of the generalized gradient approximation for exchange and correlation. *Physical Review B*, **46**, 11, (1992), pp. 6671–6687.

[107] A. D. Becke. Density-functional thermochemistry. I. The effect of the exchange-only gradient correction. *The Journal of Chemical Physics*, **96**, 3, (1992), pp. 2155–2160.

[108] A. D. Becke. Density-functional thermochemistry. II. The effect of the Perdew–Wang generalized-gradient correlation correction. *The Journal of Chemical Physics*, **97**, 12, (1992), pp. 9173–9177.

[109] A. D. Becke. Density-functional thermochemistry. III. The role of exact exchange. *The Journal of Chemical Physics*, **98**, 7, (1993), pp. 5648–5652.

[110] B. Hammer, K. W. Jacobsen, and J. K. Nørskov. Role of nonlocal exchange correlation in activated adsorption. *Physical Review Letters*, **70**, 25, (1993), pp. 3971–3974.

[111] B. Hammer and M. Scheffler. Local Chemical Reactivity of a Metal Alloy Surface. *Physical Review Letters*, **74**, 17, (1995), pp. 3487–3490.

[112] P. Philipsen, G. te Velde, and E. Baerends. The effect of density-gradient corrections for a molecule-surface potential energy surface. Slab calculations on Cu(100)c(2x2)-CO. *Chemical Physics Letters*, **226**, 5-6, (1994), pp. 583–588.

[113] D. R. Hamann. Generalized Gradient Theory for Silica Phase Transitions. *Physical Review Letters*, **76**, 4, (1996), pp. 660–663.

[114] A. Zupan, J. P. Perdew, K. Burke, and M. Caus. Density-gradient analysis for density functional theory: Application to atoms. *International Journal of Quantum Chemistry*, **61**, 5, (1997), pp. 835–845.

[115] V. Ozoliņš and M. Körling. Full-potential calculations using the generalized gradient approximation: Structural properties of transition metals. *Physical Review B*, **48**, 24, (1993), pp. 18304–18307.

[116] A. D. Becke. Density-functional exchange-energy approximation with correct asymptotic behavior. *Physical Review A*, **38**, 6, (1988), pp. 3098–3100.

[117] R. Armiento and A. E. Mattsson. Functional designed to include surface effects in self-consistent density functional theory. *Physical Review B*, **72**, 8, (2005), p. 085108.

[118] Z. Wu and R. E. Cohen. More accurate generalized gradient approximation for solids. *Physical Review B*, **73**, 23, (2006), p. 235116.

[119] J. P. Perdew, K. Burke, and M. Ernzerhof. Generalized Gradient Approximation Made Simple. *Physical Review Letters*, **77**, 18, (1996), pp. 3865–3868.

[120] J. P. Perdew, K. Burke, and M. Ernzerhof. Generalized Gradient Approximation Made Simple [Phys. Rev. Lett. 77, 3865 (1996)]. *Physical Review Letters*, **78**, 7, (1997), pp. 1396–1396.

[121] L. He, F. Liu, G. Hautier, M. J. T. Oliveira, M. A. L. Marques, F. D. Vila, J. J. Rehr, G.-M. Rignanese, and A. Zhou. Accuracy of generalized gradient approximation functionals for density-functional perturbation theory calculations. *Physical Review B*, **89**, 6, (2014), p. 064305.

[122] G.-X. Zhang, A. M. Reilly, A. Tkatchenko, and M. Scheffler. Performance of various density-functional approximations for cohesive properties of 64 bulk solids. *New Journal of Physics*, **20**, 6, (2018), p. 063020.

[123] P. Kovács, F. Tran, P. Blaha, and G. K. H. Madsen. Comparative study of the PBE and SCAN functionals: The particular case of alkali metals. *The Journal of Chemical Physics*, **150**, 16, (2019), p. 164119.

[124] H.-D. Saßnick and C. Cocchi. Electronic structure of cesium-based photocathode materials from density functional theory: performance of PBE, SCAN, and HSE06 functionals. *Electronic Structure*, **3**, 2, (2021), p. 027001.

[125] R. Van Noorden, B. Maher, and R. Nuzzo. The top 100 papers. *Nature*, **514**, 7524, (2014), pp. 550–553.

[126] John P. Perdew Google Scholar Page. URL https://scholar.google.com/citations?user=09nv75wAAAAJ&hl=en.

[127] 'Generalized gradient approximation made simple' Web of Science Entry. URL https://www.webofscience.com/wos/woscc/full-record/WOS:A1996VP22500044.

[128] A. D. Becke. A new mixing of Hartree–Fock and local density-functional theories. *The Journal of Chemical Physics*, **98**, 2, (1993), pp. 1372–1377.

[129] J. P. Perdew, M. Ernzerhof, and K. Burke. Rationale for mixing exact exchange with density functional approximations. *The Journal of Chemical Physics*, **105**, 22, (1996), pp. 9982–9985.

[130] J. Heyd, G. E. Scuseria, and M. Ernzerhof. Hybrid functionals based on a screened Coulomb potential. *Journal of Chemical Physics*, **118**, 18, (2003), pp. 8207–8215.

[131] C. Lee, W. Yang, and R. G. Parr. Development of the Colle-Salvetti correlation-energy formula into a functional of the electron density. *Physical Review B*, **37**, 2, (1988), pp. 785–789.

[132] K. Kim and K. D. Jordan. Comparison of Density Functional and MP2 Calculations on the Water Monomer and Dimer. *The Journal of Physical Chemistry*, **98**, 40, (1994), pp. 10089–10094.

[133] P. J. Stephens, F. J. Devlin, C. F. Chabalowski, and M. J. Frisch. Ab Initio Calculation of Vibrational Absorption and Circular Dichroism Spectra Using Density Functional Force Fields. *The Journal of Physical Chemistry*, **98**, 45, (1994), pp. 11623–11627.

[134] L. Lu. Can B3LYP be improved by optimization of the proportions of exchange and correlation functionals? *International Journal of Quantum Chemistry*, **115**, 8, (2015), pp. 502–509.

[135] J. Heyd, G. E. Scuseria, and M. Ernzerhof. Erratum: Hybrid functionals based on a screened Coulomb potential (Journal of Chemical Physics (2003) 118 (8207)) (2006).

[136] S. L. Dudarev, G. A. Botton, S. Y. Savrasov, C. J. Humphreys, and A. P. Sutton. Electron-energy-loss spectra and the structural stability of nickel oxide: An LSDA+U study. *Physical Review B*, **57**, 3, (1998), pp. 1505–1509.

[137] D. S. Sholl and J. A. Steckel. Density Functional Theory: A Practical Introduction, (John Wiley and Sons Inc.2009), second edition. ISBN 978 0 470 37317 0.

[138] M. C. Payne, M. P. Teter, D. C. Allan, T. A. Arias, and J. D. Joannopoulos. Iterative minimization techniques for ab initio total-energy calculations: molecular dynamics and conjugate gradients. *Reviews of Modern Physics*, **64**, 4, (1992), pp. 1045–1097.

[139] P. E. Blöchl. Projector augmented-wave method. *Physical Review B*, **50**, 24, (1994), pp. 17953–17979.

[140] H. J. Monkhorst and J. D. Pack. Special points for Brillouin-zone integrations. *Physical Review B*, **13**, 12, (1976), pp. 5188–5192.

[141] W. Setyawan and S. Curtarolo. High-throughput electronic band structure calculations: Challenges and tools. *Computational Materials Science*, **49**, 2, (2010), pp. 299–312.

[142] R. P. Feynman. Forces in Molecules. *Physical Review*, **56**, 4, (1939), pp. 340–343.

[143] P. Pulay. Ab initio calculation of force constants and equilibrium geometries in polyatomic molecules. *Molecular Physics*, **17**, 2, (1969), pp. 197–204.

[144] R. F. W. Bader. A quantum theory of molecular structure and its applications. *Chemical Reviews*, **91**, 5, (1991), pp. 893–928.

[145] G. Henkelman, A. Arnaldsson, and H. Jónsson. A fast and robust algorithm for Bader decomposition of charge density. *Computational Materials Science*, **36**, 3, (2006), pp. 354–360.

[146] E. Sanville, S. D. Kenny, R. Smith, and G. Henkelman. Improved grid-based algorithm for Bader charge allocation. *Journal of Computational Chemistry*, **28**, 5, (2007), pp. 899–908.

[147] W. Tang, E. Sanville, and G. Henkelman. A grid-based Bader analysis algorithm without lattice bias. *Journal of Physics: Condensed Matter*, **21**, 8, (2009), p. 084204.

[148] A. Otero-de-la Roza and V. Luaña. A fast and accurate algorithm for QTAIM integration in solids. *Journal of Computational Chemistry*, **32**, 2, (2011), pp. 291–305.

[149] M. Yu and D. R. Trinkle. Accurate and efficient algorithm for Bader charge integration. *The Journal of Chemical Physics*, **134**, 6, (2011), p. 064111.

[150] P. Hobza, J. Sponer, and T. Reschel. Density functional theory and molecular clusters. *Journal of Computational Chemistry*, **16**, 11, (1995), pp. 1315–1325.

[151] S. Kristyán and P. Pulay. Can (semi)local density functional theory account for the London dispersion forces? *Chemical Physics Letters*, **229**, 3, (1994), pp. 175–180.

[152] M. J. Allen and D. J. Tozer. Helium dimer dispersion forces and correlation potentials in density functional theory. *The Journal of Chemical Physics*, **117**, 24, (2002), pp. 11113–11120.

[153] S. Grimme. Accurate description of van der Waals complexes by density functional theory including empirical corrections. *Journal of Computational Chemistry*, **25**, 12, (2004), pp. 1463–1473.

[154] S. Grimme. Semiempirical GGA-type density functional constructed with a long-range dispersion correction. *Journal of Computational Chemistry*, **27**, 15, (2006), pp. 1787–1799.

[155] S. Grimme, J. Antony, S. Ehrlich, and H. Krieg. A consistent and accurate ab initio parametrization of density functional dispersion correction (DFT-D) for the 94 elements H-Pu. *The Journal of Chemical Physics*, **132**, 15, (2010), p. 154104.

[156] G. Henkelman, B. P. Uberuaga, and H. Jónsson. Climbing image nudged elastic band method for finding saddle points and minimum energy paths. *Journal of Chemical Physics*, **113**, 22, (2000), pp. 9901–9904.

[157] G. Henkelman and H. Jónsson. Improved tangent estimate in the nudged elastic band method for finding minimum energy paths and saddle points. *Journal of Chemical Physics*, **113**, 22, (2000), pp. 9978–9985.

[158] G. P. Srivastava. The Physics of Phonons, (Adam Hilger, IOP Publishing Ltd1990). ISBN 0-85274-153-7.

[159] A. Togo and I. Tanaka. First principles phonon calculations in materials science. *Scripta Materialia*, **108**, (2015), pp. 1–5.

[160] A. Togo. First-principles Phonon Calculations with Phonopy and Phono3py. *Journal of the Physical Society of Japan*, **92**, 1, (2023), p. 012001.

[161] G. Kresse and J. Hafner. Ab initio molecular dynamics for liquid metals. *Physical Review B*, **47**, 1, (1993), pp. 558–561.

[162] G. Kresse and J. Hafner. Ab initio molecular-dynamics simulation of the liquid-metal–amorphous-semiconductor transition in germanium. *Physical Review B*, **49**, 20, (1994), pp. 14251–14269.

[163] G. Kresse and J. Furthmüller. Efficiency of ab-initio total energy calculations for metals and semiconductors using a plane-wave basis set. *Computational Materials Science*, **6**, 1, (1996), pp. 15–50.

[164] G. Kresse and J. Furthmüller. Efficient iterative schemes for ab initio total-energy calculations using a plane-wave basis set. *Physical Review B*, **54**, 16, (1996), pp. 11169–11186.

[165] G. E. Blomgren. The Development and Future of Lithium Ion Batteries. *Journal of The Electrochemical Society*, **164**, 1, (2017), pp. A5019–A5025.

[166] K. Turcheniuk, D. Bondarev, G. G. Amatucci, and G. Yushin. Battery materials for low-cost electric transportation. *Materials Today*, **42**, February, (2021), pp. 57–72.

[167] B. Nykvist and M. Nilsson. Rapidly falling costs of battery packs for electric vehicles. *Nature Climate Change*, **5**, 4, (2015), pp. 329–332.

[168] K. K. Fu, J. Cheng, T. Li, and L. Hu. Flexible Batteries: From Mechanics to Devices. *ACS Energy Letters*, **1**, 5, (2016), pp. 1065–1079.

[169] G. Qian, X. Liao, Y. Zhu, F. Pan, X. Chen, and Y. Yang. Designing Flexible Lithium-Ion Batteries by Structural Engineering. *ACS Energy Letters*, **4**, 3, (2019), pp. 690–701.

[170] N. Yabuuchi, K. Kubota, M. Dahbi, and S. Komaba. Research Development on Sodium-Ion Batteries. *Chemical Reviews*, **114**, 23, (2014), pp. 11636–11682.

[171] R. Rajagopalan, Y. Tang, X. Ji, C. Jia, and H. Wang. Advancements and Challenges in Potassium Ion Batteries: A Comprehensive Review. *Advanced Functional Materials*, **30**, 12, (2020), p. 1909486.

[172] P. Saha, M. K. Datta, O. I. Velikokhatnyi, A. Manivannan, D. Alman, and P. N. Kumta. Rechargeable magnesium battery: Current status and key

challenges for the future. *Progress in Materials Science*, **66**, (2014), pp. 1–86.

[173] C. Ling, D. Banerjee, and M. Matsui. Electrochimica Acta Study of the electrochemical deposition of Mg in the atomic level : Why it prefers the non-dendritic morphology. *Electrochimica Acta*, **76**, (2012), pp. 270–274.

[174] J. Park, W. Lu, and A. M. Sastry. Numerical Simulation of Stress Evolution in Lithium Manganese Dioxide Particles due to Coupled Phase Transition and Intercalation. *Journal of The Electrochemical Society*, **158**, 2, (2011), p. A201.

[175] J. Christensen. Modeling Diffusion-Induced Stress in Li-Ion Cells with Porous Electrodes. *Journal of The Electrochemical Society*, **157**, 3, (2010), p. A366.

[176] P. Barai and P. P. Mukherjee. Stochastic Analysis of Diffusion Induced Damage in Lithium-Ion Battery Electrodes. *Journal of The Electrochemical Society*, **160**, 6, (2013), pp. A955–A967.

[177] Y. Qi and S. J. Harris. In Situ Observation of Strains during Lithiation of a Graphite Electrode. *Journal of The Electrochemical Society*, **157**, 6, (2010), p. A741.

[178] K.-Y. Oh, J. B. Siegel, L. Secondo, S. U. Kim, N. A. Samad, J. Qin, D. Anderson, K. Garikipati, A. Knobloch, B. I. Epureanu, C. W. Monroe, and A. Stefanopoulou. Rate dependence of swelling in lithium-ion cells. *Journal of Power Sources*, **267**, (2014), pp. 197–202.

[179] K. S. Novoselov, A. K. Geim, S. V. Morozov, D. Jiang, Y. Zhang, S. V. Dubonos, I. V. Grigorieva, and A. A. Firsov. Electric field in atomically thin carbon films. *Science*, **306**, 5696, (2004), pp. 666–669.

[180] A. K. Geim and K. S. Novoselov. The rise of graphene. Nanoscience and Technology: A Collection of Reviews from Nature Journals, (Co-Published with Macmillan Publishers Ltd, UK2009). ISBN 9789814287005, pp. 11–19.

[181] G. Wang, X. Shen, J. Yao, and J. Park. Graphene nanosheets for enhanced lithium storage in lithium ion batteries. *Carbon*, **47**, 8, (2009), pp. 2049–2053.

[182] Y. Wei, J. Zheng, S. Cui, X. Song, Y. Su, W. Deng, Z. Wu, X. Wang, W. Wang, M. Rao, Y. Lin, C. Wang, K. Amine, and F. Pan. Kinetics Tuning of Li-Ion Diffusion in Layered Li($Ni_xMn_yCo_z$)O_2. *Journal of the American Chemical Society*, **137**, 26, (2015), pp. 8364–8367.

[183] Q. D. Chen, S. F. Yuan, J. H. Dai, and Y. Song. Functionalized $M_2TiC_2T_x$ MXenes (M = Cr and Mo; T = F, O, and OH) as high performance electrode materials for sodium ion batteries. *Physical Chemistry Chemical Physics*, **23**, 2, (2021), pp. 1038–1049.

[184] Y. Sun, N. Liu, and Y. Cui. Promises and challenges of nanomaterials for lithium-based rechargeable batteries. *Nature Energy*, **1**, 7, (2016), pp. 1–12.

[185] J. P. Pender, G. Jha, D. H. Youn, J. M. Ziegler, I. Andoni, E. J. Choi, A. Heller, B. S. Dunn, P. S. Weiss, R. M. Penner, and C. B. Mullins. Electrode Degradation in Lithium-Ion Batteries. *ACS Nano*, **14**, 2, (2020), pp. 1243–1295.

[186] M. G. Boebinger, J. A. Lewis, S. E. Sandoval, and M. T. McDowell. Understanding Transformations in Battery Materials Using in Situ and Operando Experiments: Progress and Outlook. *ACS Energy Letters*, **5**, (2020), pp. 335–345.

[187] X. Xu, W. Liu, Y. Kim, and J. Cho. Nanostructured transition metal sulfides for lithium ion batteries: Progress and challenges. *Nano Today*, **9**, 5, (2014), pp. 604–630.

[188] T. Lu, S. Dong, C. Zhang, L. Zhang, and G. Cui. Fabrication of transition metal selenides and their applications in energy storage. *Coordination Chemistry Reviews*, **332**, (2017), pp. 75–99.

[189] M. Chhowalla, H. S. Shin, G. Eda, L.-j. Li, K. P. Loh, and H. Zhang. The chemistry of two-dimensional layered transition metal dichalcogenide nanosheets. *Nature Chemistry*, **5**, 4, (2013), pp. 263–275.

[190] S. J. McDonnell and R. M. Wallace. Atomically-thin layered films for device applications based upon 2D TMDC materials. *Thin Solid Films*, **616**, (2016), pp. 482–501.

[191] S. Fan, X. Zou, H. Du, L. Gan, C. Xu, W. Lv, Y. B. He, Q. H. Yang, F. Kang, and J. Li. Theoretical Investigation of the Intercalation Chemistry of Lithium/Sodium Ions in Transition Metal Dichalcogenides. *Journal of Physical Chemistry C*, **121**, 25, (2017), pp. 13599–13605.

[192] C. Ataca, H. Şahin, and S. Ciraci. Stable, single-layer MX_2 transition-metal oxides and dichalcogenides in a honeycomb-like structure. *Journal of Physical Chemistry C*, **116**, 16, (2012), pp. 8983–8999.

[193] A. V. Kolobov and J. Tominaga. Two-Dimensional Transition-Metal Dichalcogenides, (Springer International Publishing2016). ISBN 978-3-319-31450-1.

[194] M. Kamaratos, D. Vlachos, C. A. Papageorgopoulos, A. Schellenberger, W. Jaegermann, and C. Pettenkofer. Interaction of Li with the group IV selenide layer compounds at low temperature. *Journal of Physics: Condensed Matter*, **14**, 39, (2002), pp. 8979–8986.

[195] H. Katzke, P. Tolédano, and W. Depmeier. Phase transitions between polytypes and intralayer superstructures in transition metal dichalcogenides. *Physical Review B - Condensed Matter and Materials Physics*, **69**, 13, (2004), pp. 1–8.

[196] J. Ribeiro-Soares, R. M. Almeida, E. B. Barros, P. T. Araujo, M. S. Dresselhaus, L. G. Cançado, and A. Jorio. Group theory analysis of phonons in two-dimensional transition metal dichalcogenides. *Physical Review B*, **90**, 11, (2014), p. 115438.

[197] C. Rao and K. Pisharody. Transition metal sulfides. *Progress in Solid State Chemistry*, **10**, PART 4, (1976), pp. 207–270.

[198] Z. M. Xu, S. H. Bo, and H. Zhu. $LiCrS_2$ and $LiMnS_2$ Cathodes with Extraordinary Mixed Electron-Ion Conductivities and Favorable Interfacial Compatibilities with Sulfide Electrolyte. *ACS Applied Materials and Interfaces*, **10**, 43, (2018), pp. 36941–36953.

[199] J. H. Han, M. Kwak, Y. Kim, and J. Cheon. Recent Advances in the Solution-Based Preparation of Two-Dimensional Layered Transition Metal Chalcogenide Nanostructures. *Chemical Reviews*, **118**, 13, (2018), pp. 6151–6188.

[200] J. Zhou, C. Zhu, Y. Zhou, J. Dong, P. Li, Z. Zhang, Z. Wang, Y.-c. Lin, J. Shi, R. Zhang, Y. Zheng, H. Yu, B. Tang, F. Liu, L. Wang, L. Liu, G.-B. Liu, W. Hu, Y. Gao, H. Yang, W. Gao, L. Lu, Y. Wang, K. Suenaga, G. Liu, F. Ding, Y. Yao, and Z. Liu. Composition and phase engineering of metal chalcogenides and phosphorous chalcogenides. *Nature Materials*.

[201] C. Gong, H. Zhang, W. Wang, L. Colombo, R. M. Wallace, and K. Cho. Band alignment of two-dimensional transition metal dichalcogenides: Application in tunnel field effect transistors. *Applied Physics Letters*, **103**, 5.

[202] X. Sun, Z. Wang, Z. Li, and Y. Q. Fu. Origin of Structural Transformation in Mono- and Bi-Layered Molybdenum Disulfide. *Scientific Reports*, **6**, 1, (2016), p. 26666.

[203] W. Xu, S. Yan, and W. Qiao. Magnetism in monolayer 1T-MoS 2 and 1T-MoS 2 H tuned by strain. *RSC Advances*, , 15, , pp. 8435–8441.

[204] B. Gao, Y. Zhao, X. Du, D. Li, S. Ding, Y. Li, C. Xiao, and Z. Song. Electron injection induced phase transition of 2H to 1T MoS2 by cobalt and nickel substitutional doping. *Chemical Engineering Journal*, **411**, January, (2021), p. 128567.

[205] M. Whittingham. Chemistry of intercalation compounds: Metal guests in chalcogenide hosts. *Progress in Solid State Chemistry*, **12**, 1, (1978), pp. 41–99.

[206] Y.-P. Gao, X. Wu, K.-J. Huang, L.-L. Xing, Y.-Y. Zhang, and L. Liu. Two-dimensional transition metal diseleniums for energy storage application: a review of recent developments. *CrystEngComm*, **19**, 3, (2017), pp. 404–418.

[207] Y.-P. Gao, J. Xu, K.-J. Huang, H. Lu, Y.-X. Pang, and G.-q. Li. An overview of the current status and prospects of cathode materials based on transi-

tion metal sulfides for magnesium-ion batteries. *CrystEngComm*, **23**, 43, (2021), pp. 7546–7564.

[208] A. H. Thompson. Lithium Ordering in Li_xTiS_2. *Physical Review Letters*, **40**, 23, (1978), pp. 1511–1514.

[209] A. Emly and A. Van der Ven. Mg Intercalation in Layered and Spinel Host Crystal Structures for Mg Batteries. *Inorganic Chemistry*, **54**, 9, (2015), pp. 4394–4402.

[210] D. S. Tchitchekova, A. Ponrouch, R. Verrelli, T. Broux, C. Frontera, A. Sorrentino, F. Bardé, N. Biskup, M. E. Arroyo-de Dompablo, and M. R. Palacín. Electrochemical Intercalation of Calcium and Magnesium in TiS_2 : Fundamental Studies Related to Multivalent Battery Applications. *Chemistry of Materials*, **30**, 3, (2018), pp. 847–856.

[211] D. W. Murphy, F. J. Di Salvo, G. W. Hull, and J. V. Waszczak. Convenient preparation and physical properties of lithium intercalation compounds of Group 4B and 5B layered transition metal dichalcogenides. *Inorganic Chemistry*, **15**, 1, (1976), pp. 17–21.

[212] W. McKinnon, J. Dahn, and C. Levy-Clement. Lithium intercalation in Li_xZrS_2. *Solid State Communications*, **50**, 2, (1984), pp. 101–104.

[213] G. W. King'ori, C. N. M. Ouma, G. O. Amolo, and N. W. Makau. Ab initio insights into Graphene-Zirconium disulfide/diselenide heterostructure as electrode material for alkali-ion batteries. *Surfaces and Interfaces*, **24**, (2021), p. 101036.

[214] S. Kim, Y. J. Kim, and W.-h. Ryu. Zirconium disulfides as an electrode material alternative for Li-ion batteries. *Applied Surface Science*, **547**, December 2020, (2021), p. 149029.

[215] G. W. King'ori, C. N. M. Ouma, A. K. Mishra, G. O. Amolo, and N. W. Makau. Two-dimensional graphene–HfS_2 van der Waals heterostructure as electrode material for alkali-ion batteries. *RSC Advances*, **10**, 50, (2020), pp. 30127–30138.

[216] H. Qi, L. Wang, T. Zuo, S. Deng, Q. Li, Z. Liu, P. Hu, and X. He. Hollow Structure VS_2 @Reduced Graphene Oxide (RGO) Architecture for Enhanced Sodium-Ion Battery Performance. *ChemElectroChem*, **7**, 1, (2020), pp. 78–85.

[217] R. Sun, C. Pei, J. Sheng, D. Wang, L. Wu, S. Liu, Q. An, and L. Mai. High-rate and long-life VS_2 cathodes for hybrid magnesium-based battery. *Energy Storage Materials*, **12**, September 2017, (2018), pp. 61–68.

[218] H. Li, W. Li, L. Ma, W. Chen, and J. Wang. Electrochemical lithiation/delithiation performances of 3D flowerlike MoS_2 powders prepared by ionic liquid assisted hydrothermal route. *Journal of Alloys and Compounds*, **471**, 1-2, (2009), pp. 442–447.

[219] X. Fang, C. Hua, X. Guo, Y. Hu, Z. Wang, X. Gao, F. Wu, J. Wang, and L. Chen. Lithium storage in commercial MoS_2 in different potential ranges. *Electrochimica Acta*, **81**, (2012), pp. 155–160.

[220] T. Stephenson, Z. Li, B. Olsen, and D. Mitlin. Lithium ion battery applications of molybdenum disulfide (MoS_2) nanocomposites. *Energy Environ. Sci.*, **7**, 1, (2014), pp. 209–231.

[221] J. Xia, J. Wang, D. Chao, Z. Chen, Z. Liu, J. L. Kuo, J. Yan, and Z. X. Shen. Phase evolution of lithium intercalation dynamics in 2H-MoS_2. *Nanoscale*, **9**, 22, (2017), pp. 7533–7540.

[222] L. Zhang, D. Sun, J. Kang, J. Feng, H. A. Bechtel, L.-W. Wang, E. J. Cairns, and J. Guo. Electrochemical Reaction Mechanism of the MoS_2 Electrode in a Lithium-Ion Cell Revealed by in Situ and Operando X-ray Absorption Spectroscopy. *Nano Letters*, **18**, 2, (2018), pp. 1466–1475.

[223] A. Nadar, Y. Arora, P. Thakur, T. Narayanan, A. Bhattacharya, and D. Khushalani. ReS_2 vs MoS_2: Viable electrodes for batteries and capacitors. *Electrochemistry Communications*, **139**, July, (2022), p. 107313.

[224] K. Leng, Z. Chen, X. Zhao, W. Tang, B. Tian, C. T. Nai, W. Zhou, and K. P. Loh. Phase Restructuring in Transition Metal Dichalcogenides for Highly Stable Energy Storage. *ACS Nano*, **10**, 10, (2016), pp. 9208–9215.

[225] M. Wang, S. Xu, and J. J. Cha. Revisiting Intercalation-Induced Phase Transitions in 2D Group VI Transition Metal Dichalcogenides. *Advanced Energy and Sustainability Research*, **2**, 8, (2021), p. 2100027.

[226] R. Friend and A. Yoffe. Electronic properties of intercalation complexes of the transition metal dichalcogenides. *Advances in Physics*, **36**, 1, (1987), pp. 1–94.

[227] J. Peng, Y. Liu, Y. Pan, J. Wu, Y. Su, Y. Guo, X. Wu, C. Wu, and Y. Xie. Fast Lithium Ion Conductivity in Layered (Li–Ag)CrS_2. *Journal of the American Chemical Society*, **142**, 43, (2020), pp. 18645–18651.

[228] M. van Dijk and C. Plug. The crystal structure of $LiScS_2$ and $NaScS_2$. *Materials Research Bulletin*, **15**, 1, (1980), pp. 103–106.

[229] L. Havlák, J. Fábry, M. Henriques, and M. Dušek. Structure determination of $KScS_2$, $RbScS_2$ and $KLnS_2$ (Ln = Nd, Sm, Tb, Dy, Ho, Er, Tm and Yb) and crystal–chemical discussion. *Acta Crystallographica Section C Structural Chemistry*, **71**, 7, (2015), pp. 623–630.

[230] C. J. Price, J. Pitfield, E. A. D. Baker, and S. P. Hepplestone. First principles study of layered scandium disulfide for use as Li-ion and beyond-Li-ion batteries. *Physical Chemistry Chemical Physics*, **25**, 3, (2023), pp. 2167–2178.

[231] M. T. Janish and C. B. Carter. In situ TEM observations of the lithiation of molybdenum disulfide. *Scripta Materialia*, **107**, (2015), pp. 22–25.

[232] M. Azhagurajan, T. Kajita, T. Itoh, Y.-G. Kim, and K. Itaya. In Situ Visualization of Lithium Ion Intercalation into MoS_2 Single Crystals using Differential Optical Microscopy with Atomic Layer Resolution. *Journal of the American Chemical Society*, **138**, 10, (2016), pp. 3355–3361.

[233] P. Gao, L. Wang, Y. Y. Zhang, Y. Huang, L. Liao, P. Sutter, K. Liu, D. Yu, and E. G. Wang. High-Resolution Tracking Asymmetric Lithium Insertion and Extraction and Local Structure Ordering in SnS_2. *Nano Letters*, **16**, 9, (2016), pp. 5582–5588.

[234] P. GANAL, W. OLBERDING, T. BUTZ, and G. OUVRARD. Soft chemistry induced host metal coordination change from octahedral to trigonal prismatic in 1T-TaS_2. *Solid State Ionics*, **59**, 3-4, (1993), pp. 313–319.

[235] J. Morales, C. Perez-Vicente, and J. L. Tirado. Chemical and electrochemical lithium intercalation and staging in 2HSnS_2. *Solid State Ionics*, **51**, 3-4, (1992), pp. 133–138.

[236] J. W. Seo, J. T. Jang, S. W. Park, C. Kim, B. Park, and J. Cheon. Two-dimensional SnS_2 nanoplates with extraordinary high discharge capacity for lithium ion batteries. *Advanced Materials*, **20**, 22, (2008), pp. 4269–4273.

[237] J. Zai, K. Wang, Y. Su, X. Qian, and J. Chen. High stability and superior rate capability of three-dimensional hierarchical SnS_2 microspheres as anode material in lithium ion batteries. *Journal of Power Sources*, **196**, 7, (2011), pp. 3650–3654.

[238] B. Luo, Y. Fang, B. Wang, J. Zhou, H. Song, and L. Zhi. Two dimensional graphene-SnS_2 hybrids with superior rate capability for lithium ion storage. *Energy and Environmental Science*, **5**, 1, (2012), pp. 5226–5230.

[239] Q. Zhang, R. Li, M. Zhang, B. Zhang, and X. Gou. SnS_2/reduced graphene oxide nanocomposites with superior lithium storage performance. *Electrochimica Acta*, **115**, (2014), pp. 425–433.

[240] A. S. Hassan, K. Moyer, B. R. Ramachandran, and C. D. Wick. Comparison of Storage Mechanisms in RuO_2, SnO_2, and SnS_2 for Lithium-Ion Battery Anode Materials. *Journal of Physical Chemistry C*, **120**, 4, (2016), pp. 2036–2046.

[241] M. Wang, Y. Huang, Y. Zhu, X. Wu, N. Zhang, and H. Zhang. Binder-free flower-like SnS_2 nanoplates decorated on the graphene as a flexible anode for high-performance lithium-ion batteries. *Journal of Alloys and Compounds*, **774**, (2019), pp. 601–609.

[242] A. Jin, N. Kang, J. H. Um, I. H. Ko, M. S. Kim, K. Kim, S. H. Kim, S. H. Yu, and Y. E. Sung. Sn(salen)-derived SnS nanoparticles embedded in N-

doped carbon for high performance lithium-ion battery anodes. *Chemical Communications*, **56**, 58, (2020), pp. 8095–8098.

[243] R. Li, C. Miao, M. Zhang, and W. Xiao. Novel hierarchical structural SnS_2 composite supported by biochar carbonized from chewed sugarcane as enhanced anodes for lithium ion batteries. *Ionics*, **26**, 3, (2020), pp. 1239–1247.

[244] X. Li, Z. Liu, D. Zhu, Y. Yan, and Y. Chen. Controllable synthesis of few-layer ammoniated 1T-phase WS_2 as an anode material for lithium-ion batteries. *Nanoscale*, **14**, 15, (2022), pp. 5869–5875.

[245] M. Kan, J. Y. Wang, X. W. Li, S. H. Zhang, Y. W. Li, Y. Kawazoe, Q. Sun, and P. Jena. Structures and phase transition of a MoS_2 monolayer. *Journal of Physical Chemistry C*, **118**, 3, (2014), pp. 1515–1522.

[246] Y. Yu, G. Li, L. Huang, A. Barrette, Y.-q. Cai, Y. Yu, K. Gundogdu, Y.-w. Zhang, and L. Cao. Enhancing Multifunctionalities of Transition-Metal Dichalcogenide Monolayers via Cation Intercalation. *ACS Nano*, **11**, 9, (2017), pp. 9390–9396.

[247] A. Al Roman, M. M. Rahman, K. Hossain, S. Das, and F. Ahmed. Development of high-performance ScS_2 monolayer as cathode material: A DFT analysis. *Solid State Communications*, **352**, (2022), p. 114828.

[248] Q. Wang, L. Jiao, Y. Han, H. Du, W. Peng, Q. Huan, D. Song, Y. Si, Y. Wang, and H. Yuan. CoS_2 Hollow Spheres: Fabrication and Their Application in Lithium-Ion Batteries. *The Journal of Physical Chemistry C*, **115**, 16, (2011), pp. 8300–8304.

[249] Y. Song, J. Liao, C. Chen, J. Yang, J. Chen, F. Gong, S. Wang, Z. Xu, and M. Wu. Controllable morphologies and electrochemical performances of self-assembled nano-honeycomb WS_2 anodes modified by graphene doping for lithium and sodium ion batteries. *Carbon*, **142**, (2019), pp. 697–706.

[250] X. Xu, C. S. Rout, J. Yang, R. Cao, P. Oh, H. S. Shin, and J. Cho. Freeze-dried WS_2 composites with low content of graphene as high-rate lithium storage materials. *Journal of Materials Chemistry A*, **1**, 46, (2013), pp. 14548–14554.

[251] Y. Liu, M. Zhu, and D. Chen. Sheet-like $MoSe_2$/C composites with enhanced Li-ion storage properties. *Journal of Materials Chemistry A*, **3**, 22, (2015), pp. 11857–11862.

[252] G. K. Sung, K. J. Jeon, and C. M. Park. Highly Reversible and Superior Li-Storage Characteristics of Layered GeS_2 and Its Amorphous Composites. *ACS Applied Materials and Interfaces*, **8**, 43, (2016), pp. 29543–29550.

[253] E. Pomerantseva and Y. Gogotsi. Two-dimensional heterostructures for energy storage. *Nature Energy*, **2**, 7, (2017), p. 17089.

[254] D. K. Bediako, M. Rezaee, H. Yoo, D. T. Larson, S. Y. Zhao, T. Taniguchi, K. Watanabe, T. L. Brower-Thomas, E. Kaxiras, and P. Kim. Heterointerface effects in the electrointercalation of van der Waals heterostructures. *Nature*, **558**, 7710, (2018), pp. 425–429.

[255] Z. Xiang Huang, B. Liu, D. Kong, Y. Wang, and H. Ying Yang. $SnSe_2$ Quantum Dot/rGO composite as high performing lithium anode. *Energy Storage Materials*, **10**, August 2017, (2018), pp. 92–101.

[256] H. S. Kim, Y. H. Chung, S. H. Kang, and Y. E. Sung. Electrochemical behavior of carbon-coated SnS_2 for use as the anode in lithium-ion batteries. *Electrochimica Acta*, **54**, 13, (2009), pp. 3606–3610.

[257] R. Bhandavat, L. David, and G. Singh. Synthesis of Surface-Functionalized WS_2 Nanosheets and Performance as Li-Ion Battery Anodes. *The Journal of Physical Chemistry Letters*, **3**, 11, (2012), pp. 1523–1530.

[258] F. Wu, C. Zhao, S. Chen, Y. Lu, Y. Hou, Y.-S. Hu, J. Maier, and Y. Yu. Multi-electron reaction materials for sodium-based batteries. *Materials Today*, **21**, 9, (2018), pp. 960–973.

[259] Y. Xiao, M. Zhou, J. Liu, J. Xu, and L. Fu. Phase engineering of two-dimensional transition metal dichalcogenides. *Science China Materials*, **62**, 6, (2019), pp. 759–775.

[260] M. Jakhar, J. Singh, A. Kumar, and R. Pandey. First-Principles Study of the Hexagonal T-Phase $PdSe_2$ Monolayer and Its Application in Solar Cells. *The Journal of Physical Chemistry C*, **124**, 49, (2020), pp. 26565–26571.

[261] Y. Wu, J. Wang, Y. Li, J. Zhou, B. Y. Wang, A. Yang, L.-W. Wang, H. Y. Hwang, and Y. Cui. Observation of an intermediate state during lithium intercalation of twisted bilayer MoS_2. *Nature Communications*, **13**, 1, (2022), p. 3008.

[262] N. T. Taylor, C. J. Price, A. Petkov, M. I. Romanis Carr, J. C. Hale, and S. P. Hepplestone. The Potential of Overlayers on Tin-based Perovskites for Water Splitting. *Journal of Physical Chemistry Letters*, **11**, 10, (2020), pp. 4124–4130.

[263] S. H. Wei and A. Zunger. Calculated natural band offsets of all II-VI and III-V semiconductors: Chemical trends and the role of cation d orbitals. *Applied Physics Letters*, **72**, 16, (1998), pp. 2011–2013.

[264] F. H. Davies, C. J. Price, N. T. Taylor, S. G. Davies, and S. P. Hepplestone. Band alignment of transition metal dichalcogenide heterostructures. *Physical Review B*, **103**, 4, (2021), pp. 1–10.

[265] J. Paier, M. Marsman, K. Hummer, G. Kresse, I. C. Gerber, and J. G. Angyán. Screened hybrid density functionals applied to solids. *Journal of Chemical Physics*, **124**, 15, (2006), p. 154709.

[266] M. K. Aydinol and G. Ceder. First-Principles Prediction of Insertion Potentials in Li-Mn Oxides for Secondary Li Batteries. *Journal of The Electrochemical Society*, **144**, 11, (1997), pp. 3832–3835.

[267] M. K. Aydinol, A. F. Kohan, G. Ceder, K. Cho, and J. Joannopoulos. Ab initio study of lithium intercalation in metal oxides and metal dichalcogenides. *Physical Review B*, **56**, 3, (1997), pp. 1354–1365.

[268] M. Aydinol, A. Kohan, and G. Ceder. Ab initio calculation of the intercalation voltage of lithium-transition-metal oxide electrodes for rechargeable batteries. *Journal of Power Sources*, **68**, 2, (1997), pp. 664–668.

[269] A. Van der Ven, J. Bhattacharya, and A. A. Belak. Understanding Li Diffusion in Li-Intercalation Compounds. *Accounts of Chemical Research*, **46**, 5, (2013), pp. 1216–1225.

[270] Y. Lu, J. Li, Y. Zhao, and X. Zhu. Lithium Clustering during the Lithiation/Delithiation Process in $LiFePO_4$ Olivine-Structured Materials. *ACS Omega*, **4**, 24, (2019), pp. 20612–20617.

[271] T. Zhao, H. Shu, Z. Shen, H. Hu, J. Wang, and X. Chen. Electrochemical Lithiation Mechanism of Two-Dimensional Transition-Metal Dichalcogenide Anode Materials: Intercalation versus Conversion Reactions. *Journal of Physical Chemistry C*, **123**, 4, (2019), pp. 2139–2146.

[272] A. N. Enyashin and G. Seifert. Density-functional study of Li_xMoS_2 intercalates ($0 \leq x \leq 1$). *Computational and Theoretical Chemistry*, **999**, (2012), pp. 13–20.

[273] Z. Liu, H. Deng, and P. P. Mukherjee. Evaluating pristine and modified SnS_2 as a lithium-ion battery anode: A first-principles study. *ACS Applied Materials and Interfaces*, **7**, 7, (2015), pp. 4000–4009.

[274] M. D. Radin and A. Van der Ven. Stability of Prismatic and Octahedral Coordination in Layered Oxides and Sulfides Intercalated with Alkali and Alkaline-Earth Metals. *Chemistry of Materials*, **28**, 21, (2016), pp. 7898–7904.

[275] Y. Qi, H. Guo, L. G. Hector, and A. Timmons. Threefold Increase in the Young's Modulus of Graphite Negative Electrode during Lithium Intercalation. *Journal of The Electrochemical Society*, **157**, 5, (2010), p. A558.

[276] D. Tristant, P. Puech, and I. C. Gerber. Theoretical study of polyiodide formation and stability on monolayer and bilayer graphene. *Physical Chemistry Chemical Physics*, **17**, 44, (2015), pp. 30045–30051.

[277] Y. Qi, L. G. Hector, C. James, and K. J. Kim. Lithium Concentration Dependent Elastic Properties of Battery Electrode Materials from First Principles Calculations. *Journal of The Electrochemical Society*, **161**, 11, (2014), pp. F3010–F3018.

[278] J. Luo, C. Dai, Z. Wang, K. Liu, W. Mao, D. Fang, and X. Chen. In-situ measurements of mechanical and volume change of $LiCoO_2$ lithium-ion batteries during repeated charge–discharge cycling by using digital image correlation. *Measurement*, **94**, (2016), pp. 759–770.

[279] M. Woodcox, R. Shepard, and M. Smeu. First principles investigation into the interwoven nature of voltage and mechanical properties of the Li_xNMC-811 cathode. *Journal of Power Sources*, **516**, June, (2021), p. 230620.

[280] S. Schweidler, L. de Biasi, A. Schiele, P. Hartmann, T. Brezesinski, and J. Janek. Volume Changes of Graphite Anodes Revisited: A Combined Operando X-ray Diffraction and In Situ Pressure Analysis Study. *The Journal of Physical Chemistry C*, **122**, 16, (2018), pp. 8829–8835.

[281] L. Y. Beaulieu, S. D. Beattie, T. D. Hatchard, and J. R. Dahn. The Electrochemical Reaction of Lithium with Tin Studied By In Situ AFM. *Journal of The Electrochemical Society*, **150**, 4, (2003), p. A419.

[282] D. Uxa, B. Jerliu, E. Hüger, L. Dörrer, M. Horisberger, J. Stahn, and H. Schmidt. On the Lithiation Mechanism of Amorphous Silicon Electrodes in Li-Ion Batteries. *Journal of Physical Chemistry C*, **123**, 36, (2019), pp. 22027–22039.

[283] A. Eftekhari. Low voltage anode materials for lithium-ion batteries. *Energy Storage Materials*, **7**, January, (2017), pp. 157–180.

[284] A. Manthiram. A reflection on lithium-ion battery cathode chemistry. *Nature Communications*, **11**, 1, (2020), p. 1550.

[285] D. Zhang, Y. J. Mai, J. Y. Xiang, X. H. Xia, Y. Q. Qiao, and J. P. Tu. FeS_2/C composite as an anode for lithium ion batteries with enhanced reversible capacity. *Journal of Power Sources*, **217**, (2012), pp. 229–235.

[286] K. C. Woo, W. A. Kamitakahara, D. P. DiVincenzo, D. S. Robinson, H. Mertwoy, J. W. Milliken, and J. E. Fischer. Effect of In-Plane Density on the Structural and Elastic Properties of Graphite Intercalation Compounds. *Physical Review Letters*, **50**, 3, (1983), pp. 182–185.

[287] E. A. Suslov, O. V. Bushkova, E. A. Sherstobitova, O. G. Reznitskikh, and A. N. Titov. Lithium intercalation into TiS_2 cathode material: phase equilibria in a Li–TiS_2 system. *Ionics*, **22**, 4, (2016), pp. 503–514.

[288] B. Liu, T. Luo, G. Mu, X. Wang, D. Chen, and G. Shen. Rechargeable Mg-Ion Batteries Based on WSe_2 Nanowire Cathodes. *ACS Nano*, **7**, 9, (2013), pp. 8051–8058.

[289] F. Zhou, M. Cococcioni, C. A. Marianetti, D. Morgan, and G. Ceder. First-principles prediction of redox potentials in transition-metal compounds with LDA + U. *Physical Review B - Condensed Matter and Materials Physics*, **70**, 23, (2004), pp. 1–8.

[290] V. L. Chevrier, S. P. Ong, R. Armiento, M. K. Chan, and G. Ceder. Hybrid density functional calculations of redox potentials and formation energies of transition metal compounds. *Physical Review B - Condensed Matter and Materials Physics*, **82**, 7, (2010), pp. 1–11.

[291] Z. Hu, Z. Wu, C. Han, J. He, Z. Ni, and W. Chen. Two-dimensional transition metal dichalcogenides: Interface and defect engineering. *Chemical Society Reviews*, **47**, 9, (2018), pp. 3100–3128.

[292] E. A. D. Baker, J. Pitfield, C. J. Price, and S. P. Hepplestone. Computational analysis of the enhancement of photoelectrolysis using transition metal dichalcogenide heterostructures. *Journal of Physics: Condensed Matter*, **34**, 37, (2022), p. 375001.

[293] R. W. McKinney, P. Gorai, S. Manna, E. Toberer, and V. Stevanović. Ionic vs. van der Waals layered materials: identification and comparison of elastic anisotropy. *Journal of Materials Chemistry A*, **6**, 32, (2018), pp. 15828–15838.

[294] S. K. Saha and G. Dutta. Elastic and thermal properties of the layered thermoelectrics BiOCuSe and LaOCuSe. *Physical Review B*, **94**, 12, (2016), p. 125209.

[295] M. Güler, Uğur, G. Uğur, and E. Güler. Revealing the electronic, optical, elastic, mechanical, anisotropic, and thermoelectric responses of Sc_2NiZ (Z = Si, Ge, and Sn) Heusler alloys via DFT calculations. *International Journal of Quantum Chemistry*, **123**, 4, (2023), pp. 1–9.

[296] G. Logvenov, A. Gozar, and I. Bozovic. High-Temperature Superconductivity in a Single Copper-Oxygen Plane. *Science*, **326**, 5953, (2009), pp. 699–702.

[297] C. Scheuerlein, B. Fedelich, P. Alknes, G. Arnau, R. Bjoerstad, and B. Bordini. Elastic Anisotropy in Multifilament Nb_3Sn Superconducting Wires. *IEEE Transactions on Applied Superconductivity*, **25**, 3, (2015), pp. 1–5.

[298] K.-A. N. Duerloo, M. T. Ong, and E. J. Reed. Intrinsic Piezoelectricity in Two-Dimensional Materials. *The Journal of Physical Chemistry Letters*, **3**, 19, (2012), pp. 2871–2876.

[299] J. Zhang, C. Wang, and C. Bowen. Piezoelectric effects and electromechanical theories at the nanoscale. *Nanoscale*, **6**, 22, (2014), pp. 13314–13327.

[300] L. C. Gomes, A. Carvalho, and A. H. Castro Neto. Enhanced piezoelectricity and modified dielectric screening of two-dimensional group-IV monochalcogenides. *Physical Review B*, **92**, 21, (2015), p. 214103.

[301] Y. Liu, N. S. Hudak, D. L. Huber, S. J. Limmer, J. P. Sullivan, and J. Y. Huang. In Situ Transmission Electron Microscopy Observation of Pulverization of Aluminum Nanowires and Evolution of the Thin Surface Al_2O_3 Layers during Lithiation–Delithiation Cycles. *Nano Letters*, **11**, 10, (2011), pp. 4188–4194.

[302] Q. Li, P. Wang, Q. Feng, M. Mao, J. Liu, S. X. Mao, and H. Wang. In Situ TEM on the Reversibility of Nanosized Sn Anodes during the Electrochemical Reaction. *Chemistry of Materials*, **26**, 14, (2014), pp. 4102–4108.

[303] Q. Li, P. Wang, Q. Feng, M. Mao, J. Liu, S. X. Mao, and H. Wang. In Situ TEM on the reversibility of nanosized Sn anodes during the electrochemical reaction. *Chemistry of Materials*, **26**, 14, (2014), pp. 4102–4108.

[304] S. Prussin. Generation and Distribution of Dislocations by Solute Diffusion. *Journal of Applied Physics*, **32**, 10, (1961), pp. 1876–1881.

[305] L. Y. Beaulieu, K. W. Eberman, R. L. Turner, L. J. Krause, and J. R. Dahn. Colossal Reversible Volume Changes in Lithium Alloys. *Electrochemical and Solid-State Letters*, **4**, 9, (2001), p. A137.

[306] J. Christensen and J. Newman. A Mathematical Model of Stress Generation and Fracture in Lithium Manganese Oxide. *Journal of The Electrochemical Society*, **153**, 6, (2006), p. A1019.

[307] J. Christensen and J. Newman. Stress generation and fracture in lithium insertion materials. *Journal of Solid State Electrochemistry*, **10**, 5, (2006), pp. 293–319.

[308] X. Zhang, W. Shyy, and A. Marie Sastry. Numerical Simulation of Intercalation-Induced Stress in Li-Ion Battery Electrode Particles. *Journal of The Electrochemical Society*, **154**, 10, (2007), p. A910.

[309] Y.-T. Cheng and M. W. Verbrugge. The influence of surface mechanics on diffusion induced stresses within spherical nanoparticles. *Journal of Applied Physics*, **104**, 8, (2008), p. 083521.

[310] S. Renganathan, G. Sikha, S. Santhanagopalan, and R. E. White. Theoretical Analysis of Stresses in a Lithium Ion Cell. *Journal of The Electrochemical Society*, **157**, 2, (2010), p. A155.

[311] I. Ryu, J. W. Choi, Y. Cui, and W. D. Nix. Size-dependent fracture of Si nanowire battery anodes. *Journal of the Mechanics and Physics of Solids*, **59**, 9, (2011), pp. 1717–1730.

[312] F. Hao, X. Gao, and D. Fang. Diffusion-induced stresses of electrode nanomaterials in lithium-ion battery: The effects of surface stress. *Journal of Applied Physics*, **112**, 10, (2012), p. 103507.

[313] E. J. Seldin and C. W. Nezbeda. Elastic Constants and Electron-Microscope Observations of Neutron-Irradiated Compression-Annealed Pyrolytic and Single-Crystal Graphite. *Journal of Applied Physics*, **41**, 8, (1970), pp. 3389–3400.

[314] H. Zabel, A. Magerl, and J. J. Rush. Phonons in LiC_6. *Physical Review B*, **27**, 6, (1983), pp. 3930–3933.

[315] P. Zhou and J. E. Fischer. Interlayer interactions in LiC_6: Compressibility and thermal expansion. *Physical Review B*, **53**, 19, (1996), pp. 12643–12646.

[316] W. Kamitakahara. Dynamics of li-carbon and carbon solids. *Journal of Physics and Chemistry of Solids*, **57**, 6-8, (1996), pp. 671–676.

[317] C. Lee, X. Wei, J. W. Kysar, and J. Hone. Measurement of the Elastic Properties and Intrinsic Strength of Monolayer Graphene. *Science*, **321**, 5887, (2008), pp. 385–388.

[318] S. Bertolazzi, J. Brivio, and A. Kis. Stretching and Breaking of Ultrathin MoS_2. *ACS Nano*, **5**, 12, (2011), pp. 9703–9709.

[319] A. Castellanos-Gomez, M. Poot, G. A. Steele, H. S. J. van der Zant, N. Agraït, and G. Rubio-Bollinger. Elastic Properties of Freely Suspended MoS_2 Nanosheets. *Advanced Materials*, **24**, 6, (2012), pp. 772–775.

[320] K. Liu, Q. Yan, M. Chen, W. Fan, Y. Sun, J. Suh, D. Fu, S. Lee, J. Zhou, S. Tongay, J. Ji, J. B. Neaton, and J. Wu. Elastic Properties of Chemical-Vapor-Deposited Monolayer MoS_2, WS_2, and Their Bilayer Heterostructures. *Nano Letters*, **14**, 9, (2014), pp. 5097–5103.

[321] R. Zhang, V. Koutsos, and R. Cheung. Elastic properties of suspended multilayer WSe_2. *Applied Physics Letters*, **108**, 4, (2016), p. 042104.

[322] Y. Sun, J. Pan, Z. Zhang, K. Zhang, J. Liang, W. Wang, Z. Yuan, Y. Hao, B. Wang, J. Wang, Y. Wu, J. Zheng, L. Jiao, S. Zhou, K. Liu, C. Cheng, W. Duan, Y. Xu, Q. Yan, and K. Liu. Elastic Properties and Fracture Behaviors of Biaxially Deformed, Polymorphic $MoTe_2$. *Nano Letters*, **19**, 2, (2019), pp. 761–769.

[323] A. Sheraz, N. Mehmood, M. M. Çiçek, Ergün, H. R. Rasouli, E. Durgun, and T. S. Kasırga. High elasticity and strength of ultra-thin metallic transition metal dichalcogenides. *Nanoscale Advances*, **3**, 13, (2021), pp. 3894–3899.

[324] D. Akinwande, C. J. Brennan, J. S. Bunch, P. Egberts, J. R. Felts, H. Gao, R. Huang, J.-S. Kim, T. Li, Y. Li, K. M. Liechti, N. Lu, H. S. Park, E. J. Reed,

P. Wang, B. I. Yakobson, T. Zhang, Y.-W. Zhang, Y. Zhou, and Y. Zhu. A review on mechanics and mechanical properties of 2D materials—Graphene and beyond. *Extreme Mechanics Letters*, **13**, (2017), pp. 42–77.

[325] W. Ding, D. Han, J. Zhang, and X. Wang. Mechanical responses of WSe_2 monolayers: a molecular dynamics study. *Materials Research Express*, **6**, 8, (2019), p. 085071.

[326] Z. Islam and A. Haque. Defects and grain boundary effects in MoS_2: A molecular dynamics study. *Journal of Physics and Chemistry of Solids*, **148**, August 2020, (2021), p. 109669.

[327] N. Sakib, S. Paul, N. Nayir, A. C. T. van Duin, S. Neshani, and K. Momeni. Role of tilt grain boundaries on the structural integrity of WSe_2 monolayers. *Physical Chemistry Chemical Physics*, **24**, 44, (2022), pp. 27241–27249.

[328] P. Hess. Prediction of mechanical properties of 2D solids with related bonding configuration. *RSC Advances*, **7**, 47, (2017), pp. 29786–29793.

[329] P. Hess. Predictive modeling of intrinsic strengths for several groups of chemically related monolayers by a reference model. *Physical Chemistry Chemical Physics*, **20**, 11, (2018), pp. 7604–7611.

[330] L. D. Landau and E. M. Lifshitz. Theory of Elasticity, (Reed Educational and Professional Publishing Ltd.1986), third edition. ISBN 0-7506-2633-X.

[331] Z.-j. Wu, E.-j. Zhao, H.-p. Xiang, X.-f. Hao, X.-j. Liu, and J. Meng. Crystal structures and elastic properties of superhard IrN_2 and IrN_3 from first principles. *Physical Review B*, **76**, 5, (2007), p. 054115.

[332] M. Woodcox, J. Young, and M. Smeu. Ab initio investigation of the elastic properties of bismuth-based alloys. *Physical Review B*, **100**, 10, (2019), p. 104105.

[333] R. Hill. The Elastic Behaviour of a Crystalline Aggregate. *Proceedings of the Physical Society. Section A*, **65**, 5, (1952), pp. 349–354.

[334] O. L. Anderson. A simplified method for calculating the debye temperature from elastic constants. *Journal of Physics and Chemistry of Solids*, **24**, 7, (1963), pp. 909–917.

[335] S. Pugh. XCII. Relations between the elastic moduli and the plastic properties of polycrystalline pure metals. *The London, Edinburgh, and Dublin Philosophical Magazine and Journal of Science*, **45**, 367, (1954), pp. 823–843.

[336] L. Zhu, L. Li, T. Cheng, and D. Xu. First principles study of the elastic properties of $Li_2MnSiO_{4-y}S_y$. *Journal of Materials Chemistry A*, **3**, 10, (2015), pp. 5449–5456.

[337] S. I. Ranganathan and M. Ostoja-Starzewski. Universal elastic anisotropy index. *Physical Review Letters*, **101**, 5, (2008), pp. 3–6.

[338] Y. Ding and B. Xiao. Anisotropic elasticity, sound velocity and thermal conductivity of TiO_2 polymorphs from first principles calculations. *Computational Materials Science*, **82**, (2014), pp. 202–218.

[339] V. A. Gorodtsov and D. S. Lisovenko. The Extreme Values of Young's Modulus and the Negative Poisson's Ratios of Rhombic Crystals. *Crystals*, **11**, 8, (2021), p. 863.

[340] A. Jain, S. P. Ong, G. Hautier, W. Chen, W. D. Richards, S. Dacek, S. Cholia, D. Gunter, D. Skinner, G. Ceder, and K. A. Persson. Commentary: The Materials Project: A materials genome approach to accelerating materials innovation. *APL Materials*, **1**, 1, (2013), p. 011002.

[341] M. de Jong, W. Chen, T. Angsten, A. Jain, R. Notestine, A. Gamst, M. Sluiter, C. Krishna Ande, S. van der Zwaag, J. J. Plata, C. Toher, S. Curtarolo, G. Ceder, K. A. Persson, and M. Asta. Charting the complete elastic properties of inorganic crystalline compounds. *Scientific Data*, **2**, 1, (2015), p. 150009.

[342] S. Shang, Y. Wang, P. Guan, W. Y. Wang, H. Fang, T. Anderson, and Z.-K. Liu. Insight into structural, elastic, phonon, and thermodynamic properties of α-sulfur and energy-related sulfides: a comprehensive first-principles study. *Journal of Materials Chemistry A*, **3**, 15, (2015), pp. 8002–8014.

[343] B. Mortazavi, M. Shahrokhi, X. Zhuang, T. Rabczuk, and A. V. Shapeev. Mechanical, thermal transport, electronic and photocatalytic properties of

penta-PdPS, -PdPSe and -PdPTe monolayers explored by first-principles calculations. *Journal of Materials Chemistry C*, **10**, 1, (2022), pp. 329–336.

[344] M. Barhoumi and N. Sfina. Electronic, Optical, and Elastic Properties of CaFI Monolayer and Acoustic Phonon Dispersion at Hypersonic Frequencies Using Density Functional Theory and beyond with Random Phase Approximation and Bethe–Salpeter Equation. *ACS Omega*, **7**, 18, (2022), pp. 15338–15349.

[345] M. Barhoumi. First-principles calculations to investigate electronic band structure, optical and mechanical properties of new CaFCl monolayer. *Results in Physics*, **45**, January, (2023), p. 106251.

[346] J. Kaczkowski. Electronic structure and lattice dynamics of rhombohedral BiAlO 3 from first-principles. *Materials Chemistry and Physics*, **177**, (2016), pp. 405–412.

[347] G. Li, Q. An, S. I. Morozov, B. Duan, P. Zhai, Q. Zhang, W. A. Goddard III, and G. J. Snyder. Determining ideal strength and failure mechanism of thermoelectric $CuInTe_2$ through quantum mechanics. *Journal of Materials Chemistry A*, **6**, 25, (2018), pp. 11743–11750.

[348] T. Maxisch and G. Ceder. Elastic properties of olivine Li_xFePO_4 from first principles. *Physical Review B*, **73**, 17, (2006), p. 174112.

[349] S. A. Yamusa, A. Shaari, N. A. M. Alsaif, I. M. Alsalamah, I. Isah, and N. Rekik. Elucidating the Structural, Electronic, Elastic, and Optical Properties of Bulk and Monolayer MoS_2 Transition-Metal Dichalcogenides: A DFT Approach. *ACS Omega*, **7**, 49, (2022), pp. 45719–45731.

[350] H. Peelaers and C. G. Van de Walle. Elastic Constants and Pressure-Induced Effects in MoS 2. *The Journal of Physical Chemistry C*, **118**, 22, (2014), pp. 12073–12076.

[351] J.-n. Yuan, Y. Cheng, X.-q. Zhang, X.-r. Chen, and L.-c. Cai. First-Principles Study of Electronic and Elastic Properties of Hexagonal Layered Crystal MoS 2 Under Pressure. *Zeitschrift für Naturforschung A*, **70**, 7, (2015), pp. 529–537.

[352] L. Liu, J. Cao, W. Guo, and C. Wang. Spin and spin–orbit coupling effects in nickel-based superalloys: A first-principles study on Ni 3 Al doped with Ta/W/Re. *Chinese Physics B*, **31**, 1, (2022), p. 016105.

[353] J. Bera, A. Betal, and S. Sahu. Spin orbit coupling induced enhancement of thermoelectric performance of HfX2 (X = S, Se) and its Janus monolayer. *Journal of Alloys and Compounds*, **872**, (2021), p. 159704.

[354] M. Goyal and M. Sinha. Effect of spin-orbital coupling on the electronic, mechanical, thermoelectric, and vibrational properties of XPtBi (X = Sc and Y): A first-principles study. *Journal of Physics and Chemistry of Solids*, **153**, February, (2021), p. 110024.

[355] N. Bock, E. Holmström, T. B. Peery, R. Lizárraga, E. D. Chisolm, G. De Lorenzi-Venneri, and D. C. Wallace. Liquid-state properties from first-principles density functional theory calculations: Static properties. *Physical Review B*, **82**, 14, (2010), p. 144101.

[356] M. Ezzeldien, S. Al-Qaisi, Z. A. Alrowaili, M. Alzaid, E. Maskar, A. Es-Smairi, T. V. Vu, and D. P. Rai. Electronic and optical properties of bulk and surface of CsPbBr3 inorganic halide perovskite a first principles DFT 1/2 approach. *Scientific Reports*, **11**, 1, (2021), p. 20622.

[357] F. Mouhat and F.-X. Coudert. Necessary and sufficient elastic stability conditions in various crystal systems. *Physical Review B*, **90**, 22, (2014), p. 224104.

[358] G. Grimvall, B. Magyari-Köpe, V. Ozoliņš, and K. A. Persson. Lattice instabilities in metallic elements. *Reviews of Modern Physics*, **84**, 2, (2012), pp. 945–986.

[359] F. A. Rasmussen and K. S. Thygesen. Computational 2D Materials Database: Electronic Structure of Transition-Metal Dichalcogenides and Oxides. *The Journal of Physical Chemistry C*, **119**, 23, (2015), pp. 13169–13183.

[360] X.-F. Liu, Z.-J. Luo, X. Zhou, J.-M. Wei, Y. Wang, X. Guo, B. Lv, and Z. Ding. Structural, mechanical, and electronic properties of 25 kinds of III–V binary

monolayers: A computational study with first-principles calculation*. *Chinese Physics B*, **28**, 8, (2019), p. 086105.

[361] K. Choudhary, G. Cheon, E. Reed, and F. Tavazza. Elastic properties of bulk and low-dimensional materials using van der Waals density functional. *Physical Review B*, **98**, 1, (2018), p. 014107.

[362] H. Niu, X. Q. Chen, P. Liu, W. Xing, X. Cheng, D. Li, and Y. Li. Extra-electron induced covalent strengthening and generalization of intrinsic ductile-to-brittle criterion. *Scientific Reports*, **2**, (2012), pp. 1–6.

[363] P. Luo and Z. Huang. Fabrication of scandium-doped lithium manganese oxide as a high-rate capability cathode material for lithium energy storage. *Solid State Ionics*, **338**, May, (2019), pp. 20–24.

[364] S. Bhuvaneswari, U. Varadaraju, R. Gopalan, and R. Prakash. Structural stability and superior electrochemical performance of Sc-doped $LiMn_2O_4$ spinel as cathode for lithium ion batteries. *Electrochimica Acta*, **301**, (2019), pp. 342–351.

[365] K. Nakajima, F. L. Souza, A. L. Freitas, A. Thron, and R. H. Castro. Improving Thermodynamic Stability of nano-$LiMn_2O_4$for Li-Ion Battery Cathode. *Chemistry of Materials*, **33**, 11, (2021), pp. 3915–3925.

[366] C. J. M. Rooymans. The Crystal Structure of $LiScO_2$. *Zeitschrift fuer Anorganische und Allgemeine Chemie*, **2**, 1844, (1961), pp. 234–235.

[367] G. Zhao, I. Muhammad, K. Suzuki, M. Hirayama, and R. Kanno. Synthesis, crystal structure, and the ionic conductivity of new lithium ion conductors, M-doped $LiScO_2$ (M= Zr, Nb, Ta). *Materials Transactions*, **57**, 8, (2016), pp. 1370–1373.

[368] Z. Liu, H. Deng, S. Zhang, W. Hu, and F. Gao. A first-principles investigation of the ScO_2 monolayer as the cathode material for alkali metal-ion batteries. *Journal of Materials Chemistry A*, **6**, 7, (2018), pp. 3171–3180.

[369] Z. Liu, H. Deng, S. Zhang, W. Hu, and F. Gao. Theoretical prediction of $LiScO_2$ nanosheets as a cathode material for Li–O_2 batteries. *Physical Chemistry Chemical Physics*, **20**, 34, (2018), pp. 22351–22358.

[370] H. Zhang, X. Lin, and Z.-K. Tang. Stable ScS_2 nanostructures with tunable electronic and magnetic properties. *Solid State Communications*, **220**, (2015), pp. 12–16.

[371] J. A. Reyes-Retana and F. Cervantes-Sodi. Spin-orbital effects in metal-dichalcogenide semiconducting monolayers. *Scientific Reports*, **6**, 1, (2016), p. 24093.

[372] D. Chakraborty, M. Pandey, and P. Johari. ScS_2 Monolayer as a Potential Cathode Material for Alkali-ion Batteries and Beyond, (2022), pp. 1–25.

[373] A. Bhaskar, D. Mikhailova, N. Kiziltas-Yavuz, K. Nikolowski, S. Oswald, N. N. Bramnik, and H. Ehrenberg. 3d-Transition metal doped spinels as high-voltage cathode materials for rechargeable lithium-ion batteries. *Progress in Solid State Chemistry*, **42**, 4, (2014), pp. 128–148.

[374] H. H. Sun, U. H. Kim, J. H. Park, S. W. Park, D. H. Seo, A. Heller, C. B. Mullins, C. S. Yoon, and Y. K. Sun. Transition metal-doped Ni-rich layered cathode materials for durable Li-ion batteries. *Nature Communications*, **12**, 1, (2021), pp. 1–11.

[375] P. Wen, H. Wang, X. Wang, H. Wang, Y. Bai, and Z. Yang. Exploring the physicochemical role of Pd dopant in promoting Li-ion diffusion dynamics and storage performance of NbS_2 at the atomic scale. *Physical Chemistry Chemical Physics*, **24**, 24, (2022), pp. 14877–14885.

[376] C. J. Pickard and R. J. Needs. Ab initio random structure searching. *Journal of Physics: Condensed Matter*, **23**, 5, (2011), p. 053201.

[377] Y. Wang, J. Lv, L. Zhu, and Y. Ma. CALYPSO: A method for crystal structure prediction. *Computer Physics Communications*, **183**, 10, (2012), pp. 2063–2070.

[378] Q. Tong, J. Lv, P. Gao, and Y. Wang. The CALYPSO methodology for structure prediction*. *Chinese Physics B*, **28**, 10, (2019), p. 106105.

[379] T. Yamashita, S. Kanehira, N. Sato, H. Kino, K. Terayama, H. Sawahata, T. Sato, F. Utsuno, K. Tsuda, T. Miyake, and T. Oguchi. CrySPY: a crystal

structure prediction tool accelerated by machine learning. *Science and Technology of Advanced Materials: Methods*, **1**, 1, (2021), pp. 87–97.

[380] W. Tipton and R. G. Hennig. GASP : The Genetic Algorithm for Structure and Phase Prediction.

[381] Z. Lu, S. Carr, D. T. Larson, and E. Kaxiras. Lithium intercalation in MoS_2 bilayers and implications for moiré flat bands. *Physical Review B*, **102**, 12, (2020), p. 125424.

[382] B. Amin, N. Singh, and U. Schwingenschlögl. Heterostructures of transition metal dichalcogenides. *Physical Review B - Condensed Matter and Materials Physics*, **92**, 7, (2015), pp. 1–6.

[383] F. Zhou, C. A. Marianetti, M. Cococcioni, D. Morgan, and G. Ceder. Phase separation in Li_xFePO_4 induced by correlation effects. *Physical Review B - Condensed Matter and Materials Physics*, **69**, 20, (2004), pp. 1–4.

[384] A. Yamada, S. C. Chung, and K. Hinokuma. Optimized $LiFePO_4$ for Lithium Battery Cathodes. *Journal of The Electrochemical Society*, **148**, 3, (2001), p. A224.

[385] X. Li and Y. Xu. Spinel $LiMn_2O_4$ active material with high capacity retention. *Applied Surface Science*, **253**, 21, (2007), pp. 8592–8596.

[386] J. Barker. In-situ measurement of the thickness changes associated with cycling of prismatic lithium ion batteries based on $LiMn_2O_4$ and $LiCoO_2$. *Electrochimica Acta*, **45**, 1-2, (1999), pp. 235–242.

[387] N. K. Chaudhari, H. Jin, B. Kim, D. San Baek, S. H. Joo, and K. Lee. MXene: an emerging two-dimensional material for future energy conversion and storage applications. *Journal of Materials Chemistry A*, **5**, 47, (2017), pp. 24564–24579.

[388] M. Greaves, S. Barg, and M. A. Bissett. MXene-Based Anodes for Metal-Ion Batteries. *Batteries & Supercaps*, **3**, 3, (2020), pp. 214–235.

[389] F. Ming, H. Liang, G. Huang, Z. Bayhan, and H. N. Alshareef. MXenes for Rechargeable Batteries Beyond the Lithium-Ion. *Advanced Materials*, **33**, 1, (2021), p. 2004039.

[390] A. Sukma Aji, M. Izumoto, K. Suenaga, K. Yamamoto, H. Nakashima, and H. Ago. Two-step synthesis and characterization of vertically stacked SnS–WS_2 and SnS–MoS_2 p–n heterojunctions. *Physical Chemistry Chemical Physics*, **20**, 2, (2018), pp. 889–897.

[391] J. N. Coleman, M. Lotya, A. O'Neill, S. D. Bergin, P. J. King, U. Khan, K. Young, A. Gaucher, S. De, R. J. Smith, I. V. Shvets, S. K. Arora, G. Stanton, H.-Y. Kim, K. Lee, G. T. Kim, G. S. Duesberg, T. Hallam, J. J. Boland, J. J. Wang, J. F. Donegan, J. C. Grunlan, G. Moriarty, A. Shmeliov, R. J. Nicholls, J. M. Perkins, E. M. Grieveson, K. Theuwissen, D. W. McComb, P. D. Nellist, and V. Nicolosi. Two-Dimensional Nanosheets Produced by Liquid Exfoliation of Layered Materials. *Science*, **331**, 6017, (2011), pp. 568–571.

[392] J. Li, X. Yang, Y. Liu, B. Huang, R. Wu, Z. Zhang, B. Zhao, H. Ma, W. Dang, Z. Wei, K. Wang, Z. Lin, X. Yan, M. Sun, B. Li, X. Pan, J. Luo, G. Zhang, Y. Liu, Y. Huang, X. Duan, and X. Duan. General synthesis of two-dimensional van der Waals heterostructure arrays. *Nature*, **579**, 7799, (2020), pp. 368–374.

[393] J. Singh. Physics of Semiconductors and Their Heterostructures, (McGraw-Hill, Inc1993). ISBN 0-07-057607-6.

[394] T. Chen, D. Ding, J. Shi, G. Wang, L. Kou, X. Zheng, X. Ren, X. Liu, C. Jin, J. Zhong, and G. Hao. Lateral and Vertical $MoSe_2$-MoS_2 Heterostructures via Epitaxial Growth: Triggered by High-Temperature Annealing and Precursor Concentration. *The Journal of Physical Chemistry Letters*, **10**, 17, (2019), pp. 5027–5035.

[395] R. L. Anderson. Germanium-Gallium Arsenide Heterojunctions [Letter to the Editor]. *IBM Journal of Research and Development*, **4**, 3, (1960), pp. 283–287.

[396] M.-H. Chiu, W.-H. Tseng, H.-L. Tang, Y.-H. Chang, C.-H. Chen, W.-T. Hsu, W.-H. Chang, C.-I. Wu, and L.-J. Li. Band Alignment of 2D Transition Metal Dichalcogenide Heterojunctions. *Advanced Functional Materials*, **27**, 19, (2017), p. 1603756.

[397] D. S. Koda, F. Bechstedt, M. Marques, and L. K. Teles. Trends on band alignments: Validity of Anderson's rule in SnS_2- and SnSe-based van der Waals heterostructures. *Physical Review B*, **97**, 16, (2018), p. 165402.

[398] L. Kou, T. Frauenheim, and C. Chen. Nanoscale Multilayer Transition-Metal Dichalcogenide Heterostructures: Band Gap Modulation by Interfacial Strain and Spontaneous Polarization. *The Journal of Physical Chemistry Letters*, **4**, 10, (2013), pp. 1730–1736.

[399] K. Tang and W. Qi. Moiré-Pattern-Tuned Electronic Structures of van der Waals Heterostructures. *Advanced Functional Materials*, **30**, 32.

[400] R. Besse, J. F. R. V. Silveira, Z. Jiang, D. West, S. Zhang, and J. L. F. Da Silva. Beyond the Anderson rule: importance of interfacial dipole and hybridization in van der Waals heterostructures. *2D Materials*, **8**, 4, (2021), p. 041002.

[401] J. Sun, H.-W. Lee, M. Pasta, H. Yuan, G. Zheng, Y. Sun, Y. Li, and Y. Cui. A phosphorene–graphene hybrid material as a high-capacity anode for sodium-ion batteries. *Nature Nanotechnology*, **10**, 11, (2015), pp. 980–985.

[402] L. Shi, T. S. Zhao, A. Xu, and J. B. Xu. Ab initio prediction of a silicene and graphene heterostructure as an anode material for Li- and Na-ion batteries. *Journal of Materials Chemistry A*, **4**, 42, (2016), pp. 16377–16382.

[403] C. Chowdhury, S. Karmakar, and A. Datta. Capping Black Phosphorene by h-BN Enhances Performances in Anodes for Li and Na Ion Batteries. *ACS Energy Letters*, **1**, 1, (2016), pp. 253–259.

[404] D. T. Larson, I. Fampiou, G. Kim, and E. Kaxiras. Lithium Intercalation in Graphene–MoS_2 Heterostructures. *The Journal of Physical Chemistry C*, **122**, 43, (2018), pp. 24535–24541.

[405] Y. T. Du, X. Kan, F. Yang, L. Y. Gan, and U. Schwingenschlögl. MXene/Graphene Heterostructures as High-Performance Electrodes for Li-Ion Batteries. *ACS Applied Materials and Interfaces*, **10**, 38, (2018), pp. 32867–32873.

[406] P. Das, Q. Fu, X. Bao, and Z.-S. Wu. Recent advances in the preparation, characterization, and applications of two-dimensional heterostructures for energy storage and conversion. *Journal of Materials Chemistry A*, **6**, 44, (2018), pp. 21747–21784.

[407] H. Jiang, D. Ren, H. Wang, Y. Hu, S. Guo, H. Yuan, P. Hu, L. Zhang, and C. Li. 2D Monolayer MoS_2 -Carbon Interoverlapped Superstructure: Engineering Ideal Atomic Interface for Lithium Ion Storage. *Advanced Materials*, **27**, 24, (2015), pp. 3687–3695.

[408] K. Chang, Z. Wang, G. Huang, H. Li, W. Chen, and J. Y. Lee. Few-layer SnS_2/graphene hybrid with exceptional electrochemical performance as lithium-ion battery anode. *Journal of Power Sources*, **201**, (2012), pp. 259–266.

[409] D. Wang, L. M. Liu, S. J. Zhao, Z. Y. Hu, and H. Liu. Potential Application of Metal Dichalcogenides Double-Layered Heterostructures as Anode Materials for Li-Ion Batteries. *Journal of Physical Chemistry C*, **120**, 9, (2016), pp. 4779–4788.

[410] S. Brem, C. Linderälv, P. Erhart, and E. Malic. Tunable Phases of Moiré Excitons in van der Waals Heterostructures. *Nano Letters*, **20**, 12, (2020), pp. 8534–8540.

[411] L. Zhang, Z. Zhang, F. Wu, D. Wang, R. Gogna, S. Hou, K. Watanabe, T. Taniguchi, K. Kulkarni, T. Kuo, S. R. Forrest, and H. Deng. Twist-angle dependence of moiré excitons in WS_2/$MoSe_2$ heterobilayers. *Nature Communications*, **11**, 1, (2020), pp. 1–8.

[412] S. Luo, G. Hao, Y. Fan, L. Kou, C. He, X. Qi, C. Tang, J. Li, K. Huang, and J. Zhong. Formation of ripples in atomically thin MoS_2 and local strain engineering of electrostatic properties. *Nanotechnology*, **26**, 10.

[413] A. Chaves, J. G. Azadani, H. Alsalman, D. R. da Costa, R. Frisenda, A. J. Chaves, S. H. Song, Y. D. Kim, D. He, J. Zhou, A. Castellanos-Gomez, F. M. Peeters, Z. Liu, C. L. Hinkle, S. H. Oh, P. D. Ye, S. J. Koester, Y. H. Lee, P. Avouris, X. Wang, and T. Low. Bandgap engineering of two-dimensional semiconductor materials. *npj 2D Materials and Applications*, **4**, 1.

[414] D. Davelou, G. Kopidakis, E. Kaxiras, and I. N. Remediakis. Nanoribbon edges of transition-metal dichalcogenides: Stability and electronic properties. *Physical Review B*, **96**, 16, (2017), pp. 1–6.

[415] D. Li and F. Ding. Environment-dependent edge reconstruction of transition metal dichalcogenides: a global search. *Materials Today Advances*, **8**, (2020), pp. 1–8.

[416] H. Ma, W. Zhao, S. Yuan, H. Ren, H. Zhu, H. Ma, F. Ding, and W. Guo. Reconstructed edges of T phase transition metal dichalcogenides. *Materials Today Physics*, **19**, (2021), p. 100411.

[417] M. Born and J. R. Oppenheimer. On the Quantum Theory of Molecules (Translated by S. M. Blinder 1998). **389**, 20, (1927), pp. 457–484.

[418] M. Born and J. R. Oppenheimer. Zur Quantentheorie der Molekeln. **389**, 20, (1927), pp. 457–484.

[419] M. Born and K. Huang. Dynamical Theory of Crystal Lattices, (Oxford University Press1954).

[420] S. Baroni, S. de Gironcoli, A. Dal Corso, and P. Giannozzi. Phonons and related crystal properties from density-functional perturbation theory. *Reviews of Modern Physics*, **73**, 2, (2001), pp. 515–562.

[421] K. Lejaeghere, V. Van Speybroeck, G. Van Oost, and S. Cottenier. Error estimates for solid-state density-functional theory predictions: An overview by means of the ground-state elemental crystals. *Critical Reviews in Solid State and Materials Sciences*, **39**, 1, (2014), pp. 1–24.

[422] K. R. Kganyago and P. E. Ngoepe. Structural and electronic properties of lithium intercalated graphite LiC_6. *Physical Review B*, **68**, 20, (2003), p. 205111.

[423] K. H. Michel and B. Verberck. Theory of the elastic constants of graphite and graphene. *physica status solidi (b)*, **245**, 10, (2008), pp. 2177–2180.

[424] A. P. P. Nicholson and D. J. Bacon. A new force-constant model for graphite. *Journal of Physics C: Solid State Physics*, **10**, 13, (1977), pp. 2295–2306.

[425] L. Lang, S. Doyen-Lang, A. Charlier, and M. F. Charlier. Dynamical study of graphite and graphite intercalation compounds. *Physical Review B*, **49**, 8, (1994), pp. 5672–5681.

[426] R. Al-Jishi and G. Dresselhaus. Lattice-dynamical model for graphite. *Physical Review B*, **26**, 8, (1982), pp. 4514–4522.

[427] O. L. Blakslee, D. G. Proctor, E. J. Seldin, G. B. Spence, and T. Weng. Elastic Constants of Compression-Annealed Pyrolytic Graphite. *Journal of Applied Physics*, **41**, 8, (1970), pp. 3373–3382.

[428] H. Zabel, W. A. Kamitakahara, and R. M. Nicklow. Neutron scattering investigation of layer-bending modes in alkali-metal—graphite intercalation compounds. *Physical Review B*, **26**, 10, (1982), pp. 5919–5926.

[429] H. Zabel and A. Magerl. Inelastic neutron measurement of phonons in graphite-alkali intercalation compounds. *Physical Review B*, **25**, 4, (1982), pp. 2463–2471.

[430] M. Grimsditch. Shear elastic modulus of graphite. *Journal of Physics C: Solid State Physics*, **16**, 5, (1983), pp. L143–L144.

[431] T. M. Project. Materials Data on $LiCoO_2$ (SG:166) by Materials Project.

[432] S. Yamakawa, N. Nagasako, H. Yamasaki, T. Koyama, and R. Asahi. Phase-field modeling of stress generation in polycrystalline $LiCoO_2$. *Solid State Ionics*, **319**, February, (2018), pp. 209–217.

[433] F. X. Hart and J. B. Bates. Lattice model calculation of the strain energy density and other properties of crystalline $LiCoO_2$. *Journal of Applied Physics*, **83**, 12, (1998), pp. 7560–7566.

[434] X. Wang, I. Loa, K. Kunc, K. Syassen, and M. Amboage. Effect of pressure on the structural properties and Raman modes of $LiCoO_2$. *Physical Review B*, **72**, 22, (2005), p. 224102.

[435] E. J. Cheng, N. J. Taylor, J. Wolfenstine, and J. Sakamoto. Elastic properties of lithium cobalt oxide ($LiCoO_2$). *Journal of Asian Ceramic Societies*, **5**, 2, (2017), pp. 113–117.

[436] M. Qu, W. H. Woodford, J. M. Maloney, W. C. Carter, Y.-M. Chiang, and K. J. Van Vliet. Nanomechanical Quantification of Elastic, Plastic, and Fracture Properties of $LiCoO_2$. *Advanced Energy Materials*, **2**, 8, (2012), pp. 940–944.